Drug discovery at class A and class B GPCRs

Anna Hilser

Department of Pharmacology

University of Cambridge

This thesis is submitted for the degree of Doctor of Philosophy

Queens' college September 2022

Preface

I hereby declare that this thesis is the results of my own work and includes nothing which is the outcome of work done in collaboration except as declared in the preface and specified in the text. It is not substantially the same as any work that has already been submitted before for any degree or other qualification at the University of Cambridge, or any other university or similar institution except as declared in the preface and/or specified in the text. This thesis does not exceed the prescribed word limit of 60,000 excluding appendices, bibliography, footnotes, tables, and equations.

Drug discovery at class A and class B GPCRs, Anna Hilser

Abstract

G protein-coupled receptors (GPCRs) are a big family of membrane receptors encoded by more than 800 genes in humans. The vast number and diversity of GPCRs enables them to interact with an equally great number of ligands enabling them to regulate many physiological functions such as senses, metabolism, neurotransmission or cell growth. Given GPCRs' involvement in the regulation of many physiological functions, it then comes as no surprise that their malfunction often leads to pathological states such as cancer, diabetes mellitus, inflammation or central nervous system disorders. This makes GPCRs the focus of drug discovery with roughly 34% of all FDA (Food and drug administration) approved drugs targeting them. This thesis presents the drug discovery at adenosine receptors, class A GPCRs, and gastric inhibitory polypeptide receptor (GIPR), a class B GPCR.

Given the possible therapeutic effects of modulating GIPR signalling pathway in diabetes and obesity, the primary objective of this thesis was to discover and improve GIPR allosteric modulators using both in silico and in vitro techniques. This resulted in successful identification of potent and selective GIPR negative allosteric modulators like compound C25, while also investigating the bias of the compounds at different pathways and their selectivity. Combinational approach of in silico blind docking and in vitro mutagenesis was then used to successfully identify the GIPR allosteric binding site of the compounds located around at the top of transmembrane domain 2/3 and extracellular loop 1.

The second part of this thesis is then focused on drug discovery at adenosine receptors with the aim of developing more selective and more potent compounds. Firstly, compounds were screened for more potent adenosine 1 agonists that would retain or improve upon BnOCPA compound, which is a powerful analgesic lacking the common side effects. This was successfully achieved and some really potent and selective adenosine 1 agonists like compound 27 were identified. Secondly, potent adenosine 1 and adenosine 3 antagonists were discovered, and their potency, selectivity and binding were measured. This led to the identification of several potent dual adenosine 1 and 3 antagonists like compounds A17 and A47, which hold potential in the treatment of asthma, lowering intraocular pressure or in several central nervous system disorders.

Ultimately, these findings show how a combinational approach of in silico and in vitro pharmacology can be successfully used to identify new small molecule GPCR allosteric modulators and identify new potent adenosine receptor agonists and antagonists with potential therapeutic benefits.

Acknowledgments

The work in this thesis would not have been possible without the help of many people. First and foremost, I would like to express the sincerest gratitude to my supervisor, Prof Graham Ladds, for his guidance through the entire PhD process. This thesis would have not been possible without his constant encouragement, guidance, and inspiration throughout my study enabling me to become a better scientist. Equally sincerely I would also like to thank my second supervisor Dr Taufiq Rahman for his constant encouragement and especially for sharing some of his vast *in silico* knowledge with me. Additionally, Dr Martin Lochner (University of Bern) and Antonios Kolocouris (University of Athens) have been instrumental in collaborations on adenosine receptor projects.

At the University of Cambridge, I express my gratitude to Dr Kerry Barkan, Dr Dewi Safitri, Dr Matt Harris, Dr Sabrina Carvalho, Abigail Pearce and the rest of the Ladds' lab for teaching me various techniques, help with experiments and for making the lab a fun place to work. I would also like to thank Dr Paul Miller and Melissa Irvine from University of Cambridge for teaching me how to purify proteins for cryo-EM and generally about protein biology.

I would also like to thank my husband Pavel Hilser for his continued support over the last three years of my PhD and my family for their kind encouragement. Finally, I would like to extend my appreciation to the Cambridge Trust, who have funded my research and allowed me to undertake this PhD.

Declaration of authorship

This thesis is the result of my own work and includes nothing which is the outcome of work done in collaboration except as declared in the Preface and specified in the text.

Research from collaborators was included to deliver a complete narrative for each chapter, and the contributions are as listed below:

Abigail Pearce (University of Cambridge) measured C58 at 100 µM in Figure 3.22 and at 10 µM in Figure 3.23.

Dr Taufiq Rahman and his lab made GIPR homology models (Table 4.2) and carried out in silico blind docking using ICM-Pro (Figure 4.3), focused docking using GlideXP and in silico screen against GIPR allosteric site to identify compounds T1-T27 as potential allosteric modulators.

Dr Sabrina Carvalho (University of Cambridge) measured the cAMP accumulation data for adenosine at A_1R, $A_{2A}R$ and $A_{2B}R$ (part of Figure 5.4, 5.5 and 5.6 and Table 5.3 and 5.4).

Dr Kerry Barkan (University of Cambridge) measured the CA200645 binding to Nluc-A_1R S267$^{7.32}$ and Y271$^{7.36}$ mutants using NanoBRET binding assay (part of Figure 6.12 and Table 6.12).

Lakshiv Dhingra (University of Cambridge) measured the cAMP accumulation and NanoBRET binding assays for compounds L4, L5, L9 and L21 at human WT A_1R and A_3R (part of Figures 6.2, 6.5, 6.8 and 6.9 and Tables 6.2, 6.4, 6.7 and 6.8) and submitted the data for his BA degree.

Some of the figures/data used are adapted from other work as listed below:

Figure 1.5. is adapted from Rang (2019)

Figure 1.6 is adapted from Wootten et al. (2016)

Figures 6.2 and 6.4 are adapted from BA studies at University of Cambridge of L. Dhiangra and A. Suchankova, while the activity of compounds A17, A26 and A47 at A_1R and A_3R was measured in cAMP accumulation assay and was submitted for A. Suchankova BA degree (part of Figures 6.4 and 6.6 and Tables 6.3 and 6.5).

Part of the work has been published (or is in pre-print) as follows:

Preti B.*, **Suchankova A.***, Deganutti G.*, Leuenberger M., Barkan K., Manulak I., Huang X., Carvalho S., Ladds G, Lochner M., 2022. Discovery and Structure-Activity Relationship Studies of Novel Adenosine A_1 Receptor-Selective Agonists. Submitted to J. Med. Chem (* all three authors contributed equally)..

Stampelou M.*, **Suchankova A.***, Tzortzini E., Dhingra L., Barkan K., Lougiakis N., Marakos P., Pouli N., Ladds G., Kolocouris A., 2022. Novel 7-Anilino-Pyrazolo[3,4-c]pyridine as High Affinity Dual A_1, A_3 Adenosine Receptor Antagonists and SARs Study Using Alchemical Perturbation Binding Free-Energy Calculations. Accepted to J. Med. Chem (* both authors contributed equally)..

Suchankova, A., Harris, M., Ladds, G., 2021. Chapter 1 - Measuring the rapid kinetics of receptor-ligand interactions in live cells using NanoBRET, in: Shukla, A.K. (Ed.), Methods in Cell Biology, Biomolecular Interactions Part A. Academic Press, pp. 1–14. https://doi.org/10.1016/bs.mcb.2021.06.013

Suchankova, A.*, Stampelou, M.*, Koutsouki, K., Pousias, A., Dhingra, L., Barkan, K., Pouli, N., Marakos, P., Tenta, R., Kolocouris, A., Lougiakis, N., Ladds, G., 2022. Discovery of a High Affinity Adenosine A1/A3 Receptor Antagonist with a Novel 7-Amino-pyrazolo[3,4-d]pyridazine Scaffold. ACS Med. Chem. Lett. 13, 923–934. https://doi.org/10.1021/acsmedchemlett.2c00052 (* both authors contributed equally).

Wall, M.J., Hill, E., Huckstepp, R., Barkan, K., Deganutti, G., Leuenberger, M., Preti, B., Winfield, I., Carvalho, S., **Suchankova, A.**, Wei, H., Safitri, D., Huang, X., Imlach, W., La Mache, C., Dean, E., Hume, C., Hayward, S., Oliver, J., Zhao, F.-Y., Spanswick, D., Reynolds, C.A., Lochner, M., Ladds, G., Frenguelli, B.G., 2022. Selective activation of Gαob by an adenosine A1 receptor agonist elicits analgesia without cardiorespiratory depression. Nat. Commun. 13, 4150. https://doi.org/10.1038/s41467-022-31652-2

This thesis adheres to the word limit of 60,000 as determined by the Degree Committee of the Faculty Biology.

Word count: 56,148

Table of content

Preface iii

Abstract iv

Acknowledgments v

Declaration of authorship vi

Table of content ix

List of figures xiv

List of tables xviii

List of abbreviations xxv

Chapter 1. Introduction 1

1.1 Cellular signalling 1

1.2 The G protein-coupled receptors superfamily 1

1.2.1 Classification of GPCRs in sub-families 2

1.3 GPCR signal transduction 4

1.3.1 Ligand binding and GPCR activation 4

1.3.2 Activation and signalling of heterotrimeric G proteins by GPCRs 5

1.3.2.1 Gα subunit signalling following GPCR activation 7

1.3.2.1.1 GPCR modulation of cAMP signalling 8

1.3.2.1.2 GPCR-mediated calcium ion signalling 9

1.3.2.1.3 Rho signalling initiated from GPCR activation 10

1.3.2.2 GPCR-mediated Gβγ signalling 10

1.3.3 GPCR signalling regulation 10

1.3.3.1 The role of GPCR kinases 11

1.3.3.2 Arrestins uncouples G protein signalling from GPCRs 11

1.4 GPCR pharmacology 12

1.4.1 Different types of GPCR ligands 14

1.4.2 The operational model of pharmacological agonism 17

1.4.3 The concept of biased agonism and how this relates to GPCR signal transduction 17

1.4.4 The role of allosteric modulation in GPCR pharmacology 21

1.4.4.1 Therapeutic potential of allosteric modulators of GPCRs 23

1.5 Overview of GPCRs explored in this thesis 25

1.5.1 The adenosine receptor subfamily 25

1.5.1.1 Adenosine 1 receptor 27

1.5.1.2 Adenosine 2A and 2B receptor 28

1.5.1.3 Adenosine 3 receptor 29

1.5.2 Glucose-dependent insulinotropic polypeptide receptor 30
1.5.2.1 Type 2 diabetes mellitus and obesity 30
1.5.2.2 Current T2DM treatments 31
1.5.2.3 Incretin effect 31
1.5.2.4 Therapeutic potential of GIPR agonists in T2DM 34
1.5.2.5 Therapeutic potential of GIPR antagonists in obesity 35
1.5.2.6 Benefits and challenges of GIPR allosteric modulators 36
1.6 The process of drug discovery 38
1.6.1 Discovery and development of ARs agonists and antagonists 38
1.6.2 Discovery and development of GIPR allosteric modulators 40
1.6.3 *In silico* methods for allosteric site identification 41
1.6.3.1 Knowledge-based prediction approaches 42
1.6.3.2 Sequence-based prediction approaches 42
1.6.3.3 Geometry- and/or energy-based prediction methods 44
1.6.3.4 Dynamics-based prediction approaches 45
1.7 Aims 46
Chapter 2. Materials and methods 47
2.1 Materials 47
2.1.1 General laboratory reagents 47
2.1.2 Ligands 47
2.1.3 Compounds 47
2.1.4 Growth media 57
2.1.5 Laboratory buffer and media 57
2.1.6 DNA expression constructs 58
2.2 Methods 60
2.2.1 Mammalian cell culture 60
2.2.1.1 Cell culture 60
2.2.1.2 Generation of stable cell lines 61
2.2.1.3 Long-term cryo-storage and recovery 61
2.2.2 Molecular biology techniques 62
2.2.2.1 Escherichia coli transformation 62
2.2.2.2 Plasmid DNA purification 62
2.2.2.3 Site-directed mutagenesis 63
2.2.2.4 DNA sequencing 65
2.2.2.5 Transfections 65
2.2.3 Pharmacological investigation and signalling assays 66

2.2.3.1 cAMP accumulation assay 66
2.2.3.2 Schild analysis 67
2.2.3.3 Intracellular calcium mobilisation assay 68
2.2.3.4 NanoBRET binding assay 68
2.2.3.5 β-arrestin 1/2 recruitment assay 69
2.2.3.6 Glucose-stimulated insulin secretion 70
2.2.4 *In silico* modelling techniques 72
2.2.4.1 Docking 72
2.2.4.2 *In silico* techniques for allosteric site prediction 73
2.3 Data analysis 73
Chapter 3. Pharmacological validation and characterisation of GIPR allosteric modulators 76
3.1 Introduction 76
3.2 *In silico* screening of potential GIPR allosteric modulators 78
3.3 Compounds C22, C58, C91 and C95 are new GIPR NAMs selective for $(Ca^{2+})_i$ mobilization 80
3.4 C25 is selective for GIPR over GLP-1R and GCGR 91
3.5 C25 binds at top of TMD2/3 and ECL1 of the GIPR 98
3.6 C25 selectively inhibits GIP-potentiated insulin secretion 116
3.7 Discovery of new GIPR allosteric modulators for both $(Ca^{2+})_i$ and cAMP pathways 119
3.8 Compounds T2 and T5 are newly discovered GIPR selective compounds 136
3.9 The T compounds were confirmed to bind to site 10 141
3.10 Discussion 155
3.10.1 Drug discovery of 12 new GIPR allosteric modulators 155
3.10.2 GIPR allosteric modulators are biased towards cAMP or calcium signalling 156
3.10.3 T2, T5, T21 and C25 are selective for GIPR over GLP-1R and GCGR 158
3.10.4 GIPR allosteric binding site was identified at the top of TMD2/3 and ECL1 159
3.10.5 Inhibition of incretin-potentiated Insulin secretion 162
3.11 Conclusion 162
Chapter 4. *In silico* investigation for allosteric site identification at the GIPR 164
4.1 Introduction 164
4.2 *In silico* blind docking to GIPR homology models 166
4.2.1 Docking to GIPR homology model with bound GIP 166
4.2.3 Docking to GIPR homology models lacking the N-terminus and GIP 170
4.2.3 Detailed investigation of the compounds binding at Site 6 and Site 10 174
4.2.4 Docking of compounds to the GIPR allosteric site at ECL1 179
4.3 *In silico* methods for allosteric site identification applied to GIPR 183
4.3.1 Knowledge-based techniques 183

4.3.2 Sequence-based techniques 185
4.3.3 Geometry-based techniques 188
4.3.4 Energy-based techniques 189
4.3.5 Dynamics-based techniques 191
4.3.6 Overall summary and comparison of the *in silico* methods for allosteric site identification 193
4.4 Discussion 194
4.4.1 GIPR allosteric binding site at the top of TMD2/3 and ECL1 195
4.4.2 Exploring compound binding at Site 10 and their selectivity 196
4.4.3 Advantages and disadvantages of various *in silico* techniques 197
4.5 Conclusion 198
Chapter 5. Pharmacological characterisation of novel adenosine A_1 receptor-selective agonists ..199
5.1 Introduction 199
5.2 The effect of A_1R mutations on agonist efficacy 201
5.3 Analysing BnOCPA derivatives as potent selective agonists of the A_1R 206
5.3.1. Improved potency of 26, 27, 45, 49 and 51-54 at A_1R 206
5.3.2 Compounds 45 and 51 are 10,000-fold more selective for A_1R over other AR subtypes .. 216
5.3.3 Differences between adenosine and NECA derivates 221
5.4 Determining compound binding at ARs 222
5.4.1 Compounds 27, 28, 49, 51 and 53 have high affinity across both rat and human A_1R 222
5.4.2 Phenoxycyclopentyl derivatives have higher residence times at both human and rat A_1R 228
5.5 Data from functional and binding experiments show positive correlation 233
5.6 Discussion 234
5.6.1 Improving upon BnOCPA potency 234
5.6.2 Reaching more than 10,000-fold selectivity for A_1R over other subtypes 235
5.6.3 Assessing compound binding across human and rat A_1R 235
5.6.4 MD simulations providing insight into compound binding 236
5.7 Conclusion 238
Chapter 6. Pharmacological characterisation of novel adenosine A_1 and A_3 receptor antagonists.240
6.1 Introduction 240
6.2 Novel compound scaffold of potential A_1R and A_3R antagonists 244
6.3 Potent A_3R antagonists established using cAMP accumulation assay 246
6.4 A17 and A47 are potent dual antagonists of A_1 and A_3 receptors 253
6.5 Lead compounds A17 and A47 have low nanomolar affinities at A_1R/A_3R 262
6.6 Lead compounds have residence time between 30 and 60 mins 268

6.7 Probing A17, A26 and A47 binding at the A_1R 271
6.8 Discussion 278
6.8.1 Discovery of potent dual A_1 and A_3 receptor antagonists 278
6.8.2 Kinetic profiling of antagonists at the A_1 and A_3 receptors 278
6.8.3 MD simulations and mutagenesis give insight into compound binding 279
6.9 Conclusion 280
Chapter 7. General discussion and future directions 282
7.1 Discussion 282
7.1.1 Using combinational *in silico* and *in vitro* approach to drug discovery 282
7.1.2 Identifying the GIPR allosteric binding site at the top of TMD2/3 and ECL1 283
7.1.3 Relative advantages of orthosteric versus allosteric ligands 285
7.1.4 Common aim of drug discovery to increase compound potency 286
7.1.5 High affinity often correlates with high efficacy 287
7.1.6 Evaluating receptor-ligand binding kinetics 288
7.1.7 Understanding compounds interactions with the receptor binding site can inform future drug design 288
7.1.8 Exploring species, receptor and pathway selectivity of the compounds 289
7.2 Future directions 292
Chapter 8. Bibliography 293
Appendix 1. Suchankova, et al. 2021 334
Appendix 2. Wall, et al. 2022 349
Appendix 3. Preti, et al. 2022 372
Appendix 4. Stampelou, et al. 2022 420
Appendix 5. Suchankova, et al. 2022 444

List of figures

Figure 1.1. Schematic mechanism of heterotrimeric G protein activation cycle. 7

Figure 1.2. Representative dose-response curve. 13

Figure 1.3. Representative dose-response curves for different types of GPCR ligands. 14

Figure 1.4. Representative dose-response curves of reversible and irreversible competitive antagonists. 15

Figure 1.5. Two-state model of receptor activation. 16

Figure 1.6. Biased signalling at GLP-1R. 18

Figure 1.7. Representative dose-response curves for different types of allosteric modulators. 22

Figure 1.8. An overview adenosine receptor-mediated intracellular signalling. 26

Figure 1.9. Schematic mechanism of incretin hormone secretion from endocrine cells. 32

Figure 1.10. A schematic representation of incretin hormone-stimulated insulin secretion from pancreatic β cells. 33

Figure 1.11. Kinetic parameters of selected A_1R and A_3R ligands. 40

Figure 1.12. C3 and C25 are NAMs for $(Ca^{2+})_i$ mobilisation at GIPR 41

Figure 2.1. Principle of Europium Lance© cAMP detection kit. 67

Figure 2.2. Schematic diagram of the NanoBRET binding assay. 69

Figure 2.3. Schematic diagram of the β-arrestin 1/2 recruitment assay. 70

Figure 2.4. Principle of Insulin High Range Assay kit. 71

Figure 3.1. Compounds C3 and C25 are NAMs for $(Ca^{2+})_i$ mobilization. 78

Figure 3.2. Putative allosteric modulators at GIPR have no specific effect on $(Ca^{2+})_i$ mobilization alone. 80

Figure 3.3. Compounds C22, C58, C91 and C95 are newly identified NAMs for $(Ca^{2+})_i$ mobilization at GIPR. 81

Figure 3.4. Tested compounds do not effect ionomycin-stimulated $(Ca^{2+})_i$ mobilization at GIPR. 83

Figure 3.5. The effect of C95 on $(Ca^{2+})_i$ mobilization is concentration dependent and saturable. 85

Figure 3.6. Potential small allosteric modulators of GIPR are not agonists for cAMP accumulation. 87

Figure 3.7. Putative allosteric modulators of GIPR do not modulate cAMP pathway. 88

Figure 3.8. Selection of GIPR-Nluc for β-arrestin recruitment assay. 89

Figure 3.9. Putative allosteric modulators of GIPR do not modulate β-arrestin 1/2 recruitment. 90

Figure 3.10. Potential small allosteric modulators of GIPR do not modulate cAMP accumulation at GLP-1R and GCGR. 92

Figure 3.11. Compounds alone have no or unspecific effect on $(Ca^{2+})_i$ mobilization. 94

Figure 3.12. Compounds C3, C95 and C58 inhibit GLP-1- and glucagon-stimulated $(Ca^{2+})_i$ mobilization. 95

Figure 3.13. C25 selectively inhibits GIP-induced $(Ca^{2+})_i$ mobilization at GIPR while C58 does not. 97

Figure 3.14. GIPR allosteric binding sites 6 and 10 predicted through in silico docking. 100

Figure 3.15. GIPR mutant G198A is unable to promote cAMP accumulation. 101

Figure 3.16. GIPR mutants Y141$^{1.43}$A, L193$^{2.70}$A and G198A have significantly reduced GIP-induced $(Ca^{2+})_i$ mobilization. 103

Figure 3.17. C3 inhibits GIP-induced $(Ca^{2+})_i$ mobilization at all GIPR mutants. 105

Figure 3.18. C25 has no or little effect at GIPR mutant L193$^{2.70}$A. 107

Figure 3.19. GIPR mutants L194$^{2.71}$A, Q286$^{45.50}$A and W287$^{45.51}$A have no/little GIP-induced cAMP accumulation. 109

Figure 3.20. GIPR mutants L194$^{2.71}$A, Q286$^{45.50}$A and W287$^{45.51}$A had severally reduced GIP-induce $(Ca^{2+})_i$ mobilization. 111

Figure 3.21. C25 has no or little effect at GIPR mutant R196A, P197A, Q211$^{3.24}$A and Q220$^{3.33}$A. 112

Figure 3.22. Mutation of L193$^{2.70}$A in GIPR reduces C58 activity. 114

Figure 3.23. GIPR allosteric modulators alone do not affect GSIS from rat INS-1 WT cells. 117

Figure 3.24. NAMs selective for $(Ca^{2+})_i$ mobilization also inhibit incretin-potentiated GSIS from rat INS-1 cells. 118

Figure 3.25. The new compounds, T2, T5, T10 and T11, based upon site 10 binding alone, inhibit GIP-induced $(Ca^{2+})_i$ mobilization. 123

Figure 3.26. The new compounds T13 and T26, based upon site 10 binding alone, inhibit GIP-induced $(Ca^{2+})_i$ mobilization. 125

Figure 3.27. T19 fluorescence interferes with $(Ca^{2+})_i$ mobilization assay. 127

Figure 3.28. T10 and T11 inhibit GIP-induced $(Ca^{2+})_i$ mobilization at GIPR concentrations below 100 µM. 128

Figure 3.29. T13 and T26 do not significantly inhibit GIP-induced $(Ca^{2+})_i$ mobilization at GIPR at concentrations below 100 µM. 129

Figure 3.30. T10, T11, T18, T19 behave as NAMs, while T21 is a PAM at the GIPR. 131

Figure 3.31. Fluorescent compound T19 interferes with cAMP assay. 133

Figure 3.32. Stimulation time does not affect T10 NAM activity at the GIPR. 135

Figure 3.33. T13 inhibits GLP-1-induced $(Ca^{2+})_i$ mobilization at GLP-1R. 137

Figure 3.34. T10 is a GLP-1R NAM, while T11 and T18 are NAMs at both GLP-1R and GCGR. 139

Figure 3.35. T5 has no or little effect at many Site 10 GIPR mutants. 142

Figure 3.36. T11 has no or little effect at many GIPR mutants L193$^{2.70}$A, P197A, N210A, Q211$^{3.24}$A and Q220$^{3.33}$A. 144

Figure 3.37. GIPR mutants G198A, Q204A and N201A reduce T10 activity as a NAM. 146
Figure 3.38. GIPR mutants R196A and Q204A reduced T11 efficacy at GIPR. 149
Figure 3.39. T18 has no or little effect at GIPR mutants Q204A and E288$^{45.52}$A. 151
Figure 3.40. T21 has no or little effect in transiently transfected cells. 153
Figure 4.1. *In silico* docking of C25 to GIP-bound GIPR model 1. 168
Figure 4.2. *In silico* docking of compounds to GIPR model 1 with attached GIP. 169
Figure 4.3. Comparison of blind docking carried out by AutoDock Vina or ICM-Pro. 172
Figure 4.4. Site 6 identified by *in silico* blind docking. 175
Figure 4.5. Site 10 identified by *in silico* blind docking. 176
Figure 4.6. Site 6 is fairly conserved across GIPR, GLP-1R and GCGR. 178
Figure 4.7. Site 10 sequence varies greatly across GIPR, GLP-1R and GCGR. 179
Figure 4.8. L193$^{2.70}$ is predicted to be important for binding/activity of C9-based compounds. 181
Figure 4.9. Best C25 and C58 binding poses at GIPR homology models. 182
Figure 4.10. Potential ligand-binding sites predicted by 3DLigandSite. 184
Figure 4.11. Conservation of GIPR residues determined by GPCR-SAS and ConSurf. 186
Figure 4.12. Two sectors of coevolving GIPR residues identified by pySCA. 188
Figure 4.13. Potential ligand-binding sites predicted by POCASA. 189
Figure 4.14. Potential small molecule binding pockets predicted by FTMap server. 190
Figure 4.15. Potential ligand-binding sites determined by SPACER. 192
Figure 4.16. Potential ligand-binding pockets predicted by PARS. 193
Figure 5.1. Structures of selected A_1R agonists. 201
Figure 5.2. Effect of A_1R mutations on selective signalling of biased agonists. 202
Figure 5.3. Investigation of selective agonist coupling to $G\alpha_{o/i}$ by mutagenesis and cAMP. 205
Figure 5.4. Efficacy of synthetic adenosine and NECA Derivatives at individual A_1R. 211
Figure 5.5. Efficacy of synthetic adenosine and NECA Derivatives at individual $A_{2A}R$. 217
Figure 5.6. Efficacy of synthetic adenosine and NECA Derivatives at individual $A_{2B}R$. 218
Figure 5.7. Efficacy of synthetic adenosine and NECA Derivatives at individual A_3R. 220
Figure 5.8. Adenosine and NECA derivatives show selectivity towards A_1R subtype. 221
Figure 5.9. Binding of AR ligands at human A_1R. 224
Figure 5.10. Binding of AR ligands at rat A_1R. 225
Figure 5.11. NECA and adenosine derivatives show correlation between potency and affinity or residence time at the human A_1R. 234
Figure 5.12. Molecular dynamics docking of 20 and 27. 237
Figure 6.1. Kinetic parameters of A_1R and A_3R antagonists. 242
Figure 6.2. Potential A_3R antagonists identified during initial screening of compounds. 243

Figure 6.3. Functional characterisation of A15, A17, A26 and A47 analogues at A_3R. 248

Figure 6.4. A17, A26 and A47 are competitive antagonists of A_3R. 251

Figure 6.5. Functional characterisation of A15, A17, A26 and A47 analogues at A_1R. 254

Figure 6.6. A15, A17, A26 and A47 have no or little activity at $A_{2A}R$ and $A_{2B}R$. 258

Figure 6.7. Functional characterisation of A15, A17, A26 and A47 analogues at $A_{2A}R$ and $A_{2B}R$. 260

Figure 6.8. Binding of A15 and A17 derivates at A_1R and A_3R measured by NanoBRET. 263

Figure 6.9. Binding of A26 derivates at A_1R and A_3R measured by NanoBRET. 265

Figure 6.10. Binding of A47 derivates at A_1R and A_3R measured by NanoBRET. 267

Figure 6.11. A17, A26 and A47 docking to A_1 and A_3 receptors. 272

Figure 6.12. Kinetic measurement of CA200645 binding to WT and mutant Nluc-A_1R. 274

Figure 6.13. Binding of NECA, A17, A26 and A47 at WT and mutant A_1R. 276

List of tables

Table 1.1. Activity and members of Gα-protein families. 8

Table 2.1. 2D structures and molecular weight of potential GIPR allosteric modulators. 48

Table 2.2. List of synthetic adenosine and NECA derivatives. List of all tested compounds, their 2D structure and molecular weight. 52

Table 2.3. A17, A26 and A47 derivative compounds structures and their molecular weight. 56

Table 2.4. List of expression constructs used in this study 59

Table 2.5. Forward and reverse primers used for QuikChange Lightning site-directed mutagenesis. Bold letters indicate changed bases relative to WT protein. 64

Table 2.6. Reaction components and amounts used for QuikChange Lightning site-directed mutagenesis 65

Table 2.7. Cycle parameters used for QuikChange Lightning site-directed mutagenesis 65

Table 2.8. Dilution range for insulin samples originating from different points in the assay 72

Table 2.9. hGIPR homology models (1-10) and hGIPR model (11) used in this study 72

Table 3.1. Structures of the C3- and C25-based compounds 79

Table 3.2. Potency (pEC_{50}) and E_{max} values for $(Ca^{2+})_i$ mobilization in HEK-293S cells stably expressing GIPR in response to GIP(1-42) in the absence or presence of different concentrations of tested compounds. 82

Table 3.3. Maximal response (E_{max}) values for $(Ca^{2+})_i$ mobilization in HEK-293S cells stably expressing GIPR in response to 10 µM ionomycin in the absence or presence of 100 µM tested compound. 83

Table 3.4. Potency (pEC_{50}), E_{max} and basal values for $(Ca^{2+})_i$ mobilization in HEK-293S cells stably expressing GIPR in response to GIP(1-42) concentrations in the absence or presence of different concentrations of C95. 86

Table 3.5. Potency (pEC_{50}) and E_{max} values for cAMP accumulation in HEK-293S cells stably expressing GIPR in response to 100 µM compound or DMSO. 87

Table 3.6. Potency (pEC_{50}) and E_{max} values for cAMP accumulation in HEK-293S cells stably expressing GIPR in response to GIP(Pro3) in the presence of 100 µM compound or DMSO. 88

Table 3.7. Potency (pEC_{50}), E_{max} and basal values for β-arrestin-1/2 recruitment in response to GIP(1-42) in the presence of 100 µM compound or DMSO. 91

Table 3.8. Potency (pEC_{50}) and E_{max} values for cAMP accumulation in HEK-293S cells stably expressing GLP-1 in response to GLP-1(7-36)NH_2 and in HEK-293ΔCTR cells stably expressing GCGR in response to glucagon. 93

Table 3.9. Potency (pEC_{50}) and E_{max} values for $(Ca^{2+})_i$ mobilization in HEK-293S cells stably expressing GLP-1R or HEK-293ΔCTR cells stably expressing GCGR in response to GLP-1(7-36)NH_2 or glucagon in the absence or presence of different concentrations of tested compounds. 96

Table 3.10. Potency (pEC_{50}) and E_{max} values for $(Ca^{2+})_i$ mobilization in HEK-293S cells stably expressing GIPR or GLP-1R or HEK-293ΔCTR cells stably expressing GCGR in response to GIP(1-42), GLP-1(7-36)NH_2 or glucagon in the absence or presence of different concentrations of tested compounds. 98

Table 3.11. Potency (pEC_{50}) and E_{max} values for cAMP accumulation in HEK-293S cells transiently transfected with WT or mutant pcDNA3.2-GIPR in response to 8' stimulation with either GIP(Pro3) or GIP(1-42). 102

Table 3.12. Potency (pEC_{50}) and E_{max} values for $(Ca^{2+})_i$ mobilization in HEK-293S cells transiently transfected with WT or mutant pcDNA3.2-GIPR in response to GIP(1-42). 103

Table 3.13. Potency (pEC_{50}) and E_{max} values for $(Ca^{2+})_i$ mobilization in HEK-293S cells transiently transfected with WT or mutant pcDNA3.2-GIPR in response to with GIP(1-42) in the presence or absence of 100 µM C3. 106

Table 3.14. Potency (pEC_{50}) and E_{max} values for $(Ca^{2+})_i$ mobilization in HEK-293S cells transiently transfected with WT or mutant pcDNA3.2-GIPR in response to with GIP(1-42) in the presence or absence of 100 µM C25. 108

Table 3.15. Potency (pEC_{50}) and E_{max} values for cAMP accumulation in HEK-293S transiently transfected with WT or mutant pcDNA3.2-GIPR in response to 8' stimulation with increasing doses of either GIP(Pro3) or GIP(1-42). 110

Table 3.16. Potency (pEC_{50}) and E_{max} values for $(Ca^{2+})_i$ mobilization in HEK-293S cells transiently transfected with WT or mutant pcDNA3.2-GIPR in response to GIP(1-42). 111

Table 3.17. Potency (pEC_{50}) and E_{max} values for $(Ca^{2+})_i$ mobilization in HEK-293S cells transiently transfected with WT or mutant pcDNA3.2-GIPR in response to with GIP(1-42) in the presence or absence of 100 µM C25. 113

Table 3.18. Potency (pEC_{50}) and E_{max} values for $(Ca^{2+})_i$ mobilization in HEK-293S cells transiently transfected with WT or mutant pcDNA3.2-GIPR in response to with GIP(1-42) in the presence or absence of 100 µM C58. 115

Table 3.19. 2D structures and molecular weight of potential GIPR allosteric modulators T1-T27. 120

Table 3.29. Potency (pEC_{50}) and E_{max} values for $(Ca^{2+})_i$ mobilization in HEK-293S cells stably expressing GIPR in response to GIP(1-42) in the absence or presence of 100 µM tested compounds. 124

Table 3.21. Potency (pEC_{50}) and E_{max} values for $(Ca^{2+})_i$ mobilization in HEK-293S cells stably expressing GIPR in response to GIP(1-42) in the absence or presence of 100 µM tested compounds. 126

Table 3.22. Potency (pEC_{50}), E_{max} and basal values for $(Ca^{2+})_i$ mobilization in HEK-293S cells stably expressing GIPR in response to GIP(1-42) concentrations in the absence or presence of different concentrations of C95. 129

Table 3.23. Potency (pEC_{50}), E_{max} and basal values for $(Ca^{2+})_i$ mobilization in HEK-293S cells stably expressing GIPR in response to GIP(1-42) concentrations in the absence or presence of different concentrations of T13 and T26. 130

Table 3.24. Potency (pEC_{50}), maximal response (E_{max}) and basal response values for cAMP accumulation in HEK-293S cells stably expressing GIPR in response to 8' stimulation with increasing doses of GIP(Pro3) in the absence or presence of different concentrations of tested compounds T1-T27. 132

Table 3.25. cAMP response (FRET signal) readout from samples including no cells in the presence or absence of different concentrations of test compounds. 134

Table 3.26. Potency (pEC_{50}), basal and E_{max} values for cAMP accumulation in Flp-In CHO cells stably expressing A3R in response to NECA in the presence or absence of 100 µM T19. 134

Table 3.27. Potency (pEC_{50}) and E_{max} values for cAMP accumulation in HEK-293S cells stably expressing GIPR in response to increasing doses of GIP(Pro3) following a 0' or 30' pre-stimulation of the cells with 100 µM T10. 135

Table 3.28. Potency (pEC_{50}) and E_{max} values for $(Ca^{2+})_i$ mobilization in HEK-293S cells stably GLP-1R or HEK-293ΔCTR cells stably expressing GCGR in response to GLP-1(7-36)NH_2 or glucagon in the absence or presence of different concentrations of tested compounds. 138

Table 3.29. Potency (pEC_{50}) and E_{max} values for cAMP accumulation in HEK-293S cells stably expressing GLP-1R or HEK-293ΔCTR cells stably expressing GCGR in response to increasing doses of GLP-1(7-36)NH_2 or glucagon in the absence or presence of different concentrations of tested compounds. 140

Table 3.30. Potency (pEC_{50}) and E_{max} values for $(Ca^{2+})_i$ mobilization in HEK-293S cells transiently transfected with WT or mutant pcDNA3.2-GIPR in response to increasing doses of GIP(1-42) in the presence or absence of 100 µM T5. 143

Table 3.31. Potency (pEC_{50}) and E_{max} values for $(Ca^{2+})_i$ mobilization in HEK-293S cells transiently transfected with WT or mutant pcDNA3.2-GIPR in response to increasing doses of GIP(1-42) in the presence or absence of 100 µM T11. 145

Table 3.32. Potency (pEC_{50}) and E_{max} values for cAMP accumulation in HEK-293S transiently transfected with WT or mutant pcDNA3.2-GIPR in response to 8' stimulation with increasing doses of either GIP(Pro3) or GIP(1-42) in the presence or absence of 100 µM T10. 147

Table 3.33. Potency (pEC_{50}) and E_{max} values for cAMP accumulation in HEK-293S cells transiently transfected with WT or mutant pcDNA3.2-GIPR in response to 8' stimulation with increasing doses of GIP(1-42) in the presence or absence of 100 µM T11. 150

Table 3.34. Potency (pEC_{50}) and E_{max} values for cAMP accumulation in HEK-293S cells transiently transfected with WT or mutant pcDNA3.2-GIPR in response to 8' stimulation with increasing doses of GIP(1-42) in the presence or absence of 100 µM T18. 152

Table 3.35. Potency (pEC_{50}) and E_{max} values for cAMP accumulation in HEK-293S cells transiently transfected with WT or mutant pcDNA3.2-GIPR in response to 8' stimulation with increasing doses of GIP(1-42) in the presence or absence of 100 µM T21. 154

Table 3.36. Summary of GIPR allosteric modulators and their effect at GIPR, GLP-1R and GCGR. Cross (X) indicates the compound does not effect agonist-induced calcium/cAMP response at the indicated receptor. 157

Table 3.37. Summary of GIPR negative allosteric modulators' activity at GIPR mutants. Y indicates that the NAM retains its normal effect at that mutant GIPR, **N** indicates that the compound efficacy is significantly reduced and '-' means the compounds doesn't have any effect in that assay. 160

Table 4.1. 2D structures of the C3 and C25-based compounds proven to be allosteric modulator at GIPR. 167

Table 4.2. GIPR homology models used for *in silico* docking. The models were made by Dr Rahman and his lab. 170

Table 4.3. Compounds used for *in silico* docking at GIPR homology models 2-10. Series of allosteric modulator compounds of the GIPR based on compound C9 and their allosteric activity at GIP-induced cAMP accumulation or $(Ca^{2+})_i$ mobilisation in HEK-293S cells stably expressing the GIPR. The *in vitro* assays were performed by Dr Harris (Dr Harris' PhD thesis, 2019). 171

Table 4.4. Summary of blind docking to GIPR models 2-10 using AutoDock Vina. Percentage of all poses of tested compounds blind docked to the different sites at GIPR homology models 2-10. Poses of compounds binding to unstructured regions are written in red, poses with lowest predicted binding affinity are highlighted yellow. 173

Table 4.5. Sites 6, 7 and 10 identified as best candidate allosteric sites at GIPR. Major candidate allosteric sites identified using each technique across GIPR homology models 1-5. 194

Table 5.1. Agonist-stimulated cAMP response in WT and mutant hA_1R. pIC_{50} and E_{max} values measured by cAMP accumulation assay in Flp-In CHO cells stably expressing WT or mutant hA_1R in response to tested compounds and 10 µM forskolin. 203

Table 5.2. List of synthetic adenosine and NECA derivatives. List of all tested compounds, their 2D structure and molecular weight. 207

Table 5.3. Potency of synthetic adenosine and NECA benzyloxycyclopentyl derivatives. pIC_{50}, pEC_{50} and E_{max} values measured by cAMP accumulation assay in CHO-A_1R, CHO-$A_{2A}R$, CHO-$A_{2B}R$ or Flp-In CHO-A_3R cells in response to tested compounds. 10 and 1 µM forskolin is included in the assay for A_1R and A_3R, respectively. 212

Table 5.4. Potency of synthetic adenosine and NECA phenoxycyclopentyl derivatives. pIC_{50}, pEC_{50} and E_{max} values measured by cAMP accumulation assay in CHO-A_1R, CHO-A_{2A}R, CHO-A_{2B}R or Flp-In CHO-A_3R cells in response to tested compounds. 10 and 1 µM forskolin is included in the assay for A_1R and A_3R, respectively. 214

Table 5.5. Binding of synthetic adenosine and NECA benzyloxycyclopentyl derivatives. pK_i values were determined through NanoBRET binding assay in HEK-293 cells stably expressing human or rat Nluc-A_1R. 226

Table 5.6. Binding of synthetic adenosine and NECA phenoxycyclopentyl derivatives. pK_i values were determined through NanoBRET binding assay in HEK-293 cells stably expressing human or rat Nluc-A_1R. 227

Table 5.7. Kinetics of binding of synthetic adenosine and NECA benzyloxycyclopentyl derivatives to the orthosteric binding site at human A_1R. Kinetic parameters were determined using NanoBRET binding assays in HEK-293 cells stably expressing human Nluc-A_1R. 229

Table 5.8. Kinetics of binding of synthetic adenosine and NECA phenoxycyclopentyl derivatives to the orthosteric binding site at human A_1R. Kinetic parameters were determined using NanoBRET binding assays in HEK-293 cells stably expressing human Nluc-A_1R. 230

Table 5.9. Kinetics of binding of synthetic adenosine and NECA benzyloxycyclopentyl derivatives to the orthosteric binding site at rat A_1R. Kinetic parameters were determined using NanoBRET binding assays in HEK-293 cells stably expressing rat Nluc-A_1R. 231

Table 5.10. Kinetics of binding of synthetic adenosine and NECA phenoxycyclopentyl derivatives to the orthosteric binding site at rat A_1R. Kinetic parameters were determined using NanoBRET binding assays in HEK-293 cells stably expressing rat Nluc-A_1R. 232

Table 6.1. Chemical structures of pyrazolo[3,4-c]pyridine and pyrazolo[3,4-d]pyridazines compounds selected for further experiments following screening in Flp-In™ CHO cells stably expressing human A_3R using cAMP accumulation assay. 245

Table 6.2. Functional activities for pyrazolo[3,4-c]pyridine and pyrazolo[3,4-d]pyridazines compounds against A_3R. pIC_{50}, E_{max} and pK_d values for cAMP accumulation in Flp-In CHO cells stably expressing A_3R stimulated with 10 µM forskolin, range of NECA concentrations (1pM to 1 µM), and either 1 µM potential antagonist or DMSO for 30 minutes. Compounds A17, A26 and A47 were measured as part of my BA degree, while compounds L4, L5, L9 and L21 were measured by Lakshiv Dhingra (University of Cambridge) and were submitted for his BA degree. 250

Table 6.3. cAMP accumulation in A_3R Flp-In CHO cells following stimulation with 10 µM forskolin, compound at indicated concentration and varying concentrations of IB-MECA. A26 measurements have fairly large error bars, which is why some of the values for A26 might be coming out as not significant. This table is adapted from A. Suchankova BA studies at University of Cambridge. 252

Table 6.4. Functional activities for pyrazolo[3,4-c]pyridine and pyrazolo[3,4-d]pyridazines compounds against A_1R. pIC_{50}, E_{max} and pK_d values for cAMP accumulation in CHO-KI cells stably expressing A_1R stimulated with 10 µM forskolin, range of NECA concentrations (1pM to 1 µM), and either 1 µM potential antagonist or DMSO for 30 minutes. Compounds A17, A26 and A47 were measured as part of my BA degree, while compounds L4, L5, L9 and L21 were measured by Lakshiv Dhingra (University of Cambridge) and were submitted for his BA degree. 256

Table 6.5. Functional activities for A15, A17, A26 and A47 against $A_{2A}R$ and $A_{2B}R$. pIC_{50} and E_{max} values for cAMP accumulation in CHO-KI cells stably expressing either $A_{2A}R$ or $A_{2B}R$ stimulated with a range of NECA concentrations, and either 10 µM potential antagonist or DMSO for 30 minutes. Compounds A17, A26 and A47 were measured as part of A. Suchankova BA studies at University of Cambridge. 259

Table 6.6. Functional activities for pyrazolo[3,4-c]pyridine and pyrazolo[3,4-d]pyridazines compounds against $A_{2A}R$ and $A_{2B}R$. pIC_{50}, E_{max} and pK_d values for cAMP accumulation in CHO-KI cells stably expressing either $A_{2A}R$ or $A_{2B}R$ stimulated with a range of NECA concentrations (1pM to 1 µM), and either 10 µM potential antagonist or DMSO for 30 minutes. 261

Table 6.7. Binding affinities (pK_i) of A15, A17 and L2-L10 measured using NanoBRET against A_1R and A_3R. pK_i values determined by NanoBRET in HEK293 cells stably expressing Nluc-A_1R or Nluc-A_3R were treated with 20 nM or 5 nM CA200645, respectively, and increasing concentrations of unlabelled AR ligand, enabling concentration-dependent decreases in BRET ratio at 10 min to be determined with the response normalised to DMSO. The data at 10 min was then fitted using the "One site – Fit K_i" model derived from the Cheng and Prusoff equation built into GraphPad Prism 9.3. Compounds L4, L5 and L9 were measured by Lakshiv Dhingra (University of Cambridge) and were submitted for his BA degree. 264

Table 6.8. Binding affinities (pK_i) of A26, L12, L15 and L21 measured using NanoBRET against A_1R and A_3R. pK_i values determined by NanoBRET in HEK293 cells stably expressing Nluc-A_1R or Nluc-A_3R were treated with 20 nM or 5 nM CA200645, respectively, and increasing concentrations of unlabelled AR ligand, enabling concentration-dependent decreases in BRET ratio at 10 min to be determined with the response normalised to DMSO. The data at 10 min was then fitted using the "One site – Fit K_i" model derived from the Cheng and Prusoff equation built into GraphPad Prism 9.3. Compound L21 was measured by Lakshiv Dhingra (University of Cambridge) and were submitted for his BA degree. 266

Table 6.9. Binding affinities (pK_i) of A47, L23, L25, L26, L29 and L32 measured using NanoBRET against A_1R and A_3R. pK_i values determined by NanoBRET in HEK293 cells stably expressing Nluc-A_1R or Nluc-A_3R were treated with 20 nM or 5 nM CA200645, respectively, and increasing concentrations of unlabelled AR ligand, enabling concentration-dependent decreases in BRET ratio at 10 min to be

determined with the response normalised to DMSO. The data at 10 min was then fitted using the "One site – Fit K_i" model derived from the Cheng and Prusoff equation built into GraphPad Prism 9.3. 268

Table 6.10. Kinetic parameters of AR ligands. K_{on}, k_{off}, pK_d and RT parameters of A15/17, A26 and A47 derivates at the A_1R or A_3R orthosteric site measured using NanoBRET. 270

Table 6.11. Binding affinities (K_d) for Ca200645 measured using NanoBRET against WT A_1R and mutant A_1Rs. HEK 293 cells stably expressing WT or mutant Nluc-A_1R were stimulated with varying concentrations of CA200645 and NanoBRET ratio at 10 min from A/B was the fitted with the "One site – Specific binding" equation built in GraphPad Prism 9.3 to determine CA200645 K_d. K_d values for CA200645 binding to Nluc-A_1R S267$^{7.32}$ and Y271$^{7.36}$ mutants were measured by Dr Barkan (University of Cambridge). 275

Table 6.12. Binding affinities (pK_i) for NECA, A17 and A26 measured using NanoBRET against WT A_1R and mutant A_1Rs. pK_i values determined by NanoBRET in HEK293 cells stably expressing WT or mutant Nluc-A_1R treated with 20 nM CA200645 and increasing concentrations of unlabelled AR ligand, enabling concentration-dependent decreases in BRET ratio at 10 min to be determined with the response normalised to DMSO. The data at 10 min was then fitted using the "One site – Fit K_i" model derived from the Cheng and Prusoff equation built into GraphPad Prism 9.3. HEK293 cells stably expressing Nluc-A_1R S267$^{7.32}$ and Y271$^{7.36}$ mutants were made by Dr Barkan (University of Cambridge). 277

List of abbreviations

5-HT	serotonin
A_3R	adenosine 3 receptor
AC	adenyl cyclase
Ach	acetylcholine
AMP	adenosine monophosphate
ApoE	apolipoprotein E
ATP	adenosine triphosphate
ASK1	apoptosis signal-regulating kinase 1
cAMP	cyclic adenosine monophosphate
BA	binding affinity
BRET	bioluminescence resonance energy transfer
CADD	Computational Drug Discovery/Design
CaSR	calcium-sensing receptor
CCPs	clathrin-coated pits
CCR5	GPCR chemokine receptor type 5
CGRP	calcitonin gene-related peptide
cGMP	cyclic guanosine monophosphate
CLR	calcitonin receptor-like receptor
CNGC	cyclic nucleotide-gated ion channels
CNS	central nervous system
COPD	chronic obstructive pulmonary disease
CREB	cAMP response element binding protein
Cryo-EM	cryogenic electron microscopy
CTX	cholera toxin DAG diacylglycerol
DPP-4	dipeptidyl-peptidase 4
EC_{50}	concentration needed to produce a 50% of the maximal response
E_{max}	maximal response that the drug can produce
EPAC	exchange factor-directly activated by cAMP
ECD	extracellular domain ECLs extracellular loops
EF	edema factor
ENM	elastic network model
ERK1/2	extracellular signal-regulated kinases1/2
FDA	Food and drug administration

GABA	γ-aminobutyric acid
GAPs	GTPase-activating proteins
GCGR	glucagon receptor
GDI	guanine nucleotide dissociation inhibitor
GEFs	guanine-nucleotide exchange factors
GIP	gastric inhibitory polypeptide
GIPR	GIP receptor
GIRK	G protein-regulated inward-rectifier K^+ channels
GLP-1	glucagon-like peptide-1
GLP-1R	GLP-1 receptor
GMP	guanosine monophosphate
GPCR	G protein-coupled receptor
GPCR-SAS	GPCR—sequence analysis and statistics
GRK	GPCR kinase
GRB2	growth factor receptor-bound protein 2
GSIS	glucose-stimulated insulin secretion
IBMX	3-isobutyl-1-methylxanthine
ICLs	intracellular loops
IP_3	inositol 1,4,5-triphosphate
IP_3R	IP_3 receptor
JAK2	janus kinase 2
JNK3	c-Jun N-terminal kinase 3
LARG	leukemia-associated RhoGEF
LBDD	ligand-based drug discovery
LDL	low-density lipoprotein
LKB1	liver kinase B1
mAChR	muscarinic acetylcholine receptor
MAP	mitogen-activated protein
MAPK	mitogen-activated protein kinase kinase
MD	molecular dynamics
MEK	MAPK kinase
mGluR1	metabotropic glutamate receptor 1
MKK4/7	mitogen-activated protein kinase kinases 4 and 7
MOE	Molecular Operating Environment
MPI	myocardial perfusion imaging

MSA	multiple sequence alignment
NAM	negative allosteric modulator
NAL	neutral allosteric ligand
NEFA	non-esterified fatty acids
NMA	normal mode analysis
PAM	positive allosteric modulator
PDB	Protein Data Bank
PDE	3’,5’-cyclic nucleotide phosphodiesterase
PH	pleckstrin homology
PIP_2	phosphatidylinositol 4,5-bisphosphate
PKA	protein kinase A
PKB	protein kinase B
PKC	protein kinase C
pk_i	affinity
PLCβ	phospholipase C β
PM	plasma membrane
POCASA	POcket-Cavity Search Application
POPC	1-palmitoyl-2-oleoyl-sn-glycero-3-phosphocholine
PPARγ	peroxisome proliferator activated receptor gamma
PTX	pertussis toxin
RAMP	receptor activity-modifying protein
RGS	regulators of G protein signaling
RYGB	Roux-en-Y gastric bypass
SBDD	structure-based drug discovery
SCA	statistical coupling analysis
SGLT	sodium glucose transport protein
SLC19A1	solute carrier family 19 member 1
SLC6A4	solute carrier family 6 member 4
SNPs	single nucleotide polymorphisms
TAG	triacylglycerol
T2DM	type 2 diabetes mellitus
TMD	transmembrane domain
VGCCs	voltage-gated calcium channels

Chapter 1. Introduction

1.1 Cellular signalling

All life around us from bacteria to animals is made up of cells, also known as building blocks of life. But compared to the static and unconscious common building blocks bricks, cells are constantly sending and receiving numerous of messages enabling them to respond to a range of stimuli including physical stimuli like light or temperature or chemical stimuli like neurotransmitters, peptides or nucleotides. It is cellular signalling that enables cells to respond to outside stimuli in real time as well as manage essential communication between different cells in multicellular organisms like humans.

All cells have an outer layer surrounding them and separating it from the external environment, which is called a plasma membrane (PM) (Lodish et al., 2008). PM is a lipid bilayer composed mostly of proteins and lipids, especially phospholipids. Lipophilic (or hydrophobic) messengers like steroid hormones or various vitamins can cross the PM and exert their effects inside the cell. Lipophobic (or hydrophilic) messengers, on the other hand, are most often detected by so-called cell-surface receptors, which are proteins embedded into PM. Signal transduction is then the process, where the binding of the extracellular messenger molecule or atom to the cell-surface receptor results in the receptor recruiting and binding further intracellular proteins or other affecters including enzymes and transcription factors. This then often starts a signalling cascade, which results in changes in biochemistry, cell biology, and/or gene transcription of the cell.

The cell surface receptors can be classified into intrinsic, fully embedded in the lipid bilayer, or extrinsic, anchored to the PM by a lipid head group or another intrinsic protein (Lodish et al., 2008).The largest family of these intrinsic cell-surface receptors are the 7 transmembrane spanning G protein-coupled receptors (GPCRs), which are responsible for many cellular and physiological processes in our body and capable or binding and responding to a plethora of both natural and artificial messengers.

1.2 The G protein-coupled receptors superfamily

GPCRs compromise approximately 1.6 % of the human genome (Fredriksson and Schiöth, 2005). There are more than 800 genes coding for GPCRs according to the phylogenetic analysis done by Fredriksson et al. (2003), with splice variants (isoforms)and single nucleotide polymorphisms (SNPs) further increasing this number (Marti-Solano et al., 2020). More than half of these are believed to be odorant receptors involved in smell and taste sensations with the remainder responding to endogenous mediators. GPCRs consist of a single polypeptide chain, which is usually of 350–400 amino

acid residues long, but in some cases can be up to 1100 residues. GPCRs are defined, as their name suggests, by their ability to couple and interact with G proteins, though there are some GPCRs which do not do this.

The vast number and diversity of GPCRs enables them to interact with an equally great number of ligands, including but not limited to hormones, ions, photons, odours and lipids enabling them to regulate many physiological functions such as senses, metabolism, neurotransmission or cell growth (Bjarnadóttir et al., 2007, 2006; Hauser et al., 2017; Hu et al.). There are also many GPCRs for which a ligand has yet to be identified– termed orphan receptors (Tang et al., 2012). Given GPCRs involvement in the regulation of many physiological functions, it comes as no surprise that their malfunction often leads to pathological states such as cancer, diabetes mellitus, inflammation or central nervous system disorders (Bortolato et al., 2014; Hauser et al., 2017; Heilker et al., 2009; Hu et al., 2017). GPCRs form a target for approximately 34% of all FDA (Food and drug administration) approved drugs with many more currently in clinical trials (Hauser et al., 2017). However, all these drugs target only a small number (about 10%) of the GPCRs encoded in the human genome, leaving many more as potential drug targets (Hu et al., 2017).

1.2.1 Classification of GPCRs in sub-families

All GPCRs share the same basic architecture consisting of an N-terminal extracellular domain (ECD), 7 transmembrane domains (TMDs) as mentioned above linked by 3 extracellular loops (ECLs) and 3 intracellular loops (ICLs) and an intracellular C-terminal domain. However, despite the characteristic 3D structure, attempts to classify GPCRs into classes or clans have been greatly hindered by the lack of homology and/or protein sequence similarity between GPCRs of different species (Fredriksson et al., 2003). Initially GPCRs were classified into 6 families - the rhodopsin-like class A, secretin-like class B, metabotropic-glutamate class C, fungal mating pheromone class D, cyclic adenosine monophosphate (cAMP) class E, and frizzled/smoothened class F - with classes D and E existing only in invertebrate species or fungi (Kolakowski, 1994). Fredriksson et al. (2003) then later employed phylogenetic analysis to assess the similarities between the human GPCR gene sequences coding for the 7TMDs omitting the N- and C-termini parts of the receptors from the analysis. This approach yielded 5 families of vertebrate GPCRs called glutamate, rhodopsin, adhesion, frizzled/taste2, and adhesion, also known as the GRAFS system.

Class A, also called rhodopsin-like family, is by far the largest and most diverse of these families with over 700 members, accounting for around 80% of all GPCRs. About half of this class consists of olfactory receptors and the other half is a mix of mostly monoamine, neuropeptide, cannabinoid,

chemokine, light and odorant receptors as well as some orphan receptors. The class members are characterized by conserved sequence motifs that imply shared structural features and activation mechanisms. One of these is the Asp-Arg-Tyr (DRY) motif that sits at the bottom of TMD3 and provides a salt-bridge holding the TMD3 and TMD6 together, which was nicely demonstrated in rhodopsin, the prototypical class A receptor, where an ionic lock between Arg135 and Glu247 holds the receptor in its inactive state (Kristiansen, 2004). Second common motif is the Asn-Ser-x-x-Asn-Pro-x-x-Tyr (NSxxNPxxY) motif in TMD7 (Fredriksson et al., 2003). Class A GPCRs are also mostly characterised by a very short ECD, which makes senses from an evolutionary standpoint as these GPCRs are mainly targeted by small molecules binding typically to TMDs or ECLs (Basith et al., 2018). Class A GPCRs play a key role in many disease areas and of the 107 established GPCR drug targets, majority are aminergic and opioid receptors falling into class A (Hauser et al., 2017).

Class B1, also called the secretin receptor family, is a small GPCR class that contains only 16 members, all of which are de-orphaned. These are structurally similar to class A GPCRs. Compared to class A, their 7TMDs are also more open towards the extracellular side forming more of a V-shape and thought to help facilitate ligand binding by increasing extracellular contact surface (Hollenstein et al., 2014). An important motif for the stabilisation of class B1 GPCRs' TMDs is a Gly-Trp-Gly-x-Pro (GWGxP) motif in TMD4 (Hollenstein et al., 2014). This class has a much larger ECD approximately 120 residues long, stabilised by a number of conserved cysteine crosslinks, forming a large surface required for the binding of larger peptide hormones approximately 30-40 amino acids long (Hu et al., 2017). Secretin family receptors are important drug targets in diseases like diabetes mellitus, obesity, cancer, cardiovascular disease or psychiatric disorders (Pal et al., 2012).

Class B2, also called the adhesion receptor family, consists of 33 receptors, 24 of which occur in humans (Stacey et al., 2000). Currently, many of the adhesion receptors are orphaned. The ones that are deorphaned bind extracellular matrix proteins and facilitate cell-to-cell adhesion, which gave the name to this class (Langenhan et al., 2013). This is enabled by the large ECD containing many functional domains like epidermal growth factor-like domains and high portion of serine and threonine residues (Safaee et al., 2014). The N-termini also contains the GPCR proteolytic site (GPS) motif, which is part of the bigger GAIN (GPCR Autoproteolytic Inducing) domain (Araç et al., 2012; Lagerström and Schiöth, 2008; Rosa et al., 2021). Within the transmembrane domains there are also some conserved motifs such as the histidine and tryptophan residues in TMD3 (Bjarnadóttir et al., 2007).

Class C, also known as the metabotropic glutamate family, is a small class of 22 GPCRs. It is characterised by large ECD of approximately 600 residues that includes a clam-shaped fly trap domain connected to TMD1 by cysteine-rich loop, where ligand-binding occurs (Hu et al., 2017; Rondard et al., 2006). Despite sharing only 12 % sequence homology with class A GPCRs, the overall transmembrane

topology is similar. The short ICL3 is highly conserved in class C and receptors in this class either homo- or hetero-dimerise (Chun et al., 2012).

Class F, also known as frizzled/smoothened receptor family, consists of 10 frizzled receptors and the smoothened receptor and play an important role in developmental processes, cellular differentiation and proliferation which predisposes them as interesting cancer targets (Zhang et al., 2018). Class F GPCRs have a distinctively helical N-terminal ECD containing a Cysteine-Rich Domain (CRD) and in the case of frizzled receptors also 3 ligand binding sites (Zhang et al., 2018). Moreover, the receptors in this class seems to have highly conserved sequence and structure TMD7 (Zhang et al., 2018), but lack most of the motifs other GPCRs possess, like the DRY-motif, suggesting a possibility of different activation mechanism (Velazhahan et al, 2022).

1.3 GPCR signal transduction

1.3.1 Ligand binding and GPCR activation

The great increase in the number of solved both active and inactive GPCR crystal and cryogenic electron microscopy (Cryo-EM) structures in the past decade has provided an insight into the mechanisms of ligand binding and GPCR activation. Class A GPCRs bind mostly small ligands that dock deep into the transmembrane helix bundle (Zhang et al., 2015). Class B1 GPCRs, on the other hand, employ a two-step binding model, where in the first step the C-terminal region of the peptide ligand interacts with the ECD of the GPCR. This orients the N-terminal part of the peptide correctly to dock into the middle of the GPCR transmembrane helixes bundle (Karageorgos et al., 2018). The peptide agonists all have a amphipathic α-helix extending from the core of the GPCR until the exit of the TMD bundle and they all penetrate into the receptor core to a similar extent sitting above a well-described central polar network (Liang et al., 2020; Wootten et al., 2013b). Where the ligand binding differs among class B1 GPCRs is the distinct angle at which the peptides enter the receptor core (Liang et al., 2020). This is enabled by the dynamicity of the ECD of the class B GPCRs, which is reflected by the lower resolution of the ECD in cryo-EM structures compared to the TMDs bundle (Dal Maso et al., 2019; Liang et al., 2017, 2018b), and by the variances in the metastable positions of the ECD among the receptors (Liang et al., 2020).

GPCRs have several micro-switches that have substantially different conformations in active and inactive states of the receptors. One of these microswitches in class A is the before-mentioned $DR^{3.50}Y$ (3.50 refers to the residue position within the GPCR according to the generic GPCR residue numbering system described by Ballesteros et al (2007) motif in TMD3 that makes a salt bridge to $D/E^{6.30}$ in TMD6 to form the ionic lock holding receptor in an inactive conformation and needing to be disrupted for full

receptor activation (Schneider et al., 2010; Zhang et al., 2015). This is nicely demonstrated in the rhodopsin X-ray crystal structures, where in the inactive one $R^{3.50}$ forms an ionic interaction with both $D^{3.49}$ (of the DRY motif) and $E^{6.50}$ in TMD6 (Palczewski et al., 2000). However, in the active rhodopsin structure this interaction is absent and the $R^{3.50}$ interacts instead with the C-terminal peptide of the G protein (Taddese et al., 2013). Another microswitches would be the $W^{6.48}$xP motif in TMD6, $NP^{7.50}$xxY motif in TMD7 or conserved cysteine bond between C3.25 in the top of the TMD3 and cysteine in ECL2 (Zhang et al., 2015, 2014).

Multiple biochemical and biophysical studies indicate large structural rearrangements of the TMD helices upon receptor activation, including but not limited to the outward movement of TMD5 and TMD6, leading to distinct active state conformation (Kobilka, 2007). For example electron paramagnetic resonance spectroscopy (EPR), supported by chemical reactivity measurements and fluorescence spectroscopy, show evidence of rotation and tilting of TMD6 relative to TMD3 upon photoactivation of rhodopsin (Dunham and Farrens, 1999; Farrens et al., 1996). On the other hand, in an inactive ligand-free state of the opsin receptor the $Y^{7.53}$ residue, part of the aforementioned $NP^{7.50}$xxY motif, rotates to face into the helical bundle and blocks TMD6 from moving back towards TMD3 to adopt the inactive conformation (Park et al., 2008). The outward movement of TMD6 then results in the opening of a crevice within the intracellular surface of the receptor (Oldham and Hamm, 2008). Similar structural rearrangements involving the outward movement of TMD6 have also been reported for class B1 GPCRs like for example the glucagon-like peptide-1(GLP-1) receptor or calcitonin gene-related peptide (CGRP) receptor (Liang et al., 2018a, 2018b).

1.3.2 Activation and signalling of heterotrimeric G proteins by GPCRs

The classical signal transduction through GPCRs is dependent on receptor-mediated activation of heterotrimeric G proteins, which are molecular guanine nucleotide binding proteins that bind and hydrolyse guanine triphosphate (GTP). They are composed of three subunits, α, β and γ, and are the molecular switches that turn on intracellular signalling cascades in response to GPCR activation. They also play a crucial role in defining the specificity and temporal resolution of GPCR signal transduction.

As described above, activation of a GPCR results in structural rearrangement which exposes a G protein binding pocket, which binds an inactive GDP-bound G protein (Figure 1.1). In this inactive form Gα subunit is bound to the Gβγ subunit. Binding to the active GPCR promotes GDP dissociation from Gα and results in a nucleotide-free receptor-G protein complex, which has a very short lifetime as GTP quickly binds the Gα subunit due to being present in the cytosol in 10-fold higher concentration compared to GDP (Bos et al., 2007; Higashijima et al., 1987). This causes a conformational change in

the Gα subunit and subsequent dissociation of Gα subunit from Gβγ subunit. Both subunits have then been shown to modulate downstream signalling in the cell, which will be discussed in more detail later. Cellular response is then terminated when Gα subunit hydrolyses GTP to GDP, owing to its intrinsic GTPase activity, and reassociates with Gβγ subunit finishing the G protein cycle (Hilger et al., 2018; McCudden et al., 2005; Oldham and Hamm, 2008). The G protein cycle can be further regulated by regulatory proteins like guanine-nucleotide exchange factors (GEFs), which facilitate the release of GDP from small G proteins, which is how GPCRs themselves act in this case. GTPase-activating proteins (GAPs), including regulators of G protein signalling (RGS) proteins, can then accelerate GTP hydrolysis at the Gα subunit more than 2,000-fold and thus regulate the intensity and duration of G protein signalling (Kimple et al., 2011; Ross and Wilkie, 2000).

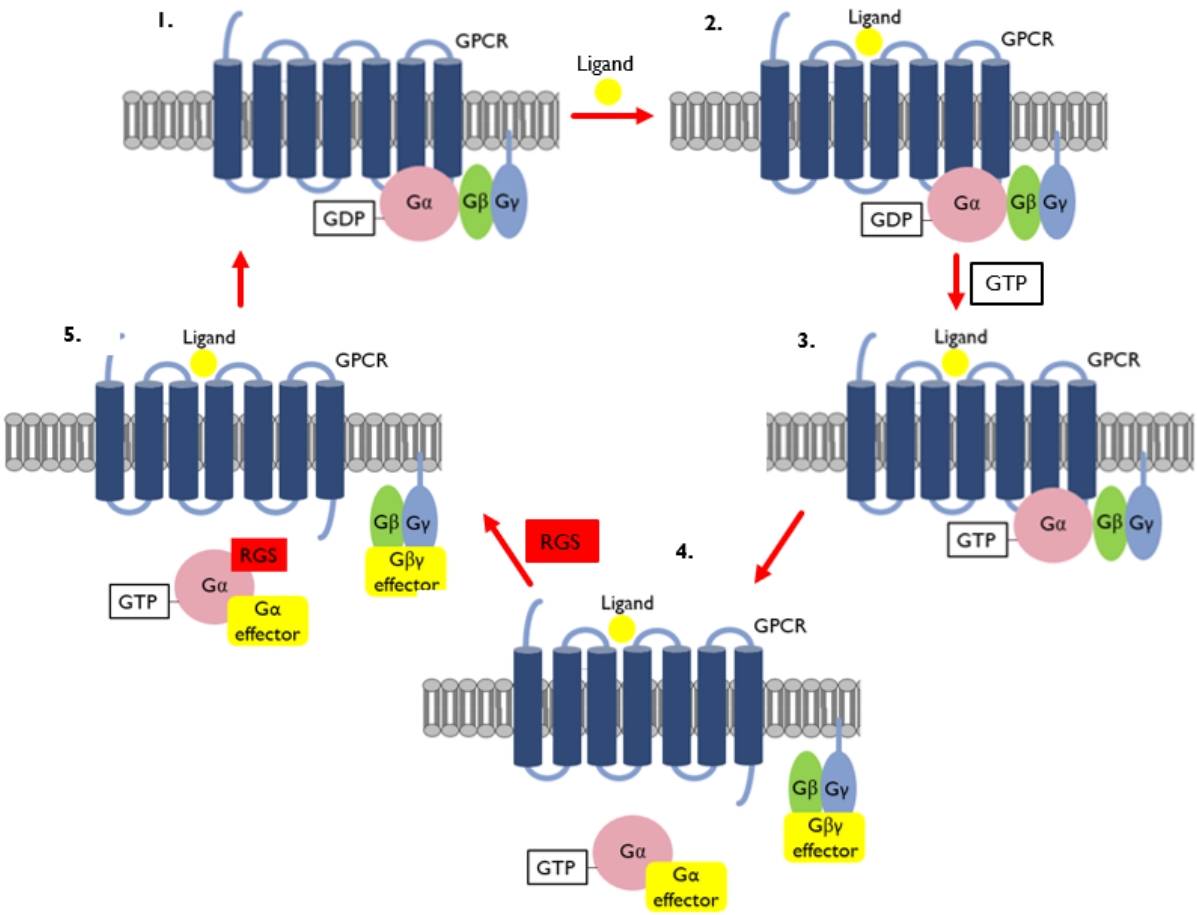

Figure 1.1. Schematic mechanism of heterotrimeric G protein activation cycle. Inactive GDP-bound Gα subunit is complexed together with the Gβγ subunit and resides at the inactive GPCR (1). When ligand binds the receptor (2), the GPCR gets activated and subsequently activated the heterotrimeric G protein resulting in exchange of GDP for GTP (3). The active Gα subunit dissociates from Gβγ subunit and both subunits can bind their own effectors and promote intracellular effects (4). G protein signalling is terminated by RGS binding the Gα subunit (5) and hydrolysis of GTP to GDP, which promotes reassociation of Gα subunit with Gβγ subunit.

1.3.2.1 Gα subunit signalling following GPCR activation

In contrast to over 800 GPCR genes, there are only 4 major Gα-protein families, called $G\alpha_s$, $G\alpha_{i/o}$, $G_{q/11}$ and $G\alpha_{12/13}$, which have been classified based on sequence homology between 23 identified human Gα isotypes encoded by 16 individual genes (Table 1.1) (Downes and Gautam, 1999; Simon et al., 1991). $G\alpha_s$ family consists of widely expressed $G\alpha_s$ and $G\alpha_{olf}$, which is only present in the olfactory sensory neurons (Jones and Reed, 1989). $G\alpha_{i/o}$ family is the largest and most diverse of all Gα families and consists of $G\alpha_{i1}$, $G\alpha_{i2}$, $G\alpha_{i3}$, $G\alpha_o$, $G\alpha_{t1}$, $G\alpha_{t2}$, $G\alpha_g$ and $G\alpha_z$. $G\alpha_o$ is highly expressed in neurons, $G\alpha_{t1}$ and $G\alpha_{t2}$ in the rod and cone cells of the eye, $G\alpha_g$ in the taste receptor cells and $G\alpha_z$ in neurons and

platelets (Kuszak et al., 2010). The $G_{q/11}$ family consists of G_q, G_{11}, G_{14} and $G_{15/16}$. The $G\alpha_{12/13}$ family consists of $G\alpha_{12}$ and $G\alpha_{13}$ ubiquitously expressed in humans. All Gα subunits except the photoreception-specific transducin (or $G\alpha_t$) contain a 16-carbon palmitate reversibly attached through a thioester bond to a cysteine near the N-terminus, which keeps the Gα subunit anchored into the PM (Wedegaertner et al., 1995).

Table 1.1. Activity and members of Gα-protein families.

Family	Members	Activity
$G\alpha_s$	$G\alpha_s$ and $G\alpha_{olf}$	Activate AC →↑cAMP
$G\alpha_{i/o}$	$G\alpha_{i1}$, $G\alpha_{i2}$, $G\alpha_{i3}$, $G\alpha_o$, $G\alpha_{t1}$, $G\alpha_{t2}$, $G\alpha_g$ and $G\alpha_z$	Activate PDE, inhibit AC →↓cAMP and cGMP
$G\alpha_q$	G_q, G_{11}, G_{14} and $G_{15/16}$	Activate PLCβ
$G\alpha_{12}$	$G\alpha_{12}$ and $G\alpha_{13}$	Activate Rho GTPases

1.3.2.1.1 GPCR modulation of cAMP signalling

Active $G\alpha_s$ subunit can catalyse all 9 isoforms of adenylyl cyclase (AC), which in turns promotes cAMP synthesis from adenosine triphosphate (ATP)(Hurley, 1999; Ross and Gilman, 1977). cAMP is an important second messenger that can then activate several other intracellular effectors – namely protein kinase A (PKA), exchange factor-directly activated by cAMP1 and 2 (EPAC1 and EPAC2) and cyclic nucleotide-gated ion channels (CNGC). PKA is a serine/threonine kinase composed of two regulatory and two catalytic subunits. Binding of cAMP to the two cAMP binding sites on each regulatory subunit activates the PKA and results in the release of an active catalytic subunit (McClendon et al., 2014; Murray, 2008). The active catalytic subunit can then phosphorylate a plethora of other intracellular targets including but not limited to cAMP response element binding protein (CREB), ion channels and other protein kinases. It can also activate Rap1-GTPase, which activates the protein kinase Raf. Raf then activates mitogen-activated protein kinase (MAPK) kinase (MEK), which then phosphorylates, and thus activates, known GPCR downstream effector extracellular signal-regulated kinases (ERK) 1/2, which is a member of the MAPK family implicated in the cellular growth and differentiation (Goldsmith and Dhanasekaran, 2007; Werry et al., 2005). cAMP can also alternatively, although with lower affinity, bind to EPAC1 and EPAC2. Similarly to PKA, binding of cAMP

induces a conformation change and activation of the EPAC1/2, which can then in turn activate small GTPases Rap1 and Rap2 (de Rooij et al., 2000, 1998).

The termination of cAMP signalling is regulated by 3',5'-cyclic nucleotide phosphodiesterases (PDEs), which degrade cAMP (or cyclic guanosine monophosphate (cGMP)) to non-cyclic nucleotide adenosine monophosphate (AMP) or guanosine monophosphate (GMP)) (Omori and Kotera, 2007). There are 11 PDE isoforms, with PDE4, 7 and 8 being specific for cAMP, while PDE5, 6 and 9 are specific for cGMP. The other isoforms are capable of breaking down both cAMP and cGMP but with differing affinities (Omori and Kotera, 2007). G protein subunits $G\alpha_{t1}$ and $G\alpha_{t2}$ activate PDEs, helping promote cyclic mononucleotides breakdown (Burns and Arshavsky, 2005; Margolskee, 2002). $G\alpha_{i1}$, $G\alpha_{i2}$ and $G\alpha_{i3}$ can then also regulate cAMP signalling by opposing $G\alpha_s$ and directly inhibiting AC by preventing the interaction AC catalytic domains (Hurley, 1999; Watts and Neve, 2005). The action of $G\alpha_o$ is less well understood, but weak inhibition of AC subtype 1 (of which there are 9) has been previously demonstrated (Taussig et al., 1994).

As one of the options, G protein regulation of cAMP signalling can be studied with the use of cholera toxin (CTX), which constitutively activates $G\alpha_s$ by decreasing the intrinsic GTPase activity of $G\alpha_s$, or pertussis toxin (PTX), which prevents $G\alpha_{i/o}$ interaction with a GPCR, leaving it inactive (Hesketh and Campbell, 1987; West et al., 1985). Another helpful compound for studying cAMP signalling is forskolin, which is a potent AC activator (Seamon et al., 1981). It is particularly useful for increasing cAMP levels prior to measuring $G\alpha_i$ activation and subsequent decrease in cAMP levels. PDE inhibitors like rolipram or 3-isobutyl-1-methylxanthine (IBMX) can then be used to prevent cAMP breakdown overtime to aid the study of Gα signalling, but their use has the disadvantage of masking the temporal component of cAMP signalling (Jin et al., 1998; Schmidt et al., 2020).

1.3.2.1.2 GPCR-mediated calcium ion signalling

All members of the $G_{q/11}$ family, upon their activation stimulate phospholipase C β1 (PLCβ) activity. PLCβ cleaves the membrane lipid phosphatidylinositol 4,5-bisphosphate (PIP_2) to generate inositol 1,4,5-trisphosphate (IP_3) and diacylglycerol (DAG), which are both important second messengers (Cabrera-Vera et al., 2003; Rhee, 2001). IP_3 is a cytosol soluble molecule that binds the IP_3 receptor (IP_3R) embedded into the endoplasmic reticulum, resulting in release of intracellular calcium $(Ca^{2+})_i$ to stimulate muscle contraction, neurotransmitter release and activation of transcription factors (Taylor et al., 2007; Thillaiappan et al., 2019). DAG, on the other hand, is a membrane bound molecule that can activate protein kinase C (PKC), which can among other targets activate Raf and start the activation cascade described above resulting in the phosphorylation of ERK1/2 (Corbit et al., 2003).

1.3.2.1.3 Rho signalling initiated from GPCR activation

$G\alpha_{12}$ and $G\alpha_{13}$ can activate p115RhoGTPase proteins PDZ-RhoGEF and leukemia-associated RhoGEF (LARG) (Fukuhara et al., 1999; Longenecker et al., 2001), while $G_{q/11}$ family subunits can activate p63RhoGEF (Booden et al., 2002; Campbell and Smrcka, 2018; Vogt et al., 2003). These proteins can then activate the small monomeric G protein Rho by promoting the exchange of GDP for GTP via stimulation of the GTPase activity. Constitutive over-activation has been shown to result in cell transformation (Fukuhara et al., 2001; Martin et al., 2001; Whitehead et al., 2001).

1.3.2.2 GPCR-mediated Gβγ signalling

There are 5 known human Gβ and 12 human Gγ subunit genes resulting in a large number of possible Gβγ dimer combinations (Clapham and Neer, 1997; Fletcher et al., 1998; Huang et al., 1999; Ray et al., 1995). However, it is the Gβ subunit that is thought to be the major determinator of cellular function, while Gγ is post-synthetically prenylated at the C-terminus localising the Gβγ dimer at the membrane (Wedegaertner et al., 1995). Originally the main Gβγ subunit function was thought to be facilitation of Gαβγ binding at a GPCR and Gα inhibitory action through its guanine nucleotide dissociation inhibitor (GDI) activity (Lodowski et al., 2003). However, Gβγ subunits, acting as a dimer have been shown to activate their own effectors like G protein-regulated inward-rectifier K^+ channels (GIRK or Kir3 channels) or neuronal N- and P/Q-type Ca^{2+} channels (Delmas et al., 2000; Kammermeier et al., 2000; Logothetis et al., 1987; Lü et al., 2001).

1.3.3 GPCR signalling regulation

There are multiple cellular proteins other than G proteins that can interact closely with GPCRs either through their C terminus (Calmodulin, endothelial nitric oxide synthase), third ICL (GPCR kinase (GRK), growth factor receptor-bound protein 2 (GRB2)) or through various motifs (e.g. janus kinase 2 (JAK2) through YIPP motif) and effect their signalling (Heuss and Gerber, 2000). For example, GPCR signalling via G proteins is terminated by the phosphorylation of active GPCRs by specific GRKs, followed by selective recognition and binding of β-arrestins and subsequent internalisation. Furthermore, β-arrestins are also capable of activating their own intracellular effectors and thus activating signalling cascades independently of G proteins.

1.3.3.1 The role of GPCR kinases

In 1989, Benovic et al. al identified a family of GRKs (named GRK-1 to GRK-7) targeting different GPCRs. GRKs are soluble proteins and thus need to be recruited to the membrane in order to be able to interact with GPCRs, which is ensured by different mechanisms for different GRKs. Visual GRK-1 and -7 are prenylated at C-termini, which ensures their permanent localisation to the membrane. On the other hand, GRK-2 and -3 have a pleckstrin homology (PH) domain, which binds Gβγ subunit (Koch et al., 1993; Lodowski et al., 2003). Activation of a GPCR results in the release of Gβγ subunit, which then recruits GRK-2/3 to the receptor (Li et al., 2003). GRK-4/5/6 lack either of these two mechanisms, but palmitoylation of their C-terminal cysteines and/or an amphipathic helix interacting with the membrane phospholipids keeps them localised to the membrane (Gurevich et al., 2012).

The difference between GRKs and other kinases is that most kinases recognise specific protein sequences in the target protein regardless on its activation state, but GRKs specifically phosphorylate active GPCRs (Gurevich and Gurevich, 2019). This is because GRKs are activated by the active GPCRs themselves, which they then in turn phosphorylate. This was nicely demonstrated for the rhodopsin receptor, where GRK-1 (previously called rhodopsin kinase) is recruited to light-activated rhodopsin receptor, even when the rhodopsin C-terminus including all the phosphorylation sites is cleaved off by proteolysis, and becomes active to phosphorylate anything in its vicinity, which normally would be the phosphorylation sites on the GPCR C-terminus (Gurevich et al., 2012; Palczewski et al., 1991). To be more precise the activation exclusively by binding to GPCRs is true for GRK-1/2/3/7, but GRK-4/5/6 can be active constitutively. Rankin et al., 2006 showed that GRK-4 constitutively phosphorylates the dopamine 1 receptor (D1R), while others have shown that GRK-5/6 can phosphorylate even inactive GPCRs both *in vitro* and in live cells (Baameur et al., 2010; Li et al., 2015, p. 4; Tran et al., 2004).

1.3.3.2 Arrestins uncouples G protein signalling from GPCRs

Arrestins are cytosolic adaptor proteins that were originally discovered for their inhibitory role in GPCR signalling via heterotrimeric G proteins (Wilden et al., 1986). There are 4 arrestin subtypes, two of which are visual arrestin-1 and -4 localised to photoreceptor cells to the retina and bind photopigments, while nonvisual arrestin-2 and -3 (commonly called β-arrestin-1 and β-arrestin-2) are ubiquitously expressed (Gurevich and Gurevich, 2019; Magalhaes et al., 2012).

The first role of arrestins is GPCR desensitisation. When an active GPCR is phosphorylated by a GRK, and binds an arrestin with high affinity, the G protein becomes decoupled from the receptor (Gurevich and Gurevich, 2004; Lefkowitz and Shenoy, 2005). As recent structural studies show, G proteins and arrestins both compete for the same binding place to the inter-helical cavity on the

cytoplasmic side of the GPCR with arrestins additionally binding also tightly to the receptor-attached phosphates that fit into positive patches on the arrestin surface (Carpenter et al., 2016; Liang et al., 2018b; Zhang et al., 2017; Zhou et al., 2017). The same binding place means that binding of one to the GPCR prevents the binding of the other. There is also the difference that G proteins readily dissociate from GPCRs in the presence of GTP, while arrestins do not and therefore arrestins outcompete G proteins, thus terminating G protein signalling (Gurevich and Gurevich, 2004).

The second important role is that β-arrestins are important adaptors for agonist-induced internalisation (Ferguson et al., 1996; Goodman et al., 1996) and ubiquitination of GPCRs (Han et al., 2013; Jean-Charles et al., 2016; Shenoy et al., 2001), thus governing the trafficking of internalized GPCRs and further reducing cell responsiveness. The classical mechanism of agonist-stimulated internalisation is via clathrin-mediated endocytosis. After β-arrestins binding to the GPCR, β-arrestins bind clathrin and its adaptor heterotetrameric adaptor protein AP2 via specific sites in their C-termini, which are made more accessible by the release of the C-terminus upon GPCR binding (Goodman et al., 1996; Kim and Benovic, 2002; Laporte et al., 1999; Zhuo et al., 2014). This recruitment of clathrin then results in the formation of clathrin-coated pits (CCPs) and subsequent endocytosis (Gurevich and Gurevich, 2019).

Thirdly, arrestins have been suggested to be able to serve as signal transducers in their own right (Gurevich and Gurevich, 2006; Hanson et al., 2006; Peterson and Luttrell, 2017). In 1999, Luttrell et al. showed that receptor-bound arrestins could promote Src-dependent activation of pro-proliferative MAP kinases ERK1/2. Another example would be the recruitment and scaffolding of the ASK1-MKK4/7-JNK3 cascade (the abbreviations stand for apoptosis signal-regulating kinase 1 (ASK1), mitogen-activated protein kinase kinases 4 and 7 (MKK4/7) and mitogen-activated protein (MAP) kinases extracellular signal-regulated kinases1/2 (ERK1/2)) resulting in an active and c-Jun N-terminal kinase 3 (JNK3) on endosomes with internalized GPCRs (Luttrell and Miller, 2013; McDonald et al., 2000). This GPCR signalling from endosomes is in contrast to the classical signalling from the plasma membrane adds another layer of complexity to GPCR signalling and this phenomenon is also called the compartmentalisation of GPCR signalling (Ellisdon and Halls, 2016). It was, however, shown that arrestins can promote these pathways also on their own without preceding GPCR activation (Han et al., 2012; Whalen et al., 2011).

1.4 GPCR pharmacology

In the traditional two-state model of GPCR activation, GPCRs are considered to exist in equilibrium between an inactive state and an active state (Del Castillo and Katz, 1957; Gether, 2000;

Makita and Iiri, 2014). As described above, a ligand binding to the receptors' orthosteric site can cause a conformational change and subsequent receptor activation which leads to a response; such a ligand is called an agonist. Response to an agonist, at varying concentrations, can be measured experimentally and plotted as a concentration–effect curve (*in vitro*) or dose–response curve (*in vivo*) (Figure 1.2) with concentration referring to compound concentration, while dose refers to compound amount administered.

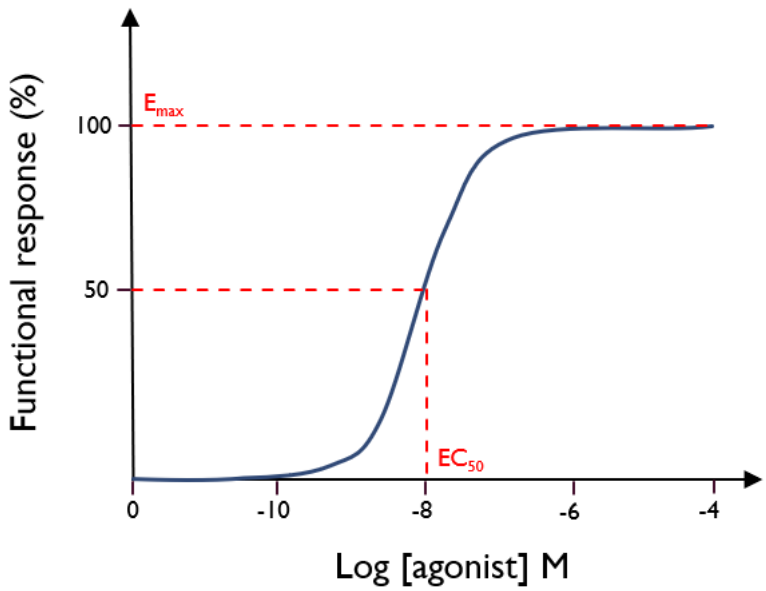

Figure 1.2. Representative concentration-response curve. Parameters that can be derived from a concentration-response curve are maximal response (E_{max}) and concentration required to produce half-maximal response (EC_{50}).

The experimentally derived concentration-response curve can then be fitted with the Hill–Langmuir equation (three-parameter logistic equation) (equation 1).

$$y = Basal + \frac{(E_{max} - Basal)}{1 + 10^{(logEC_{50} - x)^{n}}} \quad (1)$$

where y is the response, x is the agonist concentration, basal is minimal response of the system (sometimes also called E_{min}) and n is the Hill slope coefficient, which for many situations is equal to 1. This then allows for the estimation of the maximal response that the drug can produce (E_{max}), and the concentration or dose needed to produce a 50% of the maximal response (EC_{50}). These parameters describe a potency (EC_{50}) of a ligand and are useful for comparing different drugs among themselves, but it is important to keep in mind that dose-response curves cannot be used for measuring and

agonists affinity (k_i) of a drug. This is because of the existence of the so-called 'spare receptors' and the fact that maximum response of a tissue can be produced by agonists occupying less than 100% of the receptor (Stephenson, 1956). Therefore, to measure agonist affinity, it is best to measure the ligand binding to the receptor directly using techniques like radioligand binding assay.

1.4.1 Different types of GPCR ligands

There are different types of ligands that can exert their effects on GPCRs. Agonists was discussed above, which stimulate receptor response leading to changes in cell functions or other various effects. Agonist effect depends on two parameters – affinity and potency. Agonists can be further divided into full agonists that have high efficacy and can produce maximal results and partial agonists that have lower efficacy and can only produce submaximal effects (Figure 1.3) (Rang, 2019).

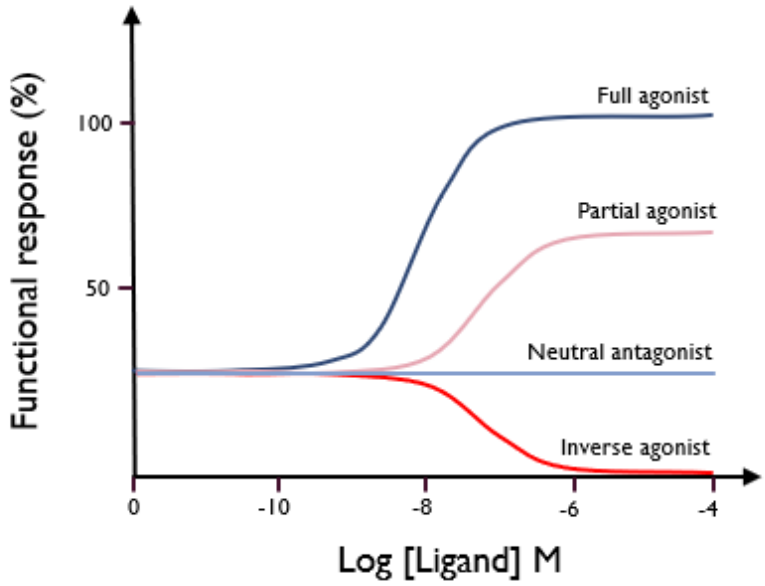

Figure 1.3. Representative dose-response curves for different types of GPCR ligands. Full agonists induce maximal response, while partial agonists induce submaximal (< 100%) response and their potency is also often reduced though it is not a rule. Inverse agonists than block constitutive receptor activity of GPCRs, resulting in reduced response overall. Neutral antagonists bind the GPCR blocking the binding site for other ligands, but on their own they elicit no response.

There is a different type of ligand that binds the receptor orthosteric site but does not activate it or cause any response. This type of ligand is called an antagonist and it has affinity for the receptor,

but no efficacy (Figure1.3). The most common type of antagonism is reversible competitive antagonism, where the antagonist competes with the agonist for the same orthosteric binding same thus reducing the receptor occupancy, i.e. proportion of receptors to which the agonist is bound. This antagonism is however surmountable as a high enough concentration of an agonist can overcome the blocking effect. This produces a characteristic reduction in agonist potency without a change in maximal response, when an antagonist is added to the experiment (Figure 1.4) (Rang, 2019). The second type of antagonism is irreversible competitive antagonism, where the antagonists also binds the orthosteric site, but because of a very slow dissociation rate from the receptor, the blocking effect cannot be overcome by increasing agonist concentration and the antagonist occupancy remains (Figure 1.4) (Rang, 2019). This also results in removing/reducing the spare receptor pool.

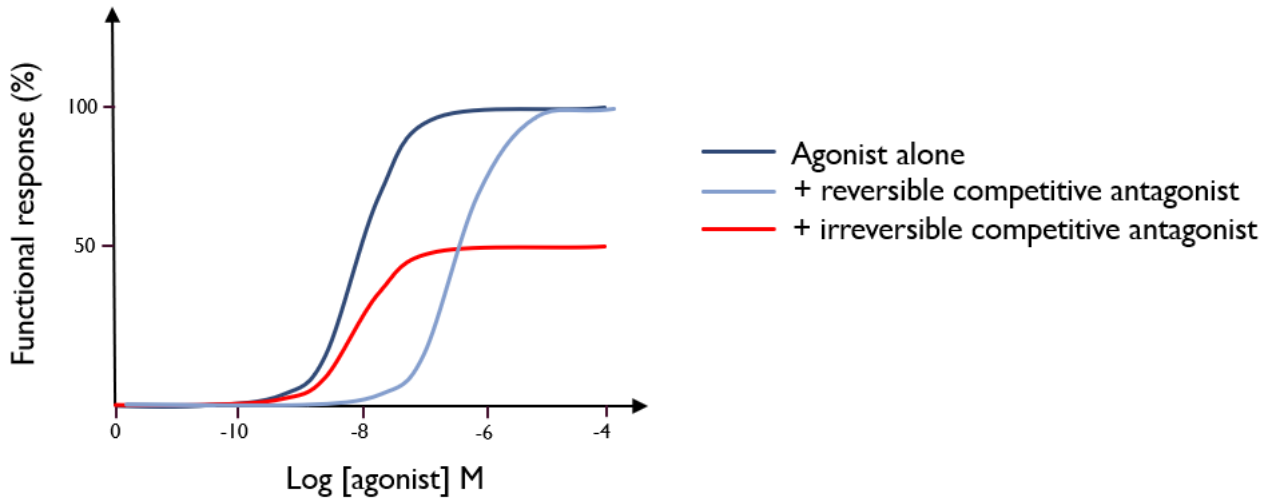

Figure 1.4. Representative dose-response curves of reversible and irreversible competitive antagonists. Addition of reversible competitive antagonist produces characteristic reduction in agonist potency without a change in maximal response as higher agonist concentration is required to outcompete the reversible competitive antagonist for its binding site. On the other hand, addition of irreversible competitive antagonists lowers the maximal response the agonist can produce by restring the number of free binding sites for the agonist.

Initially, it was postulated that a receptor could only be activated by an agonist binding. However, it was later shown that some GPCRs have appreciable levels of constitutive (agonist-independent) activity (de Ligt et al., 2000; Seifert and Wenzel-Seifert, 2002). Ligands that further diminish this inherent constitutive activity were then termed inverse agonists (Figure 1.4) (Costa and Herz, 1989; de Ligt et al., 2000; Sato et al., 2016). Both partial agonist and inverse agonists can reduce

the effects of a full agonist, which suggests that, in reality, a true neutral antagonist that has no agonistic or inverse agonistic activity is very likely to be rare.

All these different types of ligands can be inputted back into the two-state receptor model (Figure 1.5). As mentioned previously, GPCRs on their own are thought to be in an equilibrium between an inactive and active receptor state. Agonists shift this equilibrium towards the active receptor state, while inverse agonists shift it toward the inactive receptor state. Neutral antagonists do not affect the equilibrium it reduces the binding sites for other ligands by occupying the orthosteric binding pocket (Rang, 2019; Sato et al., 2016).

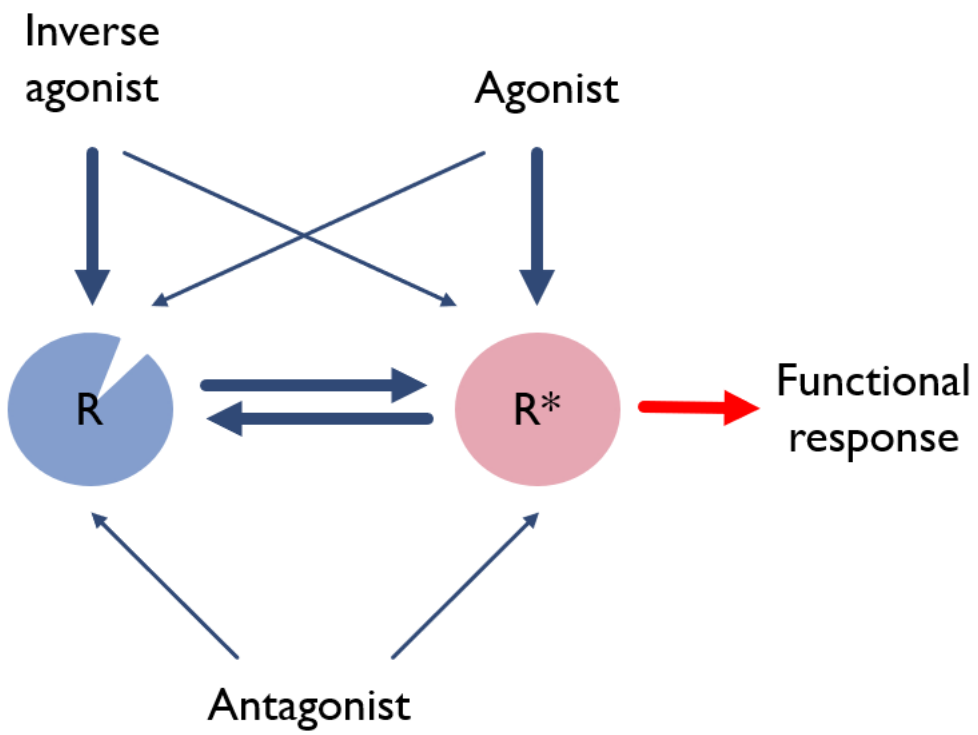

Figure 1.5. Two-state model of receptor activation. According to the two-state model, a receptor can exist in two conformations, resting (R) and activated (R*), which are in an equilibrium. Without any receptor present the receptor exist mainly in R conformation, but for constitutively active receptors, there is significant portion of the receptors in R* state. Agonists have higher affinity for the R* conformation shifting the equilibrium rightward and promoting functional response. Inverse agonists have preference for the R state shifting equilibrium leftward and inhibiting receptor constitutive activity. A neutral antagonist has same affinity for both states, so it does not shift the equilibrium on its own, but it reduces binding sites available for other ligands to bind. This figure was adapted from (Rang, 2019).

1.4.2 The operational model of pharmacological agonism

The problem with fitting dose-response curves with Hill–Langmuir equation is that it does not quantify efficacy and cannot differentiate between partial agonism and receptor depletion (Wacker et al., 2017). To overcome this, Black and Leff (1983) introduced the 'operational model of pharmacological agonism' that separates receptor occupation from agonist-mediated response (equation 2).

$$E = \frac{E_{max}\tau[A]}{K_A+(\tau+1)[A]} \tag{2}$$

where E is a response, E_{max} is the maximal response, [A] is the ligand concentration, τ is intrinsic efficacy of the agonist and K_A is intrinsic affinity. The intrinsic efficacy of the agonists can be further broken down to the total receptor concentration (R_0), and the transduction coefficient of the agonist-receptor complex (K_E) (equation 3).

$$\tau = \frac{R_0}{K_E} \tag{3}$$

It is also possible to obtain the EC_{50} parameter using the equation below (equation 4).

$$EC_{50} = \frac{K_A}{(\tau+1)} \tag{4}$$

The model therefore provides a standardised method for the estimation of ligand affinity and operational efficacy from experimentally derived hyperbolic dose-response curves and measured EC_{50} and E_{max} parameters as well as known agonist concentration.

1.4.3 The concept of biased agonism and how this relates to GPCR signal transduction

During the last few years, several important studies have revealed GPCR signalling to be much more complex and multidimensional than it was originally thought due to the concepts of biased signalling, oligomeric formation, and compartmentalized signalling (Shchepinova et al., 2020). Biased agonism (also referred to as signalling bias or functional selectivity) refers to the ability of different ligands to induce different receptor conformations which can interact with different intracellular binding partners to varying extents (Wootten and Miller, 2019). Activated GPCRs can interact with different intracellular proteins – namely heterotrimeric G proteins and β-arrestins – which then promote different signalling cascades and effects in the cells. Most ligands targeting GPCRs are thought to equally target distinct signalling pathways similarly to the endogenous reference agonist (also called the balanced agonist) and the same is thought to be true for most antagonists equally inhibiting all second messenger systems activated by the agonists (Smith et al., 2018). However, over the last two decades, it became appreciably evident that some ligands activate or block certain signalling pathways

to more than other (Jarpe et al., 1998; Luttrell, 2014). An example would be GLP-1 receptor (GLP-1R) ligand oxyntomodulin that activates the β-arrestin mediated ERK1/2 phosphorylation more that the G protein-mediated signalling compared to the endogenous reference ligand GLP-1 (Figure 1.6) (Wootten et al., 2016). Based on their effect on G proteins and β-arrestin1/2 signalling, agonists can either be balanced (affecting all signalling cascades equally), G protein biased (promoting general G protein signalling over β-arrestin1/2 signalling), β-arrestin biased (promoting β-arrestin1/2 signalling over G protein signalling) or G protein subtype biased (promoting signalling of a specific G protein over the rest of G proteins and βarrestin1/2 signalling) (Wall et al., 2022).

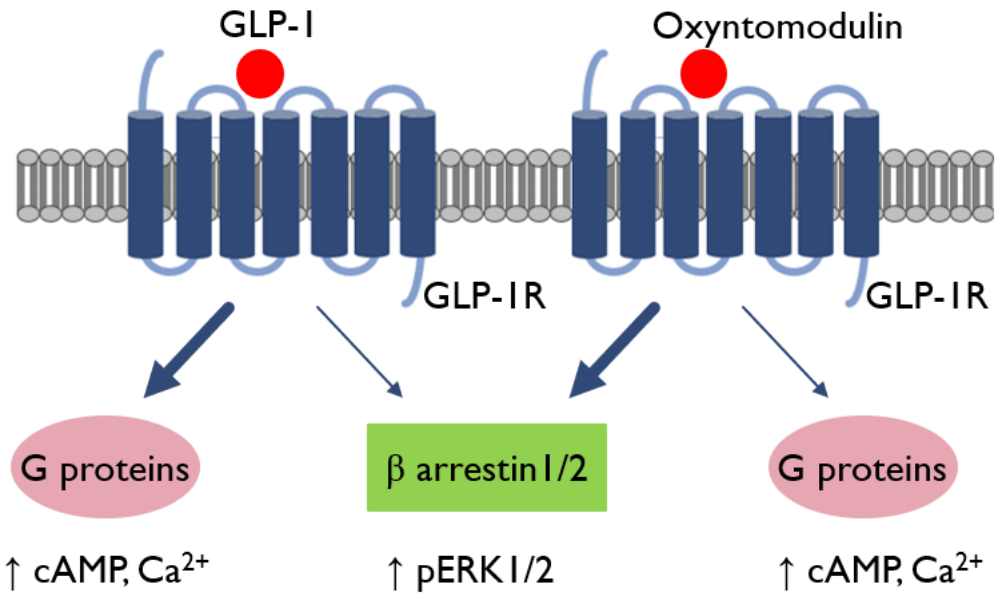

Figure 1.6. Biased signalling at GLP-1R. Oxyntomodulin is a β-arrestin1/2 biased ligand at the GLP-1R compared to the endogenous reference ligand GLP-1. The biased signalling can be measured using the functional essay measuring intracellular cAMP and calcium levels (G protein signalling) or ERK1/2 phosphorylation (β-arrestin1/2 signalling). Figure adapted from Wootten et al. (2016).

To quantify levels of bias can be tricky as bias is also relative among two or more ligands or in reference to the endogenous reference ligand. Different transducer expression profiles of different cells can also mean that a ligand that looks to be G protein subtype biased in one cell might look like a balanced agonist in another one with different G protein subtype expression. When quantifying bias, how sensitive and how much amplification there is in the methods chosen to measure each signalling pathway must also be considered. For example, a common way of measuring $G\alpha_s$ or $G\alpha_i$ activity is by measuring the accumulation of the downstream effector cAMP. By this point, however, the signalling

cascade has generated a large amount of amplification compared to, for example measuring β-arrestin recruitment assay, where the ratio of GPCR to β-arrestin is 1:1. Another important aspect is the temporal dynamics of signalling (Grundmann and Kostenis, 2017). Different signalling cascades take different times to generate their response (e.g. ERK1/2 phosphorylation vs $(Ca^{2+})_i$ mobilisation), so GPCR signalling can appear biased towards one pathway if we only look at one snapshot of the time (Klein Herenbrink et al., 2016). Typical techniques for measuring and quantifying bias at GPCRs are second messenger assays like cAMP accumulation, $(Ca^{2+})_i$ mobilisation and ERK1/2 phosphorylation. But because of the issues raised above like amplification, it is become increasingly popular to look more directly at G protein and β-arrestin recruitment using techniques like the bioluminescence resonance energy transfer (BRET) based TRUPATH system (Olsen et al., 2020).

Biased agonism can be detected with at minimum two measures of cellular function like EC_{50} and E_{max}, since EC_{50} alone will differ with different maximal response. This is where the operational model of agonism comes in handy again as it separates receptor activity into affinity, stimulus and efficacy as described above (Black and Leff, 1983). Biased agonism can than be quantified by calculating a transduction ratio (also called transduction coefficient) $Log(\tau/K_A)$, where τ is the intrinsic efficacy of the agonist and K_A is the intrinsic affinity of the agonist. This transduction ratio can then be normalised to a reference agonist and reference pathway for each agonist at each pathway allowing comparison of signalling bias among different agonists and pathways (Kenakin et al., 2011). Another measure that can be used for comparing biased agonism is relative activity (RA) (equation 5)

$$RA = \frac{E_{max} * EC_{50}(reference\ compound)}{EC_{50} * E_{max}(reference\ compound)} \quad (5)$$

where E_{max} is the maximal response and EC_{50} is the negative logarithm of the agonist concentration required to produce a half-maximal response. The Operational model of agonism and the relative activity method are mathematically identical when the Hillslope is 1. It is also common to show signalling bias graphically using either bias plots or 'web of bias'. Bias plot have the advantage of not introducing errors due to different fitting approaches, but they can not account for system bias and only compares two effector responses. Web's of bias, on the other hand, are more complex and graphically shows bias towards or away from multiple effectors.

As each ligand is chemically distinct from another, it can form distinct interactions with the receptor amino acids. These unique interactions can be propagated through the receptor and give rise to different functional effects (Kenakin, 2012; Klein Herenbrink et al., 2016; Shonberg et al., 2014). This can then result in differential recruitment of G proteins or β-arrestins or they can alter GPCRs interactions with their regulatory proteins like GRKs. A big step towards understanding the way these changes are propagated through the receptor in response to biased agonist was the first GPCR

structure bound to a biased agonist - GLP-1R bound to G protein biased exendin-P5 solved by cryo-EM (Liang et al., 2018b). Binding of exendin-P5 promotes different organization of extracellular loop 3 and proximal transmembrane segments at the extracellular surface compared to the endogenous reference ligand GLP-1. There is also slight differences in the angle of the $G\alpha_s$–α5 helix engagement between structures, which was propagated across the G protein heterotrimer and results in a different rate and extent of conformational reorganisation of $G\alpha_s$. The broad and diffuse pharmacophores of class B GPCRs like GLP-1R normally occupied by peptide ligands are not readily mimicked by small molecule ligands, gives great propensity for biased signalling at these receptors in particular (Wootten et al., 2017, 2016).

Biased signalling can be due to other reasons than simply differential recruitment of intracellular effectors. It was shown, for example that reference and biased ligands engaging a GPCR differently can be propagated down to β-arrestins and result in multiple active conformations of β-arrestin, which can then result in different trafficking and signalling functions of those β-arrestins (Lee et al., 2020; Shukla et al., 2008). For G proteins, the rate of GTP binding and G protein residence time can be affected. Following activation by biased ligands, GPCRs can also change their interactions with regulatory or scaffolding proteins resulting in a change in receptor trafficking and compartmentalization that may in turn alter the nature of cellular signalling (Wootten et al., 2017). For example, GRKs recruited by reference agonist isoproterenol andβ-arrestin biased ligand carvedilol phosphorylate the serine and threonine residues in the carboxyl-terminal tail and the intracellular loops of β2-adrenoreceptor differentially resulting in a phosphorylation barcode that imparts a specific conformation onto the recruited β-arrestin (Nobles et al., 2011).

If the signalling bias is relative and dependent on a specific system, the question remains, “is signalling bias physiologically relevant and can it be exploited in drug discovery?”. Biased agonism holds promise for improving drug efficacy, which is a major cause of drug failure, and most importantly for lowering side effects by selectively targeting specific transducers. An example would be GLP-1R agonist P5, which is a G protein biased agonist compared to GLP-1 or Exendin-4 already in the clinic and that has been shown to be more effective at reducing hyperglycaemia and haemoglobin A1c levels in diabetic mice, suggesting it might provide better treatment for diabetes mellitues type 2 than balanced agonists (Zhang, 2015).

1.4.4 The role of allosteric modulation in GPCR pharmacology

Due to commonly using radioligand binding assay for drug discovery in the past, the majority of know compounds and approved drugs targeting the GPCRs are orthosteric ligands. However, the past two decades have witnessed substantial efforts into identifying alternative methods of modulating GPCR activity, specifically by targeting topographically distinct allosteric sites. An allosteric modulator is defined as "a ligand which modifies the action of an orthosteric agonist, endogenous activator or antagonist by combining with an allosteric site on the receptor macromolecule" (Christopoulos et al., 2014). Allosteric sites being spatially distinct from orthosteric sites means that it is possible for allosteric modulators to bind simultaneously with orthosteric ligands. Well known examples of allosteric modulators approved by FDA include maraviroc, which is an antiviral drug negatively modulating class A GPCR chemokine receptor type 5 (CCR5), cinacalcet, which positively modulates calcium-sensing receptor (CaSR) in hyperparathyroidism, and ticagrelor, which targets P2Y receptor in order to prevent stroke or heart attack (Conn et al., 2009; Karlshøj et al., 2016; Wold et al., 2019).

The fact that the allosteric modulator and orthosteric ligand can potentially bind the receptor simultaneously means that they can influence the behaviour of each other, which is termed cooperativity (Christopoulos et al., 2014; Gentry et al., 2015; Wootten et al., 2013a). This cooperativity can then affect both the affinity and the efficacy of the ligand (Wootten et al., 2017). Allosteric modulators can be divided into positive allosteric modulators (PAMs), which produce a net enhanced effect on the receptor function, negative allosteric modulators (NAMs), which diminish receptor signalling or neutral allosteric ligands (NALs), which bind the allosteric site on the receptor without altering the function of the receptor (Figure 1.7) (Christopoulos et al., 2014). It is also possible to have PAMs with intrinsic activity, which are termed ago-PAMs (Foster and Conn, 2017).

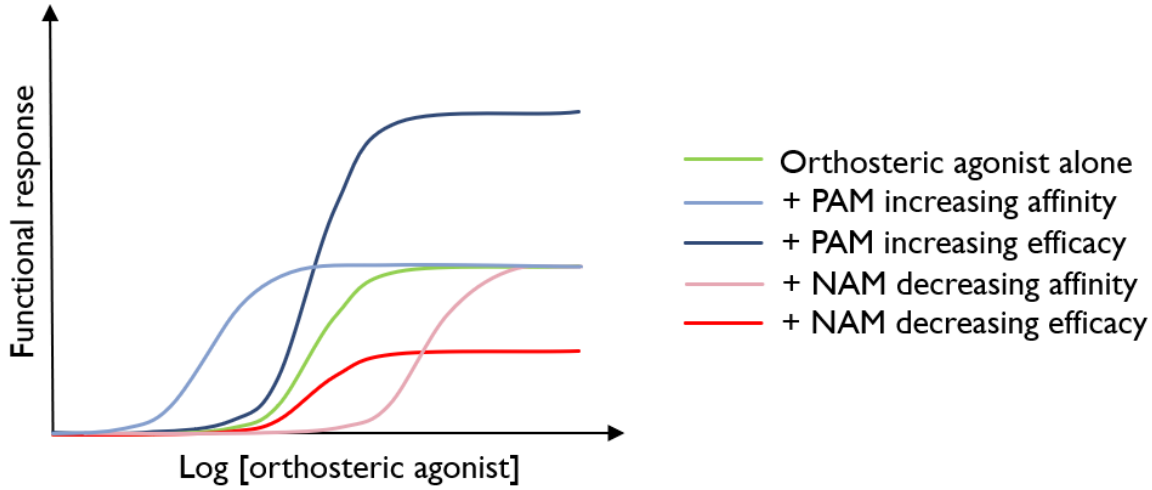

Figure 1.7. Representative dose-response curves for different types of allosteric modulators. Addition of PAM or NAM affecting efficacy results in the increase or decrease of maximal response produced by the orthosteric ligand, respectively, while addition of PAM or NAM affecting affinity will result in the leftward or rightward shift of the orthosteric ligand dose-response curve, respectively.

To be able to quantify allosteric modulators, operational model of agonism was built upon to create the operational model of allosterism, which includes an allosteric ligand (equation 6) (Leach et al., 2007).

$$E = \frac{E_{max}(\tau_A[A](K_B + \alpha\beta[B]) + \tau_B[B]K_A)^n}{([A]K_B + K_AK_B + K_A[B] + \alpha[A][B])^n + (\tau_A[A](K_B + \alpha\beta[B]) + \tau_B[B]K_A)^n} \quad (6)$$

where E is the response, E_{max} is the maximal response, EC_{50} is the concentration of the ligand required to achieve half maximal response, [A] is the concentration of the orthosteric ligand, [B] is the concentration of the allosteric ligand, n is the Hill slope, K_A is the intrinsic affinity of the orthosteric ligand, K_B is the intrinsic affinity of the allosteric ligand, τ_A is the capacity of agonism exhibited by the orthosteric ligand and τ_B is the capacity of agonism exhibited by the allosteric ligand. The τ_A and τ_B values incorporate in themselves the intrinsic efficacy of each ligand, the total density of receptors and the efficiency of stimulus-response coupling. The key factors are the cooperativity factor (α), which measures the strength and direction of allosteric effect on affinity for one binding site when the other is occupied, and β, which quantifies allosteric effect on efficacy. These two can then be combined into a cooperativity factor (Logαβ), which therefore takes into account the allosteric effect on both affinity and efficacy. When this cooperativity factor is bigger than 1, the allosteric modulator is considered as a PAM. When it is less than 0, the allosteric modulator is considered as a NAM. Otherwise, the allosteric modulator is considered NAL (Jakubík et al., 2020; Leach et al., 2007).

Allosteric modulators can be very useful, which is evidenced by their natural occurrence in the cells. GPCRs can for example be modulated by ions or lipids. Sodium ions are suggested to have their own allosteric pocket on many GPCRs, including dopaminergic ones, located in close proximity to the conserved $Asp^{2.50}$ residue (Selent et al., 2010; Yuan et al., 2013) and lipophilic 2-arachidonylglycerol negatively modulates the adenosine 3 receptor (A_3R) (Lane et al., 2010). Regarding protein allosteric modulators, receptor activity-modifying proteins (RAMPs) are important. RAMPs are single transmembrane spanning proteins about 150 amino acids long and there are 3 subtypes RAMP1, RAMP2 and RAMP3(Hay and Pioszak, 2016). RAMPs are most studied in complex with calcitonin receptor-like receptor (CLR), where they chaperone CLR to the membrane and effect its signalling. CLR complexing with RAMP1 results in affinity for calcitonin gene-related peptide (CGRP), while complexing with RAMP2 results in affinity for adrenomedulin, and with RAMP3 to both adrenomedulin and CGRP (McLatchie et al., 1998). RAMPs interaction are, however, not limited just to CLR, but have been now shown for most class B GPCRs and even few class A and C GPCRs (Mackie et al, 2017).

1.4.4.1 Therapeutic potential of allosteric modulators of GPCRs

Allosteric modulation also has a great potential for drug discovery due to several key characteristics dissimilar to orthosteric ligands. The hallmark of allosteric modulators is their probe dependency, which means that the effect of an allosteric drug is specific to the orthosteric ligand present (May et al., 2007). This is particularly true for the example for class B1 GPCRs which typically respond to some degree to more than one peptide ligand. GLP-1R, for example, responds to GLP-1, oxytomodulin and glucagon and GLP-1 allosteric modulator can have a different level of effect on GLP-1R response induced by each of these agonists due to different levels of cooperativity between the allosteric and orthosteric ligands (Wootten et al., 2017). Allosteric modulators lack intrinsic efficacy, which means their effects can only be seen when orthosteric agonist is present. This can be useful in diseases like type 2 diabetes mellitus, where PAMs of incretin receptors can promote insulin secretion only when incretin hormones are already present leading to more physiological insulin release compared to sustained insulin release following long-acting GLP-1 mimetic drugs (this will be discussed in greater detail later) (Bueno et al., 2016; Koole et al., 2013; Wootten et al., 2017).

The saturable effect of allosteric drugs can also make them safer as the maximal effect can be controlled by the endogenous ligand. This is also called the ceiling effect, where increasing doses of a drug have progressively smaller incremental effects, which is likely to prevent overdosing and related safety concerns. It was mentioned before that μ-opioid receptor is an important target in analgesia, but long-term administration of high doses of μ-opioid agonists leads to respiratory depression, nausea

and development of addiction and tolerance. Livingston and Traynor (2016) have shown that μ-opioid PAM called BMS-986122 enhance μ-opioid signalling resulting in less agonist needed and less side effects. They have also shown BMS-986122 to be G protein biased, in line with above discussed hypothesis that μ-opioid G protein biased signalling is the way forward. This is a nice example showing that allosteric ligands can also be biased and have response selectivity (Wootten et al., 2017). Another example here would be thegadolinium ion (Gd^{3+}), which is a PAM at metabotropic glutamate receptor 1 (mGluR1) promoting $G\alpha_q$-mediated calcium mobilisation while having no effect on $G\alpha_s$-mediated cAMP accumulation (Abe et al., 2003).

Moreover, allosteric modulators have great potential for subtype selectivity, as there is often much higher sequence divergence among allosteric sites of receptor subtypes relative to their orthosteric site (Gentry et al., 2015; Wootten et al., 2013a). A proof of concept of this can be seen for example at muscarinic acetylcholine (Ach) receptors (mAChRs), which have five different subtypes M_{1-5} that share a conserved ACh binding site. Lazareno et al. (2004) shows that PAM thiachrome increases ACh binding at M_4, while having no effect at the other subtypes. For class B1 GPCRs another advantage could be the better likelihood of developing small molecule drugs that are allosteric modulators rather than orthosteric agonists. The large and diffuse pharmacophores of class B GPCRs naturally bind peptide ligands and mimicking these many interactions with small molecule drugs that are orally available and cheaper has been challenging. A smaller and narrower allosteric site might therefore be more druggable (Wootten et al., 2017).

Despite the apparent benefits of allosteric modulators, there is only a handful that has yet reached the clinic. This may be partly due to the difficulties of identifying a good allosteric site. Just because a compound is binding the receptor outside of the allosteric site does not mean it will influence the orthosteric ligand affinity or efficacy. It is often this lack of understanding of the connection between binding the receptor and affecting the orthosteric ligands that is hindering the development of potent allosteric modulators (Congreve and Marshall, 2010). Secondly, allosteric sites show plasticity and many allosteric modulators bind in an induced-fit way (Chatzigoulas and Cournia, 2021; Christopher et al., 2017; Leander et al., 2020). The main technique for allosteric modulator drug discovery is combination of *in silico* screening and docking approaches with subsequent *in vitro* testing but various competition binding assays (including radioligand binding assay) used for orthosteric ligands are mostly unsuitable because there is often no compound with which to compete for binding. Furthermore, most *in silico* techniques work with a rigid snapshot of the receptor and may therefore miss some allosteric sites and compounds binding there (Chatzigoulas and Cournia, 2021; Christopher et al., 2017).

Taken all together, allosteric modulators hold great promise for therapeutical use due to their probe dependency and their potential for increasing selectivity and reduced side effects, which has been mirrored in many promising studies. However, low potency, lack of understanding or receptor function and challenging drug discovery of allosteric modulators means that not many have yet been approved and reached the clinic.

1.5 Overview of GPCRs explored in this thesis

GPCRs are important drug target for many diseases and receptors explored in this study as targets are described in more detail below. This thesis explores drug discovery namely at adenosine receptors (ARs), members of Class A GPCRs, and GIP receptor (GIPR), member of class B1 GPCRs. The *in silico* and *in vitro* pharmacological validation of GIPR allosteric modulators will be in discussed in chapters 3 and 4, while the development of ARs agonists and antagonists, targeting A_1R and A_3R in particular, will form chapters 5 and 6.

1.5.1 The adenosine receptor subfamily

Adenosine receptors family consists of 4 different receptor subtypes – A_1R, $A_{2A}R$, $A_{2B}R$ and A_3R, each with its own unique tissue distribution, pharmacological profile and effector coupling (Figure 1.8) (Chen et al., 2013). All four of the receptor subtypes are widely distributed in human tissue, however differential expression patterns varying among different cell types and in response to pathological stresses mean that each subtype is associated with unique functions and presents opportunity for medical intervention in various set of diseases. Importantly, $A_{2A}R$ and $A_{2B}R$ couple predominantly to $G\alpha_s$ leading to increase in intracellular cAMP, while A_1R and A_3R are predominantly $G\alpha_i$ coupled leading to decrease of cAMP levels in the cell (Chen et al., 2013).

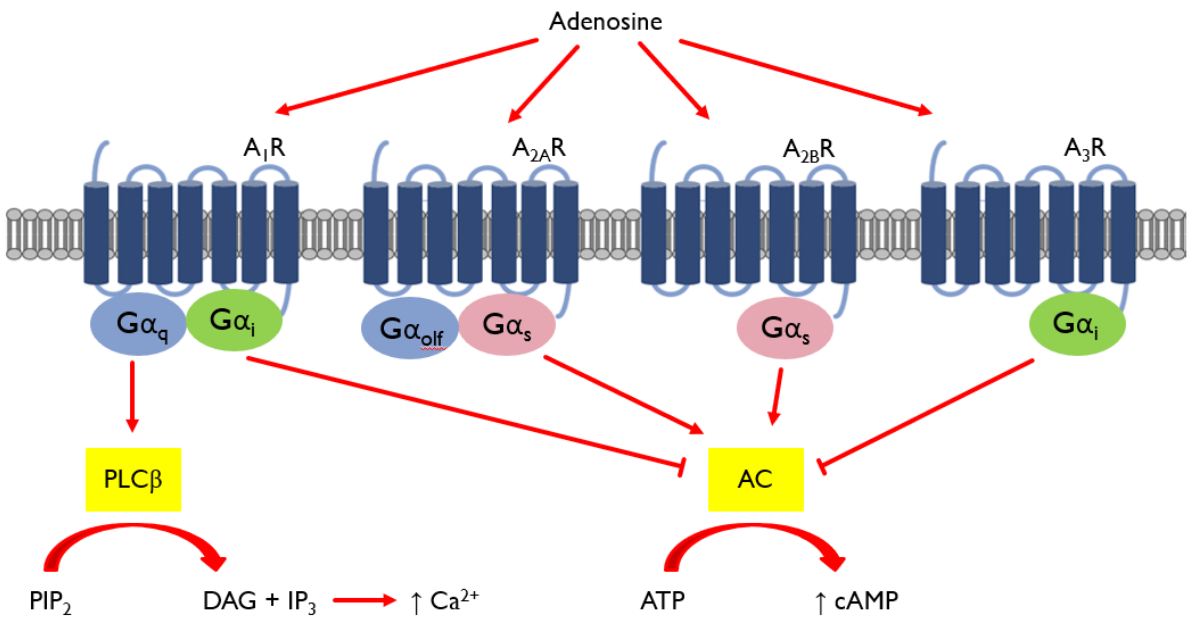

Figure 1.8. An overview adenosine receptor-mediated intracellular signalling. A_1R and A_3R couple to $G\alpha_i$ subunit resulting in inhibition of AC and decrease in intracellular cAMP levels, while $A_{2A}R$ and $A_{2B}R$ couple to $G\alpha_s$ resulting in activation of AC and increase in intracellular cAMP levels. $A_{2A}R$ can also couple to $G\alpha_{olf}$ in olfactory neurons, while A_1R can couple to $G\alpha_q$ resulting in activation of PLCβ and signalling cascade resulting in increased calcium levels in the cell.

Adenosine receptors have been implicated in many diseases including, but not limited to, cardiac disfunctions, angiogenesis, inflammatory diseases or neurodegenerative disorders (Eltzschig, 2009; Fredholm, 2007; Haskó et al., 2008; Lazarus et al., 2011) and the development of potent and selective synthetic agonists and antagonists targeting these receptors have been going for more than three decades (Jacobson and Gao, 2006). However, so far only one drug targeting the ARs have been approved by the FDA. It is Lexiscan (also known as regadenoson) that has been approved for injection as a pharmacologic stress agent in radionuclide myocardial perfusion imaging (MPI) (Al Jaroudi and Iskandrian, 2009; Buhr et al., 2008). However, despite large efforts and several big phase III clinical trials most other drugs targeting the ARs have failed owing to insufficient efficacy and/or bad side effects (Chen et al., 2013). This leaves a big untapped potential for ARs as drug targets with the need for more tissue and/or subtype selective drugs to limit the site effects.

A great promise for drug discovery in general, and for ARs in particular, is the number of crystal and cryo-EM structures solved in the past decade, which enables better understanding of compound binding and effect at the receptor and combination of *in silico* and *in vitro* approaches for drug discovery. $A_{2A}R$ receptor is one of the best structurally characterise GPCRs; there are multiple

structures available both agonist- and antagonist-bound (Cheng et al., 2017; Rucktooa et al., 2018; Segala et al., 2016). For the A_1R there are (at the time of writing) five structures available including those bound to native agonist adenosine (Draper-Joyce et al., 2021, 2018) or antagonist (Cheng et al., 2017; Glukhova et al., 2017) or even with allosteric modulator (Draper-Joyce et al., 2021). For $A_{2B}R$ and A_3R we are still waiting on the first structures to be solved, but this can be partly overcome by homology modelling, where the *in silico* structure of a receptor is model based on closely related receptor – $A_{2A}R$ or A_1R in this case (Barkan et al., 2020; Lagarias et al., 2020, 2019; Suchankova et al., 2022).

1.5.1.1 Adenosine 1 receptor

The A_1R is widely expressed in human body with highest expression levels found in the brain, especially at the excitatory nerve endings (Daly and Padgett, 1992). It is also the most conserved adenosine receptor subtype among species, which might make drug discovery and confirming *in vitro* results in animal tissues slightly easier (Fredholm et al., 2000). The A_1R predominantly couples to $G\alpha_{i/o}$ subunits leading to inhibition of AC and decrease in intracellular cAMP levels, but it can also couple to $G\alpha_q$ leading to PLC-β activation and increase of $(Ca^{2+})_i$ (Chen et al., 2013). In the nerve endings A_1R activation leads to blocking of neurotransmitter release and reducing the firing rate.

A_1R plays an important role in many conditions including the treatment of glaucoma, type 2 diabetes mellitus, cardiac disorders, pain and cerebral ischemia and agonists are of particular interest (Deganutti et al., 2020; Glukhova et al., 2017; Wall et al., 2022, 2020). Johansson et al. (2001) has shown that the A_1R gene in mice results in more anxious mice with decreased hypoxic neuroprotection and abolishment of analgesic effect of intrathecal adenosine, establishing the importance of A_1R under pathophysiological conditions including painful stimulation and hypoxia. A_1R agonists have been shown to inhibit pain in the spine (Borghi et al., 2002). The problem with using A_1R agonists for pain treatment is, however, the often-accompanying sedation. Sevoflurane has been shown to activate A_1R in primary rat hippocampus and has been advocated for use in routine anaesthesia in ambulatory surgery patients (Fredholm et al., 2011). Biased agonism or modulation could be one of the ways how to differentiate between the various promising and adverse effects of A_1R activation. Draper-Joyce et al. (2021) have introduced an A_1R PAM MIPS521 and showed it has analgesic efficacy in rats *in vivo* without affecting motor functions (like opioid analgesics) or inducing off-tissue bradycardia that is a major concern for A_1R agonist use as analgesics. A_1R partial agonists are also investigated for treatment for hypertriglyceridemia associated with diabetes (compound GS9667 by Gilead Sciences) or treatment of atrial fibrillation (compound Capadenoson by Bayer Schering Pharma) (Fredholm et al., 2011).

There has also been some investigation into antagonising the A_1R receptor and several companies are investigating selective A_1R antagonists as diuretics due to preglomerular arterioles in the kidney uncommonly constricting in response to A_1R activation. The PROTECT pilot study demonstrated that A_1R antagonist rolofylline can improve acute symptoms in patients with acute heart failure and renal impairment, although PROTECT-2 study failed to demonstrate clinical efficacy (Cotter et al., 2008; Fredholm et al., 2011).

Preceding the work in this thesis, a BnOCPA compound based on an adenosine structure has been identified from a structure-activity relationship (SAR) study (Knight et al., 2016) and was subsequently shown to selectively activate $G\alpha_{ob}$ subunit resulting in potent in vivo analgesia without causing sedation, bradycardia, hypotension or respiratory depression (Wall et al., 2022). This follows on the above discussed point that biased agonism could provide a mean to differentiate between wanted and unwanted effects following A_1R activation, but there is still a need to further improve upon BnOCPA for even more potent but still A_1R selective compounds.

The endogenous agonist adenosine is nonselective among the AR subtypes, but several A_1R-selective compounds based on adenosine scaffold have been introduced in the past few years. It has been shown that substitutions at the purine C-2 position of adenosine with for example chlorides and at the N^6 position with cycloalkyl- and bicycloalkyl groups leads to potent A_1R-selective compounds (Chen et al., 2013; Jacobson et al., 2019; Knight et al., 2016; Petrelli et al., 2018; Tosh et al., 2019). Of interest is also the C-5 position, where 5'-carboxamido group substitution yields a well-known very potent but non-selective agonist NECA, while 16 has shown that bulkier pyrazole group yields selective A_1R agonist with analgesic effects in mice.

1.5.1.2 Adenosine 2A and 2B receptor

$A_{2A}R$ is most highly expressed in the brain, immune cells of the spleen, thymus, leukocytes and blood platelets, while $A_{2B}R$ is widely expressed across the whole human body but in low quantities (Fredholm et al., 2011, 2001). $A_{2A}R$ and $A_{2B}R$ are predominantly $G\alpha_s$-coupled receptors leading to activation of PKA and increase in intracellular cAMP, but $A_{2A}R$ has also been shown to couple to $G\alpha_{olf}$ in the brain (Corvol et al., 2001; Fredholm et al., 2000; Kull et al., 2000). The endogenous agonist for both receptors is the adenosine, but $A_{2B}R$ has the lowest affinity for adenosine among all the AR subtypes requiring micromolar adenosine concentrations, which is rare under physiological conditions, but can happen in hypoxia, ischaemia or inflammation making $A_{2B}R$ a target in these conditions (Chen et al., 2013; Eckle et al., 2012, 2008). Due to its high expression in the brain, it is unsurprising to find

$A_{2A}R$ is a target in psychiatric disorders or in regulation of sleep-wake cycle, but it has also been implicated in coronary disfunctions, angiogenesis and cancer (Chen et al., 2013; Eltzschig et al., 2012)

1.5.1.3 Adenosine 3 receptor

A_3R has originally been isolated from rat testis and sequence homology of the TMD was used to identify it as part of the adenosine receptor family (Meyerhof et al., 1991). A_3R is $G\alpha_i$-coupled receptor resulting in inhibition of intracellular cAMP levels and is widely expressed in the human body with especially hight amounts in lung and liver (Salvatore et al., 1993). Somewhat limiting for drug discovery is the fact that A_3R has considerable variation in the pharmacology and distribution among species, meaning its more challenging to translate studies from human receptor to animal tissues and then to humans once more (Chen et al., 2013). A_3R signalling has been linked to, for example, rheumatoid arthritis, Crohn's disease and mast cell deregulation (Ochaion et al., 2009; Zhong et al., 2003). Salvatore et al. (2000) showed that targeted disruption of A_3R led to failure of Cl-IB-MECA (A_3R agonist) to enhance antigen-stimulated mast cell degranulation. It was also suggested that A_3R deletion has cardioprotective effect from ischemic injury by reducing myocardial mast cell degranulation (Guo et al., 2001; Rork et al., 2008), but this was negated by Ge et al. (2006) showing cardioprotective effect of A_3R activation. A_3R was also found highly upregulated in various cancer cells, particularly colon cancer, making it a possible biological tumour marker (Gessi et al., 2004).

Typical A_3R-selective agonists are IB-MECA and Cl-IB-MECA that have been widely used for pharmacological studies of A_3R. IB-MECA has about 30-fold selectivity for rat A_3R over the other subtypes (Jacobson, 1998) and is in clinical trials for treatment of autoimmune anti-inflammatory diseases, including rheumatoid arthritis (RA) and psoriasis (Fishman et al., 2012). IB-MECA was also in clinical trials for dry eye disease and glaucoma, but failed to demonstrate sufficient efficacy (Avni et al., 2010; Jacobson and Gao, 2006). A_3R agonism was also closely investigated in relation to cardio protection, primarily in the context of ischaemia-reperfusion injury. Germack and Dickenson (2006)showed that Cl-IB-MECA pre-treatment induced ischaemic preconditioning in neonatal rat cardiomyocytes.

A_3R antagonists have seen less clinical progress than agonists, but hold a great therapeutic potential in multiple pathological dysfunctions including glaucoma, respiratory disorders or inflammation (Chen et al., 2013). Avila et al. (2002) shows that A_3R-knockout mice have lower intraocular pressure, suggesting A_3R antagonists might be a nice alternative for glaucoma treatment. Adenosine-induced bronchoconstriction is a well-recognised feature of atopic asthma and it is thought that A_3R-induced mast cell degranulation and subsequent release of inflammatory mediators is partly

to blame (Leung et al., 2014; Tilley et al., 2003). This is supported by the fact that A_3R-knockout mice have reduced airway responsiveness to aerosolised adenosine, compared to wild-type mice (Tilley et al., 2003). Furthermore, this anti-inflammatory characteristic of A_3R antagonists could prove beneficial not only in asthma but also in chronic obstructive pulmonary disease (COPD). To this end, Young et al. (2004) showed that treatment of adenosine deaminase (enzyme involved in adenosine breakdown) deficient mice with A_3R-selective antagonist MRS1523 prevented airway eosinophilia and mucus production.

A_3R signalling has also been implicated in neurological disorders. A_3R has proconvulsant effect in immature brain and A_3R activation decreases stability of inhibitory GABAA signalling currents in epileptic human mesial temporal lobe (Boison, 2008; Roseti et al., 2009). This suggests that A_3R antagonists could be a useful treatment in refractory epilepsy. Furthermore, Zhu et al. (2007) shows that A_3R agonist IB-MECA stimulates serotonin (5-HT) reuptake in mouse midbrain, hippocampal, and cortical synaptosomes and this is absent in A_3R knockout mice and blocked by A_3R antagonist MRS1191. A_3R antagonist could therefore be useful for elevating extracellular 5-HT levels in hyposerotonergic disorders like major depressive disorder. Ultimately, there is a large untapped potential for novel A_3R antagonists.

1.5.2 Glucose-dependent insulinotropic polypeptide receptor

GIPR is a ubiquitous G protein-coupled receptor with the highest expression levels in pancreatic β cells, adipose tissue and in certain parts of the brain (Adriaenssens et al., 2019; Beaudry et al., 2019; Naylor et al., 2016; Nitz et al., 2007). Multiple single nucleotide polymorphisms of GIPR were also identified and associated with cardiovascular disease, increase low-density lipoprotein (LDL) cholesterol and type 2 diabetes mellitus (T2DM) (Nitz et al., 2007; Shalaby et al., 2017; Sugunan et al., 2010). GIPR expression profile and its physiological signalling, which will be explored in detail later, make it a target in T2DM, obesity, neurological disorders like Alzheimer's or Parkinson's disease and even in maintenance of bone health (Schiellerup et al., 2019; Verma et al., 2018).

1.5.2.1 Type 2 diabetes mellitus and obesity

Diabetes and obesity are huge globe health issues. The number of adult people with diabetes has increased from 108 million in 1980 to 422 million in 2014, which is almost a doubling in global prevalence from 4.7% to 8.5% (Roglic, 2016). In obesity, 108 million children and 604 million adults estimated to be clinically obese in 2015, which is more than double of what it was in 70 countries in 1980 (GBD 2015 Obesity Collaborators et al., 2017). The serious health risks associated with these

diseases are a major burden on the healthcare system. Every week diabetes leads to 169 amputations, 680 strokes and almost 2000 cases of heart failure in UK alone the and NHS spends about £10 billion a year on diabetes, which is worth ~10% of their entire budget (Diabetes UK, 2019). The global economic burden of associated healthcare risks and loss of productivity is them estimated to be approximately US $1.3 trillion for diabetes in 2015 and US $2 trillion for obesity in 2014 (Bommer et al., 2018). Out of all people diagnosed with diabetes, 90% have type 2. T2DM is a chronic metabolic disorder characterised by decreased glucose tolerance, decreased insulin production, and decreased insulin sensitivity, leading to chronic hyperglycaemia. T2DM and obesity are not the same disease but being obese is a strong predeterminant for the development of T2DM. The high incidence of both of these conditions and the astronomical healthcare costs calls for a new improved and lower costs treatment that target both T2DM and obesity.

1.5.2.2 Current T2DM treatments

Current first-line treatments for T2DM are glucose-independent anti-hyperglycaemic drugs like sulphonylureas. Sulphonylureas work by binding and inhibiting the ATP-dependent potassium channels on the membrane of pancreaticβ cells. This stops the efflux of K^+ ions outside the cell, causes depolarisation of the β cell and subsequent activation of voltage-gated calcium channels (VGCCs) resulting in exocytosis of insulin-containing vesicles (Briscoe et al., 2010). Thiazolidinediones (also known as glitazones) are another classical treatment choice and they target the peroxisome proliferator activated receptor gamma (PPARγ), which activates many genes involved in glucose and fatty acid metabolism and results in promotion of insulin sensitivity (Tyagi et al., 2011). Such treatments come with many drawbacks despite their beneficial anti-hyperglycaemic effects like the increase in insulin release and insulin sensitivity. Firstly, they do not correct all the symptoms and frequently lose efficacy as the disease progresses. Secondly, they are not glucose-dependent, instead relaying on continuous elevation of insulin levels and/or sensitivity, which carries with it the associated risk of hypoglycaemia. Thirdly, they also fail to address the fact that almost 80% of T2DM patients are clinically obese by instead promoting weight gain (Bailey, 2007; Harris et al., 1987). This means that the development of glucose-dependent drugs that do not promote weight gain is essential.

1.5.2.3 Incretin effect

Mcintyre et al. (1964) found that oral administration of glucose promotes higher insulin secretion than glucose infusion and that this is due to incretins potentiating insulin release. Oral administration of glucose promotes higher insulin secretion than glucose infusion due to incretins

potentiating insulin release and this is called the incretin effect (Mcintyre et al., 1964). Incretins are metabolic hormones released by the gut in response to nutrients that facilitates the uptake of glucose by peripheral tissues by stimulating secretion of insulin. Peptide hormones GIP and GLP-1 belong here. Incretins are secreted from enteroendocrine cells of the jejunum and ileum in response to food high in fats and carbohydrates. The incretin secretion is coupled to food ingestion by a mechanism where glucose entering the endocrine cell is co-transported with Na^+ ions, which leads to depolarisation, activation of VGCCs and influx of $(Ca^{2+})_i$ into the enteroendocrine cell. $(Ca^{2+})_i$ accumulation in the cell then promotes exocytosis of GIP and GLP-1 (Figure 1.9) (Nauck and Meier, 2018).

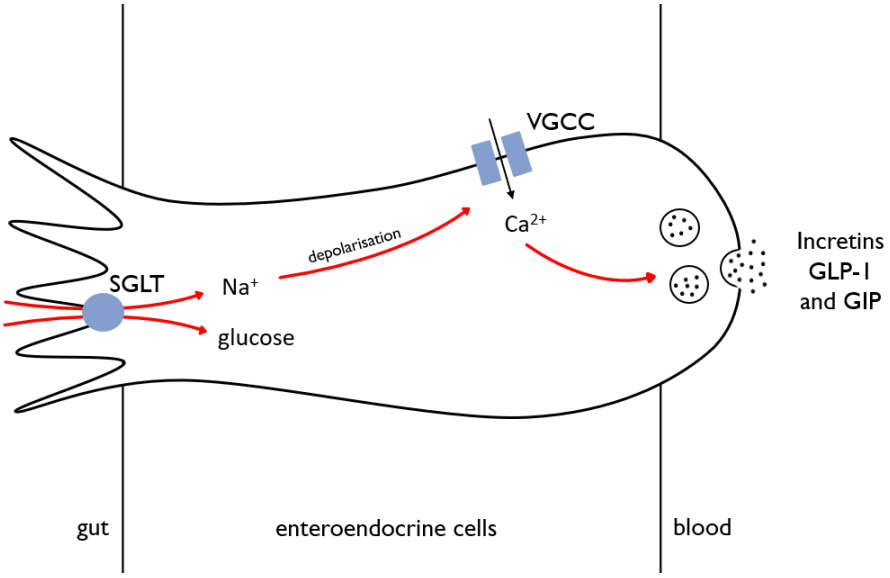

Figure 1.9. Schematic mechanism of incretin hormone secretion from endocrine cells. Glucose and sodium ions are co-transported by the sodium glucose transport protein (SGLT) into the endocrine cell. Increase of Na^+ ions in the cell results in depolarisation, opening of VGCCs and subsequent accumulation of Ca^{2+} ions inside the cell, which then triggers calcium-induced exocytosis of incretin hormones GIP and GLP-1 into the blood.

They are than carried by/through the blood to the pancreas, where they act on their receptors GIPR and GLP-1R embedded into the PM of pancreatic βcells to potentiate insulin secretion (Figure 1.10). Binding of incretin to its hormone receptor stimulates $G\alpha_s$ subunit, which activates AC resulting in the increase of intracellular cAMP. This then activates PKA, which similarly to sulphonylureas drugs mentioned above inhibits K^+ channels K_vATP and K_v2.1 leading to build up of K^+ in the cell, depolarisation and subsequent opening of VGCCs. Calcium enters the cytosol and triggers Ca^{2+}-mediated exocytosis of vesicles containing insulin. Incretin hormones receptors coupling to $G\alpha_q$

subunit then provides a second alternative way to increasing intracellular calcium, also promoting insulin release. In addition, GIP is found to promote glucagon secretion at low glucose concentrations, whereas GLP-1 suppresses its secretion (Nauck and Meier, 2018).

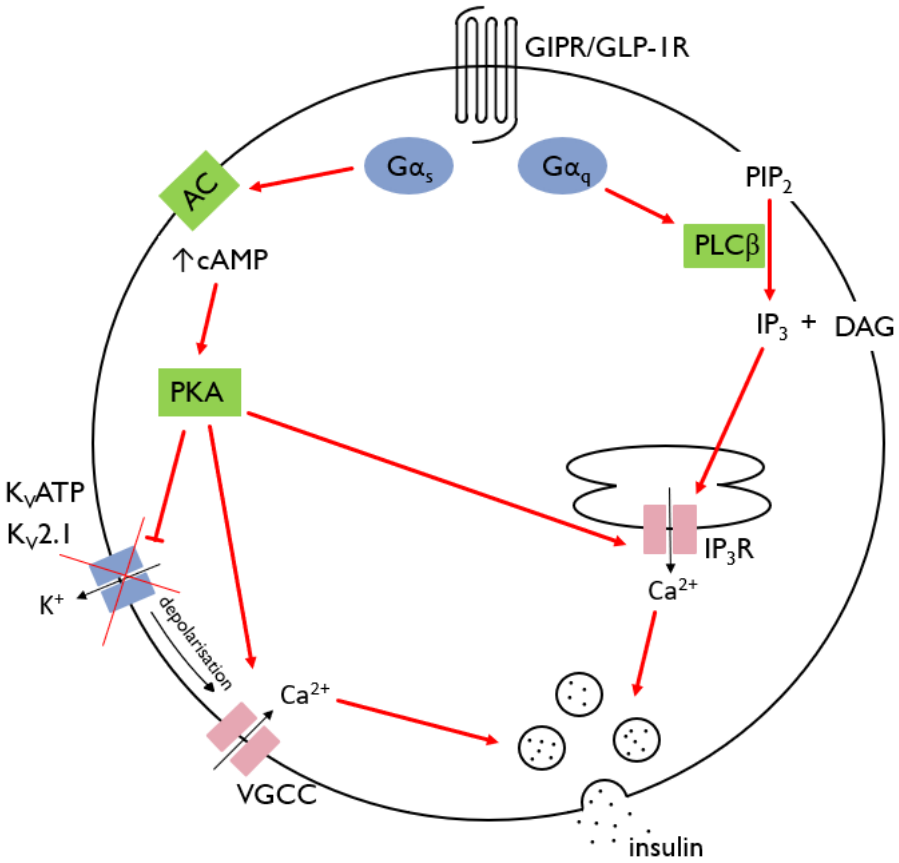

Figure 1.10. A schematic representation of incretin hormone-stimulated insulin secretion from pancreatic β cells. Incretin hormones binding at GIPR/GLP-1R causes receptor activation, which in turn activates coupled G proteins. Incretin hormone receptors can couple either to $G\alpha_s$ or $G\alpha_q$. Activated $G\alpha_s$ stimulates AC leading to cAMP accumulation in the cell, which in turn promotes PKA activity. PKA inhibits potassium channels $K_v2.1$ and K_vATP by phosphorylating them, which leads to cell depolarisation, opening of VGCC and subsequent calcium influx into the cytosol. PKA can also through a signalling cascade promote opening of IP_3R on the endoplasmic reticulum, again promoting calcium influx into the cytosol. Activated $G\alpha_q$ leads to activation of PLCβ and increase in IP_3, which then activates IP_3R resulting in Ca^{2+} influx in cytosol. This triggers Ca^{2+}-mediated exocytosis of vesicles containing insulin.

For healthy people the insulinotropic actions of incretin hormones account for 50-70% of all insulin secretion whereas it is only about 20% for T2DM patients (Nauck et al., 1986). The incretin effect impairment in T2DM patients is mostly attributed to the loss of GIP and GLP-1 insulinotropic activity (Nauck et al., 1993), but not necessarily to incretin hormone secretion decrease as the secretion of GLP-1 and GIP remains relatively unchanged, suggesting dysfunction arises at the level of the pancreatic β cells (Meier and Nauck, 2010). It is also interesting to note that although the maximum effect of GIP is reduced by around 54% in T2DM patients compared to normal, it is only reduced by 29% for GLP-1 (Nauck et al., 1993). This could be due to differences in GIPR and GLP-1R signalling and suggests GIPR as an important target in T2DM. Overall these findings stress the importance of developing therapies based upon incretins to elevate insulin release.

1.5.2.4 Therapeutic potential of GIPR agonists in T2DM

The markedly decreased (by 50%) insulinotropic action of exogenous GIP in T2DM clearly suggests that increasing GIPR signalling might benefit T2DM patients (Nauck et al., 1993). In one of the initial studies looking at this problem, Jones et al. (1987) showed that GIP infusion reduced plasma levels and increased insulin secretion by 120% in healthy people and by 27% in T2DM patients, which was still an improvement. Renner et al. (2010) then studied long-term effects of disruption of GIPR signalling. They showed that dominant negative $GIPR^{dn}$ expressing pigs had significantly decreased oral glucose tolerance and GIP-induced insulin secretion, but interestingly had enhanced response to GLP-1R agonists suggesting a compensatory effect between the signalling of the two incretin hormones. The deterioration of the glucose control and decrease in β-cell proliferation in $GIPR^{dn}$ expressing pigs without any associated weight change then suggests that GIPR agonists might be beneficial for T2DM treatment. However, GIP itself is a peptide rapidly degraded by dipeptidyl-peptidase 4 (DPP-4) enzyme and so is unsuitable for use in patients, which led to the development and use of DPP-4 inhibitors and/or DPP-4 degradation resistant incretin hormones analogues. For example, administration of DPP-4 degradation resistant GIP analog D-Ala-GIP(1-30) improved glucose tolerance and insulin secretion in obese Vancouver diabetic fatty (VDF) Zucker rats, which is an experimental model used for study of diabetes, and long-term treatment reduced degradation of βcells by reducing the levels of pro-apoptotic protein in pancreatic islets (Widenmaier et al., 2010). Another long-acting agonist AcGIP(LysPAL37) improved glucose homeostasis and insulin secretion in mice with no change in body weight (Irwin et al., 2006). Furthermore, there was interest in GLP-1R/GIPR co-agonists as they showed better control of blood glucose through actions on both incretin receptors, as well as more weight loss compared to clinically available GLP-1R agonist alone, suggesting a contribution of GIPR agonism for this weight loss (Frias et al., 2018). Yet, despite all this promising evidence it was hypothesised that

chronic GIPR agonist treatment could promote GIPR internalisation, rendering the target tissues unresponsive and hence explain why similar effects can be seen for both GIPR agonists and antagonists with respect to weight loss (Holst and Rosenkilde, 2020).

GIPR agonists have been explored for other indications apart from T2DM. Long-acting GIP analogues enhance bone strength in prediabetes via activation of skeletal GIPR and influence bone turnover, suggesting their usefulness in bone disease treatment (Holst and Rosenkilde, 2020; Vyavahare et al., 2020). Bollag et al. (2000) reported that GIP stimulates expression of collagen type I, alkaline phosphatase and other bone formation markers in osteoblasts thus promoting their anabolic function, while Zhong et al. (2007) shows that GIP inhibits the bone resorptive function of osteoclasts. This indicates that the GIPR signalling plays a role in coordinating nutrient ingestion with bone turnover to allow optimisation of nutrients available for bone formation. Furthermore, preclinical studies have associated GIPR activation with reduced progression of atherosclerotic lesions. For example, subcutaneous infusion of human GIP(1-42) in 17-week-old apolipoprotein E deficient ($ApoE^{-/-}$) mice for 4 weeks reduced aortic root atherosclerotic lesion size and macrophage infiltration (Nagashima et al., 2011).

1.5.2.5 Therapeutic potential of GIPR antagonists in obesity

Although there is a clear potential in developing GIPR agonists as viable candidates for T2DM treatment, there is also a lot of opposing evidence about GIPR signalling in adipose tissue and use of GIPR antagonists in obesity. Hauner et al. (1988) showed that GIP promotes the uptake of glucose into rat adipocytes and its conversion into lipids. In adipose tissue GIP is known to stimulate lipogenesis, increase fatty acid uptake and induce insulin resistance in adipocytes (Asmar et al., 2019, 2017, 2016; Nigel Irwin and Flatt, 2009; N. Irwin and Flatt, 2009). Lipogenesis is a process, where lipids are hydrolysed into non-esterified fatty acids (NEFA) by the enzyme lipoprotein lipase and reesterified into triacylglycerol (TAG) to be stored in adipocytes as lipid droplets (Thondam et al., 2020). GIP stimulates lipogenesis by increasing lipoprotein lipase activity via a signalling pathway involving protein kinase B (PKB), liver kinase B1(LKB1) and AMP-activated protein kinase (Kim et al., 2007). In agreement with this data, fat is a potent initiator for GIP secretion in the gut and GIP levels have been found elevated in obesity (Gasbjerg et al., 2019, Yip et al., 1998).

The elevated GIP levels in obesity are believed to be partially linked to excessive deposition of visceral and subcutaneous fat and thus supposedly increased GIP levels can predispose individuals to obesity (McClean et al., 2008; Yip et al., 1998). Further corroborating this hypothesis is the fact that bariatric surgeries such as Roux-en-Y gastric bypass (RYGB), which are the only really proven

techniques to result in sustained weight loss in humans, are often linked to decreased GIP secretion and signaling pointing to decreased GIP secretion as a primary beneficial metabolic effect of the surgical process (Flatt, 2007; Rubino et al., 2004; Salinari et al., 2009). Experiments on mice show promising results when GIPR knockout (GIPR-/-) mice on high-fat diet are protected from developing both obesity and insulin resistance (Miyawaki et al., 2002). Furthermore, when these mice are crossed with the genetically obese leptin deficient ob/ob mice, the lack of GIPR signaling leads to significant reduction in weight gain and adiposity. In another more recent promising piece of work, Killion et al. (2018) shows that prolonged administration of a GIPR neutralizing antibody enhances the weight loss induced by GLP-1 in mice.

As was mentioned above, obesity is a predisposing factor for diabetes. So, the question remains, whether it is feasible to use GIPR antagonists in obese T2DM patients when GIP promotes insulin secretion? Arguing for antagonists use is the fact that GIP-induced lipid deposition activity in adipocytes is preserved in obese T2DM patients, while the GIP insulinotropic effect is not, suggesting GIPR antagonism should not have much effect in pancreatic β-cells but should have full effect in the adipose tissue (Irwin et al., 2020; Nauck et al., 1993; Thondam et al., 2017). Additionally, both fasting and post prandial levels of peptide hormone glucagon are elevated in people with T2DM and glucagon receptor (GCGR) antagonists have been shown to lower glycaemia in T2DM patients, suggesting glucagon as a hyperglycemic agent that contributes to the pathogenesis of T2DM (Campbell and Drucker, 2015; El and Campbell, 2020). And one of the GIP known functions is a stimulation of glucagon secretion in the pancreatic α cells, on which GIPR is also expressed (DiGruccio et al., 2016; Ding et al., 1997). GIPR antagonists could therefore help lower glucagon levels.

To summarize, there is a clear potential for GIPR antagonists in obesity treatment that should not be hindered by the role of GIPR signaling in insulin secretion in T2DM patients. GIPR antagonists can be a powerful tool in preventing excessive lipogenesis in adipose tissue and excessive glucagon secretion in pancreatic α cells.

1.5.2.6 Benefits and challenges of GIPR allosteric modulators

Both GIPR agonist and antagonists target the orthosteric binding site of the GIP receptor, which has evolved for peptide hormone GIP. GIP has a short half-life of less than 2 minutes and is rapidly degraded by DPP-4, which is likely to be similar for many peptide drugs targeting the orthosteric site limiting their use in clinic (Baggio and Drucker, 2007). Current drugs licensed for treatment of diabetes, DPP-4 inhibitors or long-acting degradation resistant GLP-1 mimetics, get around the rapid degradation problem, but come with other side effects like gastrointestinal discomfort or flu-like symptoms.

Additionally, they also require subcutaneous injection and because of being peptides are very expensive costing around £956 per year per patient (Johansen et al., 2020). Therefore, there is an outstanding need for orally available, cheaper small molecule drugs in diabetes as well as in obesity.

It is very hard to design small molecules that could successfully engage all necessary amino acids in the large diffuse orthosteric binding site of class B1 GPCRs, but it might be easier to do so for a smaller allosteric binding site making it possible to develop cheaper orally available drugs. (Wootten and Miller, 2020), for example, note that the open nature of transmembrane helices of the GIPR provides many access points for small molecules which will not necessarily overlap with the region at which the orthosteric ligand binds. Furthermore, in T2DM, GIPR PAM would promote insulin secretion only when GIP is endogenously secreted making insulin secretion more physiological and lessening the probability of dangerous hypoglycaemia occurring as is the case for long-acting GLP-1 analogues (Wootten et al., 2013a). Same would be true for GIPR NAMs regulating glucagon secretion in a more natural way.

GIPR allosteric modulators may also provide an opportunity for greater subtype selectivity than orthosteric ligands (Gentry et al., 2015). GIPR, GLP-1 and GCGR are closely related class B1 GPCRs and their ligands GIP, GLP-1 and glucagon do show some cross-reactivity on all three of the receptor s (Yuliantie et al., 2020; Zhao et al., 2022, 2021). Development of selective drugs targeting the orthosteric site of these receptors might thus be hindered by the similarity between the orthosteric sites, while allosteric modulators can target less conserved parts of these receptors leading potentially to more selective drugs. This might be particularly useful for GIPR NAMs use in obese patients, where downregulation of GLP-1 signalling, which is important for insulin release, would be unwanted and could be prevented by GIPR selective NAMs.

Furthermore, GLP-1R allosteric modulator Compound 2 proves that allosterism of class B1 GPCRs is possible and also shows that allosteric modulators can be biased, when Koole et al. (2010) showed that Compound 2 inhibits GLP-1-induced cAMP accumulation but not $(Ca^{2+})_i$ mobilisation or ERK1/2 phosphorylation. GIPR biased allosteric modulators could therefore also be used to elucidate differences between GIPR signalling in pancreas and in adipose tissue.

Taken together, GIPR allosteric modulators would be useful compounds for studying GIPR signalling and because of more physiological effects and potential for development of cheaper orally available small molecule drugs show also great promise for use in clinic. In particular, GIPR PAMs could be used in T2DM treatment, while GIPR NAMs could be useful for treatment of obesity.

1.6 The process of drug discovery

Drug discovery and development is very long and very expensive process with traditional approaches relaying on stepwise synthesis and *in vitro* screening of huge compound libraries to identify potential hits/leads which are then subjected to iterative chemical optimisation followed by experimental evaluation to obtain pre-clinical candidate(s). However, over the past two decades there has been a steady increase in the application of *in silico* methods together with biological and chemistry ones in order to streamline drug discovery, design, development and optimization (Kapetanovic, 2008). *In silico* or Computational Drug Discovery/Design (CADD) can be divided into ligand-based drug discovery (LBDD) and structure-based drug discovery (SBDD), although many successful drug discovery campaigns have benefited a combined use of both (Frye et al., 2021; Lin et al., 2020; Wilson and Lill, 2011). LBDD is an approach that disregards the 3D information of the target structure (which may or may not be available) and it mainly relies on knowledge (cheminformatics and often aided by machine learning in recent time) of molecules with experimentally proven profile (potency, efficacy, affinity if known) against a desired target-related or cellular response (Bacilieri and Moro, 2006). We have also applied it here to ARs because there are a lot of known compounds targeting the ARs, which can guide design of other new compounds targeting these receptors for SAR studies. SBDD, on the other hand is an approach, where structural information of the drug target is exploited for the initial identification of hits as well as subsequent hit-to-lead transition and further lead optimisation (Wang et al., 2018). The recent rise in the number of solved crystal and cryo-EM structures means also rise in use of SBDD approach. Furthermore, in the absence of experimentally derived 3D structure of the target protein, a plausible 3D structural model can be obtained either through homology modelling (given availability of suitable templates) or ab initio folding based on A.I. methods such as AlphaFold and RosettaFold introduced in recent time (Baek et al., 2021; Jumper et al., 2021).

1.6.1 Discovery and development of ARs agonists and antagonists

LBDD effectively 'learns' from previously identified ligands, especially their structure-activity relationship (SAR) and use them as a starting point for designing new ligands. Typical ARs non-selective ligands are adenosine and NECA, while work preceding this thesis has identified a potent A_1R selective NECA derivative compound BnOCPA as discussed above (Knight et al., 2016). To identify new and improved A_1R agonists, a series of new compounds based on adenosine and NECA with extended N^6-benzyloxy- and N^6-phenoxycyclopentyl substituents was designed in collaboration with Dr Lochner's lab (University of Bern). Although to find novel scaffolds, a ligand-based approach was chosen initially

instead of virtual screening compounds libraries against AR structures, there was retrospective use of the AR structures to advise the design of the new compounds. In particular, information from the molecular dynamics (MD) simulations using the active cryo-EM A_1R structure (PDB code 6D9H20) was used, which uncovered three binding modes of BnOCPA, was used to guide the design of the adenosine and NECA derivatives (Deganutti et al., 2020). The new compounds are then characterised in chapter 5 using *in vitro* pharmacological assays such as, cAMP accumulation assay and BRET competition binding techniques.

To identify new potent A_3R antagonists in collaboration with Prof Kolocouris' group (University of Athens), a similar approach of designing a series of new compounds based on currently known A_1R and A_3R ligands (Figure 1.11) was used. There has been an emerging realization that selecting ligands based on only their affinity, which is an equilibrium parameter, does not necessarily predict in vivo efficacy (Suchankova et al., 2021). Thus, the A_1R and A_3R ligands chosen as chemical probes for selecting compounds for testing were selected based on their kinetic parameters like association constant (K_{on}), dissociation constant (K_{off}) and the residence time (RT= $1/K_{off}$). The compounds are then characterised in chapter 6 using a combination of *in vitro* techniques like cAMP accumulation assay and NanoBRET competition binding assay. This was also complimented by Prof Kolocouris' work on characterising the new compounds' binding at ARs computational techniques like MD simulations.

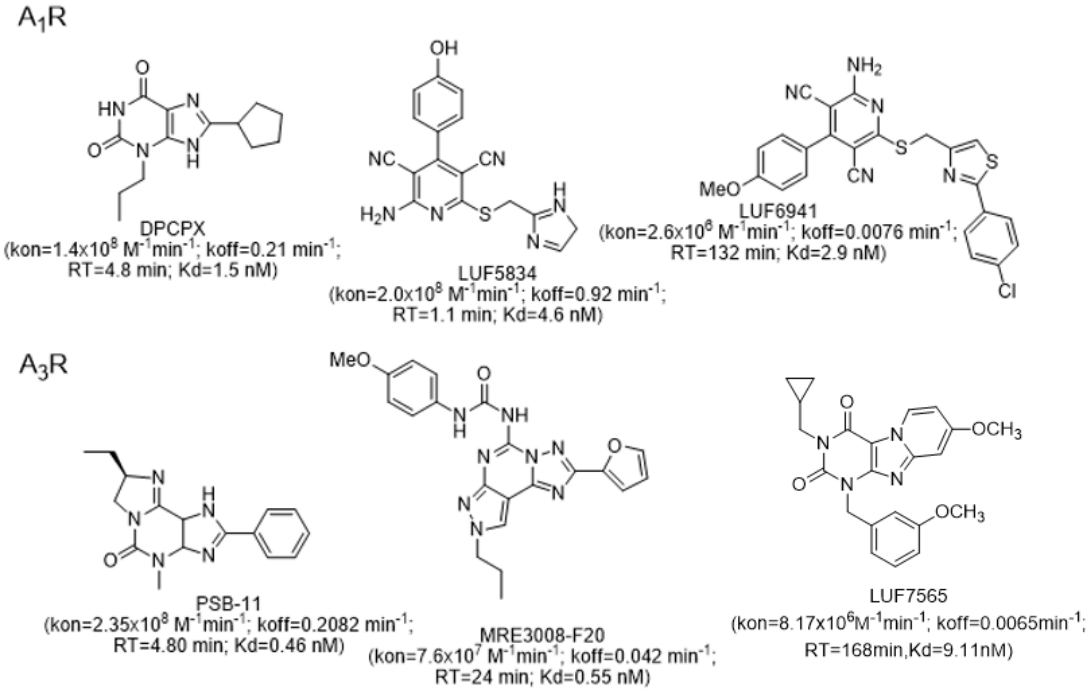

Figure 1.11. Kinetic parameters of selected A_1R and A_3R ligands. Residence time (RT), dissociation constant (K_d), association (K_{on}) and dissociation (K_{off}) rate constants of selected A_1R (DPCPX, LUF5834, LUF6941) and A_3R ligands (PSB-11, MRE3008-F20, LUF7565). Figure was adapted from Stampelou et al. (2022).

1.6.2 Discovery and development of GIPR allosteric modulators

Prior to starting this PhD, Prof Ladds' lab together with Dr Rahman's lab had identified a few unique small molecule GIPR-specific allosteric modulators. The latter were initially found through virtual screening of some commercially available, lead-like libraries against the GIPR homology model (based on active GLP-1R structure (PDB 5nx2) as template) followed by a full *in vitro* characterisation using multiple pharmacological essays. As potential allosteric sites, few regions within 5Å of the lower end of the canonical orthosteric site were used for that screening, although the binding site(s) for the positive hits remained to be experimentally determined. The identified compounds are mostly PAMs, which are able to significantly potentiate (>10-fold) GIP-enhanced glucose-stimulated insulin release from primary human islets, and few NAMs; in particular compounds C3 and C25 that selectively inhibit $(Ca^{2+})_i$ mobilisation (Figure 1.12). These compounds are the 'first-in-class' at the GIPR and they are chemically tractable, "drug-like" small molecules that contain no reactive functional groups and satisfy Lipinski's rule of 5, with high potential for oral delivery. C3 and C25 can then be used as chemical probes to search compound libraries for new compounds with similar scaffolds that will be tested for

their activity at GIPR in chapter 3 and their binding at the receptor will be explored using *in silico* docking in chapter 4.

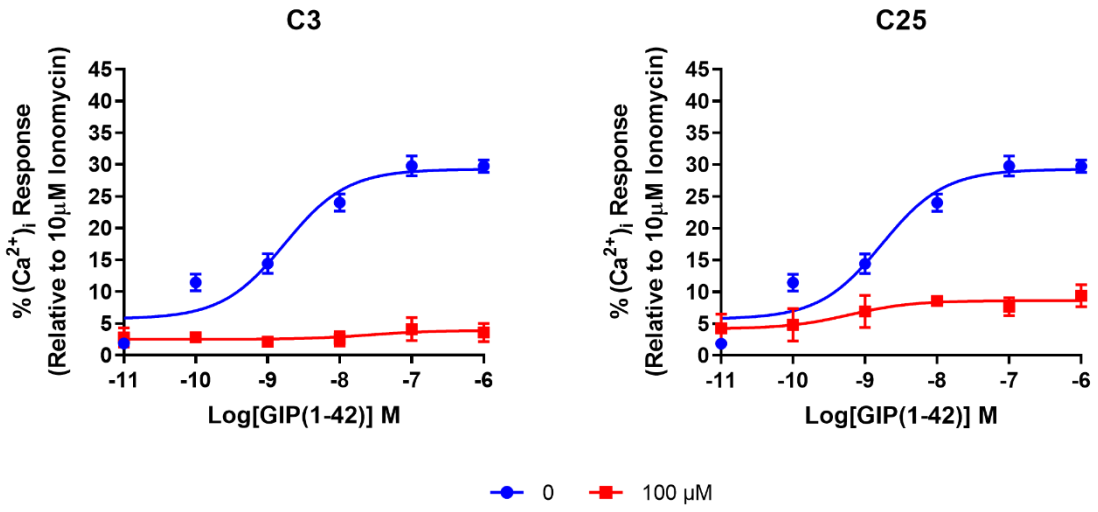

Figure 1.12. C3 and C25 are NAMs for $(Ca^{2+})_i$ mobilisation at GIPR. GIP(1-42)-induced $(Ca^{2+})_i$ mobilisation in HEK-293S cells stably expressing GIPR in the presence of either DMSO or 100 µM tested compound. Data is plotted as mean ± SEM and normalised to 10 µM ionomycin response.

A second possible approach is to first systematically and exhaustively identify suitable allosteric site(s) at the GIPR using various computational algorithms as well as comparative analyses with other GPCRs, especially those belonging to the class B1 family (Sheik Amamuddy et al., 2020; Wagner et al., 2016). Then the chosen potential allosteric site(s) can be subjected to virtual screening using various vendor libraries with scaffold diversity and lead-like properties. There are several ways how to identify suitable allosteric sites. Firstly, if there already is an identified allosteric modulator and its binding site at the receptor has been elucidated, then that allosteric site can be used for further (and possibly larger scale) screening for other potential allosteric ligands. Secondly, there is a plethora of *in silico* techniques for identification of allosteric sites on proteins, most common of which will be described in the next section and then applied to GIPR in chapter 4.

1.6.3 *In silico* methods for allosteric site identification

There are different *in silico* techniques enabling identification of good allosteric site on proteins that take into various information like evolutionary sequence conservancy, 3D information of the

protein surface or biding site of known allosteric modulators. Generally, these methods identify any binding sites on the protein including both orthosteric and allosteric sites. However, since an orthosteric site is known for a lot of receptors (and it is true also for GIPR), it is not a problem to simply exclude it from results in order to identify allosteric binding sites. The methods can be approximately divided into knowledge-, sequence-, geometry/energy- or dynamics-based approaches.

1.6.3.1 Knowledge-based prediction approaches

Knowledge based approaches like Pocketome or 3DLigandSite identify ligand binding sites by querying existing databases of already determined ligand-binding sites. Pocketome automatically gathers data from solved crystal structures in Protein Data Bank (PDB) and then superimposes the proteins in its database against the 3D structure of the queried protein to identify potential binding sites (Kufareva et al., 2012). However, since at the time of the writing Pocketome lacked class B1 GPCRs, it was not feasible for GIPR. 3DLigandSite works very similarly but offers added features of 3D structure prediction for proteins without solved structure and mapping of residue conservancy onto the protein, although this information is not factored into the ligand binding site identification automatically (http://www.sbg.bio.ic.ac.uk/3dligandsite) (Wass et al., 2010; Wass and Sternberg, 2009).

3DLigandSite was successfully used by Naushad et al. (2019) to identify loss of non-metallic-ligand-binding sites of mutant solute carrier family 19 member 1 (SLC19A1) protein that occurs in different types of cancers and systemic lupus erythematosus compared to WT protein. However, since the known ligand binding sites for GPCRS (and especially for those belonging to the class B1 family) are overwhelming represented by the orthosteric binding sites, it is unlikely for 3DLigandSite to be particularly helpful for identification of allosteric binding sites at GIPR.

1.6.3.2 Sequence-based prediction approaches

The rapid increase in availability of sequence data from many organisms allows the use of statistical sequence analysis to study relations between AA sequence and protein 3D structure or function. Multiple sequence alignment (MSA) mostly refers to the alignment of three or more biological sequences (protein or nucleic acid) of similar length, which allows insights into the evolutionary relationships between the sequences studied and how well is which part of the protein conserved. This is important, because it is expected that conservation is low in the absence of selective pressures. Hence, when a selective pressure like binding of ligands/ions to certain part of the protein is present, that part should have higher conservancy (Ng and Henikoff, 2003; Schneider et al., 1986;

Zvelebil et al., 1987). The disadvantage of this approach is that the binding of ligands is not the only selective pressure and many other parts of the protein that have structural or functional roles will be fairly well conserved as well. This makes it hard to distinguish between these and the allosteric binding site in any other way than that the binding sites are more likely to be on the protein surface while the functionally and structurally important amino acids might be a bit more buried.

The GPCR—sequence analysis and statistics (GPCR-SAS) is one of the *in silico* techniques using MSA and conservancy analysis (http://lmc.uab.cat/gpcrsas/gpcrsas/). This web application enables conservation analysis, covariance analysis and correlation analysis of the GPCRs TMD segments charting the result as a snake-plot (Gómez Tamayo et al., 2018). However, concentrating just on the TMDs means that allosteric sites particularly in the N-termini and the extracellular loops readily accessible by ligand can be missed. Another technique is ConSurf, which is an algorithmic web application for the identification of functional regions in proteins by surface mapping of phylogenetic information that maps the results onto a pdb (protein data bank format) structure and additionally constructs a phylogenetic tree (Armon et al., 2001) (https://consurf.tau.ac.il/overview.php). One of the advantages of ConSurf in comparison to other methods like GPCR-SAS is the accurate computation of the evolutionary rate by using either an empirical Bayesian method or a maximum likelihood method, which are both statistical methods (Glaser et al., 2003). Empirical Bayesian method refers to the fact that prior probability distribution is estimated from the data instead of being fixed and maximum likelihood method determines parameter values that are most likely to be the same as actual observed values.

MSA is also used by statistical coupling analysis (SCA), which identifies networks of coevolving residues (termed 'sectors') in a protein family (Lockless and Ranganathan, 1999). The sectors are thought to be functionally important and provide a molecular basis for allosteric communications between functional and allosteric sites (Lichtarge et al., 1996; Marcotte et al., 1999; Pellegrini et al., 1999). SCA was used for example by Novinec et al. (2014) and applied to a collagenolytic cysteine peptidase cathepsin K, which is a major target for the treatment of osteoporosis, leading to the identification of 14 residues and 8 allosteric sites involved in the allosteric communications of cathepsin K, which he also experimentally validated. Furthermore, by conducting a high throughput *in silico* docking of compounds against these protein sectors, he managed to identify the first small-molecule allosteric inhibitor of cathepsin K, compound NSC13345. This work shows that together with other *in silico* techniques and *in vitro* validation, SCA can be used for the discovery of druggable allosteric sites. SCA has previously been applied to class A GPCRs, but not yet to class B1 GPCRs including GIPR (Suel, 2003; dima 2005). pySCA, used in this thesis, is a prewritten python script for linux

that enables automated SCA analysis and can also be applied to class B1 GPCRs (https://github.com/ranganathanlab/pySCA) (Rivoire et al., 2016).

1.6.3.3 Geometry- and/or energy-based prediction methods

Geometry-based methods identify ligand-binding sites based on metrics like volume and shape and they view 3D structure of the target protein simply as a set of atomic coordinates (Cheng and Jiang, 2019). Too shallow binding sites are usually dropped from the analysis. There are generally three different techniques that geometry-based methods can employ: grid system scanning, probe sphere filling and alpha-shape techniques. The grid system scanning technique shows protein atoms as spheres of van der Waals radii and it sorts all the grid points into those occupied by the protein and those empty. Afterward it ranks the empty spaces as pockets by geometric metrics such as the width and depth of the pocket. Example of such method is the Fpocket (Le Guilloux et al., 2009). The probe sphere-based technique works by filling the protein pockets or cavities with a set of round probe spheres that have a set radius, which can be chosen as smaller or larger based on how the compounds we want to dock against the newly identified site look. SURFNET method uses this technique (Laskowski, 1995). Lastly, CAST method, for example, uses alpha shape and discrete-flow theory, which is a bit more mathematically and computationally complicated and more detail for those interested can be found in the references (Edelsbrunner and Mucke, 1994; Liang et al., 1998, Weiqiang et al., 2012). Then there are some methods, which employ a combination of techniques like POcket-Cavity Search Application (POCASA), which uses both the grid system and probe sphere (http://g6altair.sci.hokudai.ac.jp/g6/service/pocasa/) (Yu et al., 2010). Classifying binding sites based on geometry is also often only one part of a more complex technique and is quite commonly used since it is easy to do and doesn't require much computational power while giving a lot of information about the possible binding sites.

Energy-based approaches like FTmaps blindly dock small probes onto the target protein and then evaluate the interactions (https://ftmap.bu.edu). FTmaps samples billions of positions of small organic molecules like acetone, ethanol or urea used as probes and scores the resulting poses using a detailed energy expression (Kozakov et al., 2015). However, compared to geometry-based methods, these are much more computationally demanding. This limits their applicability to large-scale structural data sets but is still very doable for just one or a few receptor models like in this thesis.

1.6.3.4 Dynamics-based prediction approaches

The disadvantage of geometry and energy-based approaches described above is that they look on the protein as a rigid 3D structure, when in reality proteins constantly move between multiple conformations. Moreover, some allosteric sites might be open and approachable to ligands only in some of those conformations, meaning a study looking at one rigid conformation might not find them at all. Dynamics-based prediction approaches overcome this by looking at moving proteins in multiple conformations. Methods that belong here are MD simulations, Markov state models, coarse-grained and lattice modelling and normal mode analysis (NMA).

MD simulations is the most used computational method for studying protein dynamics (Karplus and McCammon, 2002). MD simulations are mostly used to investigate allosteric mechanisms of proteins, but can also be used for allosteric site identification. Laine et al. (2010, 2009) used MD simulations to study the transition of *bacillus anthracis* adenylyl cyclase toxin edema factor (EF) from its inactive to active conformation and found allosteric site present only in the intermediate structure, against which they also then found an allosteric inhibitor compound. Moreover, MD simulations can be used to generate multiple receptor models representing the snapshots of the different receptor conformations over time from one original rigid model. These receptor snapshots can then be used by other techniques to probe for allosteric sites, which might only be present in some of these models but not in all. Markov state model then further builds onto the MD simulations to calculate the probabilities of different intermediate states of the receptor (Chodera and Noé, 2014; Malmstrom et al., 2014; Pande et al., 2010).

Coarse-grained and lattice modelling has the advantage of requiring less computational power than the previous two methods. This is possible thanks to the use of ”pseudo-atoms”, which means that the method approximates and models a whole amino acid as one ball instead of modelling every single atom separately (Qi et al., 2012). The method than introduces perturbations into different sites and looks whether this has an effect on the rest of the protein structure. If it does have an effect, the perturbed site is predicted as an allosteric site. Qi et al. (2012) used this approach to successful identify new allosteric sites of Escherichia coli phosphoglycerate dehydrogenase and NAMs binding there. Finally, normal mode analysis of an elastic network model (ENM) hypothesises that the largest movements in a protein are functional and studies the functional motions of a protein (Bahar et al., 2010). Compared to MD simulations it is more suited for the study of large structural rearrangements of proteins.

SPACER is a web server application that integrates NMA with Monte Carlo simulations to predict allosteric binding sites (http://allostery.bii.a-star.edu.sg/) (Goncearenco et al., 2013). The binding sites are predicted based on local closeness, which calculates closeness between neighbouring atoms, binding leverage, which measures ability of a binding site to couple to intrinsic motions of a protein, and leverage coupling between two sites, which is a quantitative characteristic of allosteric communication. PARS is another web application that uses NMA and coarse-grained modelling to predict allosteric sites based on the alteration of protein flexibility upon ligand binding (http://bioinf.uab.cat/pars) (Panjkovich and Daura, 2014). When applied to benchmark data, PARS successfully predicted 44% of known allosteric sites (Panjkovich and Daura, 2014). Additionally, if enough structural data is available, it also measures the structural conservation of each predicted binding site.

1.7 Aims

The focus of this thesis is on the drug discovery at class A and class B GPCRs. Given the possible therapeutic effects of modulating GIPR signalling pathway in diabetes and obesity, the primary objective of this thesis was to discover and improve GIPR allosteric modulators using both *in silico* and *in vitro* techniques and also to find the allosteric binding site at GIPR. The specific aims were as follows:

- Screen potential GIPR allosteric modulators and explore their selectivity and effects on different GIPR signalling pathways.
- Use *in silico* docking to predict the GIPR binding site of the allosteric modulators and confirm these predictions using *in vitro* pharmacological techniques.
- Investigate potential allosteric binding sites at GIPR using *in silico* techniques for allosteric site identification.

The second part of this thesis is then focused on drug discovery at adenosine receptors with the aim of developing more selective and more potent compounds. The specific aims were as follows:

- Screen compounds for more potent A_1R agonists that retain or improve upon the selectivity of previously discovered compounds.
- Discover high affinity, potent A_1 and A_3 receptor antagonists.

Chapter 2. Materials and methods

2.1 Materials

2.1.1 General laboratory reagents

All general laboratory reagents were of analytical grade and purchased from Sigma-Aldrich, unless otherwise stated.

2.1.2 Ligands

Human GIP(1-42) and GIP(Pro3) were purchased from Abcam (Cambridge, U.K.) and made to 1 mM stocks in water containing 0.1% bovine serum albumin (BSA). Human GLP-1 (7–36)NH_2 and glucagon were purchased from Generon (Slough, UK) and all were made up to 1mM stocks in water containing 0.1% BSA. NECA (5'-(N-Ethylcarboxamido) adenosine), CPA (cyproterone acetate) and DPCPX (8-cyclopentyl-1,3-dipropylxanthine) were purchased from Sigma-Aldrich and made to 10 mM stocks in dimethyl-sulphoxide (DMSO). Ionomycin was bought from Cayman Biosciences (Michigan, USA) and prepared as 10 mM stock in absolute ethanol. CA200645 was purchased from Hello Bio and made up to 100 mM stocks in DMSO. All above compounds were stored at -20°C prior to use. Forskolin was purchased from Tocris Bioscience (Wiltshire, UK), made up to 10 mM stocks in DMSO and stored at room temperature (RT).

2.1.3 Compounds

All compounds tested for activity at the GIPR were purchased from either Enamine or Vitas-M Laboratories and made to 10 mM stocks in DMSO. Compounds were arbitrarily named Cx and Tx (x = number) (structures detailed in Table 2.1).

Table 2.1. 2D structures and molecular weight of potential GIPR allosteric modulators.

Compound	Structure	Molecular weight (g/mol)
C3	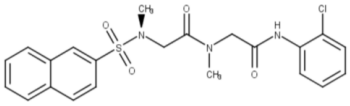	459.90
C22	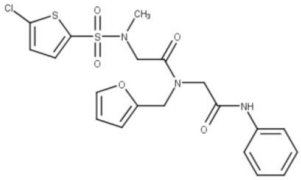	482.00
C25	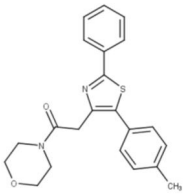	378.50
C42	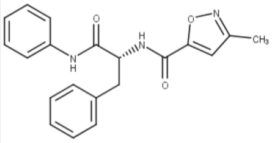	349.40
C58	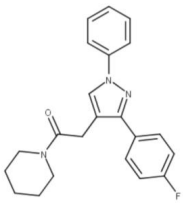	363.40
C73	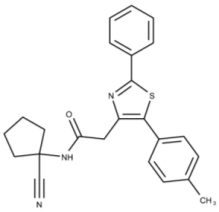	401.50
C82	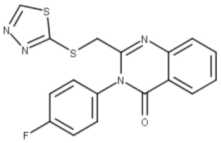	370.40
C91	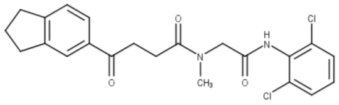	433.30
C95	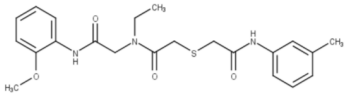	429.50
T1	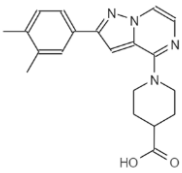	350.42

T2	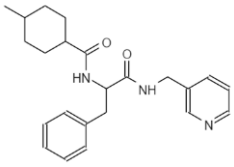	379.50
T3	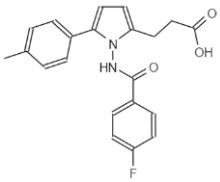	366.39
T4	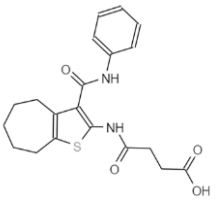	386.47
T5	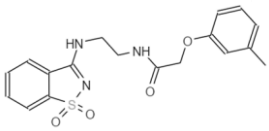	373.43
T6	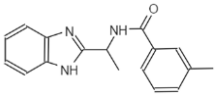	279.34
T7	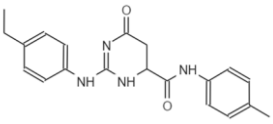	350.42
T8	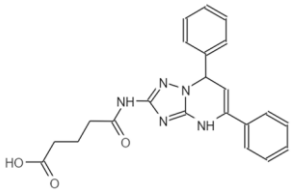	403.44
T9	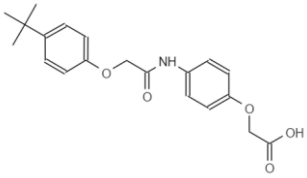	357.41
T10	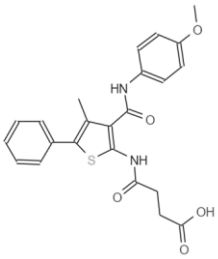	438.50
T11	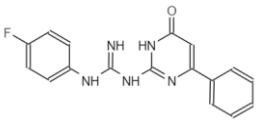	323.33

T12	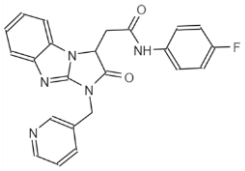	415.43
T13	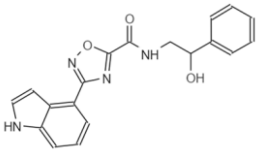	348.36
T14	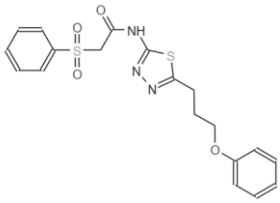	417.51
T15	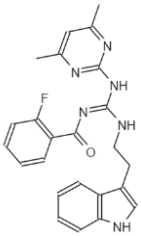	430.48
T16	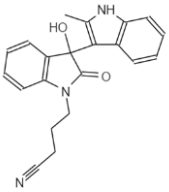	354.40
T17	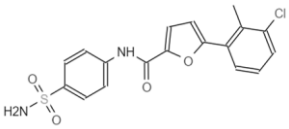	390.85
T18	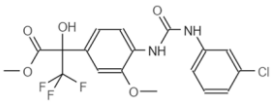	432.78
T19	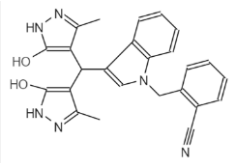	438.49
T20	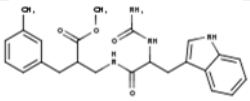	436.50
T21	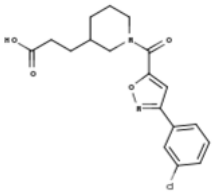	362.80
T22	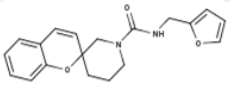	324.40

T23	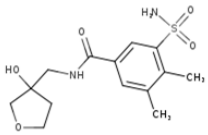	328.40
T24	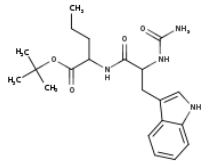	402.50
T25	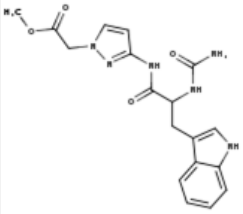	384.40
T26	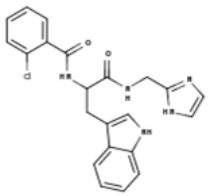	421.90
T27	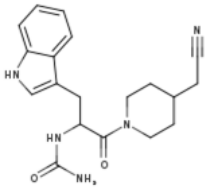	353.40

NECA and CPA derivative compounds tested for activity at ARs were synthesised by Dr Lochner's group (University of Bern) and made up to 10 mM stocks in DMSO. Compounds were arbitrarily numbered **19**-**30** and **44**-**55** (structures detailed in Table 2.2).

Table 2.2. List of synthetic adenosine and NECA derivatives. List of all tested compounds, their 2D structure and molecular weight.

Cmpd	Structure	Molecular weight (g/mol)	Type of derivate
Adenosine	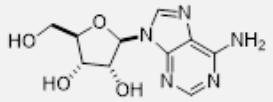	267.24	-
BnOCPA	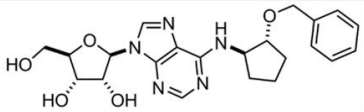	441.49	Benzyloxycyclopentyl
19	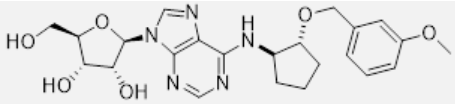	471.51	Benzyloxycyclopentyl
20	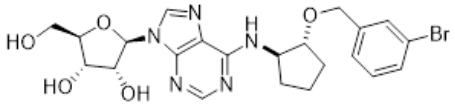	520.38	Benzyloxycyclopentyl
21	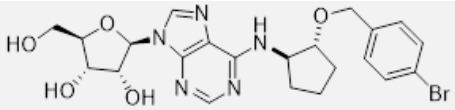	520.38	Benzyloxycyclopentyl
22	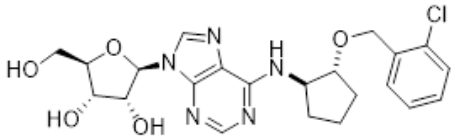	475.93	Benzyloxycyclopentyl
23	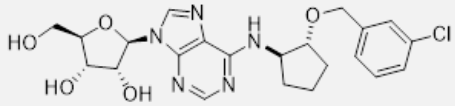	475.93	Benzyloxycyclopentyl
24	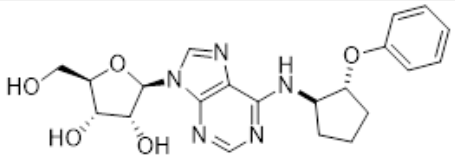	427.46	Phenoxycyclopentyl
25	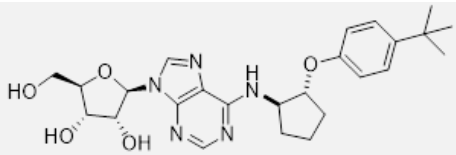	483.57	Phenoxycyclopentyl
26	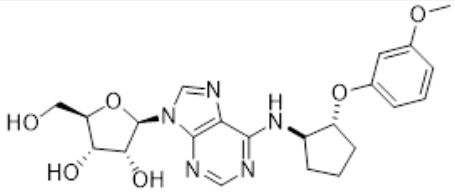	457.49	Phenoxycyclopentyl
27	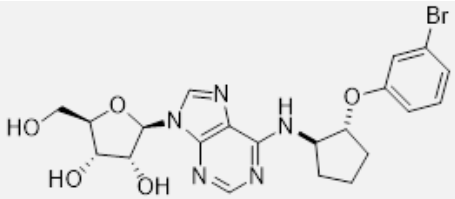	506.36	Phenoxycyclopentyl

28	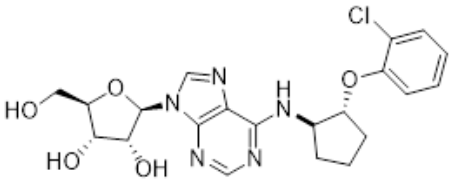	461.90	Phenoxycyclopentyl
29	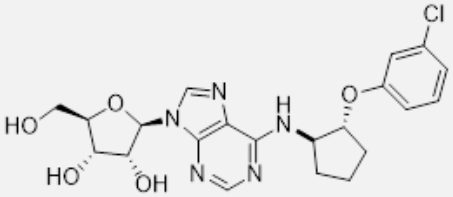	461.90	Phenoxycyclopentyl
30	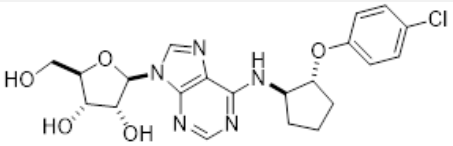	461.90	Phenoxycyclopentyl
NECA	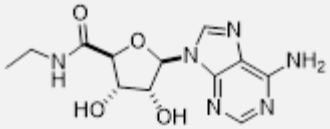	308.29	-
44	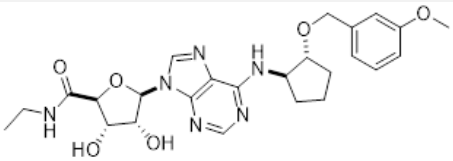	512.57	Benzyloxycyclopentyl
45	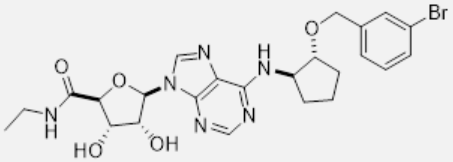	561.44	Benzyloxycyclopentyl
46	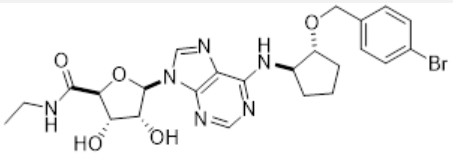	561.44	Benzyloxycyclopentyl
47	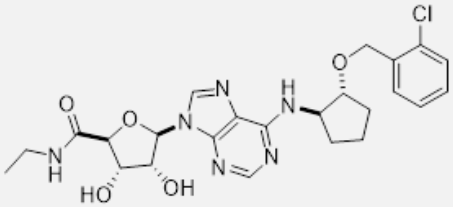	516.98	Benzyloxycyclopentyl
48	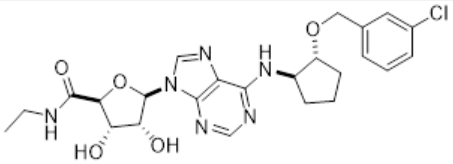	516.98	Benzyloxycyclopentyl
49	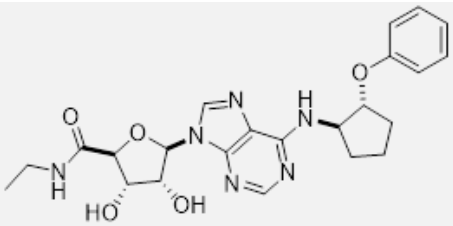	468.51	Phenoxycyclopentyl

50	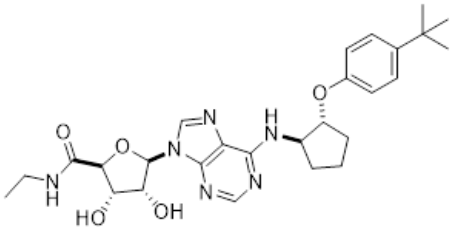	524.62	Phenoxycyclopentyl
51	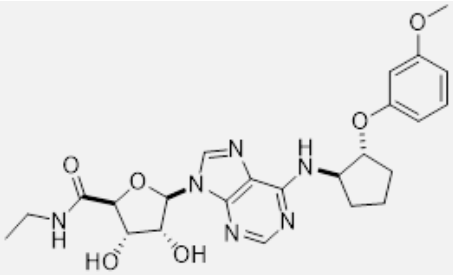	498.54	Phenoxycyclopentyl
52	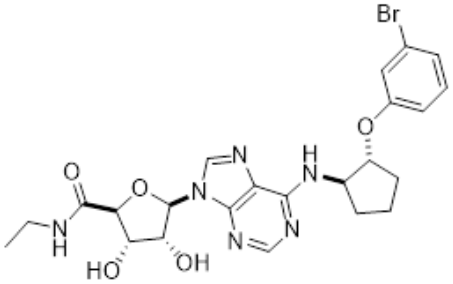	547.41	Phenoxycyclopentyl
53	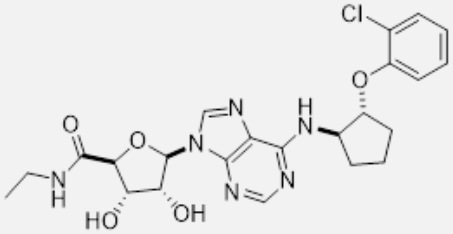	502.96	Phenoxycyclopentyl
54	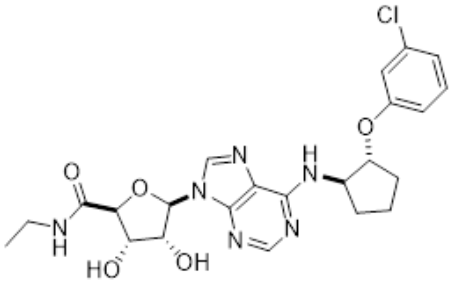	502.96	Phenoxycyclopentyl
55	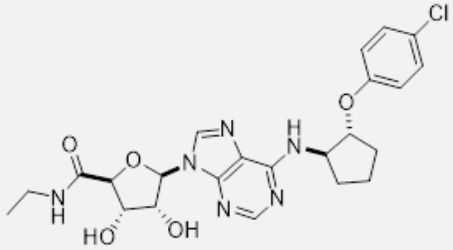	502.96	phenoxycyclopentyl

Derivative compounds based on **A17**, **A26** and **A47** (my partII undergraduate project) tested for activity at ARs were synthesised by Prof Marako's group (University of Athens) and made up to 100 mM stocks dissolved in DMSO. Compounds were arbitrarily named Ax or Lx (x = number) (structures detailed in Table 2.3).

Table 2.3. A17, A26 and A47 derivative compounds structures and their molecular weight.

Name	Structure	MW	Name	Structure	MW
A15	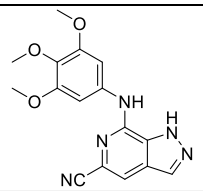	325.33	**A26**	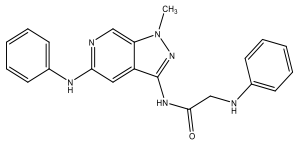	372.43
A17	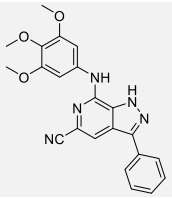	401.43	**L12**	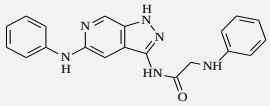	358.40
L2	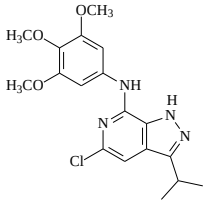	376.84	**L15**	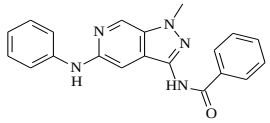	343.39
L3	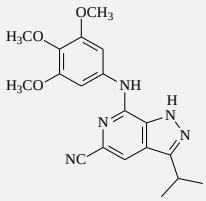	367.41	**L21**	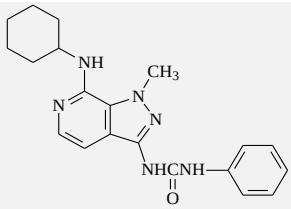	364.45
L4	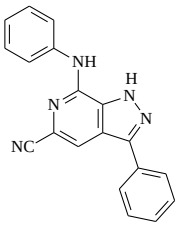	311.35	**A47**	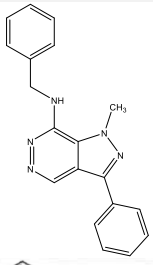	315.38
L5	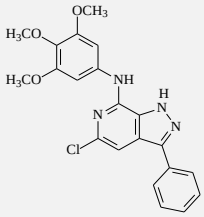	410.86	**L23**	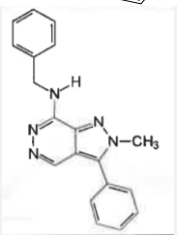	315.37
L6	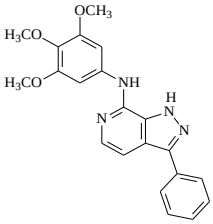	376.41	**L25**	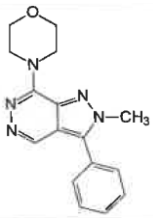	295.34
L7	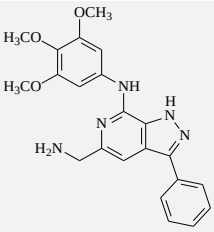	405.46	**L26**	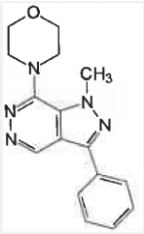	295.34

L8	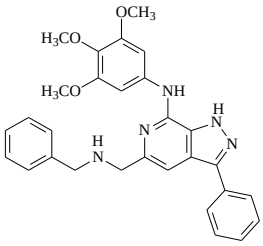	495.58	**L29**	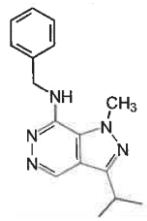	281.36
L9	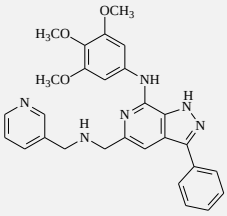	496.57	**L32**	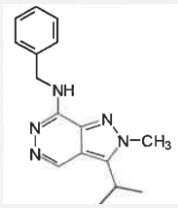	281.36
L10	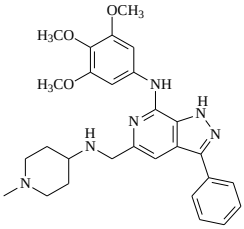	502.62			

As all the compounds were dissolved in DMSO, an equivalent amount of DMSO was used as a negative control in all experiments.

2.1.4 Growth media

The growth media used for culturing mammalian cells were Dulbecco's modified Eagle's medium (DMEM), DMEM/F-12, Ham's F12 nutrient mix and RPMI1640 media. These were all purchased from Life Technologies and supplemented with 10% v/v fetal bovine serum (FBS, Sigma-Aldrich, UK) and 1% v/v antibiotic/antimycotic (Sigma, UK).

Sterile Luria-Bertani (LB) medium, made up by adding 8 g LB powder (Sigma-Aldrich) to 400 mL distilled H_20 and autoclaving it, was used to grow *Escheriscia coli* either in solution or on an agar plate.

2.1.5 Laboratory buffer and media

Phosphate buffered saline (PBS) was made by adding one PBS tablets (Sigma-Aldrich) in 200 mL distilled H_2O and autoclaving it to produce a solution consisting of 2.7 mM KCl, 0.137 M NaCl and 0.1 M phosphate buffer at a pH of 7.4. Hank's balanced salt solution (HBSS), both with and without calcium, was purchased from Lonza.

2.1.6 DNA expression constructs

All constructs used in this study were either gifts from collaborators, purchased from commercial vendors, or generated in the laboratory by cloning or site-directed mutagenesis. The constructs and their source are detailed in Table 2.4.

Table 2.4. List of expression constructs used in this study

Construct	Source
pcDNA3.1-zeo	Invitrogen
pcDNA3.2-GIPR	Simon Dowell (GSK)
pcDNA3.2-GIPR Y141$^{1.43}$A	Site-directed mutagenesis
pcDNA3.2-GIPR L193$^{2.70}$A	Site-directed mutagenesis
pcDNA3.2-GIPR L194$^{2.71}$A	Site-directed mutagenesis
pcDNA3.2-GIPR R196A	Site-directed mutagenesis
pcDNA3.2-GIPR P197A	Site-directed mutagenesis
pcDNA3.2-GIPR G198A	Site-directed mutagenesis
pcDNA3.2-GIPR Q204A	Site-directed mutagenesis
pcDNA3.2-GIPR N210A	Site-directed mutagenesis
pcDNA3.2-GIPR Q211$^{3.24}$A	Site-directed mutagenesis
pcDNA3.2-GIPR Q220$^{3.33}$A	Site-directed mutagenesis
pcDNA3.2-GIPR Y231A	Site-directed mutagenesis
pcDNA3.2-GIPR Q286$^{45.50}$A	Site-directed mutagenesis
pcDNA3.2-GIPR W287$^{45.51}$A	Site-directed mutagenesis
pcDNA3.2-GIPR E288$^{45.52}$A	Site-directed mutagenesis
pcDNA3.2-GIPR R289A	Site-directed mutagenesis
pcDNA3.2-GIPR W296$^{5.36}$A	Site-directed mutagenesis
pcDNA3.1-myc-GIPR-RLuc	Kathleen Caron
pcDNA3.1-GIPR-Nluc	Dr Matthew Harris (Cambridge)
pEYFPN1-β-arrestin-1	Prof Kathleen Caron (UNC)
EYFPN1-β-arrestin-2	Prof Kathleen Caron (UNC)
BK(A)mGRK5	Prof Kathleen Caron (UNC)
pcDNA5/FRT	Fisher Scientific UK LTD
pOG44	Fisher Scientific UK LTD
pcDNA3.1-A_1R	Dr Steve Briddon (Nottingham)
pcDNA3.1-A_1R K291$^{7.56}$A	Site-directed mutagenesis
pcDNA3.1-A_1R I292$^{8.47}$A	Site-directed mutagenesis
pcDNA3.1-A_1R Q293$^{8.48}$A	Site-directed mutagenesis
pcDNA3.1-A_1R K294$^{8.49}$A	Site-directed mutagenesis
pcDNA3.1-Nluc- A_1R	Dr Steve Briddon (Nottingham)
pcDNA3.1-Nluc- A_1R T91$^{3.36}$A	Site-directed mutagenesis
pcDNA3.1-Nluc- A_1R F171$^{5.29}$A	Site-directed mutagenesis
pcDNA3.1-Nluc- A_1R E172$^{5.30}$A	Site-directed mutagenesis
pcDNA3.1-Nluc- A_1R L250$^{6.51}$A	Site-directed mutagenesis
pcDNA3.1-Nluc- A_1R H251$^{6.52}$A	Site-directed mutagenesis
pcDNA3.1-Nluc- A_1R N254$^{6.55}$A	Site-directed mutagenesis
pcDNA3.1-Nluc- A_1R S267$^{7.32}$A	Site-directed mutagenesis
pcDNA3.1-Nluc- A_1R Y271$^{7.36}$A	Site-directed mutagenesis

2.2 Methods

2.2.1 Mammalian cell culture

2.2.1.1 Cell culture

Cell culture procedures were conducted using proper aseptic technique in a flow laminar tissue culture hood in accordance with safe laboratory practices and standard microbiological procedures. All solutions and equipment that come into contact with cells were sterile and growth media were prewarmed in a water bath 37°C prior use. Unless otherwise stated, all cell lines were incubated in growth complete medium at 37°C in humidified 95% air and 5% CO2.

Human embryonic kidney (HEK) 293T, HEK-293S and HEK293-calcitonin receptor knock-out (ΔCTR) cells were gifted by AstraZeneca (AZ) (Cambridge, UK). HEK-293S cells stably expressing GIPR were made by Dr Harris (University of Cambridge), while HEK-293S stably expressing GLP-1R and HEK-293ΔCTR stably expressing GCGR were made by Dr Yeung (University of Cambridge). HEK-293 cells stably expressing rat Nluc-A_1R, human Nluc-A_1R or human Nluc-A_3R were made by Dr Barkan (University of Cambridge). Selection was maintained by culturing the cells with 800ng/uL G418 antibiotic (TOKU-E, Ghent, Belgium). All HEK-293 cell lines were cultured in Dulbecco's modified Eagle's medium (DMEM)/Nutrient mixture F12 supplemented with Glutamax (ThermoFisher, UK), with 10% Heat inactivated Foetal Bovine Serum (FBS) (Sigma-Aldrich, Poole, Dorset, UK) and 1% antibiotic antimycotic solution (Sigma-Aldrich, Poole, Dorset, UK) (v/v).

CHO-KI cells stably expressing A_1R, A_{2A}R or A_{2B}R and Flp-In^{TM} CHO cells stably expressing A_3R were made by Dr Barkan (University of Cambridge). Selection was maintained by culturing the CHO-A_{2A}R or CHO-A_{2B}R cells with 800ng/uL G418 antibiotic or by culturing the Flp-In^{TM} CHO-A_3R cells with 600 µg/mL hygromycin B (Thermo Fisher Scientific). Flp-In^{TM} CHO cells were purchased from Thermo Fisher Scientific (R75807) and selection was maintained by culturing the cells with 100 µg/mL Zeocin Selection Antibiotic (Thermo Fisher Scientific). All CHO cell lines were cultured in Hams F-12 nutrient mix (21765029, Thermo Fisher Scientific) supplemented with 10% Heat inactivated Foetal Bovine Serum (FBS) (Sigma-Aldrich, Poole, Dorset, UK) and 1% antibiotic antimycotic solution (Sigma-Aldrich, Poole, Dorset, UK) (v/v).

For β-arrestin recruitment assays, cells were grown in minimum essential media (MEM) with 2% heat inactivated FBS, 1% antibiotic antimycotic solution, and 1% L-Glutaine (v/v) for 24 hours before assaying.

Rat INS-1 WT cells were gifted by AZ and cultured in RPMI 1640 medium supplemented with 10% heat-inactivated FBS, 10mM HEPES, 1mM sodium pyruvate and 50μM β-mercaptoethanol.

2.2.1.2 Generation of stable cell lines

To reduce the need for transient transfections, a HEK-293 cell lines stably expressing Nluc-A_1R mutants T91$^{3.36}$A, F171$^{5.29}$A, E172$^{5.30}$A, L250$^{6.51}$A, H251$^{6.52}$A, N254$^{6.55}$A, S267$^{7.32}$A and Y271$^{7.36}$A were generated. HEK-293 cells were transfected with mutant pcDNA3.1-Nluc-A_1R and grown in 6 well plate in complete DMEM/F12 containing 800 ng/µL G418 (Sigma Aldrich), to select for transfected cells using the neomycin resistance gene contained within pcDNA3.1-Nluc-A_1R. G418-containing media was replaced every 48 hours until a well reached 100% confluency. Cells were then harvested and transferred to T25 flask for culturing. Once confluent, the cells were tested for their ability to bind CA200645 in NanoBRET binding assay. Cells were then maintained in complete DMEM/F12 containing 800 ng/µL G418 and stocks were frozen down for long-term cryo-storage as described below.

Stable Flp-In-CHO cell lines were generated through co-transfection of the Flp-In-CHO cells with pcDNA5/FRT expression vector (Thermo Fisher Scientific) containing the WT or mutant A_1R and the Flp recombinase expressing plasmid, pOG44 (Thermo Fisher Scientific). Transfection of cells seeded in a 6-well plate at a confluency of ≥80% was performed using Fugene HD transfection reagent (Promega) in accordance with the manufacturer's instructions. A total of 2 µg of DNA (receptor to pOG44 ratio of 1:1) was transfected per well at a DNA:Fugene HD reagent ratio of 1:3 (w/v). 24 h post-transfection, selection using 600 µg/mL hygromycin B (Thermo Fisher Scientific) (concentration determined through preforming a kill curve) was performed and hygromycin B-containing media was replaced every 48 hours until a well reached 100% confluency and cells were transferred into a T25 flask. Stable Flp-In-CHO cell lines expressing the receptor of interest were selected using 600 µg/mL hygromycin B whereby the media was changed every two days.

2.2.1.3 Long-term cryo-storage and recovery

To freeze down cell aliquots for long-term cryo-storage, the cells were first grown to roughly 90% confluency in an appropriate complete media in a culture vessel (T25 or T75 flask). Cells were then detached from the culture vessel using trypsin/EDTA, harvested and centrifuged. Cells were resuspended in freezing medium containing 90% of complete medium and 10% DMSO (v/v). Cells were frozen gradually in an insulated box in -70 to -80°C freezer before transferring to liquid nitrogen storage or -140°C cryo-freezer.

To recover cells from long-term cryo-storage, the cells were thawed as quickly as possible by gently swirling the vial in 37°C water bath to minimize intracellular ice crystal growth during the warming process. The cells were then diluted carefully using prewarmed complete media and the whole cell suspension was centrifuged at 1400 rpm for 4 minutes. Following centrifugation, the supernatant was decanted without disturbing the cell pellet and cells were resuspended in complete growth medium and transferred into appropriate culture vessel.

2.2.2 Molecular biology techniques

2.2.2.1 Escherichia coli transformation

DNA plasmids in this study were amplified using competent *E. coli* DH5α cells (Stratagene, San Diego, California, US), which were propagated using standard methods as described in (Glover and Hames, 1985). After slowly thawing 100 µL of competent cells' suspension on ice, approximately 100 ng plasmid DNA was added to the cells. The cell suspension was incubated on ice for 5 minutes, heat shocked at 42 °C for 1 to 2 minutes in a water bath and rested on ice for further 5 minutes. The cell suspension was then added to LB containing either ampicillin (100 mg/mL) or kanamycin (50 mg/mL), where appropriate, and cultured at 37 °C with constant shaking at 180 rpm. For cells with kanamycin resistance, the cells were cultured only in LB for 1 hour before the addition of kanamycin. Alternatively, the transformed cells could be plated on LB agar plates containing either ampicillin (100 mg/mL) or kanamycin (50 mg/mL), where appropriate, and cultured overnight at 37 °C .

2.2.2.2 Plasmid DNA purification

All plasmids used in this study were prepared by transformation and culture of competent DH5a cells described above and subsequent purification using QIAprep Spin Miniprep Kit (Qiagen, UK) following the manufacturer's instruction. First, overnight bacterial culture was centrifuged at 3200 rpm for 5 minutes and the supernatant was discarded. Bacterial pellet was then lysed under alkaline conditions using buffer P1, neutralized using buffer P2, and adjusted to high-salt binding solution using buffer N3. Cell suspension was centrifuged at 13,000 rpm for 10 minutes and the supernatant was purified on QIAprep silica membrane (QIAprep minispin column), washed with ethanol-based buffer PE, and eluted in 30 or 50 µl of warm distilled H_2O. The quality and concentration of DNA was measured using a NanoDrop™ Lite spectrophotometer (ThermoFisher Scientific), with a 260nm/280 nm absorbance ratio of 1.8 accepted as pure DNA.

2.2.2.3 Site-directed mutagenesis

pcDNA3.2-GIPR mutants Y141$^{1.43}$A, L193$^{2.70}$A, L194$^{2.71}$A, R196A, P197A, G198A, Q204A, N210A, Q211$^{3.24}$A, Q220$^{3.33}$A, Y231A, Q286$^{45.50}$A, W287$^{45.51}$A, E288$^{45.52}$A, R289A and W296$^{5.36}$A, pcDNA3.1-A_1R mutants K291$^{7.56}$A, I292$^{8.47}$A, Q293$^{8.48}$A and K294$^{8.49}$A and pcDNA3.1-Nluc-A_1R mutants T91$^{3.36}$A, F171$^{5.29}$A, E172$^{5.30}$A, L250$^{6.51}$A, H251$^{6.52}$A and N254$^{6.55}$A were made using site-directed mutagenesis using Lightning QuikChange Kit (Agilent Technologies), following the manufacturer's instructions. Forward and reverse oligonucleotides were designed using the online primer design tool for the Lightning QuikChange Kit and are detailed in Table 2.5. Reaction components and cycle parameters are stated in Table 2.6 and Table 2.7.

Table 2.5. Forward and reverse primers used for QuikChange Lightning site-directed mutagenesis. Bold letters indicate changed bases relative to WT protein.

Mutant	Primer	Primer sequence
pcDNA3.2-GIPR Y141$^{1.43}$A	Reverse	ggagtagccgacagtg**gc**catgacctgcaaccgc
	Forward	gcggttgcaggtcatg**gc**cactgtcggctactcc
pcDNA3.2-GIPR L193$^{2.70}$A	Reverse	ggtcgaggtagc**gc**acggtctcggctgaga
	Forward	tctcagccgagaccgt**gc**gctacctcgacc
pcDNA3.2-GIPR L194$^{2.71}$A	Reverse	gccaggtcgaggt**gc**cagacggtctcgg
	Forward	ccgagaccgtctg**gc**acctcgacctggc
pcDNA3.2-GIPR R196A	Reverse	gggccaggtgcaggta**gc**agacggtctc
	Forward	gagaccgtct**gc**tacctgcacctggccc
pcDNA3.2-GIPR P197A	Reverse	ggtaggggcca**g**ctcgaggtagcag
	Forward	ctgctacctcgag**c**tggcccctacc
pcDNA3.2-GIPR G198A	Reverse	cccaaggtagggg**g**caggtcgaggtag
	Forward	ctacctcgacctg**c**cccctaccttggg
pcDNA3.2-GIPR Q204A	Reverse	cagcgcaagggcc**gc**gtccccaaggtag
	Forward	ctaccttggggac**gc**ggcccttgcgctg
pcDNA3.2-GIPR N210A	Reverse	agcgagggcctgg**gc**cccacagcgcaagg
	Forward	ccttgcgctgtgg**gc**ccaggccctcgct
pcDNA3.2-GIPR Q211$^{3.24}$A	Reverse	ggcagcgagggcc**gc**gttccacagcgca
	Forward	tgcgctgtggaac**gc**ggccctcgctgcc
pcDNA3.2-GIPR Q220$^{3.33}$A	Reverse	ctgggtcacgatc**gc**ggccgtgcggcag
	Forward	ctgccgcacggcc**gc**gatcgtgacccag
pcDNA3.2-GIPR Y231A	Reverse	ccagcagccacgtg**gc**gttggcacccacgc
	Forward	gcgtgggtgccaac**gc**cacgtggctgctg
pcDNA3.2-GIPR Q286$^{45.50}$A	Reverse	cgttgcgctcccag**gc**ctgcgtgttctcgt
	Forward	acgagaacacgcag**gc**ctgggagcgcaacg
pcDNA3.2-GIPR W287$^{45.51}$A	Reverse	acttcgttgcgctcc**gc**gcactgcgtgttctc
	Forward	gagaacacgcagtgc**gc**ggagcgcaacgaagt
pcDNA3.2-GIPR E288$^{45.52}$A	Reverse	gacttcgttgcgc**g**cccagcactgcgt
	Forward	acgcagtgctggg**c**gcgcaacgaagtc
pcDNA3.2-GIPR R289A	Reverse	ccttgacttcgttg**gc**ctcccagcactgcg
	Forward	cgcagtgctgggag**gc**caacgaagtcaagg
pcDNA3.2-GIPR W296$^{5.36}$A	Reverse	gggtccgtataatccac**gc**aatggccttgacttcgttg
	Forward	caacgaagtcaaggccatt**gc**gtggattatacggaccc
pcDNA3.1-A$_1$R K291$^{7.56}$A	Reverse	cgcggaacttctggatg**gc**gaaggcatagacaatgg
	Forward	ccattgtctatgccttc**gc**catccagaagttccgcg
pcDNA3.1-A$_1$R I292$^{8.47}$A	Reverse	gacgcggaacttctgg**gc**gcggaaggcatagaca
	Forward	tgtctatgccttccgc**gc**ccagaagttccgcgtc
pcDNA3.1-A$_1$R Q293$^{8.48}$A	Reverse	ggtgacgcggaacttc**gc**gatgcggaaggcatag
	Forward	ctatgccttccgcatc**gc**gaagttccgcgtcacc
pcDNA3.1-A$_1$R K294$^{8.49}$A	Reverse	ggtgacgcggaac**gc**ctggatgcggaaggcatag
	Forward	ctatgccttccgcatccag**gc**gttccgcgtcacc
pcDNA3.1-Nluc- A$_1$R T91$^{3.36}$A	Reverse	gatggagctctggg**c**gaggatgaggaccg
	Forward	cggtcctcatcctc**g**cccagagctccatc
pcDNA3.1-Nluc- A$_1$R F171$^{5.29}$A	Reverse	tgctgatgaccttctcg**gc**ctcgcacttgatcacgg
	Forward	ccgtgatcaagtgcgag**gc**cgagaaggtcatcagca
pcDNA3.1-Nluc- A$_1$R E172$^{5.30}$A	Reverse	ccatgctgatgaccttc**g**cgaactcgcacttgatc
	Forward	gatcaagtgcgagttcg**c**gaaggtcatcagcatgg
pcDNA3.1-Nluc- A$_1$R L250$^{6.51}$A	Reverse	cagttgaggatgtgc**gc**aggcagccagctgaggg

pcDNA3.1-Nluc- A_1R H251$^{6.52}$A	Forward	Ccctcagctggctgcct**gc**gcacatcctcaactg
	Reverse	gatgcagttgaggatg**gc**caaaggcagccagctg
pcDNA3.1-Nluc- A_1R N254$^{6.55}$A	Forward	cagctggctgcctttg**gc**catcctcaactgcatc
	Reverse	cagaagagggtgatgcag**gc**gaggatgtgcaaaggcag
	Forward	ctgcctttgcacatcctc**gc**ctgcatcaccctcttctg

Table 2.6. Reaction components and amounts used for QuikChange Lightning site-directed mutagenesis

Component	Amount
10x reaction buffer	5 µL
dsDNA template	10-100 ng
Forward primer	125 ng
Reverse primer	125 ng
dNTP mix	1 µL
QuickSolution reagent	1.5 µL
ddH_2O	Up to 50 µL
QuikChange Lightning Enzyme	1 µL

Table 2.7. Cycle parameters used for QuikChange Lightning site-directed mutagenesis

Step	Number of cycles	Temperature (°C)	Time (s)
1	1	95	120
2	18	95	20
		60	10
		68	30 (per kb of plasmid length)
3	1	68	300
4	1	4	Paused

2.2.2.4 DNA sequencing

To ensure no mutation has been introduced in amplified plasmids and that all plasmids have been correctly mutated using site-directed mutagenesis, all DNA constructs were verified prior first use by double-stranded DNA sequencing using vector-specific oligonucleotides. DNA was sequenced using Sanger Sequencing by the Department of Biochemistry (University of Cambridge).

2.2.2.5 Transfections

All transient transfections of HEK-293S or HEK-293T cells in this study was performed unless otherwise stated 48 hours before assaying using polyethylenimine (PEI, with MW 25kDa, Polyscience Inc, UK), which is a stable cationic polymer that condenses DNA and generates a positive charge around

the particle allowing DNA-PEI complexes to be endocytosed by cells. PEI was made up to 1mg/ml stocks in H_2O following manufacturer's instruction. Briefly, cells were seeded 24 hours prior to transfection to allow them to reach roughly 70% confluency. PEI and DNA in 6:1 ratio (v/w) were incubated separately in 150mM NaCl for 5 minutes, before being combined and incubated for another 10 minutes at RT. The overnight culture medium was replenished with fresh complete medium before adding DNA-PEI complexes slowly to the cells

Reverse transient transfections of HEK-293S cells with WT or mutant pcDNA3.2-GIPR for $(Ca^{2+})_i$ mobilisation assays was performed 48 hours before assaying using FuGENE®HD (Promega, UK). DNA and FuGENE®HD were incubated separately in serum free DMEM/F12 at a 1:3 ratio (w/v) for 5 minutes, before being combined and incubated for another 10 minutes at RT. Meanwhile, confluent cells were harvested and resuspended in fresh complete medium and diluted 1 in 4 before adding FuGENE-DNA complexes and plating cells into 96-well plates for assaying.

2.2.3 Pharmacological investigation and signalling assays

2.2.3.1 cAMP accumulation assay

Flp-In CHO-A_3R, CHO-K1-A_1R, CHO-K1-A_{2A}R, CHO-K1-A_{2B}R, HEK-293S-GIPR, HEK-293S-GLP-1R, HEK-293ΔCTR-GCGR or HEK-293S cells transiently transfected with WT or mutant pcDNA3.2-GIPR (250 ng per 1 well of 6 well plate) were harvested using 0.05% trypsin and resuspended in stimulation buffer (SB). The SB was made up of PBS containing 0.1% BSA and either 25 µM rolipram (Sigma Aldrich) for ARs expressing cells or 0.5 mM 3-isobutyl-1-methylxanthine (IBMX, Sigma Aldrich) for other cells. Cells were then seeded in 384-well white Optiplate at a cell density of either 2,000 cells per well for ARs expressing cells or 750 cells per well for other cell lines. Cell density was counted using haemocytometer. Cells were then stimulated with an agonist and either DMSO or compound, where appropriate, for either 30 minutes for ARs expressing cells or 8 minutes per well for other cell lines. For each experiment, stimulation by forskolin in a range of concentrations (0.1 pM to 0.1 mM) was also included.

For $G_{i/o}$-coupled receptors A_1R and A_3R the cells were co-stimulated with 10 or 1 µM forskolin, respectively. Forskolin is an adenylyl cyclase activator that enables measurement of cAMP inhibition curves of $G_{i/o}$-coupled receptors.

cAMP accumulation for G_s-coupled receptors or inhibition for $G_{i/o}$-coupled receptors was measured using a Europium Lance© cAMP detection kit (Perkin Elmer), following the protocol given by the manufacturer (Figure 2.1). Briefly, after stimulation for indicated times, 10 µl of detection

reagent was applied to each cell and plate was incubated for 1-24 hours at RT. To avoid evaporation, the Optiplate was sealed with a ThermalSeal® film (EXCEL Scientific).

Plates were read using a Mithras LB 940 multimode microplate reader (Berthold Technologies) with laser excitation set at 340 nm and fluorescence from homogeneous time-resolved fluorescence resonance energy transfer (FRET) detected at 665 nm. All data were normalized to the maximal level of cAMP accumulation from cells in response to 100 µM forskolin stimulation.

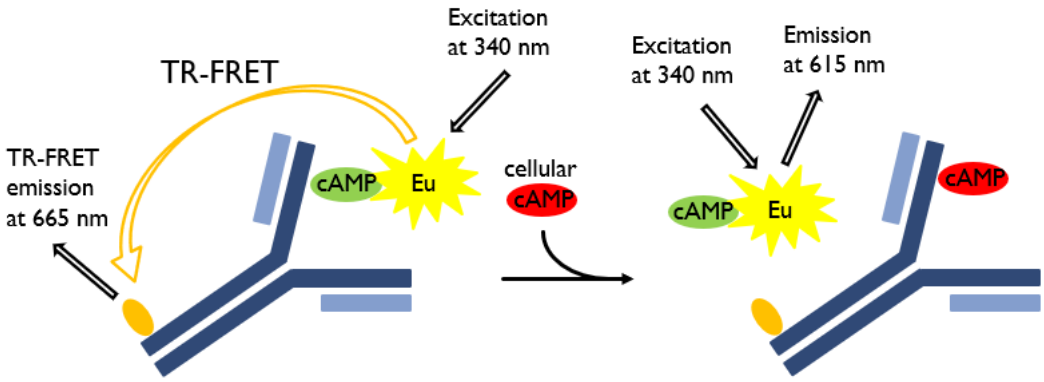

Figure 2.1. Principle of Europium Lance© cAMP detection kit. When there is no cAMP produced naturally by the cell, the supplied biotin-cAMP, which is strongly bonded to Europium-streptavidin chelate, binds the AlexaFluor®647 conjugated-anti cAMP antibody. Excitation of Europium at 340 nm then leads to homogenous time-resolved fluorescence resonance energy transfer (TR-FRET) to the Alexa Fluor® 647 antibody resulting in emission at 665 nm. When cAMP is produced by the cell, it displaces the biotin-cAMP from its binding place on the antibody resulting in the loss of TR-FRET and reduction of 665 nm emission.

2.2.3.2 Schild analysis

NECA dose-response curves were constructed in the presence of either DMSO or 1 µM tested compound using cAMP accumulation data with NECA in a range of concentrations (1 pM to 1 µM). For tested compounds A26, L5 and L21 10 µM concentration was used instead due to low efficacy of the compounds at 1 µM. Using three-parameter logistic equation built into GraphPad Prism 9.3, EC_{50} values were estimated and Schild analysis was performed manually.

2.2.3.3 Intracellular calcium mobilisation assay

HEK-293S cells stably expressing GIPR or GLP-1R, HEK-293ΔCTR cells stably expressing GCGR or HEK-293S cells reverse transfected with WT or mutant pcDNA3.2-GIPR (100 µg DNA per 100 µL cells) were seeded on 0.01% poly-l-lysine (PLL) coated black 96-well clear bottomed plates (Corning) 48 hours prior to assaying to grow to full confluency. On the assay day, cells were washed once with calcium-containing Hank's Balanced Salt solution (HBSS) before addition of 40 µl 10 µM Fluo-4/AM containing 2.5 mM probenecid to each well. Cells were then incubated for 1h at room temperature (RT), washed twice with calcium-containing HBSS containing 0.1% BSA (w/v) before addition of 100µl calcium-free HBSS containing 0.1% BSA (w/v), with or without tested compounds or DMSO. Ligands were diluted in the range 1µM to 0.1nM in calcium-free HBSS containing 0.1% BSA (w/v) and DMSO or tested compounds, where appropriate. 10 µM ionomycin was included on each column of the ligand plate as a positive control and to normalise all data to it. Ligands were added robotically using a BD Pathway 855 high-content bioimager capturing images every second for 80 seconds with an excitation wavelength set to 494 nm and an emission wavelength set to 516 nm. The sum of the fluorescence intensity for each well was obtained and corrected for background fluorescence. Maximum fluorescence intensity at each agonist concentration was then used to generate dose response curves.

2.2.3.4 NanoBRET binding assay

HEK-293 cells stably expressing rat Nluc-A_1R, human Nluc-A_1R or human Nluc-A_3R were harvested and 100 µl of cell suspension was seeded at 10,000 cells per well in into poly-L-lysine (PLL) coated white, 96-well plates (Perkin Elmer Life Sciences) and cultured overnight. After 24 hours, cells were washed with PBS and 100 µl of Nano-Glo Luciferase substrate furimazine diluted to final concentration of 0.1 µM in PBS containing 0.1% BSA was added before incubating cells for 5 minutes in dark at RT. Afterwards, 100 µl of ligands diluted in PBS containing 0.1% BSA and 20nM or 5 nM CA200645 for A_1R or A_3R expressing cells, respectively, was added and plates were immediately read using a Mithras LB 940 multimode microplate reader (Berthold Technologies). CA200645 is a high affinity AR xanthine amine congener (XAC) derivative containing a polyamide linker connected to the BY630 fluorophore that acts as a fluorescent antagonist at both A_1R and A_3R with a slow off-rate (Stoddart et al., 2012). Filtered light emission at 450 nm and > 610 nm (640-685 nm band pass filter) was measured and the raw BRET ratio calculated by dividing the 610 nm emission with the 450 nm emission (Figure 2.2). Nonspecific binding, determined by binding of a high concentration of unlabelled antagonist MRS 1220 (10 nM) for Nluc-A_3R or DPCPX for Nluc-A_1R, was subtracted from the raw

NanoBRET ration to get specific binding of compounds at A_1R or A_3R. BRET ratio at 10 minutes was then used to generate dose response curves.

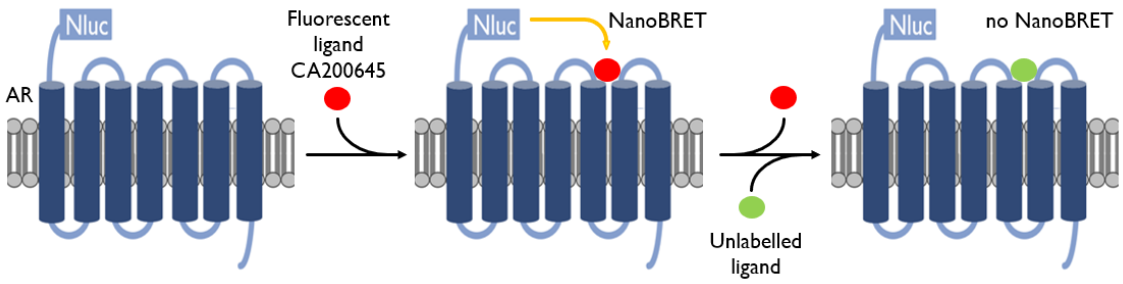

Figure 2.2. Schematic diagram of the NanoBRET binding assay. Addition of the fluorescent ligand CA200645 causes it to bind the luciferase-tagged adenosine receptor, which is called the association phase of receptor-ligand binding kinetics, and NanoBRET to occur. When an unlabelled AR ligand is added, it outcompetes the CA200645 from its binding place at the receptor, initiating the dissociation phase of the receptor-ligand binding kinetics. This figure was adapted from (Suchankova et al., 2021).

To measure the K_d of CA200645 at WT or mutant Nluc-A_1R, the experiment was conducted as described above except for the addition of 100 µl of CA200645 in a range of concentrations (1 nM to 300 nM) diluted in PBS containing 0.1% BSA instead of the addition of ligands.

2.2.3.5 β-arrestin 1/2 recruitment assay

6,000,000 HEK-293T cells were seeded in a 10 cm dish and cultured overnight in complete DMEM/F-12 media. After 24h, the cells were transfected with a 5:4:1 ratio of YFP-β-arrestin:GRK:GIPR-Nluc/Rluc . After further 24 hours, cells were resuspended in 2% MEM and seeded at 150,000 cells per well of a PLL coated white 96-well plate (Perkin Elmer). On the assay day, cells were washed once with PBS. 80 µl stimulation buffer (SB) (PBS containing 0.49 mM $MgCl_2$.6H2O, 0.9 mM $CaCl_2$.2H2O and 0.1% BSA), with or without the test compound was then added to each well, followed by 10 µL coelenterazine h (diluted in SB) with a final concentration of 5 µM in each well and the plates were incubated for 10 min at RT in the dark. Finally, varying range GIP(1-42) diluted in SB (10 pM to 1 µM) was added and emission was immediately measured at 460 or 485 nm (Nluc or Rluc donor respectively) and 530 nm (YFP acceptor) on a Berthold Mithras LB 940 multimode microplate reader (Figure 2.3).

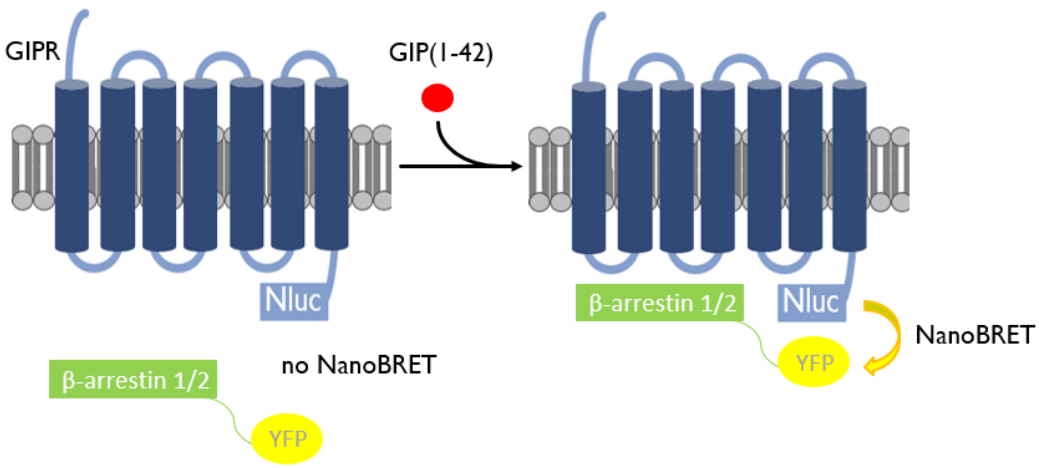

Figure 2.3. Schematic diagram of the β-arrestin 1/2 recruitment assay. Addition of GIP(1-42) causes it to bind the GIPR C-terminally tagged with Nluc. This initiates the recruitment of β-arrestin 1/2 tagged with YFP to the GIPR, which enables BRET between the Nluc and the YFP, which results in the increase of the BRET ratio signal detected.

The bioluminescence resonance energy transfer (BRET) ratio was calculated by dividing the 530 nm emission by 460 nm emission. The value at 0 minutes was subtracted from each time point to account for background emission. The BRET ratio at 10-minute time point was used to produce dose-response curves.

2.2.3.6 Glucose-stimulated insulin secretion

Rat INS-1 WT cells were harvested and resuspended in RPMI media containing 11mM glucose. The cells were then seeded at 150,000 cells per well of fibronectin coated clear 96 well plate (SLS) and cultured overnight. After 24 hours, cells were incubated in glucose-free RPMI media for 3h at 37°C. Cells were then washed once with Krebs-Ringer buffer (KRB) containing 0.2% BSA and 2.8mM glucose and incubated in 100 µl 2.8mM glucose KRB+BSA for 1h at 37°C before washing the cells twice more with 2.8mM glucose KRB+BSA. Agonists were made with or without compounds in KRB+BSA containing 16.7mM glucose, 1 in 1000 aprotinin (v/v) and 100 nM sitagliptin and 100 µl was added to the cells, which were then left at 37°C for 1h before stopping the reactions by placing cells on ice for 5 min. The supernatant was diluted 1:25 and insulin was measured using the Cisbio Insulin Ultra-Sensitive Assay kit according to the manufacturer's instructions (Figure 2.4).

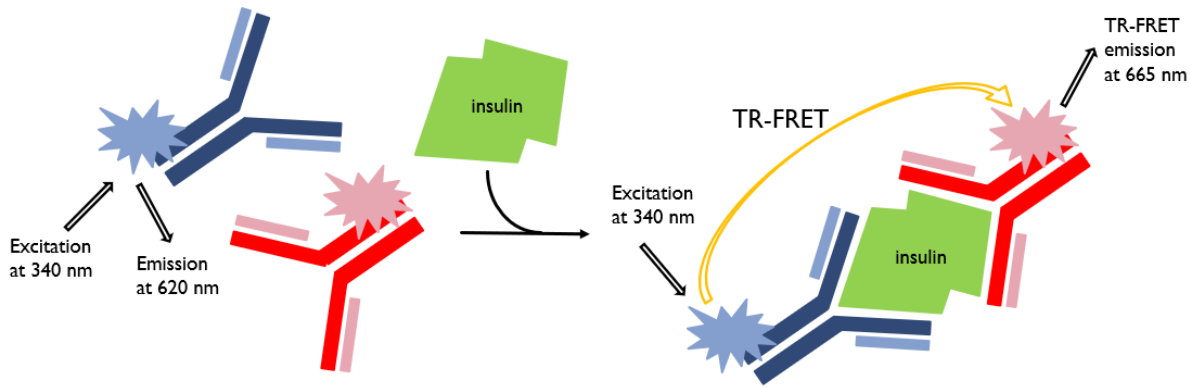

Figure 2.4. Principle of Insulin High Range Assay kit. When there is no insulin produced by the cell, the supplied fluorophores tagged anti-insulin antibodies are too far from each other, no TR-FRET occurs and emission at 620 nm occurs following 340 nm excitation. However, when insulin is present, it gets bound by the two distinct anti insulin antibodies bringing the fluorophores closer together and enabling TR-FRET to occur resulting in emission at 665 nm.

Plates were read using a Mithras LB 940 multimode microplate reader (Berthold Technologies), using excitation at 340nm and emission filters at 620nm and 665nm. The ratio of acceptor to donor was calculated (λ665/λ620) and the ΔF% calculated using equation 16 (in the data analysis section). The sample insulin content (ng/ml) was calculated by interpolating from a standard curve and then scaled as per the dilution used (Table 2.8). When whole cell measurements were taken, the response was expressed as a fraction of the whole cell insulin content. Data were expressed as a fraction of the response to 2.8mM glucose.

Table 2.8. Dilution range for insulin samples originating from different points in the assay

Sample Origin	Dilution Range
Basal insulin secretion	10-20-fold
Stimulation	20-50-fold
Whole cell insulin content	400-500-fold

2.2.4 *In silico* modelling techniques

2.2.4.1 Docking

10 hGIPR homology models made by Dr Rahman and his lab based on other GPCRs' solved structures and 1 solved hGIPR model were used (Table 2.9). Before the docking, structures of all compounds and hGIPR models were prepared using the AutoDock Tools.

Table 2.9. hGIPR homology models (1-10) and hGIPR model (11) used in this study

Model	Template GPCR[a]	PDB[b]	Modification
1	GLP-1R	5VAI	Attached GIP
2	GLP-1R	5VAI	Missing N-termini
3	GLP-1R	5NX2	Missing N-termini
4	GLP-1R	6B3J	Missing N-termini
5	GLP-1R	6ORV	Missing N-termini
6	PTHR1	6BNI	Missing N-termini
7	A2AR	5G53	Missing N-termini
8	CALCR	5UZ7	Missing N-termini
9	CALCR	6E3Y	Missing N-termini
10	CALCR	6NIY	Missing N-termini
11	GIPR	7DTY	Attached GIP

[a] The GPCR with a solved structure that the hGIPR homology model is based on
[b] Unique PDB identifier of the template GPCR from the GPCR database (gpcrdb.org)

For the blind docking, an unbiased (''blind'') docking approach (Iorga et al., 2006) was used, where the grid map in AutoGrid was generated from the hGIPR models without assuming a priori any putative binding site(s) for the ligands. Three independent docking runs for each compound were performed in AutoDock Vina with the exhaustiveness set to 24 (Trott and Olson, 2010). The relative importance of all sites identified have been assessed based on binding affinities (BA; ΔG, kcal/mol) of the compounds to that site, frequency of the compounds binding to that site in any given model (reproducibility) and the number of models the site appeared in. This information was compared to blind docking results from ICM-Pro 3.8 (Schapira et al., 2003) performed by Dr Rahman (University of Cambridge).

AutoDock Vina was then also used for focused docking around the proposed GIPR allosteric site at ECL1 using same protocol as above but restricting the docking area to the desired 3D space. Results were then supplemented by focused docking carried out by Dr Rahman using GlideXP (Friesner et al., 2004).

For the selected poses, the corresponding 2D ligand interaction diagrams were generated using PoseView™ implemented in the ProteinsPlus webserver (https://proteins.plus/).

2.2.4.2 *In silico* techniques for allosteric site prediction

To predict potential ligand-binding allosteric pockets, a variety of in silico tools and methods has been used on the GLP-1R-based hGIPR homology models made by Dr Rahman and his lab (models 1-5 in Table #). The methods utilised in this study were 3DLigandSite (http://www.sbg.bio.ic.ac.uk/3dligandsite), GPCR-SAS (http://lmc.uab.cat/gpcrsas/gpcrsas/), ConSurf (https://consurf.tau.ac.il/overview.php), PSI-BLAST (https://blast.ncbi.nlm.nih.gov/Blast.cgi) followed by pySCA (https://github.com/ranganathanlab/pySCA), POCASA (http://g6altair.sci.hokudai.ac.jp/g6/service/pocasa/), FTmap (https://ftmap.bu.edu), SPACER (http://allostery.bii.a-star.edu.sg/) and PARS (http://bioinf.uab.cat/pars). All methods have been performed using default settings following instructions on the websites.

2.3 Data analysis

Data analysis for in vitro experiments was performed using GraphPad Prism 9.3 (Graphpad software, San Diego, CA). For cAMP accumulation, $(Ca^{2+})_i$ mobilisation and β-arrestin recruitment assays, the data were fitted with log agonist vs response 3 parameter non-linear regression (equation 1) to calculate the potency (EC_{50} or IC_{50} for antagonists), basal (E_{min}) and maximal (E_{max}) signalling.

$$Response = E_{min} + \frac{(E_{min} - E_{max})}{(1+10^{(logEC_{50} - \log[Agonist])})} \quad (1)$$

To determine whether a compound was an allosteric modulator an operational model of allosterism (equation 2) was used to calculate the allosteric cooperativity factor (αβ) (Leach et al., 2007).

$$E = \frac{E_{max}(\tau_A[A](K_B + \alpha\beta[B]) + \tau_B[B]K_A)^n}{([A]K_B + K_AK_B + K_A[B] + \alpha[A][B])^n + (\tau_A[A](K_B + \alpha\beta[B]) + \tau_B[B]K_A)^n} \quad (2)$$

where E is the response, E_{max} is the maximum signalling response, [A] is the concentration of the agonist, [B] is the concentration of the compound, n is the cooperativity factor, K_A and K_B is the intrinsic

affinity of orthosteric agonist and compound, respectively, and τ_A and τ_B is the intrinsic efficacy of orthosteric agonist and compound, respectively.

To calculate the relative activities (RA) of compounds using data derived from cAMP accumulation assay equation 3 was used,

$$RA = \frac{EC_{50} \times E_{max}\ (reference\ compound)}{EC_{50} \times E_{max}\ (compound)} \quad (3)$$

where E_{max} is the maximal response and EC_{50}/IC_{50} is the agonist concentration required to produce a half-maximal response, and web plot was plotted using Microsfoft Excel. Since the receptors are expressed in the same cell background and adenosine or NECA are full potent agonists across all the adenosine subtypes, we reasoned that changes in log (RA) for a given ligand, relative to NECA or adenosine at A_1R, would provide a quantitative means of comparing receptor selectivity of individual adenosine receptor ligands.

To calculate the dissociation constant (pK_d) using Schild analysis, equation 4 was used.

$$\frac{D'}{D} = 1 + [A]K_2 \quad (4)$$

where D' and D are the IC_{50} values of NECA with and without an antagonist present, respectively, [A] is the antagonist concentration, and K_2 is the affinity constant (KA) of the antagonist used (Tallarida, 1986, Manual of Pharmacologic Calculations).

To calculate CA200645 K_d at WT and mutant Nluc-A_1R using NanoBRET binding assay, data were fitted with the "One site – Specific binding" equation built in GraphPad Prism 9.3 (equation 5).

$$Response = \frac{B_{max}[A]}{K_d + [A]} \quad (5)$$

where B_{max} is the maximum specific binding, [A] is the concentration of the fluorescent ligand and K_d is the equilibrium dissociation constant.

To calculate compound affinity (pk_i) at ARs using NanoBRET binding assay, data were fitted with the "One site – Fit K_i" model derived from the Cheng and Prusoff equation built into GraphPad Prism 9.3 (equations 6 and 7).

$$LogEC_{50} = Log10^{LogK_i\left(1+\frac{[A]}{K_A}\right)} \quad (6)$$

$$Response = Bottom + \frac{Top - Bottom}{1 + 10^{X - LogEC_{50}}} \quad (7)$$

where [A] is the concentration of the fluorescent ligand, K_A is the dissociation constant of the fluorescent ligand, top and bottom are plateaus in the units of Y axis and K_i is the equilibrium dissociation constant of the unlabelled ligand in Molar.

For the extraction of kinetic parameters from NanoBRET binding assay, the data were fitted with the 'kinetics of competitive binding' model build into GraphPad Prism 9.3 (equations 8-15).

$$K_A = k_1 \times [A] \times e^{-9} + k_2 \quad (8)$$

$$K_B = k_3 \times [B] \times e^{-9} + k_4 \quad (9)$$

$$S = SQRT((K_A - K_B)^2 + 4 \times k_1 \times k_3 \times [A] \times [B] \times e^{-18}) \quad (10)$$

$$K_F = 0.5 \times (K_A + K_B + S) \quad (11)$$

$$K_S = 0.5 \times (K_A + K_B - S) \quad (12)$$

$$DIFF = K_F - K_S \quad (13)$$

$$Q = \frac{B_{max} \times k_1 \times [A] \times e^{-9}}{DIFF}) \quad (14)$$

$$Y = Q\left(k_4 \frac{DIFF}{K_F K_S} + \frac{k_4 - k_f}{K_F}\right) \exp\left(-K_F X - \frac{k_4 - K_S}{K_S}\right) \exp\left(-K_S X\right) \quad (15)$$

where k_1 and k_3 are the association rate constants of labelled and unlabelled ligands, respectively, in M^{-1} min^{-1}, k_2 and K_4 are the dissociation rate constants of labelled and unlabelled ligands, respectively, in units of min^{-1}, K_A and K_B are the dissociation constants of the labelled and unlabelled ligands, respectively, [A] and [B] are the concentrations of the labelled and unlabelled ligands, respectively, in nM, B_{max} is the total number of receptors, X is the time in minutes and Y is the specific binding.

To calculate the ΔF% in the glucose-stimulated insulin secretion assay, equation # was used.

$$\Delta F\% = \frac{Ratio_{Sample} - Ratio_{Vehicle}}{Ratio_{Vehicle}} \times 100 \quad (16)$$

where ratio ($\lambda_{665}/\lambda_{620}$) of acceptor to donor was calculated for the sample and the vehicle.

The statistical analysis was performed using a one-way ANOVA with a Dunnett's post-test for multiple comparisons or a Student's t-test, as appropriate. Results with $p<0.05$ were deemed significant. All experiments were performed in a minimum of 3 repeats, unless otherwise stated, conducted in duplicates and data were reported as mean ± SEM.

Chapter 3. Pharmacological validation and characterisation of GIPR allosteric modulators

3.1 Introduction

GIPR is a ubiquitous GPCR predominantly expressed in the pancreatic beta cells, the adipose tissue, and certain regions of the brain (Irwin et al., 2020; El and Campbell, 2020). There is a large body of evidence implicating GIPR or its endogenous hormone ligand GIP in many pathological conditions including but not limited to T2DM, Alzheimer's disease, Parkinson's disease, neuroprotection in cerebral ischaemia and maintenance of bone health (Schiellerup et al., 2019; Verma et al., 2018). However, exploration of its physiological and pathological role has been impeded by the lack of clinically effective agents that target GIPR, which is primarily due to GIP being a peptide hormone and the unsuccessful development of small molecule agonists to the GIPR.

One of the potential clinical strategies is to promote GIPR signalling, mostly in T2DM. In their 1993 study, Nauck et al. have shown that even though T2DM patients have decreased incretin responsivity, GLP-1 potentiation of insulin secretion is relatively well preserved, while the effect of exogenous GIP is markedly decreased by about 50% even at supraphysiological doses. Furthermore, Jones et al. (1987) have shown that GIP infusion reduced plasma insulin levels and increased insulin secretion and in a rat model of diabetes and in a different study GIP analogues improved glucose tolerance and insulin secretion (Widenmaier et al., 2010). To study the long-term effects, Renner et al. (2010) generated dominant negative GIPR expressing pigs, in which the glucose tolerance deteriorated over time and β-cell proliferation was decreased with no change in weight, suggesting potentiating GIPR signalling might be beneficial. Apart from diabetes, potentiating GIP signalling might be beneficial for bone strength and heart disease – often associated with diabetes.

However, promoting GIPR signalling in the treatment of T2DM is not without controversy, as a a great deal of research points towards the benefits of inhibiting GIPR signalling in adipose tissue to combat obesity, a condition often associated with diabetes. Bariatric surgery, which despite many associated risks (as any operation) remains the only proven method to sustain weight loss in humans, is often linked to decreased GIP secretion (Flatt, 2007). Moreover, GIP levels have been found elevated in obesity (Gasbjerg et al., 2019, Yip et al., 1998). In adipose tissue, GIP is known to increase lipoprotein lipase activity and fatty acid glucose uptake, augmenting insulin-induced fatty acid incorporation into adipocytes, inhibit lipolysis (Irwin and Flatt, 2009b; Irwin and Flatt, 2009a) and inducing insulin resistance in adipocytes (Asmar et al., 2016; Asmar et al., 2017; Asmar et al., 2019). There is also evidence that GIPR-/- mice are protected against developing both obesity and insulin resistance when

placed on a high-fat diet (Miyawaki et al., 2002). Killion et al. (2018) have shown that a prolonged administration of a GIPR neutralizing antibody enhanced GLP-1-induced weight loss in mice.

GIP also stimulates secretion of glucagon, whose levels are increased in T2DM patients (Nigel Irwin and Flatt, 2009), from pancreatic α-cells. In rats fasted overnight, GIP infusion significantly reduced blood glucose and increased glucagon levels up to three-fold in a dose-dependent manner (Hinke et al., 2001). The increased glucagon secretion in T2DM patients even when hyperglycaemic might contribute to the pathogenesis of T2DM, suggesting antagonism of GIPR might be beneficial. Importantly, as the GIP insulinotropic action on β-cells is severely compromised, but the GIP-induced lipid deposition activity in adipocytes and potentiation of glucagon secretion from α-cells is well preserved in obese T2DM patients (Gasbjerg et al., 2018; Gabe et al., 2018; Perry et al., 2019), antagonising the GIPR receptor might not result in the negative effects on insulin secretion.

However, developing a potent small molecule orthosteric ligand against class B1 GPCRs like GIPR is a challenge to the large diffuse orthosteric binding site tailored towards hormone ligands. This is, where allosteric modulators can provide an alternative strategy. Allostery is a biological phenomenon describing the ability of an agent to modulate interactions at a site spatially distinct from the orthosteric binding site and can be described using the operational model of allosterism (Leach et al., 2007). Their main advantage lies in their probe dependency, lack of intrinsic selectivity, saturability and higher potential for receptor subtype selectivity among receptors with similar orthosteric binding sites (Cheng and Jiang, 2019; Wootten et al., 2017). Allosteric modulators can be either positive (PAMs), enhancing the receptor signalling, or negative (NAMs), decreasing or fully ablating the receptor response (Christopoulos, 2014; Milligan et al., 2017). PAMs represent tools to overcome reduced receptor expression, as endogenous agonist activity can be significantly amplified, thus overcoming the lack of GIPR on the surface of β-cells of T2DM patients. NAMs could be useful for the treatment of obesity.

Prior to this PhD project, there were already a few GIPR allosteric modulators available in the Ladds laboratory, identified by Dr Harris during his PhD project, the majority of which were PAMs. Given the controversy regarding GIP agonism, the focus of this chapter and Chapter 4 was to identify and characterise GIPR NAMs with the aims to 1) identify additional chemical scaffolds for GIPR-specific allosteric modulators, 2) identify an allosteric binding site at GIPR and optimize compound affinity and potency using iterative computational, functional and ligand-binding assays and 3) determine the GIPR allosteric modulators' efficacy in GIPR expressing and rat INS-1 cells. The *in silico* work described in chapter 4 was done in parallel to this chapter and especially the *in silico* docking aided the mutational analysis described in this chapter.

3.2 *In silico* screening of potential GIPR allosteric modulators

Among the GIPR allosteric modulators already available in the laboratory. prior to this PhD were some PAMs like C9 and also two NAMs C3 and C25 (Figure 3.1), selective for the $(Ca^{2+})_i$ mobilization pathway over cAMP accumulation pathway at the GIPR. These compounds were used by Miss Bowman (University of Cambridge) as query molecules to search relevant libraries for new potential ligands/modulators with different chemical backbones while maintaining the same structural and electrophysical properties. 2D structure screens were carried out using the online tool SwissSimilarity to screen Enamine, ChemBridge and ChemDiv libraries (Rodríguez et al., 2015; Sela et al., 2010; Senderowitz and Marantz, 2009). This was then followed by a 3D conformer screen using using OpenEye ROCS and 100 top candidates in were blind docked in Autodock Vina (Trott and Olson, 2010). Finally, SwissADME screen testing for pharmaceutical viability of tested compounds was performed.

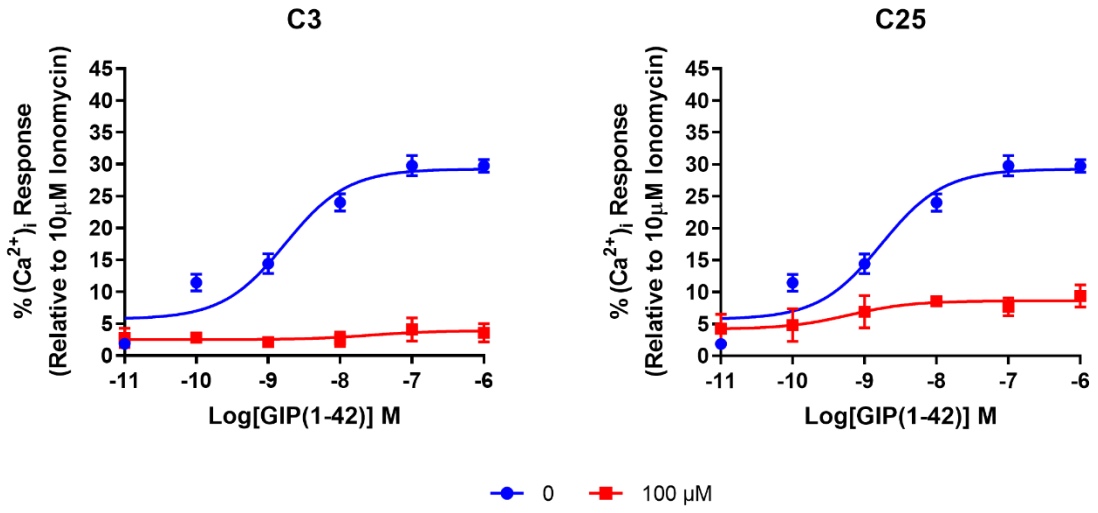

Figure 3.1. Compounds C3 and C25 are NAMs for $(Ca^{2+})_i$ mobilization. $(Ca^{2+})_i$ mobilization in HEK-293S cells stably expressing GIPR in response to GIP(1-42) in the absence or presence of 100 µM compound. Data is plotted as mean ± SEM of n≥3 individual experiments performed in duplicate and normalised to 10 µM ionomycin response.

Out of this screen, 7 compounds - C22, C42, C58, C73, C82, C91, C95 (Table 3.1) - were selected for further testing. Miss Bowman ended her involvement with the project at this point. I then took the compounds forward to do more in depth *in silico* docking to uncover their binding site and to test them in *in vitro* pharmacological assays for their activity at GIPR.

Table 3.1. Structures of the C3- and C25-based compounds

C3-based compounds	C25-based compounds
C3 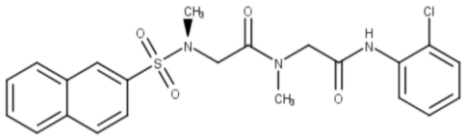	C25 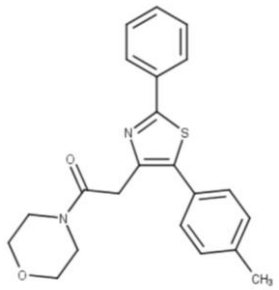
C22 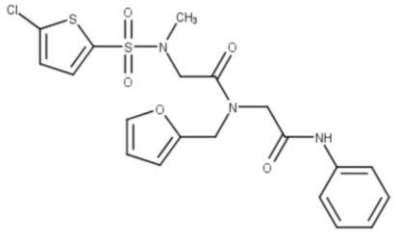	C58 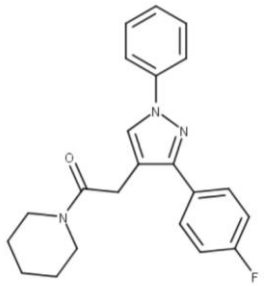
C42 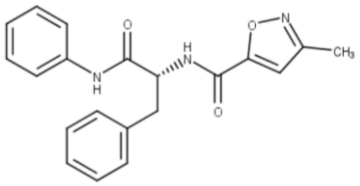	C73 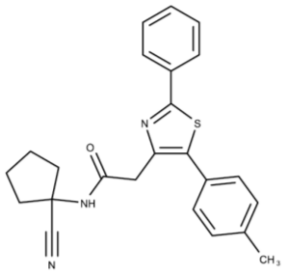
C91 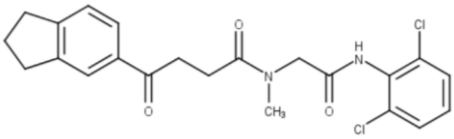	C82 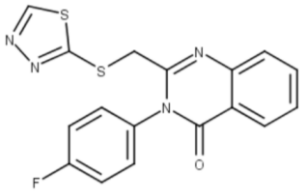
C95 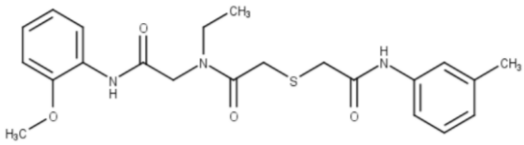	

3.3 Compounds C22, C58, C91 and C95 are new GIPR NAMs selective for $(Ca^{2+})_i$ mobilization

C3 and C25, used as baits in the above *in silico* screening, are known GIPR NAMs for $(Ca^{2+})_i$ mobilization; therefore the new compounds were first tested for any activity at this pathway using . HEK-293S cells stably expressing GIPR. To date only C3, C25, C58 and C95 have been assayed for agonistic activity and none showed any $(Ca^{2+})_i$ mobilization over 80 seconds except C58 which had an GIPR-independent effect on basal $(Ca^{2+})_i$ mobilization over time (Figure 3.2).To test the ability of the compounds to modulate GIP-induced $(Ca^{2+})_i$ mobilization, the HEK-293S cells stably expressing GIPR were stimulated with increasing doses of GIP(1-42) in the presence or absence of 10 µM or 100 µM compound (Figure 3.3, Table 3.2). GIP(1-42) was chosen for the experiment as it is the native agonist of GIPR and so the results would be most physiologically relevant. None of the compounds interfered with the 10 µM ionomycin control (Figure 3.4, Table 3.3).

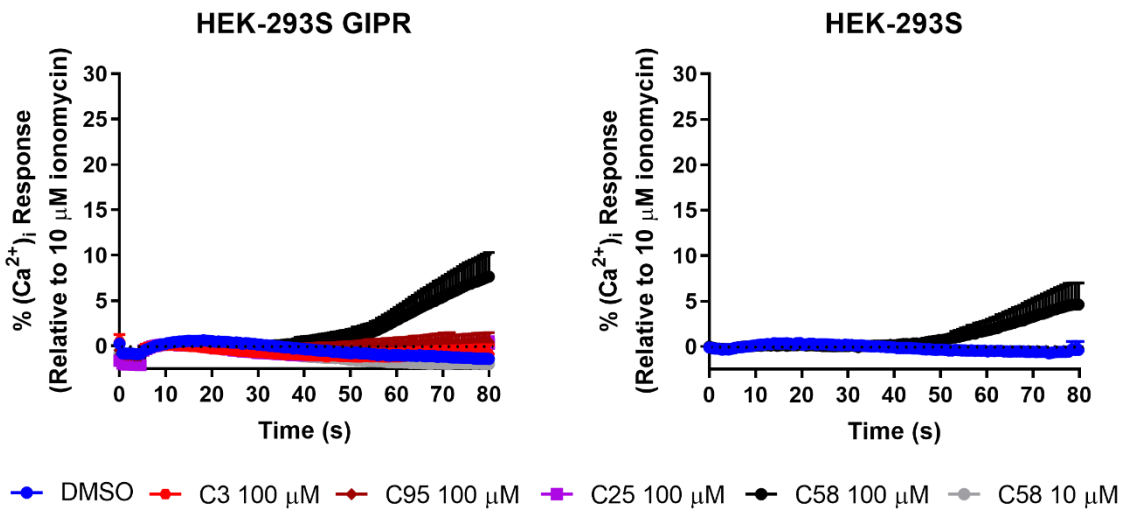

Figure 3.2. Putative allosteric modulators at GIPR have no specific effect on $(Ca^{2+})_i$ mobilization alone. $(Ca^{2+})_i$ mobilization in HEK-293S cells and HEK-293S cells stably expressing GIPR in response to different concentrations compound or DMSO. Data is plotted as mean ± SEM of n≥3 individual experiments performed in duplicate and normalised to 10 µM ionomycin response.

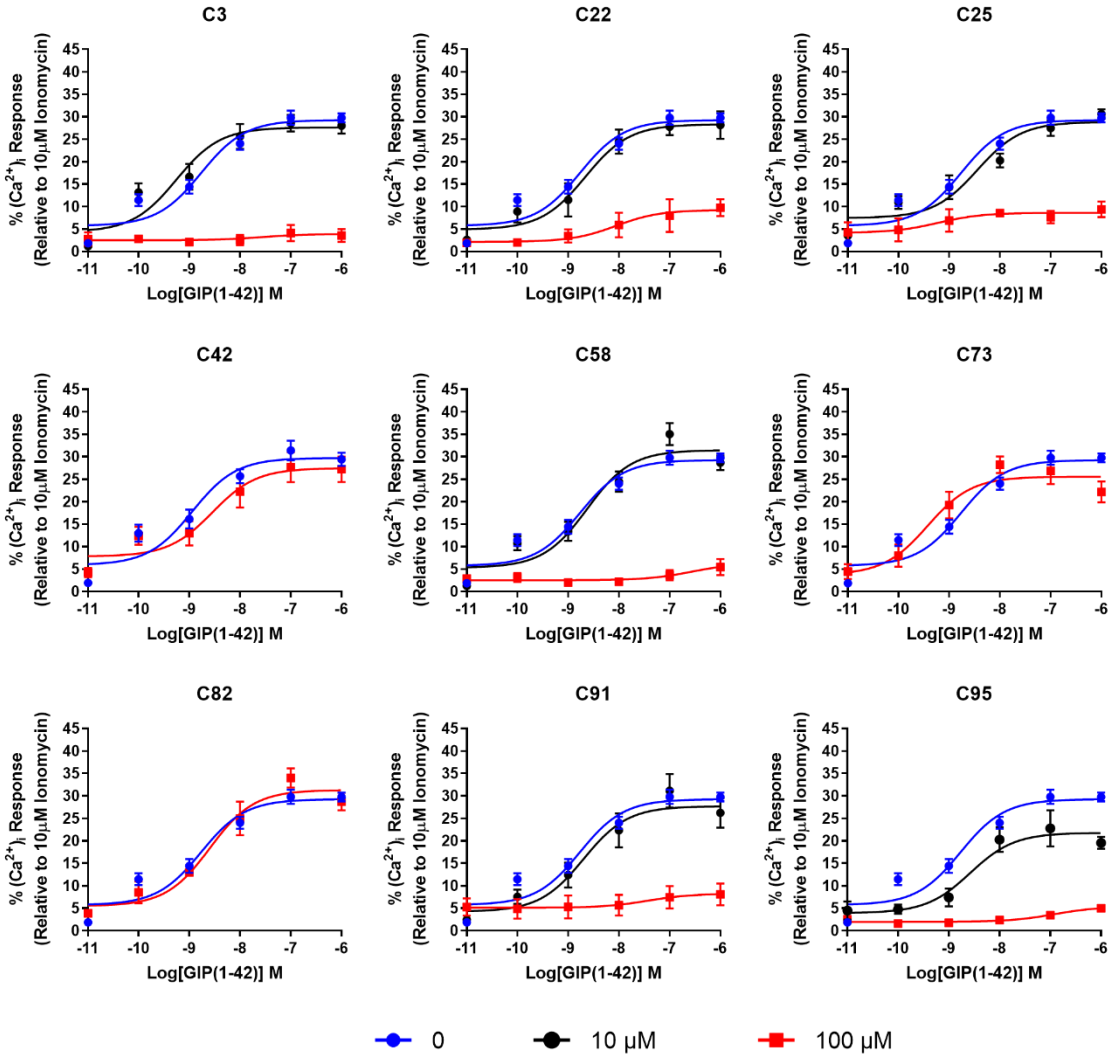

Figure 3.3. Compounds C22, C58, C91 and C95 are newly identified NAMs for $(Ca^{2+})_i$ mobilization at GIPR. $(Ca^{2+})_i$ mobilization in HEK-293S cells stably expressing GIPR in response to GIP(1-42) in the absence or presence of different concentrations of tested compounds. Data is plotted as mean ± SEM of n≥3 individual experiments performed in duplicate and normalised to 10 µM ionomycin response.

Table 3.2. Potency (pEC_{50}) and E_{max} values for $(Ca^{2+})_i$ mobilization in HEK-293S cells stably expressing GIPR in response to GIP(1-42) in the absence or presence of different concentrations of tested compounds.

Compound	µM	pEC_{50}[a]	E_{max}[b]	Basal	n
DMSO	-	8.77 ± 0.12	29.27 ± 0.93	5.70 ± 1.06	11
C3	10	9.26 ± 0.22	27.62 ± 1.64	4.35 ± 2.07	3
	100	7.58 ± 2.11	3.90 ± 1.25****	2.51 ± 0.77	3
C22	10	8.66 ± 0.24	28.32 ± 1.78	4.90 ± 1.96	3
	100	8.06 ± 0.60**	9.25 ± 1.68****	2.16 ± 1.33	3
C25	10	8.45 ± 0.20	28.85 ± 1.45	7.45 ± 1.33	4
	100	9.22 ± 0.20	28.85 ± 1.45****	7.45 ± 1.33	3
C42	10	NA	NA	NA	NA
	100	8.54 ± 0.31	27.46 ± 2.12	7.81 ± 1.97	4
C58	10	8.63 ± 0.19	31.47 ± 1.59	5.30 ± 1.71	3
	100	6.58 ± 0.98**	6.27 ± 2.47****	2.53 ± 0.56	3
C73	10	NA	NA	NA	NA
	100	9.42 ± 0.26	25.58 ± 1.47	3.72 ± 2.36	4
C82	10	NA	NA	NA	NA
	100	8.60 ± 0.19	31.31 ± 1.59	5.48 ± 1.74	3
C91	10	8.70 ± 0.26	27.70 ± 2.03	4.23 ± 2.14	4
	100	7.43 ± 1.72*	8.24 ± 2.44****	5.11 ± 1.30	3
C95	10	9.12 ± 0.40	13.68 ± 1.24*	3.23 ± 1.71	4
	100	6.92 ± 0.38**	5.35 ± 0.76****	1.98 ± 0.28	3

Data are the mean ± SEM of *n* individual data sets.

[a] The negative logarithm of the agonist concentration required to produce a half-maximal response.

[b] The maximal response to the ligand expressed as a percentage of the maximal $(Ca^{2+})_i$ mobilization as determined using 10 µM ionomycin.

Data were determined as statistically different (*, $p < 0.05$; **, $p < 0.01$; ****, $p < 0.0001$) compared to no treatment using a one-way ANOVA and Dunnett's post-hoc test.

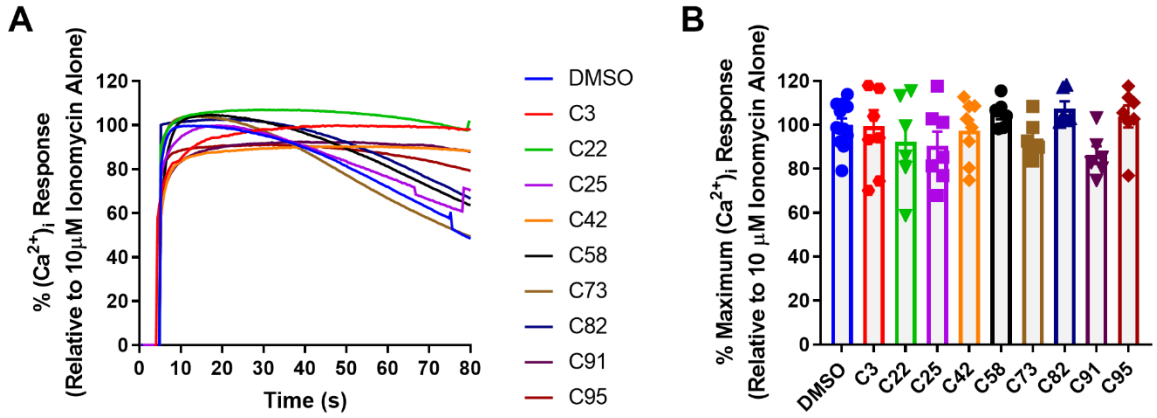

Figure 3.4. Tested compounds do not affect ionomycin-stimulated $(Ca^{2+})_i$ mobilization at GIPR. A. A representative curve from 1 day of $(Ca^{2+})_i$ mobilization in HEK-293S cells stably expressing GIPR in response to 10 µM ionomycin in the absence or presence of 100 µM tested compound. B. Maximal response of $(Ca^{2+})_i$ mobilization in HEK-293S cells stably expressing GIPR in response to 10 µM ionomycin in the absence or presence of 100 µM tested compound. All data are normalised to 10 µM ionomycin response alone.

Table 3.3. Maximal response (E_{max}) values for $(Ca^{2+})_i$ mobilization in HEK-293S cells stably expressing GIPR in response to 10 µM ionomycin in the absence or presence of 100 µM tested compound.

Compound	E_{max}[a]	n
DMSO	100.00 ± 10.03	6
C3	99.57 ± 20.40	4
C22	92.34 ± 21.61	3
C25	90.43 ± 17.38	4
C42	97.40 ± 13.80	4
C58	105.30 ± 6.46	3
C73	93.63 ± 8.85	3
C82	107.50 ± 7.90	3
C91	86.31 ± 9.90	3
C95	103.90 ± 13.14	4

Data are the mean ± SEM of *n* individual data sets.
[a] The maximal response to the ligand expressed as a percentage of the maximal $(Ca^{2+})_i$ mobilization as determined using 10 µM ionomycin alone.
Data were determined as not statistically different compared to DMSO using a one-way ANOVA and Dunnett's post-hoc test.

C42, C73 and C82 had no significant effect on GIP(1-42) mediated $(Ca^{2+})_i$ mobilization and thus were not further pursued. C3, C22, C25, C58, C91 and C95 when tested at 100 µM all significantly decreased the maximal $(Ca^{2+})_i$ response and potency of GIP(1-42), although caution is needed due to the nature of the curve fitting using GraphPad Prism 9.3 for some of these estimates. Interestingly,

only C95 significantly reduced the Emax of $(Ca^{2+})_i$ mobilization when assayed using 10 µM concentration suggesting it is the most potent of the compounds. None of the tested compounds had any significant effect on the basal value of $(Ca^{2+})_i$ mobilization. Compounds C3, C22, C25, C58, C91 and C95 behaved as NAMs for $(Ca^{2+})_i$ mobilization at GIPR.

As C95 was identified as the most potent NAM for $(Ca^{2+})_i$ mobilization among the tested compounds, its ability to modulate the $(Ca^{2+})_i$ mobilization at various concentrations was further explored. $(Ca^{2+})_i$ mobilization in HEK-293S cells stably expressing GIPR in response to GIP(1-42) in the presence or absence of various concentrations of C95 was measured (Figure 3.5, Table 3.4). Treatment with 1 µM, 10 µM, 50 µM or 100 µM C95 had no effect on basal value of $(Ca^{2+})_i$ mobilization, but treatment with 10 µM, 50 µM or 100 µM C95 significantly reduced the maximal response in a concentration-dependent manner. C95 at 100 µM also significantly reduced potency.

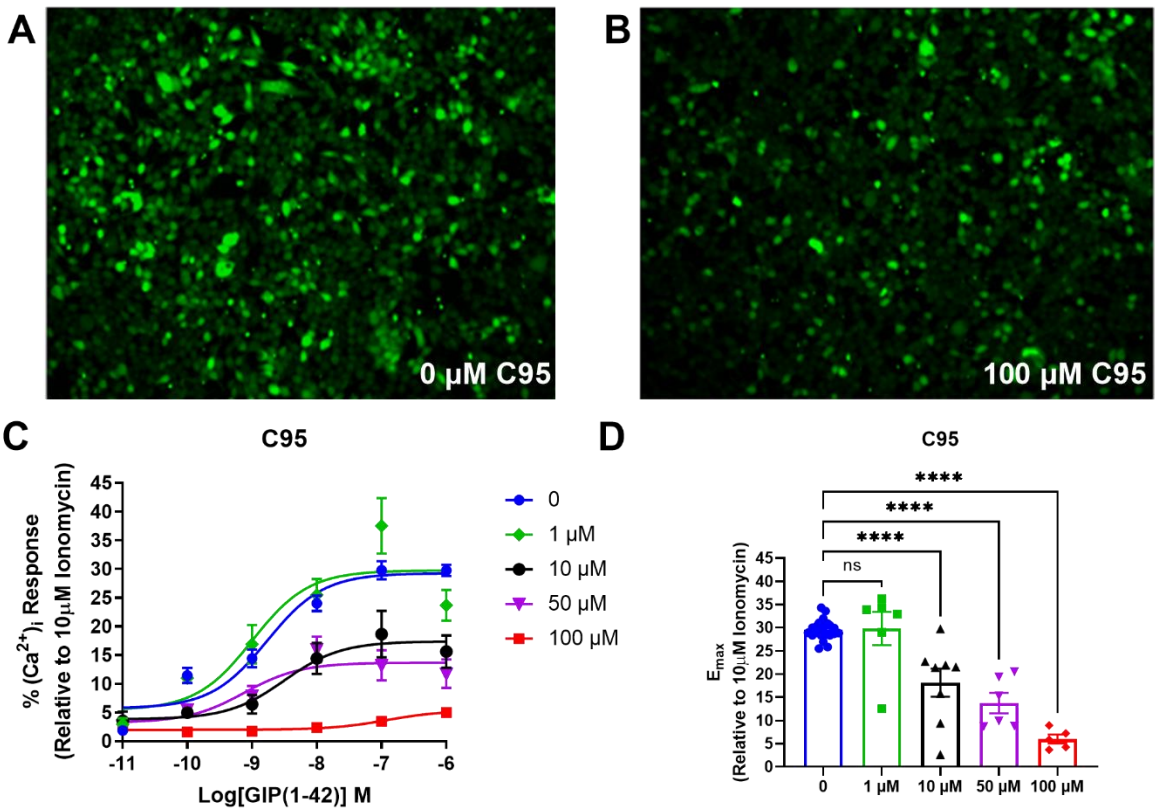

Figure 3.5. The effect of C95 on $(Ca^{2+})_i$ mobilization is concentration dependent and saturable. A-C. Representative images of the peak $(Ca^{2+})_i$ mobilization in HEK-293S cells stably expressing GIPR in response to 1 µM GIP(1-42) in the absence (A) or presence of 100 µM C95 (B). C. $(Ca^{2+})_i$ mobilization in HEK-293S cells stably expressing GIPR in response to GIP(1-42) concentrations in the absence or presence of different concentrations of C95. D. Plotted E_{max} values from C. Data is plotted as mean ± SEM of n≥3 individual experiments performed in duplicate. All data is normalised to 10 µM ionomycin response. Data were determined as statistically different (****, $p < 0.0001$) compared to DMSO using a one-way ANOVA and Dunnett's post-hoc test.

Table 3.4. Potency (pEC_{50}), E_{max} and basal values for $(Ca^{2+})_i$ mobilization in HEK-293S cells stably expressing GIPR in response to GIP(1-42) concentrations in the absence or presence of different concentrations of C95.

C95 (µM)	pEC_{50}[a]	E_{max}[b]	Basal	n
0	8.77 ± 0.12	29.27 ± 0.93	5.70 ± 1.06	11
1	9.00 ± 0.29	29.75 ± 2.19	5.41 ± 2.83	3
10	8.50 ± 0.41	17.39 ± 1.80*	3.83 ± 1.80	4
50	9.12 ± 0.40	13.68 ± 1.24****	3.23 ± 1.71	3
100	6.92 ± 0.38**	5.35 ± 0.76****	1.98 ± 0.28	3

Data are mean ± SEM of *n* individual data sets.
[a] The negative logarithm of the agonist concentration required to produce a half-maximal response.
[b] The maximal response to the ligand expressed as a percentage of the $(Ca^{2+})_i$ mobilization elicited by 10 µM ionomycin.
Data were determined as statistically different (*, $p < 0.05$; **, $p < 0.01$; ****, $p < 0.0001$) compared to DMSO using a one-way ANOVA and Dunnett's post-hoc test.

As GIPR is a pleiotropic receptor, the effects of compounds on cAMP accumulation and β-arrestin signalling pathway were investigated next. First, the compounds were tested alone and none of them showed any agonistic activity for cAMP accumulation (Figure 3.6, Table 3.5). In Figure 3.6 compound C3 seems to have a slightly lowered baseline compared to DMSO, but this decrease in baseline wasn't statistically significant. To assess the ability of each compound to modulate GIP induced cAMP accumulation, HEK-293S cells stably expressing GIPR were treated with increasing doses of the partial agonist GIP(Pro3) in the presence or absence of 100 µM of each compound (Figure 3.7, Table 3.6). In Figure 3.7 compound C82 seems to have a slightly lowered baseline compared to DMSO, but this decrease in baseline wasn't statistically significant. GIP(Pro3) was the agonist of choice for the screen instead of the natural agonist GIP(1-42), as previous experiments by Dr Harris showed that GIP(1-42) response in HEK-293S cells stably expressing GIPR is close to the system maximum (100 µM forskolin) and, thus, any increase in efficacy may manifest as an increase in potency. In contrast, the reduced potency, and E_{max} of GIP(Pro3) provides the greatest range to be able to observe any effects on either of those variables. None of the compounds had any significant effect on the potency (EC_{50}) or E_{max} of GIP(Pro3) stimulated cAMP accumulation. The compounds are diluted in DMSO, so the slight rise in the concentration-response curves in Fig 3.6 is attributable to the higher DMSO concentration and is the same for the DMSO control.

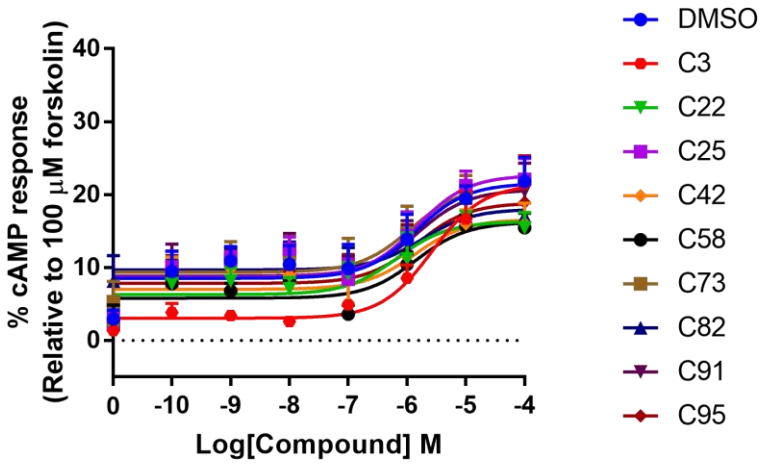

Figure 3.6. Potential small allosteric modulators of GIPR are not agonists for cAMP accumulation. cAMP accumulation in HEK-293S cells stably expressing GIPR following 8 min stimulation with 100 µM compound or DMSO. Data is plotted as mean ± SEM of n≥3 individual experiments performed in duplicate and normalised to the 100 µM forskolin.

Table 3.5. Potency (pEC_{50}) and E_{max} values for cAMP accumulation in HEK-293S cells stably expressing GIPR in response to 100 µM compound or DMSO.

Compound	pEC_{50}[a]	E_{max}[b]	n
DMSO	5.85 ± 0.42	21.53 ± 2.46	3
C3	5.57 ± 0.25	21.41 ± 2.03	3
C22	6.17 ± 0.43	16.30 ± 1.70	3
C25	5.83 ± 0.36	22.67 ± 2.3	3
C42	5.86 ± 0.51	16.64 ± 2.12	3
C58	5.85 ± 0.32	16.22 ± 1.41	3
C73	5.94 ± 0.58	21.24 ± 4.14	3
C82	5.75 ± 0.70	18.03 ± 0.71	3
C91	5.82 ± 0.48	20.68 ± 0.48	3
C95	5.82 ± 0.46	18.88 ± 2.20	3

Data are the mean ± SEM of *n* individual data sets.
[a] The negative logarithm of the agonist concentration required to produce a half-maximal response.
[b] The maximal response to the ligand expressed as a percentage of the maximal cAMP production as determined using 100 µM forskolin.
Data were determined as not statistically different compared to DMSO using a one-way ANOVA and Dunnett's post-hoc test.

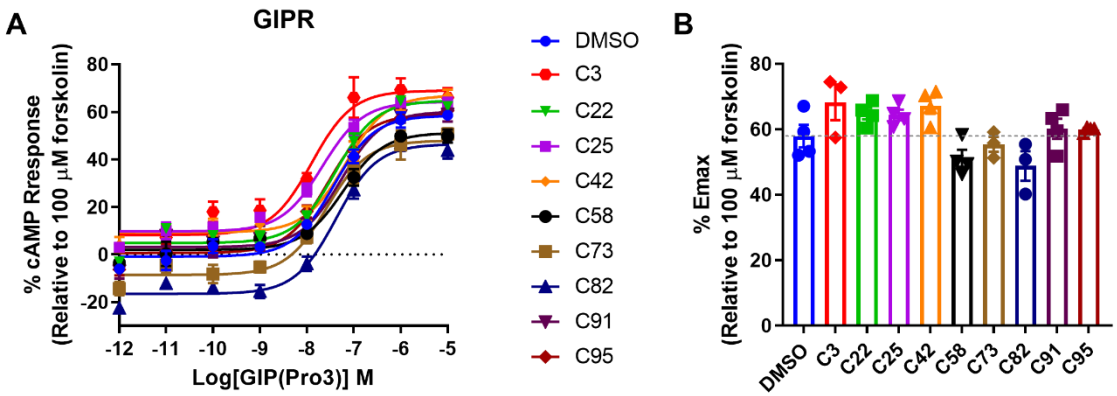

Figure 3.7. Putative allosteric modulators of GIPR do not modulate cAMP pathway. A. cAMP accumulation in HEK-293S cells stably expressing GIPR following 8 min stimulation with varying GIP(Pro3) concentrations in the presence of 100 µM compound or DMSO. B. Plotted maximal responses from A. Data is plotted as mean ± SEM of n≥3 individual experiments performed in duplicate and normalised to 100 µM forskolin.

Table 3.6. Potency (pEC_{50}) and E_{max} values for cAMP accumulation in HEK-293S cells stably expressing GIPR in response to GIP(Pro3) in the presence of 100 µM compound or DMSO.

Compound	pEC_{50}[a]	E_{max}[b]	n
DMSO	7.43 ± 0.09	58.44 ± 2.04	4
C3	7.80 ± 0.16	68.95 ± 3.30	3
C22	7.39 ± 0.08	64.77 ± 1.81	4
C25	7.67 ± 0.09	64.26 ± 1.63	4
C42	7.18 ± 0.11	66.88 ± 2.48	4
C58	7.23 ± 0.12	51.16 ± 2.31	4
C73	7.58 ± 0.15	47.91 ± 3.40	4
C82	7.38 ± 0.10	46.42 ± 2.20	4
C91	7.26 ± 0.17	60.11 ± 3.69	4
C95	7.56 ± 0.10	59.03 ± 2.08	4

Data are the mean ± SEM of n individual data sets.
[a] The negative logarithm of the agonist concentration required to produce a half-maximal response.
[b] The maximal response to the ligand expressed as a percentage of the maximal cAMP production as determined using 100 µM forskolin.
Data were determined as not statistically different compared to DMSO using a one-way ANOVA and Dunnett's post-hoc test.

C25 and C95 were further tested for any effect on β-arrestin recruitment. However, as two versions of the GIPR construct suitable for β-arrestin recruitment assay were available in the laboratory at the time (GIPR-Rluc and GIPR-Nluc), the assay needed to be optimised first. To find the most suitable of them for the assay, β-arrestin 1/2 recruitment in response to GIP(1-42) was measured (Figure 3.8).

For β-arrestin 1 the span of the resulting dose-response curve was 0.00791 ± 0.00091 for GIPR-Nluc, while it was only 0.00118 ± 0.00243 for GIPR-Rluc. For β-arrestin 2 the difference was even bigger with the span of 0.031 ± 0.00137 for GIPR-Nluc and 0.00725 ± 0.00271 for GIPR-Rluc. GIPR-Nluc has been chosen as the construct for compound testing, as the compounds' effects on β-arrestin recruitment will be easier to see given the bigger range of response.

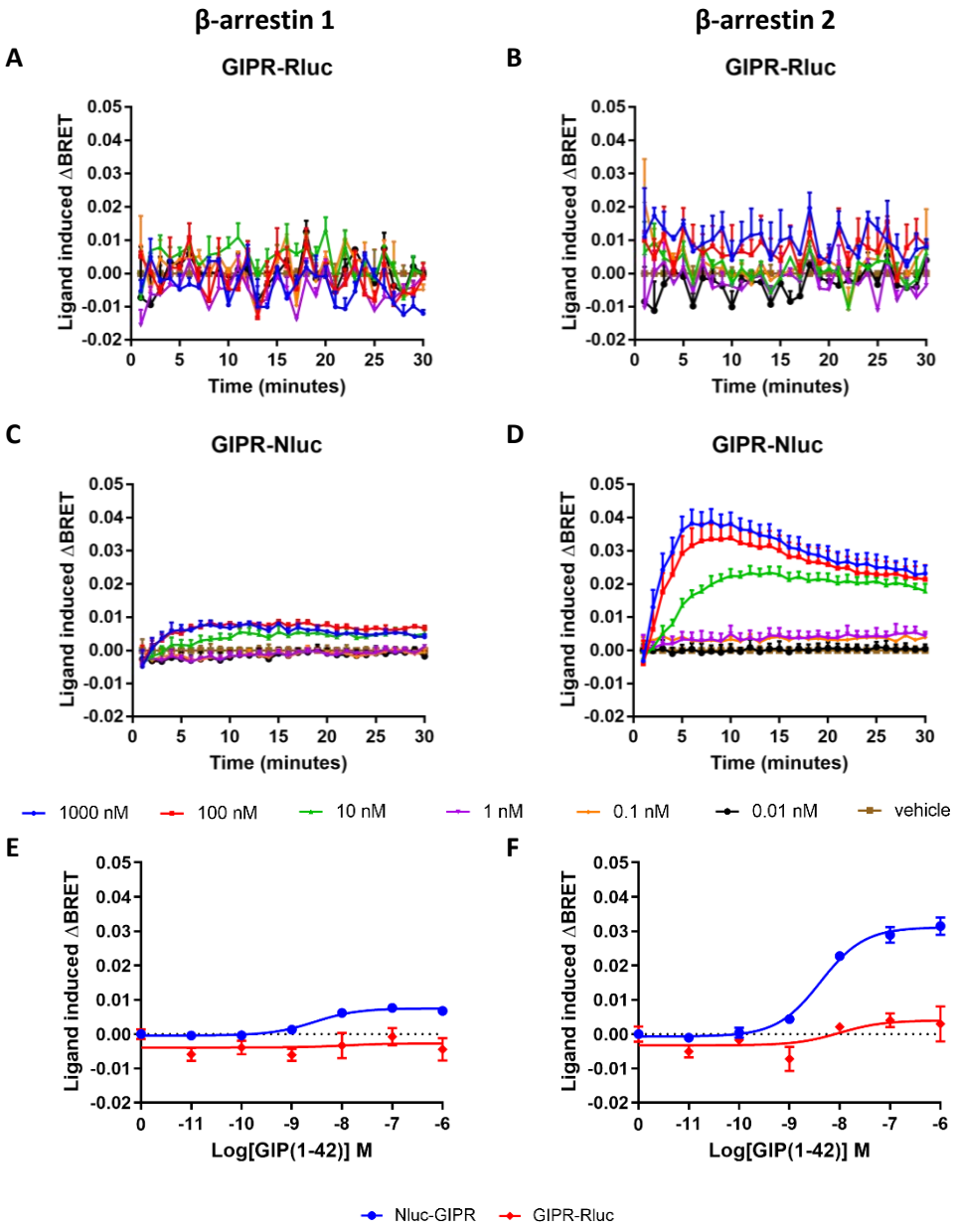

Figure 3.8. Selection of GIPR-Nluc for β-arrestin recruitment assay. A-D. HEK-293T cells were cotransfected with GIPR-Rluc (A, B)/GIPR-Nluc (C, D), GRK and YFP-β-arrestin-1/2 at a 1:4:5 ratio. β-arrestin-1/2 recruitment was measured in response to GIP(1-42) over 30-minute time period. E-F. Concentration-response curves for β-arrestin 1/2 recruitment after 10 minutes stimulation with GIP(1-42). Data is plotted as mean ± SEM of n≥3 individual experiments performed in duplicate.

To test the compounds, the HEK-293T cells co-transfected with GIPR-Nluc, GRK5 and YFP-β-arrestin 1/2 were stimulated with increasing doses of GIP(1-42) in the presence or absence of 100 µM C25 or C95 (Figure 3.9, Table 3.7). Neither of the compounds had any significant effect on the potency (EC_{50}), E_{max} and basal values of GIP(1-42) stimulated β-arrestin 1/2 recruitment. As C25 and C95 are NAMs selective for $(Ca^{2+})_i$ mobilization, these finding suggest that short-term β-arrestin 1/2 recruitment is independent of $(Ca^{2+})_i$ mobilization. If any allosteric modulators selective for cAMP accumulation were later identified, it would be interesting to test whether the G_s/cAMP pathway has any effect on β-arrestin recruitment.

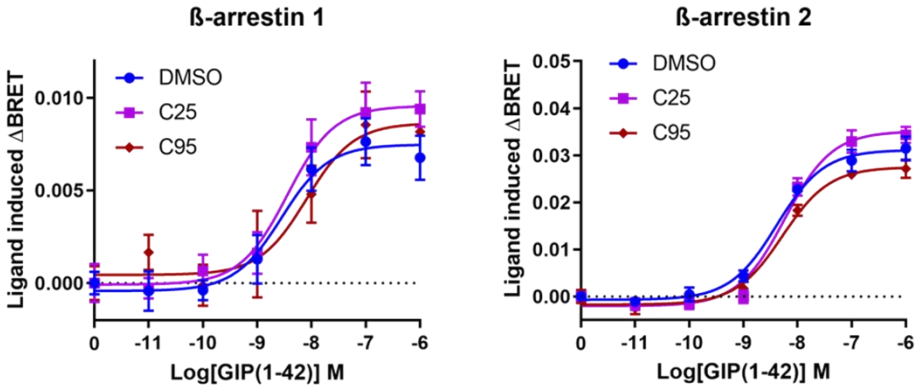

Figure 3.9. Putative allosteric modulators of GIPR do not modulate β-arrestin 1/2 recruitment. HEK-293T cells co-transfected with GIPR-Nluc, GRK5 and YFP-β-arrestin-1/2 at a 1:4:5 ratio. β-arrestin-1/2 recruitment was measured after 10 minutes stimulation with increasing doses of GIP(1-42) in the presence of 100 µM compound or DMSO. Data is plotted as mean ± SEM of n≥3 individual experiments performed in duplicate.

Table 3.7. Potency (pEC_{50}), E_{max} and basal values for β-arrestin 1/2 recruitment in response to GIP(1-42) in the presence of 100 µM compound or DMSO.

		DMSO	C25	C95
β-arrestin-1	**pEC_{50}[a]**	8.55 ± 0.27	8.45 ± 0.24	8.09 ± 0.33
	E_{max}[b] (*1000)	7.48 ± 0.75	9.56 ± 0.81	8.64 ± 1.09
	Basal[c] (*1000)	-0.43 ± 0.60	-0.08 ± 0.65	0.44 ± 0.76
	n	3	3	3
β-arrestin-2	**pEC_{50}[a]**	8.38 ± 0.10	8.23 ± 0.09	8.28 ± 0.10
	E_{max}[b] (*1000)	31.15 ± 1.15	35.12 ± 1.29	27.50 ± 1.04
	Basal[c] (*1000)	-0.70 ± 0.88	-2.02 ± 0.92	-1.73 ± 0.73
	n	3	3	3

Data are mean ± SEM of *n* individual data sets.
[a] The negative logarithm of the agonist concentration required to produce a half-maximal response.
[b] The maximal response to GIP(1-42) multiplied by 1000.
[c] Basal value multiplied by 1000.
Data were determined as not statistically different compared to DMSO using a one-way ANOVA and Dunnett's post-hoc test.

Overall, three C3-based compounds (C22, C91 and C95) and one C25-based compound (C58) were identified as GIPR NAMs for $(Ca^{2+})_i$ mobilization pathway. Out of these compounds, C95 is the most potent with lower micromolar potencies, while the rest of the compounds were only active at 100 µM. Selected compounds were also tested for their effect on cAMP accumulation and β-arrestin recruitment pathways, where they failed to have any significant effect, thus showing their selectivity for $(Ca^{2+})_i$ mobilization.

3.4 C25 is selective for GIPR over GLP-1R and GCGR

GIPR is closely related to some other class B1 GPCRs, mainly GLP-1R and GCGR. GLP-1R is another receptor playing a big role in insulin secretion and as mentioned previously both GIP and GLP-1 (an endogenous agonist of GLP-1R) regulate secretion of glucagon, an endogenous agonist of GCGR. Both receptors are also expressed in the pancreas and cells stably expressing them were already available in the laboratory. Moreover, dual and triple agonists of these receptors are known, hinting at the similarity between the orthosteric sites of these receptors (Knerr et al., 2022; Starling, 2022). Therefore, allosteric modulators binding outside the orthosteric binding site could provide a better opportunity for receptor selectivity, which is often an important characteristic to avoid too many side effects.

To test the compound cross-reactivity, selected compounds were screen for cAMP accumulation and $(Ca^{2+})_i$ mobilization at GLP-1R and GCGR. For the screen, two C3-based compounds (C3, C95) and

two C25-based compounds (C25, C58) were selected. cAMP accumulation in HEK-293S cells stably expressing GLP-1R in response to increasing doses of GLP-1(7-36)NH_2 and in HEK-293ΔCTR cells stably expressing GCGR in response to increasing doses of glucagon in the presence or absence of 100 µM compound was measured (Figure 3.10, Table 3.8). There was no significant change in concentration dependent increase in cAMP accumulation, in terms of potency and Emax, at GLP-1R or GCGR for any of the compounds.

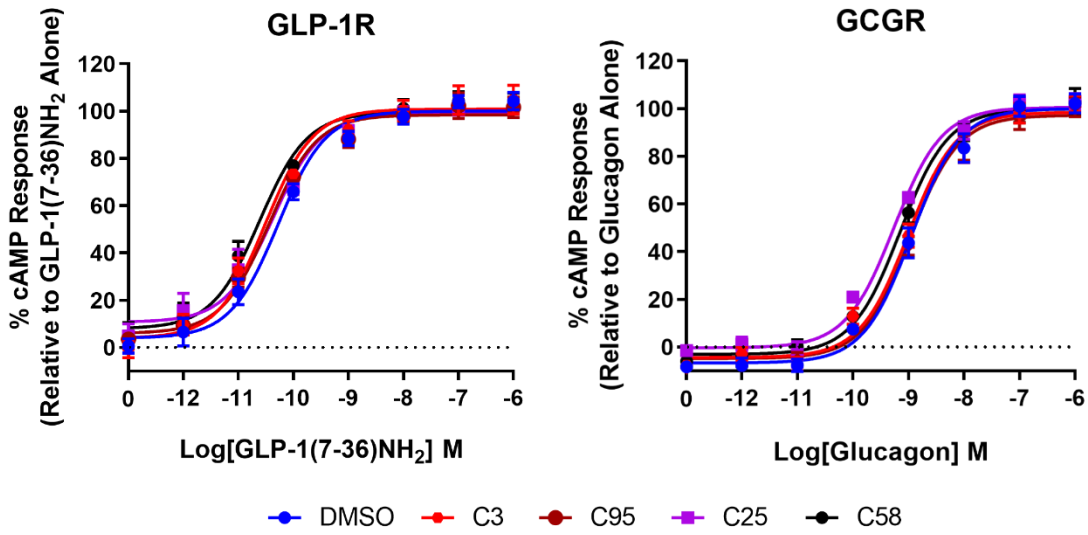

Figure 3.10. Potential small allosteric modulators of GIPR do not modulate cAMP accumulation at GLP-1R and GCGR. A. cAMP accumulation in HEK-293S cells stably expressing GLP-1R following 8 min stimulation with varying GLP-1(7-36)NH_2 concentrations in the presence of 100 µM compound or DMSO. B. cAMP accumulation in HEK-293ΔCTR cells stably expressing GCGR following 8 min stimulation with varying glucagon concentrations in the presence of 100 µM compound or DMSO. Data is plotted as mean ± SEM and normalised to agonist plus DMSO.

Table 3.8. Potency (pEC_{50}) and E_{max} values for cAMP accumulation in HEK-293S cells stably expressing GLP-1 in response to GLP-1(7-36)NH_2 and in HEK-293ΔCTR cells stably expressing GCGR in response to glucagon.

	GLP-1R			GCGR		
Compound	**pEC_{50}[a]**	**E_{max}[b]**	**n**	**pEC_{50}[a]**	**E_{max}[b]**	**n**
DMSO	10.28 ± 0.08	100.00 ± 2.07	3	8.95 ± 0.07	100 ± 2.68	3
C3	10.51 ± 0.10	100.80 ± 2.39	3	9.01 ± 0.07	98.46 ± 2.55	3
C25	10.37 ± 0.12	98.93 ± 2.53	3	9.26 ± 0.06	100.5 ± 2.02	3
C58	10.61 ± 0.10	99.51 ± 2.33	3	9.15 ± 0.07	99.85 ± 2.49	3
C95	10.44 ± 0.09	98.41 ± 1.97	3	8.96 ± 0.07	97.19 ± 2.51	3

Data are the mean ± SEM of *n* individual data sets.
[a] The negative logarithm of the agonist concentration required to produce a half-maximal response.
[b] The maximal response to the ligand expressed as a percentage of the maximal cAMP production of agonist plus DMSO.
Data were determined as not statistically different compared to DMSO using a one-way ANOVA and Dunnett's post-hoc test.

For the $(Ca^{2+})_i$ mobilization pathway, the compounds alone had no specific effect on $(Ca^{2+})_i$ mobilization in HEK-293S cells stably expressing GLP-1R or HEK-293ΔCTR cells stably expressing GCGR (Figure 3.11). To test the allosteric activity of the compounds, the HEK-293S cells stably expressing GLP-1R were stimulated with increasing doses of GLP-1(7-36)NH_2 in the presence or absence of 10 or 100 µM compound (Figure 3.12, Table 3.9). C25 had no significant effect on GLP-1(7-36)NH_2 mediated $(Ca^{2+})_i$ mobilization, however, C3, C95 and C58 at 100 µM all significantly decreased maximal response of $(Ca^{2+})_i$ mobilization, while retaining no significantly different potency, alluding to NAM activity of the compounds. C58 also slightly reduced the basal activity. C3 and C58 at 10 µM had no significant effect on $(Ca^{2+})_i$ mobilization. In the HEK-293ΔCTR cells stably expressing GCGR, C3 and C95 at 100 µM significantly decreased maximal response of glucagon stimulated $(Ca^{2+})_i$ mobilization, while not significantly changing the potency, pointing to their activity as NAMs (Figure 3.13, Table 3.10). C25 and C58 at 100 µM and C3 at 10 µM had no significant effect on glucagon stimulated $(Ca^{2+})_i$ mobilization.

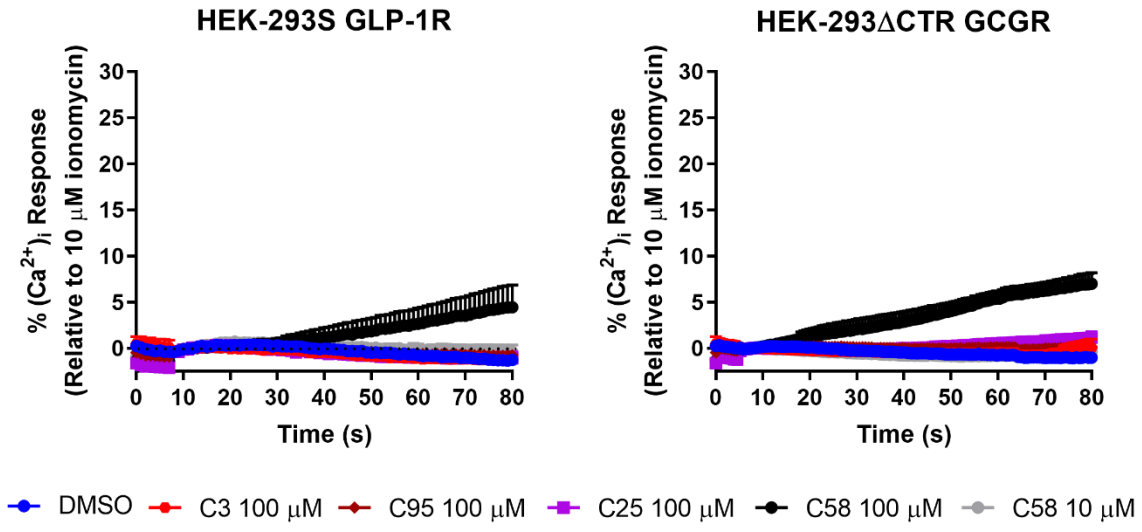

Figure 3.11. Compounds alone have no or unspecific effect on $(Ca^{2+})_i$ mobilization. $(Ca^{2+})_i$ mobilization in HEK-293S cells stably expressing GLP-1R and HEK-293ΔCTR cells stably expressing GCGR in response to different concentrations compound or DMSO. Data is plotted as mean ± SEM of n≥3 individual experiments performed in duplicate and normalised to 10 µM ionomycin response.

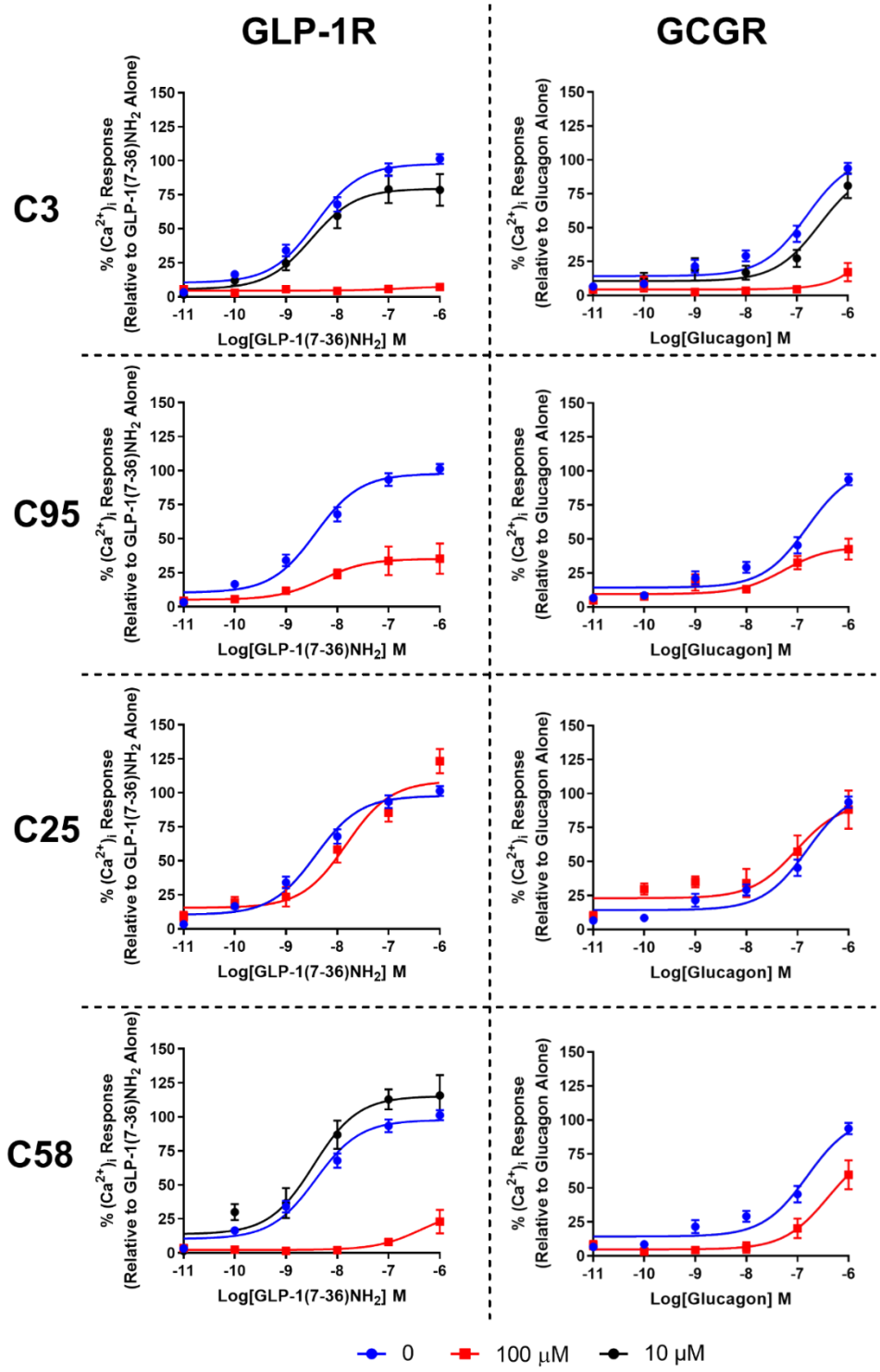

Figure 3.12. Compounds C3, C95 and C58 inhibit GLP-1- and glucagon-stimulated $(Ca^{2+})_i$ mobilization. $(Ca^{2+})_i$ mobilization in HEK-293S cells stably expressing GLP-1R or HEK-293ΔCTR cells stably expressing GCGR in response to GLP-1(7-36)NH_2 or glucagon in the absence or presence of different concentrations of test compounds. Data is plotted as mean ± SEM and normalised to GLP-1(7-36)NH_2 or glucagon with DMSO.

Table 3.9. Potency (pEC_{50}) and E_{max} values for $(Ca^{2+})_i$ mobilization in HEK-293S cells stably expressing GLP-1R or HEK-293ΔCTR cells stably expressing GCGR in response to GLP-1(7-36)NH_2 or glucagon in the absence or presence of different concentrations of tested compounds.

Cmp		GLP-1R				GCGR			
	µM	pEC_{50}[a]	E_{max}[b]	Basal	n	pEC_{50}[a]	E_{max}[b]	Basal	n
DMSO	-	8.42 ± 0.10	97.78 ± 2.96	10.34 ± 2.76	8	6.81 ± 0.11	103.00 ± 4.90	14.34 ± 2.35	9
C3	10	8.51 ± 0.23	79.47 ± 5.39	5.59 ± 5.44	4	6.55 ± 0.19	94.09 ± 7.25	10.63 ± 3.41	5
	100	6.74 ± 0.98	7.65 ± 1.91****	4.55 ± 0.59	3	NA	NA	4.41 ± 1.82	3
C95	10	NA	NA	NA	NA	NA	NA	NA	NA
	100	8.29 ± 0.45	35.16 ± 4.83****	5.13 ± 4.29	3	7.27 ± 0.33	44.54 ± 5.65***	9.51 ± 2.66	4
C25	10	NA	NA	NA	NA	NA	NA	NA	NA
	100	7.82 ± 0.18	108.7 ± 7.35	15.45 ± 4.13	4	7.02 ± 0.33	93.60 ± 13.84	23.07 ± 5.75	3
C58	10	8.46 ± 0.20	115.30 ± 7.89	13.78 ± 6.07	3	NA	NA	NA	NA
	100	6.37 ± 0.60	32.00 ± 14.26****	2.26 ± 1.86*	3	6.40 ± 0.31	81.58 ± 19.01	4.82 ± 2.69	3

Data are the mean ± SEM of *n* individual data sets.
[a] The negative logarithm of the agonist concentration required to produce a half-maximal response.
[b] The maximal response to the ligand expressed as a percentage of the maximal $(Ca^{2+})_i$ mobilization, normalised to GLP-1(7-36)NH_2 or glucagon with DMSO.
Data were determined as statistically different (*, $p < 0.05$; ***, $p < 0.001$; ****, $p < 0.0001$) compared to no treatment using a one-way ANOVA and Dunnett's post-hoc test.

It is interesting to note that C25 and C58 are structurally very similar compounds, but one is selective for GIPR over GLP-1R and GCGR, while the other is not. To look at this a bit more closely, these compounds were tested at all three receptors at more concentrations to find their real potencies and how they compare. To this end, the HEK-293S cells stably expressing GIPR or GLP-1R or HEK-293ΔCTR cells stably expressing GCGR were stimulated with increasing doses of GIP(1-42), GLP-1(7-36)NH_2 or glucagon in the presence or absence of 10, 31.6, 50 or 100 µM compound C25 or C58 (Figure 3.13 and Table 3.10). These experiments showed that C25 is active at GIPR at 100 µM and inactive at GLP-1R or GCGR at 100 µM, while C58 is active at 100 µM at all three receptors with similar potency at GIPR and GLP-1R.

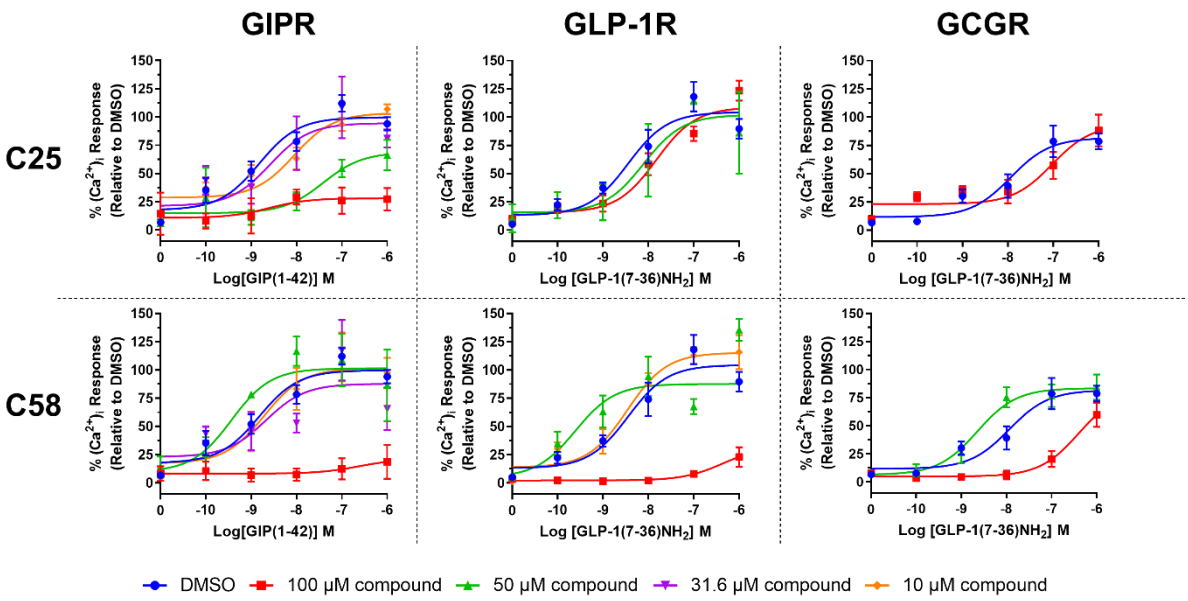

Figure 3.13. C25 selectively inhibits GIP-induced $(Ca^{2+})_i$ mobilization at GIPR while C58 does not. $(Ca^{2+})_i$ mobilization in HEK-293S cells stably expressing GIPR or GLP-1R or HEK-293ΔCTR cells stably expressing GCGR in response to GIP(1-42), GLP-1(7-36)NH_2 or glucagon in the absence or presence of different concentrations of test compounds. Data is plotted as mean ± SEM of n≥3 individual experiments performed in duplicate and normalised to GIP(1-42), GLP-1(7-36)NH_2 or glucagon with DMSO.

Table 3.10. Potency (pEC_{50}) and E_{max} values for $(Ca^{2+})_i$ mobilization in HEK-293S cells stably expressing GIPR or GLP-1R or HEK-293ΔCTR cells stably expressing GCGR in response to GIP(1-42), GLP-1(7-36)NH_2 or glucagon in the absence or presence of different concentrations of tested compounds.

Cmp	µM	GIPR			GLP-1R			GCGR		
		pEC_{50}[a]	E_{max}[b]	N	pEC_{50}[a]	E_{max}[b]	n	pEC_{50}[a]	E_{max}[b]	n
DMSO	-	8.83 ± 0.21	99.66 ± 5.55	4	8.45 ± 0.24	104.40 ± 7.54	7	7.94 ± 0.24	81.69 ± 6.97	6
C25	10	8.05 ± 0.21	103.60 ± 5.81	4	-	-	-	-	-	-
	31.6	8.58 ± 0.55	94.58 ± 12.44	3	-	-	-	-	-	-
	50	7.41 ± 0.59	68.84 ± 14.44	3	8.10 ± 0.24	102.00 ± 11.39	3	-	-	-
	100	8.61 ± 0.73	28.07 ± 3.76***	3	7.82 ± 0.18	108.70 ± 7.35	3	7.02 ± 0.33	93.60 ± 13.84	3
C58	10	8.71 ± 0.19	101.60 ± 5.32	3	8.46 ± 0.20	115.30 ± 7.88	3	-	-	-
	31.6	8.68 ± 0.63	87.77 ± 12.55	3	-	-	-	-	-	-
	50	9.44 ± 0.69	101.40 ± 12.94	3	9.61 ± 0.36	87.63 ± 8.40	3	8.65 ± 0.25	83.39 ± 5.93	3
	100	6.64 ± 0.88*	20.99 ± 7.37****	3	6.37 ± 0.60***	32.00 ± 14.26***	3	6.40 ± 0.31**	81.58 ± 19.01	3

Data are the mean ± SEM of *n* individual data sets.
[a] The negative logarithm of the agonist concentration required to produce a half-maximal response.
[b] The maximal response to the ligand expressed as a percentage of the maximal $(Ca^{2+})_i$ mobilization as determined using GIP(1-42), GLP-1(7-36)NH_2 or glucagon with DMSO.
Data were determined as statistically different (*, $p < 0.05$; **, $p < 0.01$; ***, $p < 0.001$; ****, $p < 0.0001$) compared to no treatment using a one-way ANOVA and Dunnett's post-hoc test.

Together, these findings suggest that C25 is a NAM selective for GIPR over GCGR and GLP-1R, while C3, C58 and C95 are non-selective and inhibit the agonist-stimulated $(Ca^{2+})_i$ mobilization at multiple receptors.

3.5 C25 binds at top of TMD2/3 and ECL1 of the GIPR

So far, GIPR NAMs for $(Ca^{2+})_i$ mobilization have been identified. However, the majority of these compounds are not very potent and only compound C25 showed selectivity for GIPR. It is therefore important to develop more potent selective compounds targeting the GIPR. Identifying the allosteric binding site of the compounds and better understanding their mode of binding and effect at the receptor could then help guide the development of more potent and selective compounds.

The allosteric binding site of the compounds can be found directly through, for example, solving a Cryo-Em structure, but that takes a long time, is expensive and not always works due to the difficulty of the process. To date, there is only a single Cryo-Em structure of GIPR solved (PDB ID 7DTY) (Zhao et al., 2022). Another, a bit more indirect way is to use *in silico* docking in combinations with *in vitro* mutagenesis to find which amino acids are important for compound binding or having an effect. The mutants can then be tested in *in vitro* pharmacological assays to see whether they retain GIP-induced signalling but the NAMs loose effect at them. It was this option that was pursued in this thesis.

The *in silico* docking of C25-related compounds to GIPR homology models, that will be discussed in detail in chapter 4, revealed several possible allosteric binding sites. Site 6 and Site 10 were ranked as the best candidate allosteric binding sites and the most likely place for the compounds to be binding (Figure 3.14). Site 6 lies in the top middle of transmembrane part of the receptor just below the orthosteric binding site, whereas Site 10 lies at the top of transmembrane domain 2/3 and extracellular loop 1. The *in silico* blind docking was also visualised using 2D diagrams for individual poses suggesting specific amino acids likely to interact with the compounds. Among the most likely amino acids across these 2 sites were GIPR amino acids Y141$^{1.43}$, L193$^{2.70}$, G198, Q204, N210, R289 and W296$^{5.36}$ (using the standard residue numbering for class B GPCRs by Wootten et al. (2013).

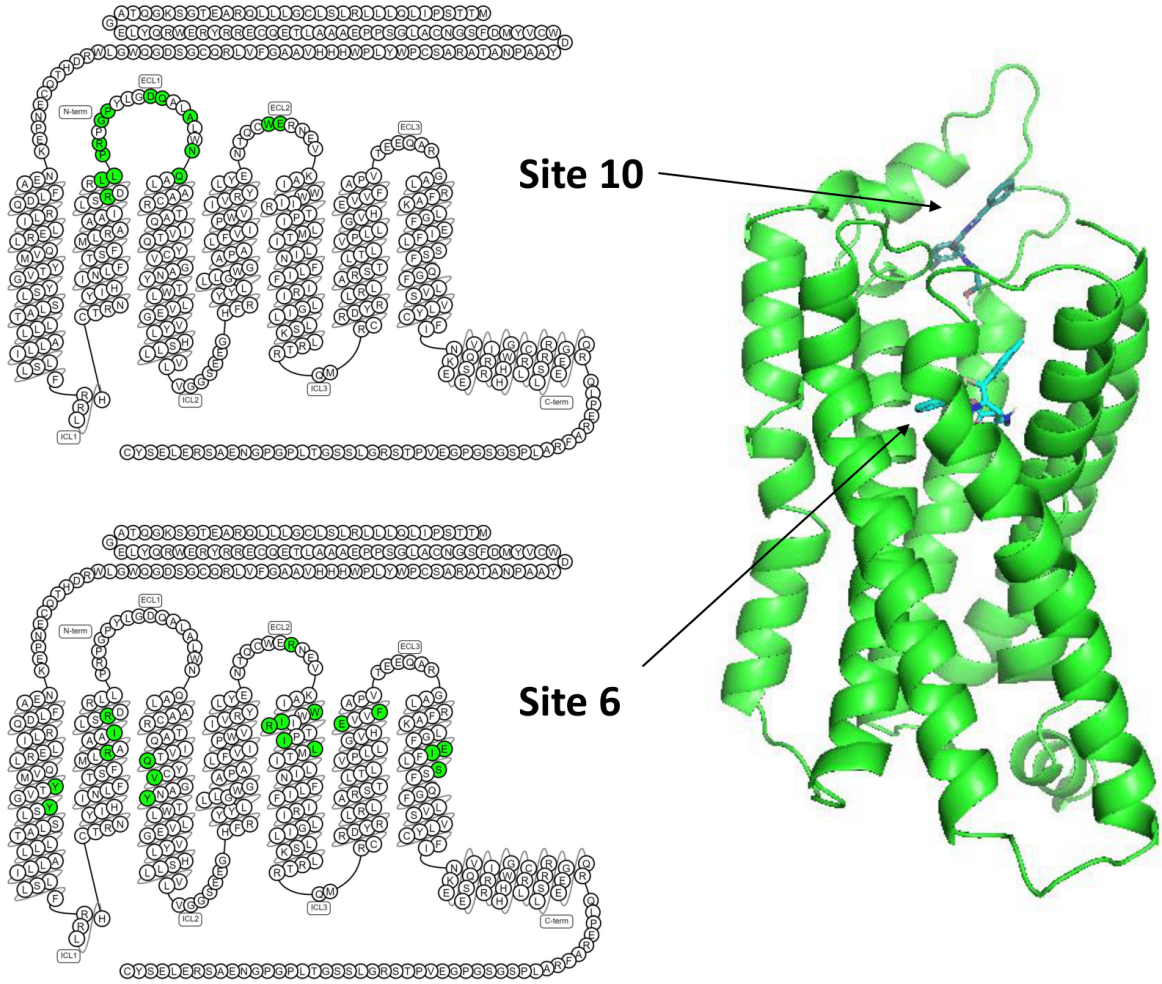

Figure 3.14. GIPR allosteric binding sites 6 and 10 predicted through in silico docking. In silico blind docking of C25-related compounds was carried out in chapter 4 using GIPR homology models excluding N-termini and GIP and identified sites 6 and 10 as most likely GIPR allosteric binding sites of the compounds. On the right, compound C25 (blue) is shown as docked to each of the sites. On the left are snake plots of GIPR indicating amino acids belonging to each side in green.

In vitro site-directed mutagenesis was then used to make alanine mutants of these amino acids resulting in GIPR mutants Y141$^{1.43}$A, L193$^{2.70}$A, G198A, Q204A, N210A, R289A and W296$^{5.36}$A. The aim was to use the mutants in second messenger assays, like the cAMP accumulation and $(Ca^{2+})_i$ mobilization assays utilised above, to see whether the GIPR NAMs lose their effects at these mutants. However, to be able to do that, the mutants first need to be characterised in the assays to see whether they retain GIP-induced signalling itself and behave normally.

To this end, HEK-293S transiently transfected with WT or mutant pcDNA3.2-GIPR were stimulated with increasing doses of either GIP(Pro3) or GIP(1-42) for 8' minutes and cAMP accumulation was measured (Figure 3.15, Table 3.11). HEK-293S cells were selected for the transfection as the GIPR stable cell line used above was made from them as well and because a trial test run with HEK-293T cells resulted in very low and inconsistent transfection, proving HEK-293S cells better. Both GIP(Pro3) and GIP(1-42) were used in this experiment as the aim was to determine which ligand would give a better assay window and would be better for future testing of any GIPR NAM for cAMP accumulation.

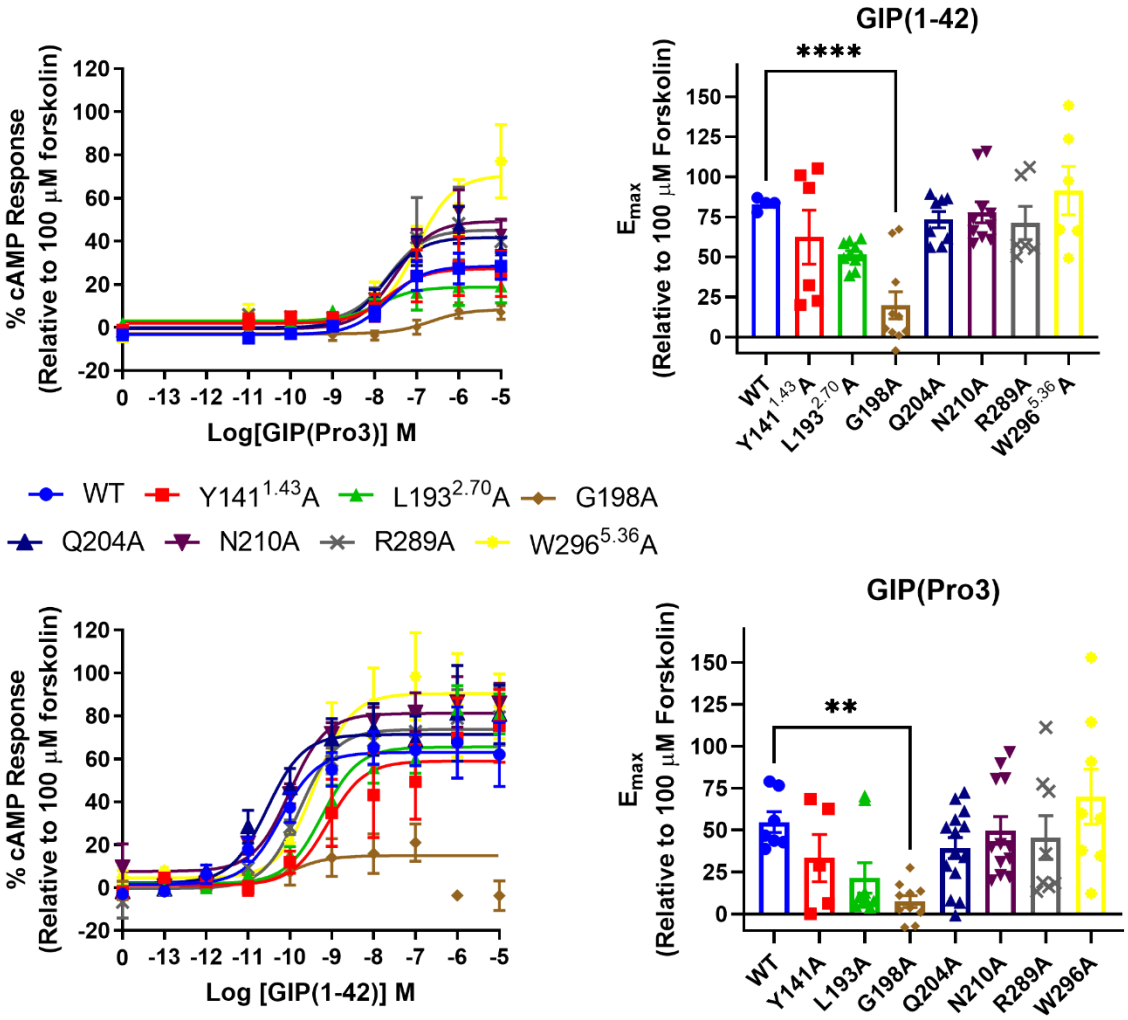

Figure 3.15. GIPR mutant G198A is unable to promote cAMP accumulation. cAMP accumulation was measured in HEK-293S transiently transfected with WT or mutant pcDNA3.2-GIPR in response to 8' stimulation with increasing doses of either GIP(Pro3) or GIP(1-42). Data is plotted as mean ± SEM of n≥3 individual experiments performed in duplicate and normalised to 100 μM forskolin response. Data

were determined as statistically different (**, $p < 0.01$; ****, $p < 0.0001$) compared to WT using a one-way ANOVA and Dunnett's post-hoc test.

Table 3.11. Potency (pEC_{50}) and E_{max} values for cAMP accumulation in HEK-293S cells transiently transfected with WT or mutant pcDNA3.2-GIPR in response to 8' stimulation with either GIP(Pro3) or GIP(1-42).

GIPR mut	GIP(Pro3)			GIP(1-42)		
	pEC_{50}[a]	E_{max}[b]	n	pEC_{50}[a]	E_{max}[b]	n
WT	7.70 ± 0.28	28.41 ± 3.02	8	10.22 ± 0.20	63.01 ± 3.46	8
Y141$^{1.43}$A	7.67 ± 0.61	27.26 ± 5.29	3	9.09 ± 0.40	58.98 ± 7.26	3
L193$^{2.70}$A	7.90 ± 0.65	18.74 ± 3.48	5	9.23 ± 0.15	65.53 ± 3.31	6
G198A	6.68 ± 0.47	8.35 ± 2.37**	5	9.94 ± 0.87	14.95 ± 3.78****	5
Q204A	7.77 ± 0.20	41.81 ± 3.00	7	10.55 ± 0.24	71.42 ± 4.39	6
N210A	7.52 ± 0.23	49.24 ± 3.87	6	10.01 ± 0.17	81.19 ± 3.59	5
R289A	7.67 ± 0.41	45.21 ± 6.09	4	9.76 ± 0.21	73.75 ± 4.05	3
W296$^{5.36}$A	7.01 ± 0.25	70.60 ± 7.13	4	9.41 ± 0.30	90.44 ± 7.15	3

Data are the mean ± SEM of *n* individual data sets.
[a] The negative logarithm of the agonist concentration required to produce a half-maximal response.
[b] The maximal response to the ligand expressed as a percentage of the maximal cAMP accumulation as determined using 100 µM forskolin.
Data were determined as statistically different (**, $p < 0.01$; ****, $p < 0.0001$) compared to WT using a one-way ANOVA and Dunnett's post-hoc test.

Of the 7 tested mutants, only mutant G198A showed a significantly reduced GIP-induced maximal cAMP response, and the GIP potency was similar across all the mutants. It is also interesting to note that while GIP(Pro3) displayed lower potency and a slightly lower maximal response, which correlates with it being known as a partial agonist, the trend for all the mutants and the relative strength of the response was very similar for both GIP(Pro3) and GIP(1-42).

The next step was then to characterize the mutants also in the intracellular $(Ca^{2+})_i$ mobilization assay. Therefore, HEK-293S transiently transfected with WT or mutant pcDNA3.2-GIPR were stimulated with increasing doses of GIP(1-42) and $(Ca^{2+})_i$ mobilization was measured (Figure 3.16, Table 3.12).

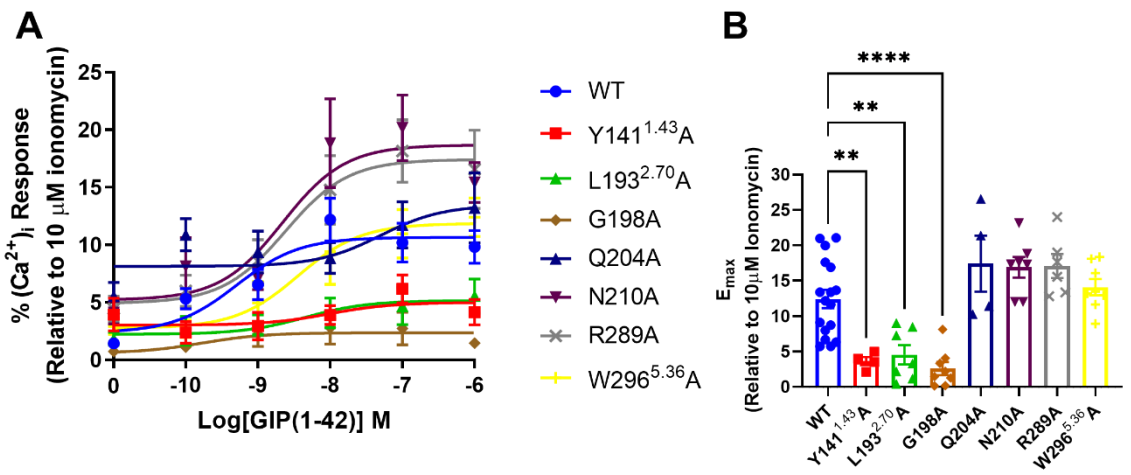

Figure 3.16. GIPR mutants Y141$^{1.43}$A, L193$^{2.70}$A and G198A have significantly reduced GIP-induced $(Ca^{2+})_i$ mobilization. $(Ca^{2+})_i$ mobilization in HEK-293S cells transiently transfected with WT or mutant pcDNA3.2-GIPR in response to GIP(1-42). Data is plotted as mean ± SEM of n≥3 individual experiments performed in duplicate. All data is normalised to 10 µM ionomycin response. Data were determined as statistically different (**, $p < 0.01$; ****, $p < 0.0001$) compared to DMSO using a one-way ANOVA and Dunnett's post-hoc test.

Table 3.12. Potency (pEC_{50}) and E_{max} values for $(Ca^{2+})_i$ mobilization in HEK-293S cells transiently transfected with WT or mutant pcDNA3.2-GIPR in response to GIP(1-42).

GIPR mut	pEC_{50}[a]	E_{max}[b]	n
WT	9.29 ± 0.38	10.66 ± 0.85	9
Y141$^{1.43}$A	8.01 ± 1.17	5.00 ± 1.05**	5
L193$^{2.70}$A	8.35 ± 0.90	5.16 ± 0.92**	4
G198A	9.76 ± 1.28	2.37 ± 0.53****	4
Q204A	7.31 ± 0.89	13.47 ± 2.26	3
N210A	8.66 ± 0.40	18.69 ± 1.73	4
R289A	8.62 ± 0.41	17.43 ± 1.64	4
W296$^{5.36}$A	8.45 ± 0.43	11.87 ± 1.32	4

Data are mean ± SEM of *n* individual data sets.
[a] The negative logarithm of the agonist concentration required to produce a half-maximal response.
[b] The maximal response to the ligand expressed as a percentage of the $(Ca^{2+})_i$ mobilization elicited by 10 µM ionomycin.
Data were determined as statistically different (**, $p < 0.01$; ****, $p < 0.0001$) compared to DMSO using a one-way ANOVA and Dunnett's post-hoc test.

First, looking at the GIP-induced $(Ca^{2+})_i$ mobilization at WT GIPR, it is slightly lower in the transfected cells (E_{max} = 10.66 ± 0.85) compared to the previous measurements in HEK 293S cells stably expressing GIPR, where the response was around 25-30% of the response induced by the 10 µM

ionomycin. This is not unexpected as not all the cells were probably perfectly transfected with the receptor and GIPR is not also so overexpressed. The potential drawback of the transient transfection approach is therefore that some of the less well expressed or worse signalling mutants have very little $(Ca^{2+})_i$ mobilization, but it was easier and less time-consuming to do the transfections than making stable cell lines of all the mutants.

Regarding the mutants, GIPR mutants $Y141^{1.43}A$, $L193^{2.70}A$ and G198A had significantly reduced GIP-induced $(Ca^{2+})_i$ mobilization. Of these G198A was the worst, producing little response, which is why this GIPR mutant was omitted from further calcium experiments.

The next step was to test the key compounds against these GIPR mutants. Compounds C3 and C25 were selected as the main compounds because they are both GIPR NAMs selective for $(Ca^{2+})_i$ mobilization and all the other compounds are based on these. Moreover, C25 is the only GIPR selective compound so far. To measure $(Ca^{2+})_i$ mobilization, HEK-293S transiently transfected with WT or mutant pcDNA3.2-GIPR were stimulated with increasing doses of GIP(1-42) in the presence or absence of 100 µM C3 (Figure 3.17, Table 3.13).

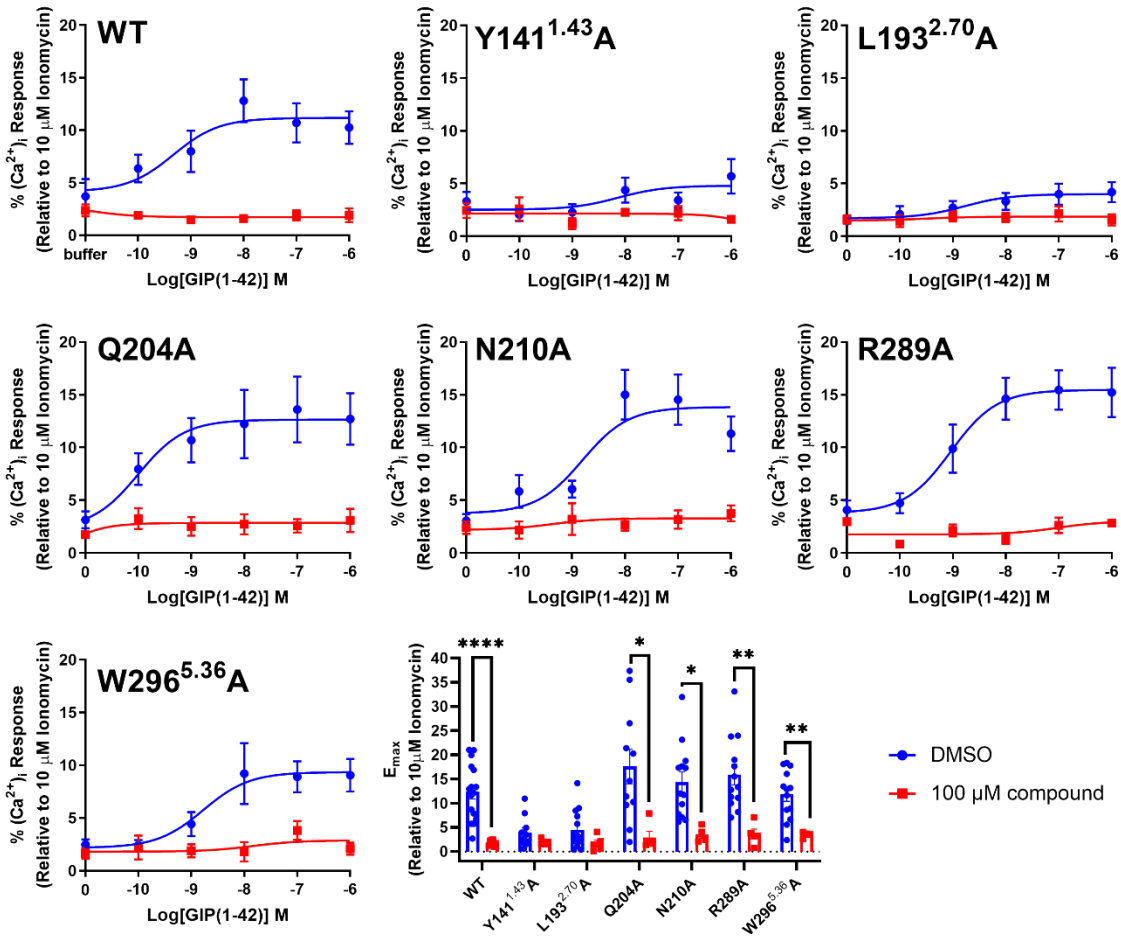

Figure 3.17. C3 inhibits GIP-induced $(Ca^{2+})_i$ mobilization at all GIPR mutants. $(Ca^{2+})_i$ mobilization was measured in HEK-293S cells stably transiently transfected with WT or mutant pcDNA3.2-GIPR in response GIP(1-42) in the presence or absence of 100 μM C3. The bottom plots then show E_{max} values plotted from the dose-response curves. Data is plotted as mean ± SEM of n≥3 individual experiments performed in duplicate and normalised to 10 μM ionomycin response. Data were determined as statistically different (*, $p < 0.05$; **, $p < 0.01$; ****, $p < 0.0001$) compared to treatment with GIP(1-42) and DMSO at each GIPR WT or mutant using Student's t-test.

Table 3.13. Potency (pEC_{50}) and E_{max} values for $(Ca^{2+})_i$ mobilization in HEK-293S cells transiently transfected with WT or mutant pcDNA3.2-GIPR in response to with GIP(1-42) in the presence or absence of 100 µM C3.

GIPR mut	µM C3	pEC_{50}[a]	E_{max}[b]	n
WT	0	9.33 ± 0.57	11.18 ± 1.07	8
	100	N.D.	1.72 ± 0.23****	4
Y141$^{1.43}$A	0	8.14 ± 0.96	4.80 ± 0.84	8
	100	N.D.	1.68 ± 0.70	3
L193$^{2.70}$A	0	8.78 ± 0.73	4.00 ± 0.52	7
	100	N.D.	1.86 ± 0.31	3
Q204A	0	10.00 ± 0.60	12.64 ± 1.27	7
	100	N.D.	2.86 ± 0.42*	3
N210A	0	8.80 ± 0.37	13.84 ± 1.17	7
	100	N.D.	3.28 ± 0.54*	3
R289A	0	9.04 ± 0.32	15.46 ± 1.14	7
	100	N.D.	3.01 ± 0.73**	3
W296$^{5.36}$A	0	8.77 ± 0.46	9.35 ± 1.04	7
	100	N.D.	2.88 ± 0.68**	4

Data are mean ± SEM of *n* individual data sets.
[a] The negative logarithm of the agonist concentration required to produce a half-maximal response.
[b] The maximal response to the ligand expressed as a percentage of the $(Ca^{2+})_i$ mobilization elicited by 10 µM ionomycin.
Data were determined as statistically different (*, $p < 0.05$; **, $p < 0.01$; ****, $p < 0.0001$) compared to treatment with GIP(1-42) and DMSO at each GIPR WT or mutant using Student's t-test.

At WT GIPR, C3 fully ablates GIP-induced $(Ca^{2+})_i$ mobilization, and the same effect was apparent on the dose-response curves of all the GIPR mutants. Furthermore, the statistical analysis showed that C3 significantly lowered the maximal response at all GIPR mutants except Y141$^{1.43}$A and L193$^{2.70}$A. However, from the curve fits of these mutants, this seems to be more because of the fact that the GIP-induced $(Ca^{2+})_i$ mobilization was so low at these mutants (E_{max} = 4.80 ± 0.84 for Y141$^{1.43}$A and E_{max} = 4.00 ± 0.52 for L193$^{2.70}$A) and because of the errors on these curves as the inhibition of the $(Ca^{2+})_i$ mobilization by C3 at these mutants was still clearly visible by eye.

The same experiment was then repeated with C25 at 100 µM (Figure 3.18, Table 3.14). At WT GIPR, C25 fully ablates GIP-induced $(Ca^{2+})_i$ mobilization, and the same effect was apparent on the dose-response curves of all the GIPR mutants except L193$^{2.70}$A. At L193$^{2.70}$A mutant, there was no significant difference between maximal GIP-induced $(Ca^{2+})_i$ mobilization with either DMSO or 100 µM C25 as is the case for WT GIPR or all the other mutants. Moreover, no inhibition of $(Ca^{2+})_i$ mobilization with C25 was visible from the dose-response either with both curves perfectly overlaid, suggesting this is a real effect. Therefore, first round of screening revealed no amino acids important for the binding or

function of C3 but suggested that L193$^{2.70}$ might be important for the negative allosteric function of C25.

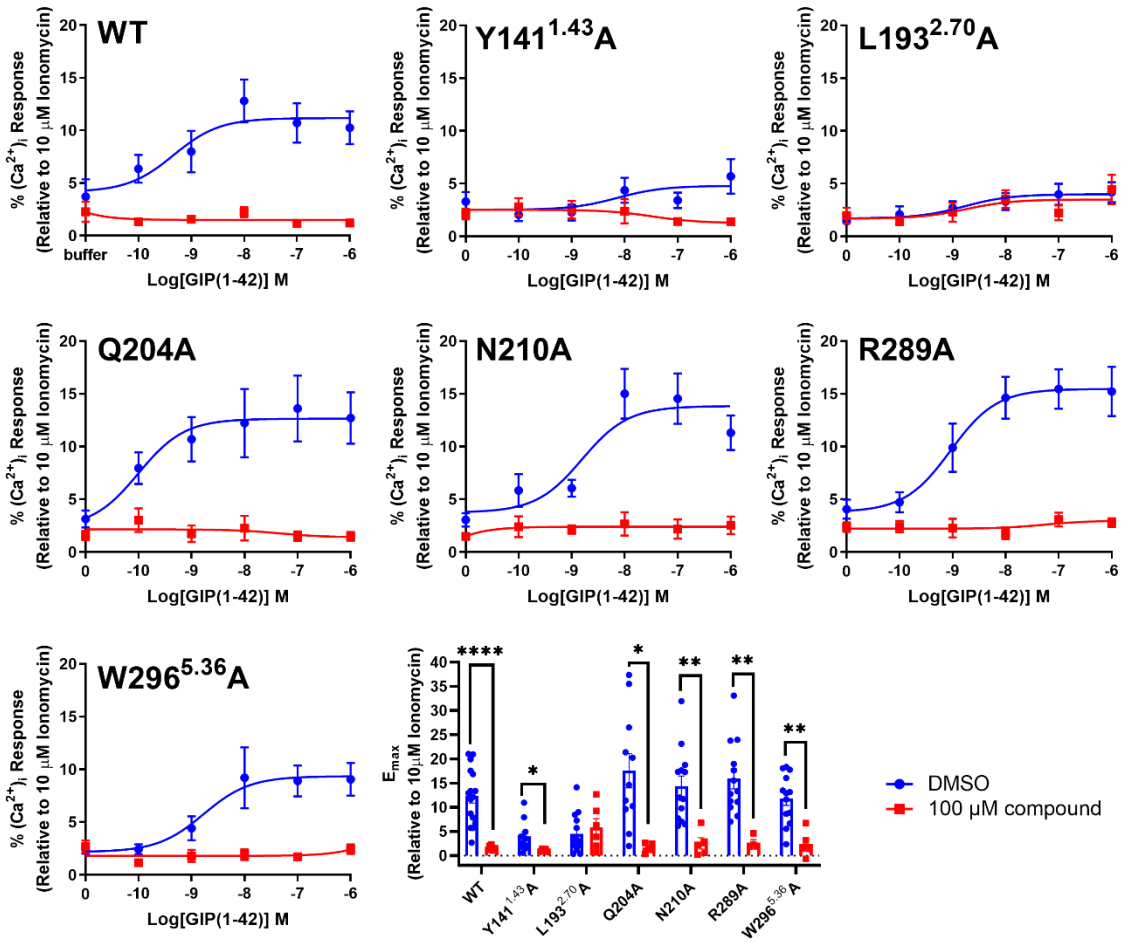

Figure 3.18. C25 has no or little effect at GIPR mutant L193$^{2.70}$A. (Ca^{2+})$_i$ mobilization was measured in HEK-293S cells stably transiently transfected with WT or mutant pcDNA3.2-GIPR in response GIP(1-42) in the presence or absence of 100 μM C25. The bottom plots then show E_{max} values plotted from the dose-response curves. Data is plotted as mean ± SEM of n≥3 individual experiments performed in duplicate and normalised to 10 μM ionomycin response. Data were determined as statistically different (*, $p < 0.05$; **, $p < 0.01$; ****, $p < 0.0001$) compared to treatment with GIP(1-42) and DMSO at each GIPR WT or mutant using Student's t-test.

Table 3.14. Potency (pEC_{50}) and E_{max} values for $(Ca^{2+})_i$ mobilization in HEK-293S cells transiently transfected with WT or mutant pcDNA3.2-GIPR in response to with GIP(1-42) in the presence or absence of 100 µM C25.

GIPR mut	µM C25	pEC_{50}[a]	E_{max}[b]	n
WT	0	9.33 ± 0.57	11.18 ± 1.07	8
	100	N.D.	1.49 ± 0.25****	4
Y141$^{1.43}$A	0	8.14 ± 0.96	4.80 ± 0.84	8
	100	N.D.	1.28 ± 0.73*	3
L193$^{2.70}$A	0	8.78 ± 0.73	4.00 ± 0.52	7
	100	8.74 ± 1.07	3.50 ± 0.61	3
Q204A	0	10.00 ± 0.60	12.64 ± 1.27	7
	100	N.D.	1.40 ± 0.88*	3
N210A	0	8.80 ± 0.37	13.84 ± 1.17	7
	100	N.D.	2.41 ± 0.41**	3
R289A	0	9.04 ± 0.32	15.46 ± 1.14	7
	100	N.D.	2.99 ± 0.68**	3
W296$^{5.36}$A	0	8.77 ± 0.46	9.35 ± 1.04	7
	100	N.D.	2.45 ± 1.24**	4

Data are mean ± SEM of *n* individual data sets.
[a] The negative logarithm of the agonist concentration required to produce a half-maximal response.
[b] The maximal response to the ligand expressed as a percentage of the $(Ca^{2+})_i$ mobilization elicited by 10 µM ionomycin.
Data were determined as statistically different (*, $p < 0.05$; **, $p < 0.01$; ****, $p < 0.0001$) compared to treatment with GIP(1-42) and DMSO at each GIPR WT or mutant using Student's t-test.

Amino acid L193$^{2.70}$, identified as possibly important for C25 binding or action, lies at the top of transmembrane 2 and is part of the predicted allosteric binding site 10. Therefore, following *more in silico* work detailed in chapter 4, a second batch of GIPR amino acids were selected, this time looking only at *in silico* poses at Site 10 (Chapter 4). These amino acids were L194$^{2.71}$, R196, P197, Q211$^{3.24}$, C216$^{3.29}$, Q220$^{3.33}$, C286$^{45.50}$, W287$^{45.51}$ and E288$^{45.52}$A.

In vitro site-directed mutagenesis was then again used to make alanine mutants of these amino acids. Of these, C216$^{3.29}$A mutant was problematic. Despite using the same protocol as for the other mutants, the DNA plasmid multiplication failed to generate sufficient DNA to enable transfection into HEK 293S cells. The reason for this was not determined and only GIPR mutants L194$^{2.71}$A, R196A, P197A, Q211$^{3.24}$A, Q220$^{3.33}$A, C286$^{45.50}$A, W287$^{45.51}$A and E288$^{45.52}$A were therefore characterised.

The characterisation of the mutants was again started with cAMP accumulation assay. The HEK-293S transiently transfected with WT or mutant pcDNA3.2-GIPR were then stimulated with increasing doses of either GIP(Pro3) or GIP(1-42) for 8' minutes and cAMP accumulation was measured (Figure 3.19, Table 3.15).

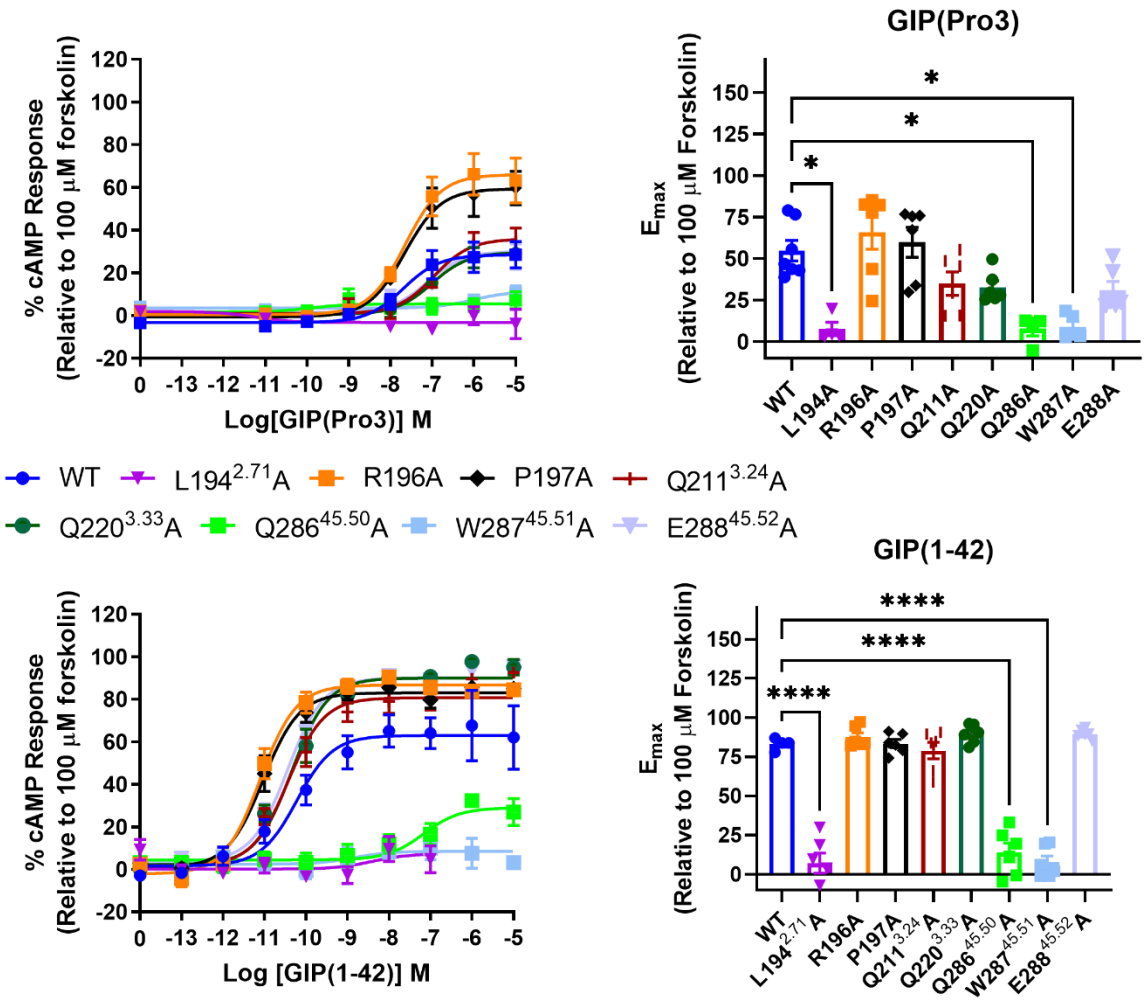

Figure 3.19. GIPR mutants L194$^{2.71}$A, Q286$^{45.50}$A and W287$^{45.51}$A have no/little GIP-induced cAMP accumulation. cAMP accumulation was measured in HEK-293S cells transiently transfected with WT or mutant pcDNA3.2-GIPR in response to 8' stimulation with increasing doses of either GIP(Pro3) or GIP(1-42). Data is plotted as mean ± SEM of n≥3 individual experiments performed in duplicate and normalised to 100 µM forskolin response. Data were determined as statistically different (*, $p < 0.05$; ****, $p < 0.0001$) compared to WT using a one-way ANOVA and Dunnett's post-hoc test.

Table 3.15. Potency (pEC_{50}) and E_{max} values for cAMP accumulation in HEK-293S transiently transfected with WT or mutant pcDNA3.2-GIPR in response to 8' stimulation with increasing doses of either GIP(Pro3) or GIP(1-42).

GIPR mut	GIP(Pro3)			GIP(1-42)		
	pEC_{50}[a]	E_{max}[b]	n	pEC_{50}[a]	E_{max}[b]	n
WT	7.70 ± 0.28	28.41 ± 3.02	8	10.22 ± 0.20	63.01 ± 3.46	8
L194$^{2.71}$A	ND	-3.22 ± 1.21*	3	ND	7.31 ± 4.69****	3
R196A	7.65 ± 0.18	66.01 ± 4.13	3	11.11 ± 0.08	86.72 ± 1.81	3
P197A	7.66 ± 0.18	59.33 ± 3.77	3	11.04 ± 0.09	83.06 ± 1.92	3
Q211$^{3.24}$A	6.96 ± 0.22	35.90 ± 3.21	3	10.44 ± 0.12	80.72 ± 2.42	3
Q220$^{3.33}$A	7.01 ± 0.18	29.60 ± 2.17	3	10.35 ± 0.09	89.98 ± 2.12	3
Q286$^{45.50}$A	ND	5.45 ± 1.57*	3	ND	29.00 ± 5.07****	3
W287$^{45.51}$A	ND	11.28 ± 3.16*	3	ND	8.85 ± 1.13****	3
E288$^{45.52}$A	7.11 ± 0.23	30.07 ± 2.54	3	10.44 ± 0.06	90.08 ± 1.43	3

Data are the mean ± SEM of *n* individual data sets.
[a] The negative logarithm of the agonist concentration required to produce a half-maximal response.
[b] The maximal response to the ligand expressed as a percentage of the maximal cAMP accumulation as determined using 100 µM forskolin.
Data were determined as statistically different (*, $p < 0.05$; ****, $p < 0.0001$) compared to WT using a one-way ANOVA and Dunnett's post-hoc test.

From this second batch of mutants, 3 displayed significantly decreased maximal response using both GIP(Pro3) and GIP(1-42). These mutants were L194$^{2.71}$A, Q286$^{45.50}$A and W287$^{45.51}$A. Since they resulted in such reduced responses, GraphPad Prism 9.3 could not reliably fit a dose-response curve for them and calculate their potency. For the other mutants, there was no significant difference in either potency or efficacy compared to WT GIPR. Also, similarly to the first batch of mutants, the relative trends for the mutants were the same when measured using either GIP(Pro3) or GIP(1-42).

The next step was then to characterize the mutants also in $(Ca^{2+})_i$ mobilization assay, similarly to the first batch of mutants. HEK-293S transiently transfected with WT or mutant pcDNA3.2-GIPR were stimulated with increasing doses of GIP(1-42) and intracellular $(Ca^{2+})_i$ mobilization quantified (Figure 3.20 and Table 3.16).

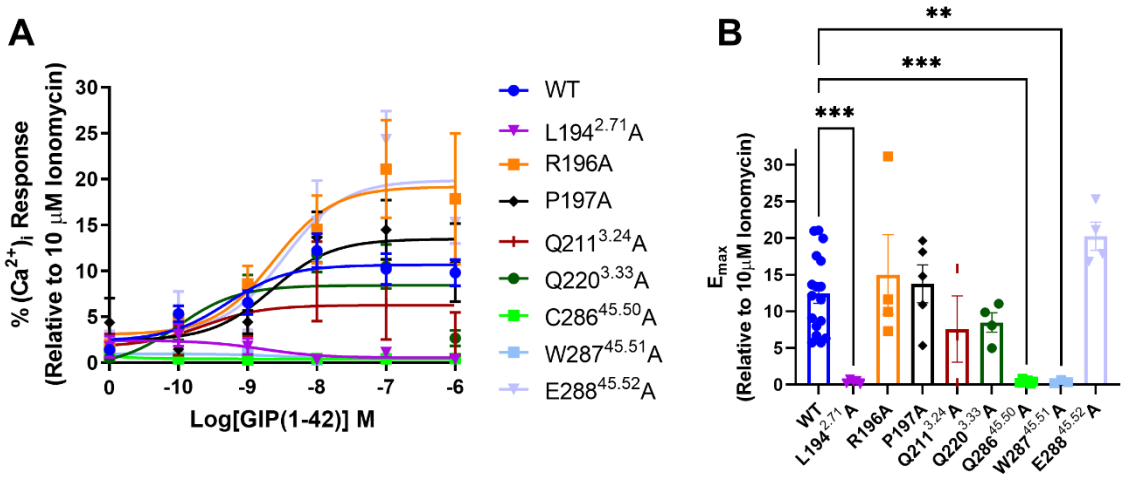

Figure 3.20. GIPR mutants L194$^{2.71}$A, Q286$^{45.50}$A and W287$^{45.51}$A had severely reduced GIP-induced (Ca^{2+})$_i$ mobilization. (Ca^{2+})$_i$ mobilization in HEK-293S cells transiently transfected with WT or mutant pcDNA3.2-GIPR in response to GIP(1-42). Data is plotted as mean ± SEM of n≥3 individual experiments performed in duplicate. All data is normalised to 10 µM ionomycin response. Data were determined as statistically different (**, $p < 0.01$; ***, $p < 0.001$) compared to DMSO using a one-way ANOVA and Dunnett's post-hoc test.

Table 3.16. Potency (pEC_{50}) and E_{max} values for (Ca^{2+})$_i$ mobilization in HEK-293S cells transiently transfected with WT or mutant pcDNA3.2-GIPR in response to GIP(1-42).

GIPR mut	pEC_{50}[a]	E_{max}[b]	n
WT	9.29 ± 0.38	10.66 ± 0.85	9
L194$^{2.71}$A	N.D.	0.55 ± 0.55***	3
R196A	8.62 ± 0.54	19.17 ± 2.75	3
P197A	8.65 ± 0.54	13.48 ± 1.91	3
Q211$^{3.24}$A	9.65 ± 1.55	6.28 ± 1.67	3
Q220$^{3.33}$A	10.01 ± 0.57	8.43 ± 1.13	3
Q286$^{45.50}$A	N.D.	0.42 ± 0.06***	3
W287$^{45.51}$A	N.D.	0.39 ± 0.30**	3
E288$^{45.52}$A	8.47 ± 0.41	19.87 ± 2.28	3

Data are mean ± SEM of *n* individual data sets.

[a] The negative logarithm of the agonist concentration required to produce a half-maximal response.

[b] The maximal response to the ligand expressed as a percentage of the (Ca^{2+})$_i$ mobilization elicited by 10 µM ionomycin.

Data were determined as statistically different (**, $p < 0.01$; ***, $p < 0.001$) compared to DMSO using a one-way ANOVA and Dunnett's post-hoc test.

From this second batch, mutants L194$^{2.71}$A, Q286$^{45.50}$A and W287$^{45.51}$ showed very little to no GIP-induced $(Ca^{2+})_i$ mobilization (E_{max} of 0.55 ± 0.55, 0.42 ± 0.06 and 0.39 ± 0.30, respectively), resulting in these mutants being excluded from further experiments. The maximal GIP-induced intracellular $(Ca^{2+})_i$ mobilization for the rest of the mutants did not significantly differ from WT for the other mutants, which were then used in further experiments.

As a next step, C25 was screened against the new GIPR mutants. To this end, HEK-293S transiently transfected with WT or mutant pcDNA3.2-GIPR were stimulated with increasing doses of GIP(1-42) in the presence or absence of 100 µM C25 (Figure 3.21, Table 3.17).

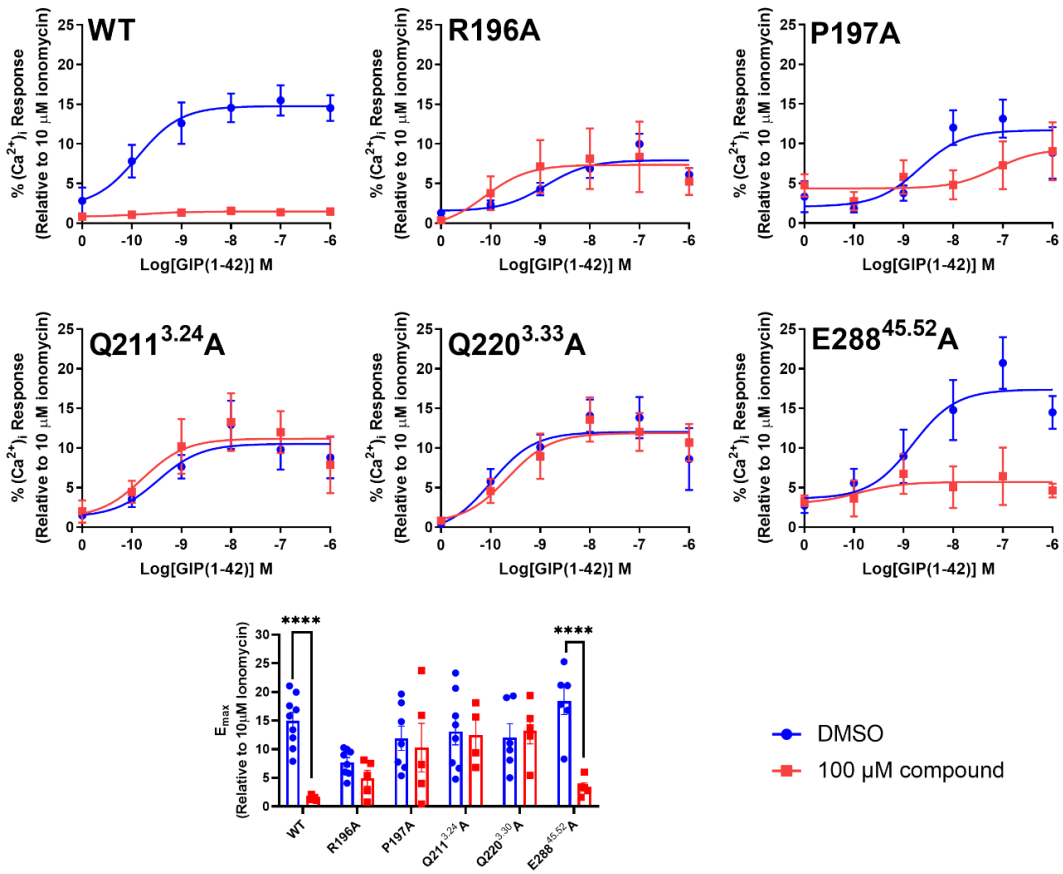

Figure 3.22. C25 has no or little effect at GIPR mutant R196A, P197A, Q211$^{3.24}$A and Q220$^{3.33}$A. $(Ca^{2+})_i$ mobilization was measured in HEK-293S cells stably transiently transfected with WT or mutant pcDNA3.2-GIPR in response GIP(1-42) in the presence or absence of 100 µM C25. The bottom plots then show E_{max} values plotted from the dose-response curves. Data is plotted as mean ± SEM of n≥3 individual experiments performed in duplicate and normalised to 10 µM ionomycin response. Data were determined as statistically different (****, $p < 0.0001$) compared to treatment with GIP(1-42) and DMSO at each GIPR WT or mutant using Student's t-test.

Table 3.17. Potency (pEC_{50}) and E_{max} values for $(Ca^{2+})_i$ mobilization in HEK-293S cells transiently transfected with WT or mutant pcDNA3.2-GIPR in response to with GIP(1-42) in the presence or absence of 100 µM C25.

GIPR mut	µM C25	pEC_{50}[a]	E_{max}[b]	n
WT	0	9.88 ± 0.36	14.77 ± 1.07	5
	100	N.D.	1.47 ± 0.15****	3
R196A	0	8.89 ± 0.31	7.95 ± 0.63	5
	100	10.11 ± 0.92	7.36 ± 1.54	3
P197A	0	8.67 ± 0.48	11.70 ± 1.48	4
	100	7.15 ± 1.10*	9.38 ± 2.94	3
$Q211^{3.24}A$	0	9.48 ± 0.53	10.52 ± 1.24	5
	100	9.78 ± 0.74	11.17 ± 1.62	3
$Q220^{3.33}A$	0	9.99 ± 0.44	12.01 ± 1.26	3
	100	9.66 ± 0.45	1.54 ± 0.89	3
$E288^{45.52}A$	0	8.81 ± 0.42	17.38 ± 1.84	3
	100	N.D.	5.70 ± 1.24****	3

Data are mean ± SEM of *n* individual data sets.
[a] The negative logarithm of the agonist concentration required to produce a half-maximal response.
[b] The maximal response to the ligand expressed as a percentage of the $(Ca^{2+})_i$ mobilization elicited by 10 µM ionomycin.
Data were determined as statistically different (****, p <0.0001) compared to treatment with GIP(1-42) and DMSO at each GIPR WT or mutant using Student's t-test.

Interestingly C25 had no significant effect on lowering maximal GIP-induced $(Ca^{2+})_i$ mobilization at 4 of the mutants R196A, P197A, $Q211^{3.24}A$ and $Q220^{3.33}A$. Analysis of the curve fitting of these mutants, confirmed that C25 did not appear to have an effect at any of these mutants except possible P197A, where the potency of GIP(1-42) is slightly lower. However, even at P197A the $(Ca^{2+})_i$ mobilization is not fully ablated as was observed for the WT GIPR and the $E288^{45.52}A$ mutant.

Combined these data suggests, that 5 amino acids ($L193^{2.70}$, R196, P197, $Q211^{3.24}$ and $Q220^{3.33}$) are important for C25 function and mutating them to alanine significantly reduces C25 efficacy. This was further corroborated by the fact that all these amino acids are located at Site 10 close to each other in the 3D GIPR structure (Chapter 4).

Previously, the second compound to screen was C3. But since no amino acid were identified as potentially important for C3 function, C3-based compounds were all unselective among GIPR, GLP-1R and GCGR and the *in silico* blind docking in chapter 4 was performed with compounds based on C9 (which includes C25 and C25-based compounds), it was decided to focus on C25-based compounds instead. Since the only other C25-based NAM identified in the original screening was compound C58, it was decided to test this compound next on all Site 10 mutants including the ones from both the first and second batch of mutants. Therefore, using same experimental setup as above, HEK-293S were

transiently transfected with WT or mutant pcDNA3.2-GIPR were stimulated with increasing doses of GIP(1-42) in the presence or absence of 100 µM C58 (Figure 3.21 and Table 3.18).

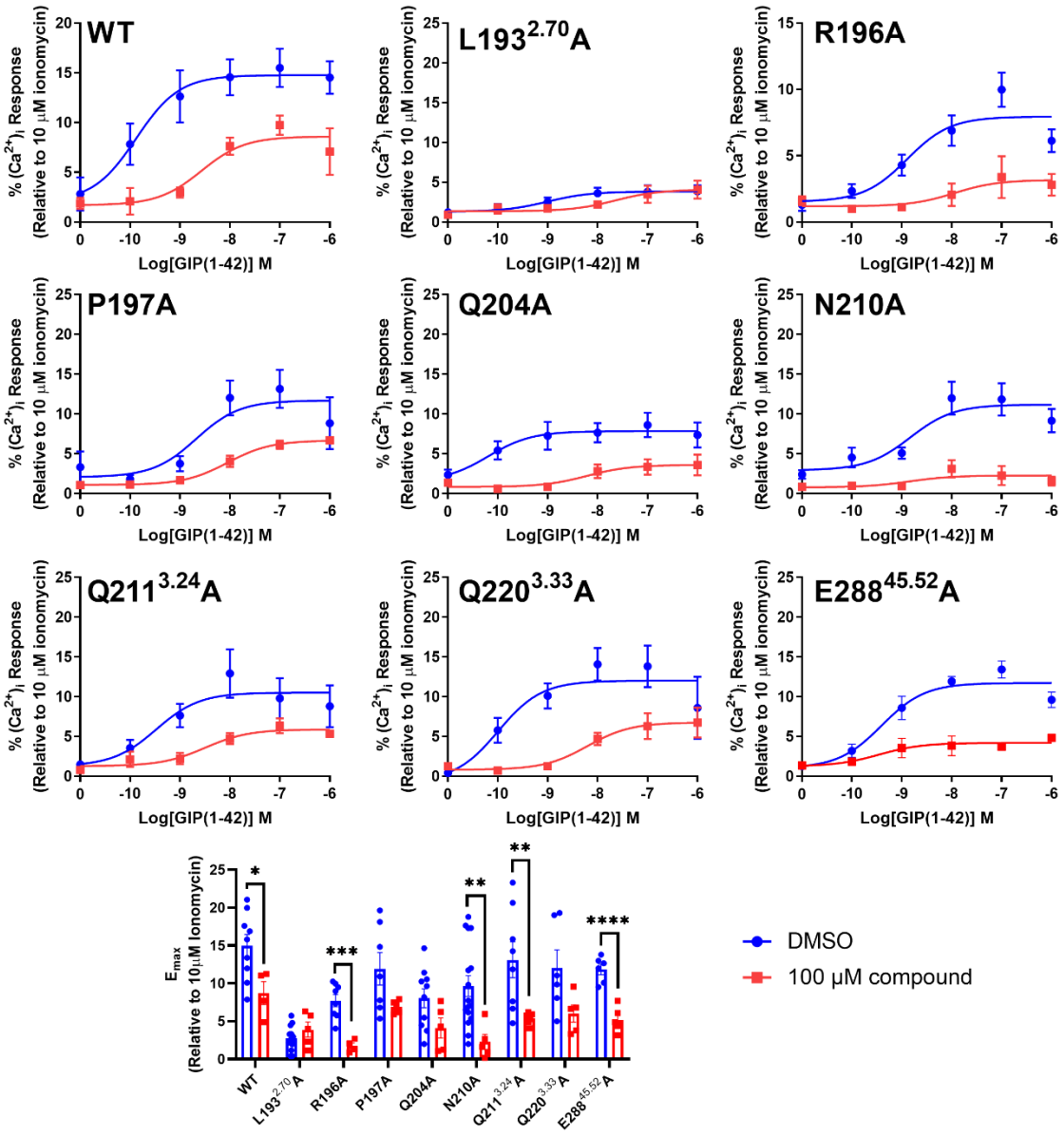

Figure 3.22. Mutation of L193$^{2.70}$A in GIPR reduces C58 activity. $(Ca^{2+})_i$ mobilization was measured in HEK-293S cells stably transiently transfected with WT or mutant pcDNA3.2-GIPR in response GIP(1-42) in the presence or absence of 100 µM C58. The bottom plots then show E_{max} values plotted from the dose-response curves. Data is plotted as mean ± SEM of n≥3 individual experiments performed in duplicate and normalised to 10 µM ionomycin response. Data were determined as statistically different (*, $p < 0.05$; **, $p < 0.01$; ***, $p < 0.001$; ****, $p < 0.0001$) compared to treatment with GIP(1-42) and DMSO at each GIPR WT or mutant using Student's t-test.

Table 3.18. Potency (pEC_{50}) and E_{max} values for $(Ca^{2+})_i$ mobilization in HEK-293S cells transiently transfected with WT or mutant pcDNA3.2-GIPR in response to with GIP(1-42) in the presence or absence of 100 µM C58.

GIPR mut	µM C58	pEC_{50}[a]	E_{max}[b]	n
WT	0	9.88 ± 0.36	14.77 ± 1.07	5
	100	8.57 ± 0.41	8.60 ± 0.90*	3
L193$^{2.70}$A	0	9.01 ± 0.52	3.84 ± 0.41	9
	100	7.64 ± 0.63	4.07 ± 0.70	4
R196A	0	8.89 ± 0.31	7.95 ± 0.63	5
	100	7.95 ± 0.85**	3.17 ± 0.68***	3
P197A	0	8.67 ± 0.48	11.70 ± 1.48	4
	100	8.05 ± 0.16*	6.68 ± 0.35	3
Q204A	0	10.19 ± 0.59	7.84 ± 0.72	9
	100	8.22 ± 0.56	3.60 ± 0.58	3
N210A	0	8.83 ± 0.38	11.18 ± 0.99	9
	100	8.85 ± 1.02	2.27 ± 0.48**	3
Q211$^{3.24}$A	0	9.48 ± 0.53	10.52 ± 1.24	5
	100	8.50 ± 0.33****	5.89 ± 0.49**	4
Q220$^{3.33}$A	0	9.99 ± 0.44	12.01 ± 1.26	3
	100	8.21 ± 0.35****	6.77 ± 0.81	3
E288$^{45.52}$A	0	9.41 ± 0.23	11.73 ± 0.63	3
	100	9.46 ± 0.60	4.20 ± 0.43****	3

Data are mean ± SEM of *n* individual data sets.
[a] The negative logarithm of the agonist concentration required to produce a half-maximal response.
[b] The maximal response to the ligand expressed as a percentage of the $(Ca^{2+})_i$ mobilization elicited by 10 µM ionomycin.
Data were determined as statistically different (*, $p < 0.05$; **, $p < 0.01$; ***, $p < 0.001$; ****, $p < 0.0001$) compared to treatment with GIP(1-42) and DMSO at each GIPR WT or mutant using Student's t-test.

At WT GIPR, C58 does not fully ablate GIP-induced $(Ca^{2+})_i$ mobilization, but it still significantly lowers the maximal response (E_{max} of 14.77 ± 1.07 and 8.60 ± 0.90 for DMSO and C58, respectively). This was true also for mutants R196A, N210A, Q211$^{3.24}$A and E288$^{45.52}$A, while there was no significant lowering at mutants L193$^{2.70}$A, P197A, Q204A and Q220$^{3.33}$A. However, looking at the dose-response curves, there seems to be some inhibition happening at some of these mutants as well masked by the bigger error rates or lower response in general. Moreover, at some of them (R196A, P197A, Q211$^{3.24}$A and Q220$^{3.33}$A) there was significant lowering of the potency of GIP(1-42). Only at mutant L193$^{2.70}$A was there no visible lowering of the maximal response with both dose-response curves overlaying quite well and no significant effect on either potency or efficacy, suggesting the amino acid L193$^{2.70}$ might be important for C58.

Overall, L193$^{2.70}$ seems important for both C25 and C58 efficacy, while R196, P197, Q211$^{3.24}$ and Q220$^{3.33}$ were identified as important for C25 only. While the statistics suggest that P197, Q204 and Q220$^{3.33}$ are also important for C58, visual analysis of the curve fitting suggests this might not be the

case as some C58 effect is still visible at alanine mutants of these amino acids. Since the compounds are structurally similar, some overlap in the binding at the GIPR would be expected and was shown with L193$^{2.70}$A, however some differences would also be expected as C25 is slightly more potent at GIPR and is GIPR selective, while C58 is not.

3.6 C25 selectively inhibits GIP-potentiated insulin secretion

Due to GIPR therapeutical relevance and its important role in insulin secretion mediated by pancreatic β-cells, the effect of compounds on GSIS was next quantified. The rat INS-1 cells were chosen for this experiment because they are a commonly used cell line for insulin secretion (Skelin et al., 2010) and grow quicker and attach better according to the Ladds laboratories past experiments than for example mouse MIN6 cells, which are also commonly used for this purpose.

C25, C58 and C95 were selected for this experiment as it was performed prior to the T compounds screening. When tested alone, none of these compounds had any significant effect on glucose-mediated insulin secretion as predicted due to them being allosteric modulators (Figure 3.23). The same compounds were then tested for their effect on both GIP- and GLP-1-potentiated glucose stimulated insulin secretion.

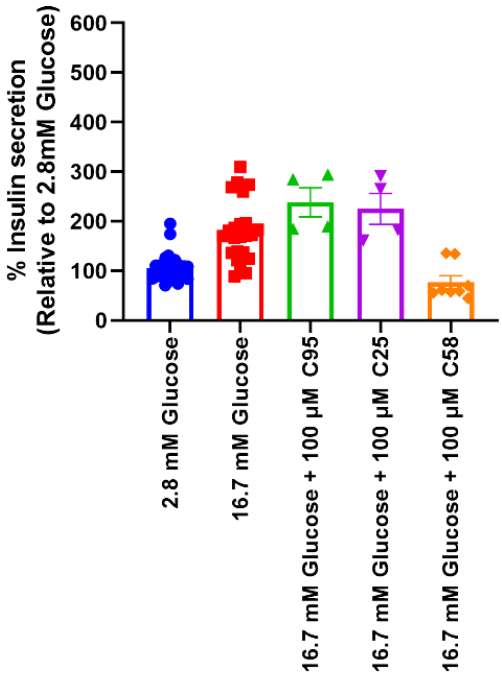

Figure 3.23. GIPR allosteric modulators alone do not affect GSIS from rat INS-1 WT cells. Insulin secretion from rat INS-1 WT cells after 1-hour pre-treatment with 2.8/16.7 mM glucose in the presence or absence of 100 µM compounds. Data is plotted as mean ± SEM of n≥3 individual experiments performed in duplicate and normalised to 2.8mM glucose. Data were determined as statistically different compared to 16.7 mM glucose using a one-way ANOVA and Dunnett's post-hoc test. Compound C58 was measured by Ms Pearce (University of Cambridge).

When tested in the presence of 0.01 µM GIP(1-45) in rat INS-1 cells, C58 at 100 µM and C25 at 10 µM and 100 µM significantly reduced GIP-potentiated GSIS (Figure 3.24.A). For C58 this was the same concentration at which the compound was active in $(Ca^{2+})_i$ mobilization assay, while C25 was only active at GIPR at 100 µM in $(Ca^{2+})_i$ mobilization assay, making it more potent in GSIS assay. C95, which was the most potent compound identified in the calcium screening, on the other hand, had no significant effect on GIP-potentiated GSIS. When tested in the presence of 0.01 µM GLP-1(7-36)NH_2 in rat INS-1 cells, C58 at 10 µM and 100 µM and C95 at 100 µM significantly reduced GLP-1-potetiated GSIS, while C25 at 100 µM had no significant effect (Figure 3.24.B).

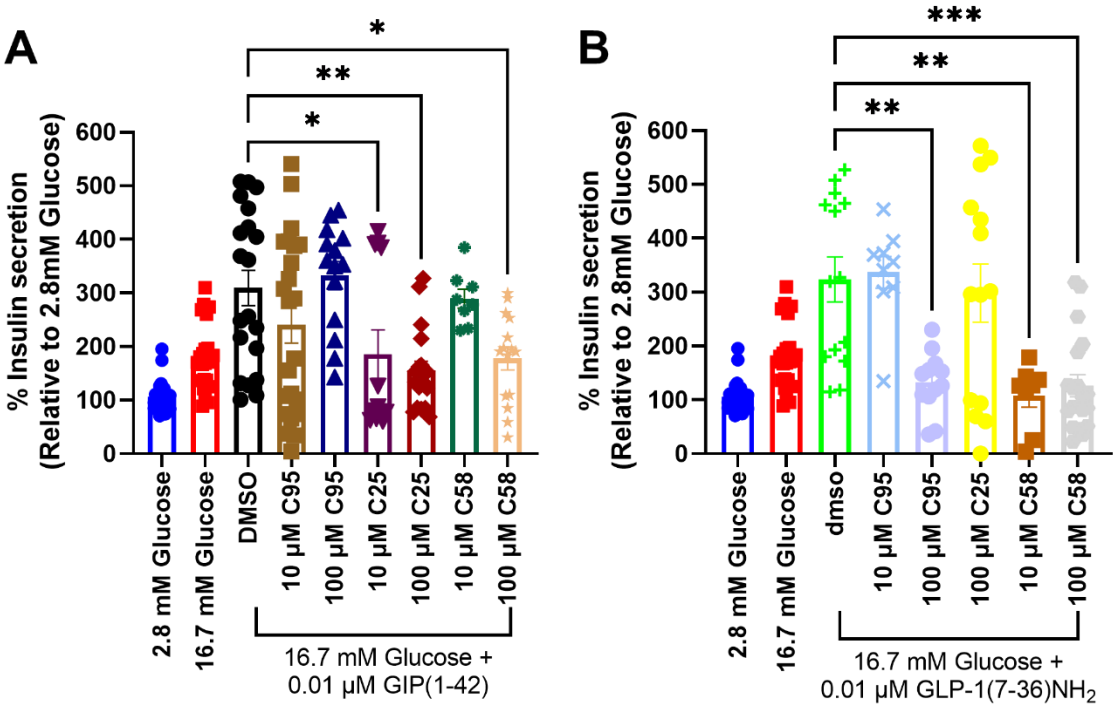

Figure 3.24. NAMs selective for $(Ca^{2+})_i$ mobilization also inhibit incretin-potentiated GSIS from rat INS-1 cells. A. Insulin secretion from rat INS-1 cells after 1-hour treatment with 2.8 or 16.7 mM glucose in the presence or absence of GIP(1-42) and DMSO or compound. B. Insulin secretion from rat INS-1 cells after 1-hour pre-treatment with 2.8 or 16.7 mM glucose in the presence or absence of GLP(1-36)NH_2 and DMSO or compound. Data is plotted as mean ± SEM of n≥3 individual experiments performed in duplicate and normalised to 2.8mM glucose. Data were determined as statistically different (*, $p < 0.05$; **, $p < 0.01$; ***, $p < 0.001$) compared to DMSO using a one-way ANOVA and Dunnett's post-hoc test. Compound C58 at 10 µM was measured by Ms Pearce (University of Cambridge).

Overall, these results suggest that in insulin secretion assay C95 is selective for GLP-1R over GIPR and even C58 is slightly more potent at GLP-1R. C25 on the other hand is selective for GIPR over GLP-1R in line with the results from $(Ca^{2+})_i$ mobilization assay.

3.7 Discovery of new GIPR allosteric modulators for both $(Ca^{2+})_i$ and cAMP pathways

The combined approach of *in silico* docking and *in vitro* experiments performed above has identified site 10 as allosteric binding site of GIPR NAMs C25 and C58. However, these are only two related compounds with a similar scaffold and potency around 100 µM. The question therefore was whether as a general allosteric binding site this could be targeted by other allosteric compounds providing a group of several varied scaffolds, which would be a better starting point for future tries to improve the potency of the compounds.

Therefore, Dr Rahman (University of Cambridge) conducted an *in silico* screen against site 10 to find new compounds binding solely at this position. He performed a structure based virtual screen using the Enamine Discovery Diversity Library (Enamine DDS) as well as VITAS. The hits were then manually inspected and ICM Pro based docking was also conducted for the most promising compounds. Finally, 2 batches of compounds (T1-T12 and T13-T27) were selected for *in vitro* screening (Table 3.19). The number of compounds was a compromise between wanting to test as many compounds as possible but also taking in regard the costs and time it would take to perform the screening.

Table 3.19. 2D structures and molecular weight of potential GIPR allosteric modulators T1-T27.

Compound	Structure	Molecular weight (g/mol)
T1	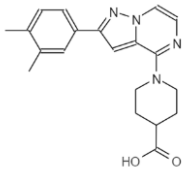	350.42
T2	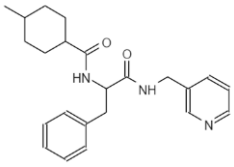	379.50
T3	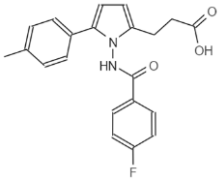	366.39
T4	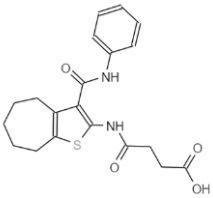	386.47
T5	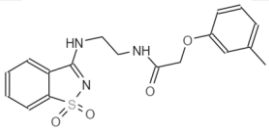	373.43
T6	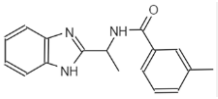	279.34
T7	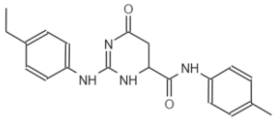	350.42
T8	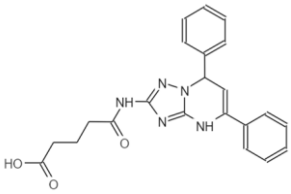	403.44
T9	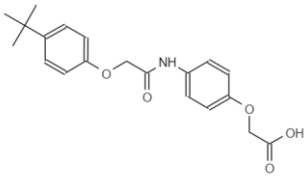	357.41

T10	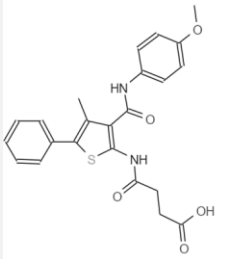	438.50
T11	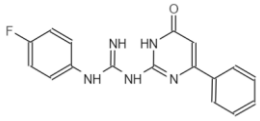	323.33
T12	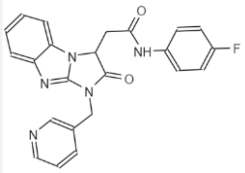	415.43
T13	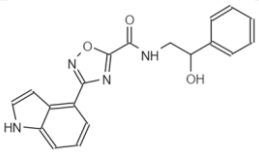	348.36
T14	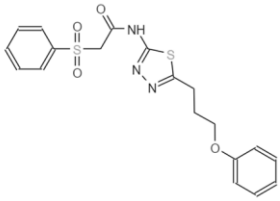	417.51
T15	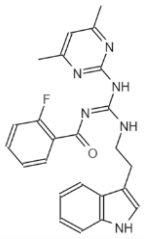	430.48
T16	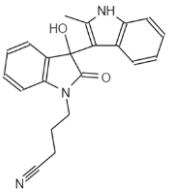	354.40
T17	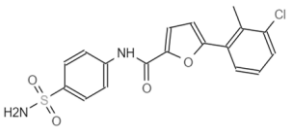	390.85
T18	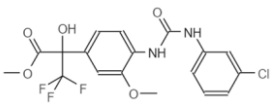	432.78
T19	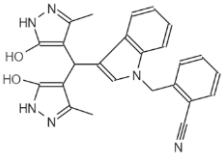	438.49

T20	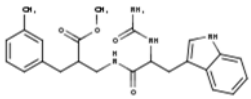	436.50
T21	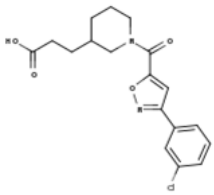	362.80
T22	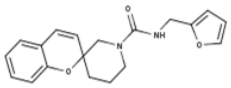	324.40
T23	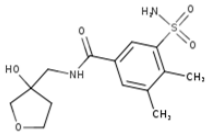	328.40
T24	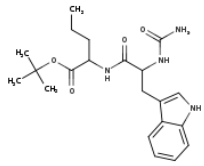	402.50
T25	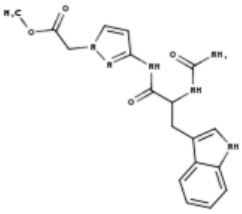	384.40
T26	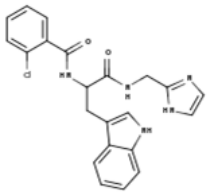	421.90
T27	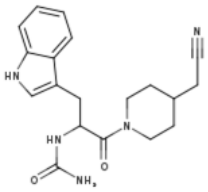	353.40

Since the original compounds binding in Site 10 are negative allosteric modulators for $(Ca^{2+})_i$ mobilization, this was the first assay used to screen the compounds. To test the ability of the compounds to modulate GIP-induced $(Ca^{2+})_i$ mobilization, the HEK-293S cells stably expressing GIPR were stimulated with increasing doses of GIP(1-42) in the presence or absence of 100 µM compound (Figure 3.25 and Table 3.20 for compounds T1-T12 and Figure 3.26 and Table 3.21 for compounds T13-T27).

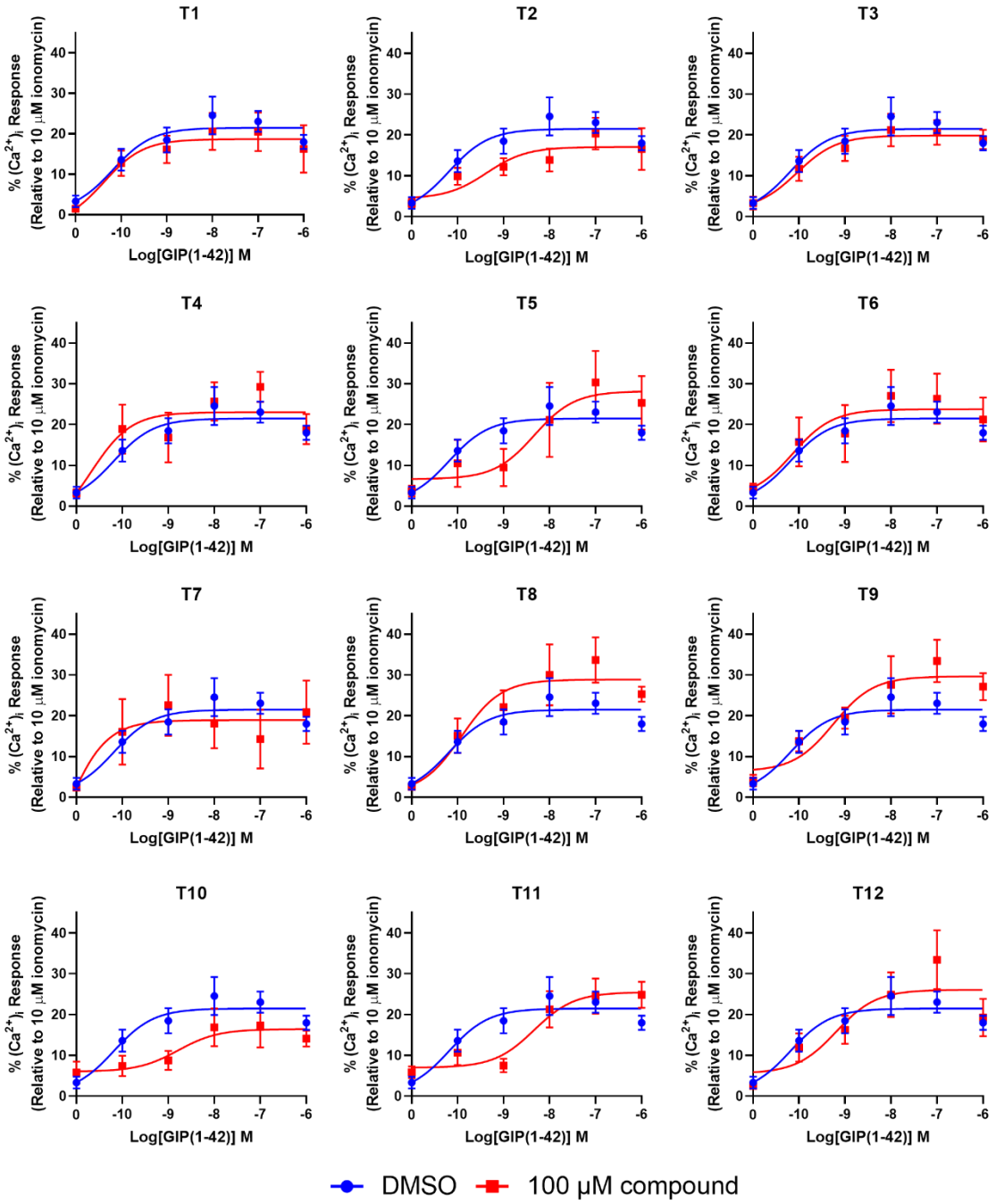

Figure 3.25. The new compounds, T2, T5, T10 and T11, based upon site 10 binding alone, inhibit GIP-induced $(Ca^{2+})_i$ mobilization. $(Ca^{2+})_i$ mobilization in HEK-293S cells stably expressing GIPR in response to GIP(1-42) in the absence or presence of 100 µM tested compounds. Data is plotted as mean ± SEM of n≥3 individual experiments performed in duplicate and normalised to 10 µM ionomycin response.

Table 3.20. Potency (pEC_{50}) and E_{max} values for $(Ca^{2+})_i$ mobilization in HEK-293S cells stably expressing GIPR in response to GIP(1-42) in the absence or presence of 100 µM tested compounds.

Cmp	pEC_{50}[a]	E_{max}[b]	Basal	n
DMSO	10.19 ± 0.37	21.48 ± 1.57	0.60 ± 4.90	9
T1	10.38 ± 0.62	18.67 ± 2.12	-2.59 ± 9.12	4
T2	9.37 ± 0.58**	17.05 ± 1.93	4.35 ± 3.14	4
T3	10.04 ± 0.39	19.86 ± 1.56	1.61 ± 4.40	4
T4	10.68 ± 0.91	23.01 ± 2.35	-6.18 ± 21.77	4
T5	8.33 ± 0.64*	28.17 ± 4.82	6.61 ± 4.50	4
T6	10.14 ± 0.68	23.74 ± 3.03	1.99 ± 9.21	5
T7	11.26 ± 4.36	18.91 ± 3.43	1.48 ± 1.04	4
T8	9.92 ± 0.39	28.86 ± 2.50	0.87 ± 6.06	4
T9	9.25 ± 0.39	29.63 ± 2.55	6.34 ± 3.79	4
T10	8.79 ± 0.70*	16.42 ± 2.30	6.00 ± 2.71	5
T11	8.33 ± 0.38*	25.49 ± 2.47	6.96 ± 2.37	4
T12	9.19 ± 0.53	26.07 ± 3.04	5.53 ± 4.80	4

Data are the mean ± SEM of *n* individual data sets.

[a] The negative logarithm of the agonist concentration required to produce a half-maximal response.

[b] The maximal response to the ligand expressed as a percentage of the maximal $(Ca^{2+})_i$ mobilization as determined using 10 µM ionomycin.

Data were determined as statistically different (*, $p < 0.05$; **, $p < 0.01$) compared to no treatment using a one-way ANOVA and Dunnett's post-hoc test.

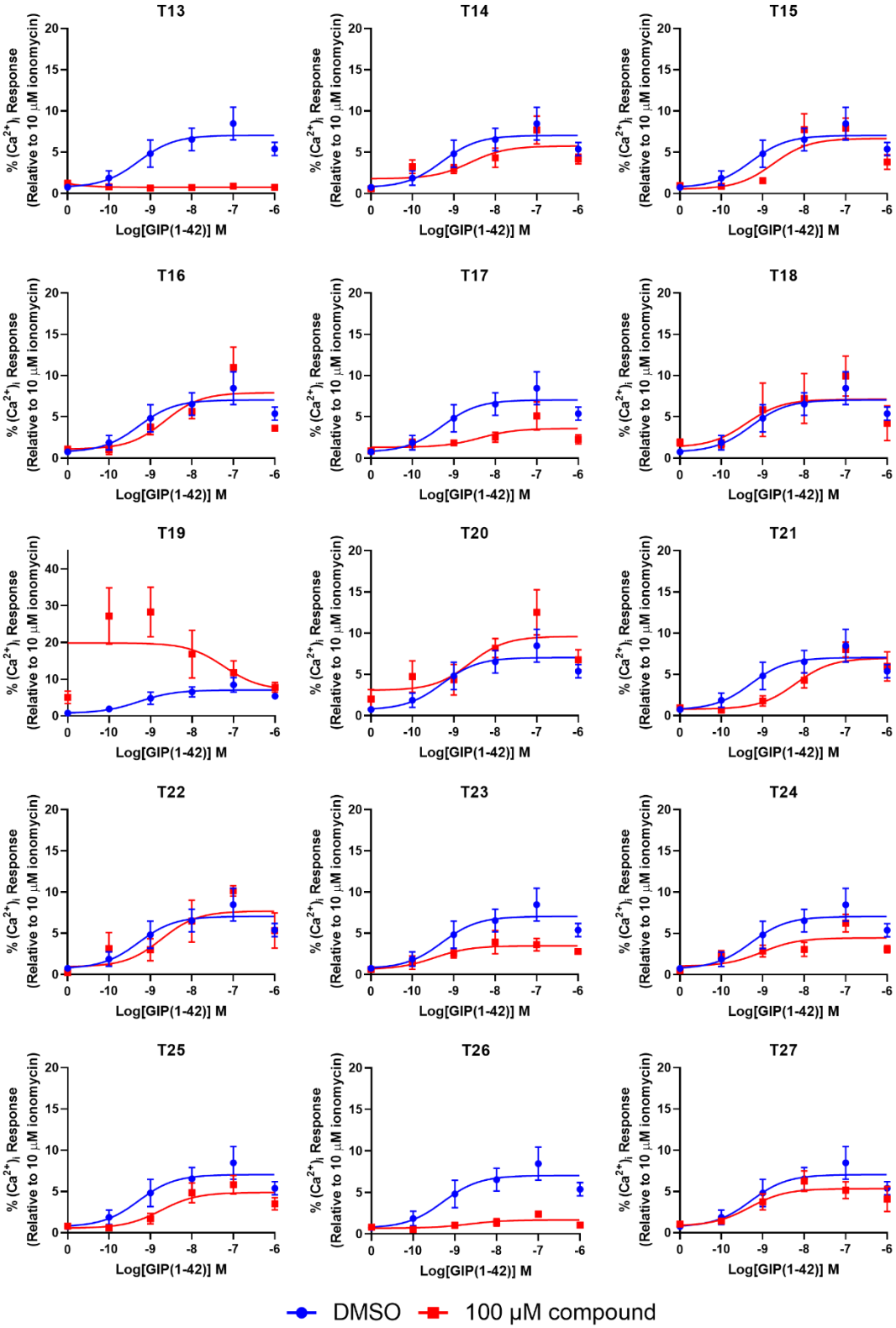

Figure 3.26. The new compounds T13 and T26, based upon site 10 binding alone, inhibit GIP-induced $(Ca^{2+})_i$ mobilization. $(Ca^{2+})_i$ mobilization in HEK-293S cells stably expressing GIPR in response to GIP(1-42) in the absence or presence of 100 µM tested compounds. Data is plotted as mean ± SEM of n≥3 individual experiments performed in duplicate and normalised to 10 µM ionomycin response.

Table 3.21. Potency (pEC_{50}) and E_{max} values for $(Ca^{2+})_i$ mobilization in HEK-293S cells stably expressing GIPR in response to GIP(1-42) in the absence or presence of 100 µM tested compounds.

Cmp	pEC_{50}[a]	E_{max}[b]	Basal	n
DMSO	9.28 ± 0.45	7.05 ± 0.85	0.72 ± 1.19	5
T13	N.D.	0.74 ± 0.04**	1.44 ± 0.36	3
T14	8.60 ± 0.60	5.77 ± 0.77	1.80 ± 0.81	3
T15	8.75 ± 0.41	6.68 ± 0.85	0.53 ± 0.91	3
T16	8.65 ± 0.42	7.93 ± 1.13	1.09 ± 0.98	3
T17	8.37 ± 0.82	3.59 ± 0.64	1.31 ± 0.60	4
T18	9.39 ± 0.89	7.12 ± 1.38	1.31 ± 2.20	4
T19	NA[1]	NA[1]	NA[1]	5
T20	8.61 ± 0.72	9.61 ± 1.37	3.07 ± 1.46	3
T21	8.21 ± 0.33	6.98 ± 0.76	0.79 ± 0.65	4
T22	8.73 ± 0.56	7.69 ± 1.18	0.94 ± 1.50	3
T23	9.46 ± 0.64	3.48 ± 0.46	0.62 ± 0.78	3
T24	9.02 ± 0.51	4.46 ± 0.57	1.02 ± 0.73	3
T25	8.75 ± 0.43	4.88 ± 0.58	0.55 ± 0.75	3
T26	N.D.	1.70 ± 0.25**	0.70 ± 0.28	4
T27	9.32 ± 0.46	5.34 ± 0.60	0.82 ± 0.85	5

Data are the mean ± SEM of *n* individual data sets.
[a] The negative logarithm of the agonist concentration required to produce a half-maximal response.
[b] The maximal response to the ligand expressed as a percentage of the maximal $(Ca^{2+})_i$ mobilization as determined using 10 µM ionomycin.
[1] Couldn't fit a proper dose-response curve due to compounds interference with the assay.
Data were determined as statistically different (**, $p < 0.01$;) compared to no treatment using a one-way ANOVA and Dunnett's post-hoc test.

From the first batch of compounds, 4 significantly lowered the potency, of GIP(1-42) . This could be an effect of either an antagonist or an allosteric modulator with an effect on orthosteric efficacy instead affinity. Since the compounds were selected based on an *in silico* screen against Site 10 instead of the orthosteric pocket, a negative allosteric modulator is slightly more likely, but this will need to be proven later through mutagenesis as was performed for C25 and C58.

The second screen of compounds T13 to T27 were identified as more interesting compounds with respect to potential NAM activity. In particular, compounds T13 and T26 fully ablate GIP(1-42) induced $(Ca^{2+})_i$ mobilization similarly to what was seen in the original screen with compound C25, marking these two as very promising compounds. Compound T19 produced an unusual dose-response curve. This compound was observed to have a yellow-colouration and was fluorescent, which strongly interfered with the $(Ca^{2+})_i$ mobilization assay making it difficulty to measure effects of this compound on $(Ca^{2+})_i$ mobilization (Figure 3.27). Therefore, T19 was excluded from further calcium experiments.

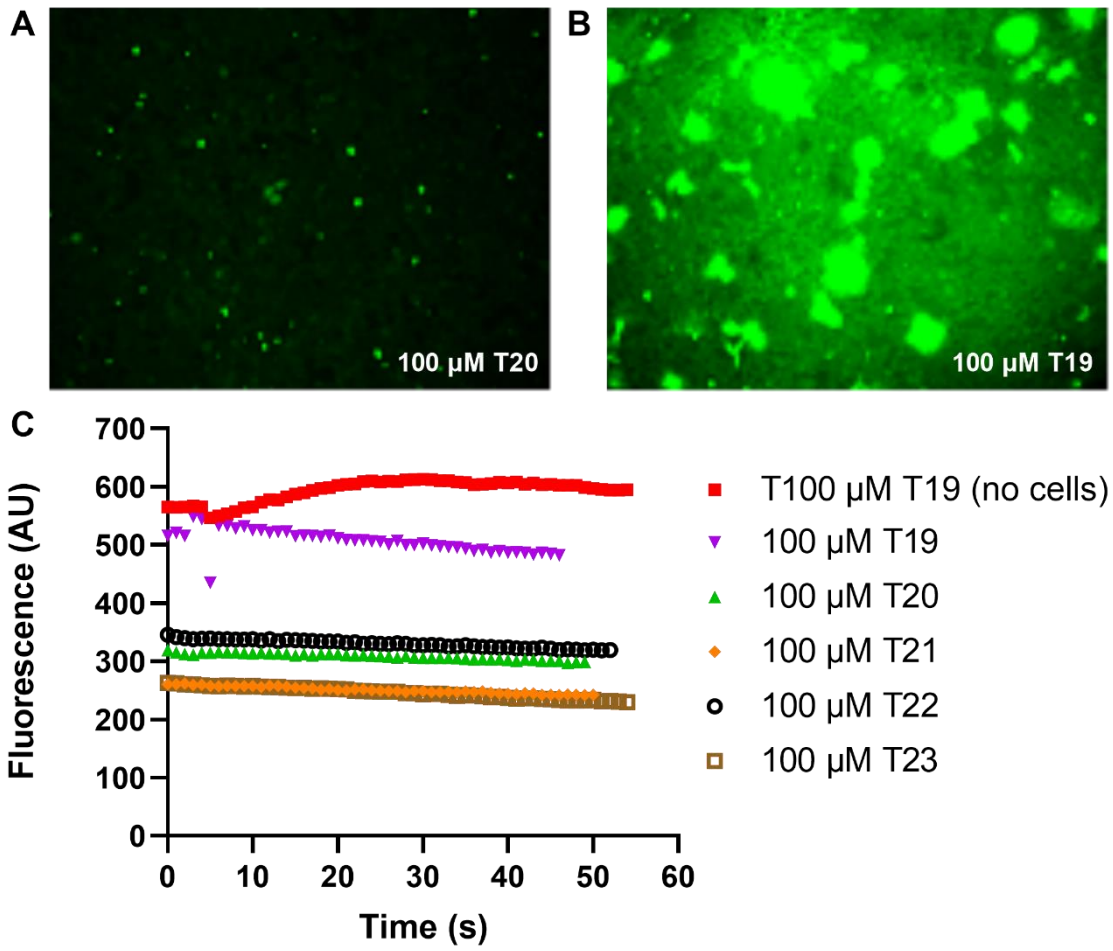

Figure 3.27. T19 fluorescence interferes with $(Ca^{2+})_i$ mobilization assay. A-B. Representative images of $(Ca^{2+})_i$ mobilization in HEK-293S cells stably expressing GIPR in response to 100 µM T20 or T19. C. $(Ca^{2+})_i$ mobilization in HEK-293S cells stably expressing GIPR or buffer with no cells in response to 100 µM compound.

The next step was then to measure the newly identified antagonist or NAMs at lower concentration to determine their true potency. HEK-293S cells stably expressing GIPR were stimulated with increasing doses of GIP(1-42) in the presence or absence of 10 µM, 31.6 µM or 50 µM compound and $(Ca^{2+})_i$ mobilization was measured (Figure 3.28 and Table 3.22 for compounds T2, T5, T10 and T11 and Figure 3.29 and Table 3.23 for compounds T13 and T26).

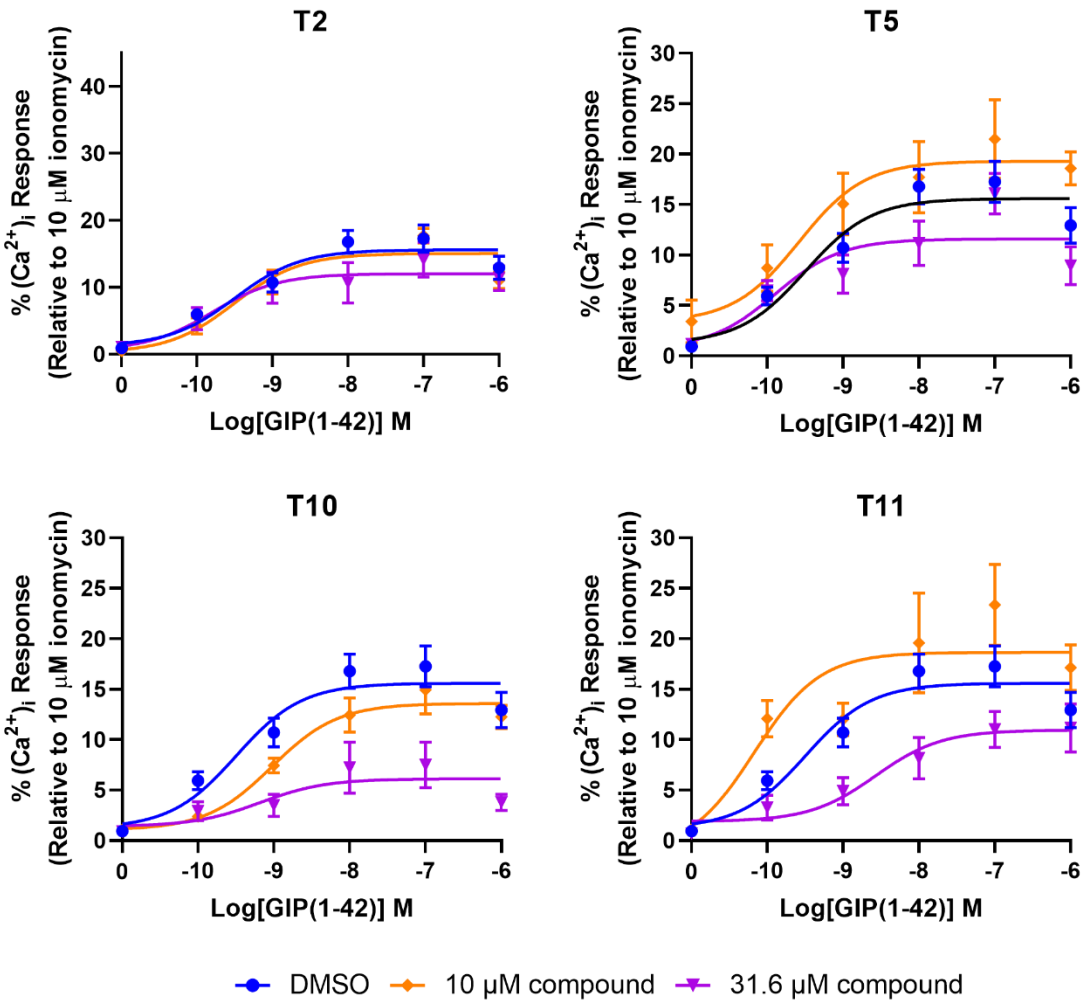

Figure 3.28. T10 and T11 inhibit GIP-induced $(Ca^{2+})_i$ mobilization at GIPR concentrations below 100 μM. $(Ca^{2+})_i$ mobilization in HEK-293S cells stably expressing GIPR in response to GIP(1-42) in the absence or presence of different concentrations of test compounds. Data is plotted as mean ± SEM of n≥3 individual experiments performed in duplicate and normalised to GIP(1-42), GLP-1(7-36)NH_2 or glucagon with DMSO.

Table 3.22. Potency (pEC_{50}), E_{max} and basal values for $(Ca^{2+})_i$ mobilization in HEK-293S cells stably expressing GIPR in response to GIP(1-42) concentrations in the absence or presence of different concentrations of C95.

Cmp	µM C95	pEC_{50}[a]	E_{max}[b]	Basal	n
DMSO	0	9.50 ± 0.25	15.60 ± 0.90	1.20 ± 1.62	9
T2	10	9.50 ± 0.23	15.05 ± 0.88	0.21 ± 1.52	3
	31.6	9.80 ± 0.44	12.02 ± 1.18	0.53 ± 2.63	5
T5	10	9.58 ± 0.43	19.30 ± 1.70	3.34 ± 3.11	3
	31.6	9.89 ± 0.41	11.59 ± 1.01	0.71 ± 2.41	5
T10	10	9.03 ± 0.22	13.60 ± 0.86	1.05 ± 1.14	5
	31.6	9.18 ± 0.72	6.12 ± 0.99*	1.40 ± 1.41	4
T11	10	10.17 ± 0.41	18.66 ± 1.65	-1.16 ± 4.98	3
	31.6	8.57 ± 0.40*	10.95 ± 1.17	1.88 ± 1.22	5

Data are mean ± SEM of *n* individual data sets.

[a] The negative logarithm of the agonist concentration required to produce a half-maximal response.

[b] The maximal response to the ligand expressed as a percentage of the $(Ca^{2+})_i$ mobilization elicited by 10 µM ionomycin.

Data were determined as statistically different (*, $p < 0.05$) compared to DMSO using a one-way ANOVA and Dunnett's post-hoc test.

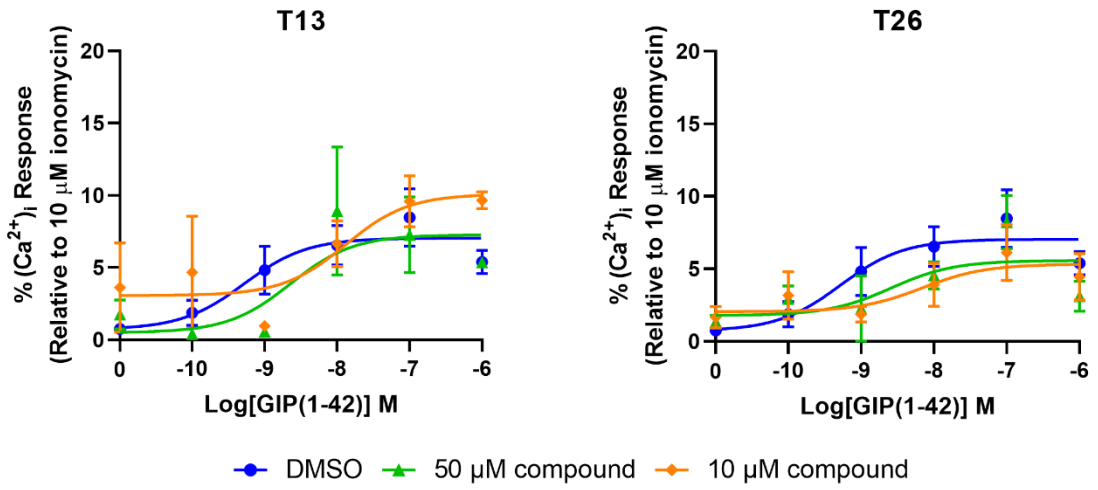

Figure 3.29. T13 and T26 do not significantly inhibit GIP-induced $(Ca^{2+})_i$ mobilization at GIPR at concentrations below 100 µM. $(Ca^{2+})_i$ mobilization in HEK-293S cells stably expressing GIPR in response to GIP(1-42) in the absence or presence of different concentrations of test compounds. Data is plotted as mean ± SEM of n≥3 individual experiments performed in duplicate except for T13, where n=1, and normalised to GIP(1-42), GLP-1(7-36)NH_2 or glucagon with DMSO.

Table 3.23. Potency (pEC_{50}), E_{max} and basal values for $(Ca^{2+})_i$ mobilization in HEK-293S cells stably expressing GIPR in response to GIP(1-42) concentrations in the absence or presence of different concentrations of T13 and T26.

Cmp	µM	pEC_{50}[a]	E_{max}[b]	Basal	n
DMSO	0	9.28 ± 0.45	7.05 ± 0.85	0.72 ± 1.19	5
T13	10	7.88 ± 0.64	10.09 ± 1.85	3.07 ± 1.35	1
	50	8.64 ± 0.73	7.28 ± 1.58	0.50 ± 1.72	1
T26	10	8.16 ± 0.89	5.53 ± 1.10	2.06 ± 1.00	3
	50	8.59 ± 0.97	5.58 ± 0.98	1.79 ± 1.19	3

Data are mean ± SEM of *n* individual data sets.
[a] The negative logarithm of the agonist concentration required to produce a half-maximal response.
[b] The maximal response to the ligand expressed as a percentage of the $(Ca^{2+})_i$ mobilization elicited by 10 µM ionomycin.
Data were determined as statistically different compared to DMSO using a one-way ANOVA and Dunnett's post-hoc test.

Out of the tested compounds, T2 and T5 had no significant effect at either 10 or 31.6 µM. On the other hand, T11 still lowered GIP(1-42) potency at 31.6 µM and at the same concentration, T10 significantly lowered Emax of GIP-induced $(Ca^{2+})_i$ mobilization. T13 and T26, which were tested next at 10 µM and 50 µM had no significant effect on either potency or maximal response of GIP. However, due to the global shortage of black 96-well plates further experiments with T13 were not possible.

Overall, the calcium screen of T compounds identified 6 new GIPR negative allosteric modulators (T2, T5, T10, T11, T13 and T26). At 100 µM most of these compounds (T2, T5, T10, T11) significantly lower GIP potency, while T13 lowered the GIP maximal response and T26 fully ablated it. This initially suggested that T26 would be the most potent compound, however further analysis showed that compounds T10 and T11 could significantly inhibit GIP-mediated $(Ca^{2+})_i$ mobilization at 31.6 µM, while T26 had no significant effect at either 10 or 50 µM. Another interesting point is that T10 significantly inhibited GIP potency at 100 µM, while also significantly lowering the maximal response at 31.6 µM. Due to the day-to-day variability of calcium mobilisation assay more testing would be desirable to confirm these results.

Despite the original NAMs C25 and C58 being only active in $(Ca^{2+})_i$ mobilization assay that does not necessarily mean that the new compounds would be also. Thus, all compounds were screened for their ability to modulate cAMP accumulation. To assess the ability of each compound to modulate GIP induced cAMP accumulation, HEK-293S cells stably expressing GIPR were treated with increasing doses of the partial agonist GIP(Pro3) in the presence or absence of 100 µM of each compound. Should any compounds display potential activity, they were then further screen using 10 µM, 31.6 µM, 50 µM

(Figure 3.30, Table 3.24). The partial agonist GIP(Pro3) was used here as it was originally used in the first screen (see Figure 3.6).

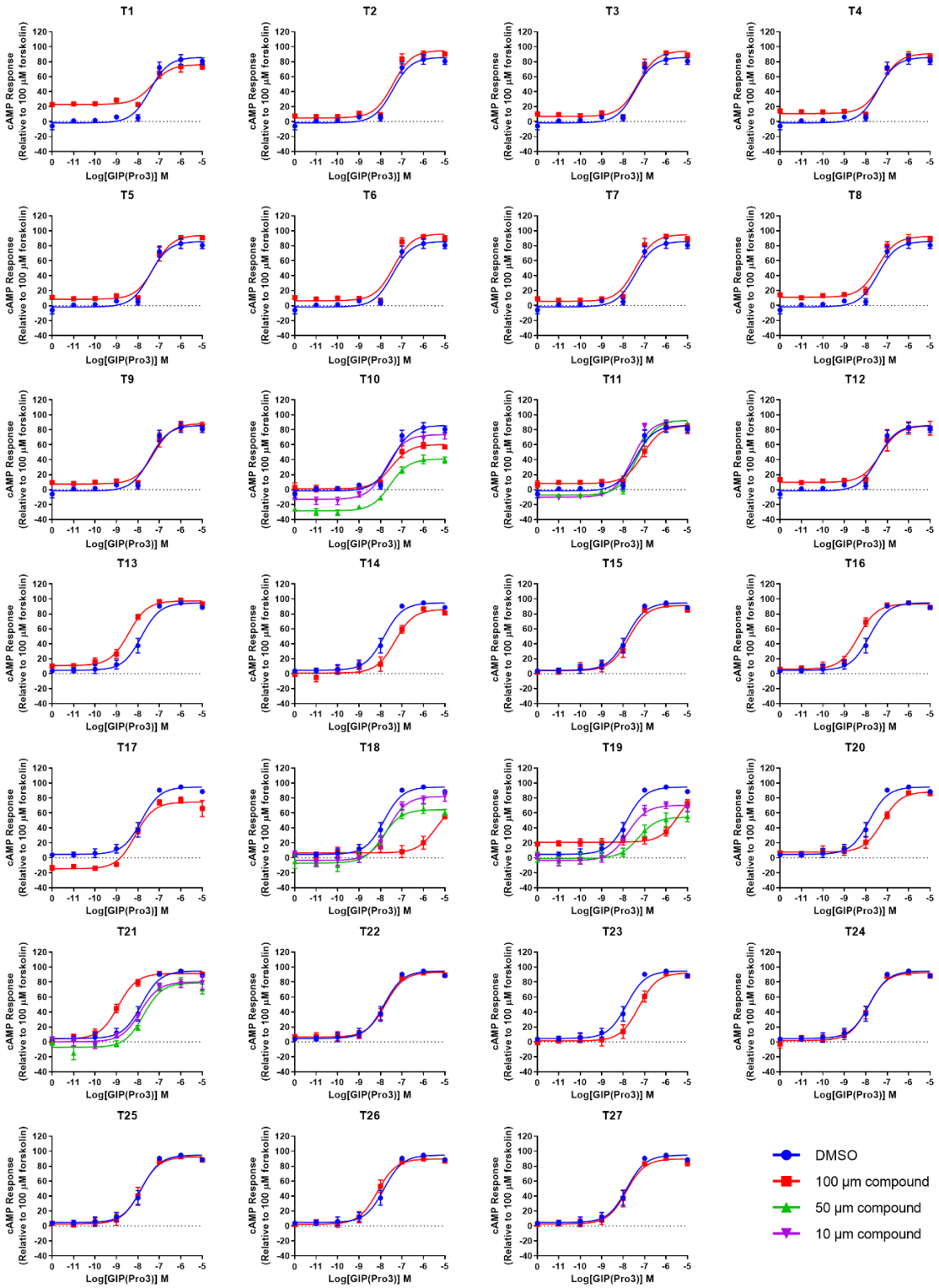

Figure 3.30. T10, T11, T18, T19 behave as NAMs, while T21 is a PAM at the GIPR. cAMP accumulation was measured in HEK-293S cells stably expressing GIPR in response to 8' stimulation with increasing doses of GIP(Pro3) in the absence or presence of different concentrations of tested compounds. Data is plotted as mean ± SEM of n≥3 individual experiments performed in duplicate and normalised to 100 µM forskolin response.

Table 3.24. Potency (pEC_{50}), maximal response (E_{max}) and basal response values for cAMP accumulation in HEK-293S cells stably expressing GIPR in response to 8' stimulation with increasing doses of GIP(Pro3) in the absence or presence of different concentrations of tested compounds T1-T27.

Cmp	µM	pEC_{50}[a]	E_{max}[b]	Basal	n
DMSO	-	7.44 ± 0.12	85.90 ± 3.85	1.68 ± 2.61	3
T1	100	7.32 ± 0.17	76.21 ± 3.29	22.94 ± 2.12****	3
T2	100	7.42 ± 0.11	95.04 ± 3.62	4.96 ± 2.44	3
T3	100	7.31 ± 0.10	94.34 ± 3.40	6.91 ± 2.19	3
T4	100	7.27 ± 0.12	91.03 ± 3.68	10.73 ± 2.33	3
T5	100	7.25 ± 0.10	94.20 ± 3.28	8.58 ± 2.05	3
T6	100	7.40 ± 0.11	95.97 ± 3.65	6.60 ± 2.44	3
T7	100	7.43 ± 0.11	95.03 ± 3.66	5.64 ± 2.47	3
T8	100	7.45 ± 0.11	92.59 ± 3.12	11.17 ± 2.13	3
T9	100	7.26 ± 0.12	88.65 ± 3.78	7.51 ± 2.38	3
T10	10	7.73 ± 0.13	73.65 ± 3.71	-12.98 ± 2.85	3
	50	7.55 ± 0.12	41.03 ± 2.76****	-28.35 ± 2.01****	3
	100	7.49 ± 0.15	60.42 ± 3.22*	1.02 ± 2.23	3
T11	10	7.57 ± 0.09	92.45 ± 3.12	-10.15 ± 2.25	3
	50	7.34 ± 0.08***	93.00 ± 3.08	-7.31 ± 2.04	3
	100	7.08 ± 0.13**	85.77 ± 4.03	8.20 ± 2.37	3
T12	100	7.31 ± 0.19	85.35 ± 5.34	9.74 ± 3.43	3
T13	100	8.43 ± 0.08	97.41 ± 1.91	10.96 ± 1.86	3
T14	100	7.33 ± 0.13	86.03 ± 4.23	0.99 ± 2.80	3
T15	100	7.74 ± 0.12	91.42 ± 3.44	4.13 ± 2.66	3
T16	100	8.34 ± 0.09	93.43 ± 2.35	6.13 ± 2.21	3
T17	100	8.12 ± 0.11	74.54 ± 3.11****	-14.70 ± 2.89*	3
T18	10	7.65 ± 0.14	82.17 ± 3.96	-3.41 ± 3.08	3
	50	7.89 ± 0.17	64.37 ± 4.06**	-7.02 ± 3.39	3
	100	5.41 ± 0.39****	73.42 ± 20.15****	6.68 ± 2.46	3
T19	10	7.78 ± 0.12	70.27 ± 3.10*	-3.49 ± 2.43	3
	50	7.29 ± 0.24****	54.70 ± 5.09****	-0.84 ± 3.31	3
	100	5.40 ± 0.32****	93.15 ± 18.11	20.90 ± 2.15*	3
T20	100	7.23 ± 0.11	88.31 ± 3.55	7.62 ± 2.21	3
T21	10	7.89 ± 0.12	80.16 ± 3.36	0.38 ± 2.80	3
	50	7.74 ± 0.13	79.06 ± 3.75	-7.22 ± 2.96	3
	100	8.92 ± 0.09*	91.48 ± 2.13	3.96 ± 2.47	3
T22	100	7.78 ± 0.10	93.15 ± 2.88	6.53 ± 2.26	3
T23	100	7.27 ± 0.12	92.42 ± 4.27	1.42 ± 2.70	3
T24	100	7.89 ± 0.10	92.73 ± 3.18	1.88 ± 2.59	3
T25	100	7.89 ± 0.11	92.48 ± 3.49	2.74 ± 2.91	3
T26	100	8.14 ± 0.10	89.71 ± 2.91	2.37 ± 2.56	3

T27	100	7.85 ± 0.12	89.75 ± 3.51	2.66 ± 2.82	3

Data are the mean ± SEM of *n* individual data sets.
[a] The negative logarithm of the agonist concentration required to produce a half-maximal response.
[b] The maximal response to the ligand expressed as a percentage of the maximal cAMP accumulation as determined using 100 µM forskolin.
Data were determined as statistically different (*, $p < 0.05$; **, $p < 0.01$; ***, $p < 0.001$; ****, $p < 0.0001$) compared to no treatment using a one-way ANOVA and Dunnett's post-hoc test.

These data suggest that T11 at 50 µM and 100 µM, T18 at 100 µM and T19 at 50 µM and 100 µM significantly lowered the pEC_{50} of GIP(Pro3), while it was increased with T21 at 100 µM. T10 at 50 µM and 100 µM, T17 at 100 µM, T18 at 50 µM and 100 µM and T19 at 10 µM and 50 µM significantly decreased maximal cAMP response.

Some of the compounds identified in the screen, namely compounds T10, T17 and T19, also influenced basal cAMP response, which suggests that they might potentially interfere with the cAMP assay. To check whether they interfere with the experiment, the cAMP accumulation assay was perform as described above, but lacking cells or GIP(Pro3) (Figure 3.31.A, Table 3.25). Indeed, T17 at 100 µM lowered the basal cAMP response, T19 at 1 µM, 10 µM and 100 µM significantly increased the response. T10 at 100 µM had no significant effect. As a second test for T19, which originally looked as a very promising compound, it was assayed against the A_3R, a class A G_i-coupled GPCR and not closely related to GIPR. The hypothesis was that if T19 is a GIPR NAM it should not have an effect on A_3R, but if it is a general interference with the assay due to the inner fluorescence of this compound, it would "work" on A_3R as well, which turned out to be the case (Figure 3.31 panels B&C, Table 3.26).

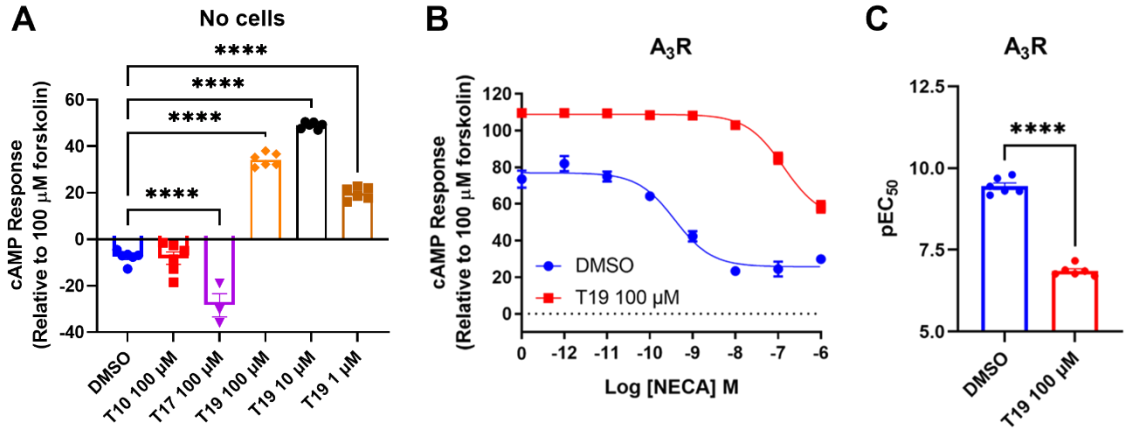

Figure 3.31. Fluorescent compound T19 interferes with cAMP assay. A. cAMP response (FRET signal) readout from samples including no cells in the presence or absence of different concentrations of test compounds. B. cAMP accumulation in Flp-In CHO cells stably expressing A3R in response to NECA in

the presence or absence of 100 µM T19. C. Plotted pEC50 values from B. Data is plotted as mean ± SEM of n≥3 individual experiments performed in duplicate and normalised to 100 µM forskolin. Data were determined as statistically different (***, p < 0.001; ****, p < 0.0001) compared to no treatment using a one-way ANOVA and Dunnett's post-hoc test.

Table 3.25. cAMP response (FRET signal) readout from samples including no cells in the presence or absence of different concentrations of test compounds.

Cmp	µM	cAMP response	n
DMSO	-	-7.55 ± 1.12	3
T10	100	-8.09 ± 2.67	3
T17	100	-28.37 ± 5.01****	3
T19	100	34.24 ± 1.16****	3
	10	49.04 ± 0.59****	3
	1	19.82 ± 1.11***	3

Data are the mean ± SEM of *n* individual data sets.
Data were determined as statistically different (***, p < 0.001; ****, p < 0.0001) compared to no treatment using a one-way ANOVA and Dunnett's post-hoc test.

Table 3.26. Potency (pEC_{50}), basal and E_{max} values for cAMP accumulation in Flp-In CHO cells stably expressing A3R in response to NECA in the presence or absence of 100 µM T19.

Cmp	pEC_{50}[a]	Basal	E_{max}[b]	n
DMSO	9.42 ± 0.13	76.90 ± 1.96	25.67 ± 2.02	3
T19	6.88 ± 0.08****	108.80 ± 0.77****	51.71 ± 2.78****	3

Data are the mean ± SEM of *n* individual data sets.
[a] The negative logarithm of the agonist concentration required to produce a half-maximal response.
[b] The maximal response to the ligand expressed as a percentage of the maximal cAMP accumulation as determined using 100 µM forskolin.
Data were determined as statistically different (***, p < 0.001; ****, p < 0.0001) compared to no treatment using a one-way ANOVA and Dunnett's post-hoc test.

Overall, these data suggests that compounds T17 and T19 interfere with the cAMP accumulation assay and the observed effects in cAMP screen were experimental artefacts. Therefore, these compounds were not continued in further cAMP experiments. However, T10 did not interfere with the assay and thus would be characterised further.

An additional point to consider is that in the cAMP screen, the potential allosteric compounds and the agonist were added simultaneously not allowing the time for the allosteric compound and the receptor to equilibrate. The reason for this is that it makes the assay set up much easier, takes less time to do and work preceding this thesis on C25- and C3-related compounds showed that it did not

make any significant difference (Dr Harris (University of Cambridge)). However, just to confirm this was also applicable to T10, a cAMP accumulation assay similar to above was performed with T10 with or without 30 minutes pre-incubation time and then addition of increasing doses of GIP(Pro3). No significant difference was observed, thereby validating the above screen (Figure 3.32, Table 3.27).

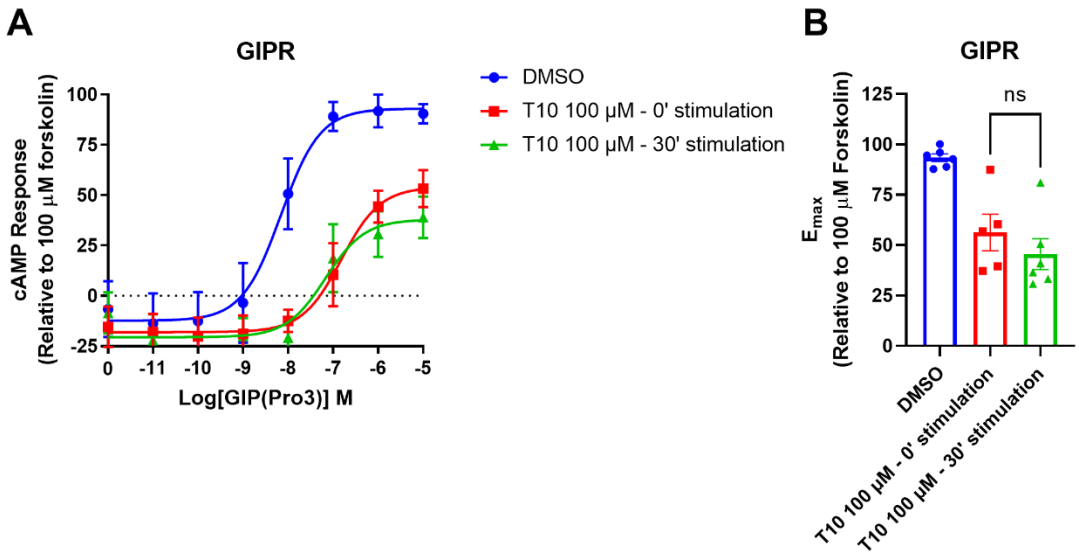

Figure 3.32. Stimulation time does not affect T10 NAM activity at the GIPR. cAMP accumulation in HEK-293S cells stably expressing GIPR in response to increasing doses of GIP(Pro3) following a 0' or 30' pre-stimulation of the cells with 100 µM T10. Data is plotted as mean ± SEM of n≥3 individual experiments performed in duplicate and normalised to 100 µM forskolin. Data were determined as statistically different compared 0' stimulation with 100 µM T10 using Student's t-test.

Table 3.27. Potency (pEC_{50}) and E_{max} values for cAMP accumulation in HEK-293S cells stably expressing GIPR in response to increasing doses of GIP(Pro3) following a 0' or 30' pre-stimulation of the cells with 100 µM T10.

Compound	pEC_{50}[a]	E_{max}[b]	n
DMSO	8.16 ± 0.10	93.00 ± 3.31	3
T10 (0' stimulation)	6.82 ± 0.27	54.10 ± 8.28	3
T10 (30' stimulation)	7.17 ± 0.40	37.93 ± 9.82	3

Data are the mean ± SEM of *n* individual data sets.
[a] The negative logarithm of the agonist concentration required to produce a half-maximal response.
[b] The maximal response to the ligand expressed as a percentage of the maximal cAMP accumulation as determined using 100 µM forskolin.
Data were determined as statistically different compared 0' stimulation with 100 µM T10 using Student's t-test.

Considering the $(Ca^{2+})_i$ and cAMP screen altogether, there are 7 new GIPR NAMs (T2, T5, T10, T11, T13, T18 and T26) and 1 new GIPR PAM T21. Compounds T10 and T11 are the most potent newly identified GIPR NAMs that significantly inhibit GIP-induced $(Ca^{2+})_i$ mobilization at 31.6 µM and cAMP response at 50 µM, which also makes them NAMs for both pathways. On the other hand, T18 also inhibited GIP-induced cAMP response at 50 µM, but has no significant effect in the $(Ca^{2+})_i$ mobilization assay.

3.8 Compounds T2 and T5 are newly discovered GIPR selective compounds

Analogous to the observations for the C3- and C25-based compounds, potency is not the only important characteristic of a compound, but its selectivity for a GIP receptor is also an important factor to consider. Therefore, T1-T27 compounds were tested for their effects on agonist induced $(Ca^{2+})_i$ mobilization and/or cAMP accumulation also at GLP-1R and GCGR.

T2, T5, T10, T11, T13 and T26 were previously identified as NAMs for $(Ca^{2+})_i$ mobilization at GIPR, which is why these compounds were further tested at the closely related GLP-1R and GCGR for their selectivity. Therefore, the HEK-293S cells stably expressing GLP-1R or HEK-293ΔCTR cells stably expressing GCGR were stimulated with increasing doses of GLP-1(7-36)NH_2 or glucagon, respectively, in the presence or absence of different concentrations of the tested compound (Figure 3.33, Table 3.28). From the dose response curves, it is visible that T13 at 100 µM ablates GLP-1-induced $(Ca^{2+})_i$ mobilization at GLP-1R, as addition of the compound resulted in little response. Furthermore, it could also be observed that T26 slightly lowered GLP-1 potency without affecting its maximal response, but this was not proven to be a statistically significant change, which might be because of the large error on the DMSO curve. Therefore, it would be ideal to add a few more repeats for DMSO/T26 and test T13 at GLP-1R at lower concentrations. At GCGR, T2, T5 and T11 had no significant effect, but the rest of the compounds were not tested due to issues with supply of black 96-well plates essential for the assays.

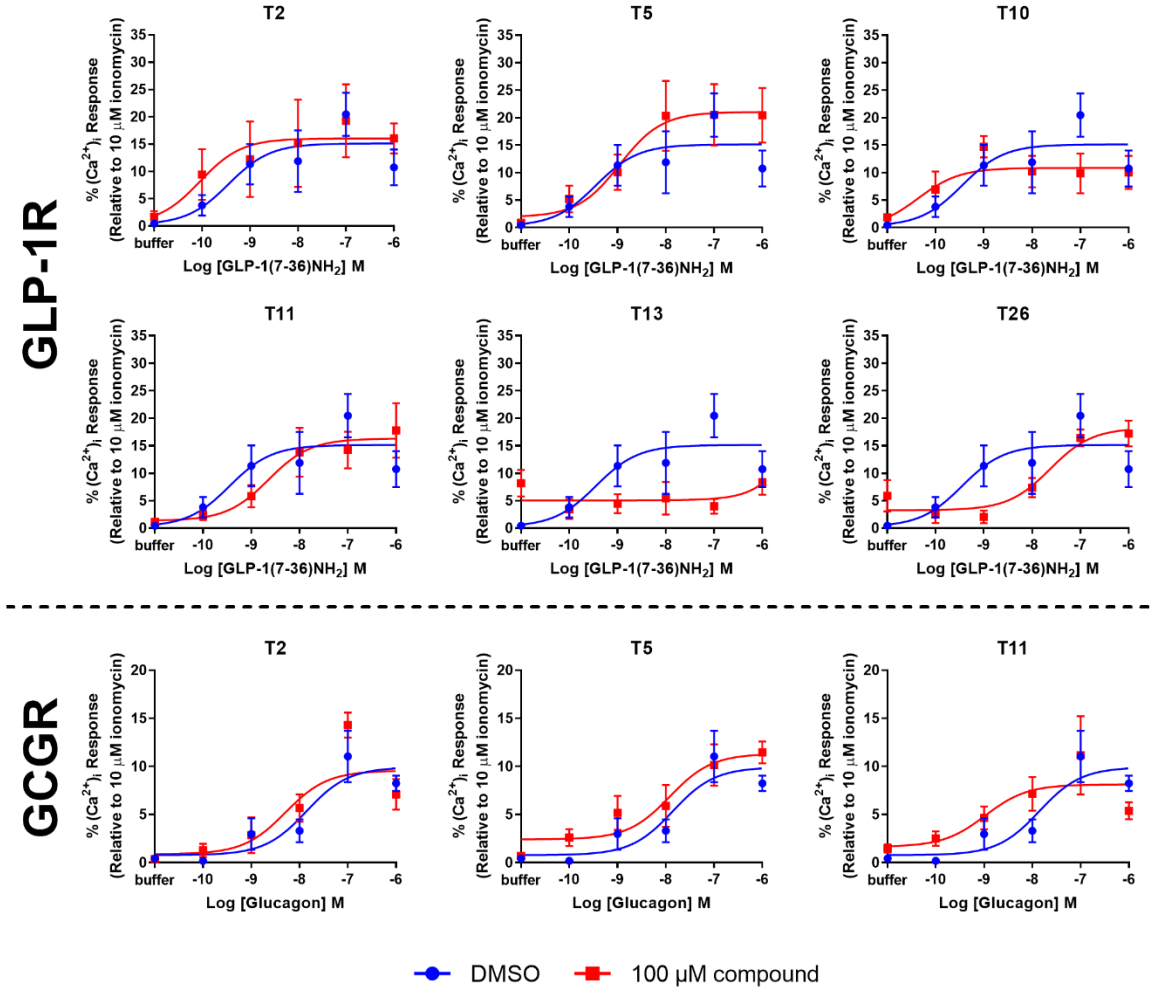

Figure 3.33. T13 inhibits GLP-1-induced $(Ca^{2+})_i$ mobilization at GLP-1R. $(Ca^{2+})_i$ mobilization in HEK-293S cells stably expressing GLP-1R or HEK-293ΔCTR cells stably expressing GCGR in response to increasing doses of GLP-1(7-36)NH_2 or glucagon in the absence or presence of different concentrations of test compounds. Data is plotted as mean ± SEM of n≥3 individual experiments performed in duplicate and normalised to 10 µM ionomycin.

Table 3.28. Potency (pEC_{50}) and E_{max} values for $(Ca^{2+})_i$ mobilization in HEK-293S cells stably GLP-1R or HEK-293ΔCTR cells stably expressing GCGR in response to GLP-1(7-36)NH_2 or glucagon in the absence or presence of different concentrations of tested compounds.

Cmp	µM	GLP-1R			GCGR		
		pEC_{50}[b]	E_{max}[c]	n	pEC_{50}[b]	E_{max}[c]	n
DMSO	-	9.45 ± 0.58	15.12 ± 2.28	3	7.86 ± 0.34	9.92 ± 1.29	3
T2	100	10.04 ± 0.81	16.04 ± 2.87	3	8.29 ± 0.39	9.56 ± 1.31	3
T5	100	8.95 ± 0.45	21.03 ± 2.74	3	7.92 ± 0.36	11.32 ± 1.32	3
T10	100	10.37 ± 0.78	10.86 ± 1.48	3	N/A[1]	N/A[1]	
T11	100	8.64 ± 0.45	16.30 ± 2.15	3	8.98 ± 0.83	8.13 ± 1.33	3
T13	100	N. D.	17.21 ± 2.34	3	N/A[1]	N/A[1]	
T26	100	7.63 ± 0.30	18.24 ± 1.93	3	N/A[1]	N/A[1]	

Data are the mean ± SEM of *n* individual data sets.
[a] The negative logarithm of the agonist concentration required to produce a half-maximal response.
[b] The maximal response to the ligand expressed as a percentage of the $(Ca^{2+})_i$ mobilization elicited by 10 µM ionomycin.
[1] These responses have not yet been measured, so no data is available on the date of the submission of this thesis.
Data were determined as statistically different compared to no treatment using a one-way ANOVA and Dunnett's post-hoc test.

To assess the ability of each compound to modulate GLP-1- or glucagon-induced cAMP accumulation, HEK-293S cells stably expressing GLP-1R or HEK-293ΔCTR cells stably expressing GCGR were treated with increasing doses of GLP-1(7-36)NH_2 or glucagon in the absence or presence of 10 µM, 50 µM or 100 µM of each compound (Figure 3.34, Table 3.29).

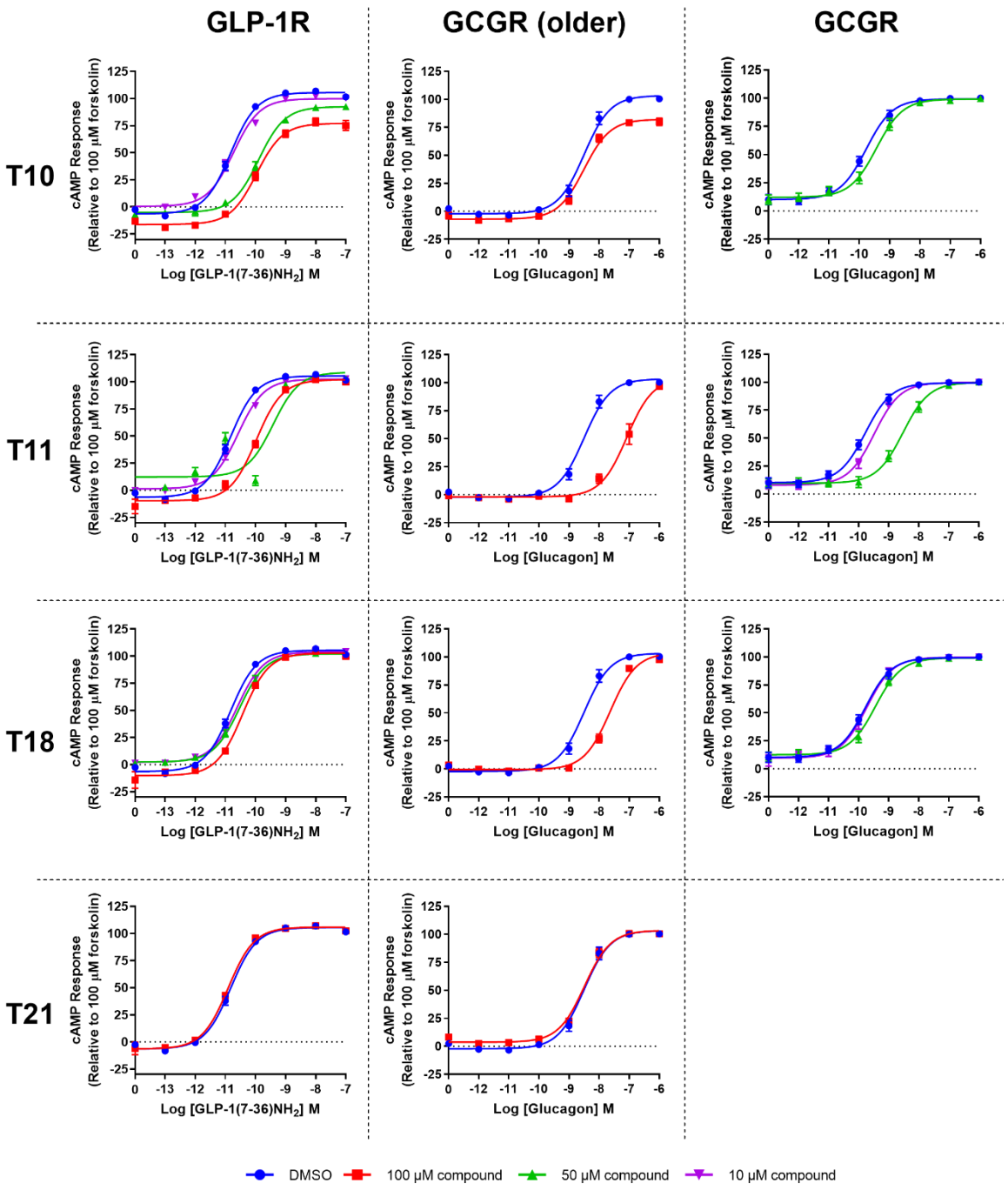

Figure 3.34. T10 is a GLP-1R NAM, while T11 and T18 are NAMs at both GLP-1R and GCGR. cAMP accumulation in HEK-293S cells stably expressing GLP-1R or HEK-293ΔCTR cells stably expressing GCGR in response to increasing doses GLP-1(7-36)NH_2 or glucagon in the absence or presence of different concentrations of test compounds. The 'GCGR (older)' data is measured with an older LANCE cAMP kit (discontinued), while the rest is measured with LANCE Ultra cAMP kit. Data is plotted as mean ± SEM of n≥3 individual experiments performed in duplicate and normalised to 100 µM forskolin.

Table 3.29. Potency (pEC_{50}) and E_{max} values for cAMP accumulation in HEK-293S cells stably expressing GLP-1R or HEK-293ΔCTR cells stably expressing GCGR in response to increasing doses of GLP-1(7-36)NH_2 or glucagon in the absence or presence of different concentrations of tested compounds.

Cmp	µM	GLP-1R			GCGR (older)[a]			GCGR		
		pEC_{50}[b]	E_{max}[c]	n	pEC_{50}[b]	E_{max}[c]	n	pEC_{50}[b]	E_{max}[c]	n
DMSO	-	10.82 ± 0.05	105.40 ± 1.48	3	8.50 ± 0.06	103.40 ± 2.25	3	9.78 ± 0.07	99.36 ± 1.72	3
T10	10	10.73 ± 0.06	99.76 ± 1.56	3	-	-	-	-	-	-
	50	9.89 ± 0.05****	92.39 ± 1.69****	3	-	-	-	9.44 ± 0.08	99.22 ± 2.10	3
	100	9.97 ± 0.06****	77.04 ± 1.90****	3	8.50 ± 0.07	82.15 ± 2.29****	3	-	-	-
T11	10	10.58 ± 0.04	102.50 ± 1.26	3	-	-	-	9.48 ± 0.07	99.80 ± 1.74	3
	50	9.42 ± 0.16****	108.80 ± 5.64	3	-	-	-	8.53 ± 0.09****	99.83 ± 2.69	3
	100	9.98 ± 0.06****	102.00 ± 2.30	3	7.08 ± 0.09****	104.30 ± 5.41	3	-	-	-
T18	10	10.60 ± 0.04	103.90 ± 1.27	3	-	-	-	9.74 ± 0.07	99.73 ± 1.78	3
	50	10.53 ± 0.05	102.10 ± 1.42	3	-	-	-	9.44 ± 0.08*	99.17 ± 1.91	3
	100	10.43 ± 0.06**	102.80 ± 1.90	3	7.63 ± 0.05***	103.80 ± 2.39	3	-	-	-
T21	100	10.91 ± 0.05	105.80 ± 1.45	3	8.49 ± 0.05	103.50 ± 1.83	3	-	-	-

Data are the mean ± SEM of *n* individual data sets.
[a] The 'GCGR (older)' data is measured with an older LANCE cAMP kit (discontinued), while the rest is measured with LANCE Ultra cAMP kit.
[b] The negative logarithm of the agonist concentration required to produce a half-maximal response.
[c] The maximal response to the ligand expressed as a percentage of the maximal cAMP accumulation as determined using 100 µM forskolin.
Data were determined as statistically different (*, $p < 0.05$; **, $p < 0.01$; ***, $p < 0.001$; ****, $p < 0.0001$) compared to no treatment using a one-way ANOVA and Dunnett's post-hoc test.

This set of experiment showed that T21 had no significant effect on either receptor, which suggests it is a PAM selective for GIPR over GLP-1R and GCGR. On the other hand, T10, T11 and T18 are non-selective and worked at all receptors. T11 is active at both GLP-1R and GCGR at 50 µM, making it equipotent for both these receptors. T10 is more potent at GLP-1R, while T18 is more potent at GCGR.

Moreover, there are some discrepancies when comparing the effects of NAMs at GLP-1R and GCGR compared to the original results obtained at GIPR. T10 only affected the maximal response at

GIPR, but at the GLP-1R and GCGR, T10 affected both potency and efficacy. T18, on the other hand, affected both potency and maximal response to the endogenous agonist at GIPR but only the potency at GLP-1R and GCGR. This was not the case for T11, which only significantly affected potency at all of them. This could be either because of the amino acid sequence difference between the binding site of these three receptors causing slightly different binding and engagement of the compounds or could be just because in some cases the effect is too low to come through as statistically significant.

Overall, looking at the results from both cAMP accumulation assay and $(Ca^{2+})_i$ mobilization assay, T2, T5 and T21 are selective allosteric modulators for GIPR over GLP-1R and GCGR, while T10, T13 and T18 are not. T11 significantly inhibited agonist-induced response at both GLP-1R and GCGR in cAMP accumulation assay, but had no significant effect in the $(Ca^{2+})_i$ mobilization assay, though more repeats to support this claim.

3.9 The T compounds were confirmed to bind to site 10

Having identified new GIPR NAMs and a PAM, the next step was to characterise their binding site. Since all the compounds were initially identified as potential GIPR allosteric modulators using an *in silico* screen against Site 10, which lies at the top of TMD2/3 and ECL1, the compounds were tested against all the previously characterised Site 10 mutants, which were L193$^{2.70}$A, R196A, P197A, Q204A, N210A, Q211$^{3.24}$A, Q220$^{3.33}$A and E288$^{45.52}$A, while L194$^{2.71}$A, G198A, Q286$^{45.50}$A and W287$^{45.51}$A were omitted due to low $(Ca^{2+})_i$ mobilization of these mutants. Moreover, since some compounds were active in both $(Ca^{2+})_i$ mobilization and cAMP accumulation assay, both of these assays were used to test the allosteric modulators against the GIPR mutants.

The compounds were first assayed against the site 10 mutants using the $(Ca^{2+})_i$ mobilization assay. To this end, HEK-293S transiently transfected with WT or mutant pcDNA3.2-GIPR were stimulated with increasing doses of GIP(1-42) in the presence or absence of 100 µM compound, starting first with compound T5 (Figure 3.35, Table 3.30). At WT, T5 significantly lowered both the potency and the maximal response. However, at mutants L193$^{2.70}$A, P197A, Q204A, N210A, Q211$^{3.24}$A and E288$^{45.52}$A it had no significant effect, which was also visible on the dose-response curves, where the two responses with and without T5 practically overlaid. This suggests that these amino acids are important for T5 binding and/or function. At mutant R196A T5 significantly lowered the pEC_{50}, while at Q220$^{3.33}$A it lowered the E_{max}.

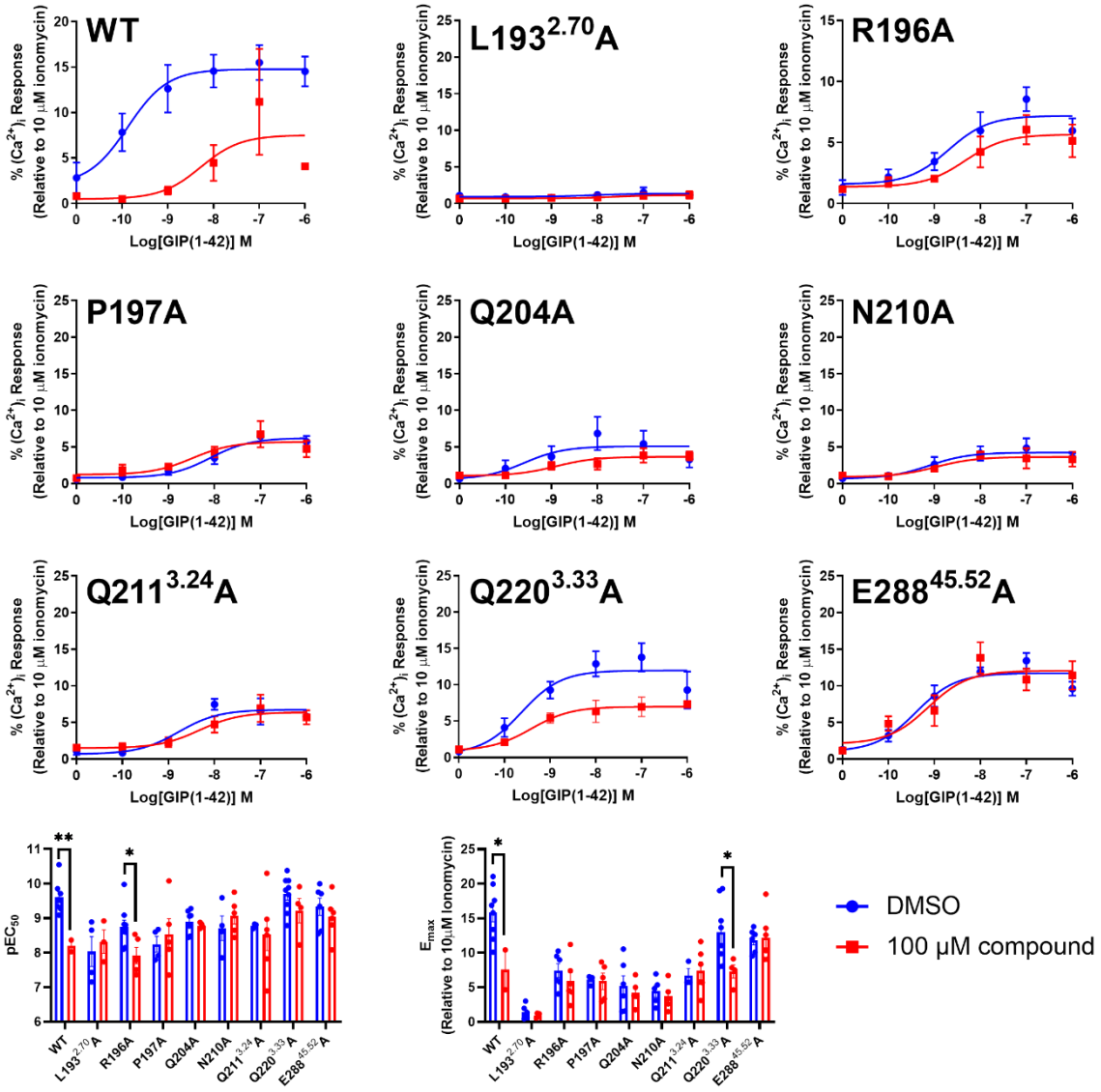

Figure 3.35. T5 has no or little effect at many Site 10 GIPR mutants. $(Ca^{2+})_i$ mobilization was measured in HEK-293S cells stably transiently transfected with WT or mutant pcDNA3.2-GIPR in response to increasing doses of GIP(1-42) in the presence or absence of 100 μM T5. The bottom plots then show pEC_{50} and E_{max} values plotted from the dose-response curves. Data is plotted as mean ± SEM of n≥3 individual experiments performed in duplicate except T5 at WT GIPR, where n=1, and normalised to 10 μM ionomycin response. Data were determined as statistically different (*, $p < 0.05$; **, $p < 0.01$) compared to treatment with GIP(1-42) and DMSO at each GIPR WT or mutant using Student's t-test.

Table 3.30. Potency (pEC_{50}) and E_{max} values for $(Ca^{2+})_i$ mobilization in HEK-293S cells transiently transfected with WT or mutant pcDNA3.2-GIPR in response to increasing doses of GIP(1-42) in the presence or absence of 100 µM T5.

GIPR mut	µM T5	pEC_{50}[a]	E_{max}[b]	n
WT	0	9.88 ± 0.36	14.77 ± 1.07	5
	100	8.28 ± 0.84**	7.52 ± 2.11*	1
L193$^{2.70}$A	0	N.D.	1.36 ± 0.31	3
	100	N.D.	1.17 ± 0.24	3
R196A	0	8.70 ± 0.38	7.20 ± 0.68	3
	100	8.33 ± 0.46*	5.66 ± 0.69	3
P197A	0	8.09 ± 0.22	6.23 ± 0.46	3
	100	8.48 ± 0.49	5.70 ± 0.72	3
Q204A	0	9.59 ± 0.81	5.09 ± 0.86	3
	100	8.90 ± 0.47	3.66 ± 0.39	3
N210A	0	9.12 ± 0.48	4.25 ± 0.52	3
	100	8.97 ± 0.55	3.63 ± 0.47	3
Q211$^{3.24}$A	0	8.78 ± 0.34	6.74 ± 0.65	3
	100	8.33 ± 0.42	6.38 ± 0.77	3
Q220$^{3.33}$A	0	9.63 ± 0.36	11.97 ± 0.97	5
	100	9.41 ± 0.34	6.99 ± 0.53*	3
E288$^{45.52}$A	0	9.41 ± 0.23	11.73 ± 0.63	3
	100	9.14 ± 0.36	12.06 ± 1.06	3

Data are mean ± SEM of *n* individual data sets.
[a] The negative logarithm of the agonist concentration required to produce a half-maximal response.
[b] The maximal response to the ligand expressed as a percentage of the $(Ca^{2+})_i$ mobilization elicited by 10 µM ionomycin.
Data were determined as statistically different (*, $p < 0.05$; **, $p < 0.01$) compared to treatment with GIP(1-42) and DMSO at each GIPR WT or mutant using Student's t-test.

Next compound T11 was then assay at the site 10 mutants using the same approach as described for T5 (Figure 3.36, Table 3.31). At WT, T11 significantly lowered the potency, without having any statistically significant or visible effect on the GIP maximal response. T11 also significantly lowered GIP potency at R196A, Q204A and E288$^{45.52}$A, while it had no significant effect at L193$^{2.70}$A, P197A, N210A, Q211$^{3.24}$A and Q220$^{3.33}$A.

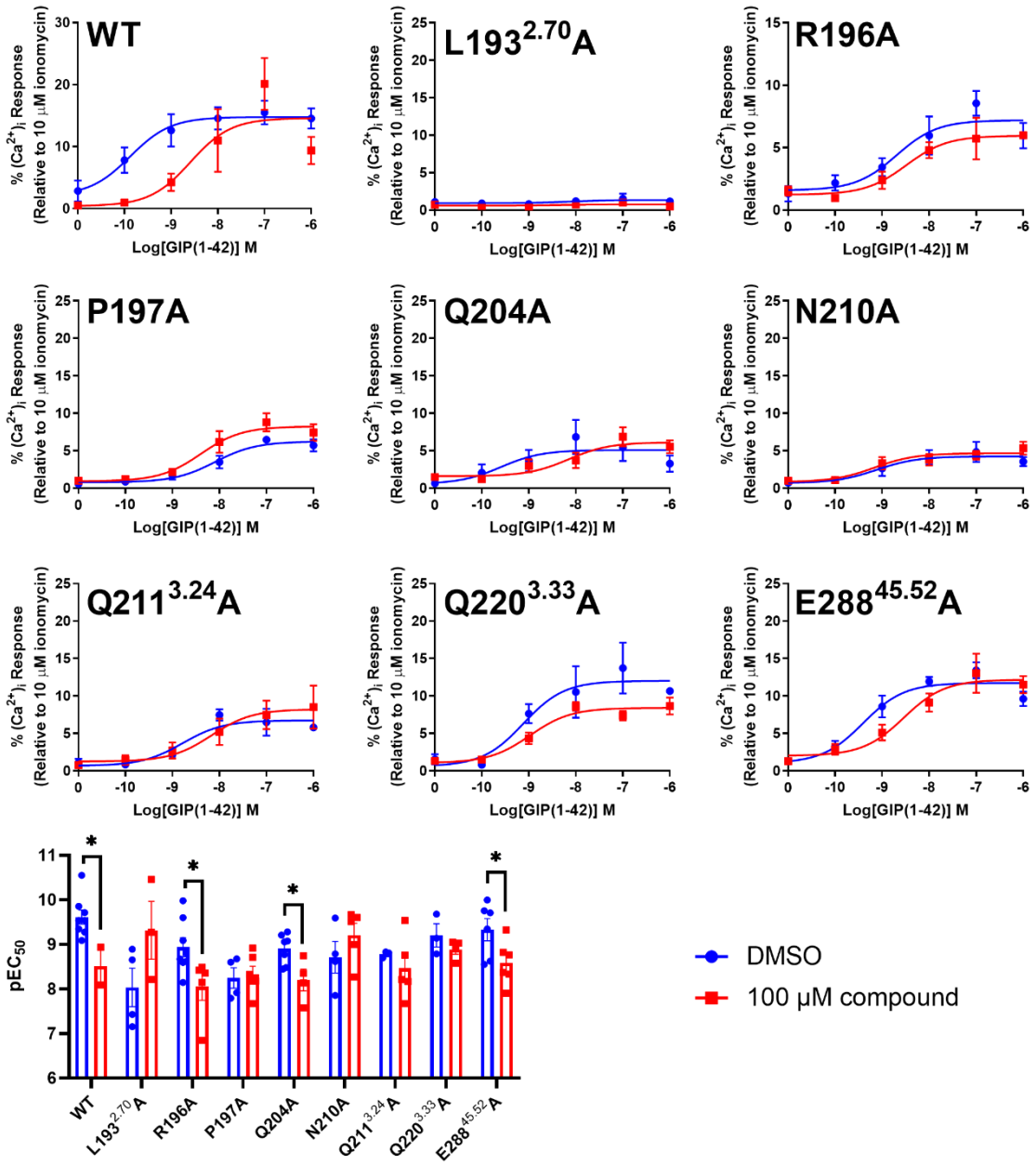

Figure 3.36. T11 has no or little effect at many GIPR mutants L193$^{2.70}$A, P197A, N210A, Q211$^{3.24}$A and Q220$^{3.33}$A. $(Ca^{2+})_i$ mobilization was measured in HEK-293S cells stably transiently transfected with WT or mutant pcDNA3.2-GIPR in response to increasing doses of GIP(1-42) in the presence or absence of 100 μM T11. The bottom plots then show pEC_{50} and E_{max} values plotted from the dose-response curves. Data is plotted as mean ± SEM of n≥3 individual experiments performed in duplicate except T11 at WT GIPR, where n=1, and normalised to 10 μM ionomycin response. Data were determined as statistically different (*, $p < 0.05$) compared to treatment with GIP(1-42) and DMSO at each GIPR WT or mutant using Student's t-test.

Table 3.31. Potency (pEC_{50}) and E_{max} values for $(Ca^{2+})_i$ mobilization in HEK-293S cells transiently transfected with WT or mutant pcDNA3.2-GIPR in response to increasing doses of GIP(1-42) in the presence or absence of 100 µM T11.

GIPR mut	µM T11	pEC_{50}[a]	E_{max}[b]	N
WT	0	9.88 ± 0.36	14.77 ± 1.07	5
	100	8.59 ± 0.55*	14.59 ± 2.52	1
L193$^{2.70}$A	0	N.D.	1.36 ± 0.31	3
	100	N.D.	0.76 ± 0.15	3
R196A	0	8.70 ± 0.38	7.20 ± 0.68	3
	100	8.49 ± 0.33*	5.96 ± 0.53	3
P197A	0	8.09 ± 0.22	6.23 ± 0.46	3
	100	8.40 ± 0.27	8.24 ± 0.64	3
Q204A	0	9.59 ± 0.81	5.09 ± 0.86	3
	100	8.15 ± 0.38*	6.12 ± 0.68	3
N210A	0	9.12 ± 0.48	4.25 ± 0.52	3
	100	9.16 ± 0.35	4.66 ± 0.39	3
Q211$^{3.24}$A	0	8.78 ± 0.34	6.74 ± 0.65	3
	100	8.17 ± 0.48	8.23 ± 1.26	3
Q220$^{3.33}$A	0	9.12 ± 0.37	12.01 ± 1.25	5
	100	8.98 ± 0.21	8.41 ± 0.46	3
E288$^{45.52}$A	0	9.41 ± 0.23	11.73 ± 0.63	3
	100	8.54 ± 0.30*	12.17 ± 0.97	3

Data are mean ± SEM of *n* individual data sets.
[a] The negative logarithm of the agonist concentration required to produce a half-maximal response.
[b] The maximal response to the ligand expressed as a percentage of the $(Ca^{2+})_i$ mobilization elicited by 10 µM ionomycin.
Data were determined as statistically different (*, $p < 0.05$) compared to treatment with GIP(1-42) and DMSO at each GIPR WT or mutant using Student's t-test.

Overall, the results from screening T5 and T11 against the Site 10 GIPR mutants are very encouraging. T5 and T11 were first identified through an *in silico* screen against site 10 looking for potential allosteric modulators. The observations that these compounds indeed behaved as NAMs and their function seemed to be effected by multiple Site 10 mutations validates Site 10 as a GIPR allosteric site. In the future, it would be good to also screen compounds T2, T10, T13 and T26 against these mutants.

Moving onto the allosteric modulators inhibiting the G_s-cAMP pathway, the compounds to test in the cAMP accumulation assay were NAMs T10, T11 and T18 and PAM T21. To measure cAMP response, HEK-293S transiently transfected with WT or Site 10 mutants pcDNA3.2-GIPR were stimulated with increasing doses of either GIP(Pro3) or GIP(1-42) in the presence or absence of 100 µM T10 (Figure 3.37, Table 3.32). Both agonists were used for compound T10 to see which one allowed a better assay window and observation of the effects.

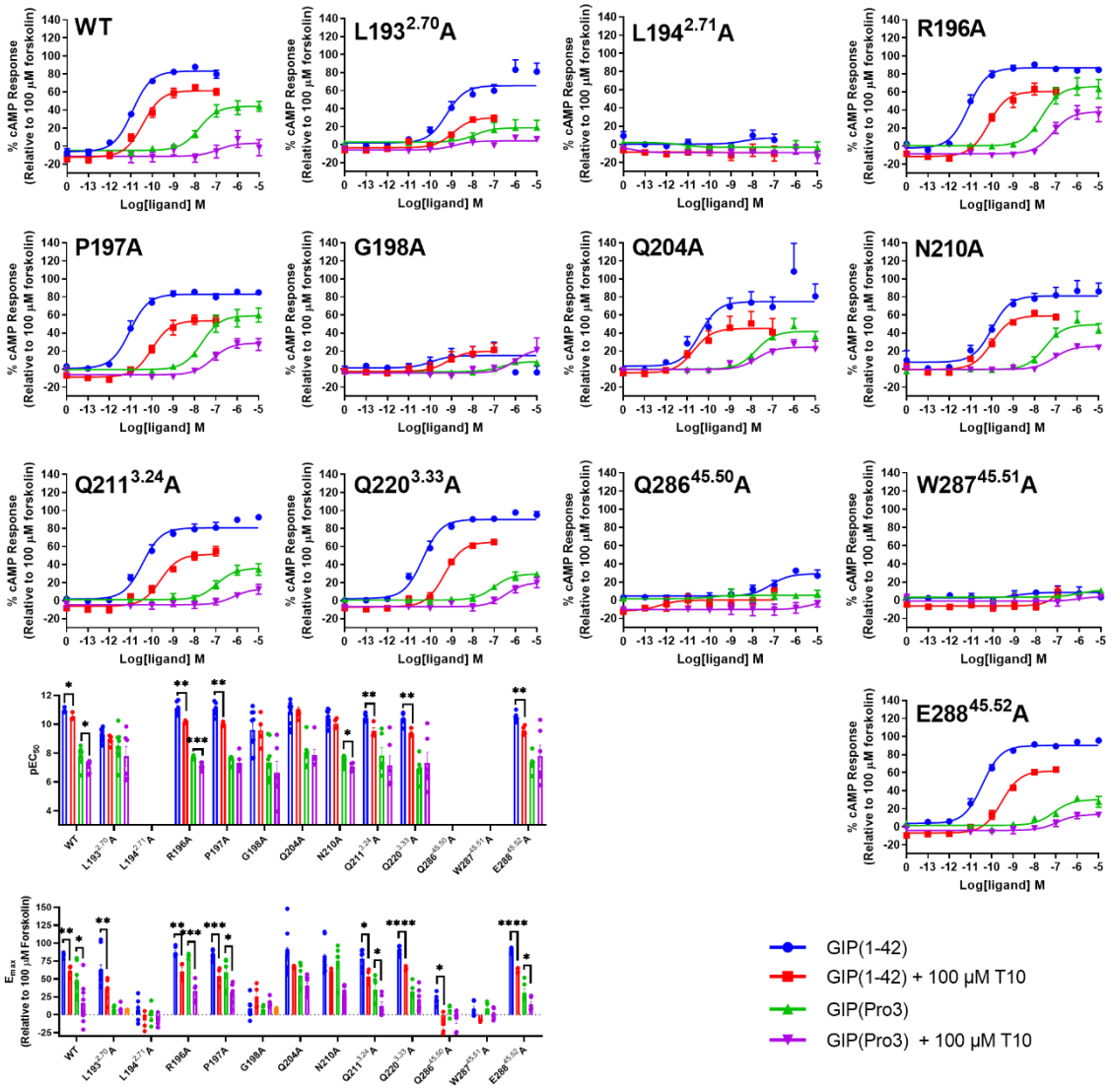

Figure 3.37. GIPR mutants G198A, Q204A and N210A reduce T10 activity as a NAM. cAMP accumulation was measured in HEK-293S transiently transfected with WT or mutant pcDNA3.2-GIPR in response to 8' stimulation with increasing doses of either GIP(Pro3) or GIP(1-42) in the presence or absence of 100 µM T10. The bottom plots then show pEC_{50} and E_{max} values plotted from the dose-response curves. Data is plotted as mean ± SEM of n≥3 individual experiments performed in duplicate and normalised to 100 µM forskolin response. Data were determined as statistically different (*, $p < 0.05$; **, $p < 0.01$; ***, $p < 0.001$; ****, $p < 0.0001$) compared to treatment with GIP(Pro3) or GIP(1-42) and DMSO at each GIPR WT or mutant using Student's t-test

Table 3.32. Potency (pEC_{50}) and E_{max} values for cAMP accumulation in HEK-293S transiently transfected with WT or mutant pcDNA3.2-GIPR in response to 8' stimulation with increasing doses of either GIP(Pro3) or GIP(1-42) in the presence or absence of 100 µM T10.

GIPR mut	µM T10	GIP(Pro3)			GIP(1-42)		
		pEC_{50}[a]	E_{max}[b]	n	pEC_{50}[a]	E_{max}[b]	n
WT	0	7.81 ± 0.18	44.17 ± 2.98	8	10.94 ± 0.07	83.13 ± 1.66	8
	100	6.93 ± 0.87*	3.45 ± 5.64*	5	10.44 ± 0.11*	61.51 ± 2.47**	3
L193$^{2.70}$A	0	7.90 ± 0.65	18.74 ± 3.48	5	9.23 ± 0.15	65.53 ± 3.31	5
	100	8.86 ± 0.42	4.20 ± 1.23	3	8.91 ± 0.15	30.13 ± 2.13**	3
L194$^{2.71}$A	0	ND	±	3	ND	±	3
	100	ND	±	3	ND	±	3
R196A	0	7.65 ± 0.18	66.01 ± 4.13	3	11.11 ± 0.08	86.72 ± 1.81	3
	100	7.15 ± 0.21***	38.06 ± 3.89***	3	10.15 ± 0.12**	60.52 ± 2.72**	3
P197A	0	7.66 ± 0.18	59.33 ± 3.77	3	11.04 ± 0.09	83.06 ± 1.92	3
	100	7.16 ± 0.20	28.93 ± 2.85*	3	10.00 ± 0.13**	53.67 ± 2.65***	3
G198A	0	6.68 ± 0.47	8.35 ± 2.37	5	9.94 ± 0.87	14.95 ± 3.78	5
	100	6.03 ± 0.44	22.87 ± 6.92	3	9.19 ± 0.50	19.92 ± 4.45	3
Q204A	0	7.77 ± 0.20	41.81 ± 3.00	7	10.41 ± 0.25	74.79 ± 4.79	6
	100	7.74 ± 0.33	24.25 ± 2.80	3	10.71 ± 0.37	44.97 ± 5.12	3
N210A	0	7.52 ± 0.23	49.24 ± 3.87	6	10.01 ± 0.17	81.19 ± 3.59	5
	100	7.09 ± 0.18*	25.41 ± 1.89	3	10.00 ± 0.10	59.16 ± 2.10	3
Q211$^{3.24}$A	0	6.96 ± 0.22	35.90 ± 3.21	3	10.44 ± 0.12	80.72 ± 2.42	3
	100	6.18 ± 0.47	13.30 ± 4.58*	3	9.60 ± 0.14**	51.44 ± 2.86*	3
Q220$^{3.33}$A	0	7.01 ± 0.18	29.60 ± 2.17	3	10.35 ± 0.09	89.98 ± 2.12	3
	100	6.47 ± 0.29	20.23 ± 3.63*	3	9.33 ± 0.09**	65.04 ± 2.32****	3
C286$^{45.50}$A	0	ND	5.45 ± 1.57	3	7.17 ± 0.35	29.00 ± 5.07	3
	100	ND	-1.03 ± 17.67	3	ND	0.10 ± 2.34**	3
W287$^{45.51}$A	0	ND	11.28 ± 3.16	3	ND	8.52 ± 2.51	3
	100	ND	4.22 ± 4.41	3	ND	ND	3
E288$^{45.52}$A	0	7.11 ± 0.23	30.07 ± 2.54	3	10.44 ± 0.06	90.08 ± 1.43	3
	100	6.96 ± 0.32	13.59 ± 2.40*	3	9.54 ± 0.08**	61.98 ±1.89****	3

Data are the mean ± SEM of *n* individual data sets.

[a] The negative logarithm of the agonist concentration required to produce a half-maximal response.

[b] The maximal response to the ligand expressed as a percentage of the maximal cAMP accumulation as determined using 100 µM forskolin.

Data were determined as statistically different (*, $p < 0.05$; **, $p < 0.01$; ***, $p < 0.001$; ****, $p < 0.0001$) compared to treatment with GIP(Pro3) or GIP(1-42) and DMSO at each GIPR WT or mutant using Student's t-test.

Analysis of the dose-response data for both GIP(Pro3) and GIP(1-42), T10 significantly lowered both pEC_{50} and E_{max} of both GIP(Pro3)- and GIP(1-42)-induced cAMP response at WT GIPR. Since both ligands showed similar response, the full agonist GIP(1-42) and not the partial agonist GIP(Pro3) was chosen as the agonist of choice for testing the other compounds against Site 10 mutants. Moreover,

mutants L194$^{2.71}$A, C286$^{45.50}$ and W287$^{45.51}$A failed to provide any measurable cAMP response in line with the original characterisation of the mutants, and thus these mutants were omitted from further experiments with the other compounds.

T10 significantly lowered pEC_{50} and E_{max} of GIP(1-42)-induced cAMP response also at GIPR mutants R196A, P197A, Q211$^{3.24}$A, Q220$^{3.33}$A and E288$^{45.52}$A. At L193$^{2.70}$A only the E_{max} was significantly lowered. Of the remaining 3 mutants, G198A displayed a small response to GIP(1-42), which was not further inhibited by T10. For mutants Q204A and N210A, there was little significant effect of T10, however for these mutants there is a larger error margin which means complete interpretation of the data for these mutants is not possible.

Compound T11 was assayed next using only GIP(1-42) using the same Site 10 mutants as described above (Figure 3.38, Table 3.33). T11 significantly reduced the potency of GIP-induced cAMP response at WT GIPR as well as at mutants L193$^{2.70}$A, Q220$^{3.33}$A and E288$^{45.52}$A. Mutants P197A, N210A and Q211$^{3.24}$A did not show a significant reduction in potency upon addition of T11, although small reductions were observed even though they did not reach significance. At G198A the response to GIP(1-42) was weak that conclusions could not be inferred from the data. However, mutants R196A and Q204A significantly reduced T11 efficacy, suggesting that these two residues are important for T11 ability to modulate GIP-induced cAMP response.

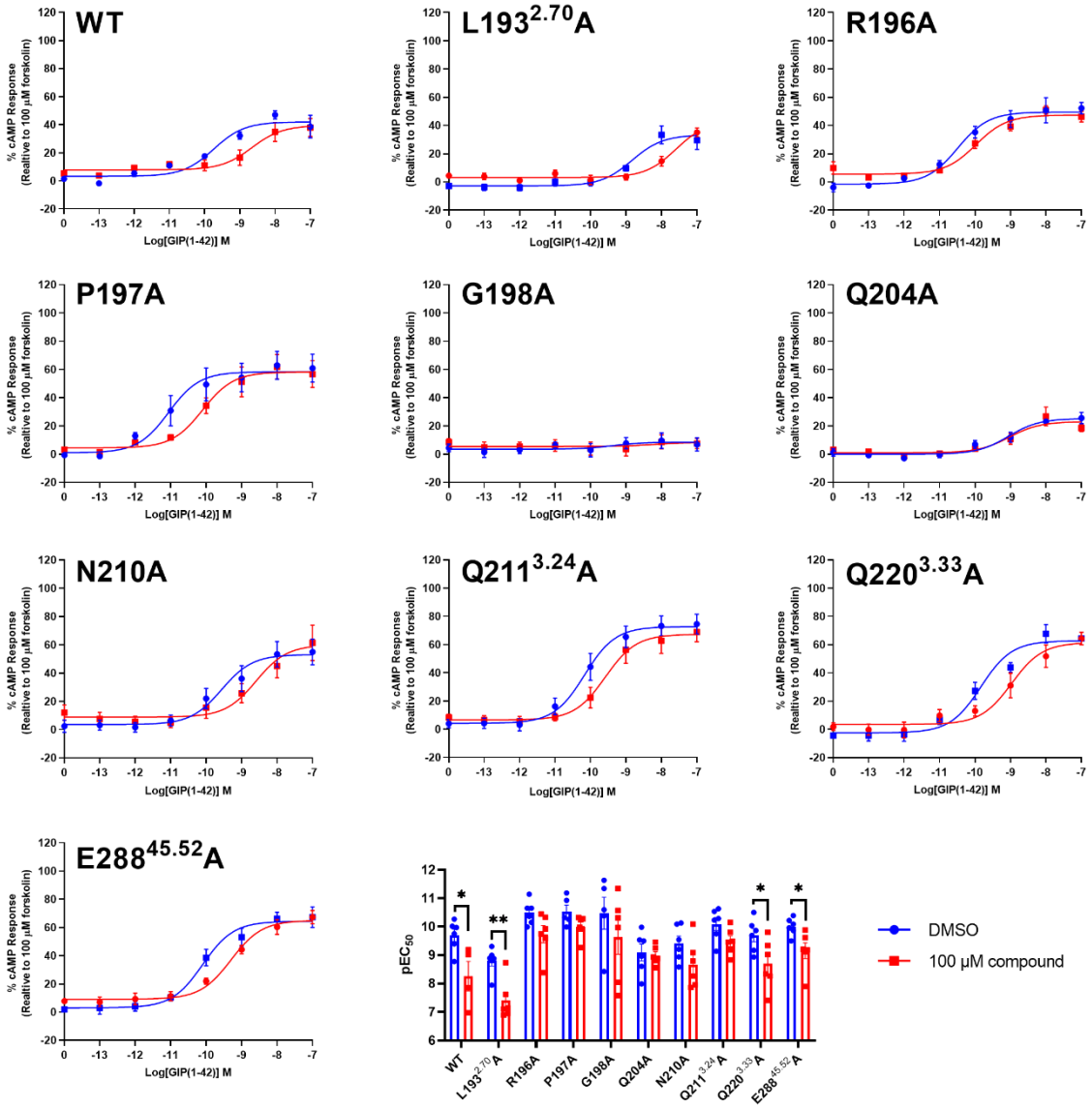

Figure 3.38. GIPR mutants R196A and Q204A reduced T11 efficacy at GIPR. cAMP accumulation was measured in HEK-293S cells stably transiently transfected with WT or mutant pcDNA3.2-GIPR in response to 8' stimulation with increasing doses of GIP(1-42) in the presence or absence of 100 µM T11. The bottom plots then show pEC_{50} values plotted from the dose-response curves. Data is plotted as mean ± SEM of n≥3 individual experiments performed in duplicate and normalised to 100 µM forskolin response. Data were determined as statistically different (*, $p < 0.05$; **, $p < 0.01$; ***, $p < 0.001$; ****, $p < 0.0001$) compared to treatment with GIP(1-42) and DMSO at each GIPR WT or mutant using Student's t-test.

Table 3.33. Potency (pEC_{50}) and E_{max} values for cAMP accumulation in HEK-293S cells transiently transfected with WT or mutant pcDNA3.2-GIPR in response to 8' stimulation with increasing doses of GIP(1-42) in the presence or absence of 100 µM T11.

GIPR mut	µM T11	pEC_{50}[a]	E_{max}[b]	n
WT	0	9.74 ± 0.17	42.02 ± 2.35	3
	100	8.66 ± 0.28*	39.52 ± 4.04	3
L193$^{2.70}$A	0	8.83 ± 0.21	33.39 ± 3.29	3
	100	7.59 ± 0.21**	43.32 ± 5.73	3
R196A	0	10.49 ± 0.18	49.54 ± 2.67	3
	100	9.97 ± 0.14	47.34 ± 1.96	3
P197A	0	11.06 ± 0.27	58.30 ± 4.32	3
	100	10.10 ± 0.22	58.17 ± 3.84	3
G198A	0	9.39 ± 1.58	8.46 ± 2.86	3
	100	8.23 ± 3.28	8.23 ± 4.77	3
Q204A	0	9.06 ± 0.20	25.28 ± 2.11	3
	100	9.04 ± 0.28	23.05 ± 2.57	3
N210A	0	9.56 ± 0.27	53.07 ± 4.64	3
	100	8.59 ± 0.31	59.89 ± 6.90	3
Q211$^{3.24}$A	0	10.17 ± 0.17	72.77 ± 3.79	3
	100	9.58 ± 0.20	67.30 ± 4.20	3
Q220$^{3.33}$A	0	9.84 ± 0.14	62.72 ± 3.01	3
	100	8.97 ± 0.19*	61.49 ± 4.61	3
E288$^{45.52}$A	0	10.10 ± 0.15	64.36 ± 3.04	3
	100	9.30 ± 0.13*	65.00 ± 2.74	3

Data are the mean ± SEM of *n* individual data sets.
[a] The negative logarithm of the agonist concentration required to produce a half-maximal response.
[b] The maximal response to the ligand expressed as a percentage of the maximal cAMP accumulation as determined using 100 µM forskolin.
Data were determined as statistically different (*, $p < 0.05$; **, $p < 0.01$) compared to treatment with GIP(1-42) and DMSO at each GIPR WT or mutant using Student's t-test.

The last of the NAMs to be test against Site 10 mutants was T18 (Figure 3.39 and Table 3.34). T18 significantly reduced potency and maximal response of GIP(1-42)-induce cAMP response at WT GIPR as well as N210A and Q220$^{3.33}$A. The potency was also significantly reduced at R196A, P197A and Q211$^{3.24}$A, while maximal response was significantly reduced at L193$^{2.70}$A. For G198A the response was again too small to see any effects. At mutants Q204A and E288$^{45.52}$A there was no significant effect of T18 on either potency or maximal response, suggesting that these two residues effect T18 ability to modulate GIP-induced cAMP response.

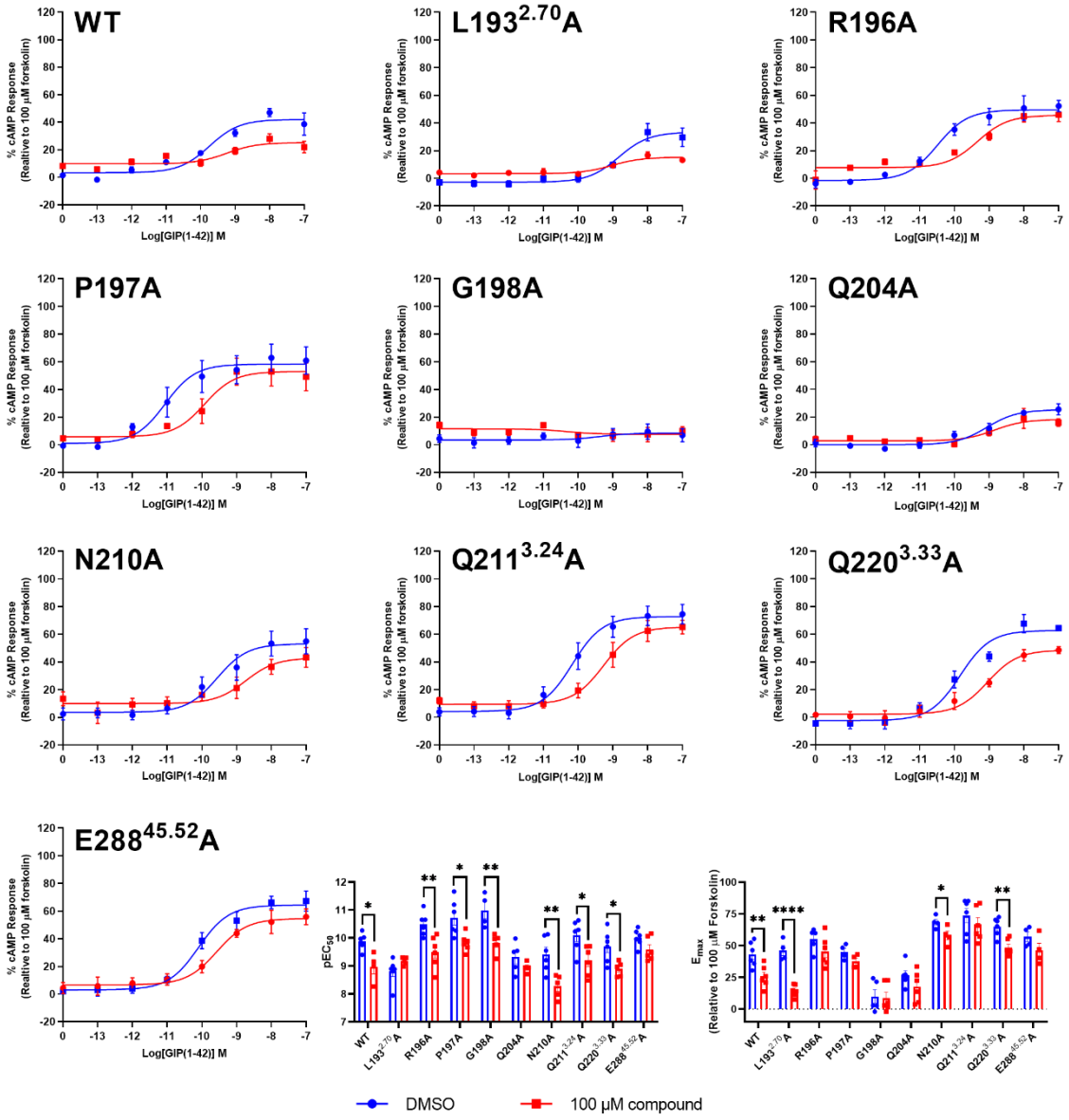

Figure 3.39. T18 has no or little effect at GIPR mutants Q204A and E288$^{45.52}$A. cAMP accumulation was measured in HEK-293S cells transiently transfected with WT or mutant pcDNA3.2-GIPR in response to 8' stimulation with increasing doses of GIP(1-42) in the presence or absence of 100 µM T18. The bottom plots then show pEC_{50} and E_{max} values plotted from the dose-response curves. Data is plotted as mean ± SEM of n≥3 individual experiments performed in duplicate and normalised to 100 µM forskolin response. Data were determined as statistically different (*, $p < 0.05$; **, $p < 0.01$; ****, $p < 0.0001$) compared to treatment with GIP(1-42) and DMSO at each GIPR WT or mutant using Student's t-test

Table 3.34. Potency (pEC_{50}) and E_{max} values for cAMP accumulation in HEK-293S cells transiently transfected with WT or mutant pcDNA3.2-GIPR in response to 8' stimulation with increasing doses of GIP(1-42) in the presence or absence of 100 µM T18.

GIPR mut	µM T18	pEC_{50}[a]	E_{max}[b]	n
WT	0	9.74 ± 0.17	42.02 ± 2.35	3
	100	9.24 ± 0.36*	25.18 ± 2.16**	3
L193A	0	8.83 ± 0.21	33.39 ± 3.29	3
	100	9.03 ± 0.26	15.25 ± 1.28****	3
R196A	0	10.49 ± 0.18	49.54 ± 2.67	3
	100	9.34 ± 0.21**	45.58 ± 2.91	3
P197A	0	11.06 ± 0.27	58.30 ± 4.32	3
	100	9.92 ± 0.28*	53.00 ± 4.44	3
G198A	0	9.39 ± 1.58	8.46 ± 2.86	3
	100	10.35 ± 1.57**	7.68 ± 1.82	3
Q204A	0	9.06 ± 0.20	25.28 ± 2.11	3
	100	8.85 ± 0.41	18.29 ± 2.73	3
N210A	0	9.56 ± 0.27	53.07 ± 4.64	3
	100	8.74 ± 0.37**	42.88 ± 5.33*	3
$Q211^{3.24}A$	0	10.17 ± 0.17	72.77 ± 3.79	3
	100	9.27 ± 0.19*	65.27 ± 3.97	3
$Q220^{3.33}A$	0	9.84 ± 0.14	62.72 ± 3.01	3
	100	9.05 ± 0.17*	48.59 ± 3.27**	3
$E288^{45.52}A$	0	10.10 ± 0.15	64.36 ± 3.04	3
	100	9.57 ± 0.22	54.59 ± 3.60	3

Data are the mean ± SEM of *n* individual data sets.
[a] The negative logarithm of the agonist concentration required to produce a half-maximal response.
[b] The maximal response to the ligand expressed as a percentage of the maximal cAMP accumulation as determined using 100 µM forskolin.
Data were determined as statistically different (*, $p < 0.05$; **, $p < 0.01$; ****, $p < 0.0001$) compared to treatment with GIP(1-42) and DMSO at each GIPR WT or mutant using Student's t-test.

From the original screen, T21 was considered to be a PAM at the GIPR. However, when re-tested at the Site 10 mutants there was no significant effect on either potency or maximal response at WT GIPR or the mutants (Figure 3.40, Table 3.35). Indeed, the only mutant that showed a visible increase in potency was R196A. The failure of T21 to reproduce its NAM activity in these assays will be discussed in the at the end of this chapter.

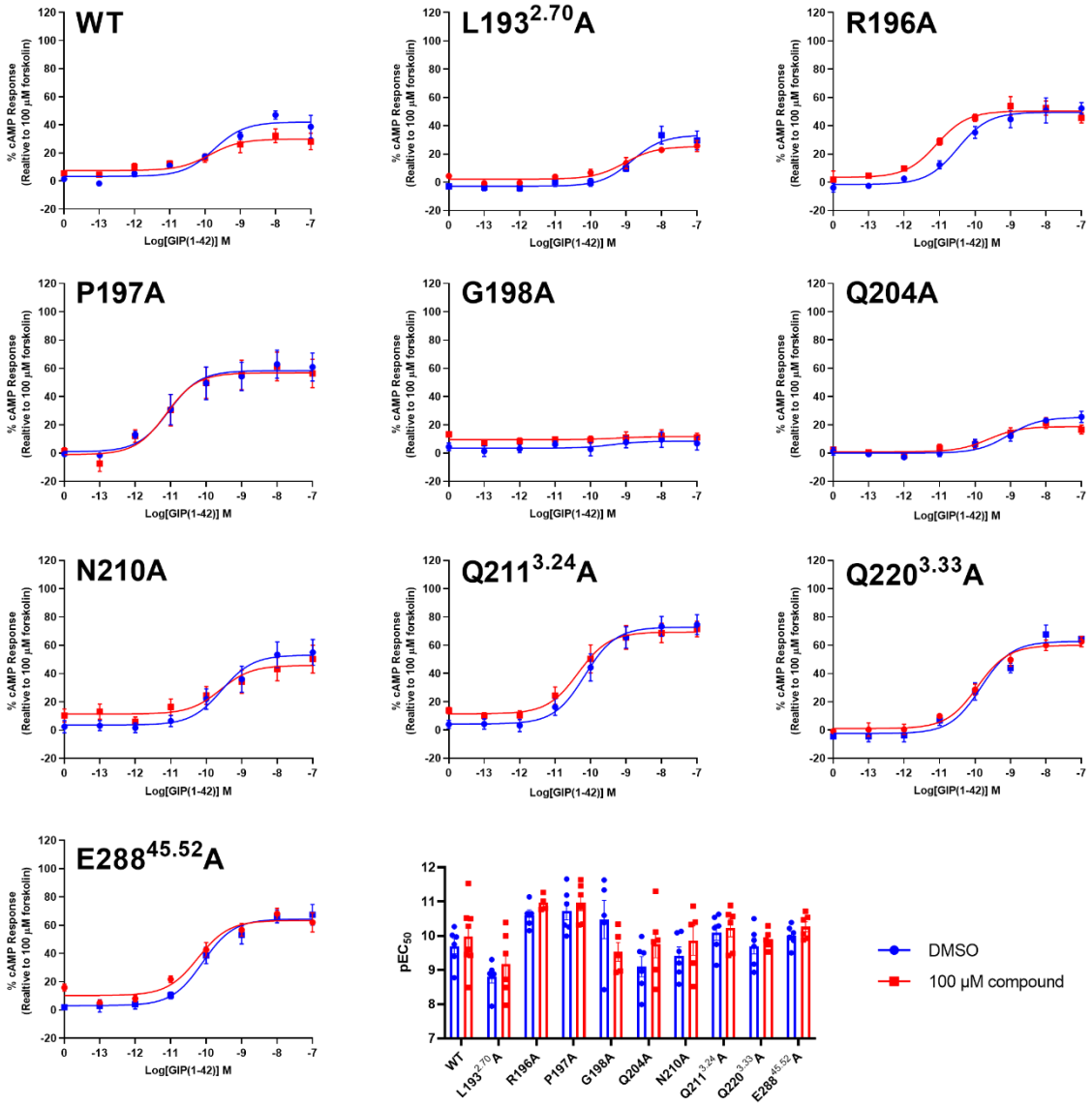

Figure 3.40. T21 has no or little effect in transiently transfected cells. cAMP accumulation was measured in HEK-293S cells transiently transfected with WT or mutant pcDNA3.2-GIPR in response to 8' stimulation with increasing doses of GIP(1-42) in the presence or absence of 100 µM T21. The bottom plots then show pEC_{50} values plotted from the dose-response curves. Data is plotted as mean ± SEM of n≥3 individual experiments performed in duplicate and normalised to 100 µM forskolin response. Data were determined as statistically different compared to treatment with GIP(1-42) and DMSO at each GIPR WT or mutant using Student's t-test

Table 3.35. Potency (pEC_{50}) and E_{max} values for cAMP accumulation in HEK-293S cells transiently transfected with WT or mutant pcDNA3.2-GIPR in response to 8' stimulation with increasing doses of GIP(1-42) in the presence or absence of 100 µM T21.

GIPR mut	µM T21	pEC_{50}[a]	E_{max}[b]	n
WT	0	9.74 ± 0.17	42.02 ± 2.35	3
	100	9.86 ± 0.33	29.84 ± 2.49	5
L193$^{2.70}$A	0	8.83 ± 0.21	33.39 ± 3.29	3
	100	9.04 ± 0.21	25.30 ± 1.97	3
R196A	0	10.49 ± 0.18	49.54 ± 2.67	3
	100	11.08 ± 0.16	50.40 ± 2.17	3
P197A	0	11.06 ± 0.27	58.30 ± 4.32	3
	100	11.13 ± 0.29	56.78 ± 4.55	3
G198A	0	9.39 ± 1.58	8.46 ± 2.86	3
	100	9.22 ± 2.57	11.74 ± 2.19	3
Q204A	0	9.06 ± 0.20	25.28 ± 2.11	3
	100	9.62 ± 0.32	18.75 ± 1.94	3
N210A	0	9.56 ± 0.27	53.07 ± 4.64	3
	100	9.60 ± 0.39	45.77 ± 4.64	3
Q211$^{3.24}$A	0	10.17 ± 0.17	72.77 ± 3.79	3
	100	10.35 ± 0.20	69.30 ± 3.56	3
Q220$^{3.33}$A	0	9.84 ± 0.14	62.72 ± 3.01	3
	100	9.94 ± 0.12	59.98 ± 2.30	3
E288$^{45.52}$A	0	10.10 ± 0.15	64.36 ± 3.04	3
	100	10.23 ± 0.15	63.34 ± 2.56	3

Data are the mean ± SEM of *n* individual data sets.
[a] The negative logarithm of the agonist concentration required to produce a half-maximal response.
[b] The maximal response to the ligand expressed as a percentage of the maximal cAMP accumulation as determined using 100 µM forskolin.
Data were determined as statistically different compared to treatment with GIP(1-42) and DMSO at each GIPR WT or mutant using Student's t-test.

Overall, all tested GIPR allosteric modulators except T21 seem to be effected by one or more of the Site 10 mutations both in cAMP accumulation and $(Ca^{2+})_i$ mobilization assays, which further validates Site 10 as a GIPR allosteric site. T11 is a GIPR NAMs for both GIP-induced cAMP accumulation and $(Ca^{2+})_i$ mobilization. In the $(Ca^{2+})_i$ mobilization assays Site 10 mutants L193$^{2.70}$A, P197A, N210A, Q211A and Q220$^{3.33}$A significantly reduced T11 efficacy, while in the cAMP accumulation assay mutants R196A and Q204A significantly reduced its efficacy. This would suggest that different amino acids that are important in modulating both responses. This could possibly be due to each pathway being mediated through different structural rearrangements of the GIPR involving different amino acids. $(Ca^{2+})_i$ mobilization assay also seems to identify generally more amino acids as potentially important, which could be related to different sensitivity of each assay.

3.10 Discussion

3.10.1 Drug discovery of 12 new GIPR allosteric modulators

In this chapter 34 new compounds were identified and *in vitro* pharmacologically tested for potential allosteric modulators activity. The 3 series of compounds tested were C3-based, C25-based and T-compounds screened against GIPR allosteric site located at the top of TMD2/3 and ECL1 (Site 10). One of the goals of this thesis was to increase the library of potential scaffolds of GIPR allosteric modulators. As potential treatment for type II diabetes or obesity, it is very advantageous to start with multiple compounds which can compensate for compounds disregarded during the drug discovery process due to insufficient effectivity or unwanted side effects. It also gives us more scaffolds, which can be tweaked and researched using structure-activity relationship studies in order to discover more potent and more selective compounds.

This goal of increasing the size of GIPR allosteric modulators library has been successful with the identification of 11 new GIPR NAMs and 1 new GIPR PAM in this chapter, although the effects of the PAM T21 are very weak and need to be further confirmed. Even more striking is the fact that these 12 new allosteric modulators were identified from overall number of only 34 screened compounds translating into a success rate of approximately 35%. Moreover, new compounds have been identified through both of the approaches used, the first one being drug discovery based on existing known GIPR NAMs C3 and C25 and the second being an *in silico* screen against potential allosteric binding site identified at the GIPR, Site 10.

But how do we know these new compounds are indeed allosteric modulators and not orthosteric ligands? The original compounds C3 and C25 were NAMs as was shown previously by Dr Harris (University of Cambridge). Moreover, C3-based and C25-based compounds showed no activity when tested alone and characteristically of NAMs lowered GIP maximal response without affecting potency. T compounds were then identified through an *in silico* screen against site 10, not against the orthosteric site, and selected as compounds predicted to bind there

But the ultimate proof is by providing a suggestion as to where they bind the GIPR which was successfully achieved indirectly by using mutagenesis (discussed later). Alternative approaches to also confirm this include solving a Cryo-Em or crystal structure of the receptor with the compounds, which due to cost and time restrictions is not feasible to do with all the compounds. Alternatively, a binding assay could be done to see whether the compounds outcompete fluorescent or radiolabelled orthosteric ligand to disprove their binding to the orthosteric site.

3.10.2 GIPR allosteric modulators are biased towards cAMP or calcium signalling

An additional aim of this chapter was to improve potency of the GIPR allosteric modulators. The starting compounds C3 and C25 both decreased GIP-induced $(Ca^{2+})_i$ mobilization at 100 µM. The most potent compound identified was C95, which inhibited GIP-induced $(Ca^{2+})_i$ mobilization at 10 µM, resulting in ~10x improved potency compared to C3, which it was based on. T10 and T11 then inhibited both GIP-induced $(Ca^{2+})_i$ mobilization and cAMP accumulation response at 31.6 µM and 50 µM, respectively, while T18 inhibited GIP-induced cAMP response at 50 µM. This means there are now four new compounds with improved potency over the original compounds C3 and C25. And while that is indeed an improvement, for GIPR allosteric compounds to be usable as potential therapeutics, there is still need for further improvement, which could be achieved by further modifying the compounds or partnering with industry to conduct a high-through put screening against Site 10. This could be performed by, for example, fluorescent- or radiolabelling one of the current compounds and then doing a high-throughput competition binding assay.

It is important to also note that C3 and C25 are both biased NAMs selective for $(Ca^{2+})_i$ mobilization pathway over cAMP accumulation pathway and this translates to being true for all C3- and C25-based compounds, which is predictable. However, it is not true for all T compounds. The T compounds were identified through screening against Site 10, which was first identified as the allosteric binding site of C25 and C58, both compounds selective for $(Ca^{2+})_i$ mobilization pathway over cAMP signalling. And indeed T2, T5, T13 and T26 still follow the same pattern (Table 3.36). On the other hand, T10 and T11 affect both calcium and cAMP signalling and moreover, T18 and T21 have an effect only on cAMP signalling at the tested concentrations. This could be because, while expected to bind in a similar site (not yet proven for all compounds), these compounds could be engaging different amino acids at this site resulting in different conformational changes in the receptor and biased signalling. In fact, the mutational studies, discussed in more detail below, do indeed point towards this.

Table 3.36. Summary of GIPR allosteric modulators and their effect at GIPR, GLP-1R and GCGR. Cross (X) indicates the compound does not effect agonist-induced calcium/cAMP response at the indicated receptor.

			GIPR		GLP-1R		GCGR	
Cmpd	**Type**	**GIPR Selective?[a]**	**Effective c - calcium (μM)[b]**	**Effective c - cAMP (μM)[c]**	**Effective c - calcium (μM)[b]**	**Effective c - cAMP (μM)[c]**	**Effective c - calcium (μM)[b]**	**Effective c - cAMP (μM)[c]**
C3	NAM	no	100	X	100	X	100	X
C22	NAM	?	100	X				
C91	NAM	?	100	X				
C95	NAM	no	10	X	100	X	100	X
C25	NAM	yes	100	X	X	X	X	X
C58	NAM	no	100	X	100	X	100	X
T2	NAM	yes	100	X	X	X	X	X
T5	NAM	yes	100	X	X	X	X	X
T10	NAM	no	31.6	50	X	50		100
T11	NAM	no	31.6	50	X	50	X	50
T13	NAM	no	100	X	100			
T18	NAM	no	X	50		100		50
T21	PAM	yes	X	100		X		X
T26	NAM	?	100	X	X			

[a] 'yes' indicates the compound is selective for GIPR over GLP-1R and GCGR

[b] Indicates lowest concentration at which the compound still effects agonist-induced $(Ca^{2+})_i$ mobilization.

[c] Indicates lowest concentration at which the compound still effects agonist-induced cAMP accumulation.

Orange indicates that lower concentration has not yet been fully measured.

GIPR signalling is truly pleiotropic, so in addition to cAMP and $(Ca^{2+})_i$ signalling, effects of compounds on β-arrestin recruitment was also assessed. The tested compounds were C3, C95, C25 and C58 and none of these showed any significant effect on this pathway. What these compounds have in common is that they are all GIPR NAMs selective for $(Ca^{2+})_i$ signalling over cAMP signalling. Therefore, it would be interesting to explore whether the β-arrestin signalling is independent of both cAMP and calcium or whether cAMP-biased compounds would have an effect on β-arrestin signalling as well.

Although the cAMP, $(Ca^{2+})_i$ and β-arrestin signalling pathways are discussed here as independent, there is most likely a crosstalk occurring between them. In order to research the compounds signalling bias in more detail, it might therefore be useful to research their effect more upstream of the signalling pathways, for example looking at the effects of compounds on G protein recruitment directly using some of the available techniques like TRUPATH system (Olsen et al., 2020).

3.10.3 T2, T5, T21 and C25 are selective for GIPR over GLP-1R and GCGR

The compounds are selective not only between GIPR signalling pathways but also between receptors. Generally, in drug discovery, there is a desire for selective compounds to limit unwanted side effects. On the other hand, especially in diabetes, dual or triple agonists of GIPR/GLP-1R/GCGR have been extensively researched as beneficial (Bastin and Andreelli, 2019; Knerr et al., 2022; Zhao et al., 2021). GLP-1R and GCGR are receptors closely related to GIPR, which is why the compounds were tested against them as well.

C25, one of the original compounds, was shown to be selective for GIPR over GLP-1R and GCGR, while C58 based on C25 was not. It would therefore be interesting to explore more, which mechanism is responsible for C58 losing the selectivity. This could be explored either through SAR studies or potentially through MD simulations of C25 and C58 at the GIPR. C3 and the most potent compound C95 are both non-selective, meaning they might not be the best candidates as starting compounds for drug development of selective GIPR allosteric modulators. T2, T5 and T21 are the newly discovered selective allosteric modulators. T10 and T11 are then selective in their effects on $(Ca^{2+})_i$ mobilization pathway, but not in their effects on cAMP accumulation. The question remains whether this is because of different sensitivity of the two assays, or it could be because of the compounds recruiting different amino acids to effect signalling of each of the assay. This was hinted at previously that cAMP and $(Ca^{2+})_i$ signalling could be propagated through the receptor differently and the compounds could be interacting with different amino acids to start this reaction. The amino acids involved in affecting $(Ca^{2+})_i$ signalling could then theoretically differ between the three receptors, while the ones affecting cAMP

signalling could be conserved. To prove or disprove this theory, the binding and effect of the compounds would need to be understood better.

3.10.4 GIPR allosteric binding site was identified at the top of TMD2/3 and ECL1

As was discussed above, finding the allosteric binding site of the compounds is important for multiple reasons including proving whether the compounds are allosteric modulators and better understanding the differences between the potency and pathway and receptor selectivity of the compounds. With the help of *in silico* docking discussed in chapter 4, multiple GIPR amino acids from Site 6 (middle of the receptor below orthosteric binding site) and 10 (top of TMD2/3 and ECL1) were selected, mutated and tested to see whether they affect the behaviour of compounds C3 and C25. Unfortunately, none of the mutants affected C3 activity, which is not that surprising since compounds used for the *in silico* docking were related to C25 instead. C25, however, lost its effect at mutant L193$^{2.70}$A pointing toward Site 10 as the potential allosteric site, which was then proven by using multiple Site 10 mutants which also had affects (Table 3.37). The identification of the new allosteric site was important as it enabled an *in silico* screen against that site resulting in successful identification of new GIPR allosteric modulators with different scaffolds like for example T2 or T10.

Table 3.37. Summary of GIPR negative allosteric modulators' activity at GIPR mutants. Y indicates that the NAM retains its normal effect at that mutant GIPR, **N** indicates that the compound efficacy is significantly reduced and '-' means the compounds doesn't have any effect in that assay.

Cmp	Assay	GIPR mutants								
		L193$^{2.70}$A	R196A	P197A	G198A	Q204A	N210A	Q211$^{3.24}$A	Q220A	E288$^{45.52}$A
C25	cAMP	-	-	-	-	-	-	-	-	-
	Ca^{2+}	**N**	**N**	**N**	-	Y	Y	**N**	**N**	Y
C58	cAMP	-	-	-	-	-	-	-	-	-
	Ca^{2+}	**N**	Y	Y	-	Y	Y	Y	Y	Y
T5	cAMP	-	-	-	-	-	-	-	-	-
	Ca^{2+}	-	Y	**N**	-	**N**	**N**	**N**	Y	**N**
T10	cAMP	Y	Y	Y	**N**	**N**	**N**	Y	Y	Y
	Ca^{2+}	N/A[1]	N/A[1]	N/A[1]	N/A[1]	N/A[1]	N/A[1]	N/A[1]	N/A[1]	N/A[1]
T11	cAMP	Y	**N**	Y	-	**N**	Y	Y	Y	Y
	Ca^{2+}	-	Y	**N**	-	Y	**N**	**N**	**N**	Y
T18	cAMP	-	-	-	-	-	-	-	-	-
	Ca^{2+}	Y	Y	Y	-	**N**	Y	Y	Y	**N**

[1] Data is not available at this time as this experiment has not yet been determined.

This was followed by C58 screening against Site 10 mutants and this time only 1 mutant was identified, mutant L193$^{2.70}$A. It was mentioned previously that C25 and C58 are structurally very similar, yet only one of them is a selective compound. As we can see in Table 3.37, amino acid L193$^{2.70}$A seems to be important for both compounds, but perhaps the rest of the amino acids they use might slightly differ. As there is only one mutant having an effect on compound C58, it would be useful to explore its binding a bit more through *in silico* docking or MD simulations coupled with the *in vitro* techniques.

Regarding compounds T5, T10, T11 and T18 there is more than one mutant affecting the actions of each of the compounds both in the cAMP accumulation and $(Ca^{2+})_i$ mobilization assays, further validating their binding to Site 10. The hypothesis is that this would be similar for compounds T2, T13 and T26 once the experiments have been completed. T10 still needs to be tested with the GIPR mutants in $(Ca^{2+})_i$ mobilization assay.

T21 is the only problematic compound from the T series where none of the mutants had any significant effect, but since it had no significant effect even on the transfected WT GIPR, it remains inconclusive whether the compound is truly a GIPR PAM. There are several possible explanations why T21 had no effect in the cAMP accumulation experiment with the transfected WT and mutant GIPR, while it did have a significant effect in the original screen. First reason could be that T21 effects in the original screen was a false positive. In line with this explanation would also be the fact that T21 had no effect at both GLP-1R and GCGR, while all the other NAMs for cAMP signalling pathways did, although it could just be because the compound is selective. This could be tested by re-doing these experiments and seeing whether the same effects would be observed once again. Secondly, the screen uses HEK-293S cells stably expressing GIPR, while this second experiment is in HEK-293S cells transiently transfected with GIPR. The smaller assay window and generally weaker response in the transfected cells could be masking the effects of T21. Lastly, the original screen used a partial agonist GIP(Pro3), while this second experiment used GIP(1-42). As was reasoned above, the high potency and maximal response of GIP(1-42) is close to a system maximum (100 µM forskolin) and could be masking effects of a PAM. The second experiment with transiently transfected WT GIPR could therefore be repeated with a GIP(Pro3).

Beyond just confirming the compounds to bind an allosteric site, the identification of amino acids important for compound binding or mediating their effects is also important for starting to understand how the compounds are working. This is particularly interesting for compound T11, where the mutants have been tested in both cAMP and calcium assay. It shows that the amino acids important for each pathway differ completely, suggesting the effect on the two pathways are propagated through two different mechanisms (Table 3.37). cAMP- or $(Ca^{2+})_i$-biased compounds could

then be used to probe the different GIPR signalling in physiological settings. Once compound T10 is tested on the mutants in $(Ca^{2+})_i$ mobilization assay, it would be interesting to see, whether the mutants identified in each assay also differ similarly to T11.

Overall, exploring the compound binding through *in silico* techniques and *in vitro* mutagenesis has resulted in successful identification of GIPR allosteric site at the top of TMD2/3 and ECL1. This then enabled identification of new GIPR allosteric modulators binding this site and slightly more insight into the compounds binding and function.

3.10.5 Inhibition of incretin-potentiated Insulin secretion

Lastly, due to these GIPR allosteric modulators being potential starting compounds for diabetes type II or obesity drugs, it is important to also research them in a more physiological setting. To start this, C25, C58 and C95 were explored for their effects on insulin secretion in rat INS WT cells, which is a cell model commonly used for insulin secretion assay and expressing both GIP and GLP-1 receptors. Confirming previous results, C25 showed selectivity for GIPR over GLP-1R, while C58 was effective at both receptors. C25 was also effective at 10 µM, which is 10x lower concentration than the one effective at $(Ca^{2+})_i$ mobilization assay. This could be because of insulin secretion assay being more sensitive or because insulin is potentiated also through other mechanisms than purely calcium.

All these tested compounds are NAMs selective for $(Ca^{2+})_i$ mobilization pathway over cAMP signalling pathway. This could therefore indicate that insulin secretion is probably at least partly potentiated through intracellular calcium mobilisation, which would be reasonable as calcium generally promotes insulin exocytosis. It would therefore be very interesting to also test GIPR allosteric modulators selective for cAMP pathway and see whether they have any effect on insulin secretion. If they did not and insulin secretion was mediated solely through calcium-related mechanisms, those could be compounds useful in lowering obesity without lowering insulin secretion.

Insulin is not the only physiological parameter that should be explored. GIP also plays a big role in glucagon secretion, which is often elevated in obesity and therefore, this parameter should be explored next as well as the effects of compounds on adipose tissue or related cell models.

3.11 Conclusion

Potentiating GIPR signalling has been explored therapeutically for type II diabetes treatment, while research shows that inhibiting GIPR signalling holds potential for weight loss in obesity. Allosteric modulators then present a more physiological solution (by being only active when an endogenous

agonist is present) and bigger opportunity for development of orally available small molecule drugs than conventional orthosteric peptide drugs targeting the GIPR. Here, we report the identification and pharmacological characterisation of new GIPR negative allosteric modulators complementing the PAM library already available in Prof Ladds' laboratory.

Out of 34 compounds screened overall, 11 new GIPR NAMs and 1 new GIPR PAM were identified translating into approximately 35% success rate. C95 is the most potent out of the new compounds with 10x improved potency over the starting compounds C3 and C25 with T10, T11 and T18 also being more potent. Moreover, compounds C25, T2, T5 and T21 are selective for GIPR over GLP-1R and GCGR giving us a promising starting point for the drug discovery of selective compounds with hopefully less side-effects.

This study also researches the bias of the new compounds and identifies NAMs selective for either the calcium or the cAMP pathway, giving us new tools to probe the different GIPR signalling pathways in a physiological setting. One such setting is GIPR signalling potentiating insulin secretion. Here we show that the negative allosteric effects of compounds translate into the inhibition of incretin potentiation of insulin secretion. It remains to be seen whether this is also true for GIPR NAMs selective for cAMP pathway over $(Ca^{2+})_i$ mobilization pathway and how it affects other GIPR physiological actions like glucagon secretion or functions in adipose tissue.

Lastly, in this chapter it was found that a new GIPR allosteric binding site at the top of TMD2/3 and ECL1 through a combinational *in silico* and *in vitro* approach. Moreover, we prove the binding of C25, C58 and T compounds to this site and start to uncover the differences between the binding and effects of these different compounds.

In conclusion, the combinational approach of *in silico* identification and *in vitro* pharmacological validation has been proven successful with the identification of new GIPR allosteric modulators and insight has been gained into the function of these compounds.

Chapter 4. *In silico* investigation for allosteric site identification at the GIPR

4.1 Introduction

As mentioned in Chapter 1, GIPR is an important target in many diseases including cardiovascular disease, increased low-density lipoprotein (LDL) cholesterol and type 2 diabetes mellitus (T2DM) (Nitz et al., 2007; Shalaby et al., 2017; Sugunan et al., 2010). In particular, promoting GIPR signalling is though to be beneficial in T2DM, while attenuating GIPR signalling has been researched with potential use in obesity in mind (Bastin and Andreelli, 2019; Cho et al., 2012; Gasbjerg et al., 2018; Irwin et al., 2020; Jones et al., 1987; Renner et al., 2010; Widenmaier et al., 2010). Apart from agonist and antagonists, this can be achieved with positive and negative allosteric modulators (PAMs and NAMs, respectively) targeting the GIPR. Since GIPR endogenous agonist is a peptide GIP, developing allosteric modulators can be considered as an attractive strategy for developing orally available and cheaper drugs for abovementioned disease areas. They also hold the advantage of being more physiologically tuned as they only work once GIP is already present at the GIPR, but they will lack activity on their own minimising risk of hypoglycaemia experienced by many T2DM drugs. They also provide potential for more receptor selectivity as GIP is active also at related receptors like GLP-1R or GCGR (Yuliantie et al., 2020; Zhao et al., 2021b, 2022).

The first approach to identify allosteric modulators could be simply to perform high throughput screening of lead/drug-like compound libraries against a receptor and then characterise the compounds using *in vitro* pharmacological assays. If any allosteric modulators are found, their exact binding site at the receptor can be possibly identified using a combination of *in silico* methods (docking +/- MD simulations) and *in vitro* mutagenesis followed by functional assays. For making initial guesses about the location of potential binding sites for allosteric ligands, *In silico* blind docking approach can be used, given this will dock a molecule to the most-likely binding sites (based on computed energy of interactions) in an unbiased manner i.e. with no binding site suggested a priori by the experimenter (Greenhalgh et al., 2020; Hajbabaie et al., 2021). Most of the available software for docking do not allow blind docking except a few such as SwissDock, AutoDock Vina and ICM-Pro (Abagyan et al., 1994; Friesner et al., 2004; Trott and Olson, 2010). Poses obtained from blind docking can further be refined (and it is better to do so) through focused docking for which one can use any of the available docking software of which few are more renowned such as Glide (especially in its extraprecision or XP mode, Schrödinger Inc.) (Friesner et al., 2004) and GOLD (CCDC, Cambridge). PoseView™ (https://proteins.plus/) or Molecular Operating Environment (MOE) (Chemical Computing Group) can

then be used to obtain 2D diagrams showing the predicted ligand-receptor interactions, which can guide the selection of amino acids for mutagenesis (Fährrolfes et al., 2017; Molecular Operating Environment, 2022; Schöning-Stierand et al., 2020). The most common approach is to use site-directed mutagenesis to mutate the selected amino acids to alanine and then test them in *in vitro* assays to see whether any of these mutations have any effect on the allosteric modulation initially observed for the molecules. If any of the mutations indeed has an effect, the information can be fed back into the focused docking models which could allow selection (done more subjectively) of plausible binding mode at a plausible allosteric pocket for the molecules.

An alternative way is to first identify potential allosteric binding sites at the target protein structure and then screen compounds only against these pockets in order to identify allosteric modulators. In an era of exponentially increasing number of solved protein structures through X-ray crystallography or Cryo-Em and large databases of sequence information from many various organisms, this approach is becoming more feasible with time. There are multiple techniques that enable identification of either good binding pockets based on metrics such as depth of the pocket of accessibility by a ligand, which identify both orthosteric and allosteric binding sites (Sheik Amamuddy et al., 2020; Wagner et al., 2016). However, since orthosteric binding site is known for many proteins now including GIPR, it can simply be excluded. Then there are other techniques that use information like sequence conservation and flexibility of the protein to identify structurally and functionally important parts of the protein, among which allosteric sites also belong. Generally, the *in silico* methods for allosteric site identification can be approximately divided into five categories: knowledge-, sequence-, geometry-, energy- and dynamics-based techniques (Sheik Amamuddy et al., 2020; Wagner et al., 2016).

In this chapter, the *in silico* blind and focused docking were performed using AutoDock Vina, ICM-Pro and GlideXP in order to predict the probable binding site(s) of few allosteric modulator compounds (already identified by Prof Ladds and Dr Rahman, detail provided in chapter 3) on GIPR structure. The predicted poses were then used to select amino acids for *in vitro* mutagenesis experiments followed by functional assays (also carried out in chapter 3). Results from these *in vitro* experiments informed subsequent refinement of the *in silico* docking protocol. Secondly, good candidate allosteric sites at the GIPR were explored using multiple non-docking type *in silico* methods for allosteric site identification with the aim of comparing these results to the *in silico* docking results and also for comparison of the different techniques against each other. The work in this chapter was done in parallel with the work in chapter 3.

4.2 *In silico* blind docking to GIPR homology models

At the beginning of this PhD project (autumn 2019), there were no resolved crystal or Cryo-Em structure of the GIPR receptor that could be used for *in silico* docking of compounds to the GIPR. However, structures for multiple other GPCRs were available including some family B GPCRs like GLP-1R. In this section multiple compounds tested for allostery at the GIPR, including compounds in chapter 3 and compounds tested by the preceding student Dr Harris in Prof Ladd's lab, were blindly docked to the GIPR homology models with the aim of finding out the allosteric binding site of these compounds at the GIPR. The results of this *in silico* blind docking also guided the *in vitro* mutagenesis experiments presented in chapter 3.

4.2.1 Docking to GIPR homology model with bound GIP

The first GIPR homology model (model 1) was based on an active GLP-1R structure (PDB id: 5VAI,), made by Dr Taufiq Rahman. The initial model (with bound GIP peptide) was then subsequently refined through 200ns of all-atoms MD simulations after embedding it in a membrane made of 1-palmitoyl-2-oleoyl-sn-glycero-3-phosphocholine (POPC) (courtesy of Dr Aneesh Chandran, Rahman lab, University of Cambridge).

C25 and C3-based compounds (Table 4.1) discussed in chapter 3 were docked to this GIPR homology model using an unbiased ('blind') docking approach in AutoDock Vina (Trott and Olson, 2010). For each compound, AutoDock Vina by default generated 9 poses ranked in order from best predicted binding affinity (BA = estimated free energy of interaction, $\Delta\Delta G$, kcal/mol) to worst. For each molecule, the blind docking was performed in three independent runs (n=3) resulting in a final 27 poses per compound.

Table 4.1. 2D structures of the C3 and C25-based compounds proven to be allosteric modulator at GIPR.

C3-based compounds	C25-based compounds
C3 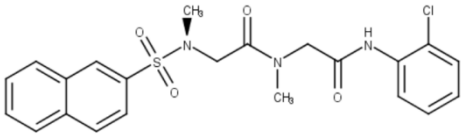	C25 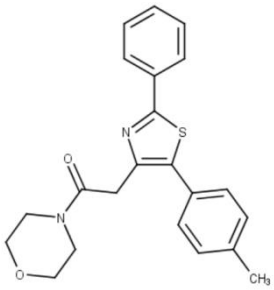
C22 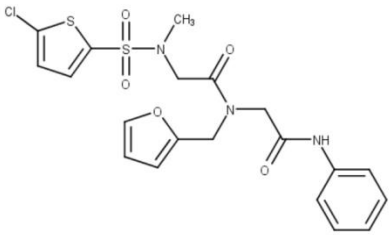	C58 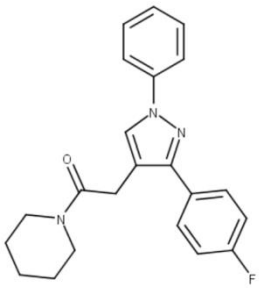
C42 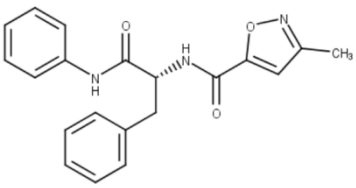	C73 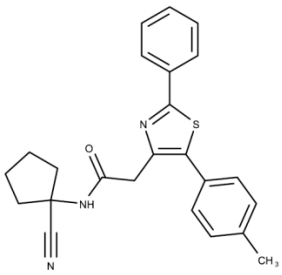
C91 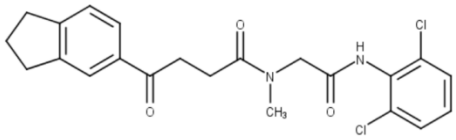	C82 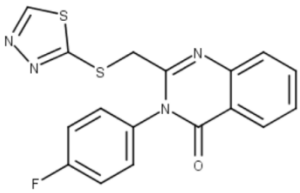
C95 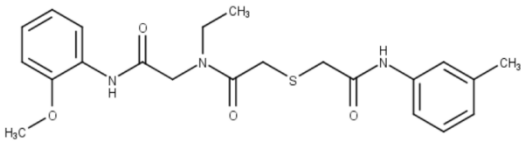	

All compounds docked into the same docking site, labelled "Site 0", although in slightly varied orientations (Figure 4.1). Site 0 is located at the interface of top of TMD3 and the orthosteric site that recognises the peptide agonist GIP, which both possibly interacts with the compounds in this predicted

pose. Furthermore, PoseView™ was unable to produce 2D interactions diagrams, suggesting the interactions might not be too strong (Fährrolfes et al., 2017; Schöning-Stierand et al., 2020).

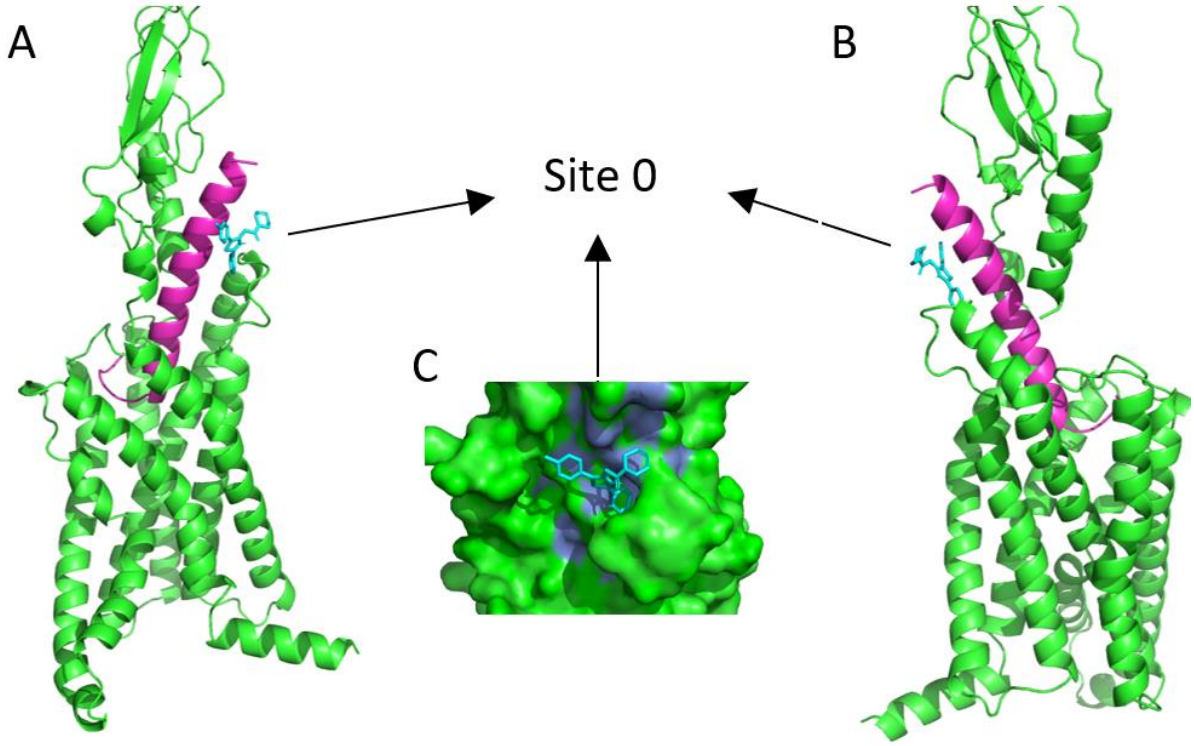

Figure 4.1. *In silico* docking of C25 to GIP-bound GIPR model 1. A-B. Different orientations of the modelled complex of GIPR (green) and GIP (pink) with C25 (blue) highest ranked pose generated by AutoDock Vina docked to Site 0. C. Close up view of C25 docked at Site 0.

Since the PoseView™ could not predict a 2D pose and the predicted binding site at the GIP seemed quite shallow, we wanted to explore other possible allosteric binding sites at the GIPR. Therefore, the area of the GIPR homology models where the compounds can dock was restricted to regions above or below Site 0. When the area was restricted below Site 0, AutoDock Vina predicted 4 new potential allosteric sites labelled Site 1-4, while restricting above Site 0 yielded a single new potential site designated as Site 5 (Figure 4.2).

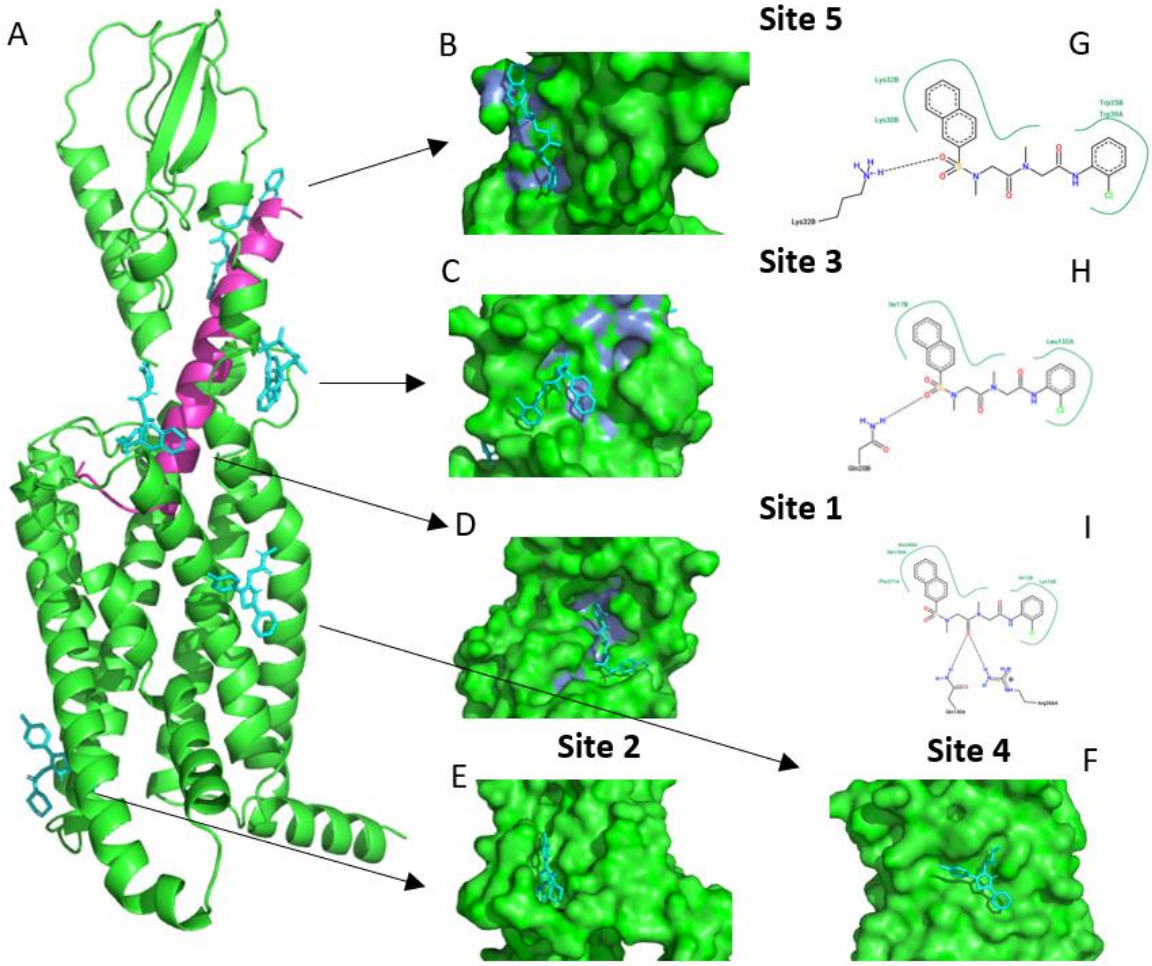

Figure 4.2. *In silico* docking of compounds to GIPR model 1 with attached GIP. A. GIPR (green) and GIP (pink) homology model 1 with tested compoundposes (blue) generated by AutoDock Vina. B-F. Close up view of tested compounds docked and individual sites. G-I. PoseView^{TM} derived ligand interaction diagrams for docked poses of C3.

Poses at Site 1 had the lowest predicted binding affinity and highest reproducibility with about 70% of all compound poses being located there. Site 1, 3 and 5 also followed similar pattern seen with poses of molecules at Site 0 and interact significantly with GIP peptide (as visible on Poseview^{TM} diagrams in Figure 4.2). At Site 2 the compounds potentially interact with the bottom of TMDs 3,4 and 5 and intracellular loop 2, while at Site 4 there are interactions with the middle of TMD 1 and 7. However, Poseview^{TM} failed to generate 2D interaction diagrams for either of these two sites. This might be because there are no receptor residue side chains likely to interact with the compound close to its 3D position.

Overall, unbiased docking to GIPR homology model 1 seemed to predict compound interacting primarily with the orthosteric peptide GIP and maybe just week interactions to the rest of the receptor like the top of TM3.

4.2.3 Docking to GIPR homology models lacking the N-terminus and GIP

Since model 1 mostly predicts compound interaction with the GIP instead of the receptor, other GIPR homology models based on class A and class B GPCRs were made by Dr Rahman (models 2-10, Table 4.2). The main difference is that compared to model 1, these models lack N-termini (deliberately excluded from the sequence during modelling) and thus, the bound GIP peptide as well. Also, the biggest proportion of these models is based on GLP-1R, which is a class B incretion hormone receptor closely related to GIPR and therefore a good choice. Also similar to GIPR, GLP1-R is predominantly G_s coupled. All the GPCR structures used for homology modelling of the N-terminally truncated GIPR are G_s-bound class B GPCRs except the A2AR structure, which is a G_s-bound class A GPCR.

Table 4.2. GIPR homology models used for *in silico* docking. The models were made by Dr Rahman and his lab.

Model	Template GPCR[a]	PDB id[b]	Modification
1	GLP-1R	5VAI	Attached GIP
2	GLP-1R	5VAI	Missing N-termini
3	GLP-1R	5NX2	Missing N-termini
4	GLP-1R	6B3J	Missing N-termini
5	GLP-1R	6ORV	Missing N-termini
6	PTHR1	6BNI	Missing N-termini
7	A2AR	5G53	Missing N-termini
8	CALCR	5UZ7	Missing N-termini
9	CALCR	6E3Y	Missing N-termini
10	CALCR	6NIY	Missing N-termini

[a] The GPCR with a solved structure that the GIPR homology model is based on
[b] Unique PDB identifier of the template GPCR from RCSB PDB (https://www.rcsb.org/)

Since the above models added considerably to the total number of GIPR homology models to dock the molecules against, I decided to use a selected sub-set of compounds from the available list of hits in order to remain time effective. The compounds selected (C9, C12, C15, C21 and C23) were

all tested by Dr Harris during his PhD in Prof Ladds lab (Table 4.3) (Dr Harris' PhD thesis, 2019). They were all structurally related compounds based on C9 (C25 is also based on C9), but the small structural changes led to big effects on their allosteric activity at the GIPR at either the cAMP accumulation and/or the $(Ca^{2+})_i$ mobilisation pathways. Of these, only compound C12 (negative control) had no effect at GIPR in either of the assays but was included for comparison.

Table 4.3. Compounds used for *in silico* docking at GIPR homology models 2-10. Series of allosteric modulator compounds of the GIPR based on compound C9 and their allosteric activity at GIP-induced cAMP accumulation or $(Ca^{2+})_i$ mobilisation in HEK-293S cells stably expressing the GIPR. The *in vitro* assays were performed by Dr Harris (Dr Harris' PhD thesis, 2019).

Compound	Structure	cAMP accumulation[a]	$(Ca^{2+})_i$ mobilisation[b]
C9	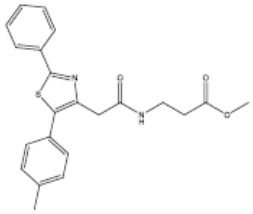	PAM	PAM
C12	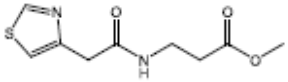	NA	NA
C15	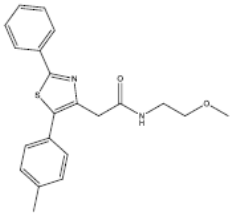	PAM	NA
C21	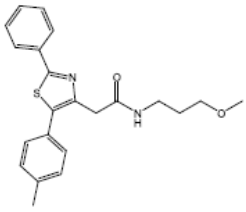	PAM	NAM
C23	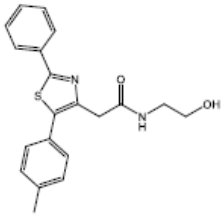	NA	PAM

[a] Allosteric modulator effect of tested compound on GIP(Pro3)-induced cAMP accumulation in HEK S cells stably expressing GIPR.
[b] Allosteric modulator effect of tested compound on GIP(1-42)-induced $(Ca^{2+})_i$ mobilisation in HEK S cells stably expressing GIPR.

The *in silico* blind docking was carried out using AutoDock Vina and for some models, also using ICM-Pro (done by Dr Rahman). The allosteric sites identified by these two different software's based on entirely different algorithms were often comparable, but not always exactly matching as can be seen for example in Figure 4.3.

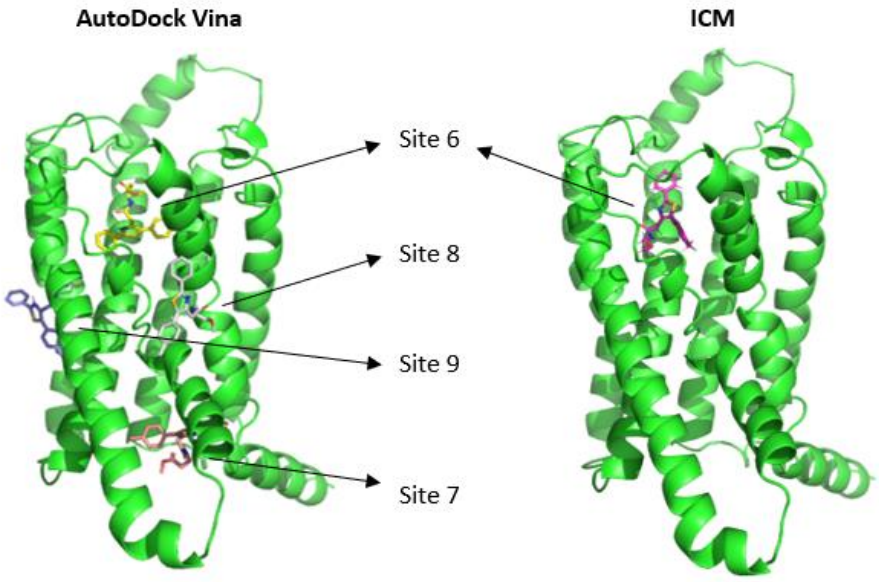

Figure 4.3. Comparison of blind docking carried out by AutoDock Vina or ICM-Pro. Compound poses from blind docking to GIPR homology model 2 (green) by Autodock Vina and ICM-Pro softwares. ICM-Pro docking was carried out by Dr Rahman.

Across all the different models of GIPR used, AutoDock Vina has identified Site 6, located in the bottom of the orthosteric site (top middle of the receptor missing and N-termini), as the most likely binding site of the compounds with the lowest predicted binding affinity in most models and the highest reproducibility (Table 4.4). The second overall most probable site is Site 10, located at the top of TMDs 2 and 3 and ECL1, which are mostly unstructured regions in the models (not identified using the particular homology model in example in Fig 4.3, but is shown for example in Fig 3.14 or 4.10). The unstructuredness might provide receptor selectivity but might be difficult to find the correct 'real-world' conformation using homology models. This site was identified most strongly, in particular, among the GLP-1R-based GIPR homology models and since GLP-1R is very close structurally and functionally to GIPR, this might be significant. ICM-Pro gave slightly different results in the less

represented poses, but generally also identified Site 6 and 10 as the best across various GIPR homology models.

Table 4.4. Summary of blind docking to GIPR models 2-10 using AutoDock Vina. Percentage of all poses of tested compounds blind docked to the different sites at GIPR homology models 2-10. Poses of compounds binding to unstructured regions are written in red, poses with lowest predicted binding affinity are highlighted yellow.

		GIPR homology model									
Site	**Description**	**2**	**3**	**4**	**5**	**6**	**7**	**8**	**9**	**10**	**Total (%)**
2	bottom TMD 3/4/5 + ICL2							2			**0.2**
6	top centre	87	99	38	59	25		39	5	88	**48.9**
7	bottom centre	6		9	4	2	25	43			**9.9**
8	middle TMD 5/6/7	1					3				**0.4**
9	middle of TMD 3/4/5	6									**0.7**
10	top TMD 2/3		1	53	37	73		3			**18.6**
11	top TMD 7/1						64	13			**8.6**
12	bottom TMD 1/2/3						7				**0.8**
13	top TMD 5/6						1				**0.1**
14	top TMD 3/4								1		**0.1**
15	unstructured region above TMD 6/7								94	12	**11.8**

Since the selected compounds had different allosteric effects at the GIPR with compound C12 having no activity in any of the conducted assays, the poses for different compounds across the GIPR homology models were also compared. However, there was not enough consensus across the different models to be able to pinpoint differences between how different compounds were engaging with the receptor to produce differential results. This might be more possible once the binding site could be found and interactions of compounds with specific amino acid side chains could then be explored jointly through *in silico* docking and *in vitro* mutagenesis experiments.

Overall, Site 6 and Site 10 appeared to be the best candidate allosteric site identified independently through two different *in silico* docking software programmes AutoDock Vina and ICM-Pro across multiple homology models of the GIPR. Therefore, these sites were focused on for subsequent experimental validation.

4.2.3 Detailed investigation of the compounds binding at Site 6 and Site 10

First, the poses of compounds in Site 6 and 10 obtained through *in silico* blind docking using AutoDock Vina and ICM-Pro were used as starting points for focused docking of the compounds in GlideXP (Schrodinger Inc), carried out by Dr Rahman. This 'extra-precision' (hence, XP) of Glide is regarded amongst the best algorithms for focused docking and pose refinement (Zhou et al., 2007). This resulted in a bit more refined poses for the compounds at these sites and 2D diagrams were also made using PoseView^{TM}. These 2D diagrams of poses obtained through all three software programmes, were then used to study the predicted interactions between the compounds and amino acid side chains. Additionally, slightly more attention was given to poses resulting from docking at the GLP-1R-based models, as it is the closest homology to GIPR amongst all the templates used for modelling the GIPR.

Site 6 was the site most consistently identified site across all the GIPR homology models and the compounds' poses there have often been predicted the lowest binding affinity. However, the slight concern remained about how accessible this site would remain if the GIP and N-termini were present and whether this site might be an artefact of the N-termini and GIP missing in these models as it might slightly overlap with the large orthosteric binding site for the endogenous peptide agonist GIP. Nevertheless, it was not the first time a similar site was suggested, as Méndez et al. (2020) showed a similar allosteric binding pocket at the GLP-1R based on their *in silico* experiments.

The 2D diagrams of compounds binding at GIPR carried out using AutoDock Vina and ICM-Pro predicted amino acids Tyr141$^{1.43}$, Arg183, Ile187, **Gln224**, Val227, Arg289, **Trp296**$^{5.36}$, **Arg300**, **Ile303**, Glu354, Phe357, Glu377 and Ile378 to be key for the binding of C9-based compounds at Site 6, while GlideXP predictedTyr141$^{1.43}$, Tyr145, **Arg183**, Ile187, **Arg190**, **Gln224**, Val227, Tyr231, Trp296$^{5.36}$, Ile299, **Arg300**, Ile303, Leu304, Glu377, Ile378 and Ser381 as most important (the ones in bold are the most important ones even from this list). Figure 4.4 shows that these amino acids are located in the top half of all the transmembrane domains except TMD4 and also shows few of the representative 2D diagrams.

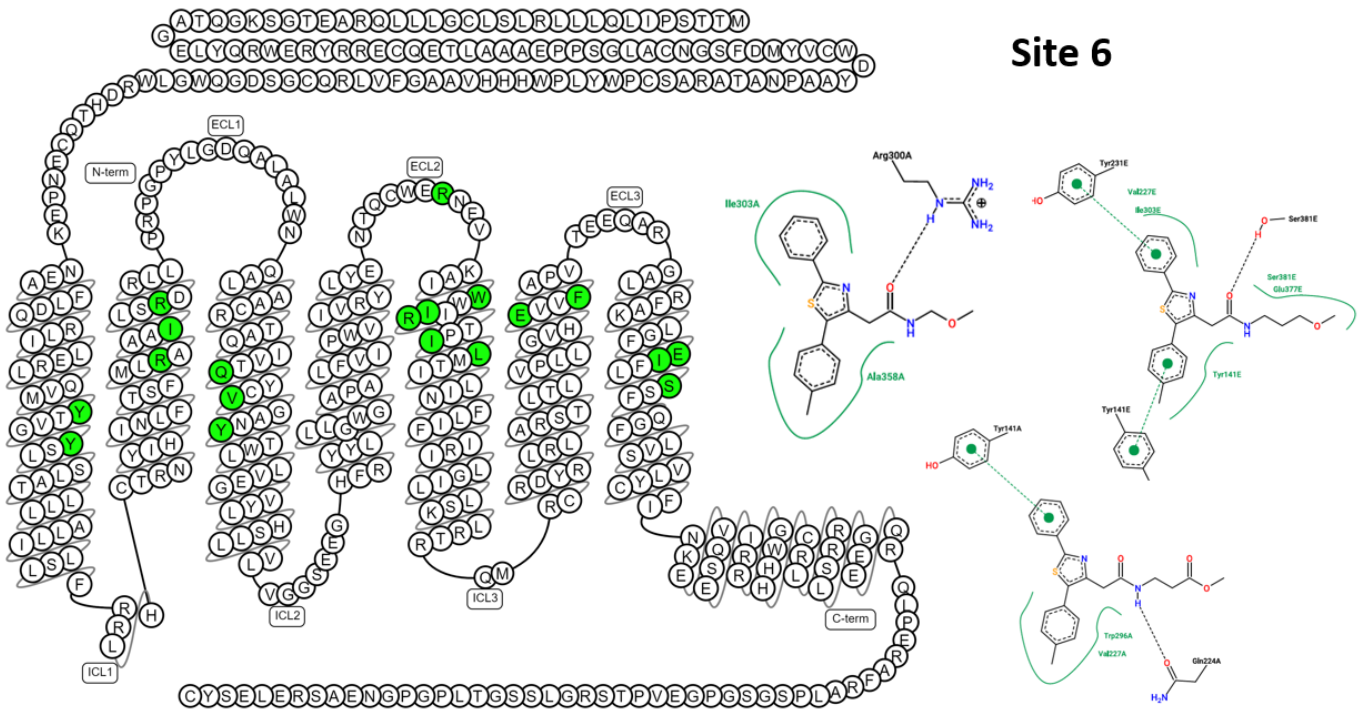

Figure 4.4. Site 6 identified by *in silico* blind docking. *In silico* blind docking of C9-based compounds to GIPR homology models without N-termini has identified site 6 as possible allosteric binding site and identified amino acids of the GIPR likely to be interacting with the compounds (green). An example of the PoseView^{TM} derived ligand interaction diagrams for site 6 is included.

Of these, some mutations had already been previously explored. Yaqub et al. (2010) showed that mutation of residues Arg183, Arg190 and Arg300 caused 76-, 71-, and 42-fold reduction in the GIP potency to induce cAMP accumulation, respectively. Furthermore, they strongly supported a binding mode of GIP to GIPR in which the N-terminal moiety of GIP was sited within TMDs 2, 3, 5, and 6 with biologically crucial GIPR amino acid Tyr1 interacting with Gln224 (TMD3), Arg300 (TMD5), and Phe357 (TMD6). Because of the known effects of these mutations on reducing the GIP binding/potency, they were excluded from the list of amino acids to be tested as it would be unlikely that these mutants would exhibit much GIP-induced cAMP accumulation or $(Ca^{2+})_i$ mobilisation needed to indirectly observe the effect of the allosteric modulators on the GIPR.

Site 10 was the second most likely allosteric binding site and deemed the most prominent across the GLP-1R-based models. It lies at the top of transmembrane domains 2 and 3 and extracellular loop 1. AutoDock Vina and ICM-Pro identified amino acids Arg190, **Leu193$^{2.70}$**, Leu194, **Asp203, Ala207**, Asn210, Gln211$^{3.24}$, Trp287$^{45.51}$, Glu288$^{45.52}$ as key for the binding of C9-based compounds at GIPR,

while GlideXP identified **Leu193**$^{2.70}$, Leu194, Pro195, Arg196, **Gly198**, Pro199, Gln204, Ala207, Asn210 as the most important (the bold ones are key even among this list) (Figure 4.5).

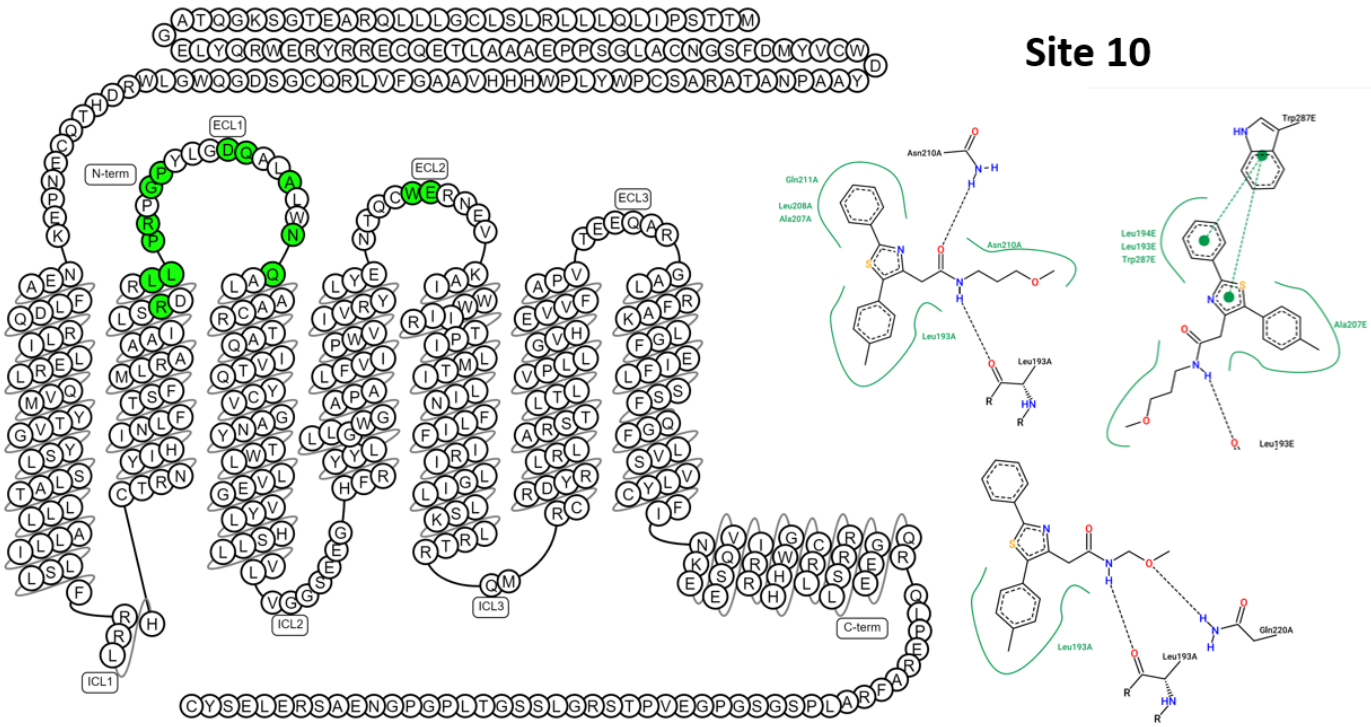

Figure 4.5. Site 10 identified by *in silico* blind docking. The site was identified through *in silico* blind docking of C9-based compounds to GIPR homology models that were devoid of the N-termini. Some specific amino acids of the GIPR that appear to be interacting with the compounds are highlighted in green in this snake diagram. To the right, few exampler 2D interaction diagrams derived from PoseView™ -based analyses of the few compounds docked to this site on GIPR models.

Interestingly for the closely-related GLP1-R, Wootten et al. (2016) showed that the extracellular surface, including ECL1 is important for signalling and especially for biased agonism. It was found that mutations L201A, M204A, W214A, L218A decreased GLP-1 binding, while mutations L201A, K202A, Y205A, Q211$^{3.24}$A decreased GLP-1-induced cAMP accumulation and K202A, W203A, Y205A, T207A decreased GLP-1-induced $(Ca^{2+})_i$ mobilisation. Mutation D215A increased GLP-1-induced $(Ca^{2+})_i$ mobilisation. There is less information about this region for GIPR, but Miyawaki (1999) showed that missense mutation (G198C) causes a decreased response of cAMP to GIP.

It is also of note, that there seemed to be more consensus among the poses in Site 10 and Site 10 is overall more defined and the poses are closer together compared to site 6. Ala207 was excluded

from the experiments since alanine mutagenesis was performed and this amino acid was already an alanine. There were also some amino acids like Arg190, Pro195, Arg196, Pro197, Gln220$^{3.33}$, Trp287$^{45.51}$ and Glu288$^{45.52}$ that overlapped between Site 6 and Site 10.

Next, the conservation of the Site 6 and Site 10 and impact on selectivity was explored by comparing sequences of the predicted allosteric sites between GIPR, GLP-1R and GCGR (Figure 4.6 and 4.7). These two class B1 receptors were picked for the initial selectivity screen because GLP-1R manifests highest sequence homology to GIPR, while also playing a role in insulin secretion and GGCG has a cross reactivity with GLP-1R. Both receptors are also expressed in the pancreas and quite conveniently, cells stably expressing either of them were already available in the lab. Generally, Site 6 seems a bit more conserved than site 10 which seems to differ a lot especially in the ECL1 region. Furthermore, these sites were identified through *in silico* docking of compound C9 and its derivatives. In previous work, Dr Harris has tested compound C9 against GIPR and other class B1 GPCRS (GLP-1R, GLP-2R, GCGR, CTR, CRFR1, CRFR2) in cAMP accumulation assay and found the compound to be selective for GIPR over the other receptor (Dr Harris' PhD thesis, 2019). Site 10 could therefore maybe give us better understanding where the selectivity is coming from than site 6.

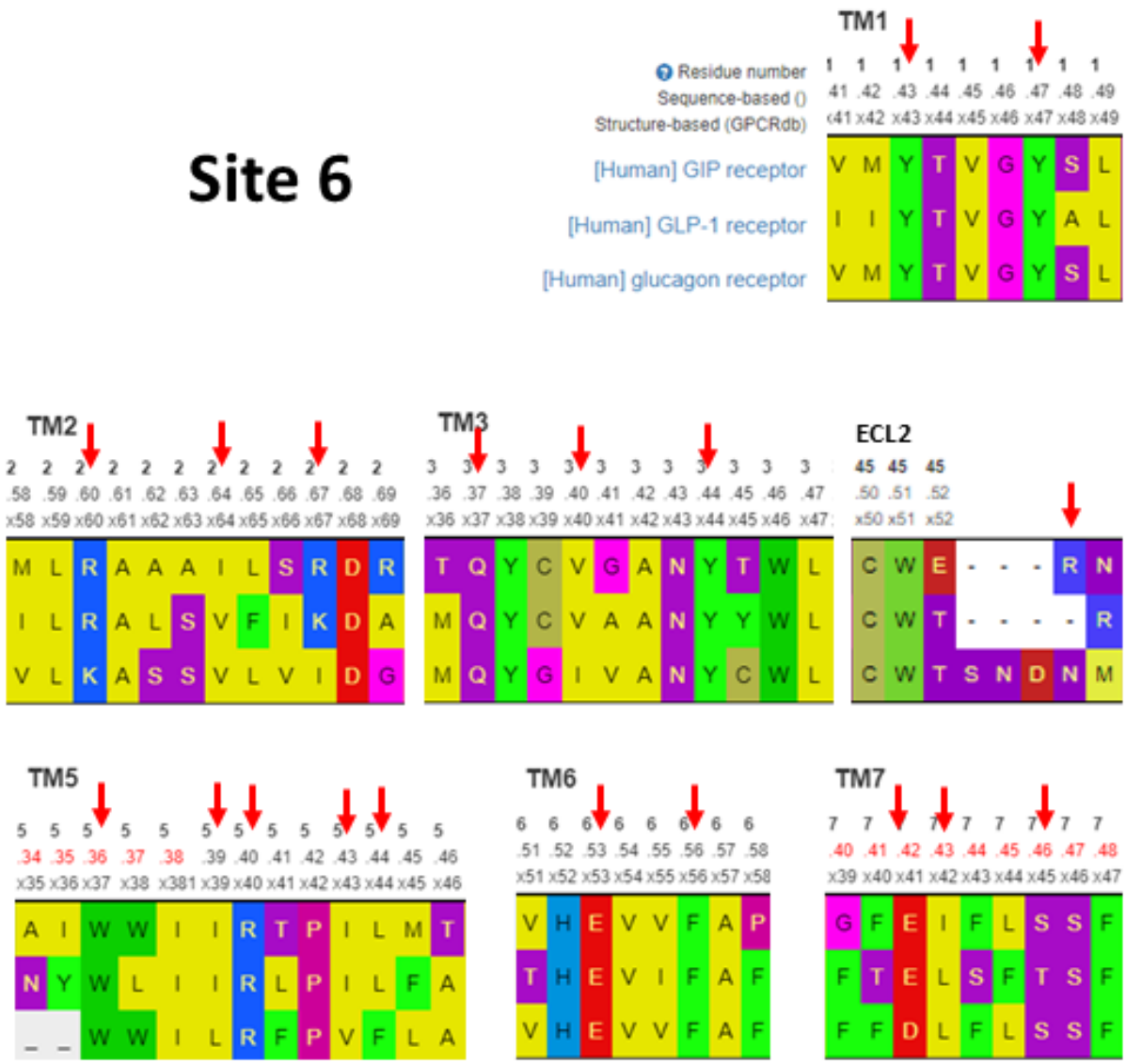

Figure 4.6. Site 6 is fairly conserved across GIPR, GLP-1R and GCGR. Comparing sequences of Site 6 identified as possible allosteric binding site at GIPR with equivalent sites at GLP-1R and GCGR using sequence alignment function at GPCRdb (https://gpcrdb.org/). Red arrows indicate residues identified as potentially important for compound binding.

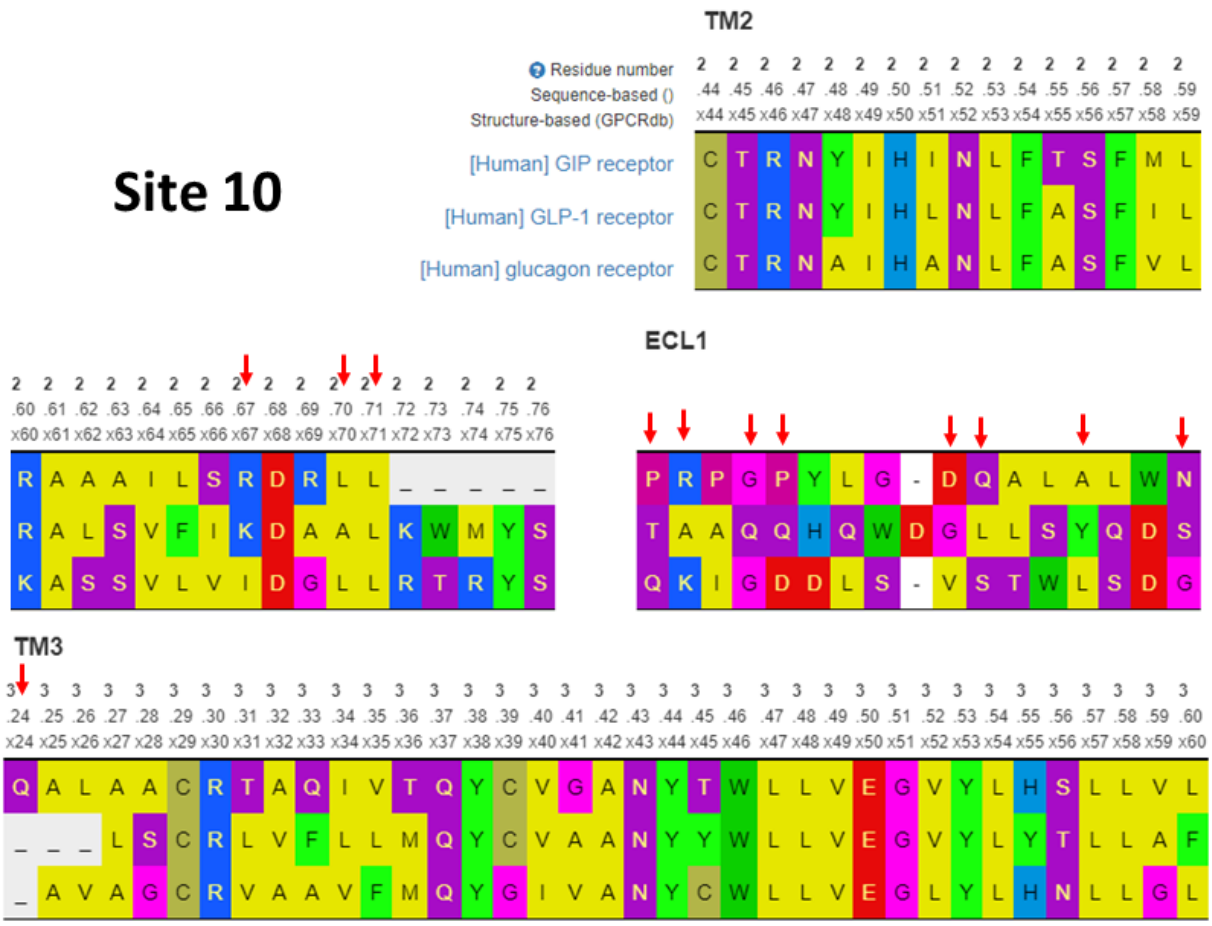

Figure 4.7. Site 10 sequence varies greatly across GIPR, GLP-1R and GCGR. Comparing sequences of Site 10 identified as possible allosteric binding site at GIPR with equivalent sites at GLP-1R and GCGR using sequence alignment function at GPCRdb (https://gpcrdb.org/). Red arrows indicate residues identified as potentially important for compound binding.

Overall, *in silico* blind docking using AutoDock Vina and ICM-Pro and focused docking in GlideXP helped identify key amino acids predicted to be important for recognising C9 and related compounds at the two potential allosteric sites namely the sites 6 and 10. First few amino acids from Site 6 and from Site 10 were then picked to be tested in the first round and to observe any effect of the alanine mutants on the activity of GIPR allosteric modulators *in vitro*. These first few amino acids were Y141$^{1.43}$A, L193$^{2.70}$A, G198A, Q204A, N210A, R289A and W296$^{5.36}$A.

4.2.4 Docking of compounds to the GIPR allosteric site at ECL1

Following the *in silico* blind docking-based analyses described above, the alanine mutants of the suggested GIPR amino acids were made and tested in cAMP accumulation and $(Ca^{2+})_i$ mobilisation

assay, first on their own in order to characterise the mutants and then with GIPR NAMs C3 and C25 (chapter 3). Following characterisation, mutant G198A was not further used in the $(Ca^{2+})_i$ mobilisation assay because its signalling was very weak. The $(Ca^{2+})_i$ mobilisation experiments with C3 yielded insignificant changes in $(Ca^{2+})_i$ levels compared to control. On the other hand, C25 had no effect at GIPR mutant L193$^{2.70}$A, while maintaining normal inhibiting effect on the other mutants.

C25 is a C9-based compound similar to the ones used for the *in silico* blind docking above, whereas C3 is structurally distinct. Therefore, it is not that surprising that C25 matched the *in silico* prediction better than C3. L193$^{2.70}$ is an amino acid located right at the top of TMD2 and shows up in mostly Site 10 poses. Therefore, the next step was to focus on Site 10 and especially the poses, where the C9-based compounds were close to or predicted to be interacting with L193$^{2.70}$ (Figure 4.8). What was encouraging about these poses was that for most molecules, the two aromatic rings that are typical to the C9 and related molecules, were nicely accommodated by some residues through hydrophobic interactions and occasionally through pi-pi stacking and the hydrogen bond interaction of the amide nitrogen from the molecules with amino acid L193$^{2.70}$ was often preserved. For most cases, the carbonyl (next to the central 5-membered thiazole or imidazole ring) oxygen of those molecules forms a hydrogen bonding with an amine group of some GIPR residues. Similar (but effectively reciprocal) hydrogen bonding could be seen between the amine group that follows that carbonyl group of those molecules and a carbonyl oxygen from some GIPR residues. So there appeared to be some consensus in the predicted mode of recognition of these molecules at this site of GIPR. Overall, these poses suggest that GIPR amino acids L193$^{2.70}$, L194, R196, P197, G198, Q204, A207, N210, Q211$^{3.24}$, C216$^{3.29}$, Q220$^{3.33}$, C286$^{45.50}$, W287$^{45.51}$ and E288$^{45.52}$ are important for the binding of C9-based compounds. Out of these, L193$^{2.70}$, G198, Q204 and N210 were already tested in the first round. Therefore, amino acids L194, R196, P197, Q211$^{3.24}$, C216$^{3.29}$, Q220$^{3.33}$, C286$^{45.50}$, W287$^{45.51}$ and E288$^{45.52}$ were picked for the next round of testing.

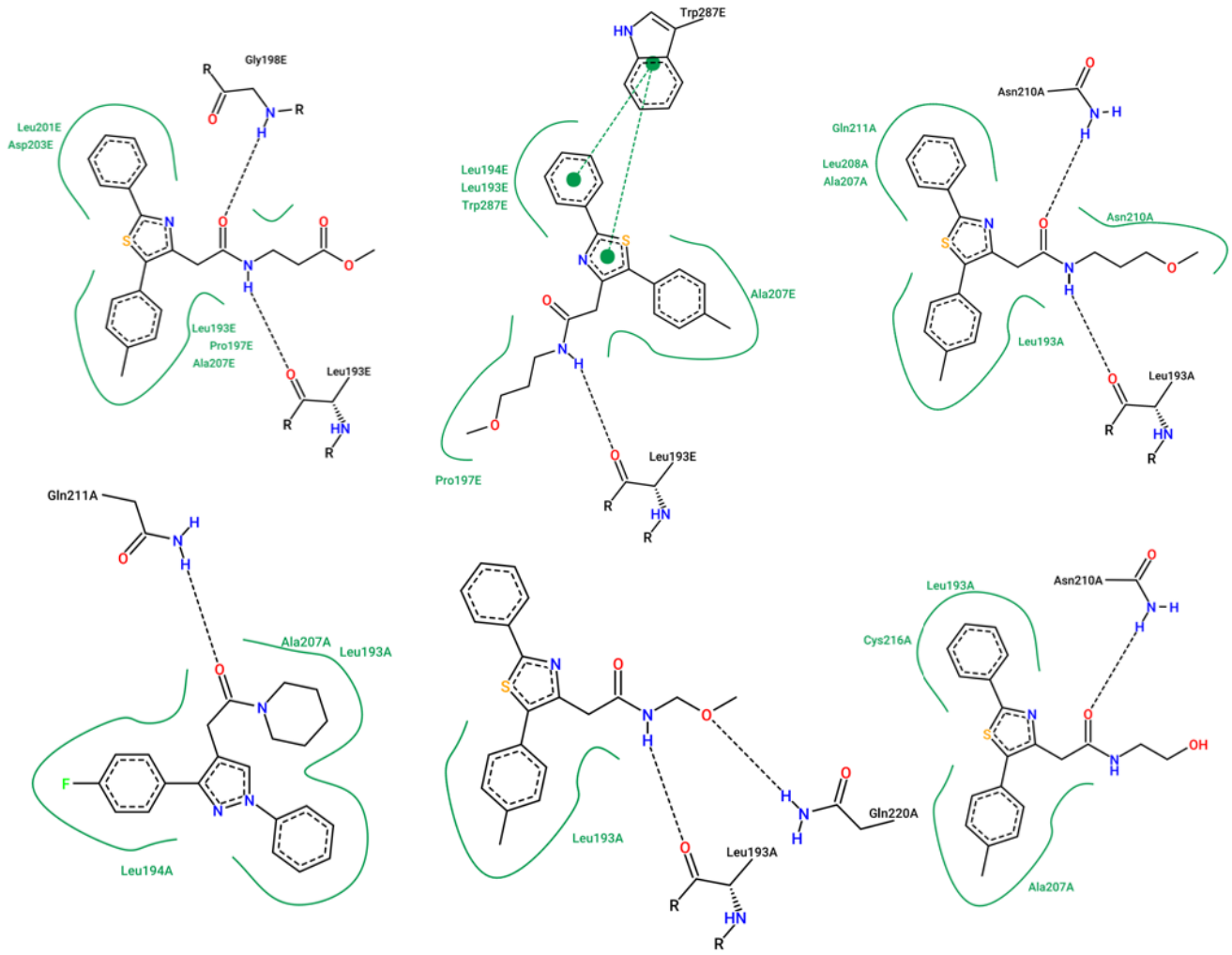

Figure 4.8. L193$^{2.70}$ is predicted to be important for binding/activity of C9-based compounds. Example of 2D diagrams of Site 10, where C9-based compounds (C9, C15, C21, C23 and C73) are predicted by the *in silico* docking to make an interaction with the GIPR amino acid L193$^{2.70}$ located at the top of TMD2. The 2D diagrams were created using Poseview^{TM}.

The second round of experiments showed that C25 hardly affected the $(Ca^{2+})_i$ mobilising response of each of specific GIPR mutants namely R196A, P197A, Q211$^{3.24}$A and Q220$^{3.33}$A. Together with L193$^{2.70}$A, these five Ala mutants at those specific residues of GIPR resulted in common outcome where C25 lost its NAM effect. Therefore, these 5 amino acids appear to be really important for C25 binding and/or mediating its effect as NAM. All these 5 amino acids belong in Site 10, suggesting the region at the top of TMD2/3 and ECL1 is an allosteric binding site of the NAM C25. There was no single pose identified through *in silico* blind or focused docking that would fully agree with the results from the *in vitro* experiments, but there were multiple poses, which did mostly agree (Figure 4.9). It is important to therefore keep in mind that *in silico* docking is just an approximation and that the

compounds are docked against a snapshot of a rigid receptor structure, which in reality is not rigid and therefore the real pose of the compound binding might differ from the prediction. The different conformations of the receptor could be further explored using MD simulations on the receptor model and then docking the compounds to multiple different conformational snapshots of the receptor.

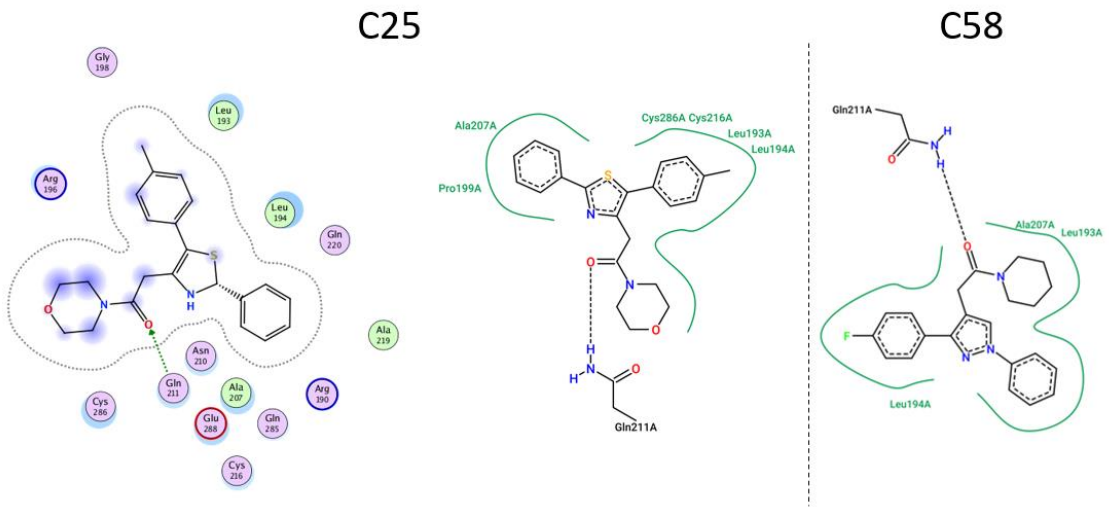

Figure 4.9. Best C25 and C58 binding poses at GIPR homology models. Sample of some of the poses of C25 and C58 binding to GIPR homology models that best agree with the results from *in vitro* pharmacological experiments using GIPR mutants. The poses where generated using AutoDock Vina, ICM-Pro or GlideXP and 2D diagrams were generated using MOE or Poseview^{TM}. In the left diagram pink indicates a polar residue, green indicates greasy residue, red circle indicates acidic residue and blue circle indicates basic residue.

Site 10 mutants were then tested with further compounds. C58, which is a GIPR NAM related to C25, lost its effect at L193$^{2.70}$A, while retaining its activity at the other Site 10 mutants of GIPR (Figure 4.9). This difference between C25 and C58 was very interesting as the compounds are both closely related GIPR NAMs with the difference of C25 being selective for GIPR over GLP-1R and GCGR, while C58 is not. C25 is also very slightly more potent. Next were tested compounds from the T series, which are few NAM type compounds identified through a virtual screening against Site 10 performed by Dr Rahman (University of Cambridge). All of the NAMs from this series lost their effect at multiple Site 10 mutants (viz chapter 3, Table 3.37). Interestingly, T11 appeared to be a NAM for both cAMP accumulation and $(Ca^{2+})_i$ mobilisation assay and testing in these two assays identified different set of amino acids important for conveying the effect of T11. This could be because of each of the two

pathways is activated through different mechanisms within the GIPR receptor and thus also different amino acids are important.

Overall, *in silico* blind docking was used to not only predict an allosteric binding site for GIPR allosteric modulators but also to predict, which amino acids are most likely key for the binding and/or efficacy of the compounds. This enabled a selection of candidate amino acids to be mutated to alanine and subsequent experimental evaluation of those mutant GIPR *in vitro* functional assay. The latter confirmed a multiple of these amino acids from Site 10 to have an impact on the binding or activity of selected compounds, thus confirming Site 10 as the allosteric binding site of the compounds at the GIPR. Among all the compounds, C25 was the most explored through both *in silico* and *in vitro* approaches and the poses showed a good correlation with the *in vitro* mutants results despite not matching perfectly. Next step would then be to dock C58 and more of the T compounds identified as GIPR NAMs and compare these *in silico* predicted poses to the *in vitro* results.

4.3 *In silico* methods for allosteric site identification applied to GIPR

As mentioned earlier, an alternative method to find allosteric modulators is to first find a good allosteric site and then compounds that dock into there. In this section, different techniques for allosteric binding site identification were applied to GLP-1R-based GIPR homology models 1-5 (mainly to save time). Many of these techniques generally identify all good binding sites including both the orthosteric and allosteric sites, but since the orthosteric site at the GIP is known, it can simply be excluded. The aim was to try to identify good allosteric sites at the GIPR and see whether the sites predicted as the compounds' binding sites through *in silico* docking are among them. Secondly, the aim was also to compare the different *in silico* techniques available for allosteric site identification and see if they agree on good binding pockets. The techniques can be approximately divided into five categories: knowledge-, sequence-, geometry-, energy- and dynamics-based techniques.

4.3.1 Knowledge-based techniques

Knowledge-based techniques work by querying existing databases and comparing the submitted protein structure against them in order to find similarities or trends and determine likely ligand-binding sites. A commonly used software application is Pocketome, however, it could not be applied to GIPR as it only works for proteins already in its database with omits all class B1 GPCRs (Kufareva et al., 2012). 3DLigandSite is another server for the prediction of ligand-binding sites that

also lacks class B1 GPCRs, but enables querying of GIPR against the rest of its database (Wass et al., 2010) (http://www.sbg.bio.ic.ac.uk/3dligandsite).

3DLigandSite did not work when applied to GIPR homology models 1,3 and 5 because of insufficient homologous structures with bound ligands identified. For models 2 and 4 several sites were identified including Sites 6,7 and 10 as the most likely ones and additional Sites 2,9,17 and 23 (Figure 4.10). Moreover, this technique identified some specific amino acids that might be important for binding and allostery. For Site 10 in model 2 these were T218, A219 and V222, which is close to the Q220$^{3.33}$ which was found through *in silico* docking and *in vitro* mutagenesis to be important for multiple allosteric modulators eliciting their effects at the GIPR.

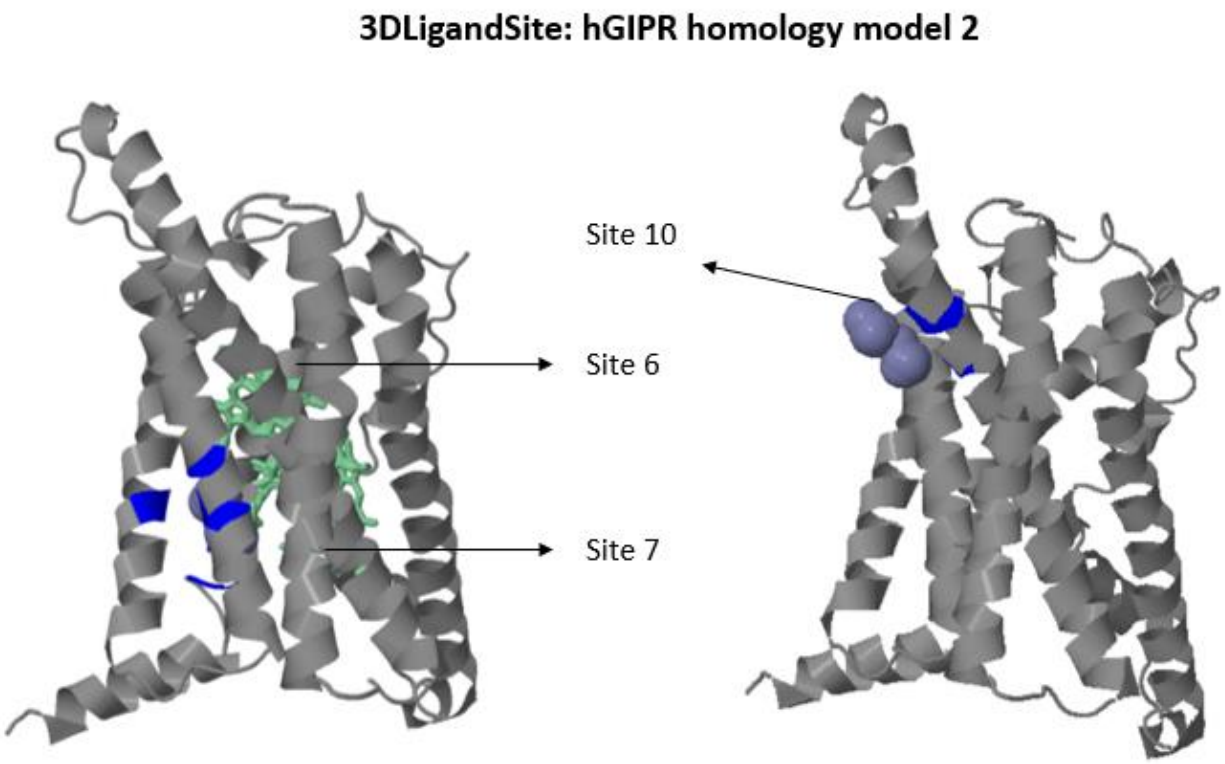

Figure 4.10. Potential ligand-binding sites predicted by 3DLigandSite. Ligand-binding sites (dark blue) are predicted by querying a library of solved structures with ligands and superimposing these onto the GIPR structure. Three main potential binding sites identified at the GIPR are sites 6, 7 and 10.

Nevertheless, this method relies on a structural library based on the PDBs available on 20th January 2010, which means it has no class B1 GPCRs in its database and it is more than 10 years out of date (Wass et al., 2010). Compared to this Pocketome (Kufareva et al., 2012) (www.pocketome.org) is more up to date (based on PDBs available on 26th April 2018) and probably better for proteins

already in its database (like 56 class A GPCRs). Moreover, the ligands co-crystallised with proteins are majorly orthosteric ligands rather than allosteric ones, making these knowledge-based techniques more suitable for identification of orthosteric binding sites, although the precise differences between the structural makeup of orthosteric versus allosteric sites isn't really known. The advantage of 3DLigandSite is that it also offers structure predicting, but since GIPR homology models were already made, this function was not used. Overall, due to the outdatedness of the database and lack of class B1 GPCR structures, the application of this method to GIPR was somewhat limited and the results should be taken with some reservation.

4.3.2 Sequence-based techniques

Sequence-based techniques also query submitted protein against an existing database, but they only compare a sequence without including structural or ligand binding sites (Allain et al., 2014; Cheng and Jiang, 2019; Gómez Tamayo et al., 2018). Multiple sequence alignment (MSA) is an *in silico* technique that aligns three or usually many more biological sequences (protein or nucleic acid) of similar length. From the output, homology can be inferred and the evolutionary relationships between the sequences studied. The theory is that the sites that are biologically and structurally important in proteins like orthosteric and allosteric sites will be more conserved among the proteins (Allain et al., 2014; Gómez Tamayo et al., 2018).

One of the web application enabling MSA of GPCRs the G Protein-Coupled Receptors—Sequence Analysis and Statistics (GPCR-SAS), which enables conservation analysis, covariance analysis and correlation analysis (Gómez Tamayo et al., 2018) (http://lmc.uab.cat/gpcrsas/gpcrsas/). This work focuses on the conservation analysis, as the second two application didn't seem to work much for GIPR. When applied to GIPR, GPCR-SAS compared the GIPR sequence against other class B GPCRs first and then against the glucagon family (GIPR, GCGR, GLP-1R, GLP-2R) second calculating the level of residue conservancy. It results in a snake-plot representations for the sequence of a specific receptor or for the consensus sequence of a group of receptors (Figure 4.11.AB).

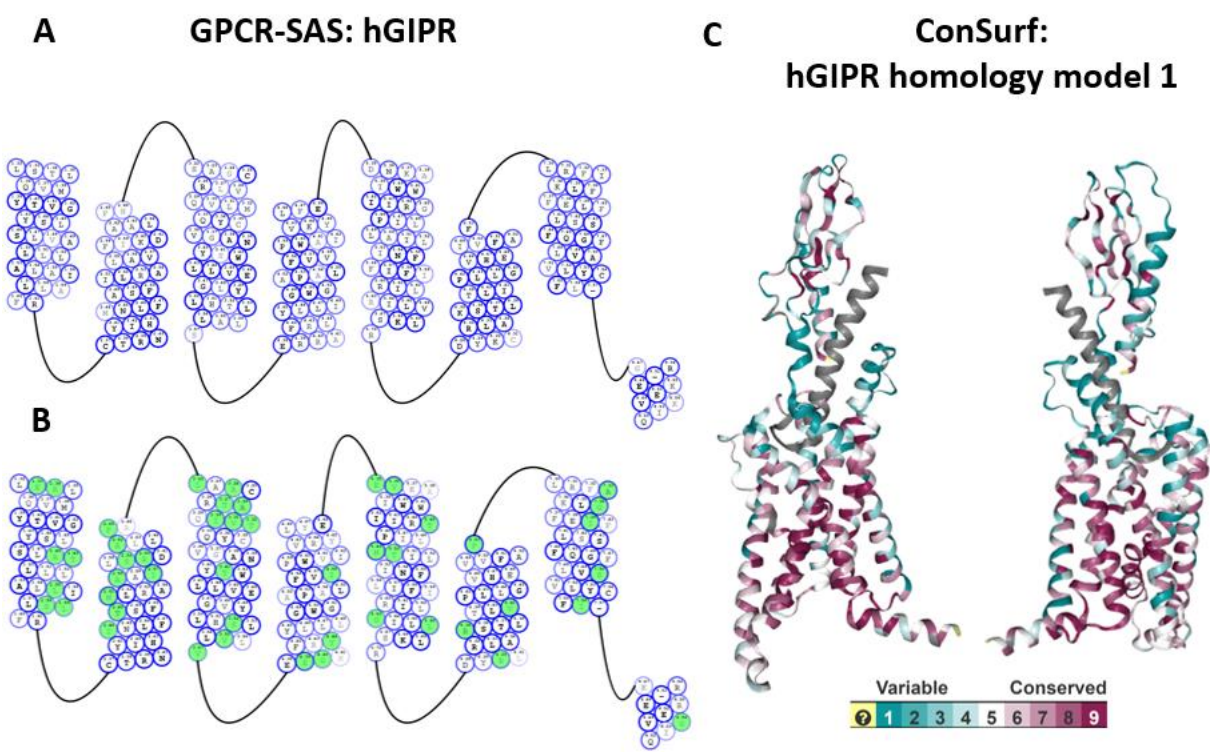

Figure 4.11. Conservation of GIPR residues determined by GPCR-SAS and ConSurf. A. Most conserved amino acids for glucagon family and their frequency of conservation determined by GPCR-SAS (more conserved are darker). B. Frequency of GIPR residue conservation compared to glucagon subfamily (darker blue) and class B GPCRs (darker black) determined by GPCR-SAS. Residues that do not match the most conserved residue for that position are coloured green. C. Residue conservation of GIPR determined by ConSurf and mapped onto GIPR homology model 1.

Another similar algorithmic tool is ConSurf (Armon et al., 2001; Glaser et al., 2003) (https://consurf.tau.ac.il/overview.php). Difference is that it maps the results onto the 3D structure submitted and additionally it also constructs a phylogenetic tree. When applied to model 1 it shows that most conserved transmembrane amino acids are facing inward, probably playing a structural role (Figure 4.11.C). Then fairly conserved is also the bottom of TMD7 and beginning of C-termini, which is known to be important for G protein recruitment. From unstructured regions and loops, ICL1 and ECL2 seem most conserved.

Overall, GPCR-SAS shows how conserved are the residues at specific positions within the class, family or subfamily. The advantage of this technique is it does not require 3D information like depth of a binding pocket, which may be useful for proteins without solved structures like GIPR. ConSurf is then a very similar technique but maps the results onto a 3D structure and also works on the whole sequence rather than just transmembrane regions like GPCR-SAS. Both techniques also miss a ranking

function to rank the sites that many other *in silico* techniques for allosteric site identification have, which makes it easier to prioritise sites.

A disadvantage is that the orthosteric and allosteric binding sites are not the only structurally or functionally important elements in the protein and 3D information like depth and size of a pocket definitely plays a role and on their own, these techniques are unlikely to be sufficient for allosteric site identification. However, once a potential allosteric binding site is identified through a different technique, these methods might be useful on advising how selective compounds docking there might be. If the site is very conserved among the family or the GPCR class, then its less likely that compounds binding there would be very selective. If we apply this to Site 6, which partly overlaps with the orthosteric site inside the protein, it is quite conserved and indeed GIP can also elicit responses at GLP-1R and GCGR. Site 10, mapped only on ConSurf, then shows the region as fairly variable so compounds docking there have potential for selectivity.

A superstructure of MSA is a statistical coupling analysis, which uses MSA to identify networks of coevolving residues (termed 'sectors') in a protein family. In theory, allosteric binding sites could be identified as such sectors (Rivoire et al., 2016). Here pySCA, a python code for running SCA on linux written by Ranganathan lab (https://github.com/ranganathanlab/pySCA, 2019 version), was applied to GIPR (Rivoire et al., 2016). First, PSI-BLAST was run to find 500 related sequences to the GIPR query sequence and the resultant MSA fasta file was fed to the pySCA code, which was slightly tweaked so that it would run (Altschul et al., 1997) (https://blast.ncbi.nlm.nih.gov/Blast.cgi). In the end, about 119 sequences were used to construct the final SCA, as the rest was eliminated due to being unusable or too similar to each other.

The pySCA method found sectors of coevolving amino acids on the hGPR, which were further divided into 10 subsections (Figure 4.12). These identified amino acids are likely key for structural and functional needs of the protein including allosteric regulation (Rivoire et al., 2016). However, SCA runs into the same problems as the MSA techniques mentioned above. It identifies too much of the GIPR protein without ranking the sites, so it makes it almost impossible to pinpoint locations of potential allosteric sites from it. It also omits the 3D information of the sites and additionally, there were problem with getting sufficiently large MSA file that would fulfil all the criteria, probably limiting the resultant SCA.

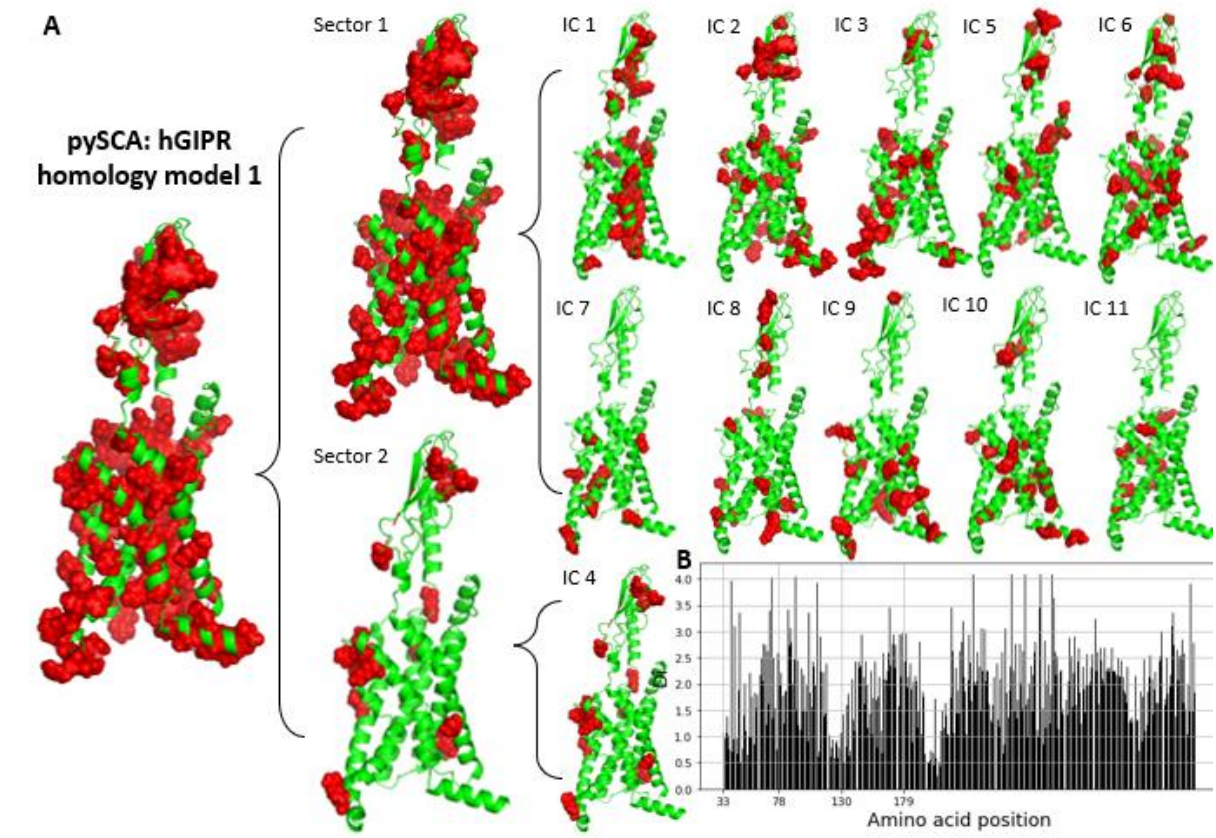

Figure 4.12. Two sectors of coevolving GIPR residues identified by pySCA. A. Sequence-based approach that uses a MSA to identify networks of coevolving residues (red) in a protein family divided into sectors and further into independent components (IC) 1-11. B. Conservation plot of individual GIPR amino acids.

4.3.3 Geometry-based techniques

Geometry-based techniques in contrast to sequence-based technique relay only on atomic coordinates of the protein and rank the sites based on geometric values such as volume and shape, while omitting sequence information. A good binding pocket is deep enough and site that is shallow or partially collapsed gets rejected. Geometry-based techniques are also often part of other web applications as will be seen later below.

A first method applied to GIPR was POcket-Cavity Search Application (POCASA), which is a purely geometric search algorithm based on a grid system and probe sphere algorithmic methods (explained in introduction) and it ranks pockets based on volume, volume depth and average volume depth (Yu et al., 2010) (http://g6altair.sci.hokudai.ac.jp/g6/service/pocasa/). Default setting of the probe range was used (larger probe spheres can be used for large ligands or large flat pockets, while small probe spheres can be used for small ligands). When applied to model 1, binding to GIP was

predicted similarly to results obtained from *in silico* blind docking. When applied to model 2 and others, sites 6, 7 and 10 were again identified as best candidates based on pure geometry (Figure 4.13).

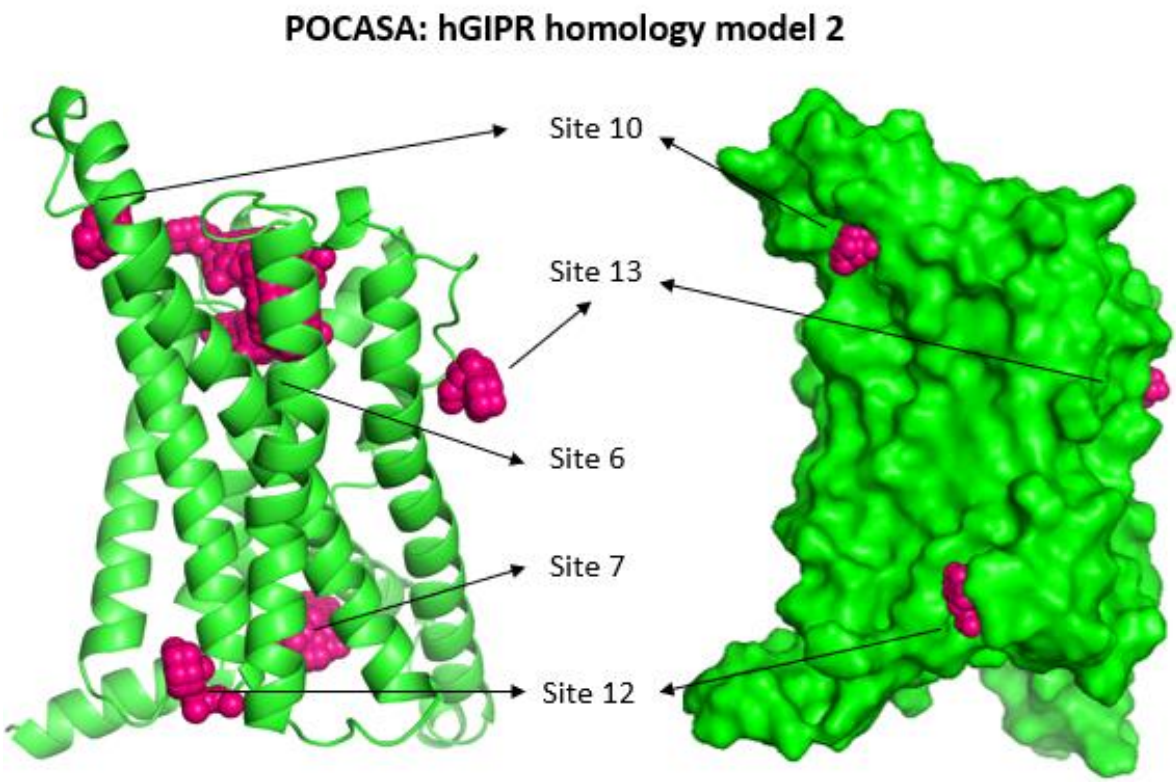

Figure 4.13. Potential ligand-binding sites predicted by POCASA. This geometry-based *in silico* method identifies ligand-binding sites considering only atomic coordinates of the protein and ranks the sites based on geometric values such as volume and shape.

Geometry is definitely an important parameter for allosteric binding site that should be taken into account. But deep cavity on its own doesn't necessarily have to have a lot of functionally important amino acids and the signal from compound binding there might not get propagated throughout the protein efficiently enough to affect the protein function. Still, geometry-based techniques remain very useful as part of the allosteric site evaluation.

4.3.4 Energy-based techniques

Compared with geometry-based methods, energetic based methods are more computationally demanding, which limits their applicability to large-scale structural data sets, but are fine for an

application to one protein like GIPR. Energy-based techniques evaluate the interactions between small organic probes and the target protein to identify binding sites. Here, FTMap, a computational solvent mapping website, which samples billions of positions of small organic molecules used as probes and scores the probe poses using a detailed energy expression, is applied to GIPR homology models (Kozakov et al., 2015) (https://ftmap.bu.edu).

FTMap failed to work on model 1, possibly because of the presence of the GIP as model 2 differs only in the exclusion of GIP and N-termini from the model. However, applied on models 2-5, FTMap identified sites 6,7, 9, 10 and19 with sites 6, 7 and 10 clearly the most dominating ones (Figure 4.14). Sites 6 and 7 were present in all 4 models, while site 10 was identified only in models 4 and 5.

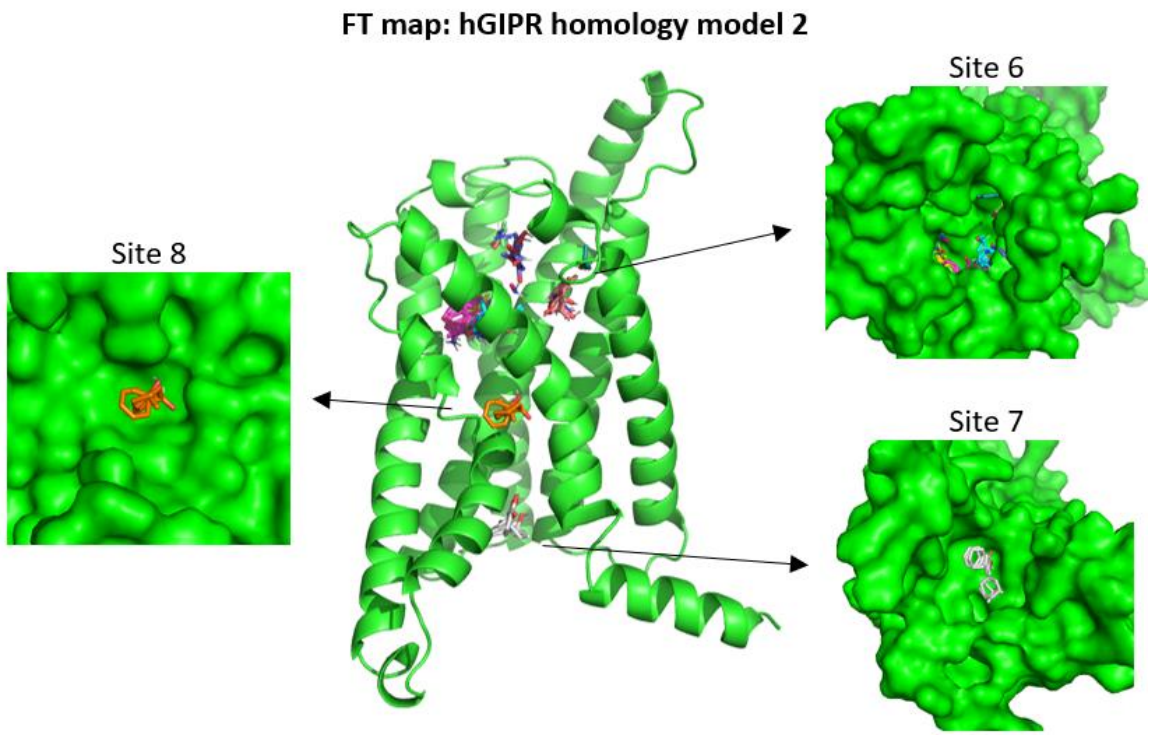

Figure 4.14. Potential small molecule binding pockets predicted by FTMap server. The algorithm uses the so called 'computational solvent mapping' approach which globally samples the surface of target proteins using molecular probes, small molecules or functional groups to identify potentially favourable binding positions (Hall et al., 2012).

4.3.5 Dynamics-based techniques

Some allosteric sites exist exclusively in the intermediate protein states, which is why the techniques above applied to a rigid snapshot of the protein captured by the Cryo-Em or X-ray crystallography may not find them. On the other hand, dynamics-based techniques like MD simulations, Markov state models or coarse-grained and lattice modelling may capture them (Cheng and Jiang, 2019). Due to high time and computational requirements the MD simulations were not used here. Instead, Markov state models and normal mode analysis (NMA) of elastic network models (ENM) using coarse grained representation of the protein structure is applied to the GIPR.

NMA is developed based on the hypothesis that the largest movements in a protein are functionally relevant and it requires less computational power compared to MD simulations, which led to the development of several web servers performing normal mode calculations. First of these is SPACER, which integrates NMA with Monte Carlo simulations to predict biologically active sites, including latent allosteric sites (Goncearenco et al., 2013) (http://allostery.bii.a-star.edu.sg/). It predicts binding sites based on local closeness of 'm' closes neighbouring atoms, binding leverage ("an ability of a binding site to couple to intrinsic motions of a protein by quantifying the cost of the binding site deformation when ligand is present and resisting the motion") and coupling leverage between 2 sites (quantitative characteristic of allosteric communication).

When applied to GIPR models 1-5 (Figure 4.15), the most local closeness was exhibited by the middle TM residues, which is what one would expect. From the known sites, this would be mostly sites 6 and 7. The binding leverage (ligand-binding modes) is calculated using the Monte Carlo docking simulations and a peptide consisting of 2−6Cα atoms was used a probe. Model 1 shows that a small probe favours N-termini, while larger middle bottom. For the other models the prevalent site was mostly site 7 and especially amino acids L165, N170, H173, C393, N396, K397, E398 and V399. This bottom part of the receptor is known to play an active role in the recruitment of signalling partners. Therefore, allosteric modulators binding there could enhance or disrupt these partnerships and thus effect GIPR signalling.

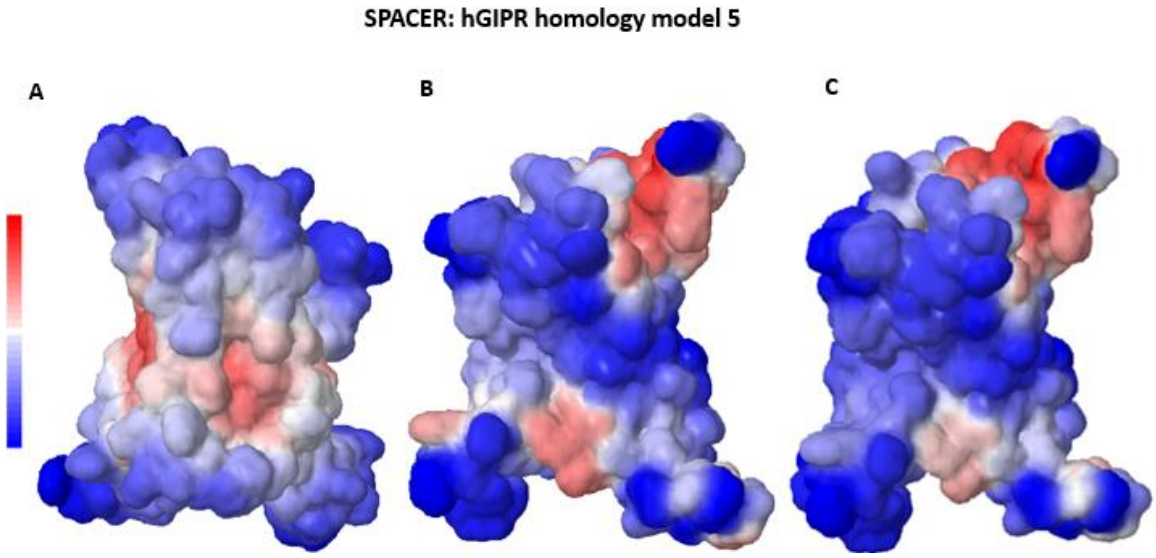

Figure 4.15. Potential ligand-binding sites determined by SPACER. *In silico* techniques using a combination of NMA and Monte Carlo simulations to predict ligand-binding sites based on local closeness (A), binding leverage (B) and allosteric communication (C). Output is normalised to colour scale 0-100 (red is highest, blue is lowest).

The quantification of allosteric communication unfortunately did not work for model 1, but for models 2, 3 and 4 site 7 was identified but it was only shown to interact with its immediate surroundings. For model 4, an additional site at the top of TMD 6 and 7 was identified but again only interacting with its immediate surroundings. For model 5, site 10 was identified and especially amino acids Ser189, **Arg190**, Asp191, Arg192, Leu193$^{2.70}$, Leu194 and Pro195. This site was shown to allosterically interact with bottom of TM6 and 7 and C-termini of the GIPR, which is where the G protein gets recruited (Cabrera-Vera et al., 2003; Hall et al., 2012). Site 10 was therefore most promising site identified showing allosteric communication with the rest of the GIPR protein.

Another NMA web server is PARS, which predicts allosteric sites based on the alteration of protein flexibility upon ligand binding (Panjkovich and Daura, 2014) (http://bioinf.uab.cat/pars). It predicts the ligand-binding sites on the protein surface using the LIGSITEcs program and then analyses the sites in terms of their structural conservation and their potential to affect protein flexibility (Huang and Schroeder, 2006; Panjkovich and Daura, 2014). Finally, the eight best pockets are then shown in ranked order. When applied to GIPR, sites 2, 6 and 7 were identified across most models and sites 6 and 7 have the most effect on protein flexibility according to the NMA (Figure 4.16). Compared to other methods, site 10 is not really that pronounced here.

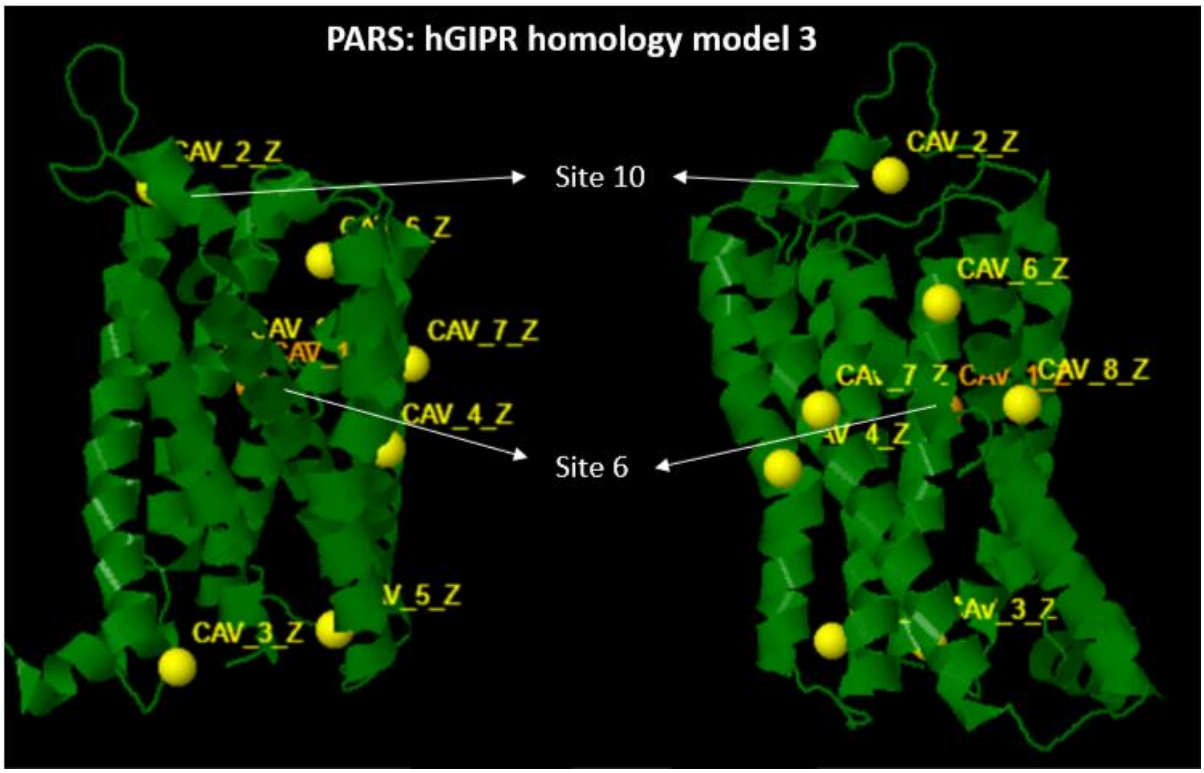

Figure 4.16. Potential ligand-binding pockets predicted by PARS. The algorithm predicts ligand-binding pockets on the GIPR surface using LIGSITEcs program (Huang and Schroeder, 2006) and ranks them in terms of their structural conservation and their potential to affect protein flexibility.

4.3.6 Overall summary and comparison of the *in silico* methods for allosteric site identification

Many different *in silico* techniques enabling allosteric site identification were introduced here. Together, they identified few sites namely the sites 6,7 and 10 as the best potential allosteric sites at the GIPR, which correlated well with the results obtained through *in silico* docking (Table 4.5). Generally, there was an overlap between these techniques and many of them combine more than one approach. For example, FTMap combines geometrical information with an energy-based approach, while SPACER combines NMA with Markov state models. The repeating themes are especially accessibility by the ligands and sequence conservation, while effect on flexibility might be a less common criterium.

Table 4.5. Sites 6, 7 and 10 identified as best candidate allosteric sites at GIPR. Major candidate allosteric sites identified using each technique across GIPR homology models 1-5.

Site	Description	3DLigandSite	POCASA	FTMap	SPACER	PARS	Total
2	bottom TMD 3/4/5 + ICL2	0.5				0.8	**0.26**
6	top centre	1	1	1		1	**0.80**
7	bottom centre	1	1	1	1	0.8	**0.96**
8	middle TMD 5/6/7			0.25		0.6	**0.17**
9	middle of TMD 3/4/5	0.5		0.25	0.2	0.4	**0.27**
10	top TMD 2/3	0.5	1	0.5		0.4	**0.48**
16	Bottom TM7					0.4	**0.08**
17	N-termini	1			0.2		**0.24**
21	Top TMD 6/7 + ECL3				0.2	0.6	**0.16**
23	Top TMD 4/5 + ECL2	0.5				0.4	**0.18**

Many of the techniques used here were also not tailored only for allosteric site identification, so the results have to be evaluated critically. This was particularly obvious for sequence-based techniques that identify any structurally and functionally important amino acids or for knowledge-based methods whose databases consists of ligands mostly docked in the orthosteric sites. The tailoring of the techniques more towards purely allosteric site identification might be hindered by the lack of many structures solved with allosteric modulators and by the poor understanding of the key differences between orthosteric and allosteric site makeup. Overall, the best techniques seem to be FTMap, which is geometry and energy-based, and PARS or SPACER, which uses a mix of NMA, Monte Carlo Simulations and even conservation analysis and geometry information. This well demonstrates the fact that together these techniques give important and relevant information about the potential allosteric binding sites at the GIPR, while individually they may be lacking.

4.4 Discussion

In this chapter, *in silico* docking was used to identify Site 6 (top middle of the receptor TMDs below the orthosteric binding site) and Site 10 (top of TMD2/3 and ECL1) as candidate allosteric sites and to identify potential key amino acids for compounds binding, which could then be tested *in vitro* resulting in confirmation of Site 10 as the binding site of GIPR allosteric modulators. Moreover, *in silico* techniques for allosteric site identification were used and confirmed Site 10 as one of the best allosteric binding sites at the GIPR.

4.4.1 GIPR allosteric binding site at the top of TMD2/3 and ECL1

Main aim of this chapter was to identify the allosteric binding site at the GIPR, where the GIPR allosteric modulators bind. Therefore, *in silico* blind docking of C9-related compounds was carried out against GIPR homology models and two main candidates were identified – Site 6 and Site 10. Site 6 was consistently predicted across all GIPR homology models used except model 7 based on $A_{2A}R$, while Site 10 was most strongly predicted for GLP-1R and PTHR1 based models 4-6. One of the reasons while Site 6 was picked up so much across the models as a possible binding site might be the fact that homology models 2-9 were missing the N-termini and had no GIP attached. This meant that the top middle of the transmembrane part of the receptor was accessible and might have contributed to the large number of dockings there. In reality, however, the N-termini most likely at least partly obstructs the access of the compounds. The second concern was then that binding so close to the orthosteric site would prevent GIP from binding even in case of PAMs like C9, although Méndez et al. (2020) suggested a similar allosteric binding pocket at the GLP-1R based on their *in silico* experiments as discussed before, so it is still possible the compounds might fit just below the orthosteric site.

Another potential concern with Site 6 lies with its classification. The numbering of the sites was purely arbitrary and created for the purpose of easy distinguishment between the sites. When one looks at the Site 6 poses, all of them did lie at the top middle part of the receptor, however, the 3D space assigned to this site was quite large and diffuse, which would account for the large number of poses assigned there. This was clearly visible on the 2D binding diagrams derived from Site 6, which showed a large range of amino acids with less repeatability. On the other hand, Site 10 was endowed with much more confined 3D space and there was large agreement in residues that appeared to be critical for the activity of those compounds.

As *in silico* experiments can only give us prediction and not proof, a combinational approach of *in silico* and *in vitro* techniques was needed. Based on the 2D diagrams of the generated poses, potential key amino acids for compounds binding at both Site 6 and Site 10 were selected. Chapter 3 discussed how alanine mutagenesis and second messenger assays were then used to confirm Site 10 as the allosteric binding site of first C25 and then also C58, both compounds related to C9.

The identification of Site 10 then enabled an *in silico* screen against Site 10 conducted by Dr Rahman (University of Cambridge), which identified potential new GIPR allosteric modulators T1-T27. In chapter 3, *in vitro* experiments confirmed T2, T5, T10, T11, T13, T18 and T26 as GIPR NAMs and T21 as potentially a weak GIPR PAM. It also showed that T5, T10, T11 and T18 do bind Site 10 as predicted based on the fact they were selected specifically against this site.

Overall, this chapter identified and together with *in vitro* experiments in chapter 3 confirmed Site 10 as the allosteric binding site for GIPR allosteric modulators.

4.4.2 Exploring compound binding at Site 10 and their selectivity

Binding to Site 10 was first confirmed for compound C25, when C25 failed to have any effect on GIPR mutant L193$^{2.70}$A, while the mutant still responded to GIP (chapter 3). This then led to a more thorough exploration of Site 10 and R196A, P197, Q211$^{3.24}$ and Q220$^{3.33}$ were first predicted *in silico* and then confirmed *in vitro* to be important for C25 binding or activity (Chapter 3, Table 3.37). On the other hand, C58 lost activity only at L193$^{2.70}$A and no other of the tested mutants. C25 and C58 are closely related and both GIPR NAMs selective for calcium pathway over cAMP pathway and β-arrestin recruitment, but C25 is selective for GIPR over GLP-1R and GCGR, while C58 is not. As shown in Figure 4.7, there is quite a bit of variability between the top of TMD2/3 and ECL1 regions of the three receptors. More specifically, GIPR amino acid L193$^{2.70}$ is conserved across GIPR and GCGR, but not GLP-1R. The rest of the amino acids important for C25 (R196, P197, Q211$^{3.24}$ and Q220$^{3.33}$) are not conserved at all across the three receptor and some of them don't even share the same charges or polarity with their counterparts. This nicely compliments the fact that C25 is GIPR selective as it acts through the non-conserved amino acids. It is unlikely that C58 only acts through one amino acid, so to better understand its action more poses of C58 need to be generated and few more amino acids specific for this compound need to be tested, but the hypothesis is that C58 acts through more conserved amino acids than C25.

Out of the T compounds identified, T2 and T5 are also selective GIPR NAMs. The mutant *in vitro* experiments were subsequently carried out for T5 in chapter 3 and P197, Q204, N210, Q211$^{3.24}$ and E288$^{45.52}$ were identified as amino acids important for T5 binding and/or activity. T5 is NAM selective for calcium pathway same as C25 and the amino acids P197 and Q211$^{3.24}$ are shared between the two compounds despite them having different chemical scaffolds. The remaining amino acids Q204, N210 and E288$^{45.52}$ are then different to C25 but again not conserved. This approach enabled us to identify multiple amino acids key for NAM activity while retaining GIPR selectivity and this knowledge could be exploited when designing new more potent GIPR allosteric modulators. This could be done for example by preferentially selecting compounds indicated to bind these amino acids or by chemically modifying other compounds to interact with these amino acids.

Another important characteristic of the compounds is their bias towards cAMP or calcium pathway. Despite Site 10 being originally identified as an allosteric binding site of C25 and C58, both NAMs selective for $(Ca^{2+})_i$ mobilisation pathway, among the T compounds there are such active at both

cAMP and calcium pathway or just cAMP pathway. It is therefore not the whole site but probably specific amino acids responsible for propagating compound effects across the receptors and selectively affecting only certain signalling pathways as discussed in chapter 3. This is further supported by Wootten et al. (2016) work, where they show that the amino acids present in the ECLs of GLP-1R, a closely related receptor to GIPR, are important for triggering biased signalling. The *in vitro* results of testing T11 with mutants in both cAMP accumulation and $(Ca^{2+})_i$ mobilisation assay also show different amino acids seem to be key for each of the pathways. To be able to better understand this signalling bias of GIPR allosteric modulators it would be useful to generate docking poses with T compounds and compare them both with the *in vitro* results and among themselves.

4.4.3 Advantages and disadvantages of various *in silico* techniques

Another aim of this chapter was to investigate potential allosteric binding sites at GIPR using *in silico* techniques for allosteric site identification and compare these techniques among themselves. Representative knowledge-, sequence-, geometry-, energy- and dynamics-based techniques were used and together they identified Site 6, Site 7 and Site 10 as best candidate allosteric binding sites at the GIPR. This closely agrees with the sites predicted through *in silico* docking for C9-related compounds. Site 6 suffers from the problems discussed above, while Site 7 is located on the intracellular side of the receptor and thus might not be reachable by all the compounds. Therefore, Site 10 has been confirmed as a good allosteric binding site to focus on for drug discovery of GIPR allosteric modulators.

Comparing the various techniques between themselves, probably the least useful for our aims were proven to be the sequence-based techniques. These are not tailored for allosteric site identification and instead they identify any structurally and functionally important amino acids. Knowledge-based methods were then largely limited by the small number of structures solved with allosteric modulators and outdated structure banks, thus majorly focusing on orthosteric sites, and also poor understanding of the key differences between orthosteric and allosteric site makeup. The geometry- and energy-based techniques have then proven the best relying on simple characteristic like the depth of the site 3D space and docking of small molecules. Since the energy-based techniques incorporate docking of small molecules it is not that surprising that results corelate well with the *in silico* docking results from the beginning of this chapter as the small molecules used there are similar to parts of the GIPR allosteric modulators' structures.

Dynamics-based techniques then offer slightly more information as SPACER can for example additionally identify regions communicating with each other. MD-simulations, which could also be

classified under dynamics-based techniques hasn't been performed in this study as they require large amounts of knowledge and computational power but exploiting them for exploration of key compounds binding and activity at GIPR might be very useful to better understand compound activity.

4.5 Conclusion

GIPR has been indicated as good target for the development of diabetes type II and obesity treatment. Instead of focusing on traditional orthosteric drugs, this work focuses on allosteric modulators instead. Allosteric modulators are compounds binding outside the orthosteric site and provide many benefits over orthosteric drugs like probe dependency or better potential for receptor selectivity and development of small molecule GIPR drugs.

In this chapter, two approaches were carried out side by side with the aim of identifying a good allosteric site at the GIPR and finding potent allosteric modulators targeting this side. In the first approach, *in silico* blind docking of already known C9-related GIPR allosteric modulators was carried out and Site 6 (top middle of the receptor TMDs below the orthosteric binding site) and Site 10 (top of TMD2/3 and ECL1) were indicated as most likely binding sites for the compounds with Site 10 being confirmed *in vitro* in chapter 3. The second approach was to use *in silico* techniques for allosteric site identification and explore the available binding sites at GIPR. This approach yielded Site 6, Site 7 (bottom middle of the receptor) and Site 10 as the best candidate allosteric site at the GIPR. Therefore, together these two approaches indicate Site 10 as an ideal allosteric binding site at the GIPR.

The successful identification of GIPR allosteric binding site enabled an *in silico* screen against this site carried out by Dr Rahman (University of Cambridge), resulting in the discovery of several new GIPR allosteric compounds including GIPR selective ones or ones biased towards certain signalling pathways. This means there are now several chemical scaffolds available for future development of GIPR targeting drugs. The next logical step would then be to explore the binding and actions of the newly identified GIPR allosteric modulators in more detail using *in silico* docking to Site 10 or even MD simulations for most important compounds. Since first structure of GIPR has also been solved last year (PDB id 7DTY)(Zhao et al., 2021a), it would be reasonable to use this structure instead of the so far used GIPR homology models.

Overall, this chapter successfully uncovered a GIPR allosteric binding site located at the top of TMD2/3 and ECL1, enabled an *in silico* screen against this site leading to the identification of new GIPR allosteric modulators and started to uncover the differences between the binding and actions of the different compounds.

Chapter 5. Pharmacological characterisation of novel adenosine A_1 receptor-selective agonists

5.1 Introduction

The A_1R is one of the four ARs that belong in class A GPCRs. While A_1R and A_3R are predominantly $G_{i/o}$-coupled leading to inhibition of intracellular cAMP, $A_{2A}R$ and $A_{2B}R$ are G_s-coupled receptors leading to increase of intracellular cAMP. A_1R is widely distributed in the human body and stimulating this receptor is thought to hold therapeutic potential in multiple disorders including but not limited to glaucoma, type 2 diabetes mellitus, pain, epilepsy and cerebral ischemia (Baltos et al., 2016; Sawynok, 2016; Varani et al., 2017; Weltha et al., 2019). A_1R has high expression in the brain and since adenosine, a natural AR ligand, is an endogenous anticonvulsant and seizure terminator in the brain, augmentation of A_1R signalling holds promise for the suppression of seizures in epilepsy and possibly even preventing its progression (Boison, 2008; Weltha et al., 2019). Furthermore, due to exerting effect on the central nervous system (CNS), A_1R has antinociceptive profile in various preclinical pain models and A_1R agonists are extensively researched as pain treatment (Sawynok, 2016; Wall et al., 2022).

Current A_1R agonists elicit various responses, particularly in the central nervous system (CNS) and in the cardiorespiratory system. In the CNS A_1Rs inhibit synaptic transmission, induce neuronal hyperpolarization, and cause sedation, while in the cardiorespiratory system A_1Rs slow the heart (bradycardia), contribute to reducing blood pressure (hypotension), and depress respiration (dyspnea) (Dunwiddie and Masino, 2001; Headrick et al., 2013; Koeppen et al., 2009; Sawynok, 2016; Vecchio et al., 2018). This wide expression profile of the A_1R in the body and the potential for many side effects caused by the none-selectiveness of many potential drugs based on the adenosine, which is near equipotent agonist across the four AR subtypes, led to the fact that despite more than four decades of intense medicinal research very few compounds have actually made it to the clinic (Chen et al., 2013; Jacobson and Gao, 2006). Therefore, in order to overcome these widespread side effects that limit the therapeutical use of A_1R agonists, more selective and possibly even biased agonists that could selectively target specific signalling pathways through selective G protein or β-arrestin coupling are needed (Kenakin, 2019; Wootten et al., 2018).

Regarding the structures of known A_1R agonists, several potent and selective compounds are based on adenosine with C-2 or N6 position substitutions (e.g. chloride or cycloalkyl-/bicycloalkyl-groups, respectively) (Jacobson et al., 2019; Knight et al., 2016; Petrelli et al., 2018; Tosh et al., 2019).

It has also been shown that the C-5' position tolerates certain substitutions resulting in compounds like for example NECA. Moreover, bulky pyrazole groups substitutions at this position resulted in some potent and selective A_1R agonists that showed analgesic effects in mice (Petrelli et al., 2018).

Another known potent A_1R agonists is BnOCPA (Knight et al., 2016). As mentioned above, the development of therapeutic GPCR agents is complicated by their pleiotropic coupling to multiple G proteins and intracellular signalling pathways and this is particularly true for A_1R, whose clinical potential is undermined by the sedation and cardiorespiratory depression caused by conventional agonists. Therefore, biased ligands that can selectively target these pathways are needed. BnOCPA is a potent A_1R-selective agonist that has been shown to be a powerful analgesic but does not cause sedation, bradycardia, hypotension or respiratory depression (Knight et al., 2016; Wall et al., 2022). Furthermore, Wall et al. (2022) have shown that BnOCPA is a selective Gα agonist in exclusively activating G_{ob} among the six members of the $G\alpha i_{/o}$ family of G protein subunits, and in the absence of β-arrestin recruitment. BnOCPA thus demonstrates a highly specific Gα-selective activation of the native A_1R making it a very therapeutically promising compound.

Deganutti et al. (2021) has then employed MD simulations to research the binding of BnOCPA to A_1R using the cryo-EM structure of the active adenosine-bound A_1R-heterotrimeric G_{i2} protein complex (PDB code 6D9H20) (Draper-Joyce et al., 2018). This work uncovered three binding modes of BnOCPA due to high flexibility of the N6-appended benzyloxy group. Based on the previous work on BnOCPA and especially the MD simulations of its binding at the A_1R, a new series of adenosine- and NECA-based compounds with extended N^6-benzyloxy- and N^6-phenoxycyclopentyl substituents was designed by Dr Lochner (University of Bern).

The aim in this chapter is to further explore BnOCPA binding to the A_1R using *in vitro* techniques like site-directed alanine mutagenesis and cAMP accumulation assays. The cAMP accumulation assay and NanoBRET binding assay will then also be used to comprehensively characterise potency, selectivity and affinity of the new adenosine- and NECA-based derivates across the four human AR subtypes and rat A_1R with the aim of identifying compounds with improved potency at A_1R while maintaining or improving the subtype-selectivity of BnOCPA (Figure 5.1). The research in this chapter was published in Preti et al. (2022), Suchankova et al. (2022) and Wall et al. (2022).

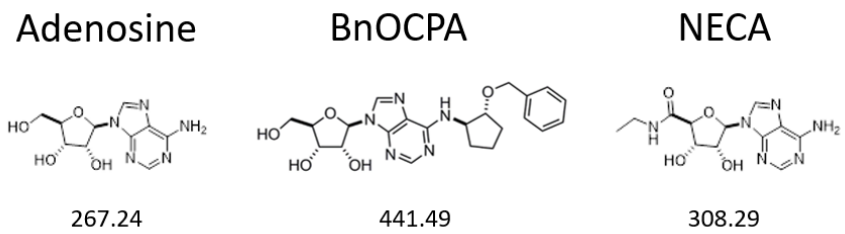

Figure 5.1. Structures of selected A_1R agonists. 2D structures and molecular weight (g/mol) of adenosine, NECA and BnOCPA compounds.

5.2 The effect of A_1R mutations on agonist efficacy

As mentioned above, MD simulations were used to probe BnOCPA binding to A_1R (Deganutti et al., 2021a). In more detailed they modelled three different systems - G_{oa} and G_{ob} subunit bound to the A_1R:BnOCPA and G_{ob} subunit bound to A_1R:HOCPA. HOCPA is another A_1R agonist based on the adenosine/CPA scaffold and it is a stereoisomer of GR79236 (Gurden et al., 1993; Knight et al., 2016; Strong et al., 1993). These MD simulations predicted that residues R291$^{7.56}$ and I292$^{8.47}$, which are located under the N7.49PXXY$^{7.53}$ motif are likely involved in A_1R/Gα coupling and show a different propensity to interact with G_{oa} or G_{ob} protein. It was therefore suggested that a particular A_1R conformation could be stabilized by BnOCPA more than by the other agonists resulting in the selective G_{ob} protein activation.

To test this hypothesis, site-directed mutagenesis of amino acids R291$^{7.56}$, I292$^{8.47}$ and the adjacent hydrophilic residues Q293$^{8.48}$ and K294$^{8.49}$ to alanine was undertaken and agonist effects on these mutants was tested compared to WT A_1R. Currently, none of these residues were reported to affect binding (GPCRdb 2022; Kooistra et al., 2021). First, Flp-In CHO cell lines stably expressing either one of these four mutants of WT A_1R were created. cAMP accumulation was then measured in Flp-In CHO cells stably expressing WT or mutant hA_1R in response to an agonist in a range (10^{-11} M to 10^{-4} M) and cAMP accumulation was measured after 30 minutes. 10 µM forskolin was also included since A_1R is a $G_{i/o}$ coupled receptor (Figure 5.2, Table 5.1). The agonists chosen for these experiments were the before-mentioned BnOCPA and HOCPA used in the MD simulations, adenosine and CPA as the compounds on which BnOCPA structure is based and NECA as a commonly used AR agonist.

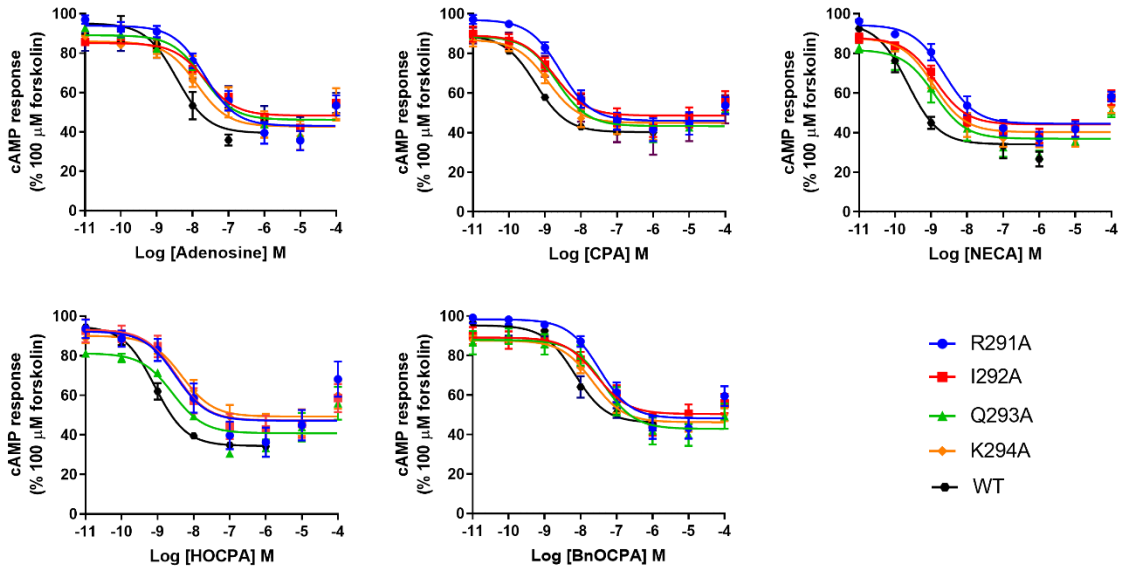

Figure 5.2. Effect of A_1R mutations on selective signalling of biased agonists. Flp-In CHO cells stably expressing WT or mutant hA_1R were co-stimulated with a range (10^{-11} M to 10^{-4} M) of agonist concentration and 10 µM forskolin and cAMP accumulation was measured after 30 minutes. Data are mean ± SEM of n≥3 individual experiments performed in duplicate, expressed as % 100 µM forskolin response.

Table 5.1. Agonist-stimulated cAMP response in WT and mutant hA_1R. pIC_{50} and E_{max} values measured by cAMP accumulation assay in Flp-In CHO cells stably expressing WT or mutant hA_1R in response to tested compounds and 10 µM forskolin.

Mutant	Adenosine			CPA			NECA			HOCPA			BNOCPA		
	pIC_{50}[a]	E_{max}[b]	n	pIC_{50}[a]	E_{max}[b]	n	pIC_{50}[a]	E_{max}[b]	n	pIC_{50}[a]	E_{max}[b]	n	pIC_{50}[a]	E_{max}[b]	n
WT	8.45 ± 0.20	55.70 ± 4.83	3	9.26 ± 0.03	48.97 ± 0.66	5	9.65 ± 0.15	61.21 ± 3.99	3	9.08 ± 0.06	60.52 ± 1.53	3	8.16 ± 0.15	49.38 ± 3.64	4
R291$^{7.56}$	7.66 ± 0.18****	50.84 ± 3.55	7	8.58 ± 0.17****	51.07 ± 3.64	8	8.63 ± 0.16****	49.89 ± 3.35**	6	8.50 ± 0.33*	45.18 ± 6.14**	5	7.49 ± 0.17****	50.15 ± 3.40	7
I292$^{8.47}$	7.66 ± 0.23****	36.82 ± 4.12****	7	8.74 ± 0.22***	40.55 ± 3.84**	8	8.88 ± 0.16****	43.79 ± 3.14****	6	8.49 ± 0.28*	45.88 ± 5.35**	5	7.56 ± 0.24***	38.72 ± 3.62***	7
Q293$^{8.48}$	7.18 ± 0.27****	42.92 ± 4.80***	6	8.68 ± 0.28***	45.37 ± 5.48	6	8.91 ± 0.22****	44.96 ± 4.52****	4	8.59 ± 0.26	40.37 ± 4.34***	4	7.36 ± 0.25****	45.03 ± 4.63	6
K294$^{8.49}$	7.89 ± 0.13**	43.12 ± 2.35***	7	8.93 ± 0.17*	42.06 ± 3.37*	7	8.93 ± 0.17****	47.57 ± 3.73****	5	8.33 ± 0.27**	40.84 ± 4.69***	5	7.67 ± 0.14**	41.37 ± 2.38**	7

Data are the mean ± SEM of n individual data sets, conducted in duplicate.

[a] The negative logarithm of agonist concentration producing half-maximal response.

[b] The % maximal inhibition of cAMP accumulation for each agonist.

Statistical significance (* $p < 0.05$, ** $p < 0.01$, *** $p < 0.001$, **** $p < 0.0001$) determined using ANOVA and Dunnett' s post-test. pIC_{50} and E_{max} values at each mutant were compared to the values at the WT A_1R for each compound.

For all the agonists the four mutations caused a reduction in efficacy when compared to the wild type A_1R, suggesting all the residues are generally most efficacious at the WT A_1R. This is not particularly surprising as these residues were predicted to be important in the transduction of the signal from the agonist:A_1R complex to the G proteins (Figure 5.3.A) and disrupting them therefore leads to reduced efficacy. Importantly in general the mutation of $K294^{8.49}$ to alanine seemed to cause the smallest loss of efficacy, except for HOCPA. On the other hand, alanine mutagenesis of $R291^{7.56}$ and $I292^{8.47}$ seems to overall cause biggest loss of efficacy of the agonists.

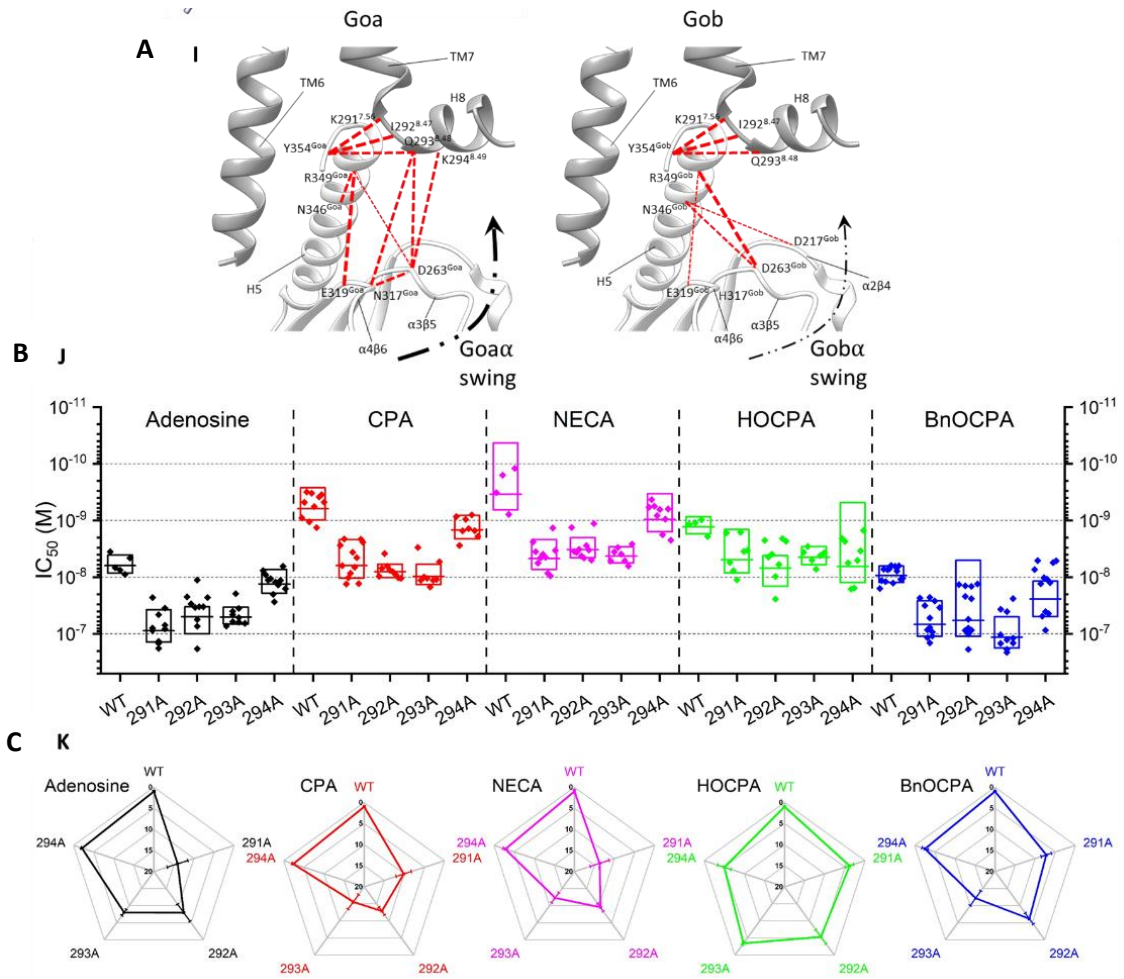

Figure 5.3. Investigation of selective agonist coupling to $G\alpha_{o/i}$ by mutagenesis and cAMP. A. MD simulations predict important residues in TM7 and H8 of the hA_1R for A_1R coupling to G_{oa} (left) and G_{ob} (right). B-C. Site directed mutagenesis was used to mutate $R291^{7.56}$, $I292^{8.47}$, $Q293^{8.48}$ and $K294^{8.49}$ to alanine in the hA_1R. cAMP accumulation was then measured in Flp-In CHO cells stably expressing WT or mutant hA_1R following 30 minutes co-stimulation with a range (10^{-11} M to 10^{-4} M) of agonist concentration and 10 µM forskolin and IC_{50} was determined (B). To easier observe how these mutants differentially affect agonist potency a web of bias plot was constructed, which normalizes the reduction in IC_{50} for each mutation and agonist relative to corresponding WT hA_1R (C). This figure was adapted from Wall et al. (2022).

To easier observe the effects of the mutations on potency (IC_{50}), bias plots were created. To this end, the IC_{50} values for individual mutants were normalized to their respective wild-type controls for each agonist (Figure 5.3.BC). The bias plot showed that residues $R291^{7.56}$, $I292^{8.47}$ and $Q293^{8.48}$ are especially important for CPA and NECA coupling, $R291^{7.56}$ for adenosine efficacy, and $Q293^{8.48}$ for

BnOCPA, while HOCPA was not appreciably affected by any of these mutations. The K294$^{8.49}$ mutation had little effect on general agonist efficacy (< 5-fold change in IC_{50}).

Overall, these observations further reinforce the MD simulations predictions that helix 8 residues are involved in the coupling of agonist-activated A_1R. In particular, residues R291$^{7.56}$, I292$^{8.47}$ and Q293$^{8.48}$ are required for selective agonist coupling to $G\alpha_{o/i}$. Subtle differences between the residue involvements may then contribute to the Gα bias observed among these agonists.

5.3 Analysing BnOCPA derivatives as potent selective agonists of the A_1R

5.3.1. Improved potency of 26, 27, 45, 49 and 51-54 at A_1R

Having looked at BnOCPA activity, the next step was to try to identify higher affinity/efficacy derivatives of BnOCPA. Dr Lochner's lab (University of Bern) synthesised a series of 24 novel synthetic AR ligands (Table 5.2). These are benzyloxycyclopentyl and phenoxycyclopentyl derivates of adenosine and NECA. Adenosine is a natural AR agonist that binds and acts at all AR subtypes with near equipotency, while NECA is an AR agonist that has efficacy and affinity at all receptors but is more potent at the A_1R (Deganutti et al., 2021a; Knight et al., 2016).

Table 5.2. List of synthetic adenosine and NECA derivatives. List of all tested compounds, their 2D structure and molecular weight.

Cmpd	Structure	Molecular weight (g/mol)	Type of derivate
Adenosine	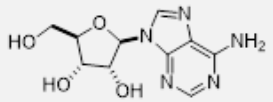	267.24	-
BnOCPA	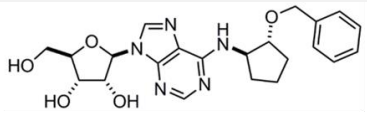	441.49	Benzyloxycyclopentyl
19	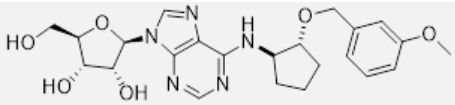	471.51	Benzyloxycyclopentyl
20	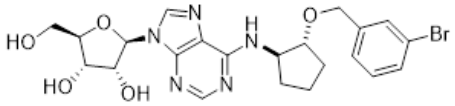	520.38	Benzyloxycyclopentyl
21	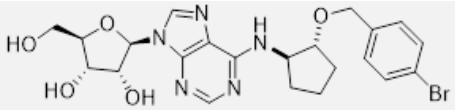	520.38	Benzyloxycyclopentyl
22	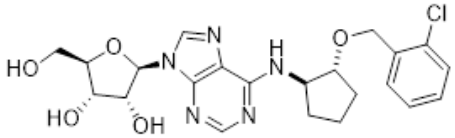	475.93	Benzyloxycyclopentyl
23	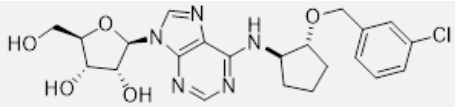	475.93	Benzyloxycyclopentyl
24	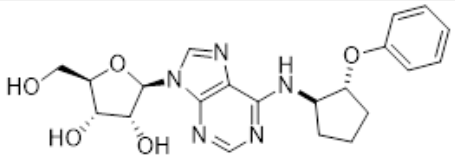	427.46	Phenoxycyclopentyl
25	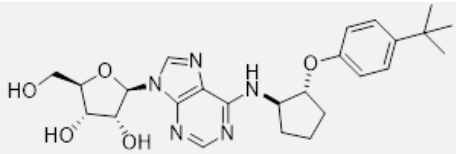	483.57	Phenoxycyclopentyl
26	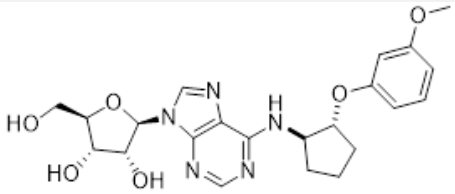	457.49	Phenoxycyclopentyl
27	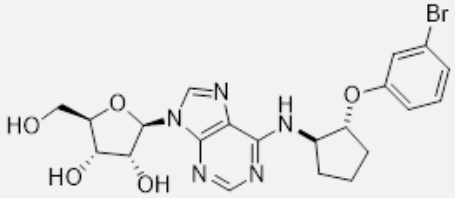	506.36	Phenoxycyclopentyl

28	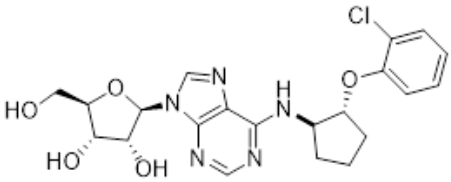	461.90	Phenoxycyclopentyl
29	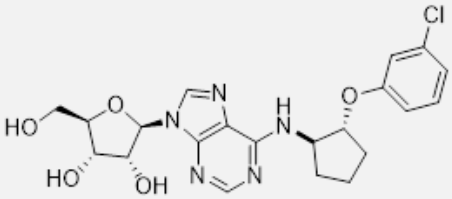	461.90	Phenoxycyclopentyl
30	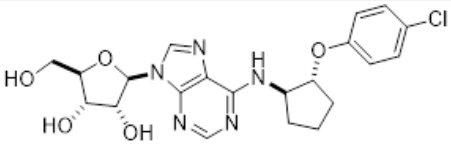	461.90	Phenoxycyclopentyl
NECA	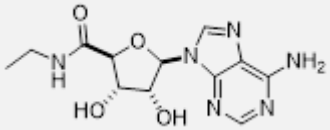	308.29	-
44	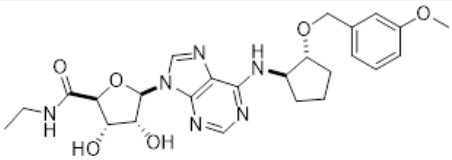	512.57	Benzyloxycyclopentyl
45	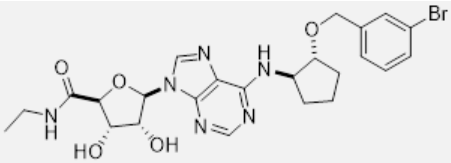	561.44	Benzyloxycyclopentyl
46	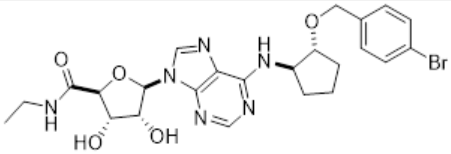	561.44	Benzyloxycyclopentyl
47	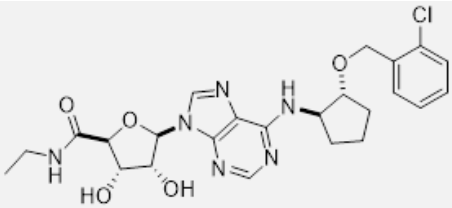	516.98	Benzyloxycyclopentyl
48	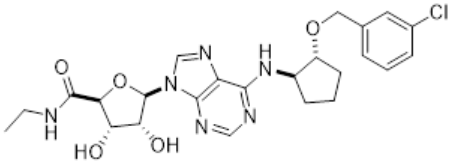	516.98	Benzyloxycyclopentyl
49	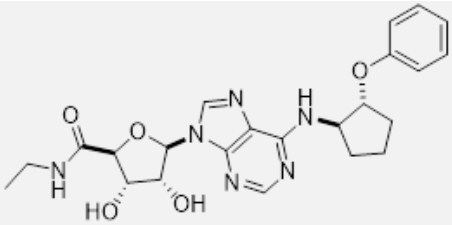	468.51	Phenoxycyclopentyl

50	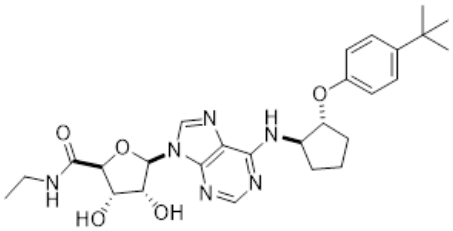	524.62	Phenoxycyclopentyl
51	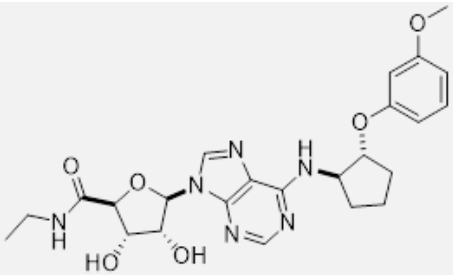	498.54	Phenoxycyclopentyl
52	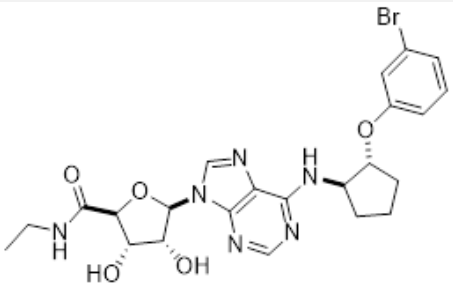	547.41	Phenoxycyclopentyl
53	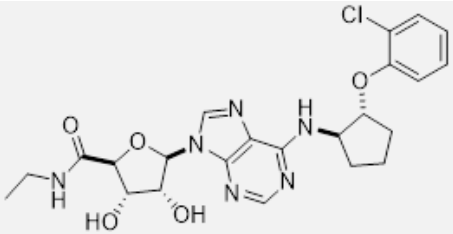	502.96	Phenoxycyclopentyl
54	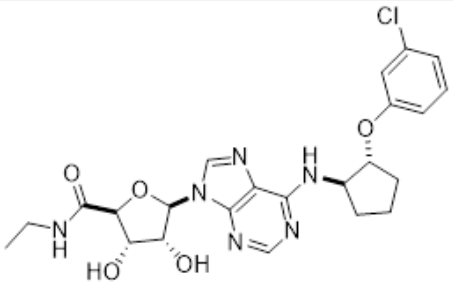	502.96	Phenoxycyclopentyl
55	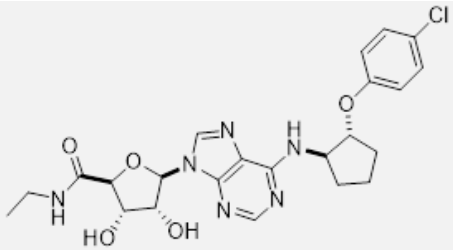	502.96	phenoxycyclopentyl

As the aim of this work was to identify more potent A_1R agonists, adenosine, NECA, BnOCPA (for reference as the best compound from work preceding this) and the new benzyloxycyclopentyl and phenoxycyclopentyl derivates of adenosine and NECA were tested for their efficacy at the A_1R using

the cAMP accumulation assay. CHO-KI cells stably expressing human A_1R were co-stimulated for 30 minutes with tested compounds in a range of concentrations (10^{-12} M to 10^{-4} M) and 10 µM forskolin, as A_1R is $G_{i/o}$ coupled (Figure 5.4, Table 5.3 and 5.4).

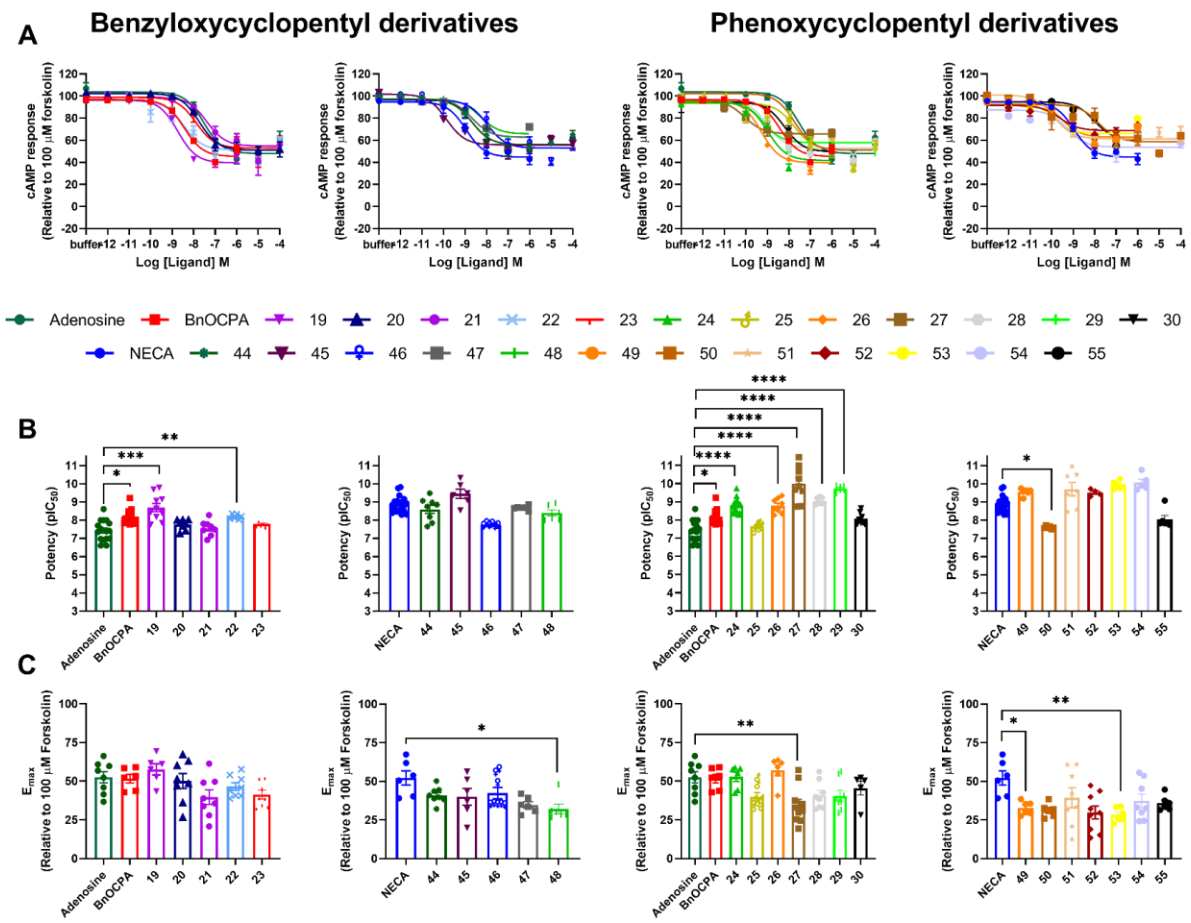

Figure 5.4. Efficacy of synthetic adenosine and NECA Derivatives at individual A_1R. A. cAMP accumulation or inhibition in CHO-KI cells stably expressing human A_1R stimulated with varying concentrations of AR ligands for 30 mins and cAMP accumulation was detected. 10 µM forskolin was included. pIC_{50} (B) and E_{max} (C) values for individual repeats derived from dose-response curves in A. Data are mean ± SEM of n≥3 individual experiments performed in duplicate, expressed as % 100 µM forskolin response.

Table 5.3. Potency of synthetic adenosine and NECA benzyloxycyclopentyl derivatives. pIC_{50}, pEC_{50} and E_{max} values measured by cAMP accumulation assay in CHO-A_1R, CHO-A_{2A}R, CHO-A_{2B}R or Flp-In CHO-A_3R cells in response to tested compounds. 10 and 1 µM forskolin is included in the assay for A_1R and A_3R, respectively.

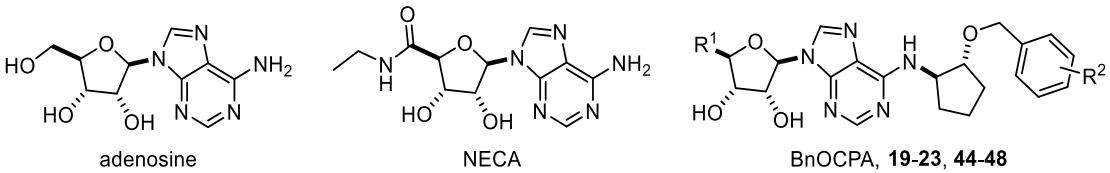

Cmpd	R^1	R^2	A_1R			A_{2A}R			A_{2B}R			A_3R		
			pIC_{50}[a]	E_{max}[b]	n	pEC_{50}[a]	E_{max}[c]	n	pEC_{50}[a]	E_{max}[c]	n	pIC_{50}[a]	E_{max}[b]	n
Adenosine	-	-	7.53 ± 0.18	52.17 ± 1.9	10	7.60 ± 0.11	21.53 ± 0.9	10	7.28 ± 0.12	59.07 ± 2.9	4	7.87 ± 0.23	24.71 ± 2.5	3
BnOCPA	-CH_2OH	H	8.43 ± 0.09*	51.49 ± 1.9	10	4.95 ± 0.38**	17.13 ± 4.6	10	N.D.		4	N.R.		5
19	-CH_2OH	m-OMe	8.74 ± 0.10***	57.41 ± 2.4	5	N.D.		5	N.D.		3	5.98 ± 0.47*	9.52 ± 2.1**	3
20	-CH_2OH	m-Br	7.74 ± 0.13	51.44 ± 2.8	4	N.R.		3	N.D.		3	5.08 ± 0.26**	12.59 ± 1.8*	3
21	-CH_2OH	p-Br	7.39 ± 0.16	44.25 ± 3.2	4	N.D.		3	N.D.		3	N.R.		3
22	-CH_2OH	o-Cl	8.47 ± 0.24**	44.66 ± 4.3	3	5.17 ± 0.33**	18.55 ± 3.5	3	4.57 ± 0.12****	96.93 ± 8.1**	3	N.R.		3
23	-CH_2OH	m-Cl	7.88 ± 0.17	45.97 ± 3.3	3	N.D.		3	N.D.		3	N.R.		3
NECA	-	-	8.96 ± 0.11	50.11 ± 2.4	10	7.95 ± 0.26	22.03 ± 2.4	4	7.20 ± 0.07	68.12 ± 2.0	6	7.83 ± 0.26	34.34 ± 3.7	7
44	-CONHEt	m-OMe	8.67 ± 0.19	41.15 ± 3.3	4	N.R.		3	4.42 ± 0.16****	73.07 ± 8.9	3	5.38 ± 0.09****	46.56 ± 2.1	4
45	-CONHEt	m-Br	9.85 ± 0.19	46.12 ± 5.2	3	N.R.		3	N.D.		3	5.56 ± 0.10****	49.17 ± 2.4*	4
46	-CONHEt	p-Br	7.97 ± 0.24	43.32 ± 4.5	3	N.D.		3	N.D.		3	5.82 ± 0.20****	30.56 ± 2.8	3
47	-CONHEt	o-Cl	8.67 ± 0.15	34.67 ± 2.2	3	5.68 ± 0.32	20.34 ± 3.1	3	5.36 ± 0.08****	87.58 ± 3.3	3	5.85 ± 0.13****	43.92 ± 2.8	3
48	-CONHEt	m-Cl	8.29 ± 0.16	31.57 ± 2.1*	3	5.04 ± 0.29**	17.18 ± 2.9	3	4.72 ± 0.11****	96.14 ± 6.8**	3	5.83 ± 0.39****	31.06 ± 5.7	3

Data are the mean ± SEM of n individual data sets, conducted in duplicate.

[a] The negative logarithm of agonist concentration producing half-maximal response.
[b] The % maximal inhibition of cAMP accumulation for each agonist.
[c] The % maximal accumulation for each agonist relative to 100 µM forskolin
N.D., not determined. Full dose-response curve was not feasible.
N.R., no response detected in the assay
Statistical significance (* $p < 0.05$, ** $p < 0.01$, *** $p < 0.001$, **** $p < 0.0001$) determined using ANOVA and Dunnett' s post-test. Adenosine derivatives were compared to adenosine, while NECA derivatives were compared to NECA.

Table 5.4. Potency of synthetic adenosine and NECA phenoxycyclopentyl derivatives. pIC_{50}, pEC_{50} and E_{max} values measured by cAMP accumulation assay in CHO-A_1R, CHO-A_{2A}R, CHO-A_{2B}R or Flp-In CHO-A_3R cells in response to tested compounds. 10 and 1 µM forskolin is included in the assay for A_1R and A_3R, respectively.

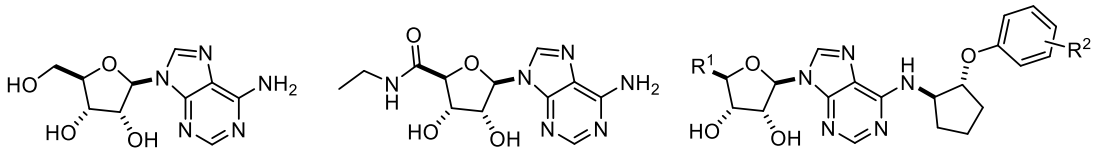

adenosine NECA **24-30**, **49-55**

Cmpd	R^1	R^2	A_1R			A_{2A}R			A_{2B}R			A_3R		
			pIC_{50}[a]	E_{max}[b]	n	pEC_{50}[a]	E_{max}[c]	n	pEC_{50}[a]	E_{max}[c]	n	pIC_{50}[a]	E_{max}[b]	n
Adenosine	-	-	7.53 ± 0.18	52.17 ± 1.9	10	7.60 ± 0.11	21.53 ± 0.9	10	7.28 ± 0.12	59.07 ± 2.9	4	7.87 ± 0.23	24.71 ± 2.5	3
24	-CH_2OH	H	8.98 ± 0.14****	52.71 ± 3.1	9	N.D.		3	4.90 ± 0.14****	64.19 ± 5.4	3	5.78 ± 0.42*	17.83 ± 3.7	3
25	-CH_2OH	p-t-Bu	7.74 ± 0.28	42.14 ± 5.1	4	N.D.		3	N.D.		3	N.R.		3
26	-CH_2OH	m-OMe	9.28 ± 0.10****	56.74 ± 2.4	4	5.24 ± 0.55**	17.25 ± 5.0	3	N.D.		3	N.R.		3
27	-CH_2OH	m-Br	10.0 ± 0.24****	30.55 ± 3.3**	4	N.D.		3	4.63 ± 0.12****	82.53 ± 6.2	3	N.R.		3
28	-CH_2OH	o-Cl	9.03 ± 0.19****	44.15 ± 3.6	4	5.96 ± 0.28*	17.01 ± 2.2	3	5.31 ± 0.09****	96.77 ± 4.4**	3	6.73 ± 0.42	13.42 ± 2.4*	3
29	-CH_2OH	m-Cl	9.21 ± 0.19****	38.25 ± 3.0	4	6.26 ± 0.34	13.63 ± 2.1	3	5.29 ± 0.07****	96.93 ± 8.1**	3	6.81 ± 0.47	11.77 ± 2.3*	3
30	-CH_2OH	p-Cl	8.19 ± 0.18	45.06 ± 3.6	4	4.86 ± 0.58**	15.15 ± 5.5	3	N.D.		3	6.88 ± 0.60	12.5 ± 3.2*	3
NECA	-	-	8.96 ± 0.11	50.11 ± 2.4	10	7.95 ± 0.26	22.03 ± 2.4	4	7.20 ± 0.07	68.12 ± 2.0	6	7.83 ± 0.26	34.34 ± 3.7	7
49	-CONHEt	H	9.53 ± 0.20	32.68 ± 2.5*	3	5.48 ± 0.42*	15.41 ± 3.0	3	6.04 ± 0.09****	87.99 ± 3.7*	3	7.17 ± 0.16	51.24 ± 3.4*	3
50	-CONHEt	p-t-Bu	7.81 ± 0.41*	33.66 ± 6.1	3	4.84 ± 0.30**	20.11 ± 3.8	3	4.77 ± 0.08****	96.35 ± 5.0**	3	6.63 ± 0.19**	39.85 ± 3.2	3
51	-CONHEt	m-OMe	9.88 ± 0.29	39.71 ± 5.9	4	5.20 ± 1.11*	5.16 ± 3.1*	3	5.10 ± 0.07****	84.76 ± 3.3	3	5.56 ± 0.14****	59.38 ± 4.0***	3

52	-CONHEt	m-Br	9.62 ± 0.35	39.71 ± 5.9	4	4.58 ± 0.87**	11.48 ± 6.7	3	5.37 ± 0.11****	61.12 ± 3.3	3	5.52 ± 0.12****	68.26 ± 3.8****	3
53	-CONHEt	o-Cl	9.91 ± 0.23	28.65 ± 2.7**	3	5.67 ± 0.46*	14.69 ± 3.2	3	6.22 ± 0.09****	80.91 ± 3.1	3	7.00 ± 0.19*	41.6 ± 3.3	3
54	-CONHEt	m-Cl	9.28 ± 0.28	34.67 ± 2.1	3	5.86 ± 0.41	13.32 ± 2.6	3	6.01 ± 0.09****	78.81 ± 3.4	3	6.79 ± 0.14**	44.20 ± 2.6	3
55	-CONHEt	*p*-Cl	7.99 ± 0.15	35.07 ± 2.5	3	4.86 ± 0.32**	25.01 ± 5.2	3	5.10 ± 0.09****	83.73 ± 4.5	3	6.92 ± 0.17*	47.16 ± 3.3	3

Data are the mean ± SEM of n individual data sets, conducted in duplicate.
[a] The negative logarithm of agonist concentration producing half-maximal response.
[b] The % maximal inhibition of cAMP accumulation for each agonist.
[c] The % maximal accumulation for each agonist relative to 100 µM forskolin
N.D., not determined. Full dose-response curve was not feasible.
N.R., no response detected in the assay
Statistical significance (* $p < 0.05$, ** $p < 0.01$, *** $p < 0.001$, **** $p < 0.0001$) determined using ANOVA and Dunnett' s post-test. Adenosine derivatives were compared to adenosine, while NECA derivatives were compared to NECA.

All the tested compounds behave as agonists at the A_1R, with compound 27 being the most potent with pIC_{50} of 10.0 ± 0.24, closely followed by compounds 26, 45, 49 and 51-54 (pIC_{50} = 9.28 ± 0.10, 9.85 ± 0.19, 9.53 ± 0.20, 9.88 ± 0.29, 9.62 ± 0.35, 9.91 ± 0.23 and 9.28 ± 0.28, respectively). Moreover, all the above-mentioned compounds display higher potency than BnOCPA or the parent compounds adenosine and NECA (pIC_{50} of 8.43 ± 0.09, 7.53 ± 0.18 and 8.96 ± 0.11, respectively), making them very promising candidate compounds.

It is also interesting to note that, except for compounds 49 and 53, all of the most potent compounds have a substituent in the *meta* position and expect for compounds 26, 49 and 51 they all have a halogen substituent. These findings seem to suggest that that a halogen substituent in the *meta* position on the aromatic ring confers high efficacy at the human A_1R. Additionally, all most potent hA_1R agonists but 45 feature a N^6-phenoxycyclopentyl moiety.

5.3.2 Compounds 45 and 51 are 10,000-fold more selective for A_1R over other AR subtypes

As was discussed, progression of promising potent A_1R agonists into clinic is often severely limited by their reduced selectivity among the four different AR subtypes and resulting side effects. Therefore, the next important step was to evaluate the selectivity of the adenosine and NECA derivatives, which was accomplished again by employing the cAMP accumulation assay to measure the compound efficacy at the remaining 3 AR subtypes.

CHO-KI cells stably expressing human $A_{2A}R$, $A_{2B}R$ or Flp-In CHO cells stably expressing A_3R were stimulated for 30 minutes with tested compounds in a range of concentrations (10^{-12} M to 10^{-4} M). In case of A_3R, 1 µM forskolin was included as well. This is because A_3R is a $G_{i/o}$-coupled receptor, whose stimulation results in the reduction of cAMP levels in the cells, while $A_{2A}R$ and $A_{2B}R$ are G_s-coupled resulting in increase of intracellular cAMP levels post stimulation.

All compounds displayed only weak or little efficacy at either $A_{2A}R$ or $A_{2B}R$ and many failed to produce full dose-response curves. NECA (pEC_{50} of 7.95 ± 0.26 and 7.20 ± 0.07 at $A_{2A}R$ and $A_{2B}R$, respectively) and adenosine (pEC_{50} of 7.60 ± 0.11 and 7.28 ± 0.12 at $A_{2A}R$ and $A_{2B}R$, respectively) remaining the only potent compounds at these receptors (Figure 5.5 and 5.6, Table 5.3 and 5.4).

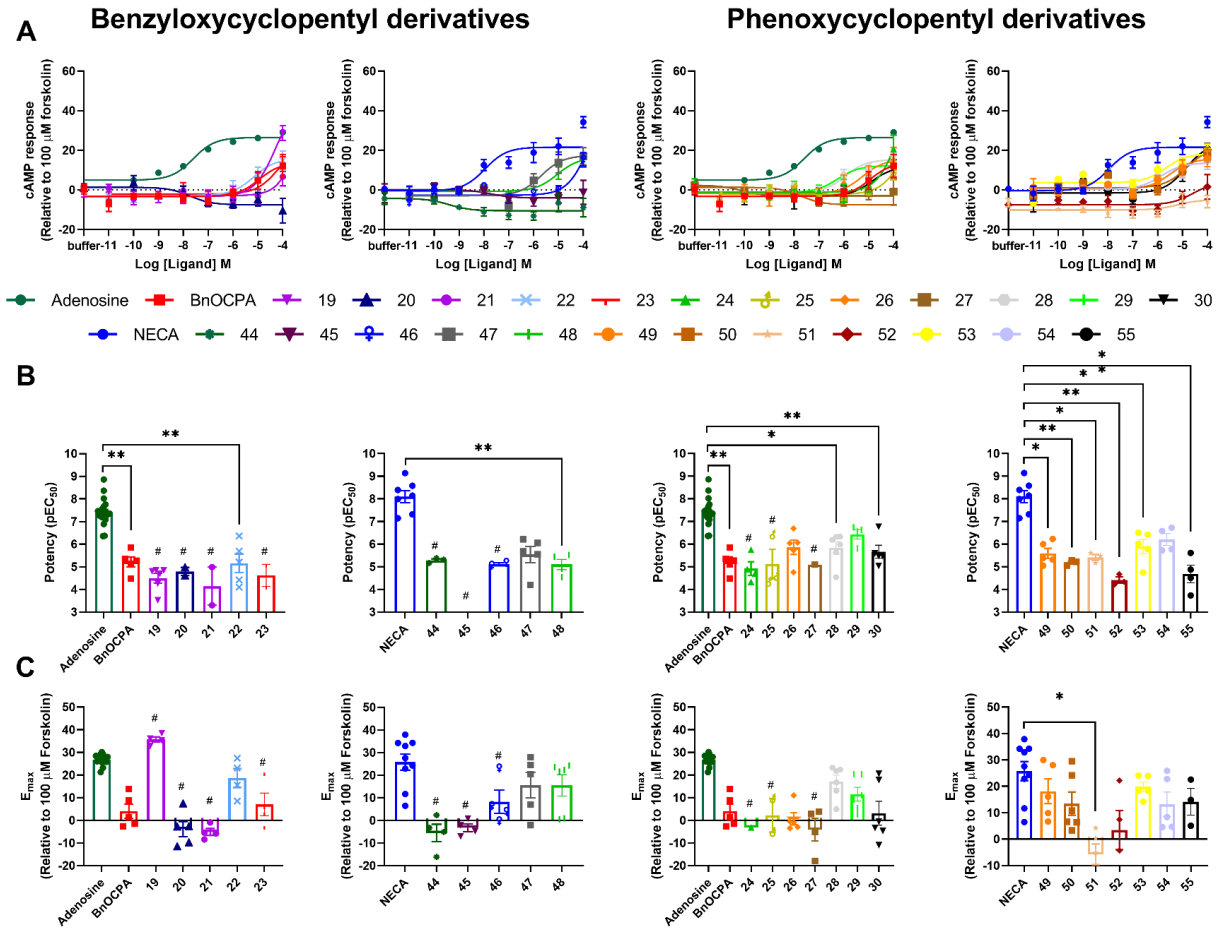

Figure 5.5. Efficacy of synthetic adenosine and NECA Derivatives at individual $A_{2A}R$. A. cAMP accumulation or inhibition in CHO-KI cells stably expressing human $A_{2A}R$ stimulated with varying concentrations of AR ligands for 30 mins and cAMP accumulation was detected. pEC_{50} (B) and E_{max} (C) values for individual repeats derived from dose-response curves in A. # Full dose-response curve wasn't feasible, so values are just an estimation. Data are mean ± SEM of n≥3 individual experiments performed in duplicate, expressed as % 100 µM forskolin response.

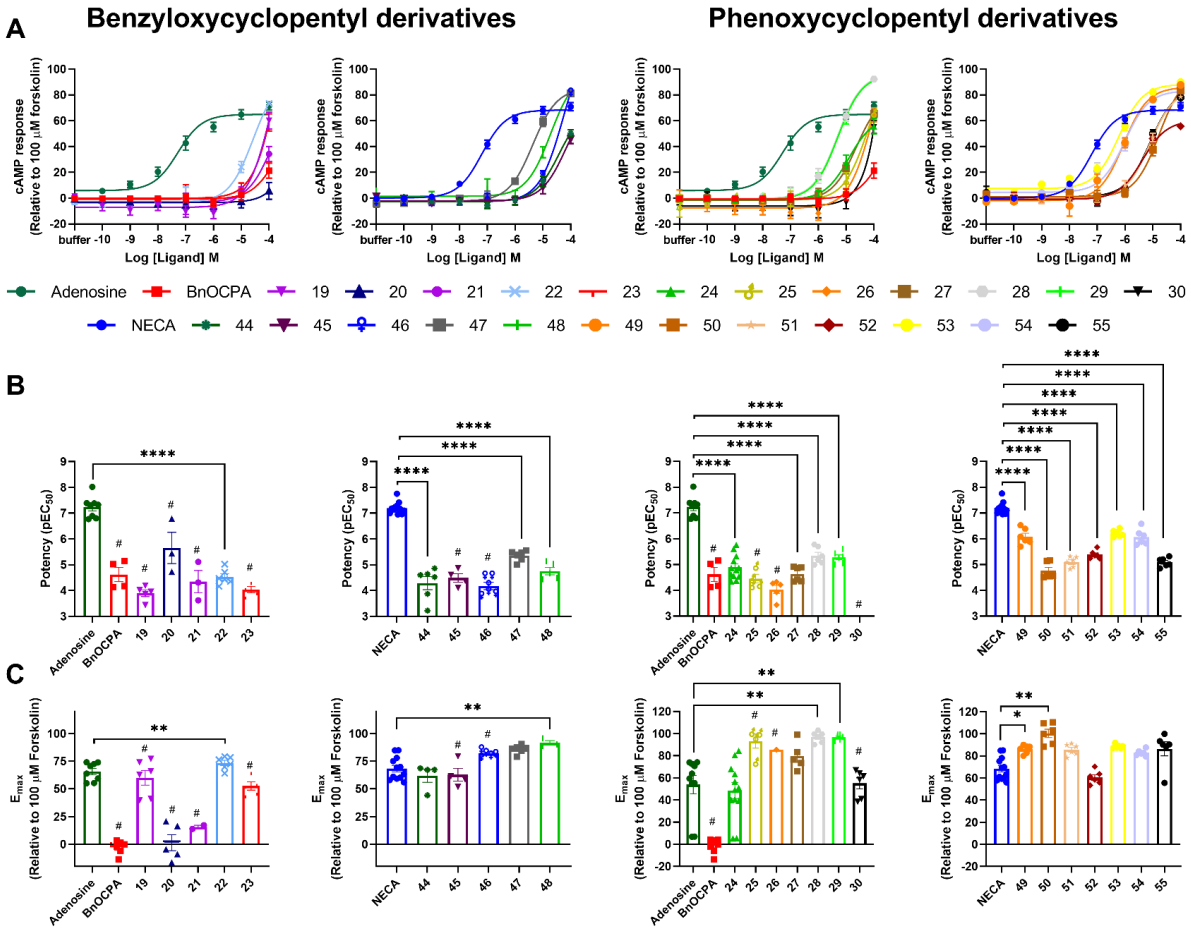

Figure 5.6. Efficacy of synthetic adenosine and NECA Derivatives at individual A_{2B}R. A. cAMP accumulation or inhibition in CHO-KI cells stably expressing human A_{2B}R stimulated with varying concentrations of AR ligands for 30 mins and cAMP accumulation was detected. pEC_{50} (B) and E_{max} (C) values for individual repeats derived from dose-response curves in A. # Full dose-response curve wasn't feasible, so values are just an estimation. Data are mean ± SEM of n≥3 individual experiments performed in duplicate, expressed as % 100 µM forskolin response.

Adenosine (pIC_{50} = 7.87 ± 0.23) and NECA (pIC_{50} = 7.83 ± 0.26) remained the most potent compound at A_3R as well, but there are several compounds that also display full agonistic activity at A_3R and near equipotency to both NECA and adenosine (Figure 5.7, Table 5.3 and 5.4). Compound 49 (pIC_{50} = 7.17 ± 0.16) was the most potent of the new AR synthetic agonists at the A_3R, followed by 28-30, 50 and 53-55 (pIC_{50} of 6.73 ± 0.42, 6.81 ± 0.47, 6.88 ± 0.60, 6.63 ± 0.19, 7.00 ± 0.19, 6.79 ± 0.14 and 6.92 ± 0.17, respectively).

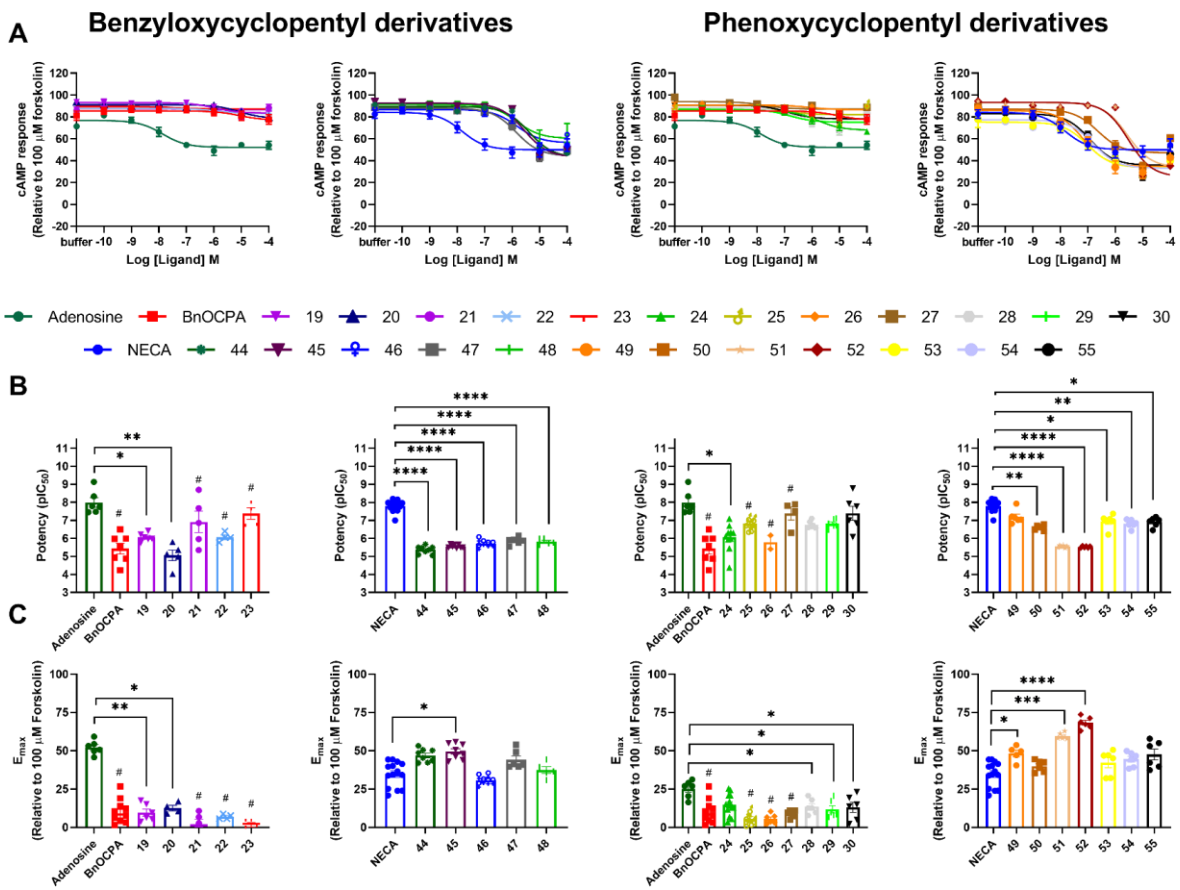

Figure 5.7. Efficacy of synthetic adenosine and NECA Derivatives at individual A_3R. A. cAMP accumulation or inhibition in Flp-In CHO cells stably expressing A_3R stimulated with varying concentrations of AR ligands for 30 mins and cAMP accumulation was detected. 1 µM forskolin was included. pIC_{50} (B) and E_{max} (C) values for individual repeats derived from dose-response curves in A. # Full dose-response curve wasn't feasible, so values are just an estimation. Data are mean ± SEM of n≥3 individual experiments performed in duplicate, expressed as % 100 µM forskolin response.

To further asses the compound selectivity, the relative activity (RA) was calculated, which was a measure incorporating pIC_{50}/pEC_{50} and E_{max} (see Chapter 2, equation 3), for all agonists at the 4 different adenosine receptor subtypes. The relative activity of each compound at each receptor was then normalised to either NECA (for NECA derivates) or adenosine (for adenosine derivatives) at A_1R (Figure 5.8). From the radar plot, it can be seen that, adenosine is near equipotent at all the receptors, but all the other tested compounds display at least partial selectivity for hA_1R.

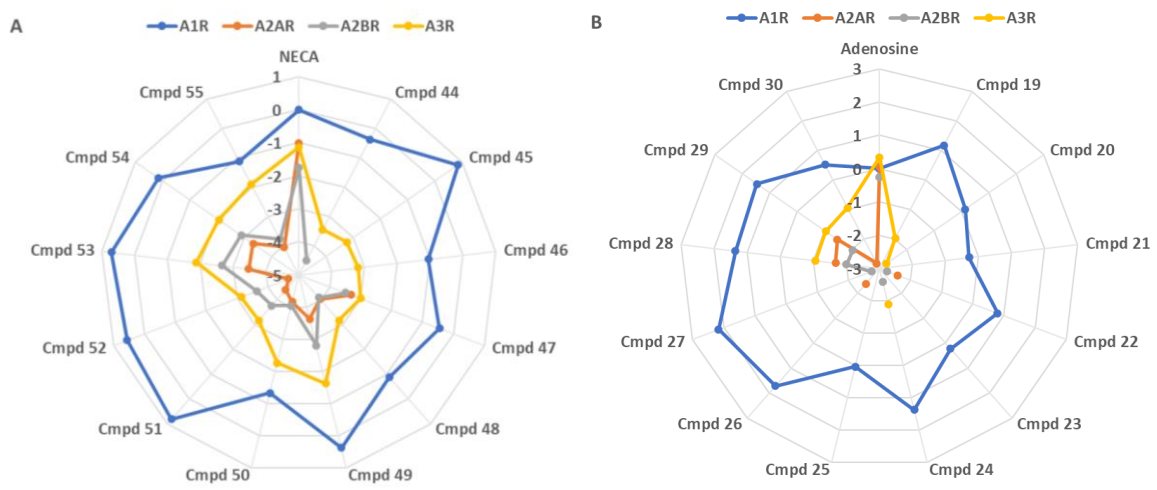

Figure 5.8. Adenosine and NECA derivatives show selectivity towards A_1R subtype. Log(RA) values of AR ligands at human A_1R, $A_{2A}R$, $A_{2B}R$ and A_3R normalized to (A) NECA or (B) adenosine response at A_1R.

With adenosine itself being near equipotent at all AR subtypes, it did not come as a big surprise that some of its derivates, like compounds 28-30, were dual agonists for hA_1R and hA_3R. However, some adenosine derivates did display A_1R selectivity, namely compounds 22, 23, 26 and 27. On the other hand, NECA itself is A_1R selective by ~10-fold. Compounds 44, 45, 51-53 display enhanced A_1R selectivity with compounds 45 and 51 being ~1500-fold more A_1R selective than NECA itself, suggesting more than 10,000-fold selectivity overall to the A_1R.

5.3.3 Differences between adenosine and NECA derivates

As was mentioned above, NECA itself is A_1R-selective, while adenosine is near equipotent at all receptors. It is thus not surprising that the new compounds based on NECA generally display higher selectivity towards A_1R than compounds based on adenosine. Moreover, NECA derivatives are generally more potent at inhibiting cAMP accumulation at A_1R than NECA, while retaining similar

potency across the other three adenosine receptor subtypes, resulting in even more A_1R-selective compounds.

When comparing the analogous derivate pairs based on adenosine or NECA more closely, it can be noticed that they often display very similar selectivity and potency across all AR subtypes (Figures 5.4, 5.5 5.6 and 5.7, Tables 5.3 and 5.4). This is the case for example for adenosine-derived 26 and its NECA-derived analogue 51, which are both potent hA_1R selective full agonists (pIC_{50} = 9.28 ± 0.10 and 9.88 ± 0.29, respectively), while compounds 30 and 55 are relatively less potent dual hA_1R and hA_3R agonists (pIC_{50} = 8.19 ± 0.18, 7.99 ± 0.15 at hA_1R and 6.88 ± 0.60, 6.92 ± 0.17 at hA_3R, respectively). Consequently, for these compounds it seems that it is the phenoxy substituent group rather than the adenosine/NECA part of the compound that has the most effect on driving compound selectivity and potency.

But this is not the case for all compounds, as some other analogue pairs show differences in their potencies across adenosine receptor subtypes. For example, compounds 25 and 50 have similar potencies at hA_1R (pIC_{50} = 7.74 ± 0.28 and 7.81 ± 0.41, respectively), but compound 50 also has a weak response at hA_3R (pIC_{50} = 6.63 ± 0.19), while adenosine-based compound 25 elicits no response at this receptor. In this case it seems to be the ribose C-5' substituent group that affects the selectivity of the compounds more with the adenosine-derived compound being more hA_1R selective.

5.4 Determining compound binding at ARs

5.4.1 Compounds 27, 28, 49, 51 and 53 have high affinity across both rat and human A_1R

A_1R agonists are promising therapeutic agents for treatment of glaucoma, type 2 diabetes mellitus, pain and epilepsy (Baltos et al., 2016; Sawynok, 2016; Varani et al., 2017; Weltha et al., 2019). It is therefore important to assess not only the efficacy of the novel synthetic AR ligands, but also their affinity at both human and rat A_1R, with rats being a common model used in the research of various pathological conditions.

The ability of all AR ligands to displace and inhibit the specific binding of CA200645, a fluorescent antagonist of A_1R and A_3R, was tested in HEK-293 cells stably expressing WT human or rat Nluc-A_1R (Stoddart et al., 2012). Briefly, HEK-293 cells stably expressing WT human or rat Nluc-A_1R were stimulated with 20 nM CA200645 and a range of ligand concentrations (10^{-11} M to 10^{-4} M). The 20 nM CA200645 concentration was chosen following previous experiments measuring the CA200645 K_d at human and rat A_1R as a concentration that elicited sufficient response without unnecessarily wasting too much compound. The BRET ratio at 10 minutes was then used to create full dose response

curves for each ligand and fitted with the "One site – Fit K_i" model derived from the Cheng and Prusoff equation built in GraphPad Prism 9.3 to enable estimates of pK_i (Figure 5.9 and 5.10, Table 5.5 and 5.6).

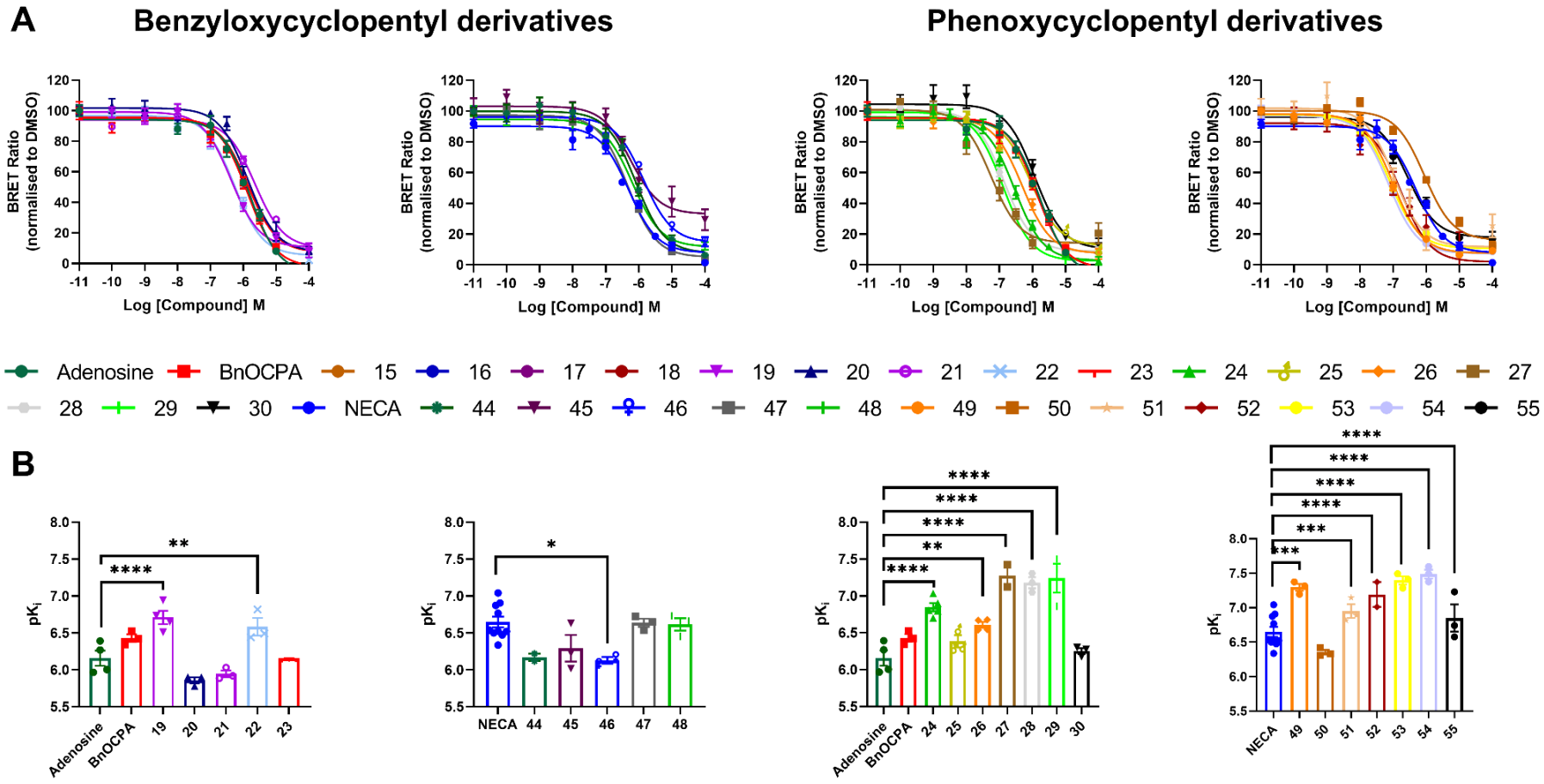

Figure 5.9. Binding of AR ligands at human A_1R. A. HEK-293 cells stably expressing human Nluc-A_1R were treated with 20nM CA200645 and increasing concentrations of unlabelled AR ligand. NanoBRET ratio at 10 minutes was calculated and fitted with the "One site – Fit K_i" model derived from the Cheng and Prusoff equation built into GraphPad Prism 9.3. B. pK_i values for individual repeats from A-B. Data are expressed as the mean ± SEM of n≥3 individual experiments performed in duplicate.

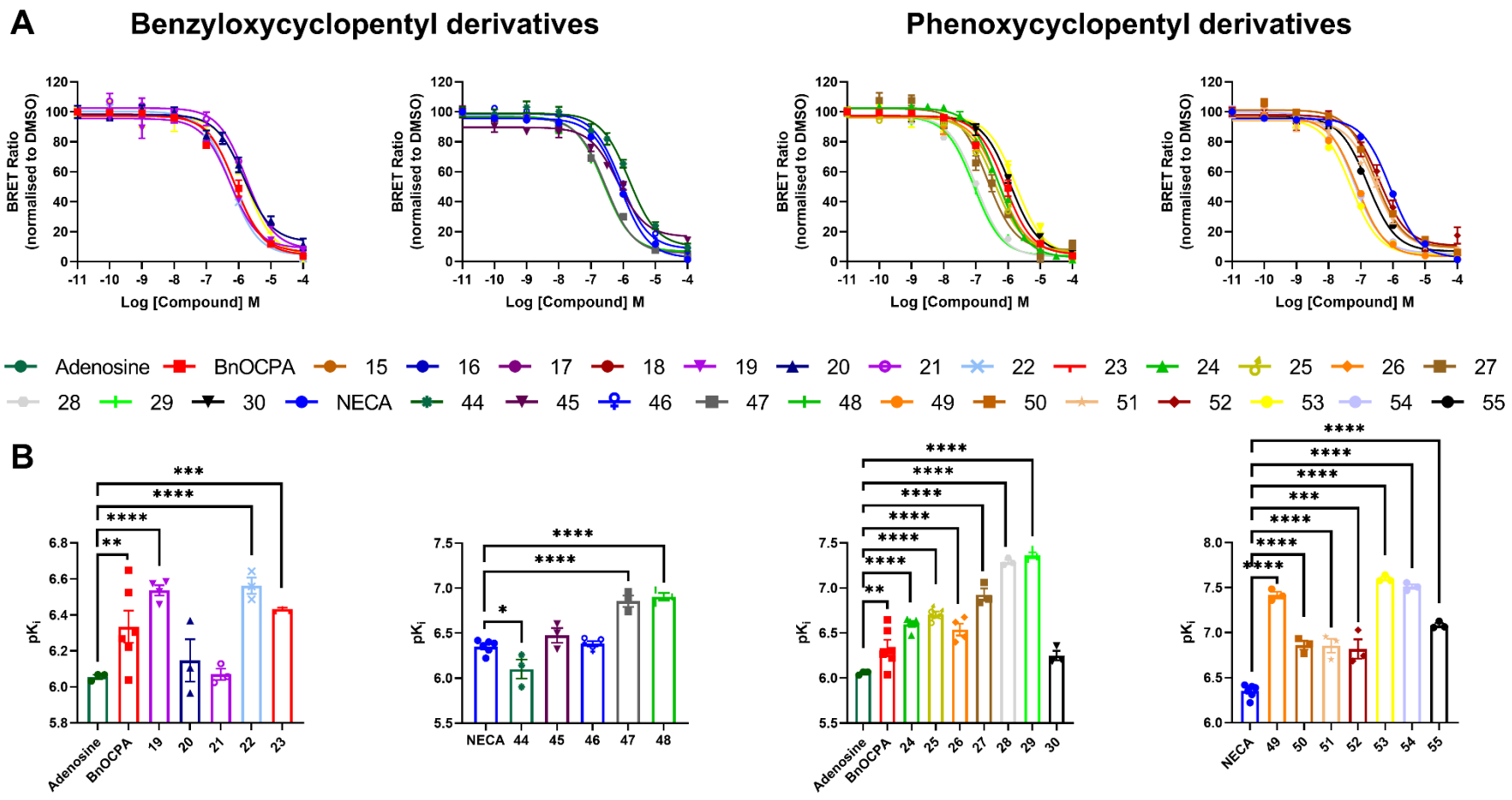

Figure 5.10. Binding of AR ligands at rat A_1R. A. HEK-293 cells stably expressing rat Nluc-A_1R were treated with 20nM CA200645 and increasing concentrations of unlabelled AR ligand. NanoBRET ratio at 10 minutes was calculated and fitted with the "One site – Fit K_i" model derived from the Cheng and Prusoff equation built into GraphPad Prism 9.3. B. pK_i values for individual repeats from A-B. Data are expressed as the mean ± SEM of n≥3 individual experiments performed in duplicate.

Table 5.5. Binding of synthetic adenosine and NECA benzyloxycyclopentyl derivatives. pK_i values were determined through NanoBRET binding assay in HEK-293 cells stably expressing human or rat Nluc-A_1R.

Cmpd	R^1	R^2	hA_1R		rA_1R	
			pK_i[a]	n	pK_i[a]	n
Adenosine	-	-	6.09 ± 0.06	4	6.06 ± 0.05	3
BnOCPA	$-CH_2OH$	H	6.18 ± 0.09	3	6.41 ± 0.06**	6
19	$-CH_2OH$	*m*-OMe	6.67 ± 0.10***	3	6.55 ± 0.06****	3
20	$-CH_2OH$	*m*-Br	6.16 ± 0.10	3	6.13 ± 0.08	3
21	$-CH_2OH$	*p*-Br	5.94 ± 0.07	3	6.06 ± 0.07	3
22	$-CH_2OH$	*o*-Cl	6.56 ± 0.07**	3	6.56 ± 0.04****	3
23	$-CH_2OH$	*m*-Cl	6.15 ± 0.07	3	6.43 ± 0.03***	3
NECA	-	-	6.61 ± 0.06	5	6.38 ± 0.04	6
44	-CONHEt	*m*-OMe	6.39 ± 0.08	3	6.11 ± 0.07*	3
45	-CONHEt	*m*-Br	6.54 ± 0.15	3	6.46 ± 0.07	3
46	-CONHEt	*p*-Br	6.15 ± 0.06*	3	6.38 ± 0.03	3
47	-CONHEt	*o*-Cl	6.63 ± 0.07	3	6.85 ± 0.05****	3
48	-CONHEt	*m*-Cl	6.49 ± 0.08	3	6.90 ± 0.05****	3

Data are the mean ± SEM of n individual data sets, conducted in duplicate.
[a] The binding affinity for each agonist.
Statistical significance (* $p < 0.05$, ** $p < 0.01$, *** $p < 0.001$, **** $p < 0.0001$) determined using ANOVA and Dunnett' s post-test. Adenosine derivatives were compared to adenosine, while NECA derivatives were compared to NECA.

Table 5.6. Binding of synthetic adenosine and NECA phenoxycyclopentyl derivatives. pK_i values were determined through NanoBRET binding assay in HEK-293 cells stably expressing human or rat Nluc-A_1R.

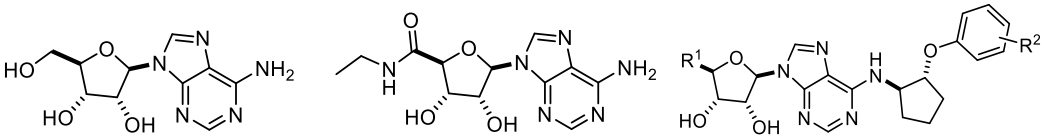

Cmpd	R^1	R^2	hA_1R		rA_1R	
			pK_i[a]	N	pK_i[a]	n
Adenosine	-	-	6.09 ± 0.06	4	6.06 ± 0.05	3
24	$-CH_2OH$	H	6.84 ± 0.06****	5	6.60 ± 0.02****	5
25	$-CH_2OH$	*p*-*t*-Bu	6.35 ± 0.08	3	6.70 ± 0.05****	3
26	$-CH_2OH$	*m*-OMe	6.61 ± 0.07**	3	6.56 ± 0.06****	3
27	$-CH_2OH$	*m*-Br	7.55 ± 0.11****	3	6.94 ± 0.08****	3
28	$-CH_2OH$	*o*-Cl	7.17 ± 0.06****	3	7.28 ± 0.04****	3
29	$-CH_2OH$	*m*-Cl	7.19 ± 0.07****	3	7.36 ± 0.03****	3
30	$-CH_2OH$	*p*-Cl	6.23 ± 0.11	3	6.22 ± 0.06	3
NECA	-	-	6.61 ± 0.06	5	6.38 ± 0.04	6
49	-CONHEt	H	7.30 ± 0.05***	3	7.41 ± 0.03****	3
50	-CONHEt	*p*-*t*-Bu	6.35 ± 0.07	3	6.85 ± 0.05****	3
51	-CONHEt	*m*-OMe	7.26 ± 0.14***	3	6.85 ± 0.06****	3
52	-CONHEt	*m*-Br	7.05 ± 0.16*	3	6.82 ± 0.10***	3
53	-CONHEt	*o*-Cl	7.39 ± 0.04****	3	7.60 ± 0.04****	3
54	-CONHEt	*m*-Cl	7.43 ± 0.05****	3	7.51 ± 0.06****	3
55	-CONHEt	*p*-Cl	6.86 ± 0.10****	3	7.09 ± 0.04****	3

Data are the mean ± SEM of n individual data sets, conducted in duplicate.
[a] The binding affinity for each agonist.
Statistical significance (* $p < 0.05$, ** $p < 0.01$, *** $p < 0.001$, **** $p < 0.0001$) determined using ANOVA and Dunnett' s post-test. Adenosine derivatives were compared to adenosine, while NECA derivatives were compared to NECA.

There is a similar binding profile across human and rat A_1R, which suggests that further studies in rats down the line would be relevant for potential therapeutical use in humans. Also, looking closer at the adenosine- and NECA-derived analogues pairs, it can be noted that they also display very similar

affinities at both human and rat A_1R. This suggest that the differences in the affinity of the compounds for the A_1R are primarily driven by the R^2 substituent on the phenoxy or benzyloxy ring.

At the human A_1R, the compound with the highest affinity is compound 27 (pK_i = 7.55 ± 0.11), followed by 28, 29, 49, 51, 53 and 54 (pK_i of 7.17 ± 0.06, 7.19 ± 0.07, 7.30 ± 0.05, 7.26 ± 0.14, 7.39 ± 0.04, 7.43 ± 0.05, respectively). All of these have higher affinity than BnOCPA and the parent compounds adenosine and NECA alone at the hA_1R. They are also all phenoxycyclopentyl derivatives. It was discussed above that a halogen substituent in the *meta* position on the aromatic ring seems to confer high efficacy at the human A_1R and similar findings can be observed here. All the above-named compounds except 49 and 51 have a halogen (chloride or bromide) substituent, mostly in the meta-position of the aromatic phenoxy ring, suggesting this substituent confers both high efficacy and high affinity at the hA_1R. At the rat A_1R, compound with the highest affinity is 49 (pK_i = 7.41 ± 0.03), followed by 28, 29, 53 and 54 (pK_i of 7.28 ± 0.04, 7.36 ± 0.03, 7.39 ± 0.04, 7.43 ± 0.05, respectively). Interestingly, compounds 27 and 52 with the bromide substituent on the phenoxy ring display reduced affinity at the rA_1R when compared to 29 and 54, respectively, that contain the chloride substituent at the same position.

5.4.2 Phenoxycyclopentyl derivatives have higher residence times at both human and rat A_1R

The NanoBRET binding assay can also be used for the determination of real-time kinetics and affinities of the compounds binding (Barkan et al., 2020; Guo et al., 2017; Sykes et al., 2019; Vauquelin, 2016). More specifically, k_{on} (k_3) and k_{off} (k_4) values for the AR ligands can be determined by fitting the kinetic traces with the 'kinetics of competitive binding' model build into GraphPad Prism 9.3 (Tables 5.7, 5.8 5.9 and 5.10) (Motulsky and Mahan, 1984). Residence time (RT) for each compound can then be calculated as a reciprocal of the k_{off}. Furthermore, pK_d of the compounds (k_4/k_3) can also be calculated from the kinetics assays and compared to the pK_i values determined from the saturation binding assays. For the human A_1R, the kinetic parameters of the fluorescent compound CA200645 binding were determined as k_{on} (k_1) = 3.67 ± 0.34 × 10^6 M^{-1} min^{-1}, k_{off} (k_2) = 0.064 ±0.0023 min^{-1} with a K_d = 18.29 ± 2.4 nM.. The kinetics of binding for CA200645 binding at rat A_1R were determined as k_{on} (k_1) = 2.93 ± 0.24 × 10^6 M^{-1} min^{-1}, k_{off} (k_2) = 0.066 ± 0.0022 min^{-1} with a K_d = 32.96 ± 2.8 nM.

Table 5.7. Kinetics of binding of synthetic adenosine and NECA benzyloxycyclopentyl derivatives to the orthosteric binding site at human A_1R. Kinetic parameters were determined using NanoBRET binding assays in HEK-293 cells stably expressing human Nluc-A_1R.

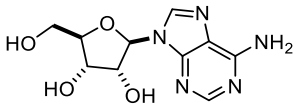
adenosine

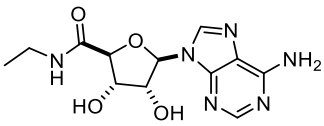
NECA

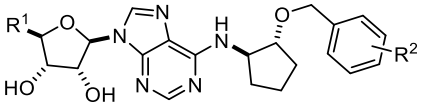
BnOCPA, **19-23**, **44-48**

Cmpd	R^1	R^2	k_{on} (k_3) ($\times 10^5$ M^{-1})[a]	k_{off} (k_4) (min^{-1})[b]	pK_d[c]	RT (min)[d]	n
Adenosine	-	-	1.65 ± 0.24	0.048 ± 0.002	6.53 ± 0.07	21.15 ± 0.84	4
BnOCPA	$-CH_2OH$	H	1.47 ± 0.33	0.068 ± 0.002	6.30 ± 0.09	14.75 ± 0.56	3
NECA	-	-	2.04 ± 0.07	0.049 ± 0.005	6.63 ± 0.06	20.97 ± 1.98	5
19	$-CH_2OH$	*m*-OMe	2.51 ± 0.36	0.041 ± 0.004	6.77 ± 0.02	24.64 ± 1.98	3
20	$-CH_2OH$	*m*-Br	0.56 ± 0.12	0.080 ± 0.016	5.84 ± 0.02	14.84 ± 3.83	3
21	$-CH_2OH$	*p*-Br	0.66 ± 0.02	0.065 ± 0.010	6.02 ± 0.06	16.72 ± 3.01	3
22	$-CH_2OH$	*o*-Cl	2.75 ± 0.14	0.055 ± 0.012	6.74 ± 0.10	22.22 ± 6.21	3
23	$-CH_2OH$	*m*-Cl	1.40 ± 0.08	0.051 ± 0.015	6.48 ± 0.09	24.12 ± 5.29	3
44	-CONHEt	*m*-OMe	1.12 ± 0.09	0.110 ± 0.024	6.04 ± 0.10	10.59 ± 2.34	3
45	-CONHEt	*m*-Br	0.83 ± 0.06	0.095 ± 0.011	5.94 ± 0.02	10.78 ± 1.28	3
46	-CONHEt	*p*-Br	1.01 ± 0.06	0.076 ± 0.007	6.13 ± 0.03	13.55 ± 1.36	3
47	-CONHEt	*o*-Cl	3.64 ± 0.33	0.044 ± 0.009	6.94 ± 0.08	25.70 ± 4.63	3
48	-CONHEt	*m*-Cl	1.80 ± 0.17	0.040 ± 0.006	6.67 ± 0.05	27.96 ± 5.57	3

Data are the mean ± SEM of n individual data sets, conducted in duplicate.
[a] k_{on} (k_3) for each ligand determined through fitting with the 'kinetics of competitive binding' model.
[a] k_{off} (k_4) for each ligand determined as in [a].
[c] Kinetic dissociation constant (pK_d) for each ligand as determined from k_{on}/k_{off}.
[d] Residence time of each ligand as determined from $1/k_{off}$.

Table 5.8. Kinetics of binding of synthetic adenosine and NECA phenoxycyclopentyl derivatives to the orthosteric binding site at human A_1R. Kinetic parameters were determined using NanoBRET binding assays in HEK-293 cells stably expressing human Nluc-A_1R.

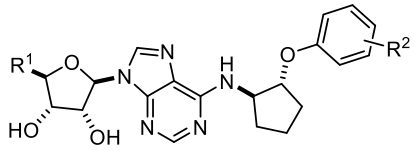

24-30, 49-55

Cmpd	R^1	R^2	k_{on} (k_3) ($\times 10^5$ M^{-1})[a]	k_{off} (k_4) (min^{-1})[b]	pK_d[c]	RT (min)[d]	n
24	$-CH_2OH$	H	4.78 ± 0.93	0.048 ± 0.004	6.97 ± 0.06	21.56 ± 2.13	5
25	$-CH_2OH$	*p*-*t*-Bu	1.48 ± 0.04	0.054 ± 0.005	6.44 ± 0.03	19.12 ± 2.01	3
26	$-CH_2OH$	*m*-OMe	2.97 ± 0.27	0.037 ± 0.003	6.90 ± 0.01	27.61 ± 2.09	3
27	$-CH_2OH$	*m*-Br	10.12 ± 1.29	0.038 ± 0.012	7.47 ± 0.09	33.13 ± 10.40	3
28	$-CH_2OH$	*o*-Cl	11.61 ± 1.31	0.052 ± 0.004	7.34 ± 0.04	19.55 ± 1.48	3
29	$-CH_2OH$	*m*-Cl	25.90 ± 2.14	0.040 ± 0.003	7.81 ± 0.02	25.37 ± 1.70	3
30	$-CH_2OH$	*p*-Cl	1.01 ± 0.31	0.056 ± 0.009	6.22 ± 0.13	19.46 ± 3.34	3
49	-CONHEt	H	16.43 ± 2.81	0.028 ± 0.002	7.63 ± 0.01	32.82 ± 1.02	3
50	-CONHEt	*p*-*t*-Bu	1.53 ± 0.11	0.091 ± 0.010	6.23 ± 0.06	11.47 ± 1.48	3
51	-CONHEt	*m*-OMe	4.27 ± 0.03	0.027 ± 0.007	7.23 ± 0.11	42.68 ± 10.88	3
52	-CONHEt	*m*-Br	5.57 ± 2.56	0.075 ± 0.038	6.91 ± 0.04	27.87 ± 14.23	3
53	-CONHEt	*o*-Cl	17.27 ± 1.12	0.041 ± 0.010	7.66 ± 0.11	29.44 ± 6.91	3
54	-CONHEt	*m*-Cl	20.28 ± 1.11	0.043 ± 0.013	7.75 ± 0.16	34.70 ± 13.43	3
55	-CONHEt	*p*-Cl	3.75 ± 1.04	0.076 ± 0.024	6.71 ± 0.03	17.48 ± 4.79	3

Data are the mean ± SEM of n individual data sets, conducted in duplicate.

[a] k_{on} (k_3) for each ligand determined through fitting with the 'kinetics of competitive binding' model.

[a] k_{off} (k_4) for each ligand determined as in [a].

[c] Kinetic dissociation constant (pK_d) for each ligand as determined from k_{on}/k_{off}.

[d] Residence time of each ligand as determined from $1/k_{off}$.

Table 5.9. Kinetics of binding of synthetic adenosine and NECA benzyloxycyclopentyl derivatives to the orthosteric binding site at rat A_1R. Kinetic parameters were determined using NanoBRET binding assays in HEK-293 cells stably expressing rat Nluc-A_1R.

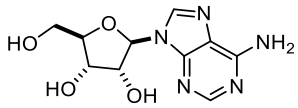
adenosine

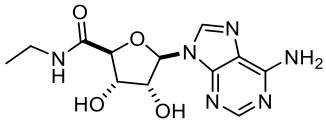
NECA

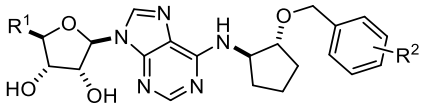
BnOCPA, **19-23**, **44-48**

Cmpd	R^1	R^2	k_{on} (k_3) ($\times 10^5$ M^{-1})[a]	k_{off} (k_4) (min^{-1})[b]	pK_d[c]	RT (min)[d]	n
Adenosine	-	-	0.52 ± 0.22	0.079 ± 0.007	5.71 ± 0.17	12.86 ± 1.10	3
BnOCPA	$-CH_2OH$	H	1.57 ± 0.54	0.054 ± 0.007	6.40 ± 0.11	19.42 ± 2.21	6
NECA	-	-	2.29 ± 0.39	0.066 ± 0.008	6.53 ± 0.04	15.84 ± 2.05	6
19	$-CH_2OH$	*m*-OMe	2.52 ± 0.31	0.083 ± 0.016	6.49 ± 0.03	13.22 ± 2.10	3
20	$-CH_2OH$	*m*-Br	1.50 ± 0.29	0.097 ± 0.008	6.17 ± 0.09	10.56 ± 0.81	3
21	$-CH_2OH$	*p*-Br	1.13 ± 0.09	0.066 ± 0.010	6.24 ± 0.03	16.05 ± 2.09	3
22	$-CH_2OH$	*o*-Cl	5.07 ± 0.26	0.090 ± 0.015	6.77 ± 0.06	12.10 ± 2.06	3
23	$-CH_2OH$	*m*-Cl	2.85 ± 0.22	0.060 ± 0.006	6.68 ± 0.06	17.13 ± 1.54	3
44	-CONHEt	*m*-OMe	1.96 ± 0.13	0.141 ± 0.018	6.15 ± 0.06	7.41 ± 0.82	3
45	-CONHEt	*m*-Br	2.95 ± 0.41	0.121 ± 0.012	6.38 ± 0.06	8.51 ± 0.82	3
46	-CONHEt	*p*-Br	2.14 ± 0.14	0.058 ± 0.003	6.56 ± 0.01	17.30 ± 1.02	3
47	-CONHEt	*o*-Cl	7.31 ± 0.61	0.046 ± 0.002	7.20 ± 0.03	21.98 ± 1.13	3
48	-CONHEt	*m*-Cl	7.54 ± 0.30	0.073 ± 0.004	7.02 ± 0.03	13.90 ± 0.72	3

Data are the mean ± SEM of n individual data sets, conducted in duplicate.
[a] k_{on} (k_3) for each ligand determined through fitting with the 'kinetics of competitive binding' model.
[a] k_{off} (k_4) for each ligand determined as in [a].
[c] Kinetic dissociation constant (pK_d) for each ligand as determined from k_{on}/k_{off}.
[d] Residence time of each ligand as determined from $1/k_{off}$.

Table 5.10. Kinetics of binding of synthetic adenosine and NECA phenoxycyclopentyl derivatives to the orthosteric binding site at rat A_1R. Kinetic parameters were determined using NanoBRET binding assays in HEK-293 cells stably expressing rat Nluc-A_1R.

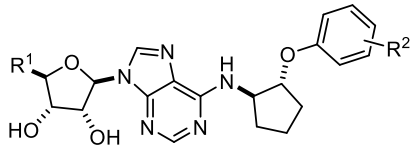

24-30, 49-55

Cmpd	R^1	R^2	k_{on} (k_3) ($\times 10^5$ M^{-1})[a]	k_{off} (k_4) (min^{-1})[b]	pK_d[c]	RT (min)[d]	n
24	-CH_2OH	H	2.70 ± 0.34	0.053 ± 0.001	6.70 ± 0.06	18.91 ± 0.30	5
25	-CH_2OH	*p*-*t*-Bu	4.84 ± 0.37	0.484 ± 0.173	6.17 ± 0.30	5.53 ± 3.31	3
26	-CH_2OH	*m*-OMe	3.32 ± 0.52	0.085 ± 0.007	6.58 ± 0.03	12.06 ± 1.03	3
27	-CH_2OH	*m*-Br	13.30 ± 1.21	0.050 ± 0.005	7.42 ± 0.03	20.40 ± 1.86	3
28	-CH_2OH	*o*-Cl	17.92 ± 1.30	0.048 ± 0.005	7.58 ± 0.01	21.46 ± 2.08	3
29	-CH_2OH	*m*-Cl	30.07 ± 4.02	0.071 ± 0.010	7.63 ± 0.12	15.20 ± 2.50	3
30	-CH_2OH	*p*-Cl	2.51 ± 0.90	0.056 ± 0.001	6.58 ± 0.15	17.90 ± 0.25	3
49	-CONHEt	H	25.12 ± 2.08	0.037 ± 0.002	7.83 ± 0.05	27.61 ± 1.66	3
50	-CONHEt	*p*-*t*-Bu	6.29 ± 0.62	0.070 ± 0.007	6.95 ± 0.01	14.76 ± 1.64	3
51	-CONHEt	*m*-OMe	11.91 ± 1.33	0.030 ± 0.006	7.62 ± 0.11	38.05 ± 8.74	3
52	-CONHEt	*m*-Br	4.46 ± 1.28	0.056 ± 0.008	6.85 ± 0.13	19.17 ± 2.68	3
53	-CONHEt	*o*-Cl	37.59 ± 1.91	0.048 ± 0.003	7.90 ± 0.00	21.23 ± 1.22	3
54	-CONHEt	*m*-Cl	35.85 ± 3.95	0.062 ± 0.007	7.76 ± 0.10	16.78 ± 2.22	3
55	-CONHEt	*p*-Cl	11.62 ± 0.26	0.064 ± 0.003	7.26 ± 0.01	15.65 ± 0.78	3

Data are the mean ± SEM of n individual data sets, conducted in duplicate.
[a] k_{on} (k_3) for each ligand determined through fitting with the 'kinetics of competitive binding' model.
[a] k_{off} (k_4) for each ligand determined as in [a].
[c] Kinetic dissociation constant (pK_d) for each ligand as determined from k_{on}/k_{off}.
[d] Residence time of each ligand as determined from $1/k_{off}$.

It was perhaps unsurprising given the previous data, which showed adenosine and NECA phenoxycyclopentyl derivatives having the highest affinities for A_1R, that these compounds also had highest residence times at both human and rat A_1R. At the human A_1R compound with highest residence time is 51 (RT = 42.68 ± 10.88 min) with compounds 27, 49, 53 and 54 all also having RT of 29-35 minutes. For the rest of the compounds, and particularly for the benzyloxycyclopentyl derivatives, the RT is lower. The pk_d values also compared quite well to the pK_i values obtained from the saturation binding assays.

Overall, adenosine and NECA phenoxycyclopentyl derivatives, and especially those with a halogen substituent as R^2 group on the aromatic ring, have higher affinity for both human and rat A_1R. Considering the substitution position on the phenoxy ring, the highest affinity was observed with the halogen in the *meta*-position (27, 29, 54), followed by *ortho*- (28, 53) and the *para*-position (30, 55).

5.5 Data from functional and binding experiments show positive correlation

Lastly, it was desirable to see how the efficacy data from cAMP accumulation assay compare with the kinetic data obtained from the NanoBRET binding assay at the human A_1R. First, potency (pIC_{50} values) was compared with the affinity (pK_i values) and a clear positive correlation was shown (r = 0.82) (Figure 5.11.A). In particular, compounds 27, 29, 49 and 51-54 were identified as both the most potent and strongest binders at the hA_1R. A second comparison between potency (pIC_{50} values) and AR ligands' residence time also revealed clear positive correlation (r = 0.65) (Figure 5.11.B) with the same compounds 27, 29, 49 and 51-54 coming up as best. Taken together with the selectivity data, very selective, potent, and high affinity hA_1R agonists were identified, namely compounds 27, 49 and 51-54.

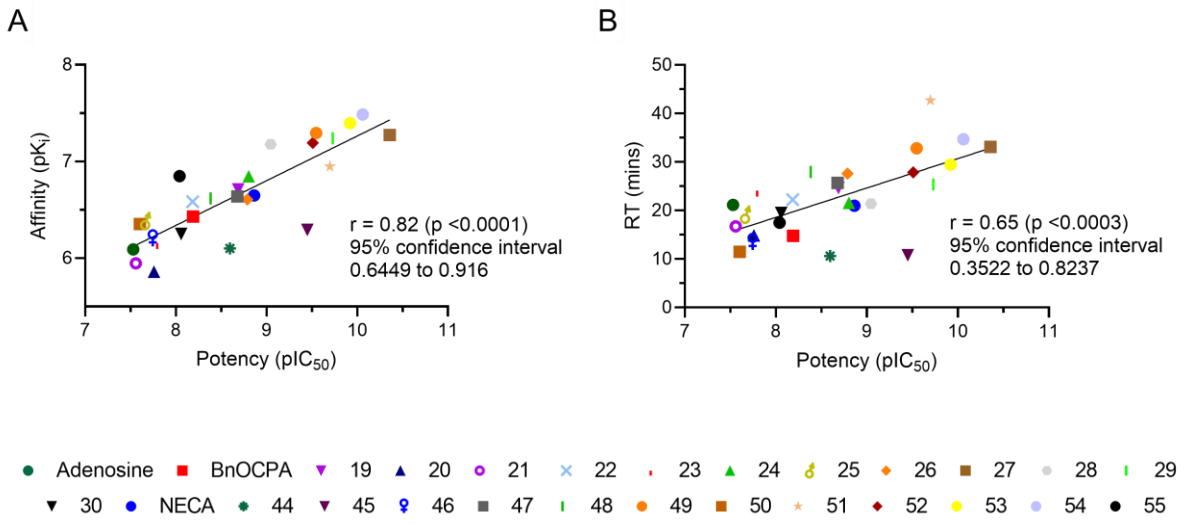

Figure 5.11. NECA and adenosine derivatives show correlation between potency and affinity or residence time at the human A_1R. A. pIC_{50} values for each AR agonist measured by cAMP accumulation assay plotted against pK_i values obtained from NanoBRET experiments at the hA_1R. B. pIC_{50} values for each AR agonist measured by cAMP accumulation assay plotted against RT values from NanoBRET experiments at hA_1R.

5.6 Discussion

5.6.1 Improving upon BnOCPA potency

BnOCPA is a high potency A_1R-selective full agonist that has been shown to be a powerful analgesic but does not cause sedation, bradycardia, hypotension or respiratory depression (Knight et al., 2016; Wall et al., 2022). What makes BnOCPA particularly interesting is the fact that it exclusively activates G_{ob} and this highly specific Gα-selective A_1R activation makes it a very therapeutically promising compound. As discussed above, MD simulations predicted that residues $R291^{7.56}$ and $I292^{8.47}$ are likely involved in A_1R/Gα coupling (Deganutti et al., 2021b; Wall et al., 2022) and here we show that, in particular, residues $R291^{7.56}$, $I292^{8.47}$ and $Q293^{8.48}$ are required for selective agonist coupling to $G\alpha_{o/i}$.

Although BnOCPA itself is a very promising compound, the main goal of this chapter was to further improve upon its potency. Preti et al. (2022) explored extended BnOCPA derivatives but found than none of these compounds improved upon BnOCPA potency or affinity at the A_1R. Instead, here we designed a new series of compounds based on adenosine (19-30) and their structural analogues based on NECA (44-55). One of the potential questions to raise is why this new series does not also include a NECA-based BnOCPA derivative (BnOCPA is an adenosine-based compound)? The answer is

that this has already been tried by (Knight et al., 2016) and they found that the resulting compound lost its selectivity, which is key to avoiding side effects like sedation.

Regarding the new compounds, they all showed full agonist activity at the A_1R except 27, 48, 50 and 53, which were partial agonists. Overall, compound 27 was the most potent A_1R agonist, closely followed by 26, 45, 49, and 51-54. What is very promising is the fact that all these compounds displayed higher potency than adenosine, NECA, or BnOCPA. We also show that a halogen in meta position on the aromatic ring confers high potency to the A_1R and all most potent A_1R agonists but 45 feature an N^6-phenoxycyclopentyl moiety.

5.6.2 Reaching more than 10,000-fold selectivity for A_1R over other subtypes

Key characteristic of BnOCPA is its selectivity for the A_1R as the structural similarity between the orthosteric site of the four adenosine receptor subtypes often results in reduced selectivity of the compounds targeting them. When tested at the remaining adenosine receptor subtypes, all compounds displayed only a very weak efficacy at both the $A_{2A}R$ and $A_{2B}R$, with many failing to generate full dose-dependent response curves at the concentrations tested, resulting in adenosine and NECA remaining the only potent compounds at these two receptors. At the A_3R, the adenosine derivatives showed either a loss of efficacy or partial activity, while all the NECA-based compounds (44-55) behaved as full agonists, although with reduced potency compared to NECA itself.

Overall, all the compounds display at least partial selectivity for A_1R except adenosine that is close to being an equipotent agonist at all the receptors. From the adenosine-based derivatives, compounds 22, 23, 26, and 27 display the most A_1R selectivity, while compounds 28-30 also show activity at A_3R. Generally, however, the NECA-based derivatives, primarily 44, 45, 51-53, are more A_1R selective than the adenosine derivatives due to NECA itself being an A_1R selective compound by approximately 10-fold. Compounds 45 and 51 are approximately 1,500-fold more A_1R selective than NECA itself, suggesting more than 10,000-fold selectivity overall.

Furthermore, we show that the selectivity can be driven both by the position of the substituent on the phenoxy group (compounds 26 and 51 or 30 and 55) or the ribose C-5' substituent group with the adenosine-derived compound being more A_1R selective (25 and 50).

5.6.3 Assessing compound binding across human and rat A_1R

Since A_1R agonists are promising compounds for the treatment of glaucoma, type 2 diabetes mellitus, pain, epilepsy and cerebral ischemia, it is important to assess their binding properties at both

human and rat A_1R, as the latter is commonly used as a model in preclinical studies (Chen et al., 2013; Sawynok, 2016). The tested compounds show overall a very similar binding profile across the human and rat A_1R, suggesting that further studies in rats would be highly relevant for the potential use of the compounds in humans.

The compounds with highest affinities at the human A_1R are 27-29, 49, 51, 53, and 54, all of which have affinities higher than the starting compounds adenosine and NECA and are all phenoxycyclopentyl derivatives. Regarding the substituents, the fact that the adenosine and NECA-derived analogue pairs display very similar affinities for both human and rat A_1R, suggests that it is the R_2 substituent on the phenoxy or benzyloxy ring that is the key to determining the compound A_1R affinity. Considering the substitution position on the phenoxy ring, we observed the highest affinity with the chloride in the meta-position (29, 54), followed by ortho- (28, 53) and the para-position (30, 55). Overall, halogen substituents as the R_2 group on the aromatic ring seem to confer high affinity for the A_1R, with chloride being preferential over bromide for binding at both the human and rat A_1R.

In this chapter we also explored the kinetics of the compounds binding at both versions of the receptor. Generally, the compounds bind slightly faster at rat A_1R, which could be because of the divergent amino acid composition of the extracellular loops between hA_1R and rA_1R, which would favour different binding paths to the orthosteric site (Deganutti et al., 2021b). Regarding the residence times at the binding site, the benzyloxycyclopentyl derivatives displayed RT comparable to adenosine and NECA on hA_1R of approximately 21 min, while the phenoxycyclopentyl analogues generally had RT over 20 min correlating to their higher affinity.

5.6.4 MD simulations providing insight into compound binding

To gain more insight into the binding of studied agonists and rationalize the selectivity displayed, Preti et al. (2022) performed in silico experiments on the phenoxycyclopentyl adenosine derivative 27, the most A_1R-selective and potent agonist, and its benzyloxycyclopentyl congener 20 using MD-derived ARs structures (Figure 5.12). The MD simulations showed that 27 stably bound to A_1R and $A_{2A}R$ but not A_3R, while 20 also stably bound to A_1R. In terms of flexibility, N^6 substituents explored divergent conformations in the different systems: the 3-bromophenyl group of 27 was highly flexible in A_3R or $A_{2A}R$ and more stable in A_1R, while the 3-bromobenzyl group of 20 displayed intermediate flexibility.

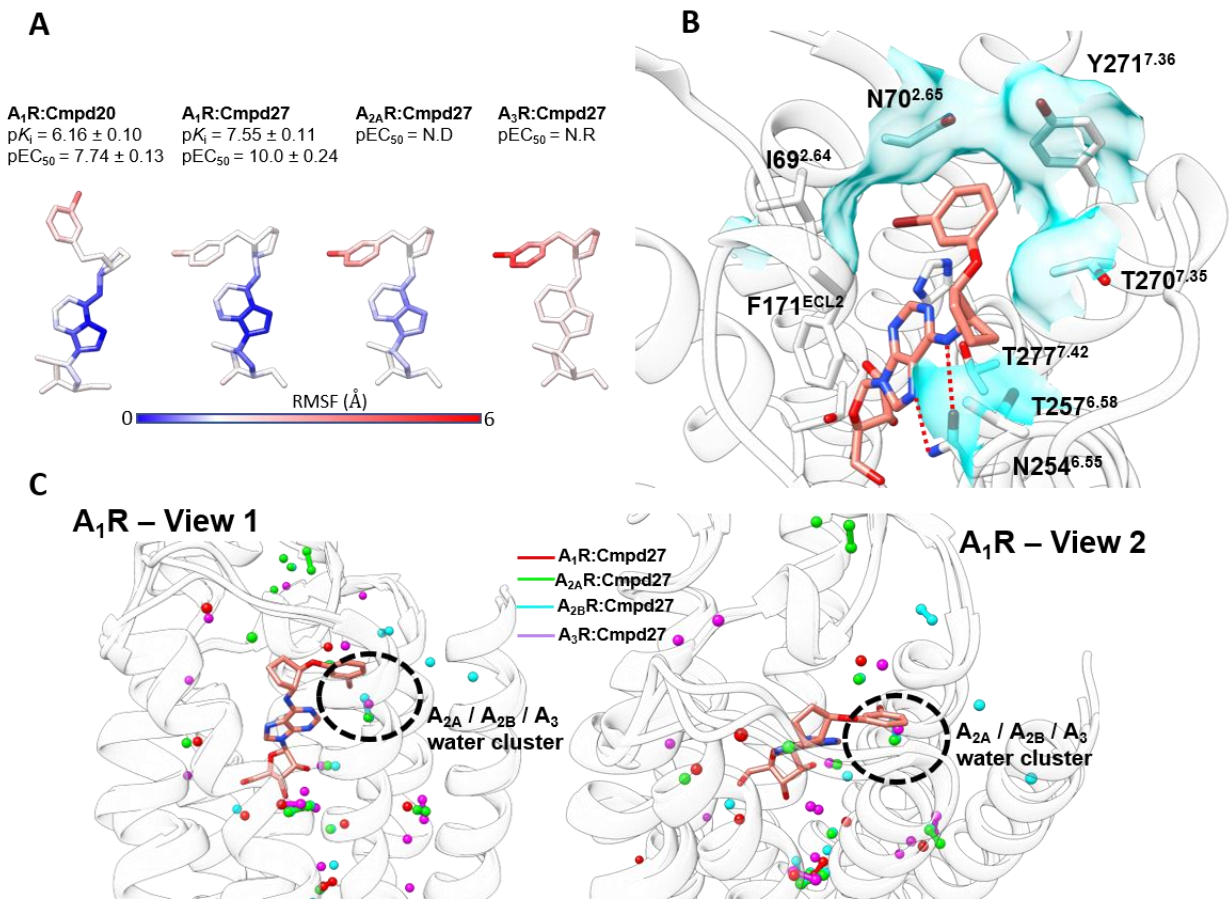

Figure 5.12. Molecular dynamics docking of 20 and 27. (A) Atomic root mean square fluctuation (RMSF) of 20 within A_1R and 27 within A_1R, $A_{2A}R$, and A_3R, plotted on the agonists' structure. (B) Compound 27 (salmon stick representation) binding mode within A_1R (white ribbon and sticks); the key hydrogen bonds with N254$^{6.55}$ are shown as red dotted lines, while the hydrophobic sub pocket is shown as cyan transparent surface. (C) Two side view comparison of the structural water molecules detected in A_1R (red spheres), $A_{2A}R$ (green), $A_{2B}R$ (cyan), and A_3R (purple). The position of the stable water cluster only present in $A_{2A}R$, $A_{2B}R$ and A_3R is highlighted. Binding mode of 27 (salmon sticks) within A_1R is superimposed for reference. This figure was adapted from Preti et al. (2022).

As shown in Figure 5.12.B, at the A_1R 27 formed key hydrogen bonds with N254$^{6.55}$, hydrophobic contacts with F171^{ECL2}, and oriented the 3-bromophenyl moiety in a hydrophobic sub pocket formed by I69$^{2.64}$, N70$^{2.65}$, Y271$^{7.36}$, and T270$^{7.35}$. On the other hand, 20, which is a bulkier compound, was not able to completely accommodate the 3-bromobenzyl group within this pocket and therefore displayed higher flexibility at the N^6 level, which could contribute to reduced affinity and efficacy of 20 compared to 27 at the A_1R. 27 is further stabilised by the hydrophobic sub-pocket that is putatively present only in A_1R, hence, 27 cannot be completely stabilized by the other AR subtypes (Figure 5.12.C).

To validate the MD simulations, Preti et al. (2022) also mutated key A_1R amino acids to observe the effects on the binding of 20, 27 and BnOCPA. They found that alanine mutagenesis of I69$^{2.64}$ and Y271$^{7.36}$ reduced affinity of BnOCPA, 20 and 27 to A_1R, proving their importance for compound binding at the receptor. Mutation of N70$^{2.65}$ then significantly reduced affinity of 20, while it had no significant effect on 27 and BnOCPA, which could be because of different orientation of the side chain between the two compounds. Mutation of T257$^{6.58}$ increased 27 and BnOCPA binding affinity, while having no effect on 20. This can be probably attributed to the increased lipophilicity of the protein environment underneath extracellular loop 3 (ECL3), which surrounds the cyclopentyl groups of the molecules. It is therefore apparent that the small molecule 27 favours a more hydrophobic environment within the binding pocket which is already suitable for 20.

5.7 Conclusion

This chapter followed on from work identifying BnOCPA as a potent A_1R-selective agonist biased towards the G_{ob} protein (Deganutti et al., 2021a; Wall et al., 2022). First, site-directed alanine mutagenesis of amino acids suggested by MD simulations coupled with cAMP accumulation assay was used to probe the transduction of the signal from various A_1R agonists, including BnOCPA, to the $G\alpha_{o/i}$ proteins. The results suggest that namely residues R291$^{7.56}$, I292$^{8.47}$ and Q293$^{8.48}$ are required for selective agonist coupling to $G\alpha_{o/i}$ proteins and may thus contribute to the Gα bias of these agonists.

Furthermore, with the aim of improving upon BnOCPA potency and affinity further without losing its selectivity, a new series of novel N^6-benzyloxycyclopentyl and N^6-phenoxycyclopentyl derivatives of adenosine and NECA was designed. These AR ligands were then evaluated for potency, selectivity and binding at adenosine receptors using cAMP accumulation assay in CHO or Flp-In CHO cells stably expressing ARs and NanoBRET binding assay in HEK-293 cells stably expressing Nluc-A_1R.

The findings presented in this chapter showed that phenoxycyclopentyl adenosine and NECA derivatives have generally higher potency and affinity at A_1R than their benzyloxycyclopentyl analogues. The results also suggest that halogen substituent (chloride or bromide) on the aromatic ring confers high affinity and efficacy at the A_1R, particularly if the halogen is in the *meta* position of the aromatic ring.

Furthermore, the study of selectivity showed that NECA-based derivatives have overall higher A_1R selectivity over the other AR subtypes. Compounds 45 and 51, especially, are showing ~1500 fold improved A_1R selectivity over NECA, which is already an A_1R selective compound.

Altogether, new very selective, very potent and high affinity A_1R agonists were identified, namely phenoxycyclopentyl compounds 27, 49, 51-54. These adenosine and NECA derivates were built upon the promising BnOCPA compound and show great therapeutic promise for overcoming insufficient receptor selectivity and potency that many current compounds face.

Chapter 6. Pharmacological characterisation of novel adenosine A_1 and A_3 receptor antagonists

6.1 Introduction

Adenosine is a naturally occurring purine nucleoside and also the endogenous agonist of adenosine receptors. AR family consists of four subtypes. A_1R and A_3R are predominantly $G_{i/o}$-coupled receptors leading to inhibition of AC and decrease of intracellular levels of the second messenger cAMP. On the other hand, $A_{2A}R$ and $A_{2B}R$ are predominantly G_s-coupled receptors leading to activation of AC and increase of intracellular cAMP.

A_1R is widely distributed in the human body and A_1R antagonists have been researched as potassium-sparing diuretic agents with kidney-protecting properties or drugs for chronic heart diseases or lung diseases such as asthma, chronic obstructive pulmonary disease and pulmonary fibrosis (Modlinger and Welch, 2003; Schenone et al., 2010; Shah and Frishman, 2009; Wilson et al., 2009). The wakefulness inducing effect of caffeine, a classical non-selective adenosine antagonist, has also inspired the search for selective antagonists endowed with CNS activity (Maemoto et al., 2004). For example, Trevitt et al. (2009) showed that A_1R-selective antagonist CPT (8-cyclopentyl-1,3-dimethylxanthine) showed promise for treatment of Parkinson's disease by improving locomotion and reducing catalepsy, a sudden physical collapse following strong emotion or laughter.

Similarly, to the A_1R, A_3R antagonists have also been explored for their role in CNS disorders. In particular, A_3R activation reduces the stability of inhibitory γ-aminobutyric acid (GABA) currents in human epileptic tissues and stimulates serotonin (5-HT) reuptake by solute carrier family 6 member 4 (SLC6A4) in the brain, meaning A_3R antagonists may be beneficial in refractory epilepsy and mental illnesses characterised by hyposerotonergic states such as major depressive disorder (Roseti et al., 2009; Zhu et al., 2007). Furthermore, A_3R antagonists hold potential for the treatment of asthma since A_3R activation promotes human mast cell degranulation and release of inflammatory mediators contributing to asthma pathogenesis (Leung et al., 2014; Tilley et al., 2003). A_3R antagonists have also proven effective in eye pathogenesis by lowering intraocular pressure. González-Fernández et al. (2014) has shown that A_3R-selective antagonist MRS1220 (N-[9-chloro-2-(2-furanyl)-1,2,4-triazolo[1,5-c]quinazolin-5-yl]benzeneacetamide) prevents oligodendrocyte damage and myelin loss in the rat eye. Apart from inhibiting cAMP levels, A_3R receptor can also couple to $G_{q/11}$ subunits and stimulate rises in $(Ca^{2+})_i$ mobilisation and MAPK activation explaining its role in cell proliferation and differentiation and in tumour progression (Borea et al., 2015; Schulte and Fredholm, 2002). Due to its overexpression

in several cancer cell types, A_3R is considered a possible biological marker for tumours (Borea et al., 2015; Cohen and Fishman, 2019). Lee et al. (2013) showed that a potent A_3R-selective antagonist LJ-1888 ((2R,3R,4S)-2-[2-chloro-6-(3-iodobenzylamino)-9H-purine-9-yl]tetrahydrothiophene-3,4-diol) blocked the development and attenuated the progression of renal interstitial fibrosis. Ultimately, there is a large untapped potential for antagonists targeting the A_1R and A_3R warranting the search for new potent and selective compounds.

Traditionally, AR selective antagonists have been discovered by either modifying AR agonists to lose their efficacy while retaining binding or by modifying wide acting non-selective AR antagonists in a bid to make them more selective (Ciancetta and Jacobson, 2017). However, increase in solved X-ray crystallography and cryo-EM structures in the last decade led to a more and more favoured approach of a simultaneous use of *in silico* and *in vitro* approaches. For example, Prof Ladds' and Prof Kolocouris' labs have previously combined *in silico* screening against the $A_{2A}R$ structure with ZM241385 (PDB ID 3EML) with *in vitro* cAMP accumulation assays to identify A_3R-selective antagonists with low micromolar affinities (Barkan et al., 2020; Jaakola et al., 2008; Lagarias et al., 2018).

Until 2017, $A_{2A}R$ had been the only AR subtype for which there were solved 3D structures, but now several A_1R structures are also available (Cheng et al., 2017; Glukhova et al., 2017; GPCRdb, 2022). Moreover, i*n silico* homology modelling enables the prediction of $A_{2B}R$ and A_3R structures based on the currently solved structures. Apart from enabling *in silico* screening of chemical compounds, these structures and homology models also enable *in silico* investigation of compounds' binding mode at the receptors, which can help in better understanding which parts of the compounds are key for potency and selectivity.

Affinity is another important parameter typically measured for interesting compounds. But there has been rising realization that selecting ligands just based on their affinity, which is an equilibrium characteristic, does not always linearly translate into good *in vivo* efficacy. Kinetic profiling allows the measurement of association rate constant k_{on}, dissociation rate constant k_{off}, residence time and dissociation constant (Guo et al., 2017; Sykes et al., 2019). These are all relevant parameters of drug candidates that can give good indication of drug performance *in vivo*. Kinetic parameters of some currently known A_1R and A_3R antagonists are shown in Figure 6.1. Thus, the identification of ligands with desired thermodynamic and kinetic binding characteristics would provide lead compounds for further development and chemical probes for the study of these receptors.

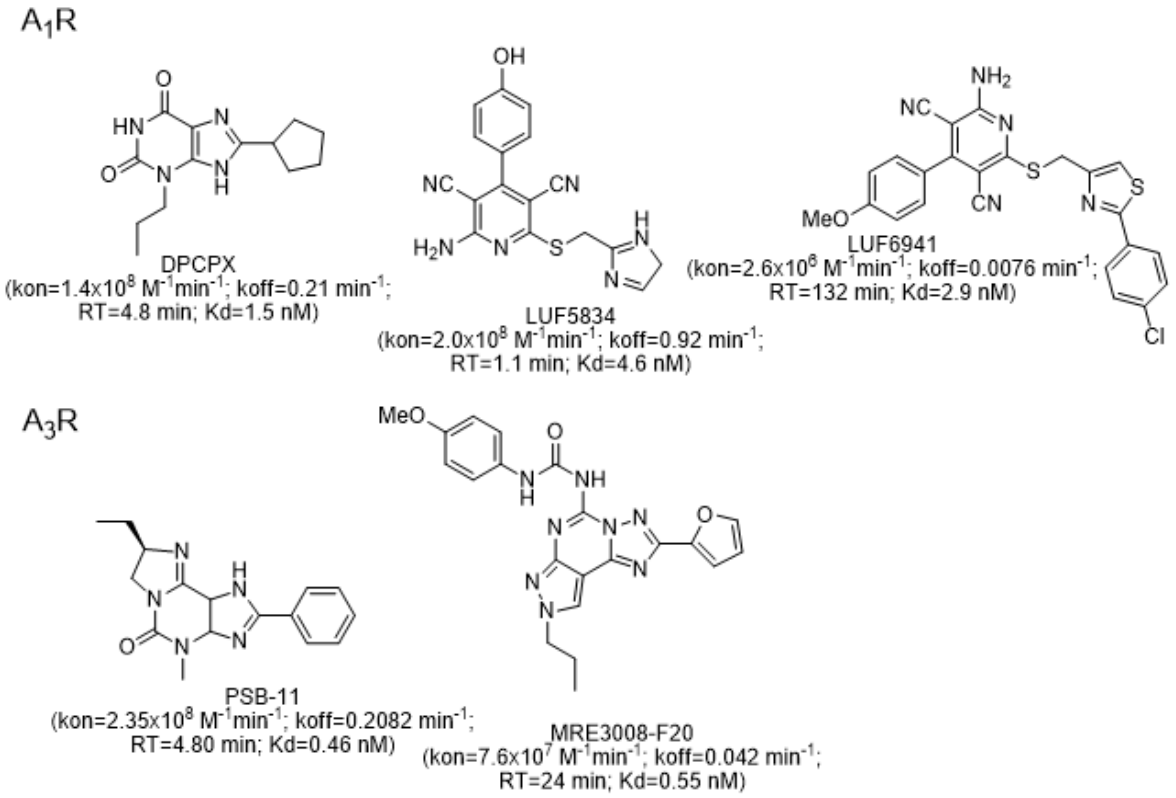

Figure 6.1. Kinetic parameters of A_1R and A_3R antagonists. K_{on}, K_{off}, RT and K_d values of selected A_1R (DPCPX, LUF5834, LUF6941) and A_3R (PSB-11, MRE3008-F20, LUF7565) antagonists (Bouzo-Lorenzo et al., 2019; Guo et al., 2014, 2013; Louvel et al., 2015; Müller et al., 2002; Varani et al., 2017). This figure was adapted from Stampelou et al. (2022).

The studies in this chapter were carried out in collaboration with Prof Kolocouris' lab (University of Athens) who supplied a series of compounds from their *in-house* library and employed computational techniques for studying them. These compounds were aromatic nitrogen heterocycles originally purposed for anti-proliferative activity, against angiogenesis, as fluorescence tracers in cells, against hepatitis B virus, and nucleosides originally tested against adenosine deaminase, hepatitis C virus, and human cytomegalovirus (Argyros et al., 2017; Evangelou et al., 2017; Gerasi et al., 2020; Lougiakis et al., 2017, 2015; Michailidou et al., 2016; Papadakis et al., 2020; Papastathopoulos et al., 2021; Xia et al., 2017). In work preceding this thesis, 96 compounds, called A1-A50 and L1-L46, were screened for potential agonistic or antagonistic activity in Flp-In A_3R CHO cells using *in vitro* second messenger assay cAMP accumulation assay (Figure 6.2) (data obtained during BA studies at University of Cambridge, L. Dhiangra and A. Suchankova). This led to identification of multiple potential new A_1R and A_3R antagonists with either the pyrazolo[3,4-c]pyridine or the pyrazolo[3,4-d]pyridazine scaffold. Full dose-response curves using the same cAMP accumulation assay were then conducted for all

significant compounds from the A series screen and only compounds A17, A26 and A47 were confirmed as A_3R antagonists (data obtained during BA studies at University of Cambridge, A. Suchankova).

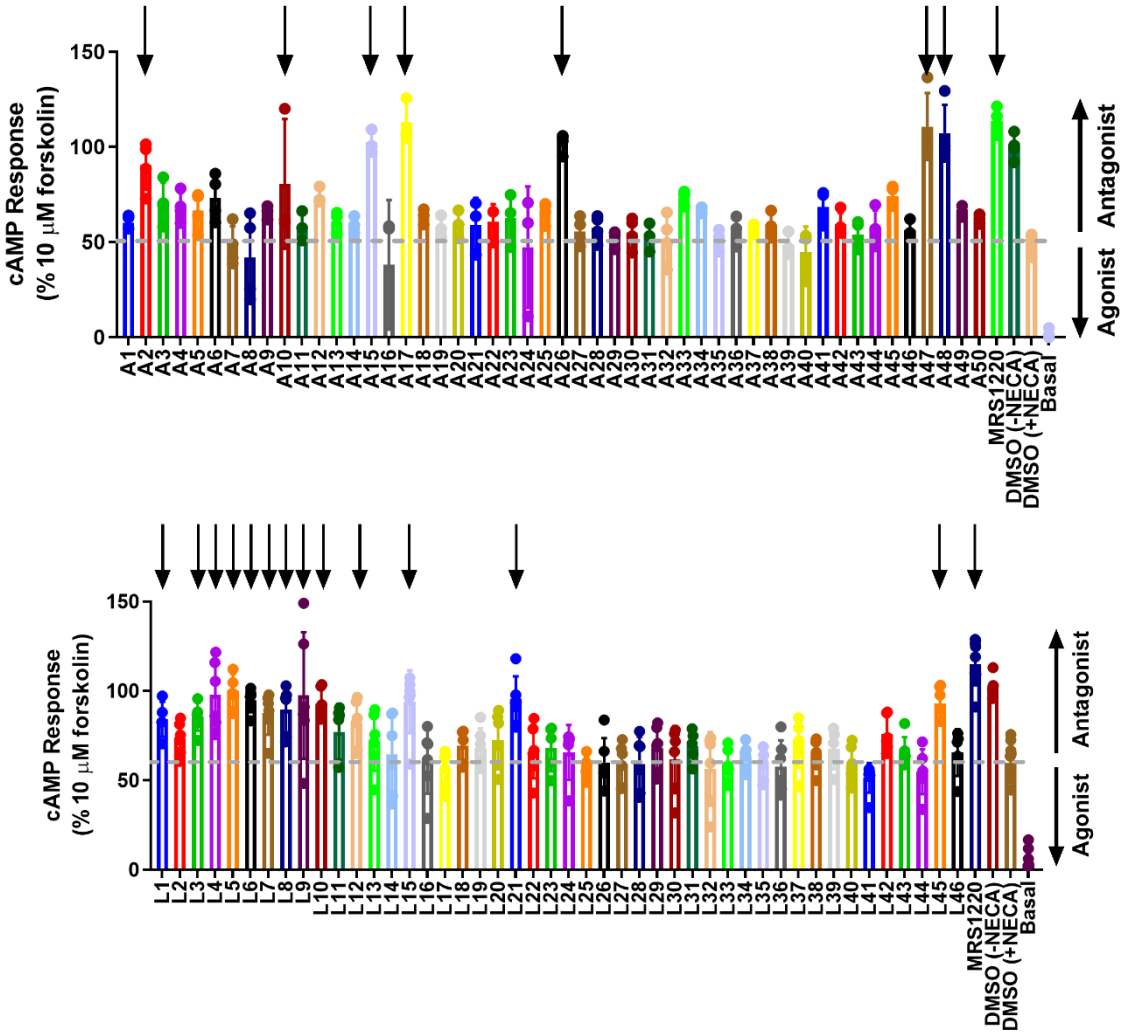

Figure 6.2. Potential A_3R antagonists identified during initial screening of compounds. Two batches of compounds (A1-A50 and L1-L46) were tested for potential activity in Flp-In A_3R CHO cells using *in vitro* second messenger assay cAMP accumulation assay. The cells were stimulated with 1 µM of the compound, 10 µM forskolin and NECA at the predetermined IC_{80} (6.32 nM) concentration. MRS1220 a known A_3R antagonist, was included as a positive control. Activation of the A_3R receptor was calculated as the % response of 10 µM forskolin alone (DMSO (-NECA)). The grey line indicates the cAMP accumulation in cells stimulated with NECA and forskolin only (DMSO (+NECA)) and any compounds below the grey line behave as potential agonists, while compounds above the grey line behave as potential antagonists. The arrows indicate statistically significant compounds in each

screen. This figure is adapted from BA studies at University of Cambridge of L. Dhiangra and A. Suchankova.

In this chapter A15/A17 derivates (L2-L10), A26 derivates (L12, L15, L21) and A47 derivates (L23, L25, L26, L29 and L32) that were either potential antagonists from the A_3R Flp-In CHO cells screening or were structurally important for the SAR studies at A_1R and A_3R were taken forward for further characterisation. To assess efficacy of the compounds, full dose-dependent response curves were produced using cAMP accumulation assays at all four ARs to test compounds selectivity. Compound affinity and other kinetic parameters at A_1R and A_3R were then measured through NanoBRET binding assay. Complimentary to this work, Prof Kolocouris' lab performed *in silico* studies of these ligands at A_1R and A_3R. Specifically, binding free energy calculations using the approximate Molecular Mechanics-Generalized Born Surface Area (MM-GBSA) method with an implicit membrane and by taking into account the waters inside the binding area were performed to further characterize the interactions of these ligands with ARs (Greene et al., 2019; Massova and Kollman, 2000). Thermodynamic Integration coupled with MD simulations (TI/MD) method and a thermodynamic cycle was also employed. Important ligand-receptor interactions were then explored *in vitro* using site-directed mutagenesis coupled with NanoBRET binding assay. Overall, this work resulted in the identification of low nanomolar antagonists A17 and A47 against both A_1R and A_3R, with A17 being slightly more potent at A_1R, while A47 is slightly more potent at A_3R and was published in Stampelou et al. (2022) and Suchankova et al. (2022). As the project was initiated during my undergraduate degree and was continued by a subsequent student (under my supervision) I have included this data to present a comprehensive story. I have fully acknowledged the work performed by others and myself in the chapter.

6.2 Novel compound scaffold of potential A_1R and A_3R antagonists

The compounds investigated in this chapter for their antagonistic activity at the ARs have a novel pyrazolo[3,4-c]pyridine or pyrazolo[3,4-d]pyridazines scaffold (Table 6.1). A15/A17 and A26 share the same pyrazolo[3,4-c]pyridine scaffold, but A15 and A17 are 3-phenyl-7-anilino(pyrazolo[3,4-c]pyridines with similar substitution pattern, while A26 is - acetamido-5-anilino(pyrazolo[3,4-c]pyridine. A15/A17 derivates (L2-L10) have an alkyl or phenyl group at 3-position, an anilino group at 7-position and a cyano-, or a chloro- or an aminomethyl or N-(arylmethyl)-2-aminomethyl group at 5-position. A26 derivates (L12, L15 and L21) have a 3-(anilinoacetamido) and 3-(N-aminobenzoyl) substitutions and a 5-anilino group or 7-(N- cyclohexanylamino) group. A47 derivates (L23, L25, L26,

L29 and L32) have a pyrazolo[3,4-d]pyridazine scaffold. The novelty of these scaffolds was confirmed by Prof Kolocouris searching the ChEMBL using similarity-based parameters for A15/A17, A26 and A47, ie. the TanimotoCombo 67 coefficient (Tc) with a value > 0.85, and not finding any similar compounds as ARs antagonists.

Table 6.1. Chemical structures of pyrazolo[3,4-c]pyridine and pyrazolo[3,4-d]pyridazines compounds selected for further experiments following screening in Flp-In™ CHO cells stably expressing human A_3R using cAMP accumulation assay.

Name	Structure	MW	Name	Structure	MW
A15	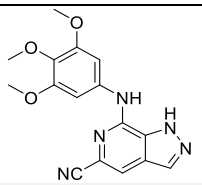	325.33	**A26**	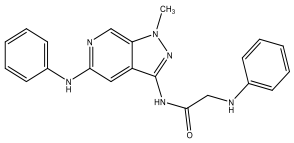	372.43
A17	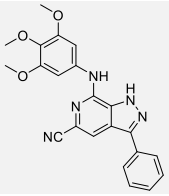	401.43	**L12**	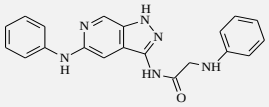	358.40
L2	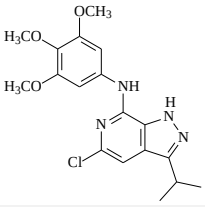	376.84	**L15**	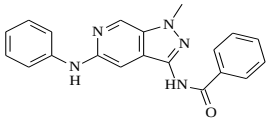	343.39
L3	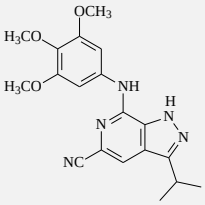	367.41	**L21**	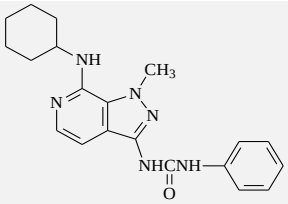	364.45
L4	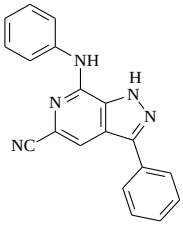	311.35	**A47**	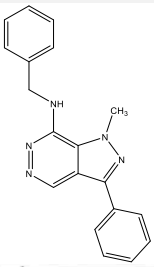	315.38
L5	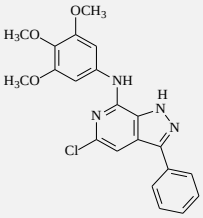	410.86	**L23**	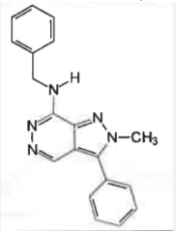	315.37

L6	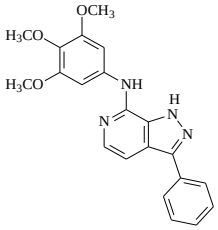	376.41	**L25**	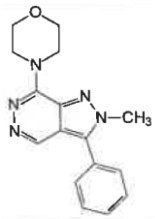	295.34
L7	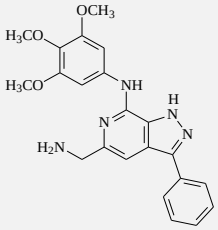	405.46	**L26**	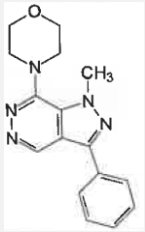	295.34
L8	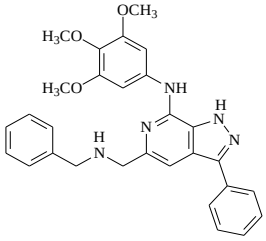	495.58	**L29**	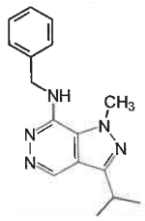	281.36
L9	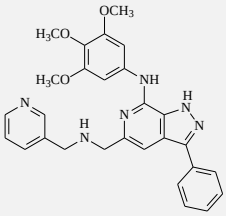	496.57	**L32**	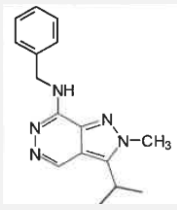	281.36
L10	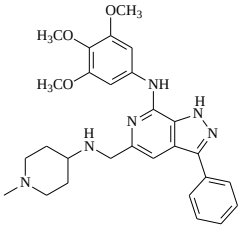	502.62			

6.3 **Potent A_3R antagonists established using cAMP accumulation assay**

As cAMP inhibition is the downstream messenger of A_3 and A_1 receptors and cAMP accumulation assay was the method used for the initial screening in the A_3R Flp-In CHO cells, it was also the assay of choice to conduct follow-on experiments to produce the full dose-response curves for all 21 compounds of interest. Flp-In CHO cells stably expressing the A_3R (Flp-In CHO-A_3R) were selected over transiently transfected CHO-KI cells to ensure a consistent level of expression between experiments and also because of easier handling. As the A17, A26 and A47 compounds are A_3R antagonists and the second screen in Flp-In CHO-A_3R cells suggested compounds L3-L10, L12, L15, L21 are also potential antagonists of the A_3R, the compounds were tested for antagonistic activity of NECA-induced cAMP inhibition response (Stampelou et al., 2022).

Since A_3R is a $G_{i/o}$-coupled receptor, the Flp-In CHO-A_3R cells were co-stimulated with 10 µM forskolin (to stimulate the CAMP accumulation by activating adenylyl cyclase), NECA in a range of concentrations (1 pM to 1 µM) and either DMSO or 1 µM of the potential antagonist A15, A17, L2-L10, A26, L12, L15, L21, A47, L23, L25, L26, L29 and L32 to obtain full inhibition curves (Figure 6.3 and Table 6.2). All A15/A17- and A26-derivatives except for L21 caused a reduction in potency without a loss of efficacy characteristic of competitive antagonists and the NECA potency was significantly reduced at A_3R by A17, L2-L10, A26, L12, L15 and L21. From these compounds, A17 was the most potent antagonist at A_3R followed by L4 (IC_{50} of 7.12 ± 0.13 and 7.22 ± 0.09, respectively). Both of these compounds decreased NECA potency ~100x fold. From A47-derivatives, only A47 (pIC_{50} of 7.26 ± 0.12) showed antagonistic activity at the A_3R, while the rest of the compounds remained inactive at this receptor.

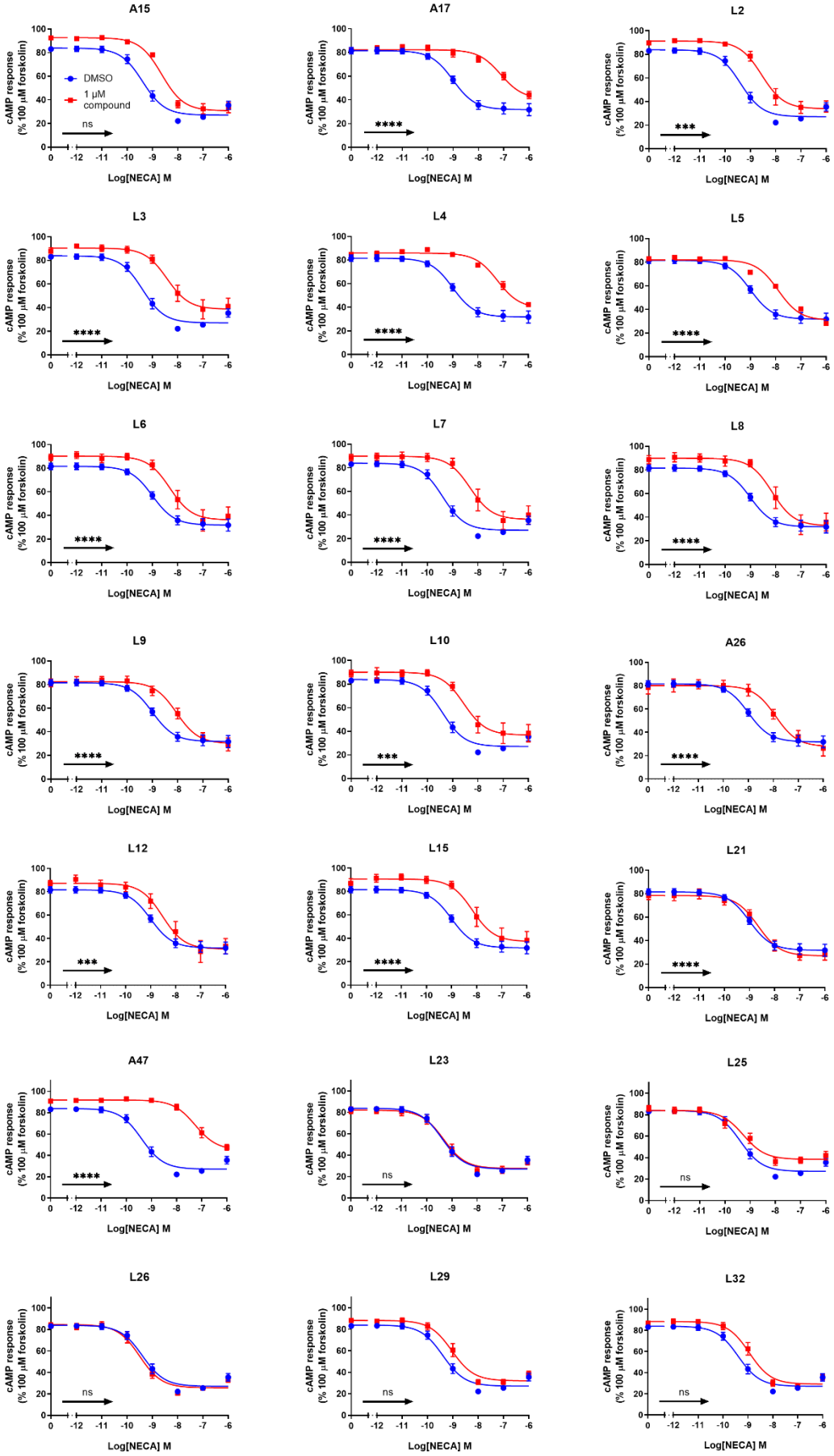
A15
A17
L2
L3
L4
L5
L6
L7
L8
L9
L10
A26
L12
L15
L21
A47
L23
L25
L26
L29
L32
cAMP response
(% 100 µM forskolin)
Log[NECA] M
DMSO
1 µM
compound
ns
****
***

Figure 6.3. Functional characterisation of A15, A17, A26 and A47 analogues at A_3R. Flp-In CHO cells stably expressing A_3R were stimulated with 10 µM forskolin, range of NECA concentrations (1 pM to 1 µM), and either 1 µM potential antagonist (red curves) or DMSO (blue curves) for 30 mins and cAMP accumulation was detected. NECA inhibition data were fitted using a three-parameter logistic equation to determine the pIC_{50} of NECA in each condition; n = 3 independent repeats, each conducted in duplicate. All values are mean ± SEM, expressed as % of 100 µM forskolin response. The black arrow indicates whether addition of the compound cause statistically significant reduction in NECA potency (pIC_{50}). Statistical significance (*** $p < 0.001$, **** $p < 0.0001$) was determined using ANOVA and Dunnett' s post-test. Compounds A17, A26 and A47 were measured as part of my BA degree, while compounds L4, L5, L9 and L21 were measured by Lakshiv Dhingra (University of Cambridge) and were submitted for his BA degree.

Table 6.2. Functional activities for pyrazolo[3,4-c]pyridine and pyrazolo[3,4-d]pyridazines compounds against A_3R. pIC_{50}, E_{max} and pK_d values for cAMP accumulation in Flp-In CHO cells stably expressing A_3R stimulated with 10 µM forskolin, range of NECA concentrations (1pM to 1 µM), and either 1 µM potential antagonist or DMSO for 30 minutes. Compounds A17, A26 and A47 were measured as part of my BA degree, while compounds L4, L5, L9 and L21 were measured by Lakshiv Dhingra (University of Cambridge) and were submitted for his BA degree.

Compound	pIC_{50} in presence of NECA [a]	E_{max} [b]	pK_d [c]	n
DMSO	9.03 ± 0.13	31.81 ± 2.17	-	6
A15	8.71 ± 0.14	30.79 ± 1.90	5.91 ± 0.19	3
A17	7.12 ± 0.13****	40.85 ± 2.73	7.87 ± 0.18	6
L2	8.55 ± 0.13***	33.86 ± 2.66	6.26 ± 0.18	3
L3	8.42 ± 0.19****	38.66 ± 3.59	6.45 ± 0.23	3
L4	7.22 ± 0.09****	39.24 ± 1.89	7.77 ± 0.16	7
L5	7.91 ± 0.10****	30.81 ± 3.27	7.05 ± 0.20	3
L6	8.29 ± 0.10****	36.21 ± 4.28	6.60 ± 0.24	3
L7	8.31 ± 0.21****	36.21 ± 4.28	6.59 ± 0.25	3
L8	8.14 ± 0.20****	32.73 ± 4.56	6.80 ± 0.24	3
L9	8.05 ± 0.10****	30.03 ± 3.21	6.89 ± 0.20	3
L10	8.56 ± 0.20***	36.79 ± 3.72	6.24 ± 0.24	3
A26	7.91 ± 0.19****	27.81 ± 4.18	7.05 ±0.22	3
L12	8.52 ± 0.21***	30.91 ± 4.36	6.31± 0.24	3
L15	8.17 ± 0.20****	37.14 ± 4.28	6.77 ± 0.24	3
L21	8.37 ± 0.19****	27.02 ± 2.70	6.52 ± 0.20	3
A47	7.26 ± 0.12****	44.94 ± 2.89*	8.13 ± 0.27	3
L23	9.33 ± 0.14	27.64 ± 2.18	N.B.	3
L25	9.27 ± 0.16	38.37 ± 2.22	N.B.	3
L26	9.50 ± 0.12	25.69 ± 2.00	N.B.	3
L29	9.04 ± 0.11	32.05 ± 2.07	N.B.	3
L32	8.94 ± 0.12	29.13 ± 2.13	N.B.	3

[a] Functional activities (pIC_{50} values in presence of NECA) for the ligands as mean ± SEM of n independent repeats, conducted in duplicate.
[b] The % maximal inhibition of cAMP accumulation for NECA with either DMSO or compound.
[c] Dissociation constant (pKd) of the ligands as mean ± SEM of n independent repeats, conducted in duplicate as determined using the Schild analysis.
N.B. – denotes no binding of the compound to A_3R
Statistical significance (* $p< 0.05$, *** $p< 0.001$, **** $p < 0.0001$) was determined using ANOVA and Dunnett' s post-test.

Furthermore, when the cAMP accumulation data in Figure 6.2 was analysed using Schild analysis (see equation 4 in chapter 2), it was possible to get a crude estimation of the potential affinity of each antagonist at the A_3R. Based upon a single concentration of antagonist the affinity constants (pK_d) of each compound except L23, L25, L26, L29 and L32 due to their inactivity at the A_3R were calculated

(Table 6.3). For compounds A26, L5 and L21 that showed only weak efficacy in the cAMP accumulation assay at 1 µM, these were measured at 10 µM as well to enable Schild analysis.

It is only possible to use Schild analysis to estimate pK_d for competitive antagonists. As it was previously shown that compounds A17, A26 and A47 are competitive antagonists at the A_3R using multiple point Schild analysis (Figure 6.4 and Table 6.3) and the decrease in potency without change in maximal response of NECA full dose response curves above is typical of competitive antagonists, it was assumed these compounds are as well (data obtained during BA studies at University of Cambridge, A. Suchankova). However, despite these facts, Schild regression analysis conducted based on a single antagonist concentration remains a little unprecise, which is, why the compound binding was confirmed below using an alternative method of NanoBRET binding assay.

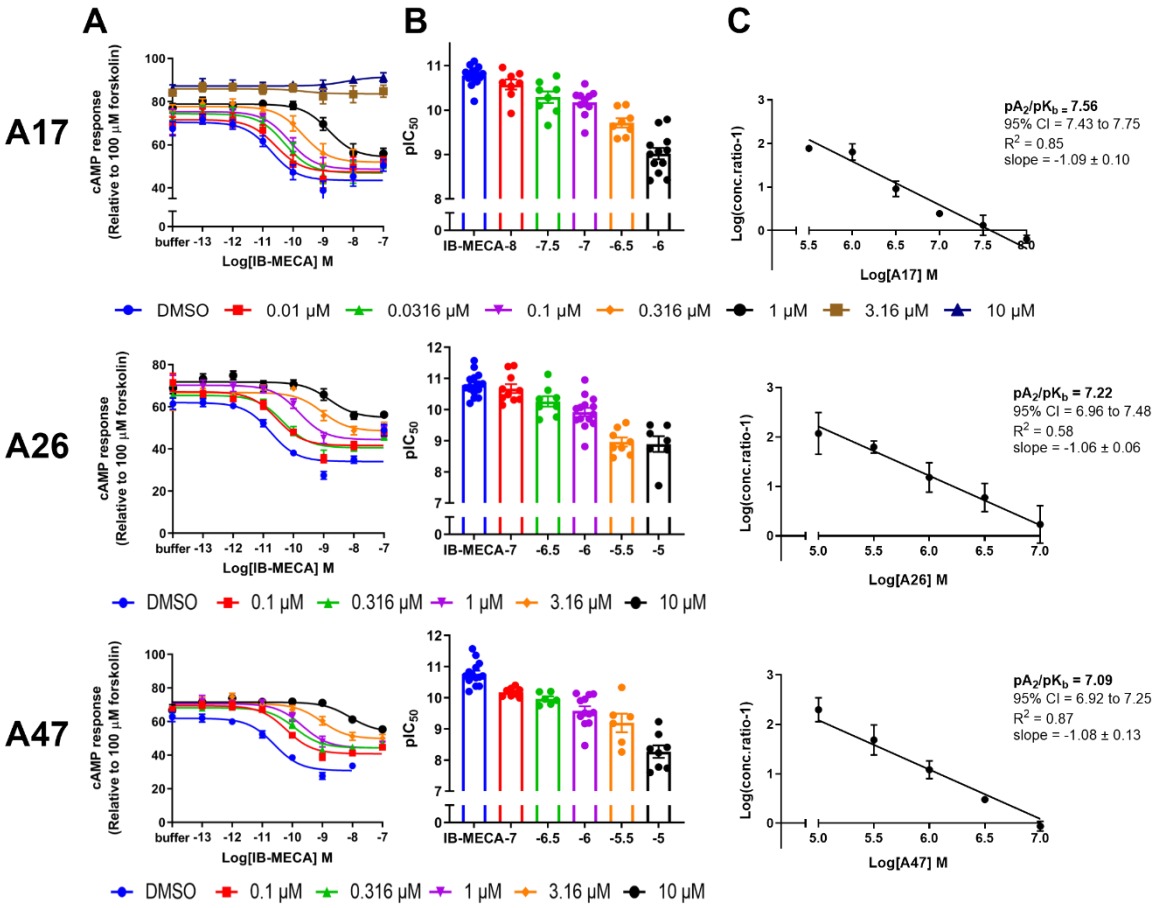

Figure 6.4. A17, A26 and A47 are competitive antagonists of A_3R. cAMP inhibition in response to 10 µM forskolin, IB-MECA (A_3R agonist) at varying concentrations and tested compound/DMSO was meassured in Flp-In CHO cells stably expressing A_3R. A. Dose-response curve normalised to 100 µM forskolin and shown as mean ± SEM. B. Potency (pIC_{50}) values derived from dose-response curves in

A. C. Schild analysis of data from A/B. Slope of ±1 indicates a competitive antagonist and for those $pA_2=pK_B$. This figure is adapted from A. Suchankova BA studies at University of Cambridge.

Table 6.3. cAMP accumulation in A_3R Flp-In CHO cells following stimulation with 10 µM forskolin, compound at indicated concentration and varying concentrations of IB-MECA. A26 measurements have fairly large error bars, which is why some of the values for A26 might be coming out as not significant. This table is adapted from A. Suchankova BA studies at University of Cambridge.

Cmpd	Concentration (µM)	pIC_{50}[a]	E_{max}[b]
DMSO	-	10.72 ±0.2	43.5 ±2.0
A17	0.1	10.13 ±0.2***	48.7 ±2.1
	1	8.81 ±0.2****	54.3 ±2.4***
	10	-[1]	-[1]
A26	0.1	10.56 ±0.2	41.6 ±1.3
	1	9.82 ±0.2****	44.4 ±1.6*
	10	8.80 ±0.3****	54.9 ±2.2****
A47	0.1	10.20 ±1.2*	40.8 ±1.2
	1	9.67 ±0.2****	44.3 ±1.4
	10	8.08 ±0.2****	53.7 ±2.4****

Data are the mean ± SEM of n individual data sets, conducted in duplicate.
[a] The negative logarithm of agonist concentration producing half-maximal response.
[b] The % maximal inhibition of cAMP accumulation for NECA with either DMSO or compound.
[1] Fully ablates IB-MECA response
Statistical significance (* $p< 0.05$;** $p<0.01$;*** $p<0.001$, **** $p<0.0001$) compared to IB-MECA only stimulation was determined by one-way ANOVA with Dunnett's post test.

According to Schild analysis, A17, L4 and A47 (pK_d of 7.87 ± 0.18, 7.77 ± 0.16 and 8.13 ± 0.27, respectively) had the strongest affinity at the A_3R which correlates with them being most potent at the receptor, while A47 derivatives failed to bind at the A_3R in the concentrations used in this assay.

6.4 A17 and A47 are potent dual antagonists of A_1 and A_3 receptors

Since A17, A26 and A47 were previously shown to have antagonistic activity at the A_1R as well, the full dose-response inhibition curves at A_1R were measured next. CHO-KI cells stably expressing A_1R (CHO-A_1R) were stimulated with 10 µM forskolin, NECA in a range of concentrations (1 pM to 1 µM) and either DMSO or 1 µM of the potential antagonist (Figure 6.5 and Table 6.4). Some of the tested compounds showed decrease in potency without change in maximal response of the NECA dose-response curve characteristic of the competitive antagonists, but the response was generally a little weaker at the A_1R than at the A_3R. The most potent compounds at the A_1R were A17 and A47 (pIC_{50} of 6.70 ± 0.10 and 7.15 ± 0.07, respectively), which lowered NECA efficacy ~100 fold (Table 6.4). Compounds A15, L2-L5, L7-L10, A26, L12, L15 and L29 also significantly lowered NECA pIC_{50}.

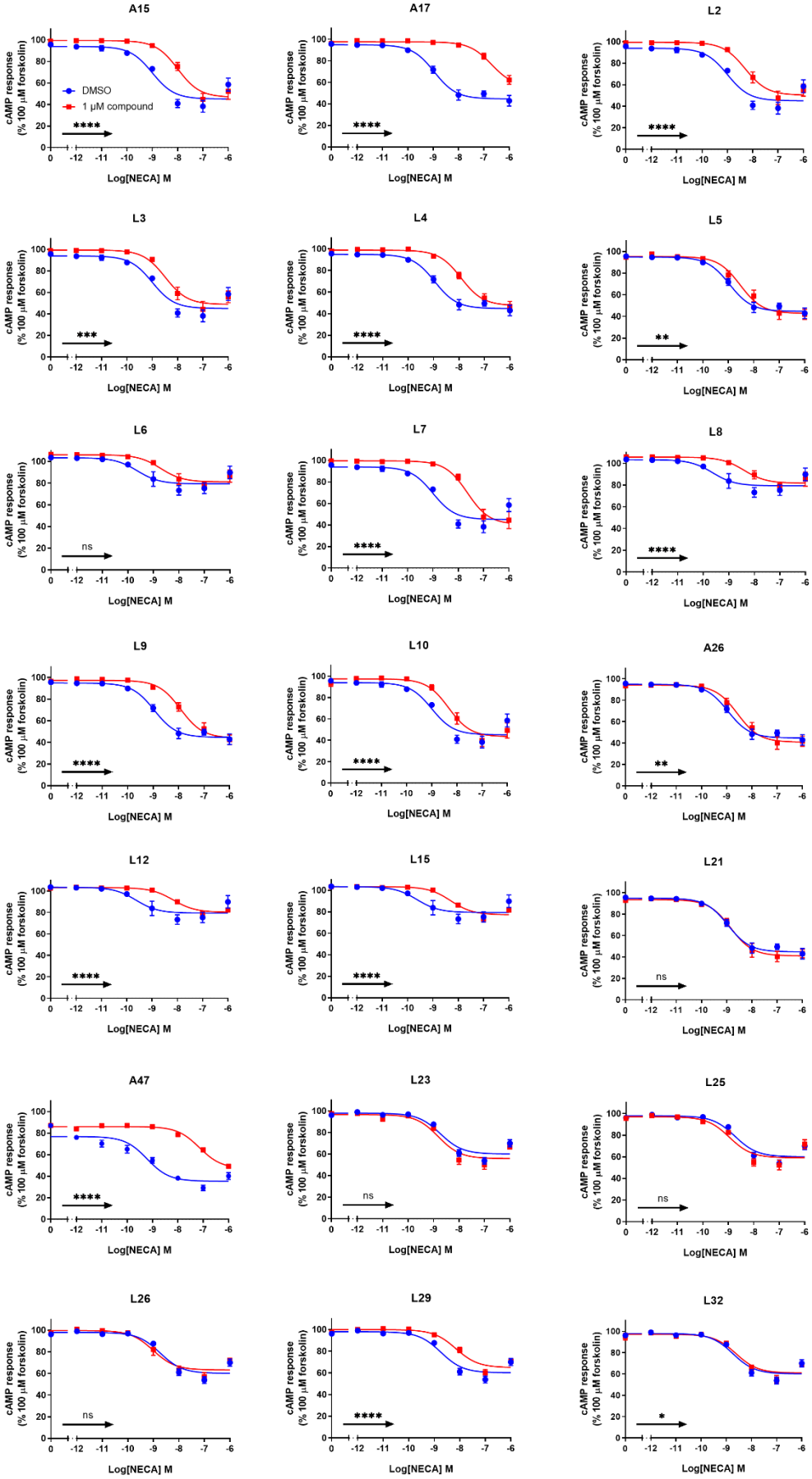
A15
A17
L2
L3
L4
L5
L6
L7
L8
L9
L10
A26
L12
L15
L21
A47
L23
L25
L26
L29
L32
cAMP response
(% 100 µM forskolin)
Log[NECA] M
DMSO
1 µM compound
****
***
**
*
ns

Figure 6.5. Functional characterisation of A15, A17, A26 and A47 analogues at A_1R. CHO-KI cells stably expressing A_1R were stimulated with 10 µM forskolin, range of NECA concentrations (1 pM to 1 µM), and either 1 µM potential antagonist (red curves) or DMSO (blue curves) for 30 mins and cAMP accumulation was detected. NECA inhibition data were fitted using a three-parameter logistic equation to determine the pIC_{50} of NECA in each condition; n = 3 independent repeats, each conducted in duplicate. All values are mean ± SEM, expressed as % 100 µM forskolin response. The black arrow indicates whether addition of the compound cause statistically significant reduction in NECA potency (pIC_{50}). Statistical significance (* $p < 0.05$, ** $p < 0.01$, *** $p < 0.001$; **** $p < 0.0001$) was determined using ANOVA and Dunnett' s post-test. Compounds A17, A26 and A47 were measured as part of my BA degree, while compounds L4, L5, L9 and L21 were measured by Lakshiv Dhingra (University of Cambridge) and were submitted for his BA degree.

Table 6.4. Functional activities for pyrazolo[3,4-c]pyridine and pyrazolo[3,4-d]pyridazines compounds against A_1R. pIC_{50}, E_{max} and pK_d values for cAMP accumulation in CHO-KI cells stably expressing A_1R stimulated with 10 µM forskolin, range of NECA concentrations (1pM to 1 µM), and either 1 µM potential antagonist or DMSO for 30 minutes. Compounds A17, A26 and A47 were measured as part of my BA degree, while compounds L4, L5, L9 and L21 were measured by Lakshiv Dhingra (University of Cambridge) and were submitted for his BA degree.

Compound	pIC_{50} in presence of NECA [a]	E_{max} [b]	pK_d [c]	n
DMSO	8.95 ± 0.10	44.70 ± 1.97[1]	-	6
A15	7.99 ± 0.14****	46.67 ± 3.06	6.91 ± 0.18	3
A17	6.70 ± 0.10****	55.82 ± 2.23**	8.25 ± 0.15	4
L2	8.30 ± 0.15****	50.32 ± 2.67	6.54 ± 0.19	3
L3	8.49 ± 0.17***	48.84 ± 2.98	6.28 ± 0.20	3
L4	7.87 ± 0.10****	47.46 ± 2.06	7.04 ± 0.14	3
L5	8.54 ± 0.14**	42.83 ± 2.55	6.20 ± 0.18	3
L7	7.64 ± 0.14****	40.56 ± 3.66	7.29 ± 0.18	3
L9	7.92 ± 0.11****	44.06 ± 2.54	6.99 ± 0.16	3
L10	8.33 ± 0.15****	43.35 ± 3.09	6.50 ± 0.19	3
A26	8.58 ± 0.10**	40.80 ± 2.50	6.13 ± 0.17	3
L21	8.85 ± 0.12	40.96 ± 2.15	<6.0	3
A47	7.15 ± 0.07****	47.07 ± 1.43	7.58 ± 0.25	3
DMSO	8.95 ± 0.10	79.32 ± 2.57[1]	-	6
L6	8.72 ± 0.23	81.09 ± 2.02	6.84 ± 0.23	3
L8	8.41 ± 0.22****	81.69 ± 2.02	7.18 ± 0.25	3
L12	8.16 ± 0.09****	80.08 ± 0.79	6.71 ± 0.14	3
L15	8.30 ± 0.14****	77.17 ± 1.13	6.54 ± 0.17	3
DMSO	8.95 ± 0.10	60.08 ± 1.91[1]	-	6
L23	8.82 ± 0.15	55.80 ± 2.08	N.B.	3
L25	8.96 ± 0.18	59.06 ± 2.34	N.B.	3
L26	9.01 ± 0.16	63.19 ± 2.00	N.B.	3
L29	8.15 ± 0.12****	64.84 ± 1.72	6.46 ± 0.27	3
L32	8.62 ± 0.15*	60.87 ± 1.85	5.50 ± 0.28	3

[a] Functional activities (pIC_{50} values in presence of NECA) for the ligands as mean ± SEM of n independent repeats, conducted in duplicate.
[b] The % maximal inhibition of cAMP accumulation for NECA with either DMSO or compound.
[c] Dissociation constant (pK_d) of the ligands as mean ± SEM of n independent repeats, conducted in duplicate as determined using the Schild analysis.
[1] The compounds were done in 3 batches over a long time on a different cell batch resulting in slightly different assay windows and thus curves E_{max}
N.B. – denotes no binding of the compound to A_1R
Statistical significance (* $p < 0.05$, ** $p < 0.01$, *** $p < 0.001$; **** $p < 0.0001$) was determined using ANOVA and Dunnett' s post-test.

Using the same approach as above, a crude estimation of the potential affinity of each antagonist at the A_1R was calculated using the Schild analysis of the cAMP accumulation data (Table 6.4). Also, similarly to above, for compounds A26, L5 and L21 showing weaker efficacy, 10 µM of the

compound was used for the Schild analysis and even under these conditions L21 did not display any activity at the A_1R same as L23, L25 and L26, which also did not bind at the A_1R in the quantities detectable by this type of assay.

Overall, the majority of the compounds displayed a small (<10-fold) selectivity for the A_3R over the A_1R receptor subtype. For example, L3, L5, L21, A26 or A47 had higher affinities at the A_3R than at the A_1R and for A26 (pK_d of 7.05 ± 0.22 and 6.13 ± 0.17 at A_3R and A_1R, respectively). L4 (pK_d of 7.77 ± 0.16 and 7.04 ± 0.14 at A_3R and A_1R, respectively) was another potent antagonist that was also A_3R selective. Interestingly, while A47 (pK_d of 8.13 ± 0.27 and 7.58 ± 0.25 at A_3R and A_1R, respectively) was selective for A_3R, most of its derivates lost efficacy at the A_3R and indeed L29 and L32 even gained selective for A_1R, although the general efficacy of A47 derivates was quite low. A17 (pK_d of 7.87 ± 0.18 and 8.25 ± 0.15 at A_3R and A_1R, respectively) was an example of a potent slightly A_1R-selective antagonist. It is important to note though that although there are some differences between compound potencies at A_1R and A_3R, these differences were small, and as such, A17 and A47 can be considered dual A_1R and A_3R antagonists.

Having established the activity of the compounds at the A_3R and A_1R, it was important to assess their subtype selectivity more closely by testing the compounds at the remaining adenosine receptor subtypes ($A_{2A}R$ and $A_{2B}R$) using the cAMP accumulation assay. As A15, A17, A26 and A47 have previously been shown to have little or no activity at $A_{2A}R$ or $A_{2B}R$ at even 10 µM concentration (Figure 6.6 and Table 6.5) (data obtained during BA studies at University of Cambridge, A. Suchankova), this concentration was picked for testing all the compounds at these receptors as well.

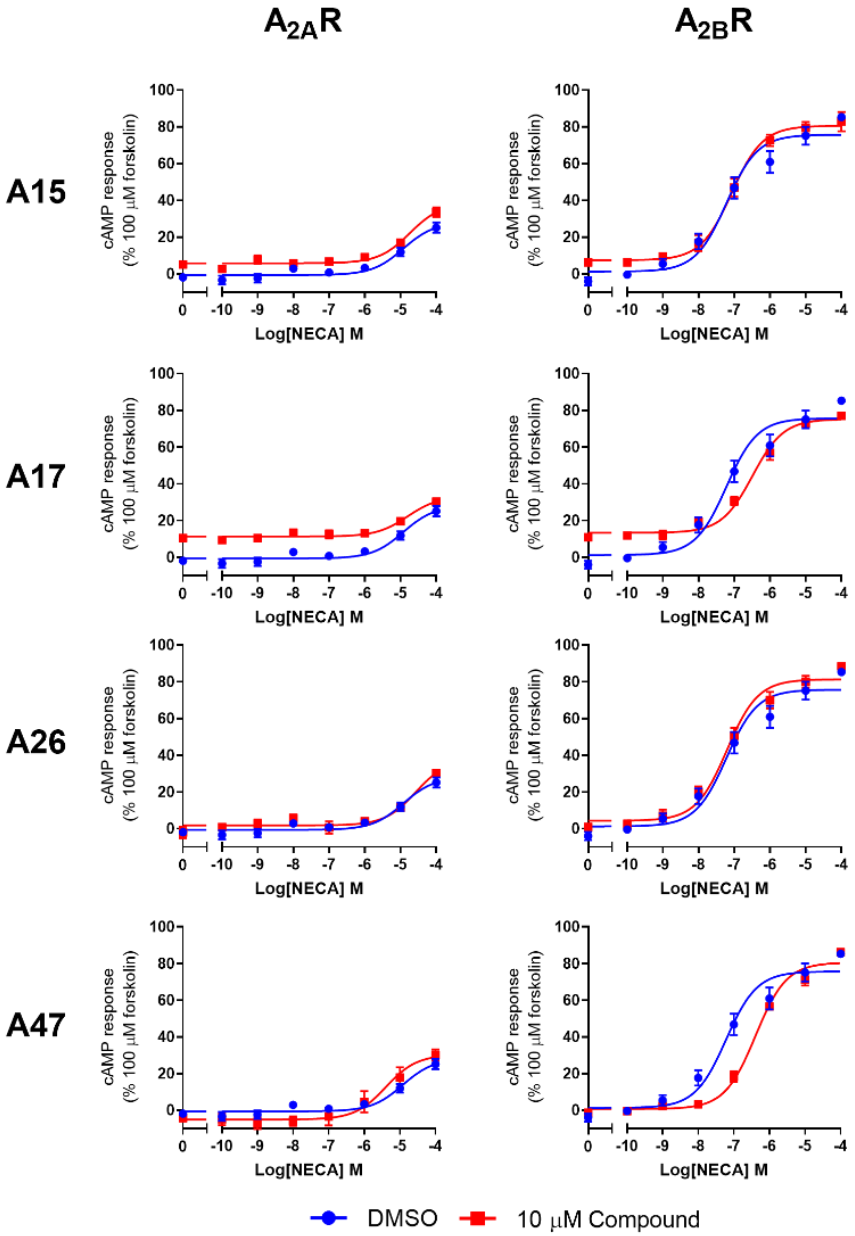

Figure 6.6. A15, A17, A26 and A47 have no or little activity at $A_{2A}R$ and $A_{2B}R$. cAMP accumulation was measured in CHO-K1 cells stably expressing either $A_{2A}R$ or $A_{2B}R$ in response to varying NECA concentration in the absence (blue) or presence of 10 µM tested compound (red). Compounds A17, A26 and A47 were measured as part of A. Suchankova BA studies at University of Cambridge.

Table 6.5. Functional activities for A15, A17, A26 and A47 against $A_{2A}R$ and $A_{2B}R$. pIC_{50}, E_{max} and E_{max} values for cAMP accumulation in CHO-KI cells stably expressing either $A_{2A}R$ or $A_{2B}R$ stimulated with a range of NECA concentrations, and either 10 µM potential antagonist or DMSO for 30 minutes. Compounds A17, A26 and A47 were measured as part of A. Suchankova BA studies at University of Cambridge.

	$A_{2A}R$			$A_{2B}R$		
Cmpd	**pIC_{50} in presence of NECA [a]**	**E_{max} [b]**	**n**	**pIC_{50} in presence of NECA [a]**	**E_{max} [b]**	**n**
DMSO	5.94 ± 0.18	28.14 ± 3.13	3	7.22 ± 0.12	75.66 ± 2.80	3
A15	5.79 ± 0.24	38.44 ± 2.91	3	7.07 ± 0.09	80.55 ± 2.13	3
A17	5.94 ± 0.2	33.31 ± 2.74	3	6.62 ± 0.07*	75.24 ± 1.79	3
A26	6.12 ± 0.43	37.80 ± 5.19	3	7.21 ± 0.09	81.29 ± 2.15	3
A47	5.69 ± 0.25	30.31 ± 4.31	4	6.39 ± 0.07****	80.56 ± 1.78	4

[a] Functional activities (pIC_{50} values in presence of NECA) for the ligands as mean ± SEM of n independent repeats, conducted in duplicate.
[b] The % maximal inhibition of cAMP accumulation for NECA with either DMSO or compound.
Statistical significance (* $p < 0.05$, **** $p < 0.0001$) was determined using ANOVA and Dunnett' s post-test.

The CHO-KI cells stably expressing the $A_{2A}R$ or $A_{2B}R$ were stimulated with NECA in a range of concentrations (1 pM to 1 µM) and either DMSO or 10 µM or the potential antagonist (Figure 6.7). Most of the tested compounds displayed no significant activity at these two adenosine receptor subtypes except for A17 and A47 which displayed weak efficacy at $A_{2B}R$ (pK_d = 6.47 ± 0.15 and pK_d = 6.76 ± 0.14, respectfully) (Table 6.6).

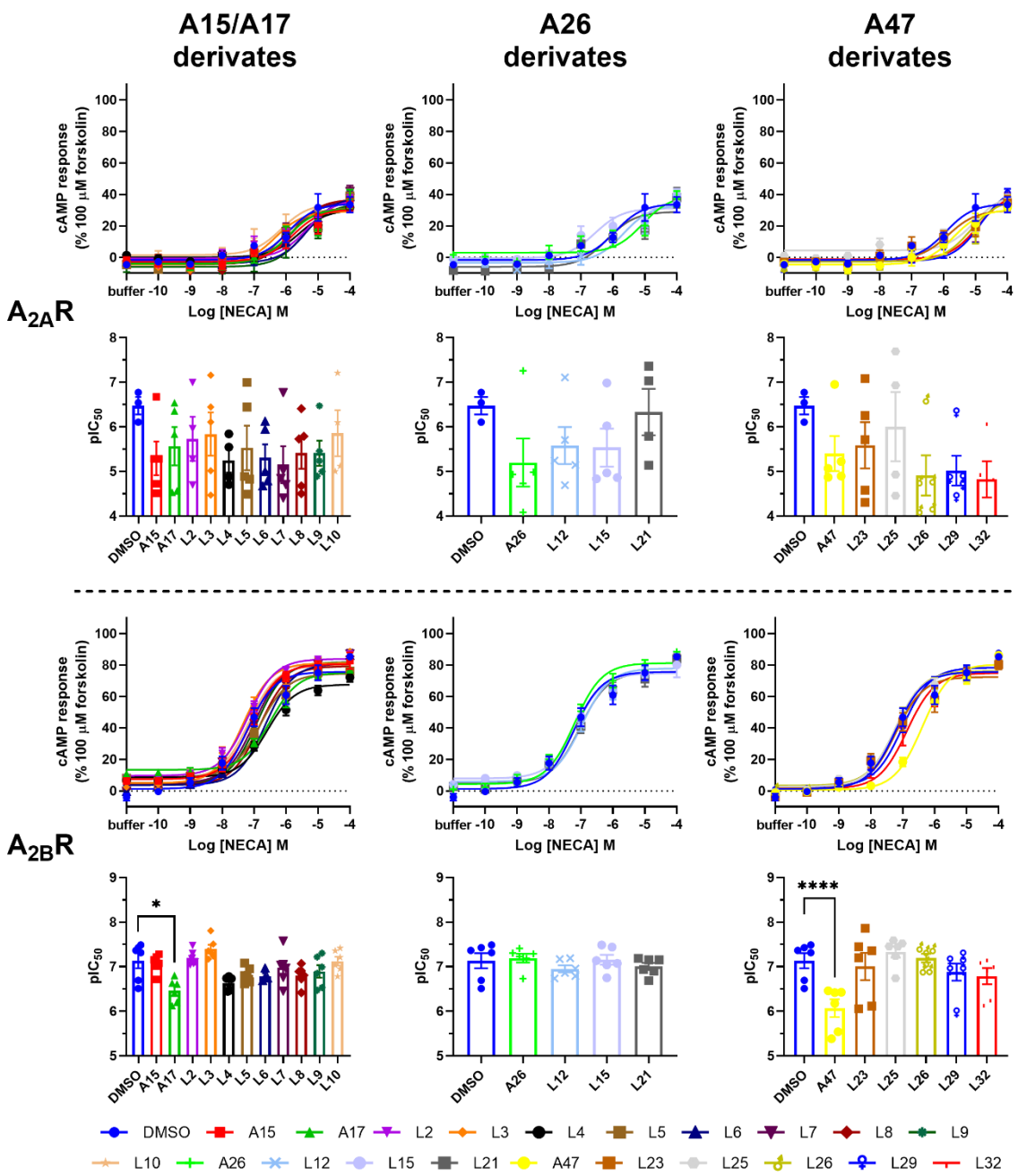

Figure 6.7. Functional characterisation of A15, A17, A26 and A47 analogues at $A_{2A}R$ and $A_{2B}R$. CHO-KI cells stably expressing $A_{2A}R$ or $A_{2B}R$ were stimulated with a range of NECA concentrations (100 pM to 100 µM), and either 10 µM potential antagonist (red curves) or DMSO (blue curves) for 30 mins and cAMP accumulation was detected. NECA inhibition data were fitted using a three-parameter logistic equation to determine the pIC_{50} of NECA in each condition; n = 3 independent repeats, each conducted in duplicate. Below are plotted pIC_{50} values from the dose response curves. All values are mean ± SEM, expressed as % 100 µM forskolin response.

Table 6.6. Functional activities for pyrazolo[3,4-c]pyridine and pyrazolo[3,4-d]pyridazines compounds against $A_{2A}R$ and $A_{2B}R$. pIC_{50}, E_{max} and pK_d values for cAMP accumulation in CHO-KI cells stably expressing either $A_{2A}R$ or $A_{2B}R$ stimulated with a range of NECA concentrations (1pM to 1 µM), and either 10 µM potential antagonist or DMSO for 30 minutes.

Cmpd	$A_{2A}R$				$A_{2B}R$			
	pIC_{50} in presence of NECA [a]	E_{max} [b]	pK_d [c]	n	pIC_{50} in presence of NECA [a]	E_{max} [b]	pK_d [c]	n
DMSO	5.94 ± 0.18	34.17 ± 2.80	-	4	7.22 ± 0.12	75.66 ± 2.80	-	3
A15	5.79 ± 0.24	30.73 ± 3.43	-	4	7.07 ± 0.09	80.55 ± 2.12	-	3
A17	5.94 ± 0.2	31.16 ± 3.30	-	4	6.62 ± 0.07*	75.24 ± 1.78	6.47 ± 0.15	3
L2	5.33 ± 0.28	36.96 ± 5.06	-	4	7.20 ± 0.07	83.89 ± 1.58	-	3
L3	6.35 ± 0.22	29.18 ± 2.81	-	4	7.33 ± 0.09	81.27 ± 2.20	-	3
L4	5.58 ± 0.22	30.35 ± 2.73	-	4	6.60 ± 0.09	67.61 ± 1.92	-	3
L5	6.09 ± 0.22	31.34 ± 3.13	-	4	6.82 ± 0.09	74.51 ± 2.03	-	3
L6	5.31 ± 0.19	38.51 ± 4.01	-	4	6.64 ± 0.10	80.91 ± 2.63	-	3
L7	5.73 ± 0.22	35.93 ± 3.59	-	4	6.99 ± 0.09	81.36 ± 2.44	-	3
L8	5.80 ± 0.19	37.00 ± 3.46	-	4	6.82 ± 0.07	79.22 ± 1.90	-	3
L9	5.46 ± 0.3	34.06 ± 5.63	-	4	6.92 ± 0.08	81.82 ± 2.16	-	3
L10	6.15 ± 0.30	34.38 ± 3.53	-	4	7.15 ± 0.08	79.99 ± 1.92	-	3
A26	6.12 ± 0.43	39.35 ± 5.66	-	4	7.21 ± 0.09	81.29 ± 2.14	-	3
L12	5.68 ± 0.25	33.38 ± 3.97	-	4	6.97 ± 0.10	77.89 ± 2.39	-	3
L15	6.56 ± 0.30	31.31 ± 2.93	-	4	7.16 ± 0.12	74.89 ± 2.62	-	3
L21	6.18 ± 0.32	29.04 ± 4.36	-	4	7.03 ± 0.11	75.62 ± 2.48	-	3
A47	5.69 ± 0.25	30.54 ± 3.80	-	4	6.39 ± 0.07****	80.56 ± 1.77	6.76 ± 0.14	3
L23	5.86 ± 0.28	29.91 ± 3.79	-	4	7.22 ± 0.13	72.44 ± 2.98	-	3
L25	5.03 ± 0.23	40.53 ± 4.71	-	4	7.24 ± 0.10	75.76 ± 2.47	-	3
L26	5.16 ± 0.28	37.12 ± 6.01	-	4	7.23 ± 0.10	76.22 ± 2.39	-	3
L29	4.83 ± 0.24	45.53 ± 7.31	-	4	7.01 ± 0.10	78.43 ± 2.55	-	3
L32	4.92 ± 0.24	40.96 ± 6.10	-	4	6.87 ± 0.09	74.94 ± 2.34	-	3

[a] Functional activities (pIC_{50} values in presence of NECA) for the ligands as mean ± SEM of n independent repeats, conducted in duplicate.
[b] The % maximal inhibition of cAMP accumulation for NECA with either DMSO or compound.
[c] Dissociation constant (pK_d) of the ligands as mean ± SEM of n independent repeats, conducted in duplicate as determined using the Schild analysis.
Statistical significance (* $p < 0.05$, **** $p < 0.0001$) was determined using ANOVA and Dunnett' s post-test.

6.5 Lead compounds A17 and A47 have low nanomolar affinities at A_1R/A_3R

As mentioned, the use of single point antagonist concentrations in Schild analysis to determine affinities constants is not the most quantitatively accurate method, because Schild analysis gives more accurate results when multiple antagonists concentrations are measured and used. Although the measurement of the effect of multiple antagonists concentrations on NECA full dose response curves using cAMP accumulation assay was possible and was previously performed for compounds A17, A26 and A47 (data obtained during BA studies at University of Cambridge, A. Suchankova), doing so for all 21 compounds would be very time consuming and expensive.

Instead NanoBRET competition binding assay can be used to determine the binding affinities for all pyrazolo[3,4-c]pyridine and pyrazolo[3,4-d]pyridazines compounds at the A_3R and A_1R. The ability of all 21 compounds to displace and inhibit the specific binding of CA200645 (also used in chapter 5), a fluorescent antagonist of A_3R and A_1R, was tested in HEK-293 cells stably expressing WT Nluc-A_3R or Nluc-A_1R, as described previously (Barkan et al., 2020; Stoddart et al., 2012). Briefly, HEK-293 cells stably expressing WT Nluc-A_3R or Nluc-A_1R were stimulated with 5 nM and 20 nM CA200645, respectively, and a range of ligand concentrations (1pM to 100 µM) (Figure 6.8, 6.9 and 6.10). BRET ratio at 10 minutes was then used to create full dose response curve for each ligand and fitted with the "One site – Fit K_i" model derived from the Cheng and Prusoff equation built in GraphPad Prism 9.3 to enable estimates of pK_i (Table 6.7, 6.8 and 6.9).

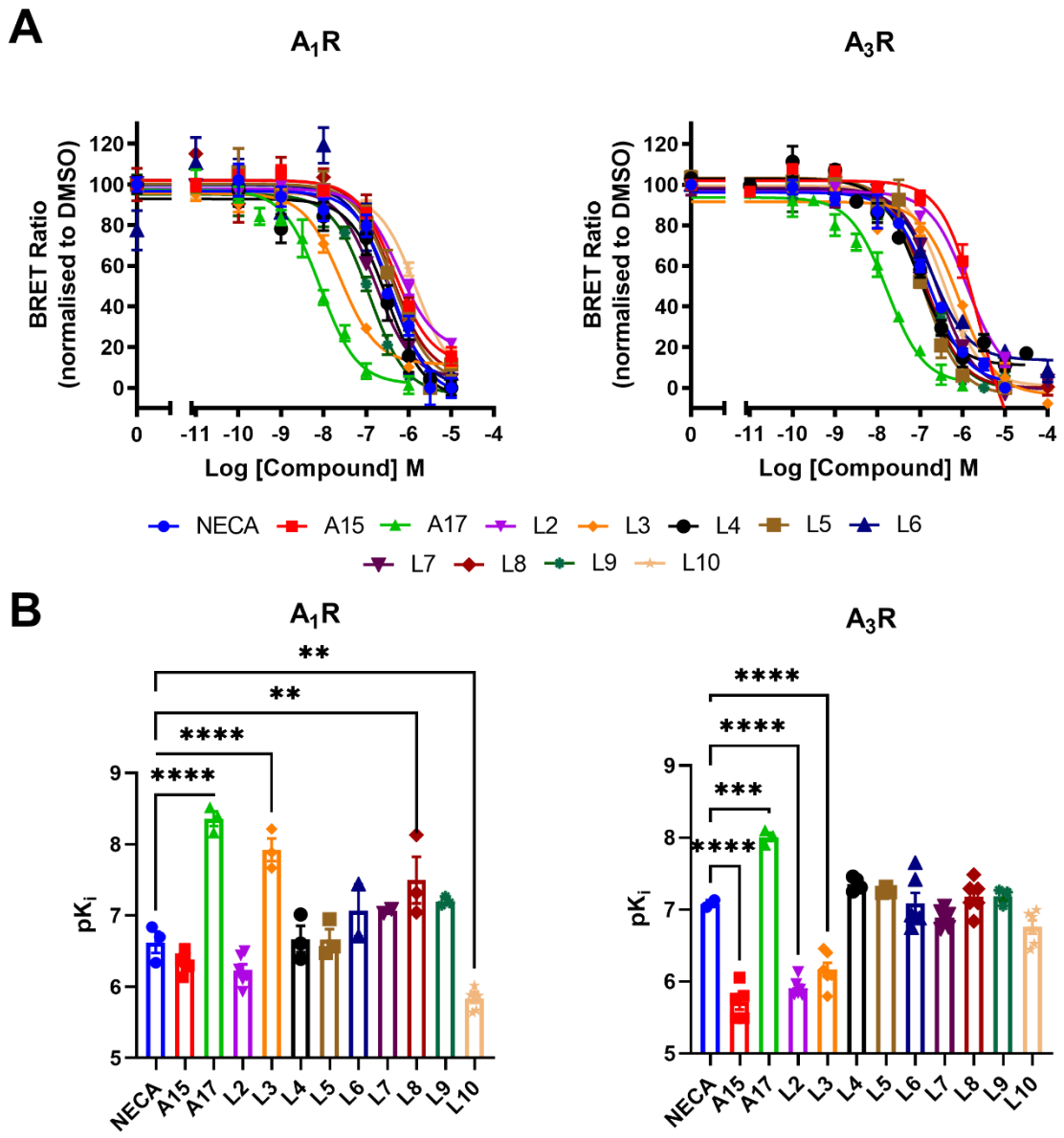

Figure 6.8. Binding of A15 and A17 derivates at A_1R and A_3R measured by NanoBRET. A. HEK293 cells stably expressing Nluc-A_1R or Nluc-A_3R were treated with 20 nM or 5 nM CA200645, respectively, and increasing concentrations of unlabelled AR ligand, enabling concentration-dependent decreases in BRET ratio at 10 min to be determined with the response normalised to DMSO. Binding curves were fitted with the "One site – Fit K_i" model derived from the Cheng and Prusoff equation built into GraphPad Prism 9.3 to enable estimates of the pK_i. B. Plotted pK_i values from A. Data are plotted at mean ± SEM of at least 3 experiments performed in duplicate. Compounds L4, L5 and L9 were measured by Lakshiv Dhingra (University of Cambridge) and were submitted for his BA degree.

Table 6.7. Binding affinities (pK_i) of A15, A17 and L2-L10 measured using NanoBRET against A_1R and A_3R. pK_i values determined by NanoBRET in HEK293 cells stably expressing Nluc-A_1R or Nluc-A_3R were treated with 20 nM or 5 nM CA200645, respectively, and increasing concentrations of unlabelled AR ligand, enabling concentration-dependent decreases in BRET ratio at 10 min to be determined with the response normalised to DMSO. The data at 10 min was then fitted using the "One site – Fit K_i" model derived from the Cheng and Prusoff equation built into GraphPad Prism 9.3. Compounds L4, L5 and L9 were measured by Lakshiv Dhingra (University of Cambridge) and were submitted for his BA degree.

Compound	A_1R		A_3R	
	pK_i[a]	n	pK_i[a]	n
DMSO	6.69 ± 0.10	3	7.06 ± 0.07	5
A15	6.64 ± 0.08	3	5.49 ± 0.10****	3
A17	8.36 ± 0.10****	3	8.01 ± 0.06***	3
L2	6.54 ± 0.07	3	6.20 ± 0.06****	3
L3	7.91 ± 0.09****	3	6.22 ± 0.10****	3
L4	6.67 ± 0.18	3	7.36 ± 0.05	4
L5	6.66 ± 0.14	3	7.26 ± 0.03	3
L6	6.78 ± 0.30	3	7.00 ± 0.10	3
L7	7.64 ± 0.57	3	6.88 ± 0.08	3
L8	6.69 ± 0.30**	3	7.19 ± 0.10	3
L9	7.20 ± 0.04	3	7.19 ± 0.07	3
L10	6.13 ± 0.08**	3	6.72 ± 0.09	3

[a] Equilibrium binding affinities (pKi) of the ligands measured with NanoBRET against WT A_1R or A_3R; NECA was used as positive control as described in ref (Barkan et al., 2020). Data are expressed as mean ± SEM of n independent repeats, conducted in duplicate.
Statistical significance (** $p < 0.01$,*** $p < 0.001$, **** $p < 0.0001$) was determined using ANOVA and Dunnett' s post-test.

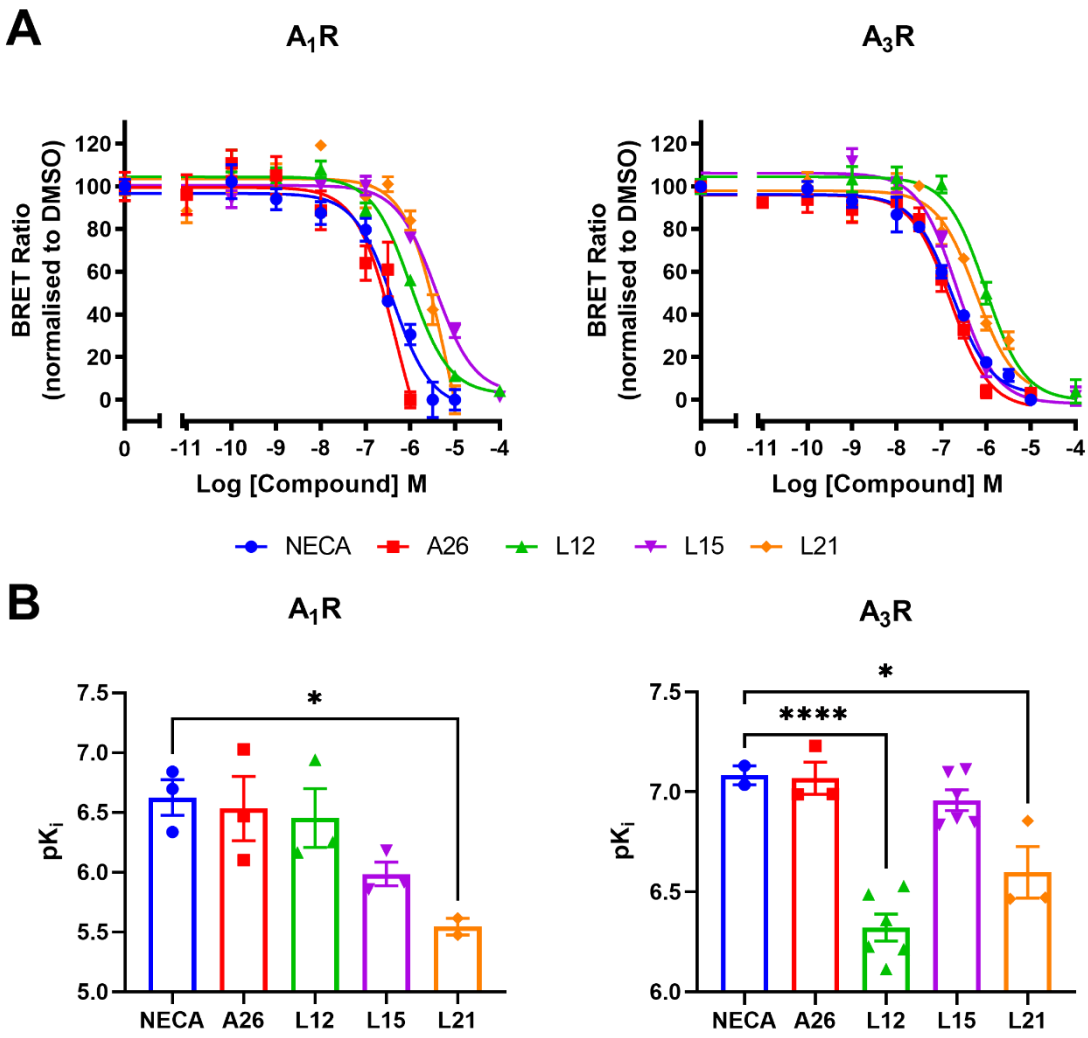

Figure 6.9. Binding of A26 derivates at A_1R and A_3R measured by NanoBRET. A. HEK293 cells stably expressing Nluc-A_1R or Nluc-A_3R were treated with 20 nM or 5 nM CA200645, respectively, and increasing concentrations of unlabelled AR ligand, enabling concentration-dependent decreases in BRET ratio at 10 min to be determined with the response normalised to DMSO. Binding curves were fitted with the "One site – Fit K_i" model derived from the Cheng and Prusoff equation built into GraphPad Prism 9.3 to enable estimates of the pK_i. B. Plotted pK_i values from A. Data are plotted at mean ± SEM of at least 3 experiments performed in duplicate. Compound L21 was measured by Lakshiv Dhingra (University of Cambridge) and were submitted for his BA degree.

Table 6.8. Binding affinities (pK_i) of A26, L12, L15 and L21 measured using NanoBRET against A_1R and A_3R. pK_i values determined by NanoBRET in HEK293 cells stably expressing Nluc-A_1R or Nluc-A_3R were treated with 20 nM or 5 nM CA200645, respectively, and increasing concentrations of unlabelled AR ligand, enabling concentration-dependent decreases in BRET ratio at 10 min to be determined with the response normalised to DMSO. The data at 10 min was then fitted using the "One site – Fit K_i" model derived from the Cheng and Prusoff equation built into GraphPad Prism 9.3. Compound L21 was measured by Lakshiv Dhingra (University of Cambridge) and were submitted for his BA degree.

Compound	A_1R		A_3R	
	pK_i[a]	n	pK_i[a]	n
DMSO	6.69 ± 0.10	3	7.06 ± 0.07	5
A26	6.53 ± 0.27	3	7.07 ± 0.08	3
L12	6.44 ± 0.11	3	6.33 ± 0.09****	3
L15	6.02 ± 0.14	3	6.95 ± 0.08	3
L21	5.51 ± 0.17*	3	6.60 ± 0.13*	3

[a] Equilibrium binding affinities (pKi) of the ligands measured with NanoBRET against WT A_1R or A_3R; NECA was used as positive control as described in ref (Barkan et al., 2020). Data are expressed as mean ± SEM of n independent repeats, conducted in duplicate.
Statistical significance (** $p < 0.01$, **** $p < 0.0001$) was determined using ANOVA and Dunnett' s post-test.

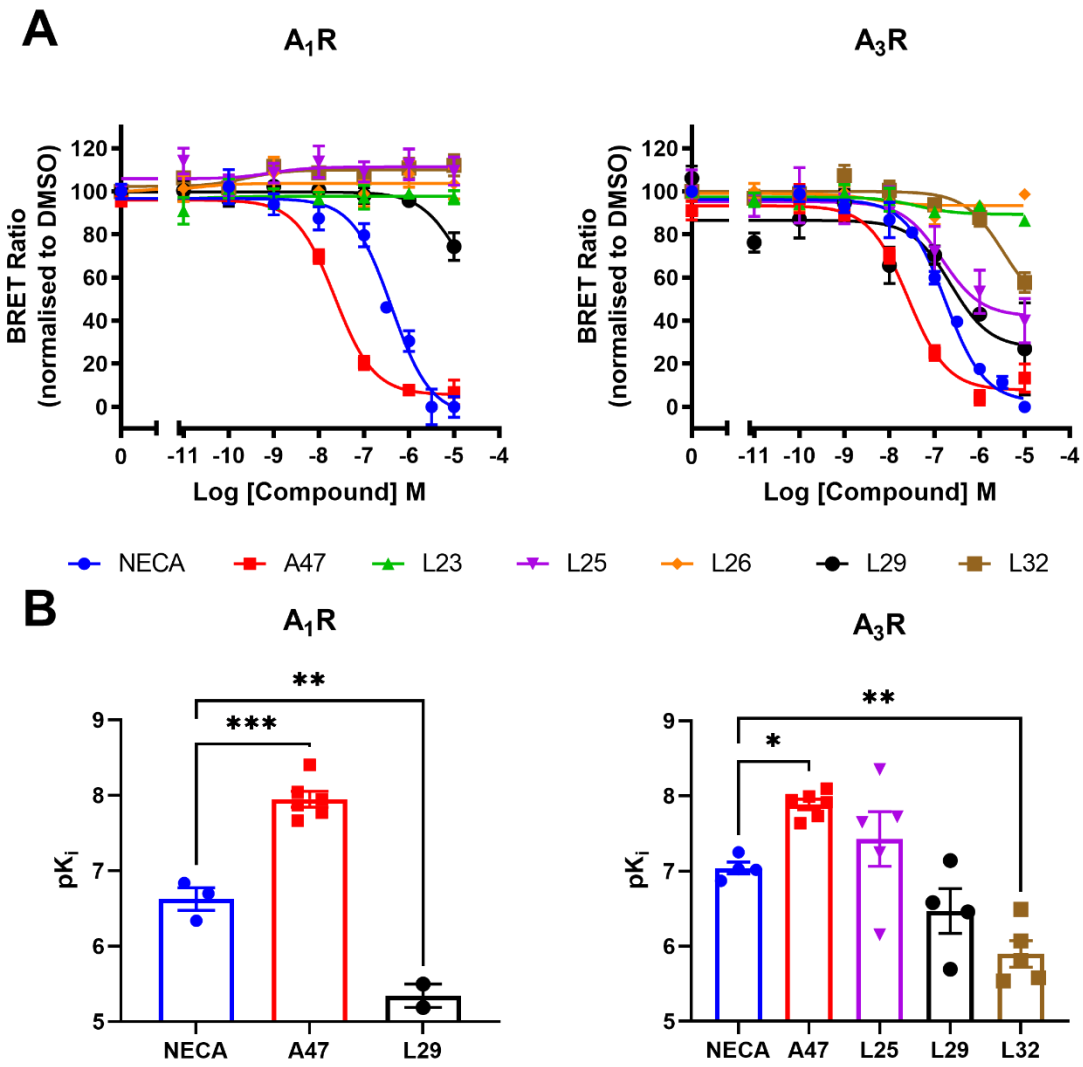

Figure 6.10. Binding of A47 derivates at A_1R and A_3R measured by NanoBRET. A. HEK293 cells stably expressing Nluc-A_1R or Nluc-A_3R were treated with 20 nM or 5 nM CA200645, respectively, and increasing concentrations of unlabelled AR ligand, enabling concentration-dependent decreases in BRET ratio at 10 min to be determined with the response normalised to DMSO. Binding curves were fitted with the "One site – Fit K_i" model derived from the Cheng and Prusoff equation built into GraphPad Prism 9.3 to enable estimates of the pK_i. B. Plotted pK_i values from A. Data are plotted at mean ± SEM of at least 3 experiments performed in duplicate.

Table 6.9. Binding affinities (pK_i) of A47, L23, L25, L26, L29 and L32 measured using NanoBRET against A_1R and A_3R. pK_i values determined by NanoBRET in HEK293 cells stably expressing Nluc-A_1R or Nluc-A_3R were treated with 20 nM or 5 nM CA200645, respectively, and increasing concentrations of unlabelled AR ligand, enabling concentration-dependent decreases in BRET ratio at 10 min to be determined with the response normalised to DMSO. The data at 10 min was then fitted using the "One site – Fit K_i" model derived from the Cheng and Prusoff equation built into GraphPad Prism 9.3.

Compound	A_1R		A_3R	
	pK_i[a]	n	pK_i[a]	n
DMSO	6.69 ± 0.10	3	7.06 ± 0.07	5
A47	7.95 ± 0.09***	3	7.89 ± 0.11*	3
L23	NA	3	NA	3
L25	NA	3	7.14 ± 0.36	3
L26	NA	3	NA	3
L29	5.17 ± 1.13**	3	6.94 ± 0.47	3
L32	NA	3	5.77 ± 0.27*	3

[a] Equilibrium binding affinities (pKi) of the ligands measured with NanoBRET against WT A_1R or A_3R; NECA was used as positive control as described in ref (Barkan et al., 2020). Data are expressed as mean ± SEM of n independent repeats, conducted in duplicate.
Statistical significance (*$p < 0.05$, ** $p < 0.01$, *** $p < 0.001$) was determined using ANOVA and Dunnett' s post-test.

The 5 nM and 20 nM of CA200645 concentrations were chosen following previous experiments measuring CA200645 K_d at WT Nluc-A_3R or Nluc-A_1R as concentrations that produced distinct NanoBRET binding curves usable for measuring compounds K_d, while using as little CA200645 compound as possible. All of the A15/A17 and A26 compounds and their derivates bind at both the A_1R and A_3R with affinities ranging between low micromolar to low nanomolar. The same was true for A47, but the affinities are generally much lower for its derivates with L23 and L26 displaying no measurable binding at either receptor, with L25 and L32 only binding at the A_3R. A17 and A47 displayed the highest affinity at the A_1R (pK_d of 8.36 ± 0.10 and 7.95 ± 0.09, respectively) followed by L3, L4, L7 and L9. A17 and A47 also had the highest affinity at the A_3R (pK_d of 8.01 ± 0.06 and 7.89 ± 0.11, respectively), followed by L4, L5, L6, L9 and A26. All the other compounds displayed weaker affinities.

6.6 Lead compounds have residence time between 30 and 60 mins

As a next step, real-time binding kinetics of the compounds were investigated (Suchankova et al., 2021) using the NanoBRET binding assay as has previously been reported at the ARs (Barkan et al., 2020; Stoddart et al., 2015, 2012). First the kinetic parameters of the fluorescent compound CA200645

were established at Nluc-A_3R as K_{on} (k_3) = 2.86± 0.45 x 106 M^{-1} min^{-1}, K_{off} (k_4) = 0.064 ±0.0023 min^{-1} with a K_d = 25 ± 4.6nM and at the Nluc-A_1R as K_{on} (k_3) = 3.67 ± 0.34 x 106 M^{-1} min^{-1}, K_{off} (k_4) = 0.067 ±0.005 min^{-1} with a K_d = 18.29 ± 2.4 nM. The real-time kinetic parameters K_{on} (k_3) and K_{off} (k_4) for the compounds were then derived using the 'kinetics of competitive binding' model build into GraphPad Prism 9.3 (Table 6.10) (Suchankova et al., 2021). Residence time (RT) of a compound was then determined as the reciprocal of the K_{off}, while pK_d of the compounds was determined as k_4/k_3. This then enabled the comparison of the pK_d derived from cAMP accumulation assay data using Schild analysis and the pK_d derived from the NanoBRET binding assay.

Table 6.10. Kinetic parameters of AR ligands. K_{on}, k_{off}, pK_d and RT parameters of A15/17, A26 and A47 derivates at the A_1R or A_3R orthosteric site measured using NanoBRET.

Compound	A_1R					A_3R				
	K_{on} (k_3) x10^5 M^{-1} [a]	K_{off} (k_4) min^{-1} [b]	pK_d Kinetics [c]	RT (mins) [d]	n	K_{on} (k_3) x10^5 M^{-1} [a]	K_{off} (k_4) min^{-1} [b]	pK_d Kinetics [c]	RT (mins) [d]	n
A15	3.2 ±1.0	0.030 ±0.006	6.99 ±0.21	38.7 ±8.8	3	<50	<0.4	N.D.	>2	3
A17	139.7 ±1.5	0.024 ±0.009	8.76 ±0.07	41.3 ±4.6	3	21.3 ±1.2	0.021 ±0.003	8.00 ±0.32	47.2 ±8.2	3
L2	1.7 ±0.3	0.048 ±0.01	6.55 ±0.03	22.9 ±4.3	3	<50	<0.4	N.D.	>2	3
L3	45.1 ±3.4	0.061 ±0.002	7.86 ±0.45	16.3 ±0.3	3	<50	<0.4	N.D.	>2	3
L4	11.5 ±4.0	0.051 ±0.004	7.21 ±0.51	20.6 ±3.4	3	8.2 ±0.5	0.026 ±0.006	7.58 ±0.32	46.7 ±4.5	3
L5	2.8 ±0.3	0.055 ±0.001	6.70 ±0.54	18.2 ±4.4	3	3.7 ±0.6	0.031 ±0.01	7.07 ±0.22	32.1 ±6.3	3
L6	5.2 ±0.5	0.036 ±0.005	6.88 ±0.23	27.7 ±3.7	3	24.7 ±3.8	0.180 ±0.02	7.13 ±0.55	5.6 ±2.6	3
L7	9.6 ±2.5	0.039 ±0.004	7.39 ±0.40	25.3 ±4.9	3	4.8 ±2.4	0.105 ±0.04	6.59 ±0.73	9.6 ±3.5	3
L8	2.3 ±0.6	0.054 ±0.005	6.37 ±0.11	18.5 ±2.6	3	<50	<0.4	N.D	>2	3
L9	8.2 ±1.4	0.020 ±0.015	7.54 ±0.10	44.0 ±2.1	3	5.6 ±1.0	0.054 ±0.02	7.00 ±0.33	17.9 ±4.3	3
L10	1.7 ±0.4	0.040 ±0.007	6.64 ±0.03	31.4 ±7.1	3	3.4 ±1.1	0.010 ±0.001	6.56 ±0.43	10.9 ±3.4	3
A26	3.4 ±1.6	0.134 ±0.003	6.40 ±0.18	7.47 ±2.2	3	12.5 ±1.8	0.096 ±0.03	7.11 ±0.45	10.4 ±3.4	3
L12	1.8 ±0.4	0.052 ±0.003	6.55 ±0.40	19.2 ±4.5	3	1.5 ±0.3	0.051 ±0.03	6.45 ±0.22	19.0 ±5.6	3
L15	0.8 ±0.3	0.071 ±0.004	6.07 ±0.22	14.1 ±2.4	3	<50	<0.4	N.D.	>2	3
L21	<50	<0.4	ND	>2	3	<50	<0.4	N.D	>2	3
A47	51.4 ±0.3	0.019 ±0.003	7.46 ±0.10	59.8 ±12.7	3	25.6 ±0.1	0.014 ±0.002	7.26 ±0.05	72.6 ±8.8	3

[a] K_{on} (k_3) for ligands as determined using NanoBRET binding assays using either Nluc-A_1R or Nluc-A_3R expressing HEK 293 cells and determined through fitting with the 'Kinetics of competitive binding' equation built in GraphPad Prism 9.3.
[b] K_{off} (k_4) for ligands determined as in a.
[c] Kinetic dissociation constant (pK_d) for each ligand as determined from K_{on}/K_{off}.
[d] Residence time of each ligand as determined by the reciprocal of the K_{off}.
Note – values in red could not be fitted using the 'kinetics of competitive binding' model.

The real-time kinetic parameters were determined for all the A15/A17 and A26 compounds and their derivates except A15, L2, L3, L8, L15 and L21 at the A_3R and L21 at the A_1R which failed to provide

a reliable fit to the data, likely due to their high K_d values. They were also only determined for A47 and not its derivates, as A47 derivates had very low if any affinity at either of the receptors and their K_{off} rate was extremely fast (> 2 min^{-1}), making the determination of the kinetic parameters unprecise.

The majority of the measured compounds showed a good agreement between the pK_d values measured through single dose Schild analysis and the NanoBRET binding assay. This was true except for compound L3 at the A_1R where the affinity determined in the NanoBRET binding assays were ~50-fold higher than in the Schild analysis, which may indicate unusual properties of the L3 compared to the other tested compounds.

The residence time for the compounds with highest affinities at the A_1R ranges around 40 to 60 minutes (A17, L9, A47) or 16 to 27 minutes (L4, L5-L8). At the A_3R, the residence time was around 35 to 73 minutes (A17, A47, L4, L5) or 10 to 17 minutes (L9, A26). Thus, in general, these compounds have between micromolar and nanomolar affinities at these receptors.

6.7 Probing A17, A26 and A47 binding at the A_1R

Having pharmacologically evaluated the different compounds at the ARs, the next step was to employ computational techniques to investigate the binding of the lead compounds (mainly A17 and A47) to the A_1 and A_3 receptor. Prof. Kolocouris and his lab used *in silico* docking with the ChemScore scoring function, unrestrained MD simulations and MM-GBSA binding free energy calculations in order to investigate the compounds biding profiles at these receptors (Figure 6.11) (Eldridge et al., 1997; Hornak et al., 2006). The MD simulations predicted A17 to make significantly interacts with $E170^{5.28}$, $F171^{5.29}$, $E172^{5.30}$, $M180^{5.38}$, $W247^{6.48}$, $L250^{6.51}$, $H251^{6.52}$, $N254^{6.55}$ $T270^{7.35}$, $Y271^{7.36}$ at the A_1R, while at the A_3R $V169^{5.30}$, $M174^{5.35}$, $I253^{6.58}$, $L264^{7.35}$, $Y265^{7.36}$ were suggested as key amino acids. For A47 the most important amino acids at the A_1R were predicted to be $A66^{2.61}$, $I69^{2.64}$ $V87^{3.32}$, $F171^{5.29}$, $M180^{5.38}$, $W247^{6.48}$, $L250^{6.51}$, $H251^{6.52}$, $N254^{6.55}$ or $H278^{7.43}$, while $L90^{3.32}$, $L91^{3.33}$, $F168^{5.29}$, $M177^{5.38}$, $L246^{6.51}$ $N254^{6.55}$, $I268^{7.39}$ or $H278^{7.43}$ were suggested to be important at the A_3R.

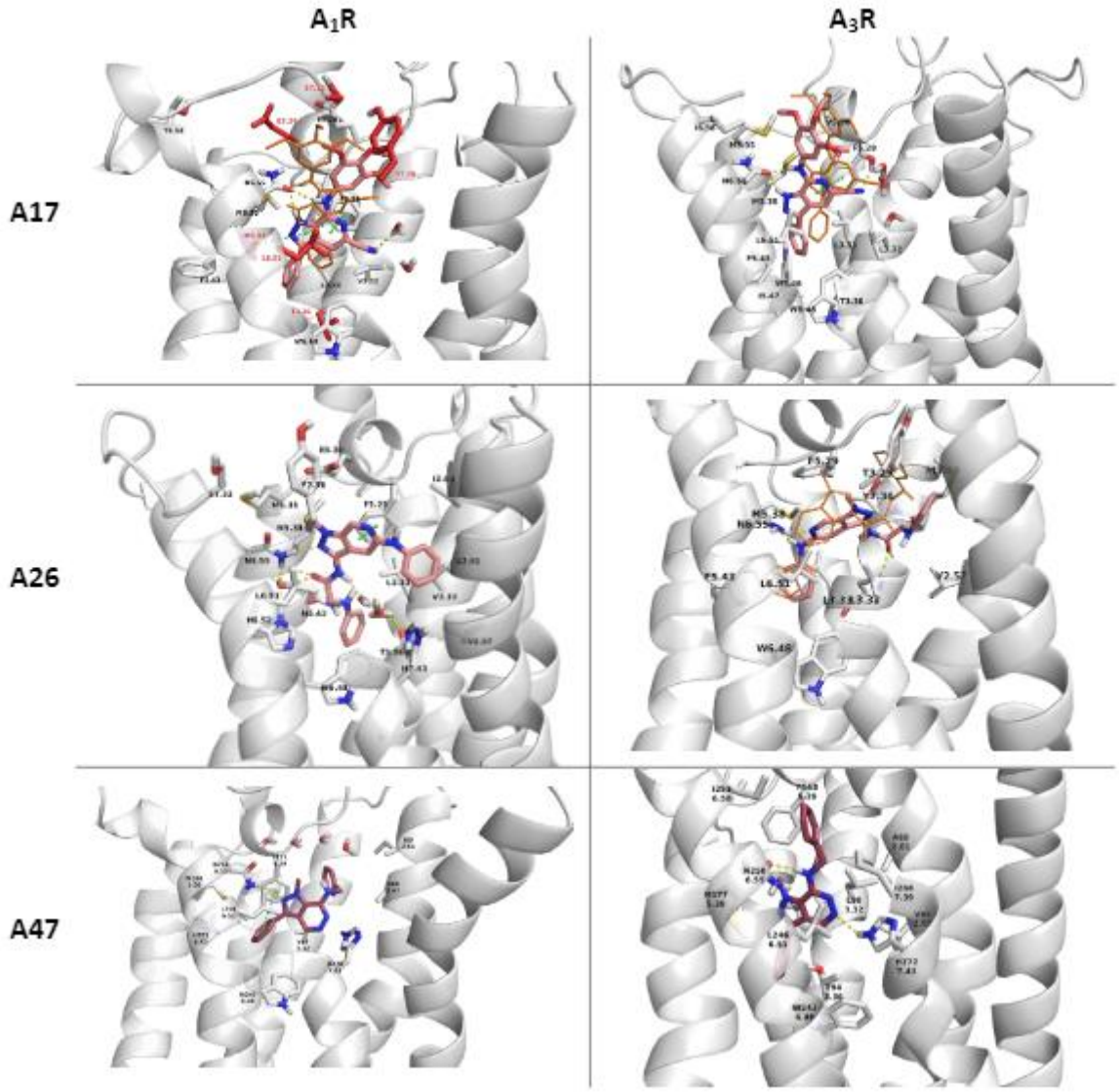

Figure 6.11. A17, A26 and A47 docking to A_1 and A_3 receptors. Representative frames of A17, A26 and A47 in the orthosteric site of WT A_1R or A_3R obtained through 100ns-MD simulations. Protein structure models are based on the inactive form for A_1R (PDB ID 5UE) or $A_{2A}R$ (PDB ID 3EML) in complex with an antagonist (Glukhova et al., 2017; Jaakola et al., 2008). Bars are plotted only for residues with interaction frequencies ≥ 0.2. Color scheme: Ligand=pink sticks, ligand's starting position=orange wire, receptor=white cartoon and sticks, hydrogen bonding interactions=yellow (dashes or bars), π-π interactions=green (dashes or bars); hydrophobic interactions=grey; water bridges-blue. Amino acids selected for the mutagenesis experiments are shown in red. These poses were produced by Prof Kolocouris.

Previously Prof Ladds and Prof Kolocouris described how mutation of residues $V169^{5.30}$, $M177^{5.38}$, $L246^{6.51}$, $F168^{5.29}$, $N250^{6.55}$ to alanine caused a reduction or negation of K18 activity, an A_3R

selective antagonist (Barkan et al., 2020; Lagarias et al., 2020, 2019; Stamatis et al., 2019). Moreover, A_1R and $A_{2A}R$ crystal structures and/or MD simulations have previously shown that residues F(5.29), M(5.38), L(6.51) and N(6.55) generally interact with all ligands in the AR orthosteric binding pocket (Amelia et al., 2021; Bolcato et al., 2020; Cheng et al., 2017; Glukhova et al., 2017; Jaakola et al., 2008; Lagarias et al., 2019; Liu et al., 2012; Matricon et al., 2021; Stamatis et al., 2019; Sun et al., 2017). To validate the *in silico* binding predictions of the lead compounds A17, A26 and A47 at A_1R, NanoBRET binding of mutagenized A_1R was used.

The amino acids selected for the single-point alanine mutagenesis at the A_1R were $T91^{3.36}A$, $F171^{5.29}$, $E172^{5.30}A$, $L250^{6.51}A$, $H251^{6.52}A$, $N254^{6.55}A$, $S267^{7.32}A$ and $Y271^{7.36}A$. This selection was guided by the *in silico* docking poses shown in Figure 6.11 and results of Prof Kolocouris' computational work. First, it was necessary to assess the affinity of CA200645 fluorescent ligand to mutant A_1R compared to the WT in order to select correct CA200645 concentrations for the NanoBRET binding experiments at the mutant A_1Rs. To this end HEK-293 cells stably expressing WT or mutants Nluc-A_1R were stimulated with a range of CA200645 concentrations (1nM to 300 nM) and BRET between Nluc tag on the A_1R and the CA200645 was measured every minute for 20 minutes (Figure 6.12.AB). BRET ratio at 10 min was the fitted with the "One site – Specific binding" equation built in GraphPad Prism 9.3 to determine CA200645 K_d (Figure 6.12.CD). $S267^{7.32}$ and $Y271^{7.36}A$ Nluc-A_1R mutants' K_ds were measured by Dr Barkan (University of Cambridge).

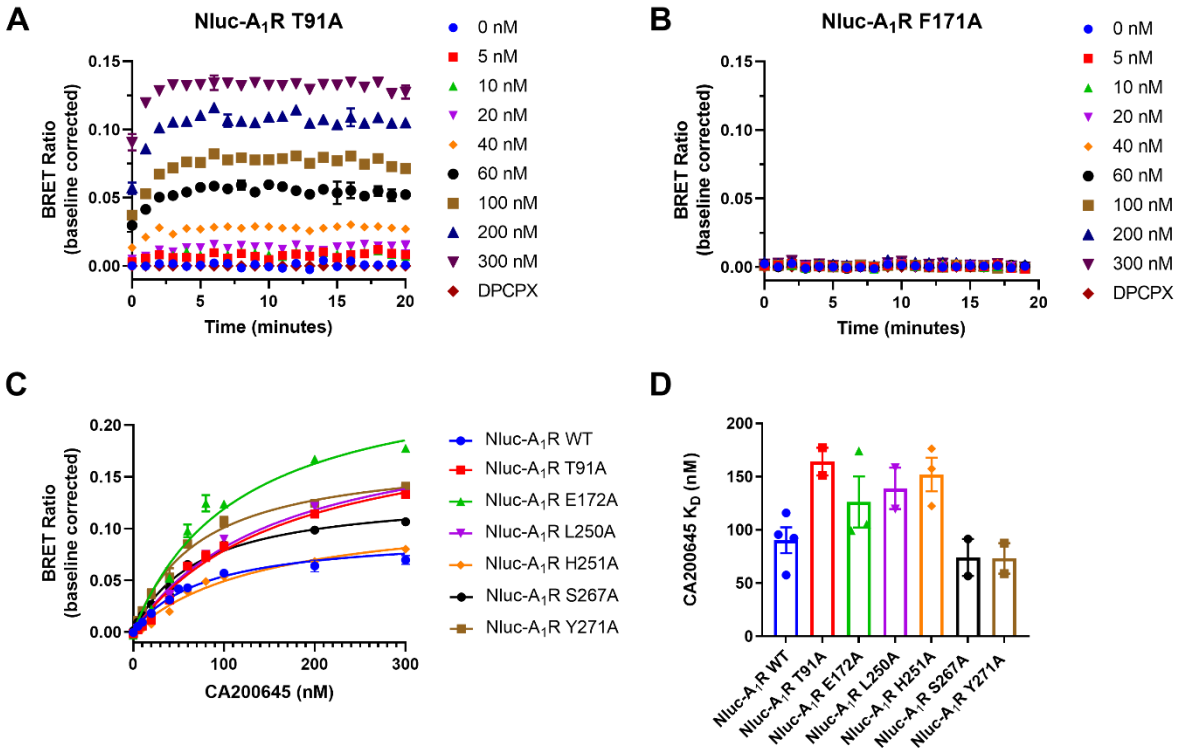

Figure 6.12. Kinetic measurement of CA200645 binding to WT and mutant Nluc-A_1R. HEK 293 cells stably expressing Nluc-A_1R T91$^{3.36}$A (A) or F171$^{5.29}$A (B) were stimulated with CA200645 at the indicated concentration. NanoBRET between the Nluc and the CA200645 was measured every 1 min for 20 min. C. NanoBRET ratio at 10 min from A/B was baseline corrected and fitted with the "One site – Specific binding" equation built in GraphPad Prism 9.3 to determine CA200645 K_d plotted in D. Data are plotted at mean ± SEM of at least 3 experiments performed in duplicate. CA200645 binding to Nluc-A_1R S267$^{7.32}$ and Y271$^{7.36}$ mutants was measured by Dr Barkan (University of Cambridge).

There was no binding of CA200645 to Nluc-A_1R mutants F171$^{5.29}$ and N254$^{6.55}$A even at the highest C200645 concentration of 300 nM. Therefore, the use of these mutants was discontinued for further experiments. For the rest of the mutants the K_d values were around 70 to 170 nM but were not significantly different from the WT Nluc-A_1R (Kd of 76.37 ± 9.37) (Table 6.11). Therefore, 20 nM was used for further NanoBRET binding experiments.

Table 6.11. Binding affinities (K_d) for Ca200645 measured using NanoBRET against WT A_1R and mutant A_1Rs. HEK 293 cells stably expressing WT or mutant Nluc-A_1R were stimulated with varying concentrations of CA200645 and NanoBRET ratio at 10 min from A/B was the fitted with the "One site – Specific binding" equation built in GraphPad Prism 9.3 to determine CA200645 K_d. K_d values for CA200645 binding to Nluc-A_1R S267$^{7.32}$ and Y271$^{7.36}$ mutants were measured by Dr Barkan (University of Cambridge).

Mutation	K_d (nM) [a]	n
WT	76.37 ± 9.37	4
T91$^{3.36}$A	166.35 ± 17.36	3
F171$^{5.29}$A	n.b.[b]	3
E172$^{5.30}$A	116.04 ± 12.22	3
L250$^{6.51}$A	158.28 ± 17.37	3
H251$^{6.52}$A	145.19 ± 19.13	3
N254$^{6.55}$A	n.b.[b]	3
S267$^{7.32}$A	70.99 ± 7.03	3
Y271$^{7.36}$A	71.10 ± 7.68	3

[a] Affinity constant (K_d) for CA200645 binding to WT or mutant A_1R receptors. Data are expressed as mean ± SEM of n independent repeats, conducted in duplicate.
[b] No binding of up to 300 nM CA200645 to Nluc-A_1R mutant.
Statistical significance was determined using ANOVA and Dunnett' s post-test.

As discussed above, A_1R amino acids T91$^{3.36}$A, F171$^{5.29}$A, E172$^{5.30}$A, L250$^{6.51}$A, H251$^{6.52}$A, N254$^{6.55}$A, S267$^{7.32}$A and Y271$^{7.36}$A were suggested to be important for the binding of A17, A26 and A47 compounds. Therefore, the ability of these three compounds to displace and inhibit the specific binding of CA200645 at the WT and mutant Nluc-A_1R was tested next. NECA was also included in this experiment, as a typical AR ligand binding to the A_1R orthosteric site. HEK-293 cells stably expressing WT or mutant Nluc-A_1R were stimulated with 20 nM CA200645 and a range of ligand concentrations (1pM to 100 µM). BRET ratio at 10 minutes was then used to create full dose response curve for each ligand and fitted with the "One site – Fit K_i" model derived from the Cheng and Prusoff equation built in GraphPad Prism 9.3 to enable estimates of pK_i (Figure 6.13 and Table 6.12).

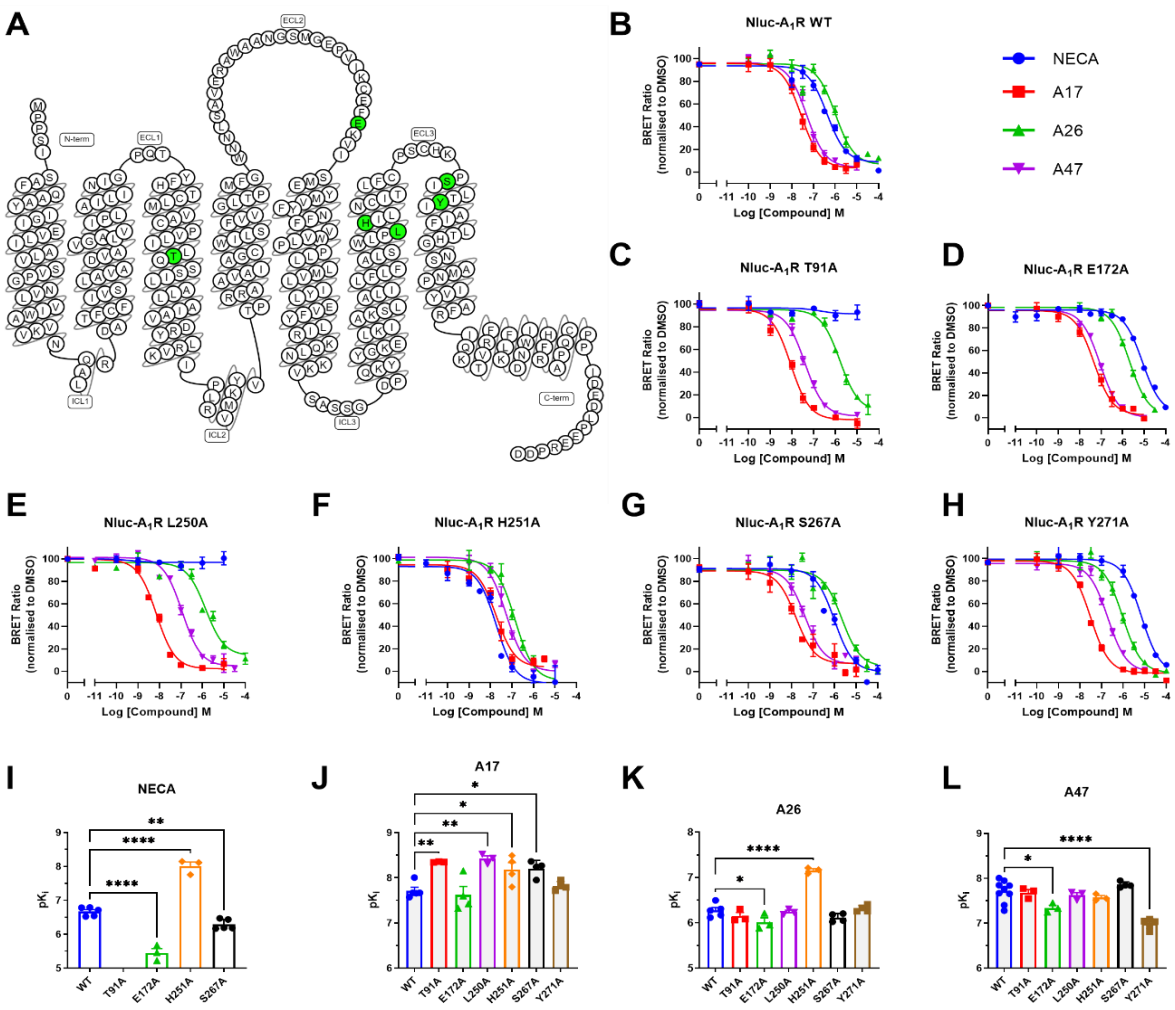

Figure 6.13. Binding of NECA, A17, A26 and A47 at WT and mutant A_1R. A. Human A_1R sequence with indicated amino acids (green) selected for mutagenesis. B-H. HEK293 cells stably expressing WT or mutant Nluc-A_1R were treated with 20 nM CA200645 and increasing concentrations of unlabelled AR ligand, enabling concentration-dependent decreases in BRET ratio at 10 min to be determined with the response normalised to DMSO. Binding curves were fitted with the "One site – Fit K_i" model derived from the Cheng and Prusoff equation built into GraphPad Prism 9.3 to enable estimates of the pK_i. I-L. Plotted pK_i values from B-H. Data are plotted at mean ± SEM of at least 3 experiments performed in duplicate. HEK293 cells stably expressing Nluc-A_1R S267$^{7.32}$ and Y271$^{7.36}$ mutants were made by Dr Barkan (University of Cambridge).

Table 6.12. Binding affinities (pK_i) for NECA, A17 and A26 measured using NanoBRET against WT A_1R and mutant A_1Rs. pK_i values determined by NanoBRET in HEK293 cells stably expressing WT or mutant Nluc-A_1R treated with 20 nM CA200645 and increasing concentrations of unlabelled AR ligand, enabling concentration-dependent decreases in BRET ratio at 10 min to be determined with the response normalised to DMSO. The data at 10 min was then fitted using the "One site – Fit K_i" model derived from the Cheng and Prusoff equation built into GraphPad Prism 9.3. HEK293 cells stably expressing Nluc-A_1R S267$^{7.32}$ and Y271$^{7.36}$ mutants were made by Dr Barkan (University of Cambridge).

Mutation	NECA		A17		A26		A47	
	pK_i[a]	n	pK_i[a]	n	pK_i[a]	n	pK_i[a]	n
WT	6.67 ± 0.05	5	7.87 ± 0.06	6	6.30 ± 0.07	5	7.62 ± 0.06	6
T91$^{3.36}$A	n.b. [b]	3	8.37 ± 0.07**	3	6.10 ± 0.07	3	7.71 ± 0.06	3
E172$^{5.30}$A	5.38 ± 0.06****	4	7.63 ± 0.08	4	5.98 ± 0.06*	3	7.35 ± 0.05*	3
L250$^{6.51}$A	n.b. [b]	4	8.44 ± 0.05**	3	6.15 ± 0.09	3	7.24 ± 0.05	3
H251$^{6.52}$A	8.04 ± 0.10****	4	8.03 ± 0.10*	4	7.15 ± 0.08****	3	7.57 ± 0.09	3
S267$^{7.32}$A	6.31 ± 0.10	5	8.10 ± 0.16*	6	5.97 ± 0.17	6	7.68 ± 0.09	5
Y271$^{7.36}$A	5.45 ± 0.06**	4	7.82 ± 0.04	5	6.33 ± 0.07	5	7.02 ± 0.05****	5

[a] Equilibrium binding affinities of the ligands measured with NanoBRET against WT or mutant A_1R.
[b] n.b. NECA was unable to displace CA200645 at the mutant receptor
Data are expressed as mean ± SEM of n independent repeats, conducted in duplicate.
Statistical significance (* $p < 0.05$, ** $p < 0.01$, **** $p < 0.0001$) was determined using ANOVA and Dunnett' s post-test.

From this data, mutants S267$^{7.32}$A and especially L250$^{6.51}$A showed significantly increased affinity for A17. This was unexpected since the L$^{6.51}$, which is a key residue for recognition and is highly conserved across all four AR subtypes (Barkan et al., 2020; Lagarias et al., 2018). On the other hand, the findings for S267$^{7.32}$A significantly increasing NECA binding affinity at the A_1R are consistent with previous findings (Jespers et al., 2018). Mutations E172$^{5.30}$A and Y271$^{7.36}$A both significantly reduced the binding affinity of NECA but had little effect upon A17 or A26 affinity. For NECA, the NanoBRET binding assay could not determine any measurable binding at the T91$^{3.36}$A mutant.

H(6.52) is an important residue in the AR orthosteric side that stabilizes both agonists and antagonists through interaction with the different modifications emerging from the core scaffold. The mutation H251$^{6.52}$ to alanine significantly increased the affinity of NECA, A17 and A26 for A_1R and for A26, especially, this was the only mutant where the compound has shown any appreciable increase in affinity. On the other hand, this mutation did not have any significant effect on A47 binding.

Compound A47 showed most significant reduction in affinity at mutant Y271$^{7.36}$A, which was in contrast to the results for A17 and A26 compounds. Looking at the MD simulations carried out by Prof Kolocouris, this might be because of the Y271$^{7.36}$A mutation affecting nearby contact of A26 with H278$^{7.43}$, as A26 isn't predicted to directly interact with Y271$^{7.36}$.

6.8 Discussion

6.8.1 Discovery of potent dual A_1 and A_3 receptor antagonists

A_1R antagonists have been indicated as potential treatment for chronic heart disease, lung diseases as asthma or as potassium-sparing diuretics, while A_3R antagonists may be beneficial in cancer or eye pathologies (Cohen and Fishman, 2019; González-Fernández et al., 2014; Schenone et al., 2010). With the aim of identifying new potent antagonists of the A_1R and A_3R, in this chapter we have investigated 21 compounds with novel pyrazolo[3,4-c]pyridine (A15/A17 and A26 series) and pyrazolo[3,4-d]pyridazines (A47 series). Compounds A15 and A17 shared the same substituents at position 5- and 7- but had isopropyl and phenyl group at the 3-position, respectively, while compound A26 had a different substitution pattern with an acetamido and anilino groups at the 3- and 5-position, respectively. Compound 47 then had a 3-phenyl group, a 7-benzylamino and 1-methyl group at the pyrazolopyridazine scaffold.

Following evaluation using cAMP accumulation assay, compounds L3, L4, L5, L7, L8, L9 and A17 showed biggest potency at A_1R and A_3R, behaving thus as dual antagonists at the two adenosine receptor subtypes. These compounds are pyrazolo-[3,4-c]pyridines with isopropyl or phenyl group at 3-position, respectively, a cyano or chloro or aminomethyl or N-(arylmethyl)aminomethyl group at 5-position and an anilino group at 7-position. A26, which is 3-acetamido-5-anilino pyrazolo-[3,4-c]pyridine, and A47, which is a pyrazolo[3,4-d]pyridazines with a 3-phenyl group, together with a 7-benzylamino and 1-methyl substitution also belong among the most potent dual A_1R and A_3R antagonists.

As many compounds targeting the ARs cause wide activation or blockage across all AR subtypes due to the similarities between the orthosteric side in the receptors, receptor subtype selectivity was also tested using cAMP accumulation assay. None of the tested compounds showed any significant activity at the $A_{2A}R$ and while A17 and A47 had slight effect at the $A_{2B}R$, this was much less that their potency at A_1R and A_3R, meaning the tested compounds are selective dual antagonists for A_1R and A_3R.

6.8.2 Kinetic profiling of antagonists at the A_1 and A_3 receptors

Another important characteristic of potential drugs is their affinity and since the newly identified compounds are dual antagonists for A_1R and A_3R, NanoBRET binding method was used to establish compound affinities at these two receptors. The compounds with the highest affinities were generally the ones based on A17, including A17 itself, showing nanomolar to mid-nanomolar binding affinities,

while 26-derived compounds had low micromolar to 100 nM binding affinities. A47 then had 21 nM affinity at the A_1R and 55 nM affinity at the A_3R with rest of the A47-derived compounds failing to show any binding.

When comparing similar compounds between themselves, it can be noted that even small changes in ligand's structure resulted in significant changes in affinity despite the broad orthosteric binding site of the ARs. For example, the replacement of the 5-cyano group in A17 by the 5-chloro group in L5 reduced the A_1R affinity approximately 30-fold, while the deletion of said 5-cyano group reduced the affinity by approximately 100-fold against A_1R. At the A_3R, there was reduction in affinity by approximately 7-fold and 20-fold, respectively.

It has been increasingly apparent in drug discovery that equilibrium characteristic like affinity is not enough to describe drug actions and the extraction of more kinetic parameters is very beneficial (Suchankova et al., 2021). Therefore, in this chapter, we have employed the NanoBRET binding assay to measure real-time kinetic parameters. At the A_1R compounds with the longest residence times of 30 to 60 minutes were A15, A17, L9, L10 and A47 compared to L3, L5, L8, A26 and L15 having some of the shortest residence times of 7.5 to 19 minutes. At the A_3R compounds with the longest residence times of 35 to 73 minutes were A17, A47, L4 and L5, while L6, L7, L10 and A26 had shortest residence times of 5.6-11 minutes. The lead compound A17 had a K_d = 5.62 nM and RT = 41.33 min for A_1R and K_d = 13.5 nM and RT = 47.23 min for A_3R. These data give us more insight into the compounds mode of binding and can advise future drug discovery.

6.8.3 MD simulations and mutagenesis give insight into compound binding

To better understand the binding mode of the compounds, in this chapter we employed *in silico* docking and MD simulations complemented by *in vitro* mutagenesis and subsequent testing of resulting mutants. The MD simulations of the most potent compound A17 showed that this compound was stabilised at the A_1R using an array of co-operative interactions. This would include interactions with TMD5 E170$^{5.28}$, F171$^{5.29}$, E172$^{5.30}$, M180$^{5.38}$, N184$^{5.42}$, TMD6 W247$^{6.48}$, L250$^{6.51}$, H251$^{6.52}$, N254$^{6.55}$, TMD7 T270$^{7.35}$ and Y271$^{7.36}$. Furthermore, the 5-cyano group of A17 seemed to be stabilized through hydrogen bonding interactions with water molecules that entered the binding area between the ligand and TMD2 and TMD3.

The residues mutated in the A_1R using single point alanine mutagenesis were T91$^{3.36}$, F171$^{5.29}$, E172$^{5.30}$, L250$^{6.51}$, H251$^{6.52}$, N254$^{6.55}$, S267$^{7.32}$ and Y271$^{7.36}$. Some of these residues like E172$^{5.30}$, Y271$^{7.36}$ or S267$^{7.32}$ in close proximity to the low nanomolar A17 left the compound affinity for the receptor unchanged or reduced, while L250$^{6.51}$ alanine mutation increased the affinity despite L$^{6.51}$ being

conserved and key for recognition across the 4 AR subtypes. This result suggests that inside the orthosteric binding area in a height where L250$^{6.51}$ is positioned a substituent can be added to A17 to increase binding affinity. Mutations T91$^{3.36}$A and H251$^{6.52}$A then increased the affinity for A17 as has been reported previously for NECA (Jespers et al., 2018; Lane et al., 2012).

The other two compounds tested with the mutants were A26 and A47. A26 showed only slight decrease in affinity at mutant E172$^{5.30}$A, while it significantly increased at mutant H251$^{6.52}$A. This is interesting since H251$^{6.52}$ is an important residue in the AR orthosteric side that stabilizes both agonists and antagonists through interaction with the different modifications emerging from the core scaffold. In contrast to A17 and A26, A47 showed most significant reduction in affinity at mutant Y271$^{7.36}$A. This might be because A47 has π-π interactions with H251$^{6.52}$, while A26 interacts with nearby H278$^{7.43}$ and not directly with Y271$^{7.36}$.

Overall, MD simulations gave us insight into the differences between the binding of individual compounds and showed good correlation with the *in vitro* results.

6.9 Conclusion

This chapter investigated 21 compounds with novel pyrazolo[3,4-c]pyridine (A15/A17 and A26 series) and pyrazolo[3,4-d]pyridazines (A47 series) for their antagonistic activity at A_1 and A_3 receptors. Through rigorous *in vitro* pharmacological testing including the use of cAMP accumulation assay and NanoBRET binding assay, several potent antagonists at these receptors were identified including L3 or L4, L5, L7,L8, L9, A17, A26 and A47. When tested against the remaining two adenosine receptor subtypes A_{2A}R and A_{2B}R, most compounds had no or little effect at either of these receptors, making them promising potential therapeutical compounds. Therefore, new selective dual antagonists for A_1R and A_3R were identified.

The A17 series is not only the most potent overall, but it also has the highest nanomolar to mid-nanomolar binding affinities measured with the NanoBRET binding method, while the A26 series has low micromolar to 100 nM binding affinity against A_1R and A_3R. A47 compound was then the only one of that series to show any significant binding with 21 nM affinity for the human A_1R and 55 nM affinity for the human A_3R. Furthermore, the NanoBRET binding assay enabled the extraction of real-time kinetic parameters and uncovered a diverse range of kinetic profiles for the tested compounds. At the A_1R compounds with the highest residence time of 40 to 60 minutes were A17, L9 and A47, while at the A_3R A17, A47, L4 and L5 had highest residence time of 35 to 73 minutes.

Subsequently, the differences in compounds binding were explored through *in silico* docking, MD simulations, *in vitro* mutagenesis and NanoBRET binding experiments. The residues mutated in the A_1R using single point alanine mutagenesis were $T91^{3.36}$, $F171^{5.29}$, $E172^{5.30}$, $L250^{6.51}$, $H251^{6.52}$, $N254^{6.55}$, $S267^{7.32}$ and $Y271^{7.36}$. The differential effect of these mutants on A17, A26 and A47 hints towards slightly different binding of these compounds that might account for their differences in selectivity, potency, and affinity.

Overall, this chapter identified some novel potent dual A_1R and A_3R antagonists with low nanomolar affinities at the A_1R and A_3R. Using computational techniques and *in vitro* experiments light was also shed on how these compounds bind in the A_1R pocket. A17 and A47, especially, show a promise as a new low nanomolar leads for future work on the A_1R and A_3R and as starting compounds for future drug discovery at these receptors.

Chapter 7. General discussion and future directions

7.1 Discussion

7.1.1 Using combinational *in silico* and *in vitro* approach to drug discovery

Drug discovery and development is very long and very expensive process with traditional approaches relaying on stepwise synthesis and *in vitro* screening of huge compound libraries to identify potential hits/leads which are then subjected to iterative chemical optimisation followed by experimental evaluation to obtain pre-clinical candidate(s). However, academic laboratories are very limited when it comes to accessing high-throughput libraries due to insufficient resources. Here I have shown how *in silico* computational techniques can be integrated to successfully streamline drug design, development, and optimization and make it more feasible for academic laboratories. In particular, I employed a combinational approach of *in silico* and *in vitro* techniques to drive drug discovery at GIPR and adenosine receptors.

Why were these receptors chosen as targets? Although GLP-1R has long been targeted in type 2 diabetes mellitus, GIPR has mostly been overlooked (Ding et al., 1997; Holst and Rosenkilde, 2020). As part of the insulin secretion experiments in chapter 3, I showed that indeed both GLP-1 and GIP potentiate glucose stimulated insulin secretion and this could be further potentiated by positive allosteric modulators already available in Ladds laboratory. But recently, there has been more and more emerging evidence arguing for inhibition of GIPR signalling in adipose tissues, suggesting that negative allosteric modulators of the GIP might be beneficial in obesity (Irwin and Flatt, 2009; Killion et al., 2018; Miyawaki et al., 2002). Regarding adenosine receptors, this work builds upon a very promising A_1R selective compound BnOCPA, that has been shown to be a powerful analgesic but does not cause sedation, bradycardia, hypotension or respiratory depression, with the aim of further improving the potency and selectivity of the compound (Knight et al., 2016; Wall et al., 2022). On the other hand, A_1R antagonists could be useful as potassium-sparing diuretic agents, drugs for chronic heart diseases or lung diseases such as asthma, chronic obstructive pulmonary disease and pulmonary fibrosis (Modlinger and Welch, 2003; Schenone et al., 2010; Shah and Frishman, 2009; Wilson et al., 2009), while A_3R antagonists hold potential as treatment for CNS disorders, asthma or eye pathogenesis (Barkan et al., 2020).

The ways in which *in silico* techniques can be applied to drug discovery of GPCRs and in particular GIPR and ARs are multiple. Firstly, there is existing knowledge of various AR ligands, for example NECA, adenosine or BnOCPA. As shown in our experiments, NECA is slightly A_1R selective, so this knowledge

can already hint that modifying the NECA scaffold as was done in chapter 4 can lead to some A_1R selective agonists like compounds 44, 45 and 51-53. Knowledge of other AR ligands and their various modifications can then further inform an *in silico* search of the available chemical space to design new NECA series that has much higher potential for being A_1R selective compounds than if a random library was screened. A similar approach was originally taken with the GIPR negative allosteric modulators building upon the already known compounds C3 and C25. This meant that out of only 7 compounds tested *in vitro*, 4 turned out to be GIPR negative allosteric modulators, translating into more than 50 % success rate. Moreover, *in silico* docking or MD simulations can then be used to research the compound's predicted binding and effects upon the receptor in more detail, which can also be used to inform for example in which direction to expand the compound further to achieve higher potency or where further expansion might cause steric hindrance.

Compared to high through-put screening, over 50% success rate is very high. However, the drawback is the need for previously known ligands for the receptor. The improvements to the compounds are also more likely to be marginal compared to discovering a truly new hit. The problem is also that this approach does not introduce new chemical scaffolds to account for attrition in drug discovery, instead building on the old ones. Alternative approaches to overcome this drawback is *in silico* screening, which is basically a computational screen of large chemical library against selected receptor or receptor site. This approach has been increasingly popular with the emergence of many solved receptor structures, including many class A and class B1 GPCRs, and here was successfully applied to GIPR to discover new NAMs like T2, T5 or T10. The challenge of this approach was first to successfully discover a good GIPR allosteric binding site, which was also achieved with the help of *in silico* docking and other computational techniques as will be discussed below.

Overall, *in silico* techniques have lately hugely benefited drug discovery as well as this thesis in making drug development less expensive, faster and more accessible to academic laboratories.

7.1.2 Identifying the GIPR allosteric binding site at the top of TMD2/3 and ECL1

Allosteric binding site can be identified using different approaches and computational techniques are again highly useful. The first approach utilised in chapter 3 and 4 was by finding the binding site of known allosteric modulators. Therefore, *in silico* blind docking of C9-related compounds (C9 is a GIPR PAM) was carried out against GIPR homology models and two main candidates were identified – Site 6 and Site 10. Site 6 lies just below the orthosteric binding site in the middle of the receptor and was consistently predicted across all GIPR homology models (Table 4.2) used except model 7 based on $A_{2A}R$. Site 10 lies at the top of TMD2/3 and was most strongly predicted for GLP-1R-

and PTHR1- based GIPR homology models. Amino acids from both sites most likely to interact with the compounds were then selected based on *in silico* binding diagrams, mutated to alanine and tested *in vitro* to see whether they affect the behaviour of GIPR NAMs C3 and C25. It was found that mutant L193$^{2.70}$A and later R196A, P197A, Q211$^{3.24}$A and Q220$^{3.33}$A significantly decreased C25 efficacy, while none of the tested mutants had any effect on C3. All these amino acids are part of Site 10, which was then confirmed as the allosteric binding site also for C58. C25 and C58 are both compounds structurally related to C9 (C3 is not), so it was not surprising these compounds bound the site predicted by the *in silico* docking of C9 and related compounds. The clever use of *in silico* blind docking meant we only had to test a handful of amino acids in pre-determined locations compared to carrying out large-scale mutagenesis study of GIPR that we would have to if we lacked the computational information.

The second approach is to use *in silico* techniques for allosteric site identification. The advantage of this approach is that there is no need for allosteric modulators to already be known, although structural information for the receptor is needed in form of a crystal, Cryo-EM or at least a homology model. The different techniques available can be roughly divided into subsequent categories: knowledge-, sequence-, geometry-, energy- and dynamics-based techniques. When applied to the same GIPR homology models as used *in silico* docking three main potential allosteric sites were identified numbered 6, 7 and 10. Site 6 and 10 are the sites mentioned above, which were in parallel also identified through the *in silico* docking approach, while site 7 wasn't that prominent in the *in silico* docking poses. Site 7 lies at the bottom middle of the receptor and thus would be only accessible by compounds capable of crossing the cell plasma membrane.

The potential issue with using this second approach is that many of the techniques are not tailored specifically towards allosteric site identification but more towards identification of any binding site including the orthosteric one or even more generally towards identifying any structurally and functionally important amino acids in the receptor. This last characteristic is particularly true for sequence-based techniques like multiple sequence alignment or a statistical coupling analysis, which were not particularly useful for our efforts. However, once potential sites have been identified using other techniques, these methods show that Site 10 is generally less conserved than Site 6 or 7, making it more promising for development of selective compounds.

Knowledge-based methods were then largely limited by the small number of structures solved with allosteric modulators and outdated structure banks, thus majorly focusing on orthosteric sites, and also poor understanding of the key differences between orthosteric and allosteric site makeup. The geometry- and energy-based techniques have proven the best for the aim of identifying a GIPR allosteric binding site. They rely on simple characteristic like the depth of the site 3D space and docking of small molecules. Since the energy-based techniques incorporate docking of small molecules it is not

that surprising that results corelate well with the *in silico* docking results as the small molecules used there are similar to parts of the GIPR allosteric modulators' structures. Dynamics-based techniques offer slightly more information as SPACER can for example additionally identify regions communicating with each other. MD-simulations, which could also be classified under dynamics-based techniques has not been performed in this study for GIPR allosteric modulators but has advised drug discovery at ARs instead. The reason they have not been used for GIPR yet, is because they require large amounts of knowledge and computational power but exploiting them for exploration of key compounds (like compound C25) binding and activity at GIPR might be very useful to better understand compound activity.

As discussed previously, finding the allosteric binding site of the GIPR allosteric modulators is important for multiple reasons including proving whether the compounds are allosteric modulators and better understanding the differences between the potency and pathway and receptor selectivity of the compounds. It has also enabled an *in silico* screen against this site carried out by Dr Rahman (University of Cambridge), which helped identify multiple new GIPR NAMs T2, T5, T10, T11, T13, T18 and T26. Using the GIPR Site 10 mutants, T5, T10, T11 and T18 were confirmed indirectly to bind this site and while T2, T13 and T26 have not been tested with the mutants yet, the hypothesis is that they are also likely to bind this site.

In silico docking paired with *in vitro* mutagenesis has managed to identify a GIPR allosteric binding site at the top of TMD2/3 and ECL1, which was confirmed as a good binding site by multiple other *in silico* techniques. However, the ultimate direct proof of the compounds binding would be a Cryo-Em structure and a collaboration has started between Ladds and Miller (University of Cambridge) laboratories to work towards a GIPR and GLP-1R Cryo-Em structure with C58, which is a NAM for both of the receptors.

7.1.3 Relative advantages of orthosteric versus allosteric ligands

This thesis has explored different types of ligands, mainly orthosteric versus allosteric ones. Orthosteric drugs are historically slightly favoured by the use of radioligand binding assays for drug discovery. It might be slightly easier to achieve higher efficacy with them having an effect straight on the orthosteric site, while the effect of allosteric modulators often has to be propagated across a receptor. For example, the dual A_1R and A_3R antagonists discussed in chapter 6 are potent at 0.1 µM (A17, A47), while the GIPR NAMs only have an effect around 50/100 µM.

Key properties of many potential drugs is selectivity. BnOCPA is such a promising compound partly due to its A_1R selectivity over the other AR subtypes, which has been even exceeded by

compounds 45 and 51 having more than 10,000-fold selectivity to the A_1R. This is, however, not true for many other AR ligands as there is a lot of sequence and structure similarity among the orthosteric pockets of the AR subtypes, evidenced by A17 and other compounds being dual antagonists for A_1R and A_3R. The orthosteric pocket of GIPR also shares partial similarity to GLP-1R and GCGR evidence by dual and triple agonists of these receptors (Bastin and Andreelli, 2019; Knerr et al., 2022; Zhao et al., 2021). Allosteric pocket, sterically different to the orthosteric pocket, might offer more potential for developing GIPR selective compounds. Indeed, the identified GIPR allosteric site at the top of TMD2/3 and ECL1 shows little conservation of residues between the three receptors (Figure 4.7) and compounds C25, T2 and T5 are GIPR-selective.

Big differences between ARs and GIPR is that ARs as class A GPCRs, have adenosine as an endogenous ligand, which is a small molecule, while class B1 GPCRs, such as GIPR, have more voluminous orthosteric site and endogenous peptide ligands such as GIP, which makes it difficult to develop small molecule orthosteric ligands against GIPR. On the other hand, all negative allosteric modulators identified in chapter 3 are small molecules. Among other advantages of allosteric modulators belong their probe dependency, lack of intrinsic selectivity and saturability (Cheng and Jiang, 2019; Wootten et al., 2017).

7.1.4 Common aim of drug discovery to increase compound potency

The common goal of the thesis was to improve compound potency. This was particularly successful for A_1R agonists with compounds 27, 26, 45, 49 and 51-54 showing pEC_{50} between 9-10, which is higher potency than BnOCPA or the parent compounds adenosine and NECA. It was also found that a halogen substituent in the *meta* position on the aromatic ring confers high efficacy at the human A_1R and all the most potent hA_1R agonists but 45 feature a N^6-phenoxycyclopentyl moiety.

More importantly, this was achieved while retaining selectivity. NECA-based compounds 44, 45, 51-53 display enhanced A_1R selectivity with compounds 45 and 51 being approximately 1500-fold more A_1R selective than NECA itself, suggesting more than 10,000-fold selectivity overall to the A_1R, while compounds 22, 23, 26, 27 are A_1R selective despite being based on near-equipotent adenosine. The selectivity can be driven both by the position of the substituent on the phenoxy group (compounds 26 and 51 or 30 and 55) or the ribose C-5' substituent group with the adenosine-derived compound being more A_1R selective (25 and 50).

With the antagonists quite high potency was still achieved, in particular L3, L4, L5, L7, L8, L9 and A17 showed biggest efficacy at A_1R and A_3R, behaving thus as dual antagonists at the tested 1 µM concentration. However, they are not that selective since they antagonise both A_1 and A_3 receptors.

Generally, it seems that orthosteric A_1R ligands are more likely to have an effect on the G_i-coupled A_3R than at the G_s-coupled $A_{2A}R$ and $A_{2B}R$, where almost none of the AR ligands tested in chapter 5 and 6 showed any activity.

The allosteric modulators then achieved slight improvement in potency with compounds T10, T11, T18 effective at 31.6/50 µM compared to the original compounds C3 and C25 effective at 100 µM. This is only a little improvement but is somewhat compensated by the increased number of chemical scaffolds now present in the GIPR allosteric modulator library, which gives better potential for future drug development.

7.1.5 High affinity often correlates with high efficacy

In addition to efficacy, affinity is also a very important characteristic. At the human A_1R, the agonists with the highest affinity are 27, 28, 29, 49, 51, 53 and 54, which all have higher affinity than BnOCPA and the parent compounds adenosine and NECA alone. They are also all phenoxycyclopentyl derivatives and not the benzyloxycyclopentyl derivatives. It is also interesting to note that the A_1R agonists show a clear positive correlation between their potency (pIC_{50} values) and affinity (pK_i values) at the human A_1R. Namely compounds 27, 29, 49 and 51-54 were identified as both the most potent and strongest binders at the hA_1R. All of these except 49 and 51 have a halogen (chloride or bromide) substituent, mostly in the meta-position of the aromatic phenoxy ring, suggesting this substituent confers both high efficacy and high affinity at the hA_1R. Overall, adenosine and NECA phenoxycyclopentyl derivatives, and especially those with a halogen substituent as R^2 group on the aromatic ring, have higher affinity for both human and rat A_1R. Considering the substitution position on the phenoxy ring, the highest affinity was observed with the halogen in the *meta*-position (27, 29, 54), followed by *ortho*- (28, 53) and the *para*-position (30, 55).

Regarding the AR antagonists, the compounds with the highest affinities were generally the ones based on A17, including A17 itself, showing nanomolar to mid-nanomolar binding affinities, while A26-derived compounds had low micromolar to 100 nM binding affinities. A47 then had 21 nM affinity at the A_1R and 55 nM affinity at the A_3R with rest of the A47-derived compounds failing to show any binding. Similarly, to agonists these are also the compounds showing highest potency, especially A17.

For allosteric modulators the affinity is harder to measure. The typical approaches would be a competition binding assay (like the NanoBRET assay employed for the AR ligands) with a fluorescent ligand or a radiolabelled ligand. Now that an allosteric binding site has been confirmed at the top of TMD2/3 and ECL1 for multiple allosteric modulators, it should be possible to tag one of the compounds with a fluorophore, measure its binding kinetics and then use it for a NanoBRET competition binding

assay to measure the other allosteric modulators binding to the same site. It is again likely that some of the most potent compounds would probably also be the best binders.

7.1.6 Evaluating receptor-ligand binding kinetics

As multiple approved drugs currently on the market show non-equilibrium binding characteristics (Schuetz et al., 2017), it is now becoming increasingly clear that a single characteristic like affinity measured at equilibrium might not be sufficient for estimating an *in vivo* efficacy and more detailed comprehension of the kinetics of association and dissociation of a receptor-ligand complex is needed to evaluate the full pharmacological effect of a drug and its mode of action (Suchankova et al., 2021).

For A_1R agonists, it was the phenoxycyclopentyl derivatives with the highest affinities for A_1R, that also had the highest residence times at both human and rat A_1R. At the human A_1R compound with highest residence time is 51 with RT of approximately 42 minutes, followed by 27, 49, 53 and 54 all also having RT of 29-35 minutes. For the rest of the A_1R agonists, and particularly for the benzyloxycyclopentyl derivatives, the RT is lower. Regarding the antagonists, the compounds with the longest residence times of 30 to 60 minutes at the human A_1R were A15, A17, L9, L10 and A47 compared to L3, L5, L8, A26 and L15 having some of the shortest residence times of 7.5 to 19 minutes. At the human A_3R antagonists with the longest residence times of 35 to 73 minutes were A17, A47, L4 and L5, while L6, L7, L10 and A26 had shortest residence times of 5.6-11 minutes.

Apart from residence times, measuring receptor-ligand kinetics has enabled the calculation of other kinetic parameters like k_{on}, k_{off} and pk_D, which can help inform future drug discovery. For example, the lead A_1 and A_3 receptor antagonist A17 had a K_d = 5.62 nM for A_1R and K_d = 13.5 nM for A_3R. It might be useful to measure these kinetic parameters also for the GIPR allosteric modulators to complement the *in silico* docking and *in vitro* efficacy data and help better understand the differences between the compounds.

7.1.7 Understanding compounds interactions with the receptor binding site can inform future drug design

Better understanding receptor-drug interactions can help inform drug development. Beyond just efficacy and kinetic parameters, insight can also be made from *in silico* docking, MD simulations and *in vitro* mutagenesis, which together give overall better picture of how a compound binds and engages the receptor.

As mentioned previously, one of the main aims was to develop more potent compounds. Preti et al. (2022) showed that 27 formed key hydrogen bonds with N254$^{6.55}$, hydrophobic contacts with F171^{ECL2}, and oriented the 3-bromophenyl moiety in a hydrophobic sub pocket formed by I69$^{2.64}$, N70$^{2.65}$, Y271$^{7.36}$, and T270$^{7.35}$ at the A_1R. Moreover, 27 is further stabilised by the hydrophobic sub-pocket that is putatively present only in A_1R, hence, 27 cannot be completely stabilized by the other AR subtypes. In contrast, compound 20, which is a structurally closely related compound but slightly bulkier, was not able to completely accommodate the 3-bromobenzyl group within this pocket and therefore displayed higher flexibility at the N^6 level, which could contribute to reduced affinity and efficacy of 20 compared to 27 at the A_1R. This knowledge already helps inform us, which interactions we might need to conserve to retain compound selectivity and in which direction the compound should not be expanded on in order not to lose efficacy and affinity like 20. Using mutagenesis, they also confirmed that 27 had significantly decreased affinity at A_1R mutants I69$^{2.64}$A and Y271$^{7.36}$A, suggesting these are likely the interactions we would want to preserve in future compounds.

Similar amino acids were then indicated as important by MD simulation with the lead dual A_1 and A_3 receptor antagonists. For example, compound A17 was predicted to be stabilised at the A_1R using an array of co-operative interactions including E170$^{5.28}$, F171$^{5.29}$, E172$^{5.30}$, M180$^{5.38}$, N184$^{5.42}$, W247$^{6.48}$, L250$^{6.51}$, H251$^{6.52}$, N254$^{6.55}$, T270$^{7.35}$ and Y271$^{7.36}$. Interestingly, the A_1R mutant L250$^{6.51}$A increased A17 affinity for the receptor despite L$^{6.51}$ being conserved and key for recognition among the four AR subtypes. This result suggests that inside the orthosteric binding area in a height where L250$^{6.51}$ is positioned a substituent can be added to A17 to increase binding affinity. Since many of the studied amino acids overlap and the agonists and antagonists share the same orthosteric site, it might be perhaps useful in future to study a bit more closely, which interactions are key for the agonist effect compared to the antagonist one.

7.1.8 Exploring species, receptor and pathway selectivity of the compounds

In silico docking, MD simulations and *in vitro* mutagenesis can also give us insight into selectivity. Compound can be selective between related receptors, pathways at one receptor or even between same receptor in different species. Good example of the interspecies differences is compound 27. As a potential drug candidate, it is important to assess affinity at both human and rat A_1R, with rats being a common model used in the research of various pathological conditions and this was carried out for all A_1R agonists in chapter 5. Of these compounds, 27 showed a significant difference between affinity at human and rat A_1R (pIC_{50} of 7.55 ± 0.11 at hA_1R compared to pIC_{50} of 6.94 ± 0.08 at rA_1R) compared to other compounds that had similar affinities across both receptors. MD simulations then showed

that 27 formed key hydrogen bonds with N254$^{6.55}$, hydrophobic contacts with F171^{ECL2}, and oriented the 3-bromophenyl moiety in a hydrophobic sub pocket formed by I69$^{2.64}$, N70$^{2.65}$, Y271$^{7.36}$, and T270$^{7.35}$ at the hA_1R. All of these amino acids are the same for rat and human A_1R except T270$^{7.35}$ (polar uncharged) which is instead an I270$^{7.35}$ (hydrophobic) in rat. Therefore, the interaction of 27 with T270$^{7.35}$ might be important for its binding or the slightly larger isoleucine in the rat receptor could be sterically hindering the compound from binding.

A good example for receptor selectivity are the GIPR allosteric modulators. It was mentioned previously that Site 10 at the top of TMD2/3 and ECL1 has a higher potential for developing selective compounds compared to Site 6 or the GIPR orthosteric site. A synergic use of *in silico* blind and focused docking together with *in vitro* mutagenesis has indicated GIPR amino acids L193$^{2.70}$A, R196A, P197, Q211$^{3.24}$ and Q220$^{3.33}$ as important for C25 binding and/or efficacy. When looking at these particular amino acids more closely and comparing them against GLP-1R and GCGR, it can be noted that only L193$^{2.70}$ is conserved across these three receptors, while the others are not and some of them do not even share the same charges or polarity with their counterparts, indicating why C25 might be a NAM selective for GIPR over GLP-1R and GCGR. On the other hand, C58, which is a NAM for both GIPR and GCGR, loses efficacy only at the L193$^{2.70}$A mutant, which is the conserved amino acid. It is unlikely that C58 acts through a single amino acid, so it would be interesting to explore its binding a bit more through either the mentioned techniques or MD simulations and see whether the other amino acids it engages are also more conserved.

T2 and T5 are the other GIPR selective NAMs and the experiments indicate that amino acids P197, Q204, N210, Q211$^{3.24}$ and E288$^{45.52}$ are important for T5 binding and/or efficacy. T5 is NAM selective for $(Ca^{2+})_i$ mobilization pathway same as C25 and the amino acids P197 and Q211$^{3.24}$ are shared between the two compounds despite them having different chemical scaffolds. The remaining amino acids Q204, N210 and E288$^{45.52}$ are then different to C25 but again not conserved across the three receptors. The combinational approach of *in silico* docking and *in vitro* mutant experiments has enabled us to identify multiple amino acids key for NAM activity while retaining GIPR selectivity and this knowledge could be exploited when designing new more potent GIPR allosteric modulators. This could be done for example by preferentially selecting compounds indicated to bind these amino acids or by chemically modifying other compounds to interact with these amino acids.

The selectivity of the A_1R agonists was then explored in a different manner using MD simulations (Preti et al., 2022). The MD simulations showed that the lead compound 27 stably bound to A_1R and A_{2A}R but not A_3R. In terms of flexibility, N^6 substituents explored divergent conformations in the different systems: the 3-bromophenyl group of 27 was highly flexible in A_3R or A_{2A}R and more stable in A_1R, which might at least partly account for the A_1R selectivity of the compound.

Apart from being receptor selective, ligands can also be pathway selective or in other words biased, meaning the preferentially effect one pathway over another (Kenakin, 2019; Wootten et al., 2018). BnOCPA is a G_{ob} selective A_1R agonist (Wall et al., 2022). MD simulations predicted that residues R291$^{7.56}$ and I292$^{8.47}$, which are located under the N7.49PXXY$^{7.53}$ motif are likely involved in A_1R/Gα coupling and show a different propensity to interact with G_{oa} or G_{ob} protein (Deganutti et al., 2021). To test this biased signalling, alanine mutants of the A_1R R291$^{7.56}$, I292$^{8.47}$, Q293$^{8.48}$ and K294$^{8.49}$ were made and tested with BnOCPA as well as other non-biased agonists. There were some general findings like the fact that mutant K294$^{8.49}$A overall caused the smallest loss of efficacy, while R291$^{7.56}$A and I292$^{8.47}$A, the two amino acids predicted directly by MD simulations, seemed to overall cause biggest loss of efficacy of the agonists. More importantly the bias plot constructed (Figure 5.3.C) showed that there were differences between the ligands. It showed that residues R291$^{7.56}$, I292$^{8.47}$ and Q293$^{8.48}$ are especially important for CPA and NECA coupling, R291$^{7.56}$ for adenosine efficacy, and Q293$^{8.48}$ for BnOCPA, while HOCPA was not appreciably affected by any of these mutations. Overall, these experiments reinforce the MD simulations predictions that helix 8 residues are involved in the coupling of agonist-activated A_1R and show that subtle differences between the residue involvements may then contribute to the Gα bias observed among these agonists.

The allosteric modulators also show pathway biased. The original compounds based on C3 and C25 together with T2, T5, T13 and T26 are all biased towards the $(Ca^{2+})_i$ mobilization pathway. On the other hand, compound T18 despite binding to the same GIPR allosteric site is biased towards cAMP accumulation pathway and then some others like T10 and T11 are NAMs for both pathways. It is therefore not the whole site but probably specific amino acids responsible for propagating compound effects across the receptors and selectively affecting only certain signalling pathways as discussed in chapter 3. This is further supported by Wootten et al. (2016) work, where they show that the amino acids present in the ECLs of GLP-1R, a closely related receptor to GIPR, are important for triggering biased signalling. *In silico* docking and *in vitro* mutant experiments can again help us gain more insight into which amino acids might be engaged for different pathways, but the trends are not clear, which might be helped by testing more of the compounds with the mutants or increasing the number of mutants. T11 is the only compound for which the mutants were tested both in $(Ca^{2+})_i$ mobilization and cAMP accumulation pathway and different amino acids were found to be important for compound efficacy/binding. To be able to better understand this signalling bias of GIPR allosteric modulators it might also be useful to generate docking poses with T compounds and compare them both with the *in vitro* results and among themselves.

7.2 Future directions

This thesis focused on the early drug development of GIPR allosteric modulators and AR ligands with the main aim of developing more potent and selective compounds. This was largely successful for the A_1R agonists, where both very potent and very selective compounds were developed. On the other hand, the GIPR allosteric modulators would benefit from further increase in efficacy. This could possibly be achieved be doing another in silico screen against the identified allosteric site at top of TMD2/3 and ECL1, partnering with industry to do a high-throughput competition binding assay screen using fluorophore-tagged allosteric modulator or doing SAR studies of the existing compounds to improve them further.

The signalling and behaviour of GIPR and AR ligands was explored in-depth within this study with major focus being on the $(Ca^{2+})_i$ mobilization and cAMP accumulation assay. Since only the effects of GIPR NAMs selective $(Ca^{2+})_i$ mobilization on β-arrestin recruitment and insulin secretion were researched, it would be worthwhile to do the same for NAMs selective for cAMP accumulation assay and see how interconnected the signalling pathways of GIPR are. Both calcium and cAMP are downstream messengers, so it would be beneficial to explore the biased signalling of both AR and GIPR ligands at G protein level using for example the TRUPATH system (Olsen et al., 2020). As it was established than not only efficacy, but also affinity and other non-equilibrium kinetic parameters can help predict compounds' success in drug discovery, the GIPR allosteric modulators should be measured in a binding assay as well using a fluorophore-tagged allosteric modulator.

While these compounds can indisputably be useful in future for example to further probe AR and GIPR physiology in tissues, the ultimate goal is to develop these into potential treatment. Following the pharmacological characterisation carried out in this thesis, the compounds should therefore be tested in more physiological systems. Due to GIPR NAMs predicted use in obesity, these compounds could be tested in glucagon secretion assay or evaluated for their effects on GIPR signalling in adipocytes and on fatty acid uptake. Eventually the most promising of the compounds could be tested in obese mice models. A_1R agonists following on the BnOCPA work of Wall et al. (2022) could then be evaluated for their pain sedative effects in mice similarly to how BnOCPA was.

Chapter 8. Bibliography

Abagyan, R., Totrov, M., Kuznetsov, D., 1994. ICM—A new method for protein modeling and design: Applications to docking and structure prediction from the distorted native conformation. J. Comput. Chem. 15, 488–506. https://doi.org/10.1002/jcc.540150503

Abe, H., Tateyama, M., Kubo, Y., 2003. Functional identification of Gd3+ binding site of metabotropic glutamate receptor 1alpha. FEBS Lett. 545, 233–238. https://doi.org/10.1016/s0014-5793(03)00569-6

Adriaenssens, A.E., Biggs, E.K., Darwish, T., Tadross, J., Sukthankar, T., Girish, M., Polex-Wolf, J., Lam, B.Y., Zvetkova, I., Pan, W., Chiarugi, D., Yeo, G.S.H., Blouet, C., Gribble, F.M., Reimann, F., 2019. Glucose-Dependent Insulinotropic Polypeptide Receptor-Expressing Cells in the Hypothalamus Regulate Food Intake. Cell Metab. 30, 987-996.e6. https://doi.org/10.1016/j.cmet.2019.07.013

Al Jaroudi, W., Iskandrian, A.E., 2009. Regadenoson: a new myocardial stress agent. J. Am. Coll. Cardiol. 54, 1123–1130. https://doi.org/10.1016/j.jacc.2009.04.089

Allain, A., Beauchêne, I.C. de, Langenfeld, F., Guarracino, Y., Laine, E., Tchertanov, L., 2014. Allosteric pathway identification through network analysis: from molecular dynamics simulations to interactive 2D and 3D graphs. Faraday Discuss. 169, 303–321. https://doi.org/10.1039/C4FD00024B

Altschul, S.F., Madden, T.L., Schäffer, A.A., Zhang, J., Zhang, Z., Miller, W., Lipman, D.J., 1997. Gapped BLAST and PSI-BLAST: a new generation of protein database search programs. Nucleic Acids Res. 25, 3389–3402. https://doi.org/10.1093/nar/25.17.3389

Amelia, T., van Veldhoven, J.P.D., Falsini, M., Liu, R., Heitman, L.H., van Westen, G.J.P., Segala, E., Verdon, G., Cheng, R.K.Y., Cooke, R.M., van der Es, D., IJzerman, A.P., 2021. Crystal Structure and Subsequent Ligand Design of a Nonriboside Partial Agonist Bound to the Adenosine A2A Receptor. J. Med. Chem. 64, 3827–3842. https://doi.org/10.1021/acs.jmedchem.0c01856

Araç, D., Boucard, A.A., Bolliger, M.F., Nguyen, J., Soltis, S.M., Südhof, T.C., Brunger, A.T., 2012. A novel evolutionarily conserved domain of cell-adhesion GPCRs mediates autoproteolysis. EMBO J. 31, 1364–1378. https://doi.org/10.1038/emboj.2012.26

Argyros, O., Lougiakis, N., Kouvari, E., Papafotika, A., Raptopoulou, C.P., Psycharis, V., Christoforidis, S., Pouli, N., Marakos, P., Tamvakopoulos, C., 2017. Design and synthesis of novel 7-aminosubstituted pyrido[2,3-b]pyrazines exhibiting anti-breast cancer activity. Eur. J. Med. Chem. 126, 954–968. https://doi.org/10.1016/j.ejmech.2016.12.025

Armon, A., Graur, D., Ben-Tal, N., 2001. ConSurf: an algorithmic tool for the identification of functional regions in proteins by surface mapping of phylogenetic information. J. Mol. Biol. 307, 447–463. https://doi.org/10.1006/jmbi.2000.4474

Asmar, M., Asmar, A., Simonsen, L., Dela, F., Holst, J.J., Bülow, J., 2019. GIP-induced vasodilation in human adipose tissue involves capillary recruitment. Endocr. Connect. 8, 806–813. https://doi.org/10.1530/EC-19-0144

Asmar, M., Asmar, A., Simonsen, L., Gasbjerg, L.S., Sparre-Ulrich, A.H., Rosenkilde, M.M., Hartmann, B., Dela, F., Holst, J.J., Bülow, J., 2017. The Gluco- and Liporegulatory and Vasodilatory Effects of Glucose-Dependent Insulinotropic Polypeptide (GIP) Are Abolished by an Antagonist of the Human GIP Receptor. Diabetes 66, 2363–2371. https://doi.org/10.2337/db17-0480

Asmar, M., Simonsen, L., Asmar, A., Holst, J.J., Dela, F., Bülow, J., 2016. Insulin Plays a Permissive Role for the Vasoactive Effect of GIP Regulating Adipose Tissue Metabolism in Humans. J. Clin. Endocrinol. Metab. 101, 3155–3162. https://doi.org/10.1210/jc.2016-1933

Avila, M.Y., Stone, R.A., Civan, M.M., 2002. Knockout of A3 Adenosine Receptors Reduces Mouse Intraocular Pressure. Invest. Ophthalmol. Vis. Sci. 43, 3021–3026.

Avni, I., Garzozi, H.J., Barequet, I.S., Segev, F., Varssano, D., Sartani, G., Chetrit, N., Bakshi, E., Zadok, D., Tomkins, O., Litvin, G., Jacobson, K.A., Fishman, S., Harpaz, Z., Farbstein, M., Yehuda, S.B., Silverman, M.H., Kerns, W.D., Bristol, D.R., Cohn, I., Fishman, P., 2010. Treatment of Dry Eye Syndrome with Orally Administered CF101: Data from a Phase 2 Clinical Trial. Ophthalmology 117, 1287–1293. https://doi.org/10.1016/j.ophtha.2009.11.029

Baameur, F., Morgan, D.H., Yao, H., Tran, T.M., Hammitt, R.A., Sabui, S., McMurray, J.S., Lichtarge, O., Clark, R.B., 2010. Role for the Regulator of G-Protein Signaling Homology Domain of G Protein-Coupled Receptor Kinases 5 and 6 in β2-Adrenergic Receptor and Rhodopsin Phosphorylation. Mol. Pharmacol. 77, 405–415. https://doi.org/10.1124/mol.109.058115

Bacilieri, M., Moro, S., 2006. Ligand-based drug design methodologies in drug discovery process: an overview. Curr. Drug Discov. Technol. 3, 155–165. https://doi.org/10.2174/157016306780136781

Baek, M., DiMaio, F., Anishchenko, I., Dauparas, J., Ovchinnikov, S., Lee, G.R., Wang, J., Cong, Q., Kinch, L.N., Schaeffer, R.D., Millán, C., Park, H., Adams, C., Glassman, C.R., DeGiovanni, A., Pereira, J.H., Rodrigues, A.V., van Dijk, A.A., Ebrecht, A.C., Opperman, D.J., Sagmeister, T., Buhlheller, C., Pavkov-Keller, T., Rathinaswamy, M.K., Dalwadi, U., Yip, C.K., Burke, J.E., Garcia, K.C., Grishin, N.V., Adams, P.D., Read, R.J., Baker, D., 2021. Accurate prediction of protein structures and interactions using a three-track neural network. Science 373, 871–876. https://doi.org/10.1126/science.abj8754

Baggio, L.L., Drucker, D.J., 2007. Biology of incretins: GLP-1 and GIP. Gastroenterology 132, 2131–2157. https://doi.org/10.1053/j.gastro.2007.03.054

Bahar, I., Lezon, T.R., Bakan, A., Shrivastava, I.H., 2010. Normal Mode Analysis of Biomolecular Structures: Functional Mechanisms of Membrane Proteins. Chem. Rev. 110, 1463–1497. https://doi.org/10.1021/cr900095e

Bailey, T.S., 2007. Diabetes Data Management in the Clinic. J. Diabetes Sci. Technol. 1, 888–891. https://doi.org/10.1177/193229680700100614

Ballesteros, J.A., Weinstein, H., 2007. Integrated methods for the construction of three-dimensional models and computational probing of structure-function relations in G protein-coupled receptors. Methods in Neurosciences. Volume 25, 1995, Pages 366-428. https://doi.org/10.1016/S1043-9471(05)80049-7

Baltos, J.-A., Gregory, K.J., White, P.J., Sexton, P.M., Christopoulos, A., May, L.T., 2016. Quantification of adenosine A(1) receptor biased agonism: Implications for drug discovery. Biochem. Pharmacol. 99, 101–112. https://doi.org/10.1016/j.bcp.2015.11.013

Barkan, K., Lagarias, P., Stampelou, M., Stamatis, D., Hoare, S., Safitri, D., Klotz, K.-N., Vrontaki, E., Kolocouris, A., Ladds, G., 2020. Pharmacological characterisation of novel adenosine A3 receptor antagonists. Sci. Rep. 10, 20781. https://doi.org/10.1038/s41598-020-74521-y

Basith, S., Cui, M., Macalino, S.J.Y., Park, J., Clavio, N.A.B., Kang, S., Choi, S., 2018. Exploring G Protein-Coupled Receptors (GPCRs) Ligand Space via Cheminformatics Approaches: Impact on Rational Drug Design. Front. Pharmacol. 9, 128. https://doi.org/10.3389/fphar.2018.00128

Bastin, M., Andreelli, F., 2019. Dual GIP–GLP1-Receptor Agonists In The Treatment Of Type 2 Diabetes: A Short Review On Emerging Data And Therapeutic Potential [WWW Document]. Diabetes Metab. Syndr. Obes. Targets Ther. https://doi.org/10.2147/DMSO.S191438

Beaudry, J.L., Kaur, K.D., Varin, E.M., Baggio, L.L., Cao, X., Mulvihill, E.E., Bates, H.E., Campbell, J.E., Drucker, D.J., 2019. Physiological roles of the GIP receptor in murine brown adipose tissue. Mol. Metab. 28, 14–25. https://doi.org/10.1016/j.molmet.2019.08.006

Benovic, J.L., DeBlasi, A., Stone, W.C., Caron, M.G., Lefkowitz, R.J., 1989. Beta-adrenergic receptor kinase: primary structure delineates a multigene family. Science 246, 235–240. https://doi.org/10.1126/science.2552582

Bjarnadóttir, T.K., Fredriksson, R., Schiöth, H.B., 2007. The adhesion GPCRs: a unique family of G protein-coupled receptors with important roles in both central and peripheral tissues. Cell. Mol. Life Sci. CMLS 64, 2104–2119. https://doi.org/10.1007/s00018-007-7067-1

Bjarnadóttir, T.K., Gloriam, D.E., Hellstrand, S.H., Kristiansson, H., Fredriksson, R., Schiöth, H.B., 2006. Comprehensive repertoire and phylogenetic analysis of the G protein-coupled receptors in human and mouse. Genomics 88, 263–273. https://doi.org/10.1016/j.ygeno.2006.04.001

Black, J.W., Leff, P., 1983. Operational Models of Pharmacological Agonism. Proc. R. Soc. Lond. B Biol. Sci. 220, 141–162.

Bohn, L.M., Gainetdinov, R.R., Lin, F.T., Lefkowitz, R.J., Caron, M.G., 2000. Mu-opioid receptor desensitization by beta-arrestin-2 determines morphine tolerance but not dependence. Nature 408, 720–723. https://doi.org/10.1038/35047086

Boison, D., 2008. The adenosine kinase hypothesis of epileptogenesis. Prog. Neurobiol. 84, 249–262. https://doi.org/10.1016/j.pneurobio.2007.12.002

Bolcato, G., Bissaro, M., Deganutti, G., Sturlese, M., Moro, S., 2020. New Insights into Key Determinants for Adenosine 1 Receptor Antagonists Selectivity Using Supervised Molecular Dynamics Simulations. Biomolecules 10, 732. https://doi.org/10.3390/biom10050732

Bollag, R.J., Zhong, Q., Phillips, P., Min, L., Zhong, L., Cameron, R., Mulloy, A.L., Rasmussen, H., Qin, F., Ding, K.H., Isales, C.M., 2000. Osteoblast-derived cells express functional glucose-dependent insulinotropic peptide receptors. Endocrinology 141, 1228–1235. https://doi.org/10.1210/endo.141.3.7366

Bommer, C., Sagalova, V., Heesemann, E., Manne-Goehler, J., Atun, R., Bärnighausen, T., Davies, J., Vollmer, S., 2018. Global Economic Burden of Diabetes in Adults: Projections From 2015 to 2030. Diabetes Care 41, 963–970. https://doi.org/10.2337/dc17-1962

Booden, M.A., Siderovski, D.P., Der, C.J., 2002. Leukemia-Associated Rho Guanine Nucleotide Exchange Factor Promotes Gαq-Coupled Activation of RhoA. Mol. Cell. Biol. 22, 4053–4061. https://doi.org/10.1128/MCB.22.12.4053-4061.2002

Borea, P.A., Varani, K., Vincenzi, F., Baraldi, P.G., Tabrizi, M.A., Merighi, S., Gessi, S., 2015. The A3 adenosine receptor: history and perspectives. Pharmacol. Rev. 67, 74–102. https://doi.org/10.1124/pr.113.008540

Borghi, V., Przewlocka, B., Labuz, D., Maj, M., Ilona, O., Pavone, F., 2002. Formalin-induced pain and mu-opioid receptor density in brain and spinal cord are modulated by A1 and A2a adenosine agonists in mice. Brain Res. 956, 339–348. https://doi.org/10.1016/s0006-8993(02)03568-0

Bortolato, A., Doré, A.S., Hollenstein, K., Tehan, B.G., Mason, J.S., Marshall, F.H., 2014. Structure of Class B GPCRs: new horizons for drug discovery. Br. J. Pharmacol. 171, 3132–3145. https://doi.org/10.1111/bph.12689

Bos, J.L., Rehmann, H., Wittinghofer, A., 2007. GEFs and GAPs: critical elements in the control of small G proteins. Cell 129, 865–877. https://doi.org/10.1016/j.cell.2007.05.018

Bouzo-Lorenzo, M., Stoddart, L.A., Xia, L., IJzerman, A.P., Heitman, L.H., Briddon, S.J., Hill, S.J., 2019. A live cell NanoBRET binding assay allows the study of ligand-binding kinetics to the adenosine A3 receptor. Purinergic Signal. 15, 139–153. https://doi.org/10.1007/s11302-019-09650-9

Briscoe, V.J., Griffith, M.L., Davis, S.N., 2010. The role of glimepiride in the treatment of type 2 diabetes mellitus. Expert Opin. Drug Metab. Toxicol. 6, 225–235. https://doi.org/10.1517/17425250903512955

Bueno, A.B., Showalter, A.D., Wainscott, D.B., Stutsman, C., Marín, A., Ficorilli, J., Cabrera, O., Willard, F.S., Sloop, K.W., 2016. Positive Allosteric Modulation of the Glucagon-like Peptide-1 Receptor by Diverse Electrophiles. J. Biol. Chem. 291, 10700–10715. https://doi.org/10.1074/jbc.M115.696039

Buhr, C., Gössl, M., Erbel, R., Eggebrecht, H., 2008. Regadenoson in the detection of coronary artery disease. Vasc. Health Risk Manag. 4, 337–340. https://doi.org/10.2147/vhrm.s1798

Burns, M.E., Arshavsky, V.Y., 2005. Beyond counting photons: trials and trends in vertebrate visual transduction. Neuron 48, 387–401. https://doi.org/10.1016/j.neuron.2005.10.014

Cabrera-Vera, T.M., Vanhauwe, J., Thomas, T.O., Medkova, M., Preininger, A., Mazzoni, M.R., Hamm, H.E., 2003. Insights into G protein structure, function, and regulation. Endocr. Rev. 24, 765–781. https://doi.org/10.1210/er.2000-0026

Campbell, A.P., Smrcka, A.V., 2018. Targeting G protein-coupled receptor signalling by blocking G proteins. Nat. Rev. Drug Discov. 17, 789–803. https://doi.org/10.1038/nrd.2018.135

Campbell, J.E., Drucker, D.J., 2015. Islet α cells and glucagon--critical regulators of energy homeostasis. Nat. Rev. Endocrinol. 11, 329–338. https://doi.org/10.1038/nrendo.2015.51

Carpenter, B., Nehmé, R., Warne, T., Leslie, A.G.W., Tate, C.G., 2016. Structure of the adenosine A2A receptor bound to an engineered G protein. Nature 536, 104–107. https://doi.org/10.1038/nature18966

Chatzigoulas, A., Cournia, Z., 2021. Rational design of allosteric modulators: Challenges and successes. WIREs Comput. Mol. Sci. 11, e1529. https://doi.org/10.1002/wcms.1529

Chen, J.-F., Eltzschig, H.K., Fredholm, B.B., 2013. Adenosine receptors as drug targets — what are the challenges? Nat. Rev. Drug Discov. 12, 265–286. https://doi.org/10.1038/nrd3955

Cheng, R.K.Y., Segala, E., Robertson, N., Deflorian, F., Doré, A.S., Errey, J.C., Fiez-Vandal, C., Marshall, F.H., Cooke, R.M., 2017. Structures of Human A1 and A2A Adenosine Receptors with Xanthines Reveal Determinants of Selectivity. Structure 25, 1275-1285.e4. https://doi.org/10.1016/j.str.2017.06.012

Cheng, X., Jiang, H., 2019. Allostery in Drug Development. Adv. Exp. Med. Biol. 1163, 1–23. https://doi.org/10.1007/978-981-13-8719-7_1

Cho, Y.M., Merchant, C.E., Kieffer, T.J., 2012. Targeting the glucagon receptor family for diabetes and obesity therapy. Pharmacol. Ther. 135, 247–278. https://doi.org/10.1016/j.pharmthera.2012.05.009

Chodera, J.D., Noé, F., 2014. Markov state models of biomolecular conformational dynamics. Curr. Opin. Struct. Biol. 25, 135–144. https://doi.org/10.1016/j.sbi.2014.04.002

Christopher, J.A., Doré, A.S., Tehan, B.G., 2017. Potential for the Rational Design of Allosteric Modulators of Class C GPCRs. Curr. Top. Med. Chem. 17, 71–78. https://doi.org/10.2174/1568026616666160719165922

Christopoulos, A., 2014. Advances in G protein-coupled receptor allostery: from function to structure. Mol. Pharmacol. 86, 463–478. https://doi.org/10.1124/mol.114.094342

Christopoulos, A., Changeux, J.-P., Catterall, W.A., Fabbro, D., Burris, T.P., Cidlowski, J.A., Olsen, R.W., Peters, J.A., Neubig, R.R., Pin, J.-P., Sexton, P.M., Kenakin, T.P., Ehlert, F.J., Spedding, M., Langmead, C.J., 2014. International Union of Basic and Clinical Pharmacology. XC. multisite pharmacology: recommendations for the nomenclature of receptor allosterism and allosteric ligands. Pharmacol. Rev. 66, 918–947. https://doi.org/10.1124/pr.114.008862

Chun, L., Zhang, W., Liu, J., 2012. Structure and ligand recognition of class C GPCRs. Acta Pharmacol. Sin. 33, 312–323. https://doi.org/10.1038/aps.2011.186

Ciancetta, A., Jacobson, K.A., 2017. Structural Probing and Molecular Modeling of the A_3 Adenosine Receptor: A Focus on Agonist Binding. Mol. Basel Switz. 22, E449. https://doi.org/10.3390/molecules22030449

Clapham, D.E., Neer, E.J., 1997. G protein beta gamma subunits. Annu. Rev. Pharmacol. Toxicol. 37, 167–203. https://doi.org/10.1146/annurev.pharmtox.37.1.167

Cohen, S., Fishman, P., 2019. Targeting the A3 adenosine receptor to treat cytokine release syndrome in cancer immunotherapy. Drug Des. Devel. Ther. 13, 491–497. https://doi.org/10.2147/DDDT.S195294

Congreve, M., Marshall, F., 2010. The impact of GPCR structures on pharmacology and structure-based drug design. Br. J. Pharmacol. 159, 986–996. https://doi.org/10.1111/j.1476-5381.2009.00476.x

Conn, P.J., Christopoulos, A., Lindsley, C.W., 2009. Allosteric modulators of GPCRs: a novel approach for the treatment of CNS disorders. Nat. Rev. Drug Discov. 8, 41–54. https://doi.org/10.1038/nrd2760

Corbit, K.C., Trakul, N., Eves, E.M., Diaz, B., Marshall, M., Rosner, M.R., 2003. Activation of Raf-1 signaling by protein kinase C through a mechanism involving Raf kinase inhibitory protein. J. Biol. Chem. 278, 13061–13068. https://doi.org/10.1074/jbc.M210015200

Corvol, J.C., Studler, J.M., Schonn, J.S., Girault, J.A., Hervé, D., 2001. Galpha(olf) is necessary for coupling D1 and A2a receptors to adenylyl cyclase in the striatum. J. Neurochem. 76, 1585–1588. https://doi.org/10.1046/j.1471-4159.2001.00201.x

Costa, T., Herz, A., 1989. Antagonists with negative intrinsic activity at delta opioid receptors coupled to GTP-binding proteins. Proc. Natl. Acad. Sci. U. S. A. 86, 7321–7325.

Cotter, G., Dittrich, H.C., Weatherley, B.D., Bloomfield, D.M., O'Connor, C.M., Metra, M., Massie, B.M., Protect Steering Committee, Investigators, and Coordinators, 2008. The PROTECT pilot study: a randomized, placebo-controlled, dose-finding study of the adenosine A1 receptor antagonist rolofylline in patients with acute heart failure and renal impairment. J. Card. Fail. 14, 631–640. https://doi.org/10.1016/j.cardfail.2008.08.010

Dal Maso, E., Glukhova, A., Zhu, Y., Garcia-Nafria, J., Tate, C.G., Atanasio, S., Reynolds, C.A., Ramírez-Aportela, E., Carazo, J.-M., Hick, C.A., Furness, S.G.B., Hay, D.L., Liang, Y.-L., Miller, L.J., Christopoulos, A., Wang, M.-W., Wootten, D., Sexton, P.M., 2019. The Molecular Control of Calcitonin Receptor Signaling. ACS Pharmacol. Transl. Sci. 2, 31–51. https://doi.org/10.1021/acsptsci.8b00056

Daly, J.W., Padgett, W.L., 1992. Agonist activity of 2- and 5'-substituted adenosine analogs and their N6-cycloalkyl derivatives at A1- and A2-adenosine receptors coupled to adenylate cyclase. Biochem. Pharmacol. 43, 1089–1093. https://doi.org/10.1016/0006-2952(92)90616-q

de Ligt, R.A.F., Kourounakis, A.P., IJzerman, A.P., 2000. Inverse agonism at G protein-coupled receptors: (patho)physiological relevance and implications for drug discovery. Br. J. Pharmacol. 130, 1–12. https://doi.org/10.1038/sj.bjp.0703311

de Rooij, J., Rehmann, H., van Triest, M., Cool, R.H., Wittinghofer, A., Bos, J.L., 2000. Mechanism of regulation of the Epac family of cAMP-dependent RapGEFs. J. Biol. Chem. 275, 20829–20836. https://doi.org/10.1074/jbc.M001113200

de Rooij, J., Zwartkruis, F.J.T., Verheijen, M.H.G., Cool, R.H., Nijman, S.M.B., Wittinghofer, A., Bos, J.L., 1998. Epac is a Rap1 guanine-nucleotide-exchange factor directly activated by cyclic AMP. Nature 396, 474–477. https://doi.org/10.1038/24884

Deganutti, G., Barkan, K., Preti, B., Leuenberger, M., Wall, M., Frenguelli, B., Lochner, M., Ladds, G., Reynolds, C.A., 2020. Deciphering the Agonist Binding Mechanism to the Adenosine A1 Receptor. bioRxiv 2020.10.22.350827. https://doi.org/10.1101/2020.10.22.350827

Deganutti, G., Barkan, K., Preti, B., Leuenberger, M., Wall, M., Frenguelli, B.G., Lochner, M., Ladds, G., Reynolds, C.A., 2021a. Deciphering the Agonist Binding Mechanism to the Adenosine A1 Receptor. https://doi.org/10.17863/CAM.63902

Deganutti, G., Barkan, K., Preti, B., Leuenberger, M., Wall, M., Frenguelli, B.G., Lochner, M., Ladds, G., Reynolds, C.A., 2021b. Deciphering the Agonist Binding Mechanism to the Adenosine A1 Receptor. ACS Pharmacol. Transl. Sci. 4, 314–326. https://doi.org/10.1021/acsptsci.0c00195

Del Castillo, J., Katz, B., 1957. Interaction at end-plate receptors between different choline derivatives. Proc. R. Soc. Lond. B Biol. Sci. 146, 369–381. https://doi.org/10.1098/rspb.1957.0018

Delmas, P., Abogadie, F.C., Buckley, N.J., Brown, D.A., 2000. Calcium channel gating and modulation by transmitters depend on cellular compartmentalization. Nat. Neurosci. 3, 670–678. https://doi.org/10.1038/76621

DeWire, S.M., Yamashita, D.S., Rominger, D.H., Liu, G., Cowan, C.L., Graczyk, T.M., Chen, X.-T., Pitis, P.M., Gotchev, D., Yuan, C., Koblish, M., Lark, M.W., Violin, J.D., 2013. A G protein-biased ligand at the μ-opioid receptor is potently analgesic with reduced gastrointestinal and respiratory dysfunction compared with morphine. J. Pharmacol. Exp. Ther. 344, 708–717. https://doi.org/10.1124/jpet.112.201616

Diabetes UK, 2019. Facts & Figures [WWW Document]. Diabetes UK. URL https://www.diabetes.org.uk/professionals/position-statements-reports/statistics (accessed 10.8.19).

DiGruccio, M.R., Mawla, A.M., Donaldson, C.J., Noguchi, G.M., Vaughan, J., Cowing-Zitron, C., van der Meulen, T., Huising, M.O., 2016. Comprehensive alpha, beta and delta cell transcriptomes reveal that ghrelin selectively activates delta cells and promotes somatostatin release from pancreatic islets. Mol. Metab. 5, 449–458. https://doi.org/10.1016/j.molmet.2016.04.007

Ding, W.G., Renström, E., Rorsman, P., Buschard, K., Gromada, J., 1997. Glucagon-like peptide I and glucose-dependent insulinotropic polypeptide stimulate Ca2+-induced secretion in rat alpha-cells by a protein kinase A-mediated mechanism. Diabetes 46, 792–800. https://doi.org/10.2337/diab.46.5.792

Doré, A.S., Okrasa, K., Patel, J.C., Serrano-Vega, M., Bennett, K., Cooke, R.M., Errey, J.C., Jazayeri, A., Khan, S., Tehan, B., Weir, M., Wiggin, G.R., Marshall, F.H., 2014. Structure of class C GPCR metabotropic glutamate receptor 5 transmembrane domain. Nature 511, 557–562. https://doi.org/10.1038/nature13396

Downes, G.B., Gautam, N., 1999. The G protein subunit gene families. Genomics 62, 544–552. https://doi.org/10.1006/geno.1999.5992

Draper-Joyce, C.J., Bhola, R., Wang, J., Bhattarai, A., Nguyen, A.T.N., Cowie-Kent, I., O'Sullivan, K., Chia, L.Y., Venugopal, H., Valant, C., Thal, D.M., Wootten, D., Panel, N., Carlsson, J., Christie, M.J., White, P.J., Scammells, P., May, L.T., Sexton, P.M., Danev, R., Miao, Y., Glukhova, A., Imlach, W.L., Christopoulos, A., 2021. Positive allosteric mechanisms of adenosine A1 receptor-mediated analgesia. Nature 597, 571–576. https://doi.org/10.1038/s41586-021-03897-2

Draper-Joyce, C.J., Khoshouei, M., Thal, D.M., Liang, Y.-L., Nguyen, A.T.N., Furness, S.G.B., Venugopal, H., Baltos, J.-A., Plitzko, J.M., Danev, R., Baumeister, W., May, L.T., Wootten, D., Sexton, P.M., Glukhova, A., Christopoulos, A., 2018. Structure of the adenosine-bound human adenosine A1 receptor–Gi complex. Nature 558, 559–563. https://doi.org/10.1038/s41586-018-0236-6

Dunham, T.D., Farrens, D.L., 1999. Conformational changes in rhodopsin. Movement of helix f detected by site-specific chemical labeling and fluorescence spectroscopy. J. Biol. Chem. 274, 1683–1690. https://doi.org/10.1074/jbc.274.3.1683

Dunwiddie, T.V., Masino, S.A., 2001. The role and regulation of adenosine in the central nervous system. Annu. Rev. Neurosci. 24, 31–55. https://doi.org/10.1146/annurev.neuro.24.1.31

Eckle, T., Faigle, M., Grenz, A., Laucher, S., Thompson, L.F., Eltzschig, H.K., 2008. A2B adenosine receptor dampens hypoxia-induced vascular leak. Blood 111, 2024–2035. https://doi.org/10.1182/blood-2007-10-117044

Eckle, T., Hartmann, K., Bonney, S., Reithel, S., Mittelbronn, M., Walker, L.A., Lowes, B.D., Han, J., Borchers, C.H., Buttrick, P.M., Kominsky, D.J., Colgan, S.P., Eltzschig, H.K., 2012. Adora2b-elicited Per2 stabilization promotes a HIF-dependent metabolic switch critical for myocardial adaptation to ischemia. Nat. Med. 18, 774–782. https://doi.org/10.1038/nm.2728

Edelsbrunner, H., Mucke, E.P., 1994. Three-Dimensional Alpha Shapes 30.

El, K., Campbell, J.E., 2020. The role of GIP in α-cells and glucagon secretion. Peptides 125, 170213. https://doi.org/10.1016/j.peptides.2019.170213

Eldridge, M.D., Murray, C.W., Auton, T.R., Paolini, G.V., Mee, R.P., 1997. Empirical scoring functions: I. The development of a fast empirical scoring function to estimate the binding affinity of ligands in receptor complexes. J. Comput. Aided Mol. Des. 11, 425–445. https://doi.org/10.1023/a:1007996124545

Ellisdon, A.M., Halls, M.L., 2016. Compartmentalization of GPCR signalling controls unique cellular responses. Biochem. Soc. Trans. 44, 562–567. https://doi.org/10.1042/BST20150236

Eltzschig, H.K., 2009. Adenosine: an old drug newly discovered. Anesthesiology 111, 904–915. https://doi.org/10.1097/ALN.0b013e3181b060f2

Eltzschig, H.K., Sitkovsky, M.V., Robson, S.C., 2012. Purinergic signaling during inflammation. N. Engl. J. Med. 367, 2322–2333. https://doi.org/10.1056/NEJMra1205750

Evangelou, K., Lougiakis, N., Rizou, S.V., Kotsinas, A., Kletsas, D., Muñoz-Espín, D., Kastrinakis, N.G., Pouli, N., Marakos, P., Townsend, P., Serrano, M., Bartek, J., Gorgoulis, V.G., 2017. Robust, universal biomarker assay to detect senescent cells in biological specimens. Aging Cell 16, 192–197. https://doi.org/10.1111/acel.12545

Fährrolfes, R., Bietz, S., Flachsenberg, F., Meyder, A., Nittinger, E., Otto, T., Volkamer, A., Rarey, M., 2017. ProteinsPlus: a web portal for structure analysis of macromolecules. Nucleic Acids Res. 45, W337–W343. https://doi.org/10.1093/nar/gkx333

Farrens, D.L., Altenbach, C., Yang, K., Hubbell, W.L., Khorana, H.G., 1996. Requirement of rigid-body motion of transmembrane helices for light activation of rhodopsin. Science 274, 768–770. https://doi.org/10.1126/science.274.5288.768

Ferguson, S.S., Downey, W.E., Colapietro, A.M., Barak, L.S., Ménard, L., Caron, M.G., 1996. Role of beta-arrestin in mediating agonist-promoted G protein-coupled receptor internalization. Science 271, 363–366. https://doi.org/10.1126/science.271.5247.363

Fishman, P., Bar-Yehuda, S., Liang, B.T., Jacobson, K.A., 2012. Pharmacological and therapeutic effects of A3 adenosine receptor agonists. Drug Discov. Today 17, 359–366. https://doi.org/10.1016/j.drudis.2011.10.007

Flatt, P.R., 2007. Effective surgical treatment of obesity may be mediated by ablation of the lipogenic gut hormone gastric inhibitory polypeptide (GIP): evidence and clinical opportunity for development of new obesity-diabetes drugs? Diab. Vasc. Dis. Res. 4, 151–153. https://doi.org/10.3132/dvdr.2007.034

Fletcher, J.E., Lindorfer, M.A., DeFilippo, J.M., Yasuda, H., Guilmard, M., Garrison, J.C., 1998. The G protein beta5 subunit interacts selectively with the Gq alpha subunit. J. Biol. Chem. 273, 636–644. https://doi.org/10.1074/jbc.273.1.636

Foster, D.J., Conn, P.J., 2017. Allosteric Modulation of GPCRs: New Insights and Potential Utility for Treatment of Schizophrenia and Other CNS Disorders. Neuron 94, 431–446. https://doi.org/10.1016/j.neuron.2017.03.016

Fredholm, B.B., 2007. Adenosine, an endogenous distress signal, modulates tissue damage and repair. Cell Death Differ. 14, 1315–1323. https://doi.org/10.1038/sj.cdd.4402132

Fredholm, B.B., Arslan, G., Halldner, L., Kull, B., Schulte, G., Wasserman, W., 2000. Structure and function of adenosine receptors and their genes. Naunyn. Schmiedebergs Arch. Pharmacol. 362, 364–374. https://doi.org/10.1007/s002100000313

Fredholm, B.B., IJzerman, A.P., Jacobson, K.A., Klotz, K.N., Linden, J., 2001. International Union of Pharmacology. XXV. Nomenclature and classification of adenosine receptors. Pharmacol. Rev. 53, 527–552.

Fredholm, B.B., IJzerman, A.P., Jacobson, K.A., Linden, J., Müller, C.E., 2011. International Union of Basic and Clinical Pharmacology. LXXXI. Nomenclature and Classification of Adenosine Receptors—An Update. Pharmacol. Rev. 63, 1–34. https://doi.org/10.1124/pr.110.003285

Fredriksson, R., Lagerström, M.C., Lundin, L.-G., Schiöth, H.B., 2003. The G-protein-coupled receptors in the human genome form five main families. Phylogenetic analysis, paralogon groups, and fingerprints. Mol. Pharmacol. 63, 1256–1272. https://doi.org/10.1124/mol.63.6.1256

Fredriksson, R., Schiöth, H.B., 2005. The repertoire of G-protein-coupled receptors in fully sequenced genomes. Mol. Pharmacol. 67, 1414–1425. https://doi.org/10.1124/mol.104.009001

Frias, J.P., Nauck, M.A., Van, J., Kutner, M.E., Cui, X., Benson, C., Urva, S., Gimeno, R.E., Milicevic, Z., Robins, D., Haupt, A., 2018. Efficacy and safety of LY3298176, a novel dual GIP and GLP-1 receptor agonist, in patients with type 2 diabetes: a randomised, placebo-controlled and active

comparator-controlled phase 2 trial. Lancet Lond. Engl. 392, 2180–2193. https://doi.org/10.1016/S0140-6736(18)32260-8

Friesner, R.A., Banks, J.L., Murphy, R.B., Halgren, T.A., Klicic, J.J., Mainz, D.T., Repasky, M.P., Knoll, E.H., Shelley, M., Perry, J.K., Shaw, D.E., Francis, P., Shenkin, P.S., 2004. Glide: A New Approach for Rapid, Accurate Docking and Scoring. 1. Method and Assessment of Docking Accuracy. J. Med. Chem. 47, 1739–1749. https://doi.org/10.1021/jm0306430

Frye, L., Bhat, S., Akinsanya, K., Abel, R., 2021. From computer-aided drug discovery to computer-driven drug discovery. Drug Discov. Today Technol. 39, 111–117. https://doi.org/10.1016/j.ddtec.2021.08.001

Fukuhara, S., Chikumi, H., Gutkind, J.S., 2001. RGS-containing RhoGEFs: the missing link between transforming G proteins and Rho? Oncogene 20, 1661–1668. https://doi.org/10.1038/sj.onc.1204182

Fukuhara, S., Murga, C., Zohar, M., Igishi, T., Gutkind, J.S., 1999. A novel PDZ domain containing guanine nucleotide exchange factor links heterotrimeric G proteins to Rho. J. Biol. Chem. 274, 5868–5879. https://doi.org/10.1074/jbc.274.9.5868

Gabe, M.B.N., Sparre-Ulrich, A.H., Pedersen, M.F., Gasbjerg, L.S., Inoue, A., Bräuner-Osborne, H., Hartmann, B., Rosenkilde, M.M., 2018. Human GIP(3-30)NH2 inhibits G protein-dependent as well as G protein-independent signaling and is selective for the GIP receptor with high-affinity binding to primate but not rodent GIP receptors. Biochem. Pharmacol. 150, 97–107. https://doi.org/10.1016/j.bcp.2018.01.040

Gasbjerg, L.S., Gabe, M.B.N., Hartmann, B., Christensen, M.B., Knop, F.K., Holst, J.J., Rosenkilde, M.M., 2018. Glucose-dependent insulinotropic polypeptide (GIP) receptor antagonists as anti-diabetic agents. Peptides 100, 173–181. https://doi.org/10.1016/j.peptides.2017.11.021

GBD 2015 Obesity Collaborators, Afshin, A., Forouzanfar, M.H., Reitsma, M.B., Sur, P., Estep, K., Lee, A., Marczak, L., Mokdad, A.H., Moradi-Lakeh, M., Naghavi, M., Salama, J.S., Vos, T., Abate, K.H., Abbafati, C., Ahmed, M.B., Al-Aly, Z., Alkerwi, A., Al-Raddadi, R., Amare, A.T., Amberbir, A., Amegah, A.K., Amini, E., Amrock, S.M., Anjana, R.M., Ärnlöv, J., Asayesh, H., Banerjee, A., Barac, A., Baye, E., Bennett, D.A., Beyene, A.S., Biadgilign, S., Biryukov, S., Bjertness, E., Boneya, D.J., Campos-Nonato, I., Carrero, J.J., Cecilio, P., Cercy, K., Ciobanu, L.G., Cornaby, L., Damtew, S.A., Dandona, L., Dandona, R., Dharmaratne, S.D., Duncan, B.B., Eshrati, B., Esteghamati, A., Feigin, V.L., Fernandes, J.C., Fürst, T., Gebrehiwot, T.T., Gold, A., Gona, P.N., Goto, A., Habtewold, T.D., Hadush, K.T., Hafezi-Nejad, N., Hay, S.I., Horino, M., Islami, F., Kamal, R., Kasaeian, A., Katikireddi, S.V., Kengne, A.P., Kesavachandran, C.N., Khader, Y.S., Khang, Y.-H., Khubchandani, J., Kim, D., Kim, Y.J., Kinfu, Y., Kosen, S., Ku, T., Defo, B.K., Kumar, G.A., Larson, H.J., Leinsalu, M., Liang, X., Lim, S.S., Liu, P., Lopez, A.D., Lozano, R., Majeed, A., Malekzadeh, R., Malta, D.C.,

Mazidi, M., McAlinden, C., McGarvey, S.T., Mengistu, D.T., Mensah, G.A., Mensink, G.B.M., Mezgebe, H.B., Mirrakhimov, E.M., Mueller, U.O., Noubiap, J.J., Obermeyer, C.M., Ogbo, F.A., Owolabi, M.O., Patton, G.C., Pourmalek, F., Qorbani, M., Rafay, A., Rai, R.K., Ranabhat, C.L., Reinig, N., Safiri, S., Salomon, J.A., Sanabria, J.R., Santos, I.S., Sartorius, B., Sawhney, M., Schmidhuber, J., Schutte, A.E., Schmidt, M.I., Sepanlou, S.G., Shamsizadeh, M., Sheikhbahaei, S., Shin, M.-J., Shiri, R., Shiue, I., Roba, H.S., Silva, D.A.S., Silverberg, J.I., Singh, J.A., Stranges, S., Swaminathan, S., Tabarés-Seisdedos, R., Tadese, F., Tedla, B.A., Tegegne, B.S., Terkawi, A.S., Thakur, J.S., Tonelli, M., Topor-Madry, R., Tyrovolas, S., Ukwaja, K.N., Uthman, O.A., Vaezghasemi, M., Vasankari, T., Vlassov, V.V., Vollset, S.E., Weiderpass, E., Werdecker, A., Wesana, J., Westerman, R., Yano, Y., Yonemoto, N., Yonga, G., Zaidi, Z., Zenebe, Z.M., Zipkin, B., Murray, C.J.L., 2017. Health Effects of Overweight and Obesity in 195 Countries over 25 Years. N. Engl. J. Med. 377, 13–27. https://doi.org/10.1056/NEJMoa1614362

Ge, Z.-D., Peart, J.N., Kreckler, L.M., Wan, T.C., Jacobson, M.A., Gross, G.J., Auchampach, J.A., 2006. Cl-IB-MECA [2-chloro-N6-(3-iodobenzyl)adenosine-5'-N-methylcarboxamide] reduces ischemia/reperfusion injury in mice by activating the A3 adenosine receptor. J. Pharmacol. Exp. Ther. 319, 1200–1210. https://doi.org/10.1124/jpet.106.111351

Gentry, P.R., Sexton, P.M., Christopoulos, A., 2015. Novel Allosteric Modulators of G Protein-coupled Receptors. J. Biol. Chem. 290, 19478–19488. https://doi.org/10.1074/jbc.R115.662759

Gerasi, M., Frakolaki, E., Papadakis, G., Chalari, A., Lougiakis, N., Marakos, P., Pouli, N., Vassilaki, N., 2020. Design, synthesis and anti-HBV activity evaluation of new substituted imidazo[4,5-b]pyridines. Bioorganic Chem. 98, 103580. https://doi.org/10.1016/j.bioorg.2020.103580

Germack, R., Dickenson, J.M., 2006. Induction of beta3-adrenergic receptor functional expression following chronic stimulation with noradrenaline in neonatal rat cardiomyocytes. J. Pharmacol. Exp. Ther. 316, 392–402. https://doi.org/10.1124/jpet.105.090597

Gessi, S., Cattabriga, E., Avitabile, A., Gafa', R., Lanza, G., Cavazzini, L., Bianchi, N., Gambari, R., Feo, C., Liboni, A., Gullini, S., Leung, E., Mac-Lennan, S., Borea, P.A., 2004. Elevated expression of A3 adenosine receptors in human colorectal cancer is reflected in peripheral blood cells. Clin. Cancer Res. Off. J. Am. Assoc. Cancer Res. 10, 5895–5901. https://doi.org/10.1158/1078-0432.CCR-1134-03

Gether, U., 2000. Uncovering molecular mechanisms involved in activation of G protein-coupled receptors. Endocr. Rev. 21, 90–113. https://doi.org/10.1210/edrv.21.1.0390

Glaser, F., Pupko, T., Paz, I., Bell, R.E., Bechor-Shental, D., Martz, E., Ben-Tal, N., 2003. ConSurf: identification of functional regions in proteins by surface-mapping of phylogenetic information. Bioinforma. Oxf. Engl. 19, 163–164. https://doi.org/10.1093/bioinformatics/19.1.163

Glover, D.M., Hames, B.D., 1985. DNA Cloning: A Practical Approach. IRL Press.

Glukhova, A., Thal, D.M., Nguyen, A.T., Vecchio, E.A., Jörg, M., Scammells, P.J., May, L.T., Sexton, P.M., Christopoulos, A., 2017. Structure of the Adenosine A1 Receptor Reveals the Basis for Subtype Selectivity. Cell 168, 867-877.e13. https://doi.org/10.1016/j.cell.2017.01.042

Goldsmith, Z.G., Dhanasekaran, D.N., 2007. G protein regulation of MAPK networks. Oncogene 26, 3122–3142. https://doi.org/10.1038/sj.onc.1210407

Gómez Tamayo, J.C., Olivella, M., Ríos, S., Hoogstraat, M., Gonzalez, A., Mayol, E., Deupi, X., Campillo, M., Cordomí, A., 2018. GPCR-SAS: A web application for statistical analyses on G protein-coupled receptors sequences. PLoS ONE 13, e0199843. https://doi.org/10.1371/journal.pone.0199843

Goncearenco, A., Mitternacht, S., Yong, T., Eisenhaber, B., Eisenhaber, F., Berezovsky, I.N., 2013. SPACER: server for predicting allosteric communication and effects of regulation. Nucleic Acids Res. 41, W266–W272. https://doi.org/10.1093/nar/gkt460

González-Fernández, E., Sánchez-Gómez, M.V., Pérez-Samartín, A., Arellano, R.O., Matute, C., 2014. A3 Adenosine receptors mediate oligodendrocyte death and ischemic damage to optic nerve. Glia 62, 199–216. https://doi.org/10.1002/glia.22599

Goodman, O.B., Krupnick, J.G., Santini, F., Gurevich, V.V., Penn, R.B., Gagnon, A.W., Keen, J.H., Benovic, J.L., 1996. Beta-arrestin acts as a clathrin adaptor in endocytosis of the beta2-adrenergic receptor. Nature 383, 447–450. https://doi.org/10.1038/383447a0

GPCRdb [WWW Document], 2022. URL https://gpcrdb.org/ (accessed 2.25.22).

Greene, D., Qi, R., Nguyen, R., Qiu, T., Luo, R., 2019. Heterogeneous Dielectric Implicit Membrane Model for the Calculation of MMPBSA Binding Free Energies. J. Chem. Inf. Model. 59, 3041–3056. https://doi.org/10.1021/acs.jcim.9b00363

Greenhalgh, J.C., Chandran, A., Harper, M.T., Ladds, G., Rahman, T., 2020. Proposed model of the Dictyostelium cAMP receptors bound to cAMP. J. Mol. Graph. Model. 100, 107662. https://doi.org/10.1016/j.jmgm.2020.107662

Grundmann, M., Kostenis, E., 2017. Temporal Bias: Time-Encoded Dynamic GPCR Signaling. Trends Pharmacol. Sci. 38, 1110–1124. https://doi.org/10.1016/j.tips.2017.09.004

Guo, D., Heitman, L.H., IJzerman, A.P., 2017. Kinetic Aspects of the Interaction between Ligand and G Protein-Coupled Receptor: The Case of the Adenosine Receptors. Chem. Rev. 117, 38–66. https://doi.org/10.1021/acs.chemrev.6b00025

Guo, D., van Dorp, E.J.H., Mulder-Krieger, T., van Veldhoven, J.P.D., Brussee, J., IJzerman, A.P., Heitman, L.H., 2013. Dual-Point Competition Association Assay: A Fast and High-Throughput Kinetic Screening Method for Assessing Ligand-Receptor Binding Kinetics. J. Biomol. Screen. 18, 309–320. https://doi.org/10.1177/1087057112464776

Guo, D., Venhorst, S.N., Massink, A., van Veldhoven, J.P.D., Vauquelin, G., IJzerman, A.P., Heitman, L.H., 2014. Molecular mechanism of allosteric modulation at GPCRs: insight from a binding kinetics

study at the human A1 adenosine receptor. Br. J. Pharmacol. 171, 5295–5312. https://doi.org/10.1111/bph.12836

Guo, Y., Bolli, R., Bao, W., Wu, W.J., Black, R.G., Murphree, S.S., Salvatore, C.A., Jacobson, M.A., Auchampach, J.A., 2001. Targeted deletion of the A3 adenosine receptor confers resistance to myocardial ischemic injury and does not prevent early preconditioning. J. Mol. Cell. Cardiol. 33, 825–830. https://doi.org/10.1006/jmcc.2001.1338

Gurden, M.F., Coates, J., Ellis, F., Evans, B., Foster, M., Hornby, E., Kennedy, I., Martin, D.P., Strong, P., Vardey, C.J., 1993. Functional characterization of three adenosine receptor types. Br. J. Pharmacol. 109, 693–698. https://doi.org/10.1111/j.1476-5381.1993.tb13629.x

Gurevich, E.V., Gurevich, V.V., 2006. Arrestins: ubiquitous regulators of cellular signaling pathways. Genome Biol. 7, 236. https://doi.org/10.1186/gb-2006-7-9-236

Gurevich, E.V., Tesmer, J.J.G., Mushegian, A., Gurevich, V.V., 2012. G protein-coupled receptor kinases: More than just kinases and not only for GPCRs. Pharmacol. Ther. 133, 40–69. https://doi.org/10.1016/j.pharmthera.2011.08.001

Gurevich, V.V., Gurevich, E.V., 2019. GPCR Signaling Regulation: The Role of GRKs and Arrestins. Front. Pharmacol. 10.

Gurevich, V.V., Gurevich, E.V., 2004. The molecular acrobatics of arrestin activation. Trends Pharmacol. Sci. 25, 105–111. https://doi.org/10.1016/j.tips.2003.12.008

Hajbabaie, R., Harper, M.T., Rahman, T., 2021. Establishing an Analogue Based In Silico Pipeline in the Pursuit of Novel Inhibitory Scaffolds against the SARS Coronavirus 2 Papain-Like Protease. Mol. Basel Switz. 26, 1134. https://doi.org/10.3390/molecules26041134

Hall, D.R., Kozakov, D., Vajda, S., 2012. Analysis of protein binding sites by computational solvent mapping. Methods Mol. Biol. Clifton NJ 819, 13–27. https://doi.org/10.1007/978-1-61779-465-0_2

Han, S., Xiao, K., Kim, J., Wu, J.-H., Wisler, J.W., Nakamura, N., Freedman, N.J., Shenoy, S.K., 2012. MARCH2 promotes endocytosis and lysosomal sorting of carvedilol-bound β(2)-adrenergic receptors. J. Cell Biol. 199, 817–830. https://doi.org/10.1083/jcb.201208192

Han, S.-O., Kommaddi, R.P., Shenoy, S.K., 2013. Distinct roles for β-arrestin2 and arrestin-domain-containing proteins in β2 adrenergic receptor trafficking. EMBO Rep. 14, 164–171. https://doi.org/10.1038/embor.2012.187

Hanson, S.M., Francis, D.J., Vishnivetskiy, S.A., Kolobova, E.A., Hubbell, W.L., Klug, C.S., Gurevich, V.V., 2006. Differential interaction of spin-labeled arrestin with inactive and active phosphorhodopsin. Proc. Natl. Acad. Sci. 103, 4900–4905. https://doi.org/10.1073/pnas.0600733103

Harris, M.I., Hadden, W.C., Knowler, W.C., Bennett, P.H., 1987. Prevalence of diabetes and impaired glucose tolerance and plasma glucose levels in U.S. population aged 20-74 yr. Diabetes 36, 523–534. https://doi.org/10.2337/diab.36.4.523

Haskó, G., Linden, J., Cronstein, B., Pacher, P., 2008. Adenosine receptors: therapeutic aspects for inflammatory and immune diseases. Nat. Rev. Drug Discov. 7, 759–770. https://doi.org/10.1038/nrd2638

Hauner, H., Glatting, G., Kaminska, D., Pfeiffer, E.F., 1988. Effects of Gastric Inhibitory Polypeptide on Glucose and Lipid Metabolism of Isolated Rat Adipocytes. Ann. Nutr. Metab. 32, 282–288. https://doi.org/10.1159/000177467

Hauser, A.S., Attwood, M.M., Rask-Andersen, M., Schiöth, H.B., Gloriam, D.E., 2017. Trends in GPCR drug discovery: new agents, targets and indications. Nat. Rev. Drug Discov. 16, 829–842. https://doi.org/10.1038/nrd.2017.178

Hay, D.L., Pioszak, A.A., 2016. RAMPs (Receptor-Activity Modifying Proteins): New Insights and Roles. Annu. Rev. Pharmacol. Toxicol. 56, 469–487. https://doi.org/10.1146/annurev-pharmtox-010715-103120

Headrick, J.P., Ashton, K.J., Rose'meyer, R.B., Peart, J.N., 2013. Cardiovascular adenosine receptors: expression, actions and interactions. Pharmacol. Ther. 140, 92–111. https://doi.org/10.1016/j.pharmthera.2013.06.002

Heilker, R., Wolff, M., Tautermann, C.S., Bieler, M., 2009. G-protein-coupled receptor-focused drug discovery using a target class platform approach. Drug Discov. Today 14, 231–240. https://doi.org/10.1016/j.drudis.2008.11.011

Hesketh, J.E., Campbell, G.P., 1987. Effects of insulin, pertussis toxin and cholera toxin on protein synthesis and diacylglycerol production in 3T3 fibroblasts: evidence for a G-protein mediated activation of phospholipase C in the insulin signal mechanism. Biosci. Rep. 7, 533–541. https://doi.org/10.1007/BF01119769

Heuss, C., Gerber, U., 2000. G-protein-independent signaling by G-protein-coupled receptors. Trends Neurosci. 23, 469–475. https://doi.org/10.1016/s0166-2236(00)01643-x

Higashijima, T., Ferguson, K.M., Sternweis, P.C., Smigel, M.D., Gilman, A.G., 1987. Effects of Mg2+ and the beta gamma-subunit complex on the interactions of guanine nucleotides with G proteins. J. Biol. Chem. 262, 762–766.

Hilger, D., Masureel, M., Kobilka, B.K., 2018. Structure and dynamics of GPCR signaling complexes. Nat. Struct. Mol. Biol. 25, 4–12. https://doi.org/10.1038/s41594-017-0011-7

Hinke, S.A., Manhart, S., Pamir, N., Demuth, H., W Gelling, R., Pederson, R.A., McIntosh, C.H., 2001. Identification of a bioactive domain in the amino-terminus of glucose-dependent insulinotropic

polypeptide (GIP). Biochim. Biophys. Acta 1547, 143–155. https://doi.org/10.1016/s0167-4838(01)00181-9

Hollenstein, K., de Graaf, C., Bortolato, A., Wang, M.-W., Marshall, F.H., Stevens, R.C., 2014. Insights into the structure of class B GPCRs. Trends Pharmacol. Sci. 35, 12–22. https://doi.org/10.1016/j.tips.2013.11.001

Holst, J.J., Rosenkilde, M.M., 2020. GIP as a Therapeutic Target in Diabetes and Obesity: Insight From Incretin Co-agonists. J. Clin. Endocrinol. Metab. 105, dgaa327. https://doi.org/10.1210/clinem/dgaa327

Hornak, V., Abel, R., Okur, A., Strockbine, B., Roitberg, A., Simmerling, C., 2006. Comparison of multiple Amber force fields and development of improved protein backbone parameters. Proteins 65, 712–725. https://doi.org/10.1002/prot.21123

Hu, G.-M., Mai, T.-L., Chen, C.-M., 2017. Visualizing the GPCR Network: Classification and Evolution. Sci. Rep. 7, 15495. https://doi.org/10.1038/s41598-017-15707-9

Huang, B., Schroeder, M., 2006. LIGSITEcsc: predicting ligand binding sites using the Connolly surface and degree of conservation. BMC Struct. Biol. 6, 19. https://doi.org/10.1186/1472-6807-6-19

Huang, L., Shanker, Y.G., Dubauskaite, J., Zheng, J.Z., Yan, W., Rosenzweig, S., Spielman, A.I., Max, M., Margolskee, R.F., 1999. Ggamma13 colocalizes with gustducin in taste receptor cells and mediates IP3 responses to bitter denatonium. Nat. Neurosci. 2, 1055–1062. https://doi.org/10.1038/15981

Hurley, J.H., 1999. Structure, mechanism, and regulation of mammalian adenylyl cyclase. J. Biol. Chem. 274, 7599–7602. https://doi.org/10.1074/jbc.274.12.7599

Irwin, Nigel, Flatt, P.R., 2009. Therapeutic potential for GIP receptor agonists and antagonists. Best Pract. Res. Clin. Endocrinol. Metab. 23, 499–512. https://doi.org/10.1016/j.beem.2009.03.001

Irwin, N., Flatt, P.R., 2009. Evidence for beneficial effects of compromised gastric inhibitory polypeptide action in obesity-related diabetes and possible therapeutic implications. Diabetologia 52, 1724–1731. https://doi.org/10.1007/s00125-009-1422-8

Irwin, N., Gault, V.A., O'Harte, F.P.M., Flatt, P.R., 2020. Blockade of gastric inhibitory polypeptide (GIP) action as a novel means of countering insulin resistance in the treatment of obesity-diabetes. Peptides 125, 170203. https://doi.org/10.1016/j.peptides.2019.170203

Irwin, N., Green, B.D., Gault, V.A., Cassidy, R.S., O'Harte, F.P.M., Harriott, P., Flatt, P.R., 2006. Effects on glucose homeostasis and insulin secretion of long term activation of the glucose-dependent insulinotropic polypeptide (GIP) receptor by N-AcGIP(LysPAL37) in normal mice. Peptides 27, 893–900. https://doi.org/10.1016/j.peptides.2005.08.003

Isberg, V., de Graaf, C., Bortolato, A., Cherezov, V., Katritch, V., Marshall, F.H., Mordalski, S., Pin, J.-P., Stevens, R.C., Vriend, G., Gloriam, D.E., 2015. Generic GPCR Residue Numbers - Aligning

Topology Maps Minding The Gaps. Trends Pharmacol. Sci. 36, 22–31. https://doi.org/10.1016/j.tips.2014.11.001

Jaakola, V.-P., Griffith, M.T., Hanson, M.A., Cherezov, V., Chien, E.Y.T., Lane, J.R., Ijzerman, A.P., Stevens, R.C., 2008. The 2.6 angstrom crystal structure of a human A2A adenosine receptor bound to an antagonist. Science 322, 1211–1217. https://doi.org/10.1126/science.1164772

Jacobson, K.A., 1998. Adenosine A3 receptors: novel ligands and paradoxical effects. Trends Pharmacol. Sci. 19, 184–191.

Jacobson, K.A., Gao, Z.-G., 2006. Adenosine receptors as therapeutic targets. Nat. Rev. Drug Discov. 5, 247–264. https://doi.org/10.1038/nrd1983

Jacobson, K.A., Tosh, D.K., Jain, S., Gao, Z.-G., 2019. Historical and Current Adenosine Receptor Agonists in Preclinical and Clinical Development. Front. Cell. Neurosci. 13, 124. https://doi.org/10.3389/fncel.2019.00124

Jakubík, J., Randáková, A., Chetverikov, N., El-Fakahany, E.E., Doležal, V., 2020. The operational model of allosteric modulation of pharmacological agonism. Sci. Rep. 10, 14421. https://doi.org/10.1038/s41598-020-71228-y

Jarpe, M.B., Knall, C., Mitchell, F.M., Buhl, A.M., Duzic, E., Johnson, G.L., 1998. [D-Arg1,D-Phe5,D-Trp7,9,Leu11]Substance P acts as a biased agonist toward neuropeptide and chemokine receptors. J. Biol. Chem. 273, 3097–3104. https://doi.org/10.1074/jbc.273.5.3097

Jean-Charles, P.-Y., Snyder, J.C., Shenoy, S.K., 2016. Chapter One - Ubiquitination and Deubiquitination of G Protein-Coupled Receptors. Prog. Mol. Biol. Transl. Sci. 141, 1–55. https://doi.org/10.1016/bs.pmbts.2016.05.001

Jespers, W., Schiedel, A.C., Heitman, L.H., Cooke, R.M., Kleene, L., van Westen, G.J.P., Gloriam, D.E., Müller, C.E., Sotelo, E., Gutiérrez-de-Terán, H., 2018. Structural Mapping of Adenosine Receptor Mutations: Ligand Binding and Signaling Mechanisms. Trends Pharmacol. Sci. 39, 75–89. https://doi.org/10.1016/j.tips.2017.11.001

Jin, S.L., Bushnik, T., Lan, L., Conti, M., 1998. Subcellular localization of rolipram-sensitive, cAMP-specific phosphodiesterases. Differential targeting and activation of the splicing variants derived from the PDE4D gene. J. Biol. Chem. 273, 19672–19678. https://doi.org/10.1074/jbc.273.31.19672

Johansen, P., Sandberg, A., Capehorn, M., 2020. A Relative Cost of Control Analysis of Once-Weekly Semaglutide Versus Exenatide Extended-Release, Dulaglutide and Liraglutide in the UK. Adv. Ther. 37. https://doi.org/10.1007/s12325-020-01242-z

Johansson, B., Halldner, L., Dunwiddie, T.V., Masino, S.A., Poelchen, W., Giménez-Llort, L., Escorihuela, R.M., Fernández-Teruel, A., Wiesenfeld-Hallin, Z., Xu, X.-J., Hårdemark, A., Betsholtz, C., Herlenius, E., Fredholm, B.B., 2001. Hyperalgesia, anxiety, and decreased hypoxic

neuroprotection in mice lacking the adenosine A1 receptor. Proc. Natl. Acad. Sci. U. S. A. 98, 9407–9412. https://doi.org/10.1073/pnas.161292398

Jones, D.T., Reed, R.R., 1989. Golf: an olfactory neuron specific-G protein involved in odorant signal transduction. Science 244, 790–795. https://doi.org/10.1126/science.2499043

Jones, I.R., Owens, D.R., Moody, A.J., Luzio, S.D., Morris, T., Hayes, T.M., 1987. The effects of glucose-dependent insulinotropic polypeptide infused at physiological concentrations in normal subjects and Type 2 (non-insulin-dependent) diabetic patients on glucose tolerance and B-cell secretion. Diabetologia 30, 707–712. https://doi.org/10.1007/BF00296993

Jumper, J., Evans, R., Pritzel, A., Green, T., Figurnov, M., Ronneberger, O., Tunyasuvunakool, K., Bates, R., Žídek, A., Potapenko, A., Bridgland, A., Meyer, C., Kohl, S.A.A., Ballard, A.J., Cowie, A., Romera-Paredes, B., Nikolov, S., Jain, R., Adler, J., Back, T., Petersen, S., Reiman, D., Clancy, E., Zielinski, M., Steinegger, M., Pacholska, M., Berghammer, T., Bodenstein, S., Silver, D., Vinyals, O., Senior, A.W., Kavukcuoglu, K., Kohli, P., Hassabis, D., 2021. Highly accurate protein structure prediction with AlphaFold. Nature 596, 583–589. https://doi.org/10.1038/s41586-021-03819-2

Kammermeier, P.J., Ruiz-Velasco, V., Ikeda, S.R., 2000. A voltage-independent calcium current inhibitory pathway activated by muscarinic agonists in rat sympathetic neurons requires both Galpha q/11 and Gbeta gamma. J. Neurosci. Off. J. Soc. Neurosci. 20, 5623–5629.

Kapetanovic, I.M., 2008. Computer-aided drug discovery and development (CADDD): in silico-chemico-biological approach. Chem. Biol. Interact. 171, 165–176. https://doi.org/10.1016/j.cbi.2006.12.006

Karageorgos, V., Venihaki, M., Sakellaris, S., Pardalos, M., Kontakis, G., Matsoukas, M.-T., Gravanis, A., Margioris, A., Liapakis, G., 2018. Current understanding of the structure and function of family B GPCRs to design novel drugs. Horm. Athens Greece 17, 45–59. https://doi.org/10.1007/s42000-018-0009-5

Karlshøj, S., Amarandi, R.M., Larsen, O., Daugvilaite, V., Steen, A., Brvar, M., Pui, A., Frimurer, T.M., Ulven, T., Rosenkilde, M.M., 2016. Molecular Mechanism of Action for Allosteric Modulators and Agonists in CC-chemokine Receptor 5 (CCR5). J. Biol. Chem. 291, 26860–26874. https://doi.org/10.1074/jbc.M116.740183

Karplus, M., McCammon, J.A., 2002. Molecular dynamics simulations of biomolecules. Nat. Struct. Biol. 9, 646–652. https://doi.org/10.1038/nsb0902-646

Kelly, E., 2013. Ligand bias at the μ-opioid receptor. Biochem. Soc. Trans. 41, 218–224. https://doi.org/10.1042/BST20120331

Kenakin, T., 2019. Biased Receptor Signaling in Drug Discovery. Pharmacol. Rev. 71, 267–315. https://doi.org/10.1124/pr.118.016790

Kenakin, T., Watson, C., Muniz-Medina, V., Christopoulos, A., Novick, S., 2011. A Simple Method for Quantifying Functional Selectivity and Agonist Bias. ACS Chem. Neurosci. 3, 193–203. https://doi.org/10.1021/cn200111m

Kenakin, T.P., 2012. Biased signalling and allosteric machines: new vistas and challenges for drug discovery. Br. J. Pharmacol. 165, 1659–1669. https://doi.org/10.1111/j.1476-5381.2011.01749.x

Killion, E.A., Wang, J., Yie, J., Shi, S.D.-H., Bates, D., Min, X., Komorowski, R., Hager, T., Deng, L., Atangan, L., Lu, S.-C., Kurzeja, R.J.M., Sivits, G., Lin, J., Chen, Q., Wang, Z., Thibault, S.A., Abbott, C.M., Meng, T., Clavette, B., Murawsky, C.M., Foltz, I.N., Rottman, J.B., Hale, C., Véniant, M.M., Lloyd, D.J., 2018. Anti-obesity effects of GIPR antagonists alone and in combination with GLP-1R agonists in preclinical models. Sci. Transl. Med. 10. https://doi.org/10.1126/scitranslmed.aat3392

Kim, S.-J., Nian, C., McIntosh, C.H.S., 2007. Activation of lipoprotein lipase by glucose-dependent insulinotropic polypeptide in adipocytes. A role for a protein kinase B, LKB1, and AMP-activated protein kinase cascade. J. Biol. Chem. 282, 8557–8567. https://doi.org/10.1074/jbc.M609088200

Kim, Y.-M., Benovic, J.L., 2002. Differential Roles of Arrestin-2 Interaction with Clathrin and Adaptor Protein 2 in G Protein-coupled Receptor Trafficking *. J. Biol. Chem. 277, 30760–30768. https://doi.org/10.1074/jbc.M204528200

Kimple, A.J., Bosch, D.E., Giguère, P.M., Siderovski, D.P., 2011. Regulators of G-protein signaling and their Gα substrates: promises and challenges in their use as drug discovery targets. Pharmacol. Rev. 63, 728–749. https://doi.org/10.1124/pr.110.003038

Klein Herenbrink, C., Sykes, D.A., Donthamsetti, P., Canals, M., Coudrat, T., Shonberg, J., Scammells, P.J., Capuano, B., Sexton, P.M., Charlton, S.J., Javitch, J.A., Christopoulos, A., Lane, J.R., 2016. The role of kinetic context in apparent biased agonism at GPCRs. Nat. Commun. 7, 10842. https://doi.org/10.1038/ncomms10842

Knerr, P.J., Mowery, S.A., Douros, J.D., Premdjee, B., Hjøllund, K.R., He, Y., Kruse Hansen, A.M., Olsen, A.K., Perez-Tilve, D., DiMarchi, R.D., Finan, B., 2022. Next generation GLP-1/GIP/glucagon triple agonists normalize body weight in obese mice. Mol. Metab. 63, 101533. https://doi.org/10.1016/j.molmet.2022.101533

Knight, A., Hemmings, J.L., Winfield, I., Leuenberger, M., Frattini, E., Frenguelli, B.G., Dowell, S.J., Lochner, M., Ladds, G., 2016. Discovery of Novel Adenosine Receptor Agonists That Exhibit Subtype Selectivity. J. Med. Chem. 59, 947–964. https://doi.org/10.1021/acs.jmedchem.5b01402

Kobilka, B.K., 2007. G Protein Coupled Receptor Structure and Activation. Biochim. Biophys. Acta 1768, 794–807. https://doi.org/10.1016/j.bbamem.2006.10.021

Koch, W.J., Inglese, J., Stone, W.C., Lefkowitz, R.J., 1993. The binding site for the beta gamma subunits of heterotrimeric G proteins on the beta-adrenergic receptor kinase. J. Biol. Chem. 268, 8256–8260. https://doi.org/10.1016/S0021-9258(18)53090-8

Koeppen, M., Eckle, T., Eltzschig, H.K., 2009. Selective deletion of the A1 adenosine receptor abolishes heart-rate slowing effects of intravascular adenosine in vivo. PloS One 4, e6784. https://doi.org/10.1371/journal.pone.0006784

Kolakowski, L.F., 1994. GCRDb: a G-protein-coupled receptor database. Receptors Channels 2, 1–7.

Kooistra, A.J., Mordalski, S., Pándy-Szekeres, G., Esguerra, M., Mamyrbekov, A., Munk, C., Keserű, G.M., Gloriam, D.E., 2021. GPCRdb in 2021: integrating GPCR sequence, structure and function. Nucleic Acids Res. 49, D335–D343. https://doi.org/10.1093/nar/gkaa1080

Koole, C., Savage, E.E., Christopoulos, A., Miller, L.J., Sexton, P.M., Wootten, D., 2013. Minireview: Signal Bias, Allosterism, and Polymorphic Variation at the GLP-1R: Implications for Drug Discovery. Mol. Endocrinol. 27, 1234–1244. https://doi.org/10.1210/me.2013-1116

Koole, C., Wootten, D., Simms, J., Valant, C., Sridhar, R., Woodman, O.L., Miller, L.J., Summers, R.J., Christopoulos, A., Sexton, P.M., 2010. Allosteric ligands of the glucagon-like peptide 1 receptor (GLP-1R) differentially modulate endogenous and exogenous peptide responses in a pathway-selective manner: implications for drug screening. Mol. Pharmacol. 78, 456–465. https://doi.org/10.1124/mol.110.065664

Kozakov, D., Grove, L.E., Hall, D.R., Bohnuud, T., Mottarella, S., Luo, L., Xia, B., Beglov, D., Vajda, S., 2015. The FTMap family of web servers for determining and characterizing ligand binding hot spots of proteins. Nat. Protoc. 10, 733–755. https://doi.org/10.1038/nprot.2015.043

Kristiansen, K., 2004. Molecular mechanisms of ligand binding, signaling, and regulation within the superfamily of G-protein-coupled receptors: molecular modeling and mutagenesis approaches to receptor structure and function. Pharmacol. Ther. 103, 21–80. https://doi.org/10.1016/j.pharmthera.2004.05.002

Kufareva, I., Ilatovskiy, A.V., Abagyan, R., 2012. Pocketome: an encyclopedia of small-molecule binding sites in 4D. Nucleic Acids Res. 40, D535–D540. https://doi.org/10.1093/nar/gkr825

Kull, B., Svenningsson, P., Fredholm, B.B., 2000. Adenosine A(2A) receptors are colocalized with and activate g(olf) in rat striatum. Mol. Pharmacol. 58, 771–777. https://doi.org/10.1124/mol.58.4.771

Kuszak, A.J., Yao, X.J., Rasmussen, S.G.F., Kobilka, B.K., Sunahara, R.K., 2010. Functional studies of isolated GPCR-G protein complexes in the membrane bilayer of lipoprotein particles, in: Milligan, G., Siehler, S. (Eds.), G Protein-Coupled Receptors: Structure, Signaling, and Physiology.

Cambridge University Press, Cambridge, pp. 32–52. https://doi.org/10.1017/CBO9780511760334.003

Lagarias, P., Barkan, K., Tzortzini, E., Stampelou, M., Vrontaki, E., Ladds, G., Kolocouris, A., 2020. Correction to Insights to the Binding of a Selective Adenosine A3 Receptor Antagonist using Molecular Dynamic Simulations, MM-PBSA and MM-GBSA Free Energy Calculations, and Mutagenesis. J. Chem. Inf. Model. 60, 2405–2406. https://doi.org/10.1021/acs.jcim.0c00240

Lagarias, P., Barkan, K., Tzortzini, E., Stampelou, M., Vrontaki, E., Ladds, G., Kolocouris, A., 2019. Insights to the Binding of a Selective Adenosine A3 Receptor Antagonist Using Molecular Dynamic Simulations, MM-PBSA and MM-GBSA Free Energy Calculations, and Mutagenesis. J. Chem. Inf. Model. 59, 5183–5197. https://doi.org/10.1021/acs.jcim.9b00751

Lagarias, P., Vrontaki, E., Lambrinidis, G., Stamatis, D., Convertino, M., Ortore, G., Mavromoustakos, T., Klotz, K.-N., Kolocouris, A., 2018. Discovery of Novel Adenosine Receptor Antagonists through a Combined Structure- and Ligand-Based Approach Followed by Molecular Dynamics Investigation of Ligand Binding Mode. J. Chem. Inf. Model. 58, 794–815. https://doi.org/10.1021/acs.jcim.7b00455

Lagerström, M.C., Schiöth, H.B., 2008. Structural diversity of G protein-coupled receptors and significance for drug discovery. Nat. Rev. Drug Discov. 7, 339–357. https://doi.org/10.1038/nrd2518

Laine, E., Blondel, A., Malliavin, T.E., 2009. Dynamics and Energetics: A Consensus Analysis of the Impact of Calcium on EF-CaM Protein Complex. Biophys. J. 96, 1249–1263. https://doi.org/10.1016/j.bpj.2008.10.055

Laine, E., Goncalves, C., Karst, J.C., Lesnard, A., Rault, S., Tang, W.-J., Malliavin, T.E., Ladant, D., Blondel, A., 2010. Use of allostery to identify inhibitors of calmodulin-induced activation of Bacillus anthracis edema factor. Proc. Natl. Acad. Sci. U. S. A. 107, 11277–11282. https://doi.org/10.1073/pnas.0914611107

Lane, J.R., Beukers, M.W., Mulder-Krieger, T., Ijzerman, A.P., 2010. The endocannabinoid 2-arachidonylglycerol is a negative allosteric modulator of the human A3 adenosine receptor. Biochem. Pharmacol. 79, 48–56. https://doi.org/10.1016/j.bcp.2009.07.024

Lane, J.R., Klein Herenbrink, C., van Westen, G.J.P., Spoorendonk, J.A., Hoffmann, C., IJzerman, A.P., 2012. A novel nonribose agonist, LUF5834, engages residues that are distinct from those of adenosine-like ligands to activate the adenosine A(2a) receptor. Mol. Pharmacol. 81, 475–487. https://doi.org/10.1124/mol.111.075937

Langenhan, T., Aust, G., Hamann, J., 2013. Sticky signaling--adhesion class G protein-coupled receptors take the stage. Sci. Signal. 6, re3. https://doi.org/10.1126/scisignal.2003825

Laporte, S.A., Oakley, R.H., Zhang, J., Holt, J.A., Ferguson, S.S.G., Caron, M.G., Barak, L.S., 1999. The β2-adrenergic receptor/βarrestin complex recruits the clathrin adaptor AP-2 during endocytosis. Proc. Natl. Acad. Sci. 96, 3712–3717. https://doi.org/10.1073/pnas.96.7.3712

Laskowski, R.A., 1995. SURFNET: a program for visualizing molecular surfaces, cavities, and intermolecular interactions. J. Mol. Graph. 13, 323–330, 307–308. https://doi.org/10.1016/0263-7855(95)00073-9

Lazareno, S., Dolezal, V., Popham, A., Birdsall, N.J.M., 2004. Thiochrome enhances acetylcholine affinity at muscarinic M4 receptors: receptor subtype selectivity via cooperativity rather than affinity. Mol. Pharmacol. 65, 257–266. https://doi.org/10.1124/mol.65.1.257

Lazarus, M., Shen, H.-Y., Cherasse, Y., Qu, W.-M., Huang, Z.-L., Bass, C.E., Winsky-Sommerer, R., Semba, K., Fredholm, B.B., Boison, D., Hayaishi, O., Urade, Y., Chen, J.-F., 2011. Arousal effect of caffeine depends on adenosine A2A receptors in the shell of the nucleus accumbens. J. Neurosci. Off. J. Soc. Neurosci. 31, 10067–10075. https://doi.org/10.1523/JNEUROSCI.6730-10.2011

Le Guilloux, V., Schmidtke, P., Tuffery, P., 2009. Fpocket: An open source platform for ligand pocket detection. BMC Bioinformatics 10, 168. https://doi.org/10.1186/1471-2105-10-168

Leach, K., Sexton, P.M., Christopoulos, A., 2007. Allosteric GPCR modulators: taking advantage of permissive receptor pharmacology. Trends Pharmacol. Sci., Special Issue on Allosterism and Collateral Efficacy 28, 382–389. https://doi.org/10.1016/j.tips.2007.06.004

Leander, M., Yuan, Y., Meger, A., Cui, Q., Raman, S., 2020. Functional plasticity and evolutionary adaptation of allosteric regulation. Proc. Natl. Acad. Sci. 117, 25445–25454. https://doi.org/10.1073/pnas.2002613117

Lee, J., Hwang, I., Lee, J.H., Lee, H.W., Jeong, L.-S., Ha, H., 2013. The selective A3AR antagonist LJ-1888 ameliorates UUO-induced tubulointerstitial fibrosis. Am. J. Pathol. 183, 1488–1497. https://doi.org/10.1016/j.ajpath.2013.07.010

Lee, Y., Warne, T., Nehmé, R., Pandey, S., Dwivedi-Agnihotri, H., Chaturvedi, M., Edwards, P.C., García-Nafría, J., Leslie, A.G.W., Shukla, A.K., Tate, C.G., 2020. Molecular basis of β-arrestin coupling to formoterol-bound β1-adrenoceptor. Nature 583, 862–866. https://doi.org/10.1038/s41586-020-2419-1

Lefkowitz, R.J., Shenoy, S.K., 2005. Transduction of receptor signals by beta-arrestins. Science 308, 512–517. https://doi.org/10.1126/science.1109237

Leung, C.T., Li, A., Banerjee, J., Gao, Z.-G., Kambayashi, T., Jacobson, K.A., Civan, M.M., 2014. The role of activated adenosine receptors in degranulation of human LAD2 mast cells. Purinergic Signal. 10, 465–475. https://doi.org/10.1007/s11302-014-9409-4

Li, J., Xiang, B., Su, W., Zhang, X., Huang, Y., Ma, L., 2003. Agonist-induced Formation of Opioid Receptor-G Protein-coupled Receptor Kinase (GRK)-Gβγ Complex on Membrane Is Required for

GRK2 Function in Vivo *. J. Biol. Chem. 278, 30219–30226. https://doi.org/10.1074/jbc.M302385200

Li, L., Homan, K.T., Vishnivetskiy, S.A., Manglik, A., Tesmer, J.J.G., Gurevich, V.V., Gurevich, E.V., 2015. G Protein-coupled Receptor Kinases of the GRK4 Protein Subfamily Phosphorylate Inactive G Protein-coupled Receptors (GPCRs) *. J. Biol. Chem. 290, 10775–10790. https://doi.org/10.1074/jbc.M115.644773

Liang, J., Edelsbrunner, H., Woodward, C., 1998. Anatomy of protein pockets and cavities: measurement of binding site geometry and implications for ligand design. Protein Sci. Publ. Protein Soc. 7, 1884–1897.

Liang, Y.-L., Belousoff, M.J., Zhao, P., Koole, C., Fletcher, M.M., Truong, T.T., Julita, V., Christopoulos, G., Xu, H.E., Zhang, Y., Khoshouei, M., Christopoulos, A., Danev, R., Sexton, P.M., Wootten, D., 2020. Toward a Structural Understanding of Class B GPCR Peptide Binding and Activation. Mol. Cell 77, 656-668.e5. https://doi.org/10.1016/j.molcel.2020.01.012

Liang, Y.-L., Khoshouei, M., Deganutti, G., Glukhova, A., Koole, C., Peat, T.S., Radjainia, M., Plitzko, J.M., Baumeister, W., Miller, L.J., Hay, D.L., Christopoulos, A., Reynolds, C.A., Wootten, D., Sexton, P.M., 2018a. Cryo-EM structure of the active, Gs-protein complexed, human CGRP receptor. Nature 561, 492–497. https://doi.org/10.1038/s41586-018-0535-y

Liang, Y.-L., Khoshouei, M., Glukhova, A., Furness, S.G.B., Zhao, P., Clydesdale, L., Koole, C., Truong, T.T., Thal, D.M., Lei, S., Radjainia, M., Danev, R., Baumeister, W., Wang, M.-W., Miller, L.J., Christopoulos, A., Sexton, P.M., Wootten, D., 2018b. Phase-plate cryo-EM structure of a biased agonist-bound human GLP-1 receptor–Gs complex. Nature 555, 121–125. https://doi.org/10.1038/nature25773

Liang, Y.-L., Khoshouei, M., Radjainia, M., Zhang, Y., Glukhova, A., Tarrasch, J., Thal, D.M., Furness, S.G.B., Christopoulos, G., Coudrat, T., Danev, R., Baumeister, W., Miller, L.J., Christopoulos, A., Kobilka, B.K., Wootten, D., Skiniotis, G., Sexton, P.M., 2017. Phase-plate cryo-EM structure of a class B GPCR-G-protein complex. Nature 546, 118–123. https://doi.org/10.1038/nature22327

Lichtarge, O., Bourne, H.R., Cohen, F.E., 1996. An evolutionary trace method defines binding surfaces common to protein families. J. Mol. Biol. 257, 342–358. https://doi.org/10.1006/jmbi.1996.0167

Lin, Xiaoqian, Li, X., Lin, Xubo, 2020. A Review on Applications of Computational Methods in Drug Screening and Design. Mol. Basel Switz. 25, E1375. https://doi.org/10.3390/molecules25061375

Liu, W., Chun, E., Thompson, A.A., Chubukov, P., Xu, F., Katritch, V., Han, G.W., Roth, C.B., Heitman, L.H., IJzerman, A.P., Cherezov, V., Stevens, R.C., 2012. Structural basis for allosteric regulation of GPCRs by sodium ions. Science 337, 232–236. https://doi.org/10.1126/science.1219218

Livingston, K.E., Traynor, J.R., 2016. A biased mu-opioid receptor positive allosteric modulator that does not alter receptor regulation. FASEB J. 30, 931.8-931.8. https://doi.org/10.1096/fasebj.30.1_supplement.931.8

Lockless, S.W., Ranganathan, R., 1999. Evolutionarily conserved pathways of energetic connectivity in protein families. Science 286, 295–299. https://doi.org/10.1126/science.286.5438.295

Lodish, H.F., Berk, A., Kaiser, C., Krieger, M., Scott, M.P., Bretscher, A., Ploegh, H.L., Matsudaira, P.T., 2008. Molecular cell biology. W.H. Freeman, New York.

Lodowski, D.T., Pitcher, J.A., Capel, W.D., Lefkowitz, R.J., Tesmer, J.J.G., 2003. Keeping G proteins at bay: a complex between G protein-coupled receptor kinase 2 and Gbetagamma. Science 300, 1256–1262. https://doi.org/10.1126/science.1082348

Logothetis, D.E., Kurachi, Y., Galper, J., Neer, E.J., Clapham, D.E., 1987. The beta gamma subunits of GTP-binding proteins activate the muscarinic K+ channel in heart. Nature 325, 321–326. https://doi.org/10.1038/325321a0

Longenecker, K.L., Lewis, M.E., Chikumi, H., Gutkind, J.S., Derewenda, Z.S., 2001. Structure of the RGS-like Domain from PDZ-RhoGEF: Linking Heterotrimeric G Protein-Coupled Signaling to Rho GTPases. Structure 9, 559–569. https://doi.org/10.1016/S0969-2126(01)00620-7

Lougiakis, N., Frakolaki, E., Karmou, P., Pouli, N., Marakos, P., Madan, V., Bartenschlager, R., Vassilaki, N., 2017. Novel nucleoside analogues targeting HCV replication through an NS5A-dependent inhibition mechanism. Chem. Biol. Drug Des. 90, 352–367. https://doi.org/10.1111/cbdd.12966

Lougiakis, N., Marakos, P., Pouli, N., Fragopoulou, E., Tenta, R., 2015. Synthesis of new nebularine analogues and their inhibitory activity against adenosine deaminase. Chem. Pharm. Bull. (Tokyo) 63, 134–142. https://doi.org/10.1248/cpb.c14-00731

Louvel, J., Guo, D., Soethoudt, M., Mocking, T.A.M., Lenselink, E.B., Mulder-Krieger, T., Heitman, L.H., IJzerman, A.P., 2015. Structure-kinetics relationships of Capadenoson derivatives as adenosine A1 receptor agonists. Eur. J. Med. Chem. 101, 681–691. https://doi.org/10.1016/j.ejmech.2015.07.023

Lü, Q., AtKisson, M.S., Jarvis, S.E., Feng, Z.P., Zamponi, G.W., Dunlap, K., 2001. Syntaxin 1A supports voltage-dependent inhibition of alpha1B Ca2+ channels by Gbetagamma in chick sensory neurons. J. Neurosci. Off. J. Soc. Neurosci. 21, 2949–2957.

Luttrell, L.M., 2014. Minireview: More Than Just a Hammer: Ligand “Bias” and Pharmaceutical Discovery. Mol. Endocrinol. 28, 281–294. https://doi.org/10.1210/me.2013-1314

Luttrell, L.M., Ferguson, S.S.G., Daaka, Y., Miller, W.E., Maudsley, S., Rocca, G.J.D., Lin, F.-T., Kawakatsu, H., Owada, K., Luttrell, D.K., Caron, M.G., Lefkowitz, R.J., 1999. β-Arrestin-Dependent Formation of β2 Adrenergic Receptor-Src Protein Kinase Complexes. Science. https://doi.org/10.1126/science.283.5402.655

Luttrell, L.M., Miller, W.E., 2013. Arrestins as regulators of kinases and phosphatases. Prog. Mol. Biol. Transl. Sci. 118, 115–147. https://doi.org/10.1016/B978-0-12-394440-5.00005-X

Mackie DI, Nielsen NR, Harris M, Singh S, Davis RB, Dy D, Ladds G, Caron KM. RAMP3 determines rapid recycling of atypical chemokine receptor-3 for guided angiogenesis. Proc Natl Acad Sci U S A. 2019 Nov 26;116(48):24093-24099. doi: 10.1073/pnas.1905561116. Epub 2019 Nov 11. PMID: 31712427; PMCID: PMC6883789

Maemoto, T., Tada, M., Mihara, T., Ueyama, N., Matsuoka, H., Harada, K., Yamaji, T., Shirakawa, K., Kuroda, S., Akahane, A., Iwashita, A., Matsuoka, N., Mutoh, S., 2004. Pharmacological Characterization of FR194921, a New Potent, Selective, and Orally Active Antagonist for Central Adenosine A1 Receptors. J. Pharmacol. Sci. 96, 42–52. https://doi.org/10.1254/jphs.fp0040359

Magalhaes, A.C., Dunn, H., Ferguson, S.S., 2012. Regulation of GPCR activity, trafficking and localization by GPCR-interacting proteins. Br. J. Pharmacol. 165, 1717–1736. https://doi.org/10.1111/j.1476-5381.2011.01552.x

Makita, N., Iiri, T., 2014. Biased agonism: a novel paradigm in G protein-coupled receptor signaling observed in acquired hypocalciuric hypercalcemia [Review]. Endocr. J. 61, 303–309. https://doi.org/10.1507/endocrj.EJ13-0453

Malmstrom, R.D., Lee, C.T., Van Wart, A.T., Amaro, R.E., 2014. Application of Molecular-Dynamics Based Markov State Models to Functional Proteins. J. Chem. Theory Comput. 10, 2648–2657. https://doi.org/10.1021/ct5002363

Marcotte, E.M., Pellegrini, M., Ng, H.L., Rice, D.W., Yeates, T.O., Eisenberg, D., 1999. Detecting protein function and protein-protein interactions from genome sequences. Science 285, 751–753. https://doi.org/10.1126/science.285.5428.751

Margolskee, R.F., 2002. Molecular mechanisms of bitter and sweet taste transduction. J. Biol. Chem. 277, 1–4. https://doi.org/10.1074/jbc.R100054200

Martin, C.B., Mahon, G.M., Klinger, M.B., Kay, R.J., Symons, M., Der, C.J., Whitehead, I.P., 2001. The thrombin receptor, PAR-1, causes transformation by activation of Rho-mediated signaling pathways. Oncogene 20, 1953–1963. https://doi.org/10.1038/sj.onc.1204281

Marti-Solano, M., Crilly, S.E., Malinverni, D., Munk, C., Harris, M., Pearce, A., Quon, T., Mackenzie, A.E., Wang, X., Peng, J., Tobin, A.B., Ladds, G., Milligan, G., Gloriam, D.E., Puthenveedu, M.A., Babu, M.M., 2020. Combinatorial expression of GPCR isoforms affects signalling and drug responses. Nature 587, 650–656. https://doi.org/10.1038/s41586-020-2888-2

Massova, I., Kollman, P.A., 2000. Combined molecular mechanical and continuum solvent approach (MM-PBSA/GBSA) to predict ligand binding. Perspect. Drug Discov. Des. 18, 113–135. https://doi.org/10.1023/A:1008763014207

Matricon, P., Duy Vo, D., Gao, Z.-G., Kihlberg, J., A. Jacobson, K., Carlsson, J., 2021. Fragment-based design of selective GPCR ligands guided by free energy simulations. Chem. Commun. 57, 12305–12308. https://doi.org/10.1039/D1CC03202J

May, L.T., Leach, K., Sexton, P.M., Christopoulos, A., 2007. Allosteric modulation of G protein-coupled receptors. Annu. Rev. Pharmacol. Toxicol. 47, 1–51. https://doi.org/10.1146/annurev.pharmtox.47.120505.105159

McClean, P.L., Gault, V.A., Irwin, N., McCluskey, J.T., Flatt, P.R., 2008. Daily administration of the GIP-R antagonist (Pro3)GIP in streptozotocin-induced diabetes suggests that insulin-dependent mechanisms are critical to anti-obesity-diabetes actions of (Pro3)GIP. Diabetes Obes. Metab. 10, 336–342. https://doi.org/10.1111/j.1463-1326.2007.00712.x

McClendon, C.L., Kornev, A.P., Gilson, M.K., Taylor, S.S., 2014. Dynamic architecture of a protein kinase. Proc. Natl. Acad. Sci. U. S. A. 111, E4623-4631. https://doi.org/10.1073/pnas.1418402111

McCudden, C.R., Hains, M.D., Kimple, R.J., Siderovski, D.P., Willard, F.S., 2005. G-protein signaling: back to the future. Cell. Mol. Life Sci. 62, 551–577. https://doi.org/10.1007/s00018-004-4462-3

McDonald, P.H., Chow, C.-W., Miller, W.E., Laporte, S.A., Field, M.E., Lin, F.-T., Davis, R.J., Lefkowitz, R.J., 2000. β-Arrestin 2: A Receptor-Regulated MAPK Scaffold for the Activation of JNK3. Science. https://doi.org/10.1126/science.290.5496.1574

Mcintyre, N., Holdsworth, C.D., Turner, D.S., 1964. NEW INTERPRETATION OF ORAL GLUCOSE TOLERANCE. Lancet Lond. Engl. 2, 20–21. https://doi.org/10.1016/s0140-6736(64)90011-x

McLatchie, L.M., Fraser, N.J., Main, M.J., Wise, A., Brown, J., Thompson, N., Solari, R., Lee, M.G., Foord, S.M., 1998. RAMPs regulate the transport and ligand specificity of the calcitonin-receptor-like receptor. Nature 393, 333–339. https://doi.org/10.1038/30666

Meier, J.J., Nauck, M.A., 2010. Is the Diminished Incretin Effect in Type 2 Diabetes Just an Epi-Phenomenon of Impaired β-Cell Function? Diabetes 59, 1117–1125. https://doi.org/10.2337/db09-1899

Méndez, M., Matter, H., Defossa, E., Kurz, M., Lebreton, S., Li, Z., Lohmann, M., Löhn, M., Mors, H., Podeschwa, M., Rackelmann, N., Riedel, J., Safar, P., Thorpe, D.S., Schäfer, M., Weitz, D., Breitschopf, K., 2020. Design, Synthesis, and Pharmacological Evaluation of Potent Positive Allosteric Modulators of the Glucagon-like Peptide-1 Receptor (GLP-1R). J. Med. Chem. 63, 2292–2307. https://doi.org/10.1021/acs.jmedchem.9b01071

Meyerhof, W., Müller-Brechlin, R., Richter, D., 1991. Molecular cloning of a novel putative G-protein coupled receptor expressed during rat spermiogenesis. FEBS Lett. 284, 155–160. https://doi.org/10.1016/0014-5793(91)80674-r

Michailidou, M., Giannouli, V., Kotsikoris, V., Papadodima, O., Kontogianni, G., Kostakis, I.K., Lougiakis, N., Chatziioannou, A., Kolisis, F.N., Marakos, P., Pouli, N., Loutrari, H., 2016. Novel

pyrazolopyridine derivatives as potential angiogenesis inhibitors: Synthesis, biological evaluation and transcriptome-based mechanistic analysis. Eur. J. Med. Chem. 121, 143–157. https://doi.org/10.1016/j.ejmech.2016.05.035

Milligan, G., Shimpukade, B., Ulven, T., Hudson, B.D., 2017. Complex Pharmacology of Free Fatty Acid Receptors. Chem. Rev. 117, 67–110. https://doi.org/10.1021/acs.chemrev.6b00056

Miyawaki, K., Yamada, Y., Ban, N., Ihara, Y., Tsukiyama, K., Zhou, H., Fujimoto, S., Oku, A., Tsuda, K., Toyokuni, S., Hiai, H., Mizunoya, W., Fushiki, T., Holst, J.J., Makino, M., Tashita, A., Kobara, Y., Tsubamoto, Y., Jinnouchi, T., Jomori, T., Seino, Y., 2002. Inhibition of gastric inhibitory polypeptide signaling prevents obesity. Nat. Med. 8, 738–742. https://doi.org/10.1038/nm727

Modlinger, P.S., Welch, W.J., 2003. Adenosine A1 receptor antagonists and the kidney. Curr. Opin. Nephrol. Hypertens. 12, 497–502. https://doi.org/10.1097/00041552-200309000-00003

Molecular Operating Environment (MOE), 2022.02 Chemical Computing Group ULC [WWW Document], n.d. URL https://www.chemcomp.com/index.htm (accessed 7.17.22).

Motulsky, H.J., Mahan, L.C., 1984. The kinetics of competitive radioligand binding predicted by the law of mass action. Mol. Pharmacol. 25, 1–9.

Müller, C.E., Diekmann, M., Thorand, M., Ozola, V., 2002. [3H]8-Ethyl-4-methyl-2-phenyl-(8R)-4,5,7,8-tetrahydro-1H-imidazo[2,1-i]-purin-5-one ([3H]PSB-11), a Novel High-Affinity Antagonist Radioligand for Human A3 Adenosine Receptors. Bioorganic Amp Med. Chem. Lett. 12, 501–503.

Murray, A.J., 2008. Pharmacological PKA inhibition: all may not be what it seems. Sci. Signal. 1, re4. https://doi.org/10.1126/scisignal.122re4

Nagashima, M., Watanabe, T., Terasaki, M., Tomoyasu, M., Nohtomi, K., Kim-Kaneyama, J., Miyazaki, A., Hirano, T., 2011. Native incretins prevent the development of atherosclerotic lesions in apolipoprotein E knockout mice. Diabetologia 54, 2649–2659. https://doi.org/10.1007/s00125-011-2241-2

Nauck, M., Stöckmann, F., Ebert, R., Creutzfeldt, W., 1986. Reduced incretin effect in type 2 (non-insulin-dependent) diabetes. Diabetologia 29, 46–52. https://doi.org/10.1007/bf02427280

Nauck, M.A., Heimesaat, M.M., Orskov, C., Holst, J.J., Ebert, R., Creutzfeldt, W., 1993. Preserved incretin activity of glucagon-like peptide 1 [7-36 amide] but not of synthetic human gastric inhibitory polypeptide in patients with type-2 diabetes mellitus. J. Clin. Invest. 91, 301–307. https://doi.org/10.1172/JCI116186

Nauck, M.A., Meier, J.J., 2018. Incretin hormones: Their role in health and disease. Diabetes Obes. Metab. 20 Suppl 1, 5–21. https://doi.org/10.1111/dom.13129

Naushad, S.M., Rama Devi, A.R., Hussain, T., Alrokayan, S.A., Janaki Ramaiah, M., Kutala, V.K., 2019. In silico analysis of the structural and functional implications of SLC19A1 R27H polymorphism. J. Genet. 98, 85.

Naylor, J., Suckow, A.T., Seth, A., Baker, D.J., Sermadiras, I., Ravn, P., Howes, R., Li, J., Snaith, M.R., Coghlan, M.P., Hornigold, D.C., 2016. Use of CRISPR/Cas9-engineered INS-1 pancreatic β cells to define the pharmacology of dual GIPR/GLP-1R agonists. Biochem. J. 473, 2881–2891. https://doi.org/10.1042/BCJ20160476

Ng, P.C., Henikoff, S., 2003. SIFT: Predicting amino acid changes that affect protein function. Nucleic Acids Res. 31, 3812–3814. https://doi.org/10.1093/nar/gkg509

Nitz, I., Fisher, E., Weikert, C., Burwinkel, B., Li, Y., Möhlig, M., Boeing, H., Schreiber, S., Schrezenmeir, J., Döring, F., 2007. Association analyses of GIP and GIPR polymorphisms with traits of the metabolic syndrome. Mol. Nutr. Food Res. 51, 1046–1052. https://doi.org/10.1002/mnfr.200700048

Nobles, K.N., Xiao, K., Ahn, S., Shukla, A.K., Lam, C.M., Rajagopal, S., Strachan, R.T., Huang, T.-Y., Bressler, E.A., Hara, M.R., Shenoy, S.K., Gygi, S.P., Lefkowitz, R.J., 2011. Distinct phosphorylation sites on the β(2)-adrenergic receptor establish a barcode that encodes differential functions of β-arrestin. Sci. Signal. 4, ra51. https://doi.org/10.1126/scisignal.2001707

Novinec, M., Korenč, M., Caflisch, A., Ranganathan, R., Lenarčič, B., Baici, A., 2014. A novel allosteric mechanism in the cysteine peptidase cathepsin K discovered by computational methods. Nat. Commun. 5, 3287. https://doi.org/10.1038/ncomms4287

Ochaion, A., Bar-Yehuda, S., Cohen, S., Barer, F., Patoka, R., Amital, H., Reitblat, T., Reitblat, A., Ophir, J., Konfino, I., Chowers, Y., Ben-Horin, S., Fishman, P., 2009. The anti-inflammatory target A(3) adenosine receptor is over-expressed in rheumatoid arthritis, psoriasis and Crohn's disease. Cell. Immunol. 258, 115–122. https://doi.org/10.1016/j.cellimm.2009.03.020

Oldham, W.M., Hamm, H.E., 2008. Heterotrimeric G protein activation by G-protein-coupled receptors. Nat. Rev. Mol. Cell Biol. 9, 60–71. https://doi.org/10.1038/nrm2299

Olsen, R.H.J., DiBerto, J.F., English, J.G., Glaudin, A.M., Krumm, B.E., Slocum, S.T., Che, T., Gavin, A.C., McCorvy, J.D., Roth, B.L., Strachan, R.T., 2020. "TRUPATH, an Open-Source Biosensor Platform for Interrogating the GPCR Transducerome." Nat. Chem. Biol. 16, 841–849. https://doi.org/10.1038/s41589-020-0535-8

Omori, K., Kotera, J., 2007. Overview of PDEs and their regulation. Circ. Res. 100, 309–327. https://doi.org/10.1161/01.RES.0000256354.95791.f1

Pal, K., Melcher, K., Xu, H.E., 2012. Structure and mechanism for recognition of peptide hormones by Class B G-protein-coupled receptors. Acta Pharmacol. Sin. 33, 300–311. https://doi.org/10.1038/aps.2011.170

Palczewski, K., Buczyłko, J., Kaplan, M.W., Polans, A.S., Crabb, J.W., 1991. Mechanism of rhodopsin kinase activation. J. Biol. Chem. 266, 12949–12955.

Palczewski, K., Kumasaka, T., Hori, T., Behnke, C.A., Motoshima, H., Fox, B.A., Le Trong, I., Teller, D.C., Okada, T., Stenkamp, R.E., Yamamoto, M., Miyano, M., 2000. Crystal structure of rhodopsin: A G protein-coupled receptor. Science 289, 739–745. https://doi.org/10.1126/science.289.5480.739

Pande, V.S., Beauchamp, K., Bowman, G.R., 2010. Everything you wanted to know about Markov State Models but were afraid to ask. Methods San Diego Calif 52, 99–105. https://doi.org/10.1016/j.ymeth.2010.06.002

Panjkovich, A., Daura, X., 2014. PARS: a web server for the prediction of Protein Allosteric and Regulatory Sites. Bioinformatics 30, 1314–1315. https://doi.org/10.1093/bioinformatics/btu002

Papadakis, G., Gerasi, M., Snoeck, R., Marakos, P., Andrei, G., Lougiakis, N., Pouli, N., 2020. Synthesis of New Imidazopyridine Nucleoside Derivatives Designed as Maribavir Analogues. Mol. Basel Switz. 25, E4531. https://doi.org/10.3390/molecules25194531

Papastathopoulos, A., Lougiakis, N., Kostakis, I.K., Marakos, P., Pouli, N., Pratsinis, H., Kletsas, D., 2021. New bioactive 5-arylcarboximidamidopyrazolo[3,4-c]pyridines: Synthesis, cytotoxic activity, mechanistic investigation and structure-activity relationships. Eur. J. Med. Chem. 218, 113387. https://doi.org/10.1016/j.ejmech.2021.113387

Park, J.H., Scheerer, P., Hofmann, K.P., Choe, H.-W., Ernst, O.P., 2008. Crystal structure of the ligand-free G-protein-coupled receptor opsin. Nature 454, 183–187. https://doi.org/10.1038/nature07063

Pellegrini, M., Marcotte, E.M., Thompson, M.J., Eisenberg, D., Yeates, T.O., 1999. Assigning protein functions by comparative genome analysis: Protein phylogenetic profiles. Proc. Natl. Acad. Sci. 96, 4285–4288. https://doi.org/10.1073/pnas.96.8.4285

Perry, R., Craig, S., Ng, M., Gault, V., Flatt, P., Irwin, N., 2019. Characterisation of Glucose-Dependent Insulinotropic Polypeptide Receptor Antagonists in Rodent Pancreatic Beta Cells and Mice. Clin. Med. Insights Endocrinol. Diabetes 12. https://doi.org/10.1177/1179551419875453

Peterson, Y.K., Luttrell, L.M., 2017. The Diverse Roles of Arrestin Scaffolds in G Protein-Coupled Receptor Signaling. Pharmacol. Rev. 69, 256–297. https://doi.org/10.1124/pr.116.013367

Petrelli, R., Scortichini, M., Belardo, C., Boccella, S., Luongo, L., Capone, F., Kachler, S., Vita, P., Del Bello, F., Maione, S., Lavecchia, A., Klotz, K.-N., Cappellacci, L., 2018. Structure-Based Design, Synthesis, and In Vivo Antinociceptive Effects of Selective A1 Adenosine Receptor Agonists. J. Med. Chem. 61, 305–318. https://doi.org/10.1021/acs.jmedchem.7b01399

Preti B., Suchankova A., Deganutti G., Leuenberger M., Barkan K., Manulak I., Huang X., Carvalho S., Ladds G, Lochner M., 2022. Discovery and Structure-Activity Relationship Studies of Novel Adenosine A_1 Receptor-Selective Agonists. Submitted to J. Med. Chem.

Qi, Y., Wang, Q., Tang, B., Lai, L., 2012. Identifying Allosteric Binding Sites in Proteins with a Two-State Gō Model for Novel Allosteric Effector Discovery. J. Chem. Theory Comput. 8, 2962–2971. https://doi.org/10.1021/ct300395h

Rang, R., 2019. Rang & Dale's Pharmacology [WWW Document]. URL https://www.uk.elsevierhealth.com/rang-dales-pharmacology-9780702074486.html (accessed 1.15.22).

Ray, K., Kunsch, C., Bonner, L.M., Robishaw, J.D., 1995. Isolation of cDNA clones encoding eight different human G protein gamma subunits, including three novel forms designated the gamma 4, gamma 10, and gamma 11 subunits. J. Biol. Chem. 270, 21765–21771. https://doi.org/10.1074/jbc.270.37.21765

Renner, S., Fehlings, C., Herbach, N., Hofmann, A., von Waldthausen, D.C., Kessler, B., Ulrichs, K., Chodnevskaja, I., Moskalenko, V., Amselgruber, W., Göke, B., Pfeifer, A., Wanke, R., Wolf, E., 2010. Glucose intolerance and reduced proliferation of pancreatic beta-cells in transgenic pigs with impaired glucose-dependent insulinotropic polypeptide function. Diabetes 59, 1228–1238. https://doi.org/10.2337/db09-0519

Rhee, S.G., 2001. Regulation of phosphoinositide-specific phospholipase C. Annu. Rev. Biochem. 70, 281–312. https://doi.org/10.1146/annurev.biochem.70.1.281

Rivoire, O., Reynolds, K.A., Ranganathan, R., 2016. Evolution-Based Functional Decomposition of Proteins. PLoS Comput. Biol. 12, e1004817. https://doi.org/10.1371/journal.pcbi.1004817

Rodríguez, D., Ranganathan, A., Carlsson, J., 2015. Discovery of GPCR Ligands by Molecular Docking Screening: Novel Opportunities Provided by Crystal Structures. Curr. Top. Med. Chem. 15, 2484–2503. https://doi.org/10.2174/1568026615666150701112853

Roglic, G., 2016. WHO Global report on diabetes: A summary [WWW Document]. URL https://www.ijncd.org/article.asp?issn=2468-8827;year=2016;volume=1;issue=1;spage=3;epage=8;aulast=Roglic;type=3 (accessed 4.14.22).

Rondard, P., Liu, J., Huang, S., Malhaire, F., Vol, C., Pinault, A., Labesse, G., Pin, J.-P., 2006. Coupling of agonist binding to effector domain activation in metabotropic glutamate-like receptors. J. Biol. Chem. 281, 24653–24661. https://doi.org/10.1074/jbc.M602277200

Rork, T.H., Wallace, K.L., Kennedy, D.P., Marshall, M.A., Lankford, A.R., Linden, J., 2008. Adenosine A2A receptor activation reduces infarct size in the isolated, perfused mouse heart by inhibiting resident cardiac mast cell degranulation. Am. J. Physiol. Heart Circ. Physiol. 295, H1825-1833. https://doi.org/10.1152/ajpheart.495.2008

Rosa, M., Noel, T., Harris, M., Ladds, G., 2021. Emerging roles of adhesion G protein-coupled receptors. Biochem. Soc. Trans. 49, 1695–1709. https://doi.org/10.1042/BST20201144

Roseti, C., Palma, E., Martinello, K., Fucile, S., Morace, R., Esposito, V., Cantore, G., Arcella, A., Giangaspero, F., Aronica, E., Mascia, A., Gennaro, G.D., Quarato, P.P., Manfredi, M., Cristalli, G., Lambertucci, C., Marucci, G., Volpini, R., Limatola, C., Eusebi, F., 2009. Blockage of A2A and A3 adenosine receptors decreases the desensitization of human GABAA receptors microtransplanted to Xenopus oocytes. Proc. Natl. Acad. Sci. 106, 15927–15931. https://doi.org/10.1073/pnas.0907324106

Ross, E.M., Gilman, A.G., 1977. Resolution of some components of adenylate cyclase necessary for catalytic activity. J. Biol. Chem. 252, 6966–6969.

Ross, E.M., Wilkie, T.M., 2000. GTPase-activating proteins for heterotrimeric G proteins: regulators of G protein signaling (RGS) and RGS-like proteins. Annu. Rev. Biochem. 69, 795–827. https://doi.org/10.1146/annurev.biochem.69.1.795

Routledge, S.J., Ladds, G., Poyner, D.R., 2017. The effects of RAMPs upon cell signalling. Mol. Cell. Endocrinol. 449, 12–20. https://doi.org/10.1016/j.mce.2017.03.033

Rubino, F., Gagner, M., Gentileschi, P., Kini, S., Fukuyama, S., Feng, J., Diamond, E., 2004. The Early Effect of the Roux-en-Y Gastric Bypass on Hormones Involved in Body Weight Regulation and Glucose Metabolism. Ann. Surg. 240, 236–242. https://doi.org/10.1097/01.sla.0000133117.12646.48

Rucktooa, P., Cheng, R.K.Y., Segala, E., Geng, T., Errey, J.C., Brown, G.A., Cooke, R.M., Marshall, F.H., Doré, A.S., 2018. Towards high throughput GPCR crystallography: In Meso soaking of Adenosine A2A Receptor crystals. Sci. Rep. 8, 41. https://doi.org/10.1038/s41598-017-18570-w

Safaee, M., Ivan, M.E., Oh, M.C., Oh, T., Sayegh, E.T., Kaur, G., Sun, M.Z., Bloch, O., Parsa, A.T., 2014. The Role of Epidermal Growth Factor-Like Module Containing Mucin-Like Hormone Receptor 2 in Human Cancers. Oncol. Rev. 8, 242. https://doi.org/10.4081/oncol.2014.242

Salinari, S., Bertuzzi, A., Asnaghi, S., Guidone, C., Manco, M., Mingrone, G., 2009. First-phase insulin secretion restoration and differential response to glucose load depending on the route of administration in type 2 diabetic subjects after bariatric surgery. Diabetes Care 32, 375–380. https://doi.org/10.2337/dc08-1314

Salvatore, C.A., Jacobson, M.A., Taylor, H.E., Linden, J., Johnson, R.G., 1993. Molecular cloning and characterization of the human A3 adenosine receptor. Proc. Natl. Acad. Sci. U. S. A. 90, 10365–10369. https://doi.org/10.1073/pnas.90.21.10365

Salvatore, C.A., Tilley, S.L., Latour, A.M., Fletcher, D.S., Koller, B.H., Jacobson, M.A., 2000. Disruption of the A(3) adenosine receptor gene in mice and its effect on stimulated inflammatory cells. J. Biol. Chem. 275, 4429–4434. https://doi.org/10.1074/jbc.275.6.4429

Sato, J., Makita, N., Iiri, T., 2016. Inverse agonism: the classic concept of GPCRs revisited [Review]. Endocr. J. 63, 507–514. https://doi.org/10.1507/endocrj.EJ16-0084

Sawynok, J., 2016. Adenosine receptor targets for pain. Neuroscience 338, 1–18. https://doi.org/10.1016/j.neuroscience.2015.10.031

Schenone, S., Brullo, C., Musumeci, F., Bruno, O., Botta, M., 2010. A1 receptors ligands: past, present and future trends. Curr. Top. Med. Chem. 10, 878–901. https://doi.org/10.2174/156802610791268729

Schiellerup, S.P., Skov-Jeppesen, K., Windeløv, J.A., Svane, M.S., Holst, J.J., Hartmann, B., Rosenkilde, M.M., 2019. Gut Hormones and Their Effect on Bone Metabolism. Potential Drug Therapies in Future Osteoporosis Treatment. Front. Endocrinol. 10, 75. https://doi.org/10.3389/fendo.2019.00075

Schmidt, M., Cattani-Cavalieri, I., Nuñez, F.J., Ostrom, R.S., 2020. Phosphodiesterase isoforms and cAMP compartments in the development of new therapies for obstructive pulmonary diseases. Curr. Opin. Pharmacol. 51, 34–42. https://doi.org/10.1016/j.coph.2020.05.002

Schneider, E.H., Schnell, D., Strasser, A., Dove, S., Seifert, R., 2010. Impact of the DRY motif and the missing “ionic lock” on constitutive activity and G-protein coupling of the human histamine H4 receptor. J. Pharmacol. Exp. Ther. 333, 382–392. https://doi.org/10.1124/jpet.109.163220

Schneider, T.D., Stormo, G.D., Gold, L., Ehrenfeucht, A., 1986. Information content of binding sites on nucleotide sequences. J. Mol. Biol. 188, 415–431. https://doi.org/10.1016/0022-2836(86)90165-8

Schöning-Stierand, K., Diedrich, K., Fährrolfes, R., Flachsenberg, F., Meyder, A., Nittinger, E., Steinegger, R., Rarey, M., 2020. ProteinsPlus: interactive analysis of protein–ligand binding interfaces. Nucleic Acids Res. 48, W48–W53. https://doi.org/10.1093/nar/gkaa235

Schulte, G., Fredholm, B.B., 2002. Signaling pathway from the human adenosine A(3) receptor expressed in Chinese hamster ovary cells to the extracellular signal-regulated kinase 1/2. Mol. Pharmacol. 62, 1137–1146. https://doi.org/10.1124/mol.62.5.1137

Seamon, K.B., Padgett, W., Daly, J.W., 1981. Forskolin: unique diterpene activator of adenylate cyclase in membranes and in intact cells. Proc. Natl. Acad. Sci. U. S. A. 78, 3363–3367. https://doi.org/10.1073/pnas.78.6.3363

Segala, E., Guo, D., Cheng, R.K.Y., Bortolato, A., Deflorian, F., Doré, A.S., Errey, J.C., Heitman, L.H., IJzerman, A.P., Marshall, F.H., Cooke, R.M., 2016. Controlling the Dissociation of Ligands from the Adenosine A2A Receptor through Modulation of Salt Bridge Strength. J. Med. Chem. 59, 6470–6479. https://doi.org/10.1021/acs.jmedchem.6b00653

Seifert, R., Wenzel-Seifert, K., 2002. Constitutive activity of G-protein-coupled receptors: cause of disease and common property of wild-type receptors. Naunyn. Schmiedebergs Arch. Pharmacol. 366, 381–416. https://doi.org/10.1007/s00210-002-0588-0

Sela, I., Golan, G., Strajbl, M., Rivenzon-Segal, D., Bar-Haim, S., Bloch, I., Inbal, B., Shitrit, A., Ben-Zeev, E., Fichman, M., Markus, Y., Marantz, Y., Senderowitz, H., Kalid, O., 2010. G protein coupled receptors -in silico drug discovery and design. Curr. Top. Med. Chem. 10, 638–656. https://doi.org/10.2174/156802610791111498

Selent, J., Sanz, F., Pastor, M., Fabritiis, G.D., 2010. Induced Effects of Sodium Ions on Dopaminergic G-Protein Coupled Receptors. PLOS Comput. Biol. 6, e1000884. https://doi.org/10.1371/journal.pcbi.1000884

Senderowitz, H., Marantz, Y., 2009. G Protein-Coupled Receptors: target-based in silico screening. Curr. Pharm. Des. 15, 4049–4068. https://doi.org/10.2174/138161209789824821

Shah, R.H., Frishman, W.H., 2009. Adenosine1 receptor antagonism: a new therapeutic approach for the treatment of decompensated heart failure. Cardiol. Rev. 17, 125–131. https://doi.org/10.1097/CRD.0b013e31819f1a98

Shalaby, S.M., Zidan, H.E., Shokry, A., Saeed, J., El-Sokkary, R.H., 2017. Association of incretin receptors genetic polymorphisms with type 2 diabetes mellitus in Egyptian patients. J. Gene Med. 19. https://doi.org/10.1002/jgm.2973

Shchepinova, M.M., Hanyaloglu, A.C., Frost, G.S., Tate, E.W., 2020. Chemical biology of noncanonical G protein-coupled receptor signaling: Toward advanced therapeutics. Curr. Opin. Chem. Biol. 56, 98–110. https://doi.org/10.1016/j.cbpa.2020.04.012

Sheik Amamuddy, O., Veldman, W., Manyumwa, C., Khairallah, A., Agajanian, S., Oluyemi, O., Verkhivker, G.M., Tastan Bishop, Ö., 2020. Integrated Computational Approaches and Tools for Allosteric Drug Discovery. Int. J. Mol. Sci. 21, 847. https://doi.org/10.3390/ijms21030847

Shenoy, S.K., McDonald, P.H., Kohout, T.A., Lefkowitz, R.J., 2001. Regulation of receptor fate by ubiquitination of activated beta 2-adrenergic receptor and beta-arrestin. Science 294, 1307–1313. https://doi.org/10.1126/science.1063866

Shonberg, J., Lopez, L., Scammells, P.J., Christopoulos, A., Capuano, B., Lane, J.R., 2014. Biased agonism at G protein-coupled receptors: the promise and the challenges--a medicinal chemistry perspective. Med. Res. Rev. 34, 1286–1330. https://doi.org/10.1002/med.21318

Shukla, A.K., Violin, J.D., Whalen, E.J., Gesty-Palmer, D., Shenoy, S.K., Lefkowitz, R.J., 2008. Distinct conformational changes in beta-arrestin report biased agonism at seven-transmembrane receptors. Proc. Natl. Acad. Sci. U. S. A. 105, 9988–9993. https://doi.org/10.1073/pnas.0804246105

Simon, M.I., Strathmann, M.P., Gautam, N., 1991. Diversity of G proteins in signal transduction. Science 252, 802–808. https://doi.org/10.1126/science.1902986

Skelin, M., Rupnik, M., Cencic, A., 2010. Pancreatic beta cell lines and their applications in diabetes mellitus research. ALTEX 27, 105–113. https://doi.org/10.14573/altex.2010.2.105

Smith, J.S., Lefkowitz, R.J., Rajagopal, S., 2018. Biased Signalling: From Simple Switches to Allosteric Microprocessors. Nat. Rev. Drug Discov. 17, 243–260. https://doi.org/10.1038/nrd.2017.229

Stacey, M., Lin, H.H., Gordon, S., McKnight, A.J., 2000. LNB-TM7, a group of seven-transmembrane proteins related to family-B G-protein-coupled receptors. Trends Biochem. Sci. 25, 284–289. https://doi.org/10.1016/s0968-0004(00)01583-8

Stamatis, D., Lagarias, P., Barkan, K., Vrontaki, E., Ladds, G., Kolocouris, A., 2019. Structural Characterization of Agonist Binding to an A3 Adenosine Receptor through Biomolecular Simulations and Mutagenesis Experiments. J. Med. Chem. 62, 8831–8846. https://doi.org/10.1021/acs.jmedchem.9b01164

Stampelou M., Suchankova A., Tzortzini E., Dhingra L., Barkan K., Lougiakis N., Marakos P., Pouli N., Ladds G., Kolocouris A., 2022. Novel 7-Anilino-Pyrazolo[3,4-c]pyridine as High Affinity Dual A_1, A_3 Adenosine Receptor Antagonists and SARs Study Using Alchemical Perturbation Binding Free-Energy Calculations. Accepted to J. Med. Chem.

Starling, S., 2022. A new GLP1, GIP and glucagon receptor triagonist. Nat. Rev. Endocrinol. 18, 135–135. https://doi.org/10.1038/s41574-021-00631-w

Stephenson, R.P., 1956. A modification of receptor theory. Br. J. Pharmacol. Chemother. 11, 379–393. https://doi.org/10.1111/j.1476-5381.1956.tb00006.x

Stoddart, L.A., Johnstone, E.K.M., Wheal, A.J., Goulding, J., Robers, M.B., Machleidt, T., Wood, K.V., Hill, S.J., Pfleger, K.D.G., 2015. Application of BRET to monitor ligand binding to GPCRs. Nat. Methods 12, 661–663. https://doi.org/10.1038/nmeth.3398

Stoddart, L.A., Vernall, A.J., Denman, J.L., Briddon, S.J., Kellam, B., Hill, S.J., 2012. Fragment Screening at Adenosine-A3 Receptors in Living Cells Using a Fluorescence-Based Binding Assay. Chem. Biol. 19, 1105–1115. https://doi.org/10.1016/j.chembiol.2012.07.014

Strong, P., Anderson, R., Coates, J., Ellis, F., Evans, B., Gurden, M.F., Johnstone, J., Kennedy, I., Martin, D.P., 1993. Suppression of non-esterified fatty acids and triacylglycerol in experimental animals by the adenosine analogue GR79236. Clin. Sci. Lond. Engl. 1979 84, 663–669. https://doi.org/10.1042/cs0840663

Suchankova, A., Harris, M., Ladds, G., 2021. Chapter 1 - Measuring the rapid kinetics of receptor-ligand interactions in live cells using NanoBRET, in: Shukla, A.K. (Ed.), Methods in Cell Biology, Biomolecular Interactions Part A. Academic Press, pp. 1–14. https://doi.org/10.1016/bs.mcb.2021.06.013

Suchankova, A., Stampelou, M., Koutsouki, K., Pousias, A., Dhingra, L., Barkan, K., Pouli, N., Marakos, P., Tenta, R., Kolocouris, A., Lougiakis, N., Ladds, G., 2022. Discovery of a High Affinity Adenosine A1/A3 Receptor Antagonist with a Novel 7-Amino-pyrazolo[3,4-d]pyridazine Scaffold. ACS Med. Chem. Lett. 13, 923–934. https://doi.org/10.1021/acsmedchemlett.2c00052

Sugunan, D., Nair, A.K., Kumar, H., Gopalakrishnapillai, A., 2010. A case-control analysis of common variants in GIP with type 2 diabetes and related biochemical parameters in a South Indian population. BMC Med. Genet. 11, 118. https://doi.org/10.1186/1471-2350-11-118

Sun, B., Bachhawat, P., Chu, M.L.-H., Wood, M., Ceska, T., Sands, Z.A., Mercier, J., Lebon, F., Kobilka, T.S., Kobilka, B.K., 2017. Crystal structure of the adenosine A2A receptor bound to an antagonist reveals a potential allosteric pocket. Proc. Natl. Acad. Sci. U. S. A. 114, 2066–2071. https://doi.org/10.1073/pnas.1621423114

Sykes, D.A., Stoddart, L.A., Kilpatrick, L.E., Hill, S.J., 2019. Binding kinetics of ligands acting at GPCRs. Mol. Cell. Endocrinol. 485, 9–19. https://doi.org/10.1016/j.mce.2019.01.018

Taddese, B., Simpson, L.M., Wall, I.D., Blaney, F.E., Reynolds, C.A., 2013. Modeling active GPCR conformations. Methods Enzymol. 522, 21–35. https://doi.org/10.1016/B978-0-12-407865-9.00002-9

Tang, X., Wang, Y., Li, D., Luo, J., Liu, M., 2012. Orphan G protein-coupled receptors (GPCRs): biological functions and potential drug targets. Acta Pharmacol. Sin. 33, 363–371. https://doi.org/10.1038/aps.2011.210

Taussig, R., Tang, W.J., Hepler, J.R., Gilman, A.G., 1994. Distinct patterns of bidirectional regulation of mammalian adenylyl cyclases. J. Biol. Chem. 269, 6093–6100.

Taylor, E.A., Clinch, K., Kelly, P.M., Li, L., Evans, G.B., Tyler, P.C., Schramm, V.L., 2007. Acyclic Ribooxacarbenium Ion Mimics as Transition State Analogues of Human and Malarial Purine Nucleoside Phosphorylases. J. Am. Chem. Soc. 129, 6984–6985. https://doi.org/10.1021/ja071087s

Thillaiappan, N.B., Chakraborty, P., Hasan, G., Taylor, C.W., 2019. IP3 receptors and Ca2+ entry. Biochim. Biophys. Acta BBA - Mol. Cell Res., 15th European Symposium on Calcium 1866, 1092–1100. https://doi.org/10.1016/j.bbamcr.2018.11.007

Thondam, S.K., Cuthbertson, D.J., Wilding, J.P.H., 2020. The influence of Glucose-dependent Insulinotropic Polypeptide (GIP) on human adipose tissue and fat metabolism: Implications for obesity, type 2 diabetes and Non-Alcoholic Fatty Liver Disease (NAFLD). Peptides 125, 170208. https://doi.org/10.1016/j.peptides.2019.170208

Thondam, S.K., Daousi, C., Wilding, J.P.H., Holst, J.J., Ameen, G.I., Yang, C., Whitmore, C., Mora, S., Cuthbertson, D.J., 2017. Glucose-dependent insulinotropic polypeptide promotes lipid deposition in subcutaneous adipocytes in obese type 2 diabetes patients: a maladaptive response. Am. J. Physiol. Endocrinol. Metab. 312, E224–E233. https://doi.org/10.1152/ajpendo.00347.2016

Tilley, S.L., Tsai, M., Williams, C.M., Wang, Z.-S., Erikson, C.J., Galli, S.J., Koller, B.H., 2003. Identification of A3 receptor- and mast cell-dependent and -independent components of adenosine-mediated

airway responsiveness in mice. J. Immunol. Baltim. Md 1950 171, 331–337. https://doi.org/10.4049/jimmunol.171.1.331

Tosh, D.K., Rao, H., Bitant, A., Salmaso, V., Mannes, P., Lieberman, D.I., Vaughan, K.L., Mattison, J.A., Rothwell, A.C., Auchampach, J.A., Ciancetta, A., Liu, N., Cui, Z., Gao, Z.-G., Reitman, M.L., Gavrilova, O., Jacobson, K.A., 2019. Design and in Vivo Characterization of A1 Adenosine Receptor Agonists in the Native Ribose and Conformationally Constrained (N)-Methanocarba Series. J. Med. Chem. 62, 1502–1522. https://doi.org/10.1021/acs.jmedchem.8b01662

Tran, T.M., Friedman, J., Qunaibi, E., Baameur, F., Moore, R.H., Clark, R.B., 2004. Characterization of Agonist Stimulation of cAMP-Dependent Protein Kinase and G Protein-Coupled Receptor Kinase Phosphorylation of the β2-Adrenergic Receptor Using Phosphoserine-Specific Antibodies. Mol. Pharmacol. 65, 196–206. https://doi.org/10.1124/mol.65.1.196

Trevitt, J., Vallance, C., Harris, A., Goode, T., 2009. Adenosine antagonists reverse the cataleptic effects of haloperidol: implications for the treatment of Parkinson's disease. Pharmacol. Biochem. Behav. 92, 521–527. https://doi.org/10.1016/j.pbb.2009.02.001

Trott, O., Olson, A.J., 2010. AutoDock Vina: improving the speed and accuracy of docking with a new scoring function, efficient optimization and multithreading. J. Comput. Chem. 31, 455–461. https://doi.org/10.1002/jcc.21334

Tyagi, S., Gupta, P., Saini, A.S., Kaushal, C., Sharma, S., 2011. The peroxisome proliferator-activated receptor: A family of nuclear receptors role in various diseases. J. Adv. Pharm. Technol. Res. 2, 236–240. https://doi.org/10.4103/2231-4040.90879

Varani, K., Vincenzi, F., Merighi, S., Gessi, S., Borea, P.A., 2017. Biochemical and Pharmacological Role of A1 Adenosine Receptors and Their Modulation as Novel Therapeutic Strategy. Adv. Exp. Med. Biol. 1051, 193–232. https://doi.org/10.1007/5584_2017_61

Vauquelin, G., 2016. Effects of target binding kinetics on in vivo drug efficacy: koff , kon and rebinding. Br. J. Pharmacol. 173, 2319–2334. https://doi.org/10.1111/bph.13504

Vecchio, E.A., Baltos, J.-A., Nguyen, A.T.N., Christopoulos, A., White, P.J., May, L.T., 2018. New paradigms in adenosine receptor pharmacology: allostery, oligomerization and biased agonism. Br. J. Pharmacol. 175, 4036–4046. https://doi.org/10.1111/bph.14337

Velazhahan V, Ma N, Vaidehi N, Tate CG. Activation mechanism of the class D fungal GPCR dimer Ste2. Nature. 2022 Mar;603(7902):743-748. doi: 10.1038/s41586-022-04498-3. Epub 2022 Mar 16. PMID: 35296853; PMCID: PMC8942848.

Verma, M.K., Goel, R., Krishnadas, N., Nemmani, K.V.S., 2018. Targeting glucose-dependent insulinotropic polypeptide receptor for neurodegenerative disorders. Expert Opin. Ther. Targets 22, 615–628. https://doi.org/10.1080/14728222.2018.1487952

Vogt, S., Grosse, R., Schultz, G., Offermanns, S., 2003. Receptor-dependent RhoA activation in G12/G13-deficient cells: genetic evidence for an involvement of Gq/G11. J. Biol. Chem. 278, 28743–28749. https://doi.org/10.1074/jbc.M304570200

Vyavahare, S.S., Mieczkowska, A., Flatt, P.R., Chappard, D., Irwin, N., Mabilleau, G., 2020. GIP analogues augment bone strength by modulating bone composition in diet-induced obesity in mice. Peptides 125, 170207. https://doi.org/10.1016/j.peptides.2019.170207

Wacker, D., Stevens, R.C., Roth, B.L., 2017. How Ligands Illuminate GPCR Molecular Pharmacology. Cell 170, 414–427. https://doi.org/10.1016/j.cell.2017.07.009

Wagner, J.R., Lee, C.T., Durrant, J.D., Malmstrom, R.D., Feher, V.A., Amaro, R.E., 2016. Emerging Computational Methods for the Rational Discovery of Allosteric Drugs. Chem. Rev. 116, 6370–6390. https://doi.org/10.1021/acs.chemrev.5b00631

Wall, M.J., Hill, E., Huckstepp, R., Barkan, K., Deganutti, G., Leuenberger, M., Preti, B., Winfield, I., Carvalho, S., Suchankova, A., Wei, H., Safitri, D., Huang, X., Imlach, W., La Mache, C., Dean, E., Hume, C., Hayward, S., Oliver, J., Zhao, F.-Y., Spanswick, D., Reynolds, C.A., Lochner, M., Ladds, G., Frenguelli, B.G., 2022. Selective activation of Gαob by an adenosine A1 receptor agonist elicits analgesia without cardiorespiratory depression. Nat. Commun. 13, 4150. https://doi.org/10.1038/s41467-022-31652-2

Wall, M.J., Hill, E., Huckstepp, R., Barkan, K., Deganutti, G., Leuenberger, M., Preti, B., Winfield, I., Wei, H., Imlach, W., Dean, E., Hume, C., Hayward, S., Oliver, J., Zhao, F.-Y., Spanswick, D., Reynolds, C.A., Lochner, M., Ladds, G., Frenguelli, B.G., 2020. A biased adenosine A1R agonist elicits analgesia without cardiorespiratory depression. https://doi.org/10.1101/2020.04.04.023945

Wang, X., Song, K., Li, L., Chen, L., 2018. Structure-Based Drug Design Strategies and Challenges. Curr. Top. Med. Chem. 18, 998–1006. https://doi.org/10.2174/1568026618666180813152921

Wass, M.N., Kelley, L.A., Sternberg, M.J.E., 2010. 3DLigandSite: predicting ligand-binding sites using similar structures. Nucleic Acids Res. 38, W469–W473. https://doi.org/10.1093/nar/gkq406

Wass, M.N., Sternberg, M.J.E., 2009. Prediction of ligand binding sites using homologous structures and conservation at CASP8. Proteins 77, 147–151. https://doi.org/10.1002/prot.22513

Watts, V.J., Neve, K.A., 2005. Sensitization of adenylate cyclase by Galpha i/o-coupled receptors. Pharmacol. Ther. 106, 405–421. https://doi.org/10.1016/j.pharmthera.2004.12.005

Wedegaertner, P.B., Wilson, P.T., Bourne, H.R., 1995. Lipid modifications of trimeric G proteins. J. Biol. Chem. 270, 503–506. https://doi.org/10.1074/jbc.270.2.503

Weiqiang Zhou, Hong Yan, Alpha shape and Delaunay triangulation in studies of protein-related interactions, Briefings in Bioinformatics, Volume 15, Issue 1, January 2014, Pages 54–64, https://doi.org/10.1093/bib/bbs077

Weltha, L., Reemmer, J., Boison, D., 2019. The role of adenosine in epilepsy. Brain Res. Bull. 151, 46–54. https://doi.org/10.1016/j.brainresbull.2018.11.008

Werry, T.D., Sexton, P.M., Christopoulos, A., 2005. "Ins and outs" of seven-transmembrane receptor signalling to ERK. Trends Endocrinol. Metab. TEM 16, 26–33. https://doi.org/10.1016/j.tem.2004.11.008

West, R.E., Moss, J., Vaughan, M., Liu, T., Liu, T.Y., 1985. Pertussis toxin-catalyzed ADP-ribosylation of transducin. Cysteine 347 is the ADP-ribose acceptor site. J. Biol. Chem. 260, 14428–14430. https://doi.org/10.1016/S0021-9258(17)38585-X

Whalen, E.J., Rajagopal, S., Lefkowitz, R.J., 2011. Therapeutic potential of β-arrestin- and G protein-biased agonists. Trends Mol. Med. 17, 126–139. https://doi.org/10.1016/j.molmed.2010.11.004

Whitehead, I.P., Zohn, I.E., Der, C.J., 2001. Rho GTPase-dependent transformation by G protein-coupled receptors. Oncogene 20, 1547–1555. https://doi.org/10.1038/sj.onc.1204188

Widenmaier, S.B., Kim, S.-J., Yang, G.K., De Los Reyes, T., Nian, C., Asadi, A., Seino, Y., Kieffer, T.J., Kwok, Y.N., McIntosh, C.H.S., 2010. A GIP receptor agonist exhibits beta-cell anti-apoptotic actions in rat models of diabetes resulting in improved beta-cell function and glycemic control. PloS One 5, e9590. https://doi.org/10.1371/journal.pone.0009590

Wilden, U., Hall, S.W., Kühn, H., 1986. Phosphodiesterase activation by photoexcited rhodopsin is quenched when rhodopsin is phosphorylated and binds the intrinsic 48-kDa protein of rod outer segments. Proc. Natl. Acad. Sci. 83, 1174–1178. https://doi.org/10.1073/pnas.83.5.1174

Wilson, C.N., Nadeem, A., Spina, D., Brown, R., Page, C.P., Jamal Mustafa, S., 2009. Adenosine Receptors and Asthma. Handb. Exp. Pharmacol. 10.1007/978-3-540-89615–9_11. https://doi.org/10.1007/978-3-540-89615-9_11

Wilson, G.L., Lill, M.A., 2011. Integrating structure-based and ligand-based approaches for computational drug design. Future Med. Chem. 3, 735–750. https://doi.org/10.4155/fmc.11.18

Wold, E.A., Chen, J., Cunningham, K.A., Zhou, J., 2019. Allosteric Modulation of Class A GPCRs: Targets, Agents, and Emerging Concepts. J. Med. Chem. 62, 88–127. https://doi.org/10.1021/acs.jmedchem.8b00875

Wootten, D., Christopoulos, A., Marti-Solano, M., Babu, M.M., Sexton, P.M., 2018. Mechanisms of signalling and biased agonism in G protein-coupled receptors. Nat. Rev. Mol. Cell Biol. 19, 638–653. https://doi.org/10.1038/s41580-018-0049-3

Wootten, D., Christopoulos, A., Sexton, P.M., 2013a. Emerging paradigms in GPCR allostery: implications for drug discovery. Nat. Rev. Drug Discov. 12, 630–644. https://doi.org/10.1038/nrd4052

Wootten, D., Miller, L.J., 2020. Structural Basis for Allosteric Modulation of Class B G Protein-Coupled Receptors. Annu. Rev. Pharmacol. Toxicol. 60, 89–107. https://doi.org/10.1146/annurev-pharmtox-010919-023301

Wootten, D., Miller, L.J., Koole, C., Christopoulos, A., Sexton, P.M., 2017. Allostery and Biased Agonism at Class B G Protein-Coupled Receptors. Chem. Rev. 117, 111–138. https://doi.org/10.1021/acs.chemrev.6b00049

Wootten, D., Reynolds, C.A., Smith, K.J., Mobarec, J.C., Koole, C., Savage, E.E., Pabreja, K., Simms, J., Sridhar, R., Furness, S.G.B., Liu, M., Thompson, P.E., Miller, L.J., Christopoulos, A., Sexton, P.M., 2016. The Extracellular Surface of the GLP-1 Receptor Is a Molecular Trigger for Biased Agonism. Cell 165, 1632–1643. https://doi.org/10.1016/j.cell.2016.05.023

Wootten, D., Simms, J., Miller, L.J., Christopoulos, A., Sexton, P.M., 2013b. Polar transmembrane interactions drive formation of ligand-specific and signal pathway-biased family B G protein-coupled receptor conformations. Proc. Natl. Acad. Sci. U. S. A. 110, 5211–5216. https://doi.org/10.1073/pnas.1221585110

Xia, L., Burger, W.A.C., van Veldhoven, J.P.D., Kuiper, B.J., van Duijl, T.T., Lenselink, E.B., Paasman, E., Heitman, L.H., IJzerman, A.P., 2017. Structure–Affinity Relationships and Structure–Kinetics Relationships of Pyrido[2,1-f]purine-2,4-dione Derivatives as Human Adenosine A3 Receptor Antagonists. J. Med. Chem. 60, 7555–7568. https://doi.org/10.1021/acs.jmedchem.7b00950

Yaqub, T., Tikhonova, I.G., Lättig, J., Magnan, R., Laval, M., Escrieut, C., Boulègue, C., Hewage, C., Fourmy, D., 2010. Identification of determinants of glucose-dependent insulinotropic polypeptide receptor that interact with N-terminal biologically active region of the natural ligand. Mol. Pharmacol. 77, 547–558. https://doi.org/10.1124/mol.109.060111

Yip, R.G., Boylan, M.O., Kieffer, T.J., Wolfe, M.M., 1998. Functional GIP receptors are present on adipocytes. Endocrinology 139, 4004–4007. https://doi.org/10.1210/endo.139.9.6288

Young, H.W.J., Molina, J.G., Dimina, D., Zhong, H., Jacobson, M., Chan, L.-N.L., Chan, T.-S., Lee, J.J., Blackburn, M.R., 2004. A3 adenosine receptor signaling contributes to airway inflammation and mucus production in adenosine deaminase-deficient mice. J. Immunol. Baltim. Md 1950 173, 1380–1389. https://doi.org/10.4049/jimmunol.173.2.1380

Yu, J., Zhou, Y., Tanaka, I., Yao, M., 2010. Roll: a new algorithm for the detection of protein pockets and cavities with a rolling probe sphere. Bioinforma. Oxf. Engl. 26, 46–52. https://doi.org/10.1093/bioinformatics/btp599

Yuan, S., Vogel, H., Filipek, S., 2013. The Role of Water and Sodium Ions in the Activation of the μ-Opioid Receptor. Angew. Chem. Int. Ed. 52, 10112–10115. https://doi.org/10.1002/anie.201302244

Yuliantie, E., Darbalaei, S., Dai, A., Zhao, P., Yang, D., Sexton, P.M., Wang, M.-W., Wootten, D., 2020. Pharmacological characterization of mono-, dual- and tri-peptidic agonists at GIP and GLP-1 receptors. Biochem. Pharmacol. 177, 114001. https://doi.org/10.1016/j.bcp.2020.114001

Zhang, D., Zhao, Q., Wu, B., 2015. Structural Studies of G Protein-Coupled Receptors. Mol. Cells 38, 836–842. https://doi.org/10.14348/molcells.2015.0263

Zhang, K., Zhang, J., Gao, Z.-G., Zhang, D., Zhu, L., Han, G.W., Moss, S.M., Paoletta, S., Kiselev, E., Lu, W., Fenalti, G., Zhang, W., Müller, C.E., Yang, H., Jiang, H., Cherezov, V., Katritch, V., Jacobson, K.A., Stevens, R.C., Wu, B., Zhao, Q., 2014. Structure of the human P2Y12 receptor in complex with an antithrombotic drug. Nature 509, 115–118. https://doi.org/10.1038/nature13083

Zhang, X., Dong, S., Xu, F., 2018. Structural and Druggability Landscape of Frizzled G Protein-Coupled Receptors. Trends Biochem. Sci. 43, 1033–1046. https://doi.org/10.1016/j.tibs.2018.09.002

Zhang, Y., Sun, B., Feng, D., Hu, H., Chu, M., Qu, Q., Tarrasch, J.T., Li, S., Sun Kobilka, T., Kobilka, B.K., Skiniotis, G., 2017. Cryo-EM structure of the activated GLP-1 receptor in complex with a G protein. Nature 546, 248–253. https://doi.org/10.1038/nature22394

Zhao, F., Zhang, C., Zhou, Q., Hang, K., Zou, X., Chen, Y., Wu, F., Rao, Q., Dai, A., Yin, W., Shen, D.-D., Zhang, Y., Xia, T., Stevens, R.C., Xu, H.E., Yang, D., Zhao, L., Wang, M.-W., 2021a. Structural insights into hormone recognition by the human glucose-dependent insulinotropic polypeptide receptor. eLife 10, e68719. https://doi.org/10.7554/eLife.68719

Zhao, F., Zhou, Q., Cong, Z., Hang, K., Zou, X., Zhang, C., Chen, Y., Dai, A., Liang, A., Ming, Q., Wang, M., Chen, L., Xu, P., Chang, R., Feng, W., Xia, T., Zhang, Y., Wu, B., Yang, D., Zhao, L., Xu, H.E., Wang, M.-W., 2021b. Structural basis for the therapeutic advantage of dual and triple agonists at the human GIP, GLP-1 or GCG receptors. https://doi.org/10.1101/2021.07.29.454286

Zhao, F., Zhou, Q., Cong, Z., Hang, K., Zou, X., Zhang, C., Chen, Y., Dai, A., Liang, A., Ming, Q., Wang, M., Chen, L.-N., Xu, P., Chang, R., Feng, W., Xia, T., Zhang, Y., Wu, B., Yang, D., Zhao, L., Xu, H.E., Wang, M.-W., 2022. Structural insights into multiplexed pharmacological actions of tirzepatide and peptide 20 at the GIP, GLP-1 or glucagon receptors. Nat. Commun. 13, 1057. https://doi.org/10.1038/s41467-022-28683-0

Zhong, H., Shlykov, S.G., Molina, J.G., Sanborn, B.M., Jacobson, M.A., Tilley, S.L., Blackburn, M.R., 2003. Activation of murine lung mast cells by the adenosine A3 receptor. J. Immunol. Baltim. Md 1950 171, 338–345. https://doi.org/10.4049/jimmunol.171.1.338

Zhong, Q., Itokawa, T., Sridhar, S., Ding, K.-H., Xie, D., Kang, B., Bollag, W.B., Bollag, R.J., Hamrick, M., Insogna, K., Isales, C.M., 2007. Effects of glucose-dependent insulinotropic peptide on osteoclast function. Am. J. Physiol.-Endocrinol. Metab. 292, E543–E548. https://doi.org/10.1152/ajpendo.00364.2006

Zhou, X.E., He, Y., Waal, P.W. de, Gao, X., Kang, Y., Eps, N.V., Yin, Y., Pal, K., Goswami, D., White, T.A., Barty, A., Latorraca, N.R., Chapman, H.N., Hubbell, W.L., Dror, R.O., Stevens, R.C., Cherezov, V., Gurevich, V.V., Griffin, P.R., Ernst, O.P., Melcher, K., Xu, H.E., 2017. Identification of Phosphorylation Codes for Arrestin Recruitment by G Protein-Coupled Receptors. Cell 170, 457-469.e13. https://doi.org/10.1016/j.cell.2017.07.002

Zhou, Z., Felts, A.K., Friesner, R.A., Levy, R.M., 2007. Comparative performance of several flexible docking programs and scoring functions: enrichment studies for a diverse set of pharmaceutically relevant targets. J. Chem. Inf. Model. 47, 1599–1608. https://doi.org/10.1021/ci7000346

Zhu, C.-B., Steiner, J.A., Munn, J.L., Daws, L.C., Hewlett, W.A., Blakely, R.D., 2007. Rapid Stimulation of Presynaptic Serotonin Transport by A3 Adenosine Receptors. J. Pharmacol. Exp. Ther. 322, 332–340. https://doi.org/10.1124/jpet.107.121665

Zhuo, Y., Vishnivetskiy, S.A., Zhan, X., Gurevich, V.V., Klug, C.S., 2014. Identification of Receptor Binding-induced Conformational Changes in Non-visual Arrestins *. J. Biol. Chem. 289, 20991–21002. https://doi.org/10.1074/jbc.M114.560680

Zvelebil, M.J., Barton, G.J., Taylor, W.R., Sternberg, M.J., 1987. Prediction of protein secondary structure and active sites using the alignment of homologous sequences. J. Mol. Biol. 195, 957–961. https://doi.org/10.1016/0022-2836(87)90501-8

Appendix 1. Suchankova, et al. 2021

This appendix contains:

Suchankova, A., Harris, M., Ladds, G., 2021. Chapter 1 - Measuring the rapid kinetics of receptor-ligand interactions in live cells using NanoBRET, in: Shukla, A.K. (Ed.), Methods in Cell Biology, Biomolecular Interactions Part A. Academic Press, pp. 1–14. https://doi.org/10.1016/bs.mcb.2021.06.013

Chapter 1 (Measuring the rapid kinetics of receptor-ligand interactions in live cells using NanoBRET) is removed for copyright reasons. Copyright holder is Elsevier Inc.

Chapter 1 (Measuring the rapid kinetics of receptor-ligand interactions in live cells using NanoBRET) is removed for copyright reasons. Copyright holder is Elsevier Inc.

Chapter 1 (Measuring the rapid kinetics of receptor-ligand interactions in live cells using NanoBRET) is removed for copyright reasons. Copyright holder is Elsevier Inc.

Chapter 1 (Measuring the rapid kinetics of receptor-ligand interactions in live cells using NanoBRET) is removed for copyright reasons. Copyright holder is Elsevier Inc.

Chapter 1 (Measuring the rapid kinetics of receptor-ligand interactions in live cells using NanoBRET) is removed for copyright reasons. Copyright holder is Elsevier Inc.

Chapter 1 (Measuring the rapid kinetics of receptor-ligand interactions in live cells using NanoBRET) is removed for copyright reasons. Copyright holder is Elsevier Inc.

Chapter 1 (Measuring the rapid kinetics of receptor-ligand interactions in live cells using NanoBRET) is removed for copyright reasons. Copyright holder is Elsevier Inc.

Chapter 1 (Measuring the rapid kinetics of receptor-ligand interactions in live cells using NanoBRET) is removed for copyright reasons. Copyright holder is Elsevier Inc.

Chapter 1 (Measuring the rapid kinetics of receptor-ligand interactions in live cells using NanoBRET) is removed for copyright reasons. Copyright holder is Elsevier Inc.

Chapter 1 (Measuring the rapid kinetics of receptor-ligand interactions in live cells using NanoBRET) is removed for copyright reasons. Copyright holder is Elsevier Inc.

Chapter 1 (Measuring the rapid kinetics of receptor-ligand interactions in live cells using NanoBRET) is removed for copyright reasons. Copyright holder is Elsevier Inc.

Chapter 1 (Measuring the rapid kinetics of receptor-ligand interactions in live cells using NanoBRET) is removed for copyright reasons. Copyright holder is Elsevier Inc.

Chapter 1 (Measuring the rapid kinetics of receptor-ligand interactions in live cells using NanoBRET) is removed for copyright reasons. Copyright holder is Elsevier Inc.

Chapter 1 (Measuring the rapid kinetics of receptor-ligand interactions in live cells using NanoBRET) is removed for copyright reasons. Copyright holder is Elsevier Inc.

Appendix 2. Wall, et al. 2022

This appendix contains:

Wall, M.J., Hill, E., Huckstepp, R., Barkan, K., Deganutti, G., Leuenberger, M., Preti, B., Winfield, I., Carvalho, S., **Suchankova, A.**, Wei, H., Safitri, D., Huang, X., Imlach, W., La Mache, C., Dean, E., Hume, C., Hayward, S., Oliver, J., Zhao, F.-Y., Spanswick, D., Reynolds, C.A., Lochner, M., Ladds, G., Frenguelli, B.G., 2022. Selective activation of Gαob by an adenosine A1 receptor agonist elicits analgesia without cardiorespiratory depression. Nat. Commun. 13, 4150. https://doi.org/10.1038/s41467-022-31652-2

nature COMMUNICATIONS

ARTICLE

Check for updates

OPEN

Selective activation of Gαob by an adenosine A_1 receptor agonist elicits analgesia without cardiorespiratory depression

Mark J. Wall[1,10✉], Emily Hill[1,10], Robert Huckstepp[1,10], Kerry Barkan[2,10], Giuseppe Deganutti[3,4,10], Michele Leuenberger[5,10], Barbara Preti[5,10], Ian Winfield[2,10], Sabrina Carvalho[2], Anna Suchankova[2], Haifeng Wei[6], Dewi Safitri[2,7], Xianglin Huang[2], Wendy Imlach[8], Circe La Mache[1], Eve Dean[1], Cherise Hume[1], Stephanie Hayward[1], Jess Oliver[1], Fei-Yue Zhao[6], David Spanswick[6,8,9], Christopher A. Reynolds[3,4], Martin Lochner[5], Graham Ladds[2✉] & Bruno G. Frenguelli[1✉]

The development of therapeutic agonists for G protein-coupled receptors (GPCRs) is hampered by the propensity of GPCRs to couple to multiple intracellular signalling pathways. This promiscuous coupling leads to numerous downstream cellular effects, some of which are therapeutically undesirable. This is especially the case for adenosine A_1 receptors (A_1Rs) whose clinical potential is undermined by the sedation and cardiorespiratory depression caused by conventional agonists. We have discovered that the A_1R-selective agonist, benzyloxy-cyclopentyladenosine (BnOCPA), is a potent and powerful analgesic but does not cause sedation, bradycardia, hypotension or respiratory depression. This unprecedented discrimination between native A_1Rs arises from BnOCPA's unique and exquisitely selective activation of Gob among the six Gαi/o subtypes, and in the absence of β-arrestin recruitment. BnOCPA thus demonstrates a highly-specific Gα-selective activation of the native A_1R, sheds new light on GPCR signalling, and reveals new possibilities for the development of novel therapeutics based on the far-reaching concept of selective Gα agonism.

[1] School of Life Sciences, University of Warwick, Gibbet Hill Rd, Coventry CV4 7AL, UK. [2] Department of Pharmacology, University of Cambridge, Tennis Court Road, Cambridge CB2 1PD, UK. [3] Centre for Sport, Exercise and Life Sciences (CSELS), Faculty of Health and Life Sciences, Coventry University, Coventry CV1 2DS, UK. [4] School of Biological Sciences, University of Essex, Wivenhoe Park, Colchester CO4 3SQ, UK. [5] Institute of Biochemistry and Molecular Medicine, University of Bern, 3012 Bern, Switzerland. [6] NeuroSolutions Ltd, Coventry, UK. [7] Pharmacology and Clinical Pharmacy Research Group, School of Pharmacy, Bandung Institute of Technology, Bandung 40132, Indonesia. [8] Department of Physiology, Monash Biomedicine Discovery Institute, Monash University, Innovation Walk, Clayton, VIC 3800, Australia. [9] Warwick Medical School, University of Warwick, Gibbet Hill Rd, Coventry CV4 7AL, UK. [10] These authors contributed equally: Mark J. Wall, Emily Hill, Robert Huckstepp, Kerry Barkan, Giuseppe Deganutti, Michele Leuenberger, Barbara Preti, Ian Winfield. ✉email: mark.wall@warwick.ac.uk; grl30@cam.ac.uk; b.g.frenguelli@warwick.ac.uk

protein-coupled receptors (GPCRs) are the targets of many FDA-approved drugs[1,2]. However, the promiscuity with which they couple to multiple G protein- and β-arrestin-activated intracellular signalling cascades leads to unwanted side effects. These side effects limit both the range of GPCRs suitable for drug-targeting, and the number of conditions for which treatments could be developed[3,4]. One family of GPCRs that have particularly suffered as drug targets from their promiscuous coupling and wide-ranging cellular actions are the four GPCRs for the purine nucleoside adenosine, despite the potential for using adenosine receptor agonists to treat many pathological conditions including cancer, and various cardiovascular, neurological and inflammatory diseases[5–7]. For example, activation of the widely-distributed adenosine A_1 receptor (A_1R) with currently available agonists elicits multiple actions in both the central nervous system (CNS) and the cardiorespiratory system. In the CNS A_1Rs inhibit synaptic transmission, induce neuronal hyperpolarization, reduce seizure activity and cause sedation, while in the cardiorespiratory system A_1Rs slow the heart (bradycardia), and contribute to reducing blood pressure (hypotension), and depress respiration (dyspnoea)[7–12]. These multiple effects severely limit the prospects of A_1R agonists as life-changing medicines, despite their potential use in a wide range of clinical conditions, such as glaucoma, type 2 diabetes mellitus, pain, epilepsy and cerebral ischaemia[7,13–16], and in which there are clear unmet clinical needs that could be addressed with novel therapeutics.

The therapeutic limitations of promiscuous GPCR coupling might be overcome through the development of biased agonists—compounds that preferentially recruit one intracellular signalling cascade over another[4,17,18]. This signalling bias has most frequently been expressed in terms of Gα vs β-arrestin signalling[19] and has been pursued at a variety of receptors[20,21], for example, at the angiotensin II type 1 receptor (AT1R)[22], and at neurotensin receptors in the treatment of drug addiction[23]. Agonist bias has been sought in the context of opioid receptors, but with some controversy[24], for compounds producing analgesia with reduced respiratory depression, gastrointestinal disturbance and tolerance[4].

However, while other forms of bias exist, including between individual Gα subunits[17,25,26], the challenge remains in translating GPCR signalling bias observed in vitro to tangible, and physiologically- and clinically-relevant, selectivity at native receptors in vivo[3,4,27,28]. Accordingly, while the potential to preferentially drive the G protein-coupling of A_1Rs has been described in several in vitro studies[29–32], to date no A_1R-specific agonist has been reported that can elicit biased Gα agonism at native A_1Rs in intact physiological systems, let alone the selective activation of one Gα subunit. To achieve such selectivity among Gα subunits would introduce novel therapeutic opportunities across a wide range of debilitating clinical conditions.

Here we show, utilising molecular dynamics (MD) simulations, and Gαi/o subunit- and β-arrestin-specific cellular signalling assays, how one A_1R-selective agonist, BnOCPA[33,34], fulfils the criteria for a selective Gα agonist in exclusively activating Gob among the six members of the Gαi/o family of G protein subunits, and in the absence of β-arrestin recruitment. In addition, through a combination of CNS electrophysiology, physiological recordings of cardiorespiratory parameters, a sensitive assay of attention and locomotor function, and the use of a clinically-relevant model of chronic neuropathic pain, we demonstrate selective activation of native A_1Rs and the delivery of potent analgesia without sedation, motor impairment or cardiorespiratory depression. Our data thus demonstrate the translation of agonist Gα selectivity in vitro to therapeutically tangible clinically-relevant observations in vivo. Such observations reveal the possibility of achieving Gα selectivity at native receptors, highlight the physiological benefits of such selectivity, and specifically speak to the possibility of unlocking the widespread clinical potential of A_1R agonists.

Results

The novel A_1R agonist BnOCPA exquisitely discriminates between native pre- and postsynaptic A_1Rs in the intact mammalian CNS. BnOCPA (Fig. 1a), a molecule first described in a patent as a potential treatment for glaucoma or ocular hypertension[34], is a cyclopentyl derivative of adenosine and a highly selective and potent, full agonist at human adenosine A_1Rs (hA_1Rs; Fig. 1b; Supplementary Table 1)[33]. Our characterisation of BnOCPA, synthesised independently as part of a screen for suitable scaffolds for the generation of fluorescent ligands for the A_1R, began with an exploration of the binding characteristics of BnOCPA at the hA_1R using classical radioligand binding (where the antagonist [^{3}H]DPCPX was used as a tracer), and a NanoBRET agonist binding assay (using a novel NECA-TAMRA compound, which acts as a full agonist (pEC_{50} −7.23 ± 0.13; See Methods). Using both assays we observed that BnOCPA was able to bind to the hA_1R with an affinity equal to that of the prototypical A_1R agonists CPA and NECA, and higher than that of the endogenous agonist adenosine (Fig. 1b; Supplementary Table 1). Significantly, using NECA-TAMRA as the fluorescent agonist tracer, the high-affinity state of the biphasic binding profile observed in the NanoBRET assay was equivalent to that reported previously for BnOCPA (3.8 nM compared to 1.7 nM[34]).

These initial pharmacological studies at recombinant hA_1Rs in cell lines did not reveal anything extraordinary about BnOCPA. However, when we investigated BnOCPA at native A_1Rs in rat hippocampal slices, against which BnOCPA is also a potent agonist, with ~8000- and >150-fold greater efficacy at rat A_1Rs (rA_1Rs) than at rat $A_{2A}Rs$ ($rA_{2A}Rs$) and A_3Rs (rA_3Rs), respectively (Supplementary Table 2), we discovered properties of BnOCPA that were not consistent with those of typical A_1R agonists such as adenosine, CPA and NECA. In accordance with the effects of standard A_1R agonists, BnOCPA potently inhibited excitatory synaptic transmission in rat hippocampal slices (IC_{50} ~65 nM; Fig. 1c–g and Supplementary Fig. 1a–d). This effect was attributable to the activation of native presynaptic A_1Rs on glutamatergic terminals[9] (Fig. 1c; Supplementary Fig. 1e, f), and cannot be attributed to any action of BnOCPA at A_3Rs since even a high concentration (1 μM) of the potent and selective A_3R agonist 2-Cl-IB-MECA[35] had no effect on synaptic transmission (Supplementary Fig. 1g, h). However, in stark contrast to adenosine and CPA, BnOCPA did not activate postsynaptic A_1Rs (Fig. 1c) to induce membrane hyperpolarisation, even at concentrations 15 times the IC_{50} for the inhibition of synaptic transmission (Fig. 1h, i).

This peculiar and unique discrimination between pre- and postsynaptic A_1Rs might possibly be explained in terms of either some hindrance in the binding of BnOCPA to A_1Rs on postsynaptic neurones, or, and unprecedented for an A_1R agonist, binding to the postsynaptic A_1R, but without the ability to activate the receptor. To test the latter hypothesis—that BnOCPA actually bound to postsynaptic A_1Rs, but without efficacy—we reasoned that BnOCPA might behave in a manner analogous to a receptor antagonist in preventing or reversing activation by other A_1R agonists, a property that has been predicted and observed for biased agonists at other receptors[17,27]. To test this, we pre-applied BnOCPA and then applied CPA (in the continued presence of BnOCPA). Remarkably, the co-application of CPA and BnOCPA resulted in a significant reduction of the effects of CPA on membrane potential (Fig. 1i; Supplementary Fig. 2a, b). In addition, membrane hyperpolarisation induced by the endogenous

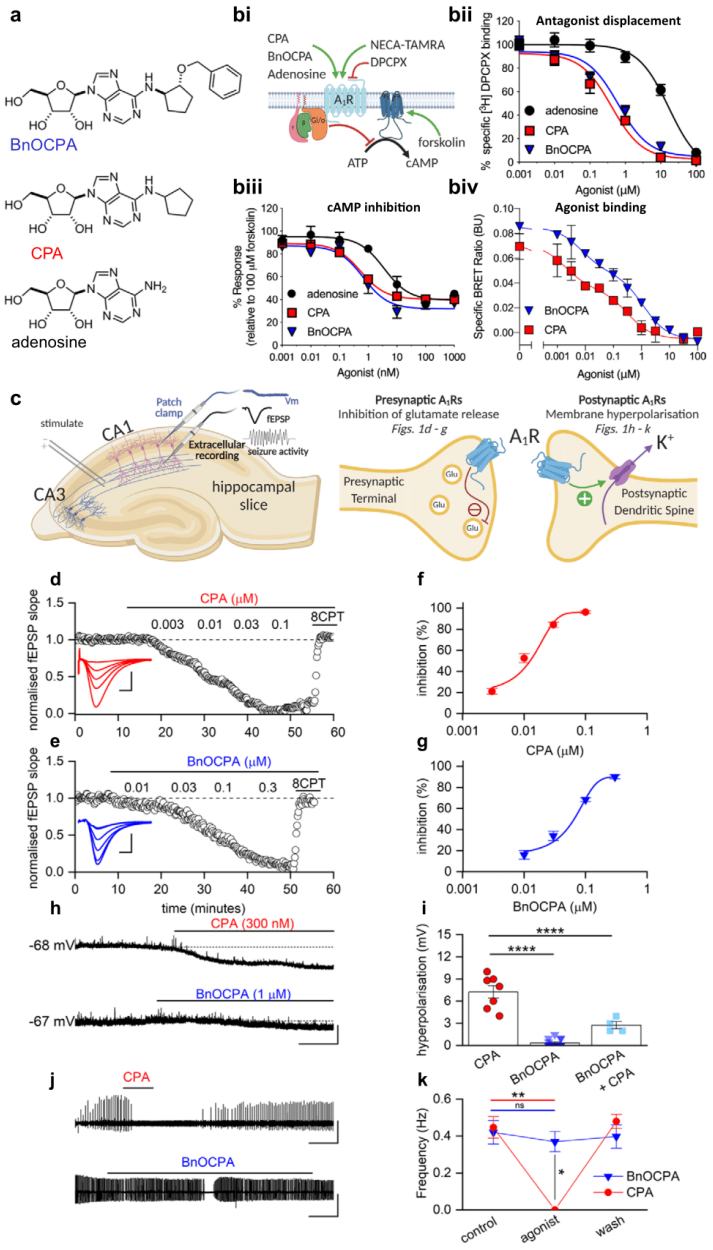

agonist adenosine was reversed by BnOCPA (Supplementary Fig. 2c). In contrast, the A_3R agonist 2-Cl-IB-MECA had no effect on membrane potential and did not interfere with the membrane hyperpolarisation caused by adenosine (Supplementary Fig. 2d, e), further reaffirming the actions of BnOCPA as being selectively mediated by A_1Rs.

To test whether the inability of BnOCPA to affect membrane potential was a trivial action due to BnOCPA blocking K^+ channels mediating the postsynaptic hyperpolarisation, or in some other way non-specifically interfering with G protein signalling, we applied the $GABA_B$ receptor agonist baclofen to CA1 pyramidal neurons. BnOCPA had no effect on membrane

Fig. 1 BnOCPA is an A_1R agonist that discriminates between pre- and postsynaptic A_1Rs in the CNS. a Chemical structures of adenosine, CPA and BnOCPA[33]. **bi** Schematic representing assays used to characterise the affinity and efficacy of agonists (green arrows) to the human (h) A_1R. **bii** agonist displacement of [^{3}H]DPCPX, a selective antagonist for the hA_1R ($n = 5$–10 individual repeats). **biii** cAMP levels measured in CHO-K1-hA_1R cells following co-stimulation with 1 μM forskolin and each agonist ($n = 4$–10 individual repeats). **biv** Both CPA and BnOCPA displace the fluorescent AR agonist NECA-TAMRA in a biphasic manner indicating that both agonists display high affinity and low affinity binding ($n = 4$ individual repeats). **c** Diagram illustrating: left, hippocampal slice preparation showing position of stimulating, patch-clamp and extracellular recording electrodes together with representative electrophysiological recordings: membrane potential (Vm), a fEPSP (field excitatory postsynaptic potential) and seizure activity; right, pre- and postsynaptic A_1Rs at hippocampal synapses and their physiological effects upon activation. **d**, **e** Increasing concentrations of CPA or BnOCPA reduced the fEPSP, an effect reversed by the A_1R antagonist 8-CPT (2 μM). Inset, superimposed fEPSP averages in control (largest fEPSP) and becoming smaller with increasing concentrations of CPA or BnOCPA. Scale bars measure 0.2 mV or 0.1 mV and 5 ms for CPA and BnOCPA, respectively. **f**, **g** Concentration-response curves for the inhibition of synaptic transmission by CPA ($IC_{50} = 11.8 \pm 2.7$ nM; $n = 17$ slices) or BnOCPA ($IC_{50} = 65 \pm 0.3$ nM; $n = 11$ slices). **h** CPA hyperpolarised the membrane potential while BnOCPA had little effect. Scale bars measure 4 mV and 30 s. **i** Summary data for membrane potential changes. The mean hyperpolarisation produced by CPA (300 nM; 7.26 ± 0.86 mV, $n = 7$ cells) was significantly different (one-way ANOVA; $F(2,23) = 70.46$; $P = 1.55 \times 10^{-10}$) from that produced by BnOCPA (300 nM or 1 μM; 0.33 ± 0.14 mV, $n = 10$ and 5 cells, respectively; $P = 8.26 \times 10^{-11}$) and for CPA (300 nM) applied in the presence of BnOCPA (300 nM; 2.75 ± 0.48 mV, $n = 4$ cells, $P = 2.89 \times 10^{-5}$; See Supplementary Fig. 2a for an example trace). **j** In an in vitro model of seizure activity, represented as frequent spontaneous spiking from baseline, CPA (300 nM) reversibly blocked activity while BnOCPA (300 nM) had little effect. Scale bars measure 0.5 mV and 200 s. **k** Summary data for seizure activity expressed in terms of the frequency of spontaneous spiking before, during and after CPA or BnOCPA. CPA abolished seizure activity ($n = 4$) whereas BnOCPA did not significantly reduce seizure frequency ($n = 6$). Data represented as mean ± SEM; Two-way RM ANOVA (BnOCPA vs CPA slices): $F(1, 3) = 186.11$, $P = 8.52 \times 10^{-4}$ with the following Bonferroni post hoc comparisons: BnOCPA vs Control; $P = 1$; CPA vs control; $P = 0.010$; BnOCPA vs CPA; $P = 0.027$. Averaged data are presented as mean ± SEM. ns, not significant; *, $P < 0.05$; **, $P < 0.02$; ****, $P < 0.0001$. Source data are provided as a Source Data file.

hyperpolarisation produced by baclofen (Supplementary Fig. 2f, g), confirming that the actions of BnOCPA were specific to the A_1R. These observations, of a lack of effect of BnOCPA on postsynaptic membrane potential, likely explained why, in a model of seizure activity, (low Mg^{2+}/high K^+), with prominent postsynaptic depolarisation that promotes neuronal firing, BnOCPA had little effect (Fig. 1j, k). In contrast, equivalent concentrations of CPA completely suppressed neuronal firing (Fig. 1j, k).

BnOCPA demonstrates unique Gα signalling in the selective activation of Gob. The observation that BnOCPA discriminated between pre- and postsynaptic A_1Rs might be explained if these receptors were to activate different intracellular pathways to mediate their effects, and that BnOCPA was not able to activate the pathway responsible for postsynaptic membrane hyperpolarisation. To test whether the actions of BnOCPA and the prototypical A_1R agonists were mediated via β-arrestins (β-arrestin1 and β-arrestin2), we used a BRET assay[36–40] for β-arrestin recruitment (Supplementary Fig. 3). We observed no β-arrestin recruitment at the A_1R using either BnOCPA, CPA or adenosine, regardless of whether β-arrestin1 or β-arrestin2 was expressed (Supplementary Fig. 3). This was in contrast to β-arrestin2 recruitment by the A_3R in response to adenosine and NECA, but not BnOCPA (Supplementary Fig. 3). Moreover, the lack of recruitment of β-arrestin1 and β-arrestin2 by the A_1R was independent of any of the six G protein receptor kinase (GRK) isoforms co-expressed with β-arrestin1 and β-arrestin2; only low levels of recruitment were observed even when GRKs were highly (five-fold) overexpressed compared to the levels in the A_3R assays (Supplementary Fig. 4). These observations of a lack of β-arrestin recruitment by A_1Rs are consistent with those previously reported for recombinant A_1Rs expressing native sequences[41–45], and are likely due to the absence of serine and threonine residues in the A_1R cytoplasmic tail, which makes the A_1R intrinsically biased against β-arrestin signalling[19,46]. Accordingly, the differential actions of BnOCPA at pre- and postsynaptic A_1Rs are more likely to reside in selective activation of one Gα-mediated pathway over another.

To investigate whether BnOCPA has the ability to discriminate between the various Gαi/o subunits activated by adenosine, we generated a recombinant cell system (CHO-K1 cells) expressing both the hA_1R and individual pertussis toxin (PTX)-insensitive variants of individual Gαi/o subunits. Against these individual Gαi/o subunits we tested adenosine, CPA, NECA, BnOCPA, and the agonist HOCPA[33,47], a stereoisomer of GR79236[48,49], which behaved similarly to adenosine and CPA in both inhibiting synaptic transmission and causing membrane hyperpolarisation (Supplementary Fig. 5). In cells treated with PTX to inhibit endogenous Gαi/o[30,33] we observed that adenosine, CPA, NECA and HOCPA activated a range of Gαi/o subunits. Common to all of these agonists was the activation of both Gαo isoforms, Goa and Gob, with differential activation of Gi1 (HOCPA), Gi2 (NECA, CPA) and Gz (adenosine; Fig. 2a–e; Supplementary Figs. 5 and 6). Such promiscuous and biased Gα coupling has been described previously for adenosine, CPA, and NECA at recombinant A_1Rs in cell lines[29,50], including using novel BRET-based assays for adenosine at some Gαi/o[51]. These previous observations are in keeping with ours, confirming the validity of the PTX-based approach. In stark contrast, BnOCPA displayed a unique and highly distinctive Gαi/o subunit activation profile: BnOCPA was not able to activate Gi1, Gi2, Gi3 or Gz, and was furthermore capable of discriminating between the two Gαo isoforms via the selective activation of Gob, and not of Goa (Fig. 2a–e; Supplementary Fig. 6).

The selective and unique activation of Gob among the six Gαi/o subunits by BnOCPA could be observed in a comparison of the activation of Goa and Gob by the native and selective A_1R agonists in their ability to inhibit the forskolin-stimulated accumulation of cAMP (Fig. 2f). Whereas adenosine, CPA and HOCPA activated both Goa and Gob to inhibit cAMP accumulation, BnOCPA selectively activated Gob, with no discernible activation of Goa. Further quantification of this Gα selectivity, through the application of the operational model of receptor agonism[52–54] to remove potential issues of system bias, confirmed selective activation of Gob by BnOCPA, with no detectable response at Goa (Fig. 2g). As further validation of the ability of BnOCPA to discriminate between the activation of Goa and Gob, we took advantage of BRET assays of GPCR activation[55,56], which utilise a reduction in a Gα-Gβγ BRET signal to infer agonist-induced G protein activation, including for Goa and Gob[57] (Fig. 2h; Supplementary Fig. 7a). Using the TRUPATH GPCR BRET assay[55], adenosine, CPA, and HOCPA

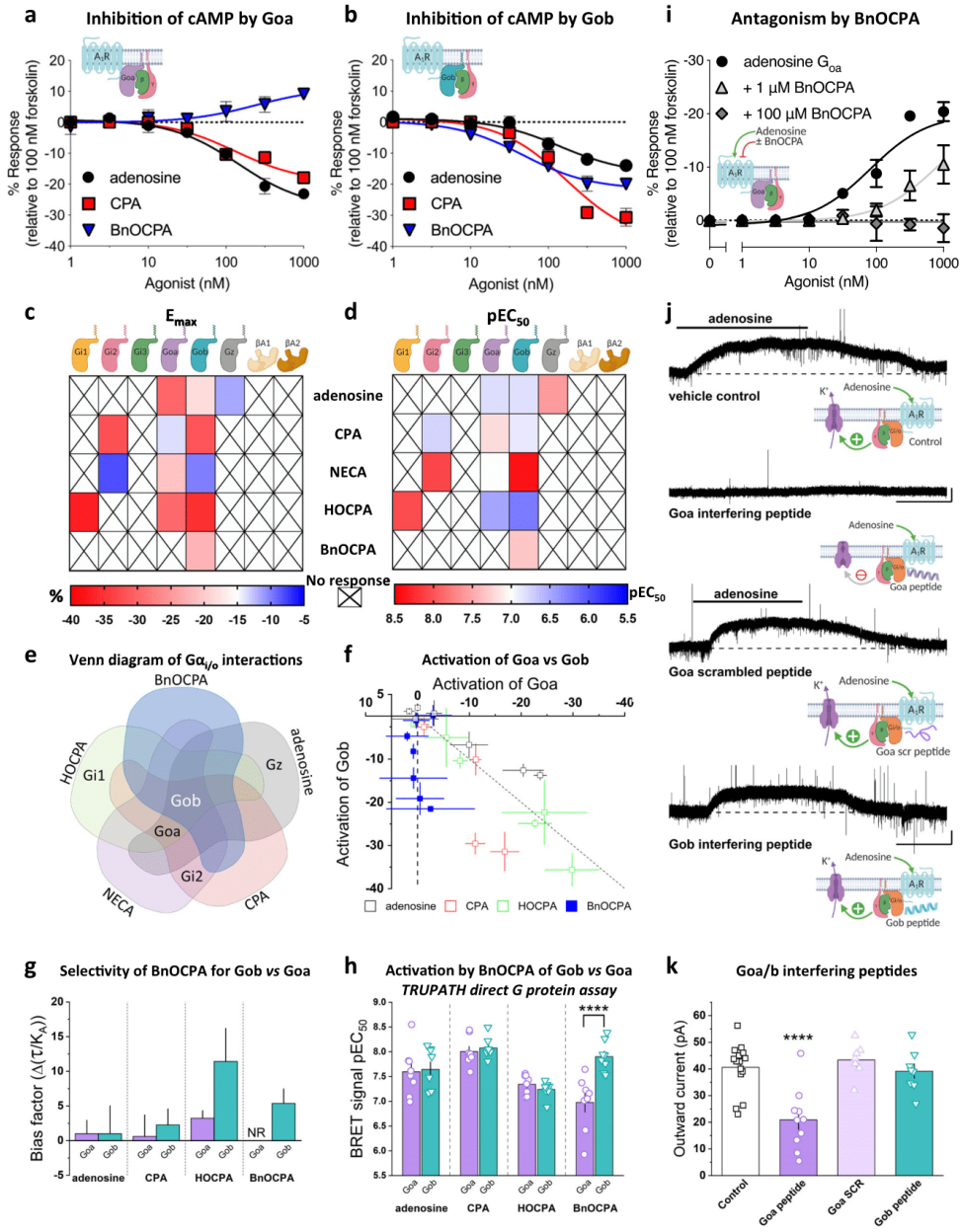

elicited equipotent activation of both Goa and Gob. In stark contrast to these agonists, BnOCPA was >10-fold more efficacious in activating Gob than Goa, and, of all the agonists tested, BnOCPA displayed the weakest potency at Goa. While subtle differences between the Goa and Gob response exist across the two very different in vitro assays, these data nonetheless confirm that BnOCPA demonstrates a previously unprecedented ability for an A_1R agonist to discriminate between Gα subtypes, and in particular between Goa and Gob.

To establish the functional implications of BnOCPA's profound selectivity for Gob over Goa, we hypothesised that BnOCPA should reduce the actions of adenosine on the

Fig. 2 BnOCPA selectively activates Gob. a cAMP accumulation in PTX-pre-treated CHO-K1-hA_1R cells expressing PTX-insensitive Goa following co-stimulation with 1 μM forskolin and each agonist (1 nM–1 μM; $n = 6$ individual repeats). **b** as for **a** but cells were transfected with PTX-insensitive Gob ($n = 6$ individual repeats). Stimulation of cAMP production in **a** reflects BnOCPA's activation of endogenous, PTX-resistant Gs by the A_1R (see Supplementary Figs. 5 and 6 and[29,153,154]). **c**, **d** Heatmaps summarising E_{max} (**c %**) and potency (**d** pEC_{50}; −log [agonist concentration] required for 50% inhibition of cAMP accumulation) for individual Gα subunit and β-arrestin1 and 2 activation by selective A_1R agonists for the inhibition of forskolin-stimulated cAMP production. Data taken from: adenosine, CPA, BnOCPA Fig. 1, Supplementary Figs. 3, 6; NECA, Supplementary Fig. 3, 6; HOCPA, Supplementary Fig. 5. **e** Venn diagram of agonist interactions with individual Gαo/i subunits. **f** The inhibition of cAMP accumulation via A_1R:Goa or A_1R:Gob by adenosine, CPA, HOCPA and BnOCPA. Each data point represents a concentration of agonist from the data in Supplementary Figs. 5 and 6. Line of unity (broken grey line) represents no bias. Data presented as mean ± SEM. **g** Signalling bias of A_1R-selective agonists for A_1R-Goa and A_1R-Gob (Δ(τ/KA)) was determined relative to the natural agonist adenosine using the change in (τ/KA) ratio. The values were calculated for all compounds at each individual G protein and the data was fitted globally to determine single values for τ and KA and then normalised to a reference agonist (adenosine). This approach, used by others[155], precludes the provision of individual data points. Compared to adenosine, BnOCPA elicits no measurable response (NR) at Goa. **h** The TRUPATH assay for direct G protein activation reveals no preference between Goa and Gob by adenosine, CPA or HOCPA, but a significant >10-fold greater activation of Gob *vs* Goa by BnOCPA (two-tailed unpaired Student's t-test; $P = 0.0009$; see also Supplementary Fig. 7a; $n = 8$ individual repeats for each agonist). **i** Adenosine/Goa-mediated inhibition of cAMP accumulation was antagonised by BnOCPA in a concentration-dependent manner ($n = 3$–4 individual repeats). **j** Example current traces produced by adenosine (10 μM) in control conditions or in the presence of intracellular Goa interfering peptide, scrambled Goa peptide or Gob interfering peptide (all at 100 μM). Scale bars measure 25 pA and 100 s. **k** Summary data of adenosine-induced outward current experiments. The mean amplitude of the outward current induced by adenosine (40.6 ± 2.2 pA, $n = 16$ cells) was significantly reduced (one-way ANOVA; $F(3,37)=12.40$, $P = 9.22 \times 10^{-6}$) to 20.9 ± 3.6 pA ($n = 10$ cells, $P = 2.65 \times 10^{-5}$) in 100 μM Goa interfering peptide. Neither the scrambled Goa peptide (Goa SCR; 43.4 ± 2.4 pA, $n = 7$ cells, $P = 1$) nor the Gob interfering peptide (39. 2 ± 2.7 pA, $n = 8$ cells, $P = 1$) reduced the amplitude of the adenosine-induced outward current compared to control, but each were significantly different from the Goa interfering peptide ($P = 8.20 \times 10^{-5}$; $P = 8.86 \times 10^{-4}$, respectively). Averaged data are presented as mean ± SEM. ****, $P < 0.0001$ relative to other groups. Source data are provided as a Source Data file.

inhibition of cAMP accumulation via Goa. This was indeed the case (Fig. 2i): BnOCPA antagonised the Goa-mediated inhibition of cAMP production by adenosine in a concentration-dependent manner. This classic attribute of an antagonist enabled a Schild analysis estimate of BnOCPA's affinity (Kd) to be 113 nM, with a pKd ~6.9[58], a value that was quantitatively similar to BnOCPA's ability to bind to the hA_1R (pK_i ~6.6; Fig. 1b). Importantly, this observation, of the ability of BnOCPA to antagonise the actions of adenosine on cAMP inhibition (Fig. 2i), revealed no agonist action of BnOCPA at Goa at concentrations up to 100 μM (>10^5 greater than the IC_{50} against cAMP accumulation; Fig. 1b and ~10^4 greater than the EC_{50} in the TRUPATH assay; Fig. 2h), and, moreover, had parallels with the antagonising effects of BnOCPA on membrane potential in the CNS (Fig. 1h, i; Supplementary Fig. 2a, c). These data suggest that BnOCPA has the unique ability of displaying both agonist and antagonist-like properties at both recombinant and native A_1Rs; properties that are expected of a truly Gα subunit-selective agonist.

The data from whole-cell patch-clamp recordings showed that BnOCPA did not influence neuronal membrane potential at native A_1Rs (Fig. 1h, i), while experiments in recombinant hA_1Rs showed that BnOCPA did not activate Goa (Fig. 2a, c–f), and indeed *prevented* the activation of Goa by adenosine (Fig. 2i). We thus predicted that A_1Rs in the hippocampus, where Goa is found at levels 10–15 times higher than Gob[59], should act via Goa to induce membrane hyperpolarisation, and thereby providing a potential explanation for the lack of effect of BnOCPA on membrane potential. To test this prediction, we injected a series of previously-validated interfering peptides against Goa and Gob[60–69] into CA1 pyramidal cells during whole-cell voltage-clamp recordings. Introduction of the Goa interfering peptide caused a significant attenuation of the adenosine-induced outward current (Fig. 2j, k). In contrast, neither the scrambled Goa peptide, nor the Gob peptide, which reduced the modulation of Ca^{2+} channels by muscarinic M_4 receptors in striatal cholinergic interneurons[63], had any effect on outward current amplitude (Fig. 2j, k). To confirm the specificity and potency of the interfering peptides used in hippocampal neurons, we transfected plasmids coding for the last 11 C-terminal amino acids of either Goa, Gob and the scrambled version of Goa, into the Goa and Gob vectors in the TRUPATH assay used in Fig. 2h (Supplementary Fig. 7b). The interfering peptides reduced the activation of their cognate G protein in a dose-dependent manner, but had no effect on the alternate Go isoform. The scrambled peptide sequence had no effect on Goa or Gob activation.

Thus, adenosine-mediated membrane potential hyperpolarisation occurs mainly through A_1R activation of Goa, in keeping with the high levels of expression of Goa *vs* Gob in the hippocampus[59], and with the observation that the Goa-activating agonists adenosine, CPA and HOCPA (Fig. 2c–e, Supplementary Figs. 5 and 6) all induced membrane hyperpolarisation (Fig. 1h, i; Supplementary Figs. 2 and 5). Moreover, the absence of an effect of adenosine on membrane potential in Gz knockout mice[70] argues against the possibility that the selective activation of Gz by adenosine observed in our PTX assays (Fig. 2c, d; Supplementary Fig. 6) contributes to membrane hyperpolarisation. The data from recombinant receptors demonstrating the inability of BnOCPA to activate Goa (Fig. 2a, c–g) thus explains why BnOCPA did not cause membrane hyperpolarisation, and indeed prevented or reversed the hyperpolarisation induced by CPA or adenosine, respectively (Fig. 1h, i; Supplementary Fig. 2a, c).

The Gα selectivity displayed by BnOCPA is reflected in non-canonical binding modes and selective interaction with Gαi/o subunits. To better understand the unusual signalling properties of BnOCPA and the highly specific Gα coupling to Gob, we carried out dynamic docking simulations to study the basic orthosteric binding mode of BnOCPA in an explicit, fully flexible environment using the active cryo-EM structure of the A_1R (PDB code 6D9H; Supplementary Movie 1). We previously reported that modifications at position N^6 of the adenine scaffold modulated the agonist binding path to A_1R[71]. More precisely, N^6-cyclopentyl analogues (CPA and HOCPA) markedly interact with the extracellular loop 2 (ECL2) compared to adenosine, while BnOCPA (which bears the N^6-cyclopentyl-2-benzyloxy group) is most prone to engage residues of the A_1R located at the top of transmembrane helix 1 (TM1) and TM7. In the present study, we compared the bound-state BnOCPA to the non-Gα selective

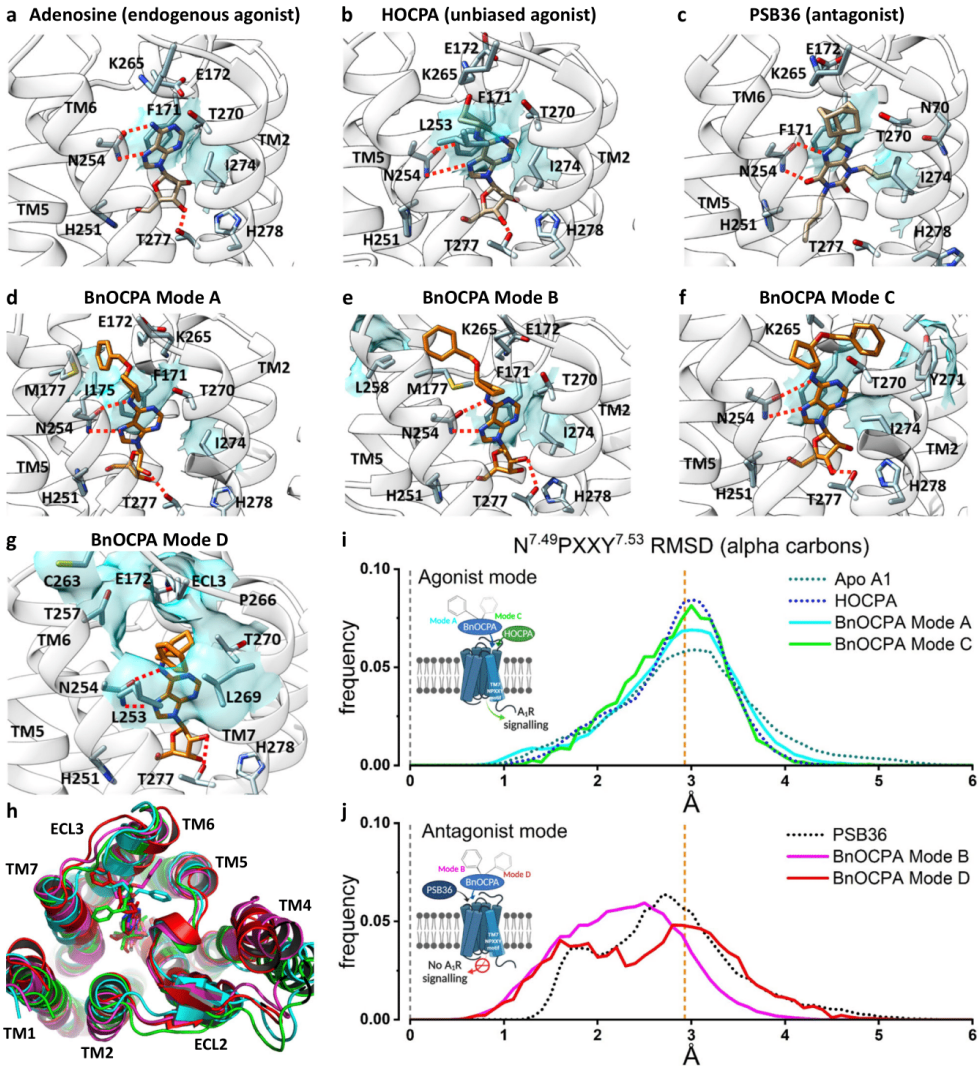

agonists adenosine and HOCPA, and an antagonist (PSB36) of the A_1R (Fig. 3a–c). BnOCPA engaged the receptor with the same fingerprint as adenosine[72] (Fig. 3a) and HOCPA (Fig. 3b, Supplementary Movie 2). Further explorations of the BnOCPA docked state using metadynamics (MetaD) simulations[73] revealed interchangeable variations on this fingerprint (namely Modes A, B, and C; Fig. 3d–f; Supplementary Fig. 8) that could be distinguished by the orientation of the BnOCPA-unique benzyl group. Having established the possible BnOCPA binding modes, we examined the respective contribution of the orthosteric agonists, the G protein α subunit α5 (C-terminal) helix (GαCT), and the Gα protein subunit[74,75] to the empirically-observed G protein selectivity displayed by BnOCPA (Fig. 2a–h, Supplementary Fig. 6).

Firstly, following Dror et al.[76], we compared the dynamics of the BnOCPA-bound A_1R with the corresponding dynamics of the receptor[77,78] bound to either HOCPA (Fig. 3b), the A_1R antagonist PSB36 (Fig. 3c), or the apo receptor in the absence of G protein, our hypothesis being that there may be ligand-dependent differences in the way that the intracellular region of the receptor responds in the absence of the G protein. In these simulations the G protein was omitted so that inactivation was possible and so that the results were not G protein-dependent. The BnOCPA binding Modes A–C were interchangeable during MD simulations (Table 1) but were associated with distinctly different dynamics, as monitored by changes in a structural hallmark of GPCR activation, the $N^{7.49}PXXY^{7.53}$ motif[79] (Supplementary Fig. 9). Given the high flexibility shown by the

Fig. 3 Molecular dynamics simulations reveal that BnOCPA binding modes can uniquely drive both agonist- and antagonist-like intracellular conformations of the A_1R. a Adenosine binding pose: N254$^{6.55}$ (Ballesteros-Weinstein superscript enumeration) is engaged in key hydrogen bonds, while important hydrophobic contacts are shown as cyan transparent surfaces (F171^{ECL2} and I274$^{7.39}$). **b** On the basis of structural similarities and the dynamic docking (Supplementary Movie 2), HOCPA was predicted to bind with a geometry analogous to adenosine; the cyclopentyl group makes further hydrophobic contacts with L253$^{6.54}$, as shown by simulation. **c** The xanthine scaffold of the antagonist PSB36 makes hydrogen bonds with N254$^{6.55}$ side chains and hydrophobic contacts with F171^{ECL2} and I274$^{7.39}$. **d** BnOCPA agonist-like binding Mode A (Supplementary Movie 1): the benzyl group orients towards the ECL2 and makes hydrophobic contacts with I175^{ECL2} (and M177$^{5.35}$) side chains. **e** BnOCPA antagonist-like binding Mode B: the benzyl group orients towards the top of TM5/TM6 and makes hydrophobic contacts with L258$^{6.59}$ side chain. **f** BnOCPA agonist-like binding Mode C: the benzyl group orients towards the top of TM7 and makes hydrophobic contacts with Y271$^{7.36}$ side chain. **g** Binding orientation of BnOCPA in antagonist-like Mode D: the benzyl group orients under ECL3 and occupies the hydrophobic pocket defined by L253$^{6.54}$, T257$^{6.58}$, T270$^{7.35}$, and L269$^{7.34}$. Key hydrogen bonds with N254$^{6.55}$ and T277$^{7.42}$ are shown as dotted lines; main hydrophobic contacts are highlighted as cyan transparent surfaces. **h** Extracellular view of the A_1R showing the four BnOCPA binding Modes A (cyan), B (magenta), C (green), and D (red) as randomly extracted from the MD simulations. **i, j** Root-mean-square deviation (RMSD) distributions considering the inactive N$^{7.49}$PXXY$^{7.53}$ motif on the distal part of TM7 as reference. **i** HOCPA (blue broken line), BnOCPA Mode A (cyan curve), BnOCPA Mode C (green curve) and the apo receptor (dark green broken line) have a common distribution centring around the active confirmation of the A_1R (orange broken line; Supplementary Fig. 9) leading to A_1R signalling. In contrast, **j** PSB36 (black broken line), BnOCPA Mode B (magenta curve) and BnOCPA Mode D (red curve) RMSD values have the tendency to move closer to the inactive N$^{7.49}$PXXY$^{7.53}$ geometry (leftward shift of the curves towards broken grey line at x = 0) preventing A_1R signalling.

BnOCPA benzyl group during the simulations and its lipophilic character, we hypothesised and simulated a further binding mode (namely Mode D) not explored during MD or MetaD simulations. This conformation involves a hydrophobic pocket underneath ECL3 (Fig. 3g) which is responsible for the A_1/A_{2A} selectivity[72]. Superimposition of the four BnOCPA binding Modes A–D reveals the highly motile nature of the benzyl group of BnOCPA (Fig. 3h) under the simulated conditions.

Quantification of the N$^{7.49}$PXXY$^{7.53}$ dynamics revealed that HOCPA, BnOCPA Mode A, BnOCPA Mode C and the apo receptor show a similar distribution of the RMSD of the conserved N$^{7.49}$PXXY$^{7.53}$ motif (Fig. 3i; Supplementary Fig. 9). In contrast, the non-canonical BnOCPA binding Modes B and D were responsible for a partial transition of the N$^{7.49}$PXXY$^{7.53}$ backbone from the active conformation to the inactive conformation (Supplementary Fig. 9) in a manner analogous with the antagonist PSB36 (Fig. 3j). Overall, the simulations revealed Mode D as the most stable BnOCPA pose (6.8 µs out of 9 µs simulated starting from this configuration – Table 1), while Mode B accounted for 3.6 µs out of 30 µs.

Next, to simulate the agonist-driven interaction between the A_1R and the G protein, the α5 (C-terminal) helix (GαCT) of the G protein (Gi2, Goa, Gob) was dynamically docked to the HOCPA- and BnOCPA-bound active A_1R structure (again lacking G protein; Supplementary Movie 3). This allowed us to evaluate the effect of different GαCT on the formation of the complex with A_1R to test the hypothesis that, of Goa, Gob and Gi2, only the GαCT of Gob would fully engage with the BnOCPA-bound active A_1R, in line with the empirical observations of G protein selectivity summarised in Fig. 2c, d. Figure 4a shows that the GαCT of Gob docked to the A_1R via a metastable state (MS1) relative to the canonical state (CS1; Supplementary Movie 3), regardless of whether HOCPA or BnOCPA was bound. Figure 4b, c show that the CS1 geometry corresponds to the canonical arrangement as found in the cryo-EM A_1R:Gi protein complex, whereas state MS1 resembles the recently reported non-canonical state observed in the neurotensin receptor, believed to be an intermediate on the way to the canonical state[80]. In contrast, fig. 4d–f shows that the GαCT of Goa and Gi2 docks to the A_1R to form metastable states MS2 and MS3. MS2 is similar to the β_2-adrenergic receptor:GsCT fusion complex[81], proposed to be an intermediate on the activation pathway and a structure relevant to G protein specificity. In this case, however, it appears to be on an unproductive pathway.

To test the hypothesis that the non-functional BnOCPA:A_1R:Goa complex showed anomalous dynamics, we next increased the complexity of the simulations by considering the Gα subunit of the Goa and Gob protein bound to the A_1R:BnOCPA (Mode B or D) complex or the Gob protein bound to A_1R:HOCPA (a functional system). The most visible differences between Goa (Supplementary Movie 4) and Gob (Supplementary Movie 5) comprised the formation of transient hydrogen bonds between the α4-β6 and α3-β5 loops of Goa and helix 8 (H8) of the receptor (Supplementary Table 3). Similar contacts are present in the non-canonical state of the neurotensin receptor:Gi protein complex[80]. Overall, Goa interacted more with TM3 and ICL2 residues (Fig. 4g, h), while TM5 and TM6, along with ICL1, were more engaged by Gob (Fig. 4g, h). Interestingly, R291$^{7.56}$ and I292$^{8.47}$, which are located under the N$^{7.49}$PXXY$^{7.53}$ motif, showed a different propensity to interact with Goa or Gob. In this scenario, it is plausible that a particular A_1R conformation stabilised by BnOCPA (as suggested by the simulations in the absence of G protein, Fig. 3i, j) may favour different intermediate states during the activation process of Goa and Gob.

To test the prediction from the MD simulations that R291$^{7.56}$ and I292$^{8.47}$ were involved in A_1R/Gα coupling, we performed a series of site-directed mutagenesis (to alanine) against R291$^{7.56}$, I292$^{8.47}$ and the adjacent hydrophilic residues Q293$^{8.48}$ and K294$^{8.49}$ (Fig. 4i) and compared the inhibition of forskolin-stimulated cAMP production in response to adenosine, CPA, NECA, HOCPA and BnOCPA in Flp-In-CHO cells against the wild-type (WT) hA_1R (Fig. 4j). Of these residues, none of which are reported to affect binding[82,83], K294$^{8.49}$ had the least impact on potency; of the agonists, the mutations had minimal effects on HOCPA. In contrast A_1R/Gα coupling induced by adenosine, CPA, NECA and BnOCPA was affected, but differentially so. These effects on potency (IC_{50} values) can be readily observed when individual mutant IC_{50} values are normalised to their respective WT controls (Fig. 4k), and revealed that R291$^{7.56}$, I292$^{8.47}$ and Q293$^{8.48}$ are especially important for CPA and NECA coupling, R291$^{7.56}$ for adenosine potency, and Q293$^{8.48}$ for BnOCPA. These observations reinforce the MD simulations predictions related to H8 residues involved in G protein coupling of the agonist-stimulated A_1R, and in particular suggest that R291$^{7.56}$, I292$^{8.47}$ and Q293$^{8.48}$ are especially required for selective agonist coupling to Gαo/i, and may thus contribute to the Gα bias observed among these agonists (Fig. 2c, d). A more detailed analysis, involving saturation mutagenesis of these residues, is required to provide a full characterisation of their actions to direct agonist bias but is beyond the scope of this current study.

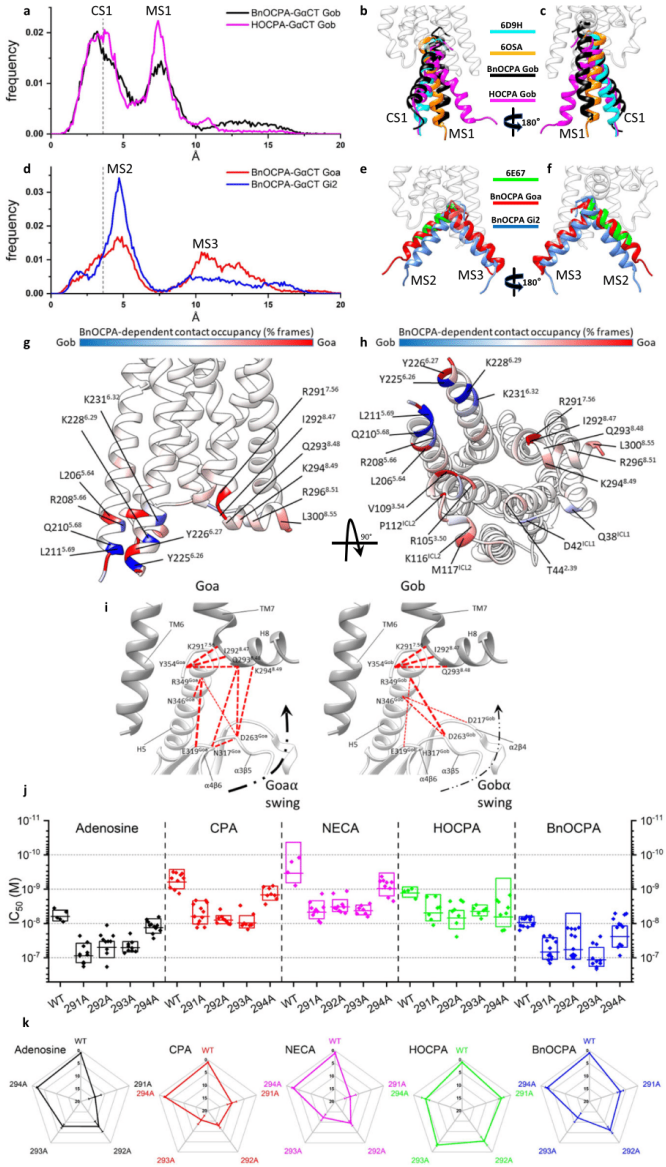

BnOCPA does not depress heart rate, blood pressure or respiration: evidence for in vivo physiological selectivity at native A_1Rs. Given BnOCPA's clear differential effects in a native physiological system (Fig. 1), strong Gob selectivity (Fig. 2), unique binding characteristics (Fig. 3) and selective Gob interaction (Fig. 4), we hypothesised that these properties might circumvent a key obstacle to the development of A_1R agonists for therapeutic use—their powerful effects in the cardiovascular system (CVS) where their activation markedly reduces both heart rate and blood pressure[12]. These cardiovascular effects are likely through Goa, which is expressed at high levels in the heart[84,85], particularly in the atria[86], and which plays an important role in regulating cardiac function[87]. In contrast, and with parallels of differential Goa vs Gob expression in the hippocampus[59], Gob may be absent or expressed at very low levels in the heart[86,88]. Given this differential expression of Goa and Gob, and the lack of functional effect of BnOCPA on Goa (Fig. 2a–g), we predicted that BnOCPA would have minimal effects on the CVS. Moreover,

Fig. 4 BnOCPA selectively induces canonical activation states at A_1R:Gob, but non-productive metastable states at other Gαi/o subunits. a–c Dynamic docking of the Gob-GαCT (last 27 residues) performed on the BnOCPA-A_1R (black) and the HOCPA-A_1R (magenta) complex, respectively. **a** Frequency distribution of the RMSD of the last 15 residues of Gob-GαCT (alpha carbon atoms) relative to the Gi2-GαCT conformation reported in the A_1R structure PDB code 6D9H (dashed grey line indicates 3.6 Å resolution). The two most probable RMSD ranges, canonical state (CS) CS1 and metastable state (MS) MS1, can be observed. **b**, **c** Side views of representative MD frames of the most populated α5 clusters from CS1 and MS1. The last 15 residues of Gob-GαCT in CS1 of both BnOCPA and HOCPA resemble the Gi2-bound state (PDB code 6D9H; cyan). MS1 is characterised by a binding geometry similar to the non-canonical Gi intermediate state reported for the neurotensin receptor structure (PDB Code 6OSA; orange). **d–f** Dynamic docking of the Goa- and Gi2-GαCT (last 27 residues) performed on the BnOCPA-A_1R complex. **d** As for **a** except Gob was replaced with Goa (red) and compared to Gi2 (blue), with the two most probable RMSD ranges labelled as MS2 and MS3. **e**, **f** Side views of representative MD frames of the most populated GαCT clusters from MS2 and MS3. The Goa and Gi2 last 15 residues in MS2 overlap well with the putative Gs intermediate state (PDB code 6E67; green). In MS3, the GαCT helix orients in unique conformations that differ from those previously described. **g**, **h** For each residue the interaction plotted on the backbone is the difference between the Goa and Gob occupancies in the presence of orthosteric BnOCPA (% of MD frames in which interaction occurred). BnOCPA/A_1R/Goa (inactive coupling) had the tendency to interact more with ICL2, TM3 TM7, and H8 (red), while BnOCPA/A_1R/Gob (active coupling) formed more contacts with TM5 and TM6 (blue). **i** Residues in TM7 and H8 of the hA_1R predicted by MD simulations to be of importance to A_1R coupling to Goa (left) and Gob (right). **j**, **k** Mutations of R291$^{7.56}$, I292$^{8.47}$, Q293$^{8.48}$ and K294$^{8.49}$ to alanine in the hA_1R differentially affect agonist efficacy against stimulated cAMP production. **j** Data points represent individual IC_{50} values ($n = 5$-13 individual experiments), with the mean represented as the horizontal bar and the box limits indicating ±1 SD. **k** Spider plot summarising data from **j**. Source data are provided as a Source Data file.

given the antagonism of Goa-mediated actions by BnOCPA at native and recombinant A_1Rs (Fig. 1h, i, Supplementary Fig. 2a, c, Fig. 2i), we further predicted that the actions of adenosine on the CVS may be attenuated by BnOCPA.

In initial experiments, we screened BnOCPA for its effects on heart rate using an isolated frog heart preparation. In contrast to adenosine and CPA, which depress heart rate through hyperpolarisation caused by activation of cardiac sinoatrial K^+ channels[89], BnOCPA had no effect on heart rate, but markedly reduced the bradycardia evoked by adenosine (Supplementary Fig. 10a). Thus, BnOCPA appears not to activate A_1Rs in the heart, but instead behaves like an antagonist in preventing the actions of the endogenous agonist. These observations have parallels with BnOCPA's inability to activate A_1Rs to hyperpolarise neurones, and indeed inhibiting or reversing the post-synaptic hyperpolarisation induced by typical A_1R agonists (Fig. 1h, i; Supplementary Fig. 2a, c), and in preventing the A_1R/Goa-mediated inhibition of cAMP accumulation by adenosine (Fig. 2i). Such antagonist-like behaviour may be explained by BnOCPA causing unique A_1R conformations unlike those of conventional agonists (Fig. 3i, j), and driving non-canonical and ultimately non-productive interactions with Goa (Fig. 4).

To investigate the effects of BnOCPA in an intact mammalian system, we measured the influence of BnOCPA on heart rate and blood pressure in urethane-anaesthetised, spontaneously breathing adult rats. As expected, both resting heart rate and arterial blood pressure were significantly reduced by adenosine and CPA (Fig. 5a–d). In complete contrast, BnOCPA had no effect on either heart rate (Fig. 5a, c) or blood pressure (Fig. 5b, d), even when applied at two or three times the initial dose (Supplementary Fig. 11; Fig. 6e, f). These negative observations could not be explained by metabolism of BnOCPA to an inactive substance since BnOCPA is a very stable compound (half-life ($t_{1/2}$) >240 min in PBS at 37 °C) with a human plasma stability of ~100% remaining after 120 mins suggesting a $t_{1/2} > 240$ min at 37 °C. In addition, the in vitro metabolic $t_{1/2}$ of BnOCPA was determined as >60 mins using human liver microsomes (0.1 mg/mL, 37 °C), and the intrinsic clearance (CL_{int}) calculated as <115.5 µL/min/mg. This was in contrast to the reference compounds verapamil and terfenadine (0.1 µM) with $t_{1/2}$ in human plasma determined as 33 and 10 min and CL_{int} as 213.1 and 683.0 µl/min/mg, respectively (see Supporting Data File 1). Further evidence that BnOCPA was present and active during these experiments was obtained from studies analogous to those in frog heart when BnOCPA was applied together with adenosine. In the intact anaesthetised rat, when co-applied with adenosine or CPA, BnOCPA abolished the bradycardia induced by both agonists, indicating its ability to bind to the A_1R at the dose applied (Fig. 5a, c; Fig. 6g, Supplementary Figs. 10b and 11). Volumes of saline equivalent to the drug injections had no effect on either heart rate or blood pressure and there was no waning in the effects of adenosine responses with repeated doses (Supplementary Fig. 10c, d). Thus, BnOCPA does not appear to act as an agonist at CVS A_1Rs, but instead antagonises the bradycardic effects of A_1R activation on the heart.

Since adverse effects on respiration (dyspnoea) limit the use of systemic A_1R agonists[7], we additionally examined the effects of BnOCPA on respiration. In urethane-anaesthetised, spontaneously breathing adult rats, intravenous injection of BnOCPA had no appreciable effect on respiration (Fig. 6a–d), even if the dose of BnOCPA was doubled or trebled (Fig. 6e, f). In stark contrast the selective A_1R agonist CPA caused significant respiratory depression (Fig. 6a–d). Paralleling BnOCPA's antagonism of adenosine- and CPA-induced depressions of heart rate (Fig. 5a, c; Supplementary Figs. 10b and 11), BnOCPA reduced the depression of respiratory frequency and minute ventilation caused by CPA (Fig. 6g, Supplementary Fig. 11). These data suggest that while BnOCPA targets and clearly engages the A_1Rs responsible for adenosine and CPA's cardiorespiratory depression, BnOCPA has no agonist action at these A_1Rs.

BnOCPA is a potent analgesic. Our observations of a lack of effect of BnOCPA on the CVS and respiration prompted an investigation into a potential application of A_1R agonists that had previously been severely curtailed by adverse cardiorespiratory events[7,16], namely the use of A_1R agonists as analgesics. Since sedation or motor impairment can be mistaken for analgesia, we tested BnOCPA in a sensitive assay for balance and motor coordination, the rotarod, in which the ability of a rodent to remain upon a slowly accelerating rotating cylinder is a measure of alertness and motor function. As a positive control for the sensitivity of the test, we showed that the ability of animals treated with morphine to remain on the rotating cylinder was strongly impaired (Fig. 7a). In contrast, the performance of animals treated with BnOCPA, delivered either intravenously or intraperitoneally, was indistinguishable from vehicle-treated mice (Fig. 7a). This was true even if BnOCPA was injected intravenously at three times the dose (Fig. 7a), which, while having no cardiorespiratory actions on its own, prevented cardiorespiratory depression caused by adenosine and CPA (Figs. 5 and 6; Supplementary Figs. 10 and 11). Thus, BnOCPA does not induce

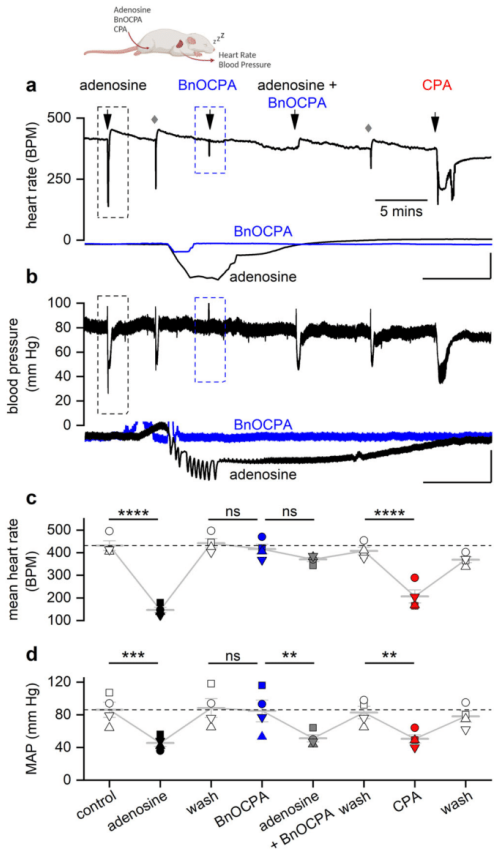

Fig. 5 BnOCPA does not affect heart rate or blood pressure. a Examples of heart rate (HR) and **b** arterial blood pressure traces from a urethane-anaesthetised, spontaneously breathing rat showing the effects of adenosine (1 mg kg^{-1}), BnOCPA (8 μg kg^{-1}) and CPA (6 μg kg^{-1}). Grey diamonds reflect saline flushing of the femoral vein catheter. Insets are expanded HR and blood pressure responses to adenosine and BnOCPA (black and blue traces, respectively; boxed regions in **a** and **b**). Scale bars measure: HR, 200 BPM and 6 s; blood pressure, 40 mm Hg and 6 s. **c, d** Summary data for 4 rats where each rat is shown as a different symbol with the means (± SEM, light grey bars) connected. One-way RM ANOVA for: **c** HR, Greenhouse-Geisser corrected F(2.33, 7.00) = 68.27, $P = 2.07 \times 10^{-5}$; **d** mean arterial blood pressure (MAP), Greenhouse-Geisser corrected F(1.84, 5.52) =10.51, $P = 0.014$; with the following Bonferroni post hoc comparisons: The resting HR of 432 ± 21 BPM was significantly reduced to 147 ± 12 BPM (~66%, $P = 2.76 \times 10^{-11}$) by adenosine. BnOCPA had no effect on HR (~6%, 442 ± 20 vs 416 ± 21 BPM; $P = 1$) but prevented the bradycardic effects of adenosine ($P = 2.71 \times 10^{-9}$ vs adenosine) when co-injected (mean change 51 ± 4 BPM; ~12%; $P = 0.67$). CPA significantly decreased HR (from 408 ± 17 to 207 ± 29 BPM; ~50%, $P = 1.85 \times 10^{-8}$), a decrease that was not different to the effect of adenosine ($P = 0.12$), but was significantly different to the effect of both BnOCPA ($P = 9.00 \times 10^{-9}$) and adenosine in the presence of BnOCPA ($P = 6.69 \times 10^{-7}$). The resting MAP (86 ± 9 mm Hg) was significantly reduced by adenosine (~47%, 46 ± 4 mm Hg; $P = 0.001$). BnOCPA had no effect on its own on MAP (88 ± 11 vs 85 ± 13 mm Hg; $P = 1$) and did not prevent adenosine in lowering MAP to a value similar to adenosine on its own (51 ± 4 mm Hg; $P = 1$ vs adenosine; $P = 0.012$ vs BnOCPA alone). CPA significantly decreased MAP (from 83 ± 8 to 51 ± 5 mm Hg; $P = 0.017$), a decrease that was not different to the effect of adenosine in the absence or presence of BnOCPA ($P = 1$ for both). ns, not significant; **, $P < 0.02$; ***, $P < 0.001$; ****, $P < 0.0001$. Source data are provided as a Source Data file.

sedation or locomotor impairment that could confound interpretations of analgesia.

To assess the potential of BnOCPA as an analgesic, we used a rat model of chronic neuropathic pain (spinal nerve ligation)[90] a feature of which is mechanical allodynia whereby the affected limb is rendered sensitive to previously innocuous tactile stimuli, and which models the debilitating human clinical condition of chronic pain, which affects between 20 and 50% of the population[91,92], and which carries a major global burden of disability[93].

Both intrathecal (Fig. 7b) and intravenous (Fig. 7c) BnOCPA potently reversed mechanical allodynia in a dose-dependent manner. Thus, BnOCPA exhibits powerful analgesic properties at doses devoid of sedative or cardiorespiratory effects, and at several orders of magnitude lower than the non-opioid analgesics pregabalin and gabapentin[94]. To test if this analgesia was mediated by the activation of A_1Rs by BnOCPA, we used the selective A_1R antagonist, DPCPX. Prior administration of DPCPX prevented the reversal of mechanical allodynia by BnOCPA (Fig. 7d), confirming the importance of A_1Rs in mediating the analgesic actions of BnOCPA. In contrast, the rat A_3R-selective antagonist MRS1523[95,96], which is effective in reversing analgesia caused by selective A_3R agonists[97–99], had no effect on the analgesia caused by BnOCPA, and indeed may have provoked a slight facilitation. This may be due to the reported elevated adenosine tone[100] and activation of A_3Rs[101] in the neuropathic spinal cord, which may have resulted in the desensitisation of A_1R-mediated responses[102]. These observations confirm that the analgesia provoked by BnOCPA is mediated via the selective activation of A_1Rs.

Discussion

Biased agonists at GPCRs offer great potential for the preferential activation of desirable intracellular signalling pathways, while avoiding, or indeed blocking those pathways that lead to adverse or unwanted effects[3,27]. While this, and the potential to exploit previously unattractive drug targets such as the A_1R, have been appreciated, translation of in vitro observations, particularly of Gα bias, to native receptors in vivo has been problematic[3,4,27]. Here we have shown that translation of in vitro selectivity among Gα subunits, identified using two separate assays, to an intact physiological system is possible through a benzyloxy derivative (BnOCPA) of the selective A_1R agonist CPA. Moreover, this Gα selectivity has occurred in the context of the A_1R, an attractive, but notoriously intractable drug target by virtue of the profound cardiorespiratory consequences of its activation by conventional A_1R agonists.

BnOCPA was first reported as a final compound in a patent where it was described to be selective for the A_1R with respect to its binding affinity, and effective in reducing elevated intraocular pressure for the potential treatment of glaucoma or ocular hypertension[34]. We have previously prepared BnOCPA (and HOCPA)[33] for assessment as part of our synthetic campaign to develop potent and A_1R-selective fluorescent ligands. The N^6-substituent (1*R*,2*R*)-2-aminocyclopentan-1-ol) present in BnOCPA and HOCPA is also found in the experimental and later discontinued[103] drug CVT-3619 (later named GS 9667), which

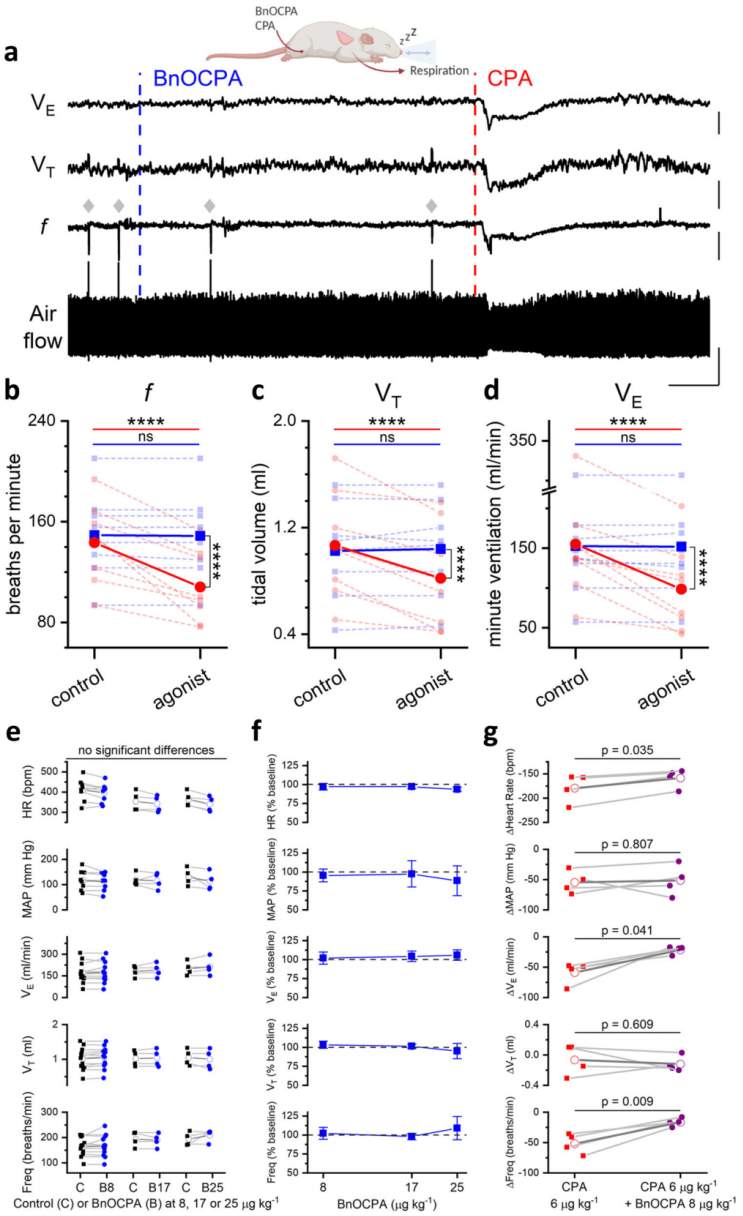

has been described as a partial, selective agonist of the A_1R and shown to reduce cAMP content and lipolysis in rat adipocytes[104].

Having identified BnOCPA as a selective Gob agonist at recombinant A_1Rs in vitro, we established that this unusual property can be translated into the selective activation of native A_1Rs in both the in vitro CNS and in vivo cardiorespiratory and peripheral nervous systems. Moreover, these properties of BnOCPA were observed at A_1Rs expressed by three different species: amphibian, rat, and human. While BnOCPA bound to and induced A_1R coupling to Gαi/o subunits recruited by prototypical A_1R agonists such as adenosine and CPA, BnOCPA selectively activated Gob among the six Gαi/o subunits. This likely reflected BnOCPA's non-canonical binding profile at the A_1R, which had profound implications for the interaction with the

Fig. 6 BnOCPA does not cause respiratory depression. a Examples of tracheal airflow, respiratory frequency (*f*), tidal volume (V_T) and minute ventilation (V_E) from a urethane-anaesthetised, spontaneously breathing rat showing the lack of effect of BnOCPA on respiration and the respiratory depression caused by CPA. BnOCPA or CPA were given intravenously at the times indicated by the vertical broken lines (BnOCPA, 8 μg kg^{-1}, blue; CPA, 6 μg kg^{-1}, red). Grey diamonds indicate spontaneous sighs. Scale bars measure: 180 s and: airflow, 0.5 mL; *f*, 50 breaths per minute (BrPM); V_T, 0.25 mL; V_E, 50 mL/min. **b**–**d** Summary data for 8 animals. Data from each rat is shown before and after the injection of BnOCPA (blue squares and broken lines) or CPA (red circles and broken lines) together with the mean value for all animals (solid lines) for *f*, V_T and V_E, respectively. One-way RM ANOVA: For: **b** *f*, Greenhouse-Geisser corrected F(1.20, 8.38) = 30.4, $P = 3.48 \times 10^{-4}$; **c** V_T, F(3, 21) = 15.9, $P = 1.25 \times 10^{-5}$, and **d** V_E, Greenhouse-Geisser corrected F(1.19, 8.34) =15.77, $P = 0.003$, with the following Bonferroni post hoc comparisons: Following BnOCPA, *f* (149 ± 12 BrPM), V_T (1.0 ± 0.1 mL), and V_E (152 ± 26 ml/min) were not altered ($P = 1$) compared to resting values *f* (149 ± 12 BPM), V_T (1.0 ± 0.1 mL), and V_E (153 ± 26). In contrast to CPA, which reduced *f* (108 ± 10 BrPM), V_T (0.8 ± 0.1 mL), and V_E (99 ± 19 ml/min) compared to resting values *f* (143 ± 11 BrPM; $p = 4.05 \times 10^{-6}$), V_T (1.1 ± 0.1 mL; $P = 2.58 \times 10^{-5}$), and V_E (155 ± 28; $P = 5.52 \times 10^{-5}$). The control resting values before administration of BnOCPA and CPA were not different to one another ($P = 1$). The effects of CPA were significantly greater than BnOCPA for *f* ($P = 4.48 \times 10^{-7}$), V_T ($P = 1.15 \times 10^{-4}$), and V_E ($P = 1.16 \times 10^{-4}$). Horizontal significance indicators above the data show differences between resting values and following IV administration of either BnOCPA (blue line) or CPA (red line). Vertical significance indicators show differences between the effects of BnOCPA and CPA. **e** Individual data ($n = 4$–12 rats) for the three doses of BnOCPA (blue circles) compared to their preceding baseline (black squares). The mean is shown as an open symbol. One-way ANOVA with Bonferroni corrections found no differences in: HR ($p = 0.07$), MAP ($p = 1$), Freq ($P = 0.2$), V_T ($p = 1$), or V_E ($p = 0.9$). **f** Average data from the animals in **e** showing cardiorespiratory variables as a percentage of their preceding baseline and as a function of increasing dose of BnOCPA ($\log_{10}$ scale). **g** Individual data from four rats showing the effect (difference from the previous baseline) of CPA in the absence (red squares) and presence (purple circles) of BnOCPA (8 μg kg^{-1}). The mean is shown as an open symbol. Two-tailed paired t-tests indicated a significant reduction in the effects of CPA by BnOCPA on: HR (CPA: 179 ± 15 bpm vs BnOCPA: 159 ± 10 bpm; $p = 0.035$), V_E (CPA: 59 ± 9 ml/min vs BnOCPA: 21 ± 3 ml/min; p = 0.041) and Freq (CPA: 52 ± 8 breaths/min vs BnOCPA: 17 ± 3 breaths/min; $p = 0.009$), with no change in: MAP ($p = 0.807$) or V_T ($p = 0.609$). Data are shown as mean ± SEM. Raw traces from a representative experiment can be found in Supplementary Fig. 11. Source data are provided as a Source Data file.

GαCT in terms of different binding pathways and intermediate states, and in the different intra- and intermolecular hydrogen bond patterns and contacts observed in the simulations of the A_1R in complex with either Goa (inactive) or Gob (active). Predictions from the MD simulations suggested four hitherto uncharacterised residues as being important for the interaction between the A_1R and Gαi/o. Individual mutations in three of these contacts, R291$^{7.56}$, I292$^{8.47}$, Q293$^{8.48}$, differentially impacted agonist efficacy, with adenosine and HOCPA being relatively unaffected compared to the stronger effects on the efficacy of CPA, NECA and BnOCPA. These and other molecular differences in the coupling of the A_1R to Gαi/o are likely to underlie the ability of the BnOCPA-bound A_1R to selectively trigger Gob activation among the six Gαi/o subtypes.

The unique and unprecedented Gα selectivity displayed by BnOPCA has physiological importance since it is able to inhibit excitatory synaptic transmission without causing neuronal membrane hyperpolarisation, sedation, bradycardia, hypotension or dyspnoea. BnOCPA thus overcomes cardiovascular and respiratory obstacles to the development of adenosine-based therapeutics that have plagued the field since their first description nine decades ago[105]. As a first, but significant, step towards this, we demonstrate that BnOCPA has powerful analgesic properties via A_1Rs in an in vivo model of chronic neuropathic pain, potentially through a mechanism that may involve a combination of inhibition of synaptic transmission in peripheral and spinal pain pathways, and the hyperpolarisation of Gob-containing nociceptive neurons. Chronic pain, a condition that a large proportion of the population suffers on a constant or frequent basis[91,92] and associated with a major global burden of disability[93] is, however, a disorder for which the current treatments are either severely lacking in efficacy[106] or, in the case of opioids, come with unacceptable harms such as adverse gastrointestinal effects, respiratory depression, tolerance, dependence and abuse potential[107]. Accordingly, novel treatments for chronic pain are urgently required.

We have shown that highly selective Gα agonism in vitro can be translated into selective activation of native A_1Rs to mediate differential physiological effects, and have identified a novel molecule capable of doing so. We have also explored molecular mechanisms by which this could occur, and demonstrated pain as one potential and wide-reaching therapeutic application. Such discoveries are of importance in both understanding GPCR-mediated signalling, and in the generation of both new research tools and therapeutics based on the untapped potential of biased, and indeed Gα-selective, agonists such as BnOCPA.

Methods

Approvals. All experiments involving animals were conducted with the knowledge and approval of the University of Warwick Animal Welfare and Ethical Review Board, and in accordance with the U.K. Animals (Scientific Procedures) Act (1986) and the EU Directive 2010/63/EU. In vivo cardiorespiratory studies were conducted under the auspices of UK PPL 70/8936 and chronic neuropathic pain studies under the auspices of P9D9428A9. Rotarod studies were approved by the Monash University Animal Ethics Committee in accordance with the Australian Code for the Care and Use of Animals for Scientific Purposes (2013) under Monash AEC protocol number 13333.

Preparation of hippocampal slices. Sagittal slices of hippocampus (300–400 μm) were prepared from male Sprague–Dawley rats, at postnatal days 12–20[108]. Rats were kept on a 12-hour light-dark cycle with slices made 90 min after entering the light cycle. In accordance with the U.K. Animals (Scientific Procedures) Act (1986), rats were killed by cervical dislocation and then decapitated. The brain was removed, cut down the midline and the two sides of the brain stuck down to a metal base plate using cyanoacrylate glue. Slices were cut along the midline with a Microm HM 650 V microslicer in cold (2–4 °C), high Mg^{2+}, low Ca^{2+} artificial cerebrospinal fluid (aCSF), composed of (mM): 127 NaCl, 1.9 KCl, 8 $MgCl_2$, 0.5 $CaCl_2$, 1.2 KH_2PO_4, 26 $NaHCO_3$, 10 D-glucose (pH 7.4 when bubbled with 95% O_2 and 5% CO_2, 300 mOSM). Slices were stored at 34 °C for 1–6 h in aCSF (1 mM $MgCl_2$, 2 mM $CaCl_2$) before use.

Extracellular recording. A slice was transferred to the recording chamber, submerged in aCSF and perfused at 4–6 ml min^{-1} (32 ± 0.5 °C). The slice was placed on a grid allowing perfusion above and below the tissue and all tubing was gastight (to prevent loss of oxygen). An aCSF-filled glass microelectrode was placed within stratum radiatum in area CA1 and recordings were made using either a differential model 3000 amplifier (AM systems, WA USA) or a DP-301 differential amplifier (Warner Instruments, Hampden, CT USA). Field excitatory postsynaptic potentials (fEPSPs) were evoked with either an isolated pulse stimulator model 2100 (AM Systems, WA) or ISO-Flex (AMPI, Jerusalem, Israel). For fEPSPs a 10–20 min baseline was recorded at a stimulus intensity that gave 40-50% of the maximal response. Signals were acquired at 10 kHz, filtered at 3 kHz, and digitised on line (10 kHz) with a Micro CED (Mark 2) interface controlled by Spike software (Vs 6.1, Cambridge Electronic Design, Cambridge UK) or with WinLTP[109]. For fEPSP slope, a 1 ms linear region after the fibre volley was measured. Extracellular recordings were made independently on two electrophysiology rigs. As the data obtained from each rig was comparable, both sets of data have been pooled.

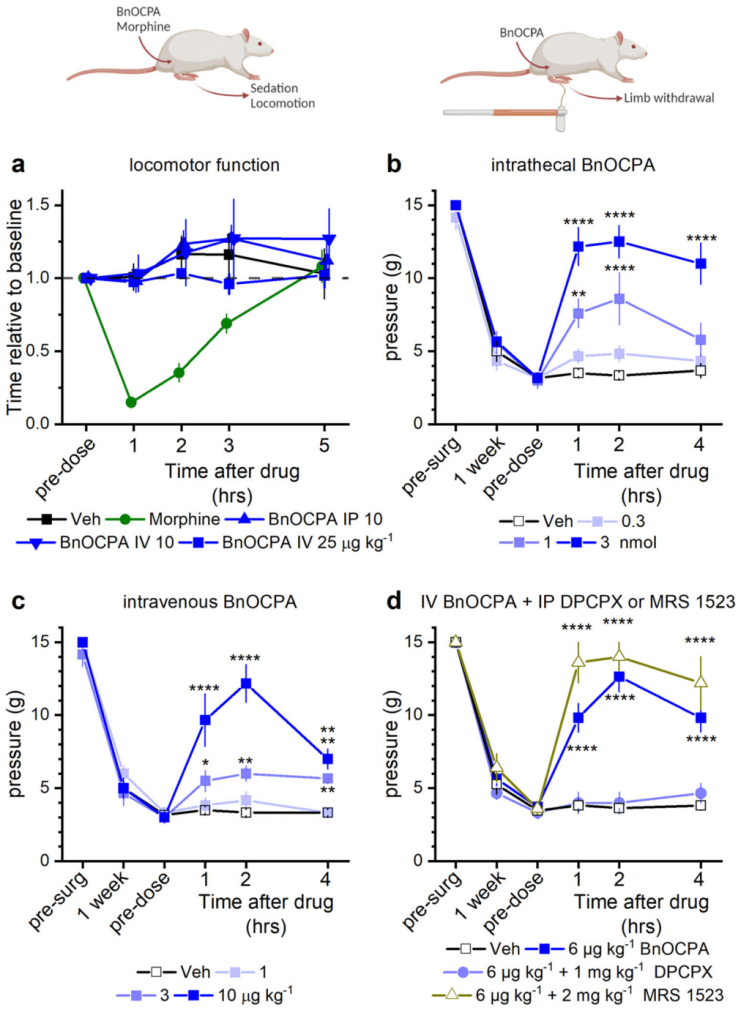

Seizure model. Seizure activity was induced in hippocampal slices using nominally Mg^{2+}-free aCSF that contained no added Mg^{2+} and with the total K^+ concentration increased to 6 mM with KCl. Removal of extracellular Mg^{2+} facilitates depolarisation via glutamate N-methyl-D-aspartate (NMDA) receptor activation. Increasing the extracellular concentration of K^+ depolarises neurons leading to firing and release of glutamate to sustain activity. Both the increase in K^+ concentration and removal of Mg^{2+} are required to produce spontaneous activity in hippocampal slices[110]. Spontaneous activity was measured with an aCSF-filled microelectrode placed within stratum radiatum in area CA1.

Whole-cell patch-clamp recording from hippocampal pyramidal cells. A slice was transferred to the recording chamber and perfused at 3 ml min^{-1} with aCSF at 32 ± 0.5 °C. Slices were visualised using IR-DIC optics with an Olympus BX151W microscope (Scientifica) and a CCD camera (Hitachi). Whole-cell current- and voltage-clamp recordings were made from pyramidal cells in area CA1 of the hippocampus using patch pipettes (5–10 MΩ) manufactured from thick walled glass (Harvard Apparatus, Edenbridge UK) and containing (mM): potassium gluconate 135, NaCl 7, HEPES 10, EGTA 0.5, phosphocreatine 10, MgATP 2, NaGTP 0.3 and biocytin 1 mg ml^{-1} (290 mOSM, pH 7.2). Voltage and current recordings were obtained using an Axon Multiclamp 700B amplifier (Molecular Devices, USA) and digitised at 20 KHz. Data acquisition and analysis was performed using pClamp 10 (Molecular Devices, USA). For voltage-clamp experiments, CA1 pyramidal cells were held at −60 mV. Peptides to interfere with G protein signalling were introduced via the patch pipette into the recorded cell. The cell was held for at least 10 min before adenosine (10 μM) was added to induce an outward current.

Frog heart preparation. Young adult male *Xenopus leavis* frogs were obtained from Portsmouth Xenopus Resource Centre. Frogs were euthanized with MS222 (0.2% at a pH of 7), decapitated and pithed. The animals were dissected to reveal the heart and the pericardium was carefully removed. Heart contractions were measured with a force transducer (AD instruments). Heart rate was acquired via a PowerLab 26 T (AD instruments) controlled by LabChart 7 (AD instruments). The heart was regularly washed with Ringer solution and drugs were applied directly to the heart.

In vivo anaesthetised rat preparation for cardiorespiratory recordings. Anaesthesia was induced in adult male Sprague–Dawley rats (230-330 g) with isofluorane (2–4%; Piramal Healthcare). The femoral vein was catheterised for drug delivery. Anaesthesia was maintained with urethane (1.2–1.7 g kg^{-1}; Sigma) in sterile saline delivered via the femoral vein catheter. Body temperature was

Fig. 7 BnOCPA is a potent analgesic without causing sedation or motor impairment. a BnOCPA did not induce sedation or affect motor function when injected intraperitoneally (IP; 10 μg kg^{-1}) or intravenously (IV; 10 or 25 μg kg^{-1}). In contrast, morphine caused sedation and motor impairment (15 mg kg^{-1} subcutaneously, SC). Saline (Veh, SC) did not affect rotarod performance. Data points (mean ± SEM; $n = 6$ for each compound) are normalised to pre-dose performance and are offset for clarity. **b**, **c** BnOCPA alleviates mechanical allodynia in neuropathic pain when administered **b** via an intrathecal (IT) or **c** IV route. Pre-surgery (pre-surg) animals had similar sensitivity to tactile stimulation as assessed by von Frey hair stimulation. Spinal nerve ligation caused hypersensitivity to touch (mechanical allodynia) at 1 week after surgery as evidenced by the reduction in the tactile pressure necessary to elicit paw withdrawal (paw withdrawal threshold; PWT). PWT reaches a similar nadir across all groups prior to the vehicle or BnOCPA infusion (pre-dose). Administration of BnOCPA significantly increased PWT in the limb ipsilateral to the site of injury in a dose-dependent manner (one-way ANOVA (pre-dose, 1, 2 and 4 hrs) for IT BnOCPA $F(3,88) = 21.9$, $P = 1.10 \times 10^{-10}$; for IV BnOCPA $F(3,92) = 18.1$, $P = 2.70 \times 10^{-9}$). Fisher LSD post hoc comparisons showed significant differences at: IT 1 nmol at 1 and 2 hrs, $P = 0.001$ and 4.16×10^{-5}, respectively, and 3 nmol at 1, 2 and 4 hrs, $P = 9.52 \times 10^{-11}$, 1.42×10^{-11} and 1.41×10^{-8}, respectively; IV 3 μg kg^{-1} at 1, 2 and 4 hrs, $P = 0.044$, 0.008 and 0.019, respectively, and 10 μg kg^{-1} at 1, 2 and 4 hrs, $P = 1.37 \times 10^{-8}$, 6.81×10^{-14} and 3.23×10^{-4}, respectively. **b**, **c** $n = 6$ per treatment, except for 1 nmol BnOCPA, $n = 5$. **d** The analgesic effects of BnOCPA (6 μg kg^{-1} IV) were prevented by the A_1R antagonist DPCPX (1 mg kg^{-1} IP), but not the A_3R-selective antagonist MRS1523 (2 mg kg^{-1} IP). Post hoc LSD comparisons across all four groups and four-time points (pre-dose, 1, 2 and 4 hrs; $F(15,116) = 26.8$, $P = 0$) revealed that BnOCPA at 6 μg kg^{-1} (IV) elicited significant analgesia compared to vehicle-treated animals at 1, 2, and 4 h post-dosing ($P = 4.69 \times 10^{-9}$, 3.50×10^{-16}, 4.69×10^{-9}, respectively), which persisted in the presence of the selective A_3R antagonist MRS1523 over the same time period ($P = 4.42 \times 10^{-13}$, 3.38×10^{-14}, 1.81×10^{-10}, respectively). In contrast, the PWT in DPCPX-treated animals did not differ from those in the vehicle group ($P = 0.872$, 0.748, 0.453 at 1, 2, and 4 h, respectively). $n = 11$ for BnOCPA and vehicle groups; $n = 6$ for the DPCPX group and $n = 5$ for the MRS1523 group. Averaged data are presented as mean ± SEM. ns, not significant; *, $P < 0.05$; **, $P < 0.02$; ***, $P < 0.001$; ****, $P < 0.0001$. Source data are provided as a Source Data file.

maintained at 36.7 °C via a thermocoupled heating pad (TCAT 2-LV; Physitemp). The trachea was cannulated and the femoral artery catheterised, and both were connected to pressure transducers (Digitimer) to record respiratory airflow and arterial blood pressure, respectively. Blood pressure and airflow signals were amplified using the NeuroLog system (Digitimer) connected to a micro1401 interface and acquired on a computer using Spike2 software (v7.08a; Cambridge Electronic Design). Arterial blood pressure recordings were used to derive heart rate (HR: beats.$minute^{-1}$; BPM), and to calculate mean arterial blood pressure (MAP: Diastolic pressure + 1/3*[Systolic Pressure−Diastolic pressure]). Airflow measurements were used to calculate: tidal volume (V_T; mL; pressure sensors were calibrated with a 3 mL syringe), and respiratory frequency (f; breaths min^{-1}; BrPM). Minute ventilation (V_E; mL min^{-1}) was calculated as $f \times V_T$.

Cardiovascular and respiratory parameters were allowed to stabilise before experiments began. A_1R agonists were administered by intravenous (IV) injection and the changes in HR, MAP, f, V_T, and V_E were measured. In pilot studies, the optimal dose of adenosine was determined by increasing the dose until robust and reliable changes in HR and MAP were produced (1 mg kg^{-1}). The dose of CPA was adjusted until equivalent effects to adenosine were produced on HR and MAP (6 μg kg^{-1}). For BnOCPA we initially used 1 μg kg^{-1}, but saw no agonist effect on HR and MAP. To ensure this was not a false negative we increased the dose of BnOCPA (8 μg kg^{-1}), which still gave no agonist effect on HR and MAP. However, as BnOCPA produced an antagonistic effect when co-administered with adenosine (Fig. 5, Supplementary Fig. 10b) and CPA (Fig. 6, Supplementary Fig. 11), it must have reached A_1Rs at a high enough concentration to be physiologically active. These observations confirmed that the lack of agonistic effects on HR and MAP were not due to a type II error. 8 μg kg^{-1} BnOCPA was used for all further experiments. All injections were administered IV as a 350 μl·kg^{-1} bolus.

In the experimental studies, rats either:

1. received an injection of adenosine. After cardiorespiratory parameters returned to baseline (5–10 min), rats were given BnOCPA. After allowing sufficient time for any effect of BnOCPA to be observed, rats received adenosine with BnOCPA co-administered in a single injection. After cardiorespiratory parameters returned to baseline, rats were injected with CPA, or
2. received an injection of CPA. After cardiorespiratory parameters returned to baseline (5-10 min) rats were given 8 μg kg^{-1} BnOCPA. After allowing sufficient time for any effect of BnOCPA to be observed, rats received CPA with 8 μg kg^{-1} BnOCPA co-administered in a single injection. After cardiorespiratory parameters returned to baseline, rats were injected with successive injections of 17 μg kg^{-1} and 25 μg kg^{-1} BnOCPA, with sufficient time given for any effect of BnOCPA to be observed.

To check that the volume of solution injected with each drug did not itself induce a baroreflex response leading to spurious changes in cardiorespiratory responses, equivalent volumes of saline (0.9%) were injected. These had no effect on either heart rate or MAP (Supplementary Fig. 10c). To confirm that repeated doses of adenosine produced the same response and that the responses did not run-down, rats were given two injections of adenosine (1 mg kg^{-1}). There was no significant difference in the changes in cardiovascular parameters produced by each adenosine injection (Supplementary Fig. 10d).

An additional series of experiments ($n = 4$) were undertaken to directly compare BnOCPA and CPA on respiration. Adult male Sprague–Dawley rats (400-500 g) were anaesthetised with urethane and instrumented as described above, with the exception that the arterial cannulation was not performed.

After allowing the animal to stabilise following surgery, BnOCPA (8 μg kg^{-1}) was administered. After a 20 min recovery period CPA (6 μg kg^{-1}) was administered. All injections were administered IV as a 350 μl kg^{-1} bolus. Changes in f, V_T, and V_E were measured. If the dosing occurred close to a respiratory event such as a sigh a second IV dose was administered, with 20 min recovery periods either side of the injection. Measurements for the effect of BnOCPA were time-matched to when CPA induced a change in respiration in the same preparation. As no difference was observed between the respiratory responses to BnOCPA in these rats ($n = 4$) and those instrumented for both cardiovascular and respiratory recordings ($n = 4$), the data were pooled ($n = 8$; Fig. 6a–d).

Spinal nerve ligation (Chung model[90]). Adult male Sprague–Dawley rats, 7-8 weeks old, weighing around 250 g at the time of Chung model surgery, were purchased from Charles River UK Ltd. The animals were housed in groups of 4 in an air-conditioned room on a 12-hour light/dark cycle. Food and water were available *ad libitum*. They were allowed to acclimatise to the experimental environment for three days by leaving them on a raised metal mesh for at least 40 min. The baseline paw withdrawal threshold (PWT) was examined using a series of graduated von Frey hairs (see below) for 3 consecutive days before surgery and re-assessed on the 6th to 8th day after surgery and on the 13th to 17th day after surgery before drug dosing.

Prior to surgery each rat was anaesthetised with 3% isoflurane mixed with oxygen (2 L min^{-1}) followed by an intramuscular injection of ketamine (60 mg kg^{-1}) plus xylazine (10 mg kg^{-1}). The back was shaved and sterilised with povidone-iodine. The animal was placed in a prone position and a para-medial incision was made on the skin covering the L4-6 level. The L5 spinal nerve was carefully isolated and tightly ligated with 6/0 silk suture. The wound was then closed in layers after a complete haemostasis. A single-dose of antibiotics (Amoxipen, 15 mg/rat, intraperitoneally, IP) was routinely given for prevention of infection after surgery. The animals were placed in a temperature-controlled recovery chamber until fully awake before being returned to their home cages. The vehicle (normal saline or DMSO) was administered via the IV route at 1 ml·kg^{-1} and via the intrathecal (IT) route at 10 μl for each injection. The A_1R-selective antagonist DPCPX (1 mg kg^{-1}) and the A_3R-selective antagonist MRS1523 (2 mg kg^{-1}) were delivered IP 30 mins before vehicle or BnOCPA treatment. The rats with validated neuropathic pain state were randomly divided into 11 groups: vehicle IV, BnOCPA at 1, 3, 6, 10 μg kg^{-1} IV; vehicle IT, BnOCPA at 0.3, 1, 3 nmol IT; 6 μg kg^{-1} BnOCPA IV plus 1 mg kg^{-1} DPCPX IP; 6 μg kg^{-1} BnOCPA IV plus 2 mg kg^{-1} MRS1523 IP groups and tested blind to treatment.

To test for mechanical allodynia the animals were placed in individual Perspex boxes on a raised metal mesh for at least 40 min before the test. Starting from the filament of lower force, each filament was applied perpendicularly to the centre of the ventral surface of the paw until slightly bent for 6 seconds. If the animal withdrew or lifted the paw upon stimulation, then a hair with force immediately lower than that tested was used. If no response was observed, then a hair with force immediately higher was tested. The highest value was set at 15 g. The lowest amount of force required to induce reliable responses (positive in 3 out of 5 trials) was recorded as the value of PWT. On the testing day, PWT were assessed before and 1, 2 and 4 h following BnOCPA or vehicle administration. The animals were returned to their home cages to rest (about 30 min) between two neighbouring testing time points. At the end of each experiment, the animals were deeply anaesthetised with isoflurane and killed by decapitation.

Rotarod test for motor function. A rotarod test was used to assess motor coordination following intravenous and intraperitoneal administration of BnOCPA. An accelerating rotarod (Ugo Basile) was set so speed increased from 6 to 80 rpm over 170 seconds. Male Sprague–Dawley rats ($n = 24$), 7 weeks of age (212-258 g) were trained on the rotarod twice daily for two days (≥2 trials per session) until performance times were stable. On the day of the experiment, three baseline trials were recorded. The compound was administered IP (10 μg kg^{-1}, $n = 6$) or IV via tail vein injection (10 and 25 μg kg^{-1}, $n = 6$ per group). The control group received subcutaneous saline and the positive control group received subcutaneous morphine (15 mg kg^{-1}). Latency to fall (seconds) was measured in triplicate at 1, 2, 3 and 5 h post drug administration.

Constructs, transfections and generation of stable cell lines. Cell lines were maintained using standard subculturing routines as guided by the European Collection of Cell Culture (ECACC) and checked annually for mycoplasma infection using an EZ-PCR mycoplasma test kit from Biological Industries (Kibbutz Beit-Haemek, Israel). To investigate the signalling properties of the rat A_3R (rA_3R) and mutants of the human A_1R (hA_1R), stable cell lines were generated using Flp-In-CHO cells (ThermoFisher - R75807). Untagged hA_1R from sigNanoLuciferase (Nluc)-A_1R in pcDNA3.1+ and untagged rA_3R from sigNluc-A_3R in pcDNA3.1 + (both gifted by Dr Steve Briddon (University of Nottingham)) were cloned into the pcDNA5/FRT expression vector (Thermo Fisher Scientific). Mutations within the hA_1R were made using the QuikChange Lightening Site-Directed Mutagenesis Kit (Agilent Technologies) in accordance with the manufacturer's instructions. Constructs for generating Goa/b interfering and scrambled peptides were generated by PCR and cloned into the B*amH*I/H*ind*III site of pcDNA3.1- as described in Gilchrist et al.[60],. Prior to the initiator codon a Kozak sequence was included for enhanced translation. The peptide sequences used were: for Goa MGIANNLRGCGLY, for Gob MGIAKNLRGCGLY, and for the scrambled peptide MGLNRGNAYLCIGMG was used. Constructs were sequenced to confirm fidelity. Flp-In-CHO cells were generated through co-transfection of the cell line with pcDNA5/FRT expression vector (Thermo Fisher Scientific) containing the WT or mutant hA_1R, or rA_3R, and the Flp recombinase expressing plasmid, pOG44 (Thermo Fisher Scientific), in accordance with the manufacturer's instructions. Co-transfection of cells in a T25 flask, with a total of 5 μg of adenosine receptor (AR)/pcDNA5/FRT and pOG44 (AR:pOG44 ratio of 1:9), was performed using Fugene HD (Promega), at a ratio of 3:1 (v/w) (Fugene:DNA). 24 h after transfection, cells were harvested and resuspended in growth media containing 600 μg/ml Hygromycin B (Thermo Fisher Scientific), and subsequently seeded into a fresh T25 flask. Media was replaced every 2–3 days and cells stably expressing the receptor of interest were selected using 600 μg/ml Hygromycin B. To generate CHO-K1 (European Collection of Authenticated Cell Cultures (ECAC) catalogue number 85051005) cells stably expressing the rat $A_{2A}R$ (CHO-K1-$rA_{2A}R$), CHO-K1 cells were seeded onto a 6-well plate and transfected with 1 μg $rA_{2A}R$ using Fugene HD (Promega) at a ratio of 3:1 (v/w) (Fugene:DNA). 48 h after transfection, media was replaced with growth media containing 800 μg/ml G418 (Thermo Fisher Scientific) and changed every 2–3 days until cells were >80% confluent. To investigate rat A_1R-mediated signalling, CHO-K1 cells seeded onto a 6-well plate were transiently transfected with 1 μg rat A_1R (rA_1R) using Fugene HD (Promega) at a ratio of 3:1 (v/w) (Fugene:DNA), for 48 h. The plasmids encoding the rA_1R and $rA_{2A}R$ (Nluc-A_1R/pcDNA3.1(+) and Nluc-$A_{2A}R$/pcDNA3.1(+), respectively) were kindly gifted by Stephen Hill and Stephen Briddon (University of Nottingham).

Cell signalling assays. CHO cell lines expressing ARs of interest (including mutants of the hA_1R) were routinely cultured in Ham's F-12 nutrient mix supplemented with 10% foetal bovine serum (FBS), at 37 °C with 5% CO_2, in a humidified atmosphere. For cAMP accumulation experiments, cells were seeded at a density of 2000 cells per well of a white 384-well optiplate and stimulated, for 30 min, with a range of agonist concentrations (100 pM – 100 μM) in the presence of 25 μM rolipram (Cayman Chemicals). For cAMP inhibition experiments, cells were co-stimulated with 1 μM forskolin and a range of agonist concentrations (1 pM–100 μM), in the presence or absence of 1 μM antagonist. cAMP levels were then determined using a LANCE® cAMP kit as described previously[33,111].

For determination of individual Gαi/o/z couplings, CHO-K1-hA_1R cells (made in-house) were transfected with pcDNA3.1-GNAZ or, pcDNA3.1 containing pertussis toxin (PTX) insensitive Gαi/o protein mutants (C351I, C352I, C351I, C351I, C351I, C351I, for Gi1, Gi2, Gi3, Goa, Gob, respectively, obtained from cDNA Resource Centre; www.cdna.org), using 500 ng plasmid and Fugene HD at a 3:1 (v/w) (Fugene:Plasmid) ratio. Cells were then incubated for 24 h before addition of 100 ng/ml PTX, to inhibit activity of endogenous Gαi/o, and then incubated for a further 16-18 h. Transfected cells were then assayed as per cAMP inhibition experiments, but co-stimulated with agonist and 100 nM forskolin.

β-arrestin recruitment assays. HEK 293 T cells (ATCC CRL-3216) were routinely grown in DMEM/F-12 GlutaMAX™ (Thermo Fisher Scientific) supplemented with 10% foetal bovine serum (FBS; F9665, Sigma-Aldrich) and 1x antibiotic-antimycotic solution (DMEM complete; Thermo Fisher Scientific). For analysis of β-arrestin recruitment following ligand stimulation at the hA_1R or hA_3R, HEK 293 T cells in a single well of 6-well plate (confluency ≥ 80%) were transiently co-transfected with either A_1R-Nluc or A_3R-Nluc, β-arrestin1/2-YFP and hGRK1-6, or pcDNA3.1 vector (total 2 μg, at a AR:β-arrestin:hGRK ratio of 1:5:4) using polyethyleneimine (PEI, 1 mg/ml, MW = 25,000 g/mol; Polysciences Inc) at a DNA:PEI ratio of 1:6 (w/v). As a negative control for the A_1R, transfections were also set up in the absence of β-arrestin1/2-YFP. Briefly, in sterile tubes containing 150 mM NaCl, DNA or PEI was added (final volume 50 μl) and allowed to incubate at room temperature for 5 min before mixing together and incubating for a further 10 min prior to adding the combined mix dropwise to the cells. 24 h post-transfection, HEK 293 T cell were harvested, resuspended in reduced serum media (MEM, NEAA; Thermo Fisher Scientific) supplemented with 1% L-glutamine (2 mM final; Thermo Fisher Scientific), 2% FBS and 1x antibiotic-antimycotic solution and seeded (50,000 cells/well) in a poly-L-lysine-coated (MW: 150,000-300,000 Da; Sigma-Aldrich) white 96-well plate (PerkinElmer Life Sciences). 24 h post seeding, media was removed, cells gently washed in PBS and 90 μl of furimazine (4 μM)-containing solution added (PBS supplemented with 0.49 mM $MgCl_2$, 0.9 mM $CaCl_2$ and 0.1% BSA) to each well before incubating in the dark for 10 min. After incubation, 10 μl of agonist (NECA, CPA, adenosine, BnOCPA) was added (0.01 μM to 10 μM) and filtered light emissions measured at 450 nm and 530 nm every minute for 1 h using a Mithras LB 940 (Berthold technology) using MikroWin 2000 software. Here, Nluc on the C-terminus of A_1R or A_3R acted as the BRET donor (luciferase oxidising its substrate) and YFP acted as the fluorescent acceptor. Vehicle control (1% DMSO) was added to determine background emission, and data was corrected for baseline reading, vehicle and the response obtained in the absence of YFP-β-arrestin1/2, when appropriate.

Radioligand binding. Radioligand displacement assays were conducted using crude membrane preparations (100 μg protein per tube) acquired from homogenisation of CHO-K1-hA_1R cells in ice-cold buffer (2 mM $MgCl_2$, 20 mM HEPES, pH 7.4). The ability to displace binding of the A_1R-selective antagonist radioligand, 1,3-[^{3}H]-dipropyl-8-cyclopentylxanthine ([^{3}H]-DPCPX) at a concentration (1 nM) around the Kd value (1.23 nM, as determined by saturation binding experiments) by increasing concentrations of NECA, adenosine, CPA, BnOCPA or HOCPA (0.1 nM − 10 μM) allowed the binding affinities (Ki) to be determined. Non-specific binding was determined in the presence of 10 μM DPCPX. Membrane incubations were conducted in Sterilin™ scintillation vials (Thermo Fisher Scientific; Wilmington, Massachusetts, USA) for 60 min at room temperature. Free radioligand was separated from bound radioligand by filtration through Whatman® glass microfiber GF/B 25 mm filters (Sigma-Aldrich). Each filter was then placed in a Sterilin™ scintillation vial and radioactivity determined by: addition of 4 mL of Ultima Gold XR liquid scintillant (PerkinElmer), overnight incubation at room temperature and the retained radioactivity determined using a Beckman Coulter LS 6500 Multi-purpose scintillation counter (Beckman Coulter Inc.; Indiana, USA).

NanoBRET ligand-binding studies. Real-time pharmacological interactions between ligands and receptors was quantitated using NanoBRET as described previously[112]. In brief, using N-terminally Nluc-tagged rA_1R-, $rA_{2A}R$- or rA_3R-expressing HEK 293 cell lines, competition binding assays were conducted. In all antagonist assays CA200645, which acts as a fluorescent antagonist with a slow off-rate[113], was used, with the exception of the rat A_3R where the fluorescent compound was AV039[114]. The data was fitted with the 'one-site – Ki model' derived from the Cheng and Prusoff equation, built into Prism to determine affinity (pK_i) values for all unlabelled agonists at all AR subtypes assayed. For the hA_1R we also performed an agonist binding competition assay using NECA-TAMRA (Noel et al., unpublished). Here data was fitted with the 'two-site Ki model', build into Prism to determine high affinity and low affinity values for the unlabelled agonists. For all ARs, filtered light emission at 450 nm and >610 nm (640-685 nm band pass filter) was measured using a Mithras LB 940 and the raw BRET ratio calculated by dividing the 610 nm emission with the 450 nm emission. The Nluc acts as the BRET donor (luciferase oxidising its substrate) and CA200645/AV039/NECA-TAMRA acted as the fluorescent acceptor. CA200645 was used at 25 nM, as previously reported[115], AV039 was used at 100 nM[112] and NECA-TAMRA at its Kd of 15.2 μM (Noel et al., unpublished). BRET was measured following the addition of the Nluc substrate, Furimazine (0.1 μM). Non-specific binding was determined using a high concentration of unlabelled antagonist, DPCPX for rA_1R, ZM241385 for the $rA_{2A}R$ and MRS1220 for rA_3R.

TRUPATH G protein dissociation assay. Cells were plated in a density of 1,500,000 cells/well in a 6-well plate and grown in DMEM /F-12 GlutaMAX™ media (Thermo Fisher Scientific, UK) supplemented with 10% FBS (Sigma, UK) and 1% AA (Sigma, UK). After being grown overnight, cells in each well were transfected using polyethylenimine 25 kDa (PEI, Polysciences Inc., Germany) at a 6:1 ratio of PEI to DNA, diluted in 150 mM NaCl. Cells were transfected with hA_1R, Goa-RLuc8 or Gob-RLuc8, $G\beta_3$, $G\gamma_8$-GFP2, and pcDNA3.1 with the ratio of 1:1:1:1:1 (400 ng per construct) in accordance with previously published methods[55]. Gα (either Goa-RLuc8, or Gob-RLuc8), Gβ3 and Gγ8-GFP2 constructs were purchased as part of the TRUPATH sensor kit from Addgene, pcDNA3.1-A_1R was obtained from cDNA resource centre, and pcDNA3.1 (-) zeo was purchased from Invitrogen. After 24 h, cells were trypsinised and re-seeded onto poly-L-lysine (PLL)-coated white 96-well plates (Greiner, UK) at the density of 50,000 cells/well in a complete DMEM/F-12 medium. After grown overnight, the culture

media was discarded and replaced with 80 µl assay buffer (1× Hank's balanced salt solution (HBSS) with calcium, supplemented with 20 mM HEPES and 0.1% BSA at pH 7.4). The assay was started by adding 10 µl of coelenterazine 400a (Nanolight technology, USA) to a final concentration of 5 µM. The plates were then incubated in the dark for 5 min, prior to the addition of 10 µl compounds (in a range of 0.01 nM – 1 µM). In order to investigate the effect of interfering peptides on Goa and Gob activation, cells were transfected with the TRUPATH constructs for Goa and Gob with the A_1R as described above. However, the vector was replaced by either interfering or scrambled peptides, as appropriate, with increasing concentration: 0, 100, and 400 ng and was complemented by pcDNA3.1(-) up to 400 ng. CPA 10 µl was used as the ligand in a range of 1 nM–1 µM. BRET signal was recorded for 30 min on a Mithras LB940 plate reader allowing sequential integration of signal detected from GFP2 and Rluc8. The BRET ratio corresponds to the ratio of light emission from GFP2 (515 nm) over Rluc8 (400 nm). Net BRET ratio was used to generate the concentration-response curve by taking 11-minute time-point after baseline correction. Data was analysed as change in the presence of the interfering peptides relative to control alone at 1 µM CPA.

Statistics and reproducibility

Data and statistical analysis. Concentration-response curves for the effects of A_1R agonists on synaptic transmission were constructed in OriginPro 2018 (OriginLab; Northampton, MA, USA) and fitted with a logistic curve using the Levenberg Marquadt iteration algorithm. OriginPro 2018 was also used for statistical analysis. Statistical significance was tested as indicated in the text using paired or unpaired two-tailed t-tests or one-way or two-way ANOVAs with repeated measures (RM) as appropriate. Bonferroni corrections for multiple comparisons were performed. All in vitro cell signalling assay data was analysed using Prism 8.4 (Graphpad software, San Diego, CA), with all concentration-response curves being fitted using a 3 parameter logistic equation to calculate response range and IC_{50}. All cAMP data was normalised to a forskolin concentration-response curve ran in parallel to each assay. Where appropriate the operational model of receptor agonism[52,111] was used to obtain efficacy (log τ) and equilibrium disassociation constant (log K_A) values. Calculation of bias factors (Δlog(Tau/K_A)) relative to adenosine was performed as described in Weston et al. (2016)[111]. Error for this composite measure was propagated by applying the following Eq. (1).

$$Pooled\ SEM = \sqrt{(SEM_A)^2 + (SEM_B)^2} \quad (1)$$

Where, σ_A and σ_B are the standard deviations of measurement A and B with mean of $\bar{x}_A$ and $\bar{x}_B$ is the composite mean and n is the number of repeats.

Single-dose Schild analysis was performed on data using BnOCPA as an antagonist to adenosine in the cAMP assays so enabling determination of BnOCPA's affinity constant (K_A) using the following Eq. (2)

$$\frac{D'}{D} = 1 + [A]K_2 \quad (2)$$

where D' and $D = EC_{50}$ values of adenosine with and without BnOCPA present, respectively, $[A]$ = the concentration of BnOCPA, and K_2 = the affinity constant (K_A) of the BnOCPA[58].

Statistical significance relative to adenosine was calculated using a one-way ANOVA with a Dunnett's post-test for multiple comparisons. Radioligand displacement curves were fitted to the one-site competition binding equation yielding log(Ki) values. One-way ANOVA (Dunnett's post-test) was used to determine significance by comparing the log(Ki) value for each compound when compared to adenosine. To determine the extent of ligand-induced recruitment of β-arrestin2-YFP to either the A_1R or A_3R, the BRET signal was calculated by subtracting the 530 nm/450 nm emission for vehicle-treated cells from ligand-treated cells (ligand-induced ΔBRET). ΔBRET for each concentration at 5 min (maximum response) was used to produce concentration-response curves.

All in vivo cardiovascular and respiratory data were analysed using OriginPro 2018. One-way ANOVAs, with repeated measures as appropriate, and with Bonferroni correction for multiple comparisons were used. Statistical significance for the effects of IV saline and the antagonist effect of BnOCPA on CPA were tested using two-tailed paired t-tests. Data are reported throughout as mean ± SEM and n values are reported for each experiment. For the neuropathic pain studies, one-way ANOVAs with Fisher's Least Significant Difference (LSD) post hoc test was used to compare drug treatment groups to the vehicle group (OriginPro 2018). The significance level was set at $P < 0.05$, with actual P values reported in the figure legends and summaries, by way of abbreviations and asterisks, on the graphs: ns, not significant; * $P < 0.05$; **, $P < 0.02$; ***, $P < 0.001$; ****, $P < 0.0001$.

Reproducibility. Samples sizes for in vitro pharmacological or in vivo cardiorespiratory experiments were based on prior experience and were routinely in excess of 4 individual biological replicates. In many instances the pool of replicates was added to over time via interleaved experiments with other compounds and often by other investigators, ensuring the consistency and reproducibility of experimental observations. Data was only excluded when technical failures occurred. Randomisation and blinding was not performed for in vitro or cardiorespiratory studies. In the pain and rotarod studies, the sample sizes for which (typically 6 animals) were based on prior experience, the experimenters were blinded to the reagents used. For the pain studies, all animals were pre-screened for hypersensitivity (von Frey hair) when they arrived, and those that showed this, i.e., a paw withdrawal threshold (PWT) less than 8 g, were eliminated from the study. Those rats successfully developing mechanical allodynia (with PWT lower than 4 g) were randomly assigned into different groups according to their PWT values of pre-surgery, 1 week post-surgery and pre-dosing to ensure a balanced distribution across groups. For the rotarod studies, rats were randomly assigned to treatment groups by animal care technicians not involved in the experimental studies. Experiments occurred over a period of time with various types of manipulations interleaved to avoid batch effects. Key observations were replicated with different batches of animals and reagents and by different experimenters. Results across different independent labs working in different experimental systems were consistent with the main themes and conclusions of the study.

Drugs and substances. Drugs were made up as stock solutions (1-10 mM) and then diluted in aCSF or saline on the day of use. BnOCPA[34] ((2 *R*,3 *R*,4 *S*,5 *R*)−2-(6-{[(1 *R*,2 *R*)−2-benzyloxycyclopentyl]amino}−9*H*-purin-9-yl)−5-(hydroxymethyl)oxolane-3,4-diol) and HOCPA[47] ((2 *R*,3 *R*,4 *S*,5 *R*)−2-(6-{[(1 *R*,2 *R*)−2-hydroxycyclopentyl]amino}−9*H*-purin-9-yl)−5-(hydroxymethyl)oxolane-3,4-diol), the [(1 *R*,2 *R*)−2-hydroxycyclopentyl]amino bis-epimer of known A_1R agonist GR79236[49], were synthesised as described previously[33] and dissolved in dimethyl-sulphoxide (DMSO, 0.01% final concentration). Adenosine, 8-CPT (8-cyclopentyltheophylline), NECA (5′-(*N*-Ethylcarboxamido) adenosine), DPCPX, ZM241385, MRS1220 and CPA (N^6-Cyclopentyladenosine) were purchased from Sigma-Aldrich (Poole, Dorset, UK). MRS1523 was purchased from Cayman Chemicals (Cambridge Bioscience Ltd., Cambridge UK). [^{3}H]-DPCPX was purchased from PerkinElmer (Life and Analytical Sciences, Waltham, MA). CA200645 and peptides for interfering with G protein signalling were obtained from Hello Bio (Bristol, UK) and were based on published sequences[60]. NECA-TAMARA was synthesised in-house (Noel et al., in preparation), while AV039, a highly potent and selective fluorescent antagonist of the human A_3R based on the 1,2,4-Triazolo[4,3-a]quinoxalin-1-one linked to BY630 was kindly gifted to us by Stephen Hill and Stephen Briddon (University of Nottingham). For G_{oa} the peptide had a sequence of MGIANNLRGCGLY. The scrambled version was LNRGNAYLCIGMG. For G_{ob} the peptide had a sequence of MGIAKNLRGCGLY. Peptides were made up as stock solutions (2 mM) and stored at −20 °C. The stock solutions were dissolved in filtered intracellular solution just before use.

BnOCPA Pharmacokinetics. The stability in solution and metabolism of BnOCPA (0.1 µM or 1 µM) was assessed by Eurofins Panlabs (Supplementary Data 1). The parameters examined were: half-life ($t_{1/2}$) in PBS (1 µM BnOCPA, 37 °C, pH 7.4; Assay #600); $t_{1/2}$ in human plasma (1 µM BnOCPA, 37 °C; Assay #887) and intrinsic clearance by human liver microsomes (0.1 µM BnOCPA, 0.1 mg/ml, 37 °C; Assay #607).

Half-life determination in PBS. At the end of the incubation at each of the time points (0, 1, 2, 3, 4 h), an equal volume of an organic mixture (acetonitrile/methanol, 50/50 v/v) was added to the incubation mixture. Samples were analysed by HPLC-MS/MS and corresponding peak areas were recorded for each analyte. The ratio of precursor compound remaining after each time-point relative to the amount present at time 0, expressed as a percentage, is reported as chemical stability. The $t_{1/2}$ was estimated from the slope of the initial linear range of the logarithmic curve of compound remaining (%) versus time, assuming first-order kinetics.

Half-life determination in human plasma. At the end of incubation at each of the time points (0, 0.5, 1, 1.5, 2 h), acetonitrile was added to the incubation mixture followed by centrifugation. Samples were analysed by HPLC-MS/MS and peak areas were recorded for each analyte. The area of precursor compound remaining after each of the time points relative to the amount remaining at time 0, expressed as a percentage, was calculated. Subsequently, the $t_{1/2}$ is estimated from the slope of the initial linear range of the logarithmic curve of compound remaining (%) versus time, assuming first-order kinetics.

Intrinsic clearance by human liver microsomes. Metabolic stability, expressed as a percentage of the parent compound remaining, was calculated by comparing the peak area of the compound at the time-point (0, 15, 30, 45, 60 min) relative to that at time 0. The $t_{1/2}$ was estimated from the slope of the initial linear range of the logarithmic curve of compound remaining (%) vs. time, assuming the first-order kinetics. The apparent intrinsic clearance (CL_{int}, in µL/min/mg) was calculated according to the following Eq. (3):

$$CL_{int} = \frac{0.693}{t_{1/2} \times (0.0001\text{mg protein}/\mu\text{L})} \quad (3)$$

The behaviour of BnOCPA was compared to appropriate standards. Data is available in Supplemental Data File 1

Molecular dynamics simulations

Ligand parameterisation. The CHARMM36[116,117]/CGenFF[118–120] force field combination was employed in all the MD simulations performed. Initial topology and parameter files of BnOCPA, HOCPA, and PSB36 were obtained from the

Table 1 Summary of the simulations performed.

Ligand	MD approach	# Replicas	Total simulated time♦
BnOCPA	SuMD	6	1.9 μs
BnOCPA	SuMD-Metadynamics	5	4.3 μs
HOCPA	SuMD	5	3.4 μs
BnOCPA (bound state after dynamic docking)	Metadynamics	3	0.75 μs
BnOCPA(A)	Classic MD	6	9.0 μs
BnOCPA(B)	Classic MD	6	9.0 μs
BnOCPA(C)	Classic MD	3	3.0 μs
BnOCPA(D)	Classic MD	6	9.0 μs
HOCPA	Classic MD	4	8.0 μs
PSB36	Classic MD	4	6.0 μs
Apo A_1	Classic MD	4	8.0 μs
GαCT Goa (BnOCPA)	SuMD + Classic MD	10	0.36 μs + 3.0 μs
GαCT Gob (BnOCPA)	SuMD + Classic MD	10	0.33 μs + 3.0 μs
GαCT Gi2 (BnOCPA)	SuMD + Classic MD	10	0.37 μs + 3.0 μs
GαCT Gob (HOCPA)	SuMD + Classic MD	10	0.29 μs + 3.0 μs
BnOCPA(D):Gob	Classic MD	4	4.0 μs
BnOCPA(B):Gob	Classic MD	3	3.0 μs
HOCPA:Gob	Classic MD	4	4.0 μs
BnOCPA(D):Goa	Classic MD	5	5.0 μs
BnOCPA(B):Goa	Classic MD	4	4.0 μs

♦For SuMD and SuMD-metadynamics simulations the time is the sum of productive SuMD time windows.
(A), (B), (C) and (D) indicate the respective BnOCPA binding modes.

Paramchem webserver[118]. Higher penalties were associated with a few BnOCPA dihedral terms, which were therefore optimised at the HF/6-31 G* level of theory using both the high throughput molecular dynamics (HTMD)[121] parameterise functionality and the visual molecular dynamics (VMD)[122] Force Field Toolkit (ffTK)[123], after fragmentation of the molecule. Short MD simulations of BnOCPA in water were performed to visually inspect the behaviour of the optimised rotatable bonds.

Systems preparation for fully dynamic docking of BnOCPA and HOCPA. Coordinates of the A_1R in the active, adenosine- and G protein-bound state were retrieved from the Protein Data Bank[124,125] database (PDB ID 6D9H[77]). Intracellular loop 3 (ICL3) which is missing from PDB ID 6D9H was rebuilt using Modeller 9.19[126,127]. The G protein, with the exception of the C-terminal helix (helix 5) of the G protein alpha subunit (the key region responsible for the receptor TM6 active-like conformation) was removed from the system as in previous work[128,129]. BnOCPA and HOCPA were placed in the extracellular bulk, in two different systems, at least 20 Å from the receptor vestibule. The resulting systems were prepared for simulations using in-house scripts able to exploit both python HTMD[121] and Tool Command Language (TCL) scripts. Briefly, this multistep procedure performs the preliminary hydrogen atoms addition by means of the pdb2pqr[130] and propka3[131] software, considering a simulated pH of 7.0 (the proposed protonation of titratable side chains was checked by visual inspection). Receptors were then embedded in a square 80 Å × 80 Å 1-palmitoyl-2-oleyl-sn-glycerol-3-phosphocholine (POPC) bilayer (previously built by using the VMD Membrane Builder plugin 1.1, Membrane Plugin, Version 1.1.; http://www.ks.uiuc.edu/Research/vmd/plugins/membrane/) through an insertion method[132], considering the A_1R coordinates retrieved from the OPM database[133] to gain the correct orientation within the membrane. Lipids overlapping the receptor transmembrane bundle were removed and TIP3P water molecules[134] were added to the simulation box (final dimensions 80 Å × 80 Å × 125 Å) using the VMD Solvate plugin 1.5 (Solvate Plugin, Version 1.5; http://www.ks.uiuc.edu/Research/vmd/plugins/solvate/). Finally, overall charge neutrality was achieved by adding Na^+/Cl^- counter ions (concentration of 0.150 M) using the VMD Autoionize plugin 1.3 (Autoionize Plugin, Version 1.3; http://www.ks.uiuc.edu/Research/vmd/plugins/autoionize/). All histidine side chains were considered in the delta tautomeric state, with the exception of H251 (epsilon tautomer) and H278 (protonated).

The MD engine ACEMD[135] was employed for both the equilibration and productive simulations. Systems were equilibrated in isothermal-isobaric conditions (NPT) using the Berendsen barostat[136] (target pressure 1 atm), the Langevin thermostat[137] (target temperature 300 K) with a low damping factor of 1 ps^{-1} and with an integration time step of 2 fs. Clashes between protein and lipid atoms were reduced through 2000 conjugate-gradient minimisation steps before a 2 ns long MD simulation was run with a positional constraint of 1 kcal mol^{-1} $Å^{-2}$ on protein and lipid phosphorus atoms. Twenty nanoseconds of MD simulation were then performed constraining only the protein atoms. Lastly, positional constraints were applied only to the protein backbone alpha carbons for a further 5 ns.

Dynamic docking of BnOCPA and HOCPA. The supervised MD (SuMD) approach is an adaptive sampling method[138] for simulating binding events in a timescale one or two orders of magnitudes faster than the corresponding classical (unsupervised) MD simulations[139]. SuMD has been successfully applied to small molecules and peptides[140–146]. In the present work, the distances between the centres of mass of the adenine scaffold of the A_1R agonist and $N254^{6.55}$, $F171^{ECL2}$, $T277^{7.42}$ and $H278^{7.43}$ of the receptor were considered for the supervision during the MD simulations. The dynamic docking of BnOCPA was hindered by the ionic bridge formed between the $E172^{ECL2}$ and $K265^{ECL3}$ side chains. A metadynamics[147–149] energetic bias was therefore introduced in order to facilitate the rupture of this ionic interaction, thus favoring the formation of a bound complex. More precisely, Gaussian terms (height = 0.01 kcal mol^{-1} and widths = 0.1 Å) were deposited every 1 ps along the distance between the $E172^{ECL2}$ carboxyl carbon and the positively charged $K265^{ECL3}$ nitrogen atom using PLUMED 2.3[150]. A similar SuMD-metadynamics hybrid approach was previously employed to study binding/unbinding kinetics[151] on the $A_{2A}R$ subtype. For each replica (Table 1), when the ligands reached a bound pose (i.e. a distance between the adenine and the receptor residues centres of mass <3 Å), a classic (unsupervised and without energetic bias) MD simulation was performed for at least a further 100 ns.

BnOCPA bound state metadynamics. We decided to perform a detailed analysis of the role played by the $E172^{ECL2}$–$K265^{ECL3}$ ionic interaction in the dynamic docking of BnOCPA. Three 250 ns long well-tempered[152] metadynamics simulations were performed using the bound state obtained from a previous dynamic docking simulation, which resulted in binding mode A, as a starting point. The collective variables (CVs) considered were: i) the distance between the $E172^{ECL2}$ carboxyl carbon and the positively charged $K265^{ECL3}$ nitrogen atom and ii) the dihedral angle formed by the 4 atoms linking the cyclopentyl ring to the phenyl moiety (which was the most flexible ligand torsion during the previous SuMD simulations). Gaussian widths were set at 0.1 Å and 0.01 radians respectively, heights at 0.01 kcal/mol^{-1}, and the deposition was performed every 1 ps (bias-factor = 5). Although complete convergence was probably not reached, three replicas (Table 1) allowed sampling of three main energetic minima on the energy surface (Supplementary Fig. 8); these correspond to the representative binding poses shown in Fig. 3d to f.

Classic MD simulations of BnOCPA binding modes A, B, C and D. To test the hypothesis that BnOCPA and HOCPA may differently affect TM6 and/or TM7 mobility when bound to A_1R (and to further sample the stability of each BnOCPA binding mode), putative binding conformations A, B and C (Fig. 3) were superposed to the experimental A_1R active state coordinates with the modelled ICL3. This should have removed any A_1R structural artefacts, possibly introduced by metadynamics. As reference and control, two further systems were considered: i) the pseudo-apo A_1R and ii) the selective A_1R antagonist PSB36[72] superposed in the same receptor active conformation (Table 1). The BnOCPA binding mode D was modelled from mode B by rotating the dihedral angle connecting the cyclopentyl ring and the N6 nitrogen atom in order to point the benzyl of the agonist toward the hydrophobic pocket underneath ECL3 (Fig. 3g) delimited by $L253^{6.56}$, $T257^{6.52}$, $K265^{ECL3}$, $T270^{7.35}$, and $L269^{7.34}$. The G protein atoms were removed, and the resulting systems prepared for MD as reported above. A similar comparison was performed in a milestone study on the β_2 adrenergic receptor[76] which sought to describe the putative deactivation mechanism of the receptor.

Dynamic docking of the Goa, Gob and Gi2-GαCT helix. A randomly extracted frame from the classic MD performed on the BnOCPA:A_1R complex was prepared for three sets of simulations placing the GαCT helix 5 (last 27 residues) of the Gα proteins Goa, Gob and Gi2 in the intracellular solvent bulk side of the simulation boxes. As a further control, a frame from the classic MD performed on the unbiased ligand HOCPA:A_1R complex was randomly extracted and prepared along with the Gob-GαCT. The resulting four systems were embedded in a POPC membrane and prepared as reported above.

The different structural effects putatively triggered by BnOCPA and HOCPA on the recognition mechanism of Goa, Gob and Gi2-GαCT were studied by performing 10 SuMD replicas (Table 1). During each replica (Video S3), the distance between the centroid of the GαCT residues 348-352 and the centroid of the A1R residues D42$^{2.37}$, I232$^{6.33}$, and Q293$^{8.48}$ was supervised until it reached a value lower than 8 Å. A classic MD simulation was then run for a further 300 ns.

Classic MD simulations on the A_1R:Goa and Gob complexes. The A_1R cryo-EM structure (PDB ID 6D9H) was used as template for all the five systems simulated (Table 1). The endogenous agonist adenosine was removed and HOCPA and BnOCPA (modes B and D) were inserted in the orthosteric site superimposing 6D9H to the systems prepared for the classic MD simulations in the absence of G protein. ICL3 was not modelled, nor were the missing part of the G protein α subunit. As subunits β and γ were removed, the Gα NT helix was truncated to residue 27 to avoid unnatural movements (NT is constrained by Gβ in 6D9H). The Gα subunit was mutated according to the Goa and Gob primary sequences[87] using in-house scripts. The resulting five systems (Table 1) were embedded in a POPC membrane and prepared as reported above.

Analysis of the classic MD simulations. During the classic MD simulations that started from Modes A-C (Fig. 3d–g), BnOCPA had the tendency to explore the three conformations by rapidly interchanging between the three binding modes. In order to determine the effect exerted on the TM domain by each conformation, 30 µs of MD simulations (Table 1: BnOCPA mode A, BnOCPA mode B, BnOCPA mode C, BnOCPA mode D) were subjected to a geometric clustering. More precisely, a simulation frame was considered in pose A if the distance between the phenyl ring of BnOCPA and the I175^{ECL2} alpha carbon was less than 5 Å; in pose B if the distance between the phenyl ring of BnOCPA and the L258$^{6.59}$ alpha carbon was less than 6 Å, and in pose C if the distance between the phenyl ring of BnOCPA and the Y271$^{7.36}$ alpha carbon was less than 6 Å. During the MD simulations started from mode D (Fig. 3g), a frame was still considered in mode D if the root mean square deviation (RMSD) of the benzyl ring to the starting equilibrated conformation was less than 3 Å. For each of the resulting four clusters, the RMSD of the GPCR conserved motif NPXXY (N$^{7.49}$ PIV Y$^{7.53}$ in the A_1R; Supplementary Fig. 9) was computed using Plumed 2.3[150] considering the inactive receptor state as reference, plotting the obtained values as frequency distributions (Fig. 3i, j). Rearrangement of the NPXXY motif, which is located at the intracellular half of TM7, is considered one of the structural hallmarks of GPCR activation[79]. Upon G protein binding, it moves towards the centre of the receptor TM bundle (Supplementary Fig. 9). Unlike other activation micro-switches (e.g. the break/formation of the salt bridge between R$^{3.50}$ and E$^{6.30}$), this conformational transition is believed to occur in timescales accessible to MD simulations[76].

Hydrogen bonds and atomic contacts were computed using the GetContacts analysis tool (https://github.com/getcontacts/getcontacts) and expressed in terms of occupancy (the percentage of MD frames in which the interaction occurred).

Analysis of the Goa, Gob and Gi2-GαCT classic MD simulations after SuMD. For each system, only the classic MD simulations performed after the GαCT reached the A_1R intracellular binding site were considered for the analysis.

The RMSD values to the last 15 residues of the Gi2-GαCT reported in the A_1R cryo-EM PDB structure 6D9H were computed using VMD[122]. The MD frames associated with the peaks in the RMSD plots (states CS1, MS1, MS2 and MS3 in Fig. 4a, d) were clustered employing the VMD Clustering plugin (https://github.com/luisico/clustering) by selecting the whole GαCT helixes alpha carbon atoms and a cutoff of 3 Å.

Reporting summary. Further information on research design is available in the Nature Research Reporting Summary linked to this article.

Data availability

The active cryo-EM structure of the A_1R (PDB code 6D9H) was retrieved from https://www.rcsb.org/structure/6d9h; the human neurotensin receptor 1 (PDB code 6OSA) from https://www.rcsb.org/structure/6OSA, and the β2 adrenergic receptor (PDB code 6E67) from https://www.rcsb.org/3d-view/6e67. Source data are provided with this paper.

Code availability

SuMD scripts used for this manuscript, and newer versions, are provided as Supplemental Data File 2. AceMD software is available from Acellera's website www.acellera.com.

Received: 21 July 2020; Accepted: 23 June 2022;
Published online: 18 July 2022

References

1. Hauser, A. S., Attwood, M. M., Rask-Andersen, M., Schiöth, H. B. & Gloriam, D. E. Trends in GPCR drug discovery: new agents, targets and indications. *Nat. Rev. Drug Discov.* **16**, 829 (2017).
2. Congreve, M., de Graaf, C., Swain, N. A. & Tate, C. G. Impact of GPCR structures on drug discovery. *Cell* **181**, 81–91 (2020).
3. Kenakin, T. Is the quest for signaling bias worth the effort? *Mol. Pharm.* **93**, 266–269 (2018).
4. Michel, M. C. & Charlton, S. J. Biased agonism in drug discovery-is it too soon to choose a path? *Mol. Pharm.* **93**, 259–265 (2018).
5. Jacobson, K. A. & Muller, C. E. Medicinal chemistry of adenosine, P2Y and P2X receptors. *Neuropharmacology* **104**, 31–49 (2016).
6. Borea, P. A., Gessi, S., Merighi, S., Vincenzi, F. & Varani, K. Pharmacology of adenosine receptors: the state of the art. *Physiol. Rev.* **98**, 1591–1625 (2018).
7. Sawynok, J. Adenosine receptor targets for pain. *Neuroscience* **338**, 1–18 (2016).
8. Headrick, J. P., Ashton, K. J., Rose'meyer, R. B. & Peart, J. N. Cardiovascular adenosine receptors: expression, actions and interactions. *Pharm. Ther.* **140**, 92–111 (2013).
9. Dunwiddie, T. V. & Masino, S. A. The role and regulation of adenosine in the central nervous system. *Annu Rev. Neurosci.* **24**, 31–55 (2001).
10. Vecchio, E. A. et al. New paradigms in adenosine receptor pharmacology: allostery, oligomerization and biased agonism. *Br. J. Pharm.* **175**, 4036–4046 (2018).
11. Kaczynska, K. & Szereda-Przestaszewska, M. The potential role of the nodose ganglion adenosine A_1 receptor in regulation of breathing in anaesthetized rats. *J. Physiol. Pharm.* **59**, 759–770 (2008).
12. Koeppen, M., Eckle, T. & Eltzschig, H. K. Selective deletion of the A_1 adenosine receptor abolishes heart-rate slowing effects of intravascular adenosine in vivo. *PLoS ONE* **4**, e6784 (2009).
13. Varani, K., Vincenzi, F., Merighi, S., Gessi, S. & Borea, P. A. Biochemical and pharmacological role of A_1 adenosine receptors and their modulation as novel therapeutic strategy. *Adv. Exp. Med. Biol.* **1051**, 193–232 (2017).
14. Baltos, J. A. et al. Quantification of adenosine A_1 receptor biased agonism: Implications for drug discovery. *Biochem. Pharm.* **99**, 101–112 (2016).
15. Weltha L., Reemmer J., Boison D. The role of adenosine in epilepsy. *Brain Res. Bull.* **151**, 46–54 (2018).
16. Deb, P. K., Deka, S., Borah, P., Abed, S. N. & Klotz, K. N. Medicinal chemistry and therapeutic potential of agonists, antagonists and allosteric modulators of A_1 adenosine receptor: current status and perspectives. *Curr. Pharm. Des.* **25**, 2697–2715 (2019).
17. Kenakin, T. Biased receptor signaling in drug discovery. *Pharm. Rev.* **71**, 267–315 (2019).
18. Wootten, D., Christopoulos, A., Marti-Solano, M., Babu, M. M. & Sexton, P. M. Mechanisms of signalling and biased agonism in G protein-coupled receptors. *Nat. Rev. Mol. Cell Biol.* **19**, 638–653 (2018).
19. Violin, J. D. & Lefkowitz, R. J. Beta-arrestin-biased ligands at seven-transmembrane receptors. *Trends Pharm. Sci.* **28**, 416–422 (2007).
20. Smith, J. S., Lefkowitz, R. J. & Rajagopal, S. Biased signalling: from simple switches to allosteric microprocessors. *Nat. Rev. Drug Discov.* **17**, 243–260 (2018).
21. Foster, D. J. & Conn, P. J. Allosteric modulation of GPCRs: new insights and potential utility for treatment of schizophrenia and other CNS disorders. *Neuron* **94**, 431–446 (2017).
22. Wingler, L. M. et al. Angiotensin and biased analogs induce structurally distinct active conformations within a GPCR. *Science* **367**, 888–892 (2020).
23. Slosky L. M., et al. Beta-arrestin-biased allosteric modulator of NTSR1 selectively attenuates addictive behaviors. *Cell* **181**, 1364–1379.e14 (2020).
24. Kliewer, A. et al. Morphine-induced respiratory depression is independent of beta-arrestin2 signalling. *Br. J. Pharm.* **177**, 2923–2931 (2020).
25. Yano, H. et al. Gs- versus Golf-dependent functional selectivity mediated by the dopamine D1 receptor. *Nat. Commun.* **9**, 486 (2018).
26. Von Moo, E. et al. Ligand-directed bias of G protein signaling at the dopamine D2 receptor. *Cell Chem. Biol.* **29**, 226–238.e224 (2022).
27. Luttrell, L. M., Maudsley, S. & Gesty-Palmer, D. Translating in vitro ligand bias into in vivo efficacy. *Cell Signal.* **41**, 46–55 (2018).
28. Benredjem, B. et al. Exploring use of unsupervised clustering to associate signaling profiles of GPCR ligands to clinical response. *Nat. Commun.* **10**, 4075 (2019).
29. Cordeaux, Y., Ijzerman, A. P. & Hill, S. J. Coupling of the human A_1 adenosine receptor to different heterotrimeric G proteins: evidence for agonist-specific G protein activation. *Br. J. Pharm.* **143**, 705–714 (2004).

30. Stewart, G. D. et al. Determination of adenosine A1 receptor agonist and antagonist pharmacology using Saccharomyces cerevisiae: implications for ligand screening and functional selectivity. *J. Pharm. Exp. Ther.* **331**, 277–286 (2009).
31. Valant, C. et al. Separation of on-target efficacy from adverse effects through rational design of a bitopic adenosine receptor agonist. *Proc. Natl Acad. Sci. USA* **111**, 4614–4619 (2014).
32. Aurelio, L. et al. A Structure-Activity Relationship Study of Bitopic N(6)-Substituted Adenosine Derivatives as Biased Adenosine A_1 Receptor Agonists. *J. Med Chem.* **61**, 2087–2103 (2018).
33. Knight, A. et al. Discovery of novel adenosine receptor agonists that exhibit subtype selectivity. *J. Med Chem.* **59**, 947–964 (2016).
34. Jagtap P. Adenosine compounds and their use thereof Patent WO2011/119919 A1 (2011).
35. Jacobson, K. A. et al. A_3-adenosine receptors: design of selective ligands and therapeutic prospects. *Drugs Future* **20**, 689–699 (1995).
36. Angers, S. et al. Detection of β_2-adrenergic receptor dimerization in living cells using bioluminescence resonance energy transfer (BRET). *Proc. Natl Acad. Sci.* **97**, 3684–3689 (2000).
37. Hamdan F. F., Percherancier Y., Breton B., Bouvier M. Monitoring protein-protein interactions in living cells by bioluminescence resonance energy transfer (BRET). *Curr Protoc Neurosci* **Chapter 5**, Unit 5.23 (2006).
38. Kocan, M. & Pfleger, K. D. Study of GPCR-protein interactions by BRET. *Methods Mol. Biol.* **746**, 357–371 (2011).
39. Pfleger, K. D., Seeber, R. M. & Eidne, K. A. Bioluminescence resonance energy transfer (BRET) for the real-time detection of protein-protein interactions. *Nat. Protoc.* **1**, 337–345 (2006).
40. Salahpour, A. et al. BRET biosensors to study GPCR biology, pharmacology, and signal transduction. *Front Endocrinol. (Lausanne)* **3**, 105 (2012).
41. Ciruela, F. et al. Ligand-induced phosphorylation, clustering, and desensitization of A_1 adenosine receptors. *Mol. Pharm.* **52**, 788–797 (1997).
42. Escriche, M. et al. Ligand-induced caveolae-mediated internalization of A_1 adenosine receptors: morphological evidence of endosomal sorting and receptor recycling. *Exp. Cell Res.* **285**, 72–90 (2003).
43. Ferguson, G., Watterson, K. R. & Palmer, T. M. Subtype-specific regulation of receptor internalization and recycling by the carboxyl-terminal domains of the human A_1 and rat A_3 adenosine receptors: consequences for agonist-stimulated translocation of arrestin3. *Biochemistry* **41**, 14748–14761 (2002).
44. Gines, S. et al. Involvement of caveolin in ligand-induced recruitment and internalization of A_1 adenosine receptor and adenosine deaminase in an epithelial cell line. *Mol. Pharm.* **59**, 1314–1323 (2001).
45. Iacovelli, L., Franchetti, R., Grisolia, D. & De Blasi, A. Selective regulation of G protein-coupled receptor-mediated signaling by G protein-coupled receptor kinase 2 in FRTL-5 cells: analysis of thyrotropin, $alpha_{1B}$-adrenergic, and A_1 adenosine receptor-mediated responses. *Mol. Pharm.* **56**, 316–324 (1999).
46. Yin, W. et al. A complex structure of arrestin-2 bound to a G protein-coupled receptor. *Cell Res.* **29**, 971–983 (2019).
47. Evans B. Adenosine Derivatives Patent EP0322242 (1989).
48. Gurden, M. F. et al. Functional characterization of three adenosine receptor types. *Br. J. Pharm.* **109**, 693–698 (1993).
49. Strong, P. et al. Suppression of non-esterified fatty acids and triacylglycerol in experimental animals by the adenosine analogue GR79236. *Clin. Sci. (Lond.)* **84**, 663–669 (1993).
50. Wise, A., Sheehan, M., Rees, S., Lee, M. & Milligan, G. Comparative analysis of the efficacy of A_1 adenosine receptor activation of Gi/o alpha G proteins following coexpression of receptor and G protein and expression of A_1 adenosine receptor-Gi/o alpha fusion proteins. *Biochemistry* **38**, 2272–2278 (1999).
51. Avet C., et al. Selectivity landscape of 100 therapeutically relevant GPCR profiled by an effector translocation-based BRET platform. *bioRxiv*, https://www.biorxiv.org/content/10.1101/2020.04.20.052027v1 (2020).
52. Black, J. W. & Leff, P. Operational models of pharmacological agonism. *Proc. R. Soc. Lond. B Biol. Sci.* **220**, 141–162 (1983).
53. Gomes, I. et al. Biased signaling by endogenous opioid peptides. *Proc. Natl Acad. Sci. USA* **117**, 11820–11828 (2020).
54. Kenakin, T., Watson, C., Muniz-Medina, V., Christopoulos, A. & Novick, S. A simple method for quantifying functional selectivity and agonist bias. *ACS Chem. Neurosci.* **3**, 193–203 (2012).
55. Olsen, R. H. J. et al. TRUPATH, an open-source biosensor platform for interrogating the GPCR transducerome. *Nat. Chem. Biol.* **16**, 841–849 (2020).
56. Galés, C. et al. Probing the activation-promoted structural rearrangements in preassembled receptor–G protein complexes. *Nat. Struct. Mol. Biol.* **13**, 778–786 (2006).
57. Busnelli, M. et al. Functional selective oxytocin-derived agonists discriminate between individual G protein family subtypes. *J. Biol. Chem.* **287**, 3617–3629 (2012).
58. Tallarida R. J., Murray R. B. Analysis of the Regression Line. In: *Manual of Pharmacologic Calculations: With Computer Programs*). Springer New York (1987).
59. Kolasa, K., Harrell, L. E. & Parsons, D. S. Effects of pertussis toxin and galpha-protein-specific antibodies on phosphoinositide hydrolysis in rat brain membranes after cholinergic denervation and hippocampal sympathetic ingrowth. *Exp. Neurol.* **161**, 724–732 (2000).
60. Gilchrist, A., Li, A. & Hamm, H. E. G alpha COOH-terminal minigene vectors dissect heterotrimeric G protein signaling. *Sci. STKE* **2002**, pl1 (2002).
61. Gilchrist A., et al. Antagonists of the receptor-G protein interface block Gi-coupled signal transduction. *J. Biol. Chem.* **273**, 14912–14919 (1998).
62. McPherson, K. B. et al. Regulators of G-protein signaling (RGS) proteins promote receptor coupling to G-protein-coupled inwardly rectifying potassium (GIRK) channels. *J. Neurosci.* **38**, 8737–8744 (2018).
63. Ding, J. et al. RGS4-dependent attenuation of M4 autoreceptor function in striatal cholinergic interneurons following dopamine depletion. *Nat. Neurosci.* **9**, 832–842 (2006).
64. Vanhauwe, J. F. et al. Thrombin receptors activate Go proteins in endothelial cells to regulate intracellular calcium and cell shape changes. *J. Biol. Chem.* **277**, 34143–34149 (2002).
65. Goldsmith P., et al. Antibodies directed against synthetic peptides distinguish between GTP-binding proteins in neutrophil and brain. *J. Biol. Chem.* **262**, 14683–14688 (1987).
66. Mousli, M., Bronner, C., Bockaert, J., Rouot, B. & Landry, Y. Interaction of substance P, compound 48/80 and mastoparan with the alpha-subunit C-terminus of G protein. *Immunol. Lett.* **25**, 355–357 (1990).
67. McIntire, W. E., Dingus, J., Schey, K. L. & Hildebrandt, J. D. Characterization of the major bovine brain Go alpha isoforms. Mapping the structural differences between the alpha subunit isoforms identifies a variable region of the protein involved in receptor interactions. *J. Biol. Chem.* **273**, 33135–33141 (1998).
68. Oleskevich, S. G alpha o1 decapeptide modulates the hippocampal 5-HT1A potassium current. *J. Neurophysiol.* **74**, 2189–2193 (1995).
69. Rouot, B. et al. Specific antibodies against Go isoforms reveal the early expression of the Go2 alpha subunit and appearance of Go1 alpha during neuronal differentiation. *Mol. Pharm.* **41**, 273–280 (1992).
70. Oleskevich, S., Leck, K. J., Matthaei, K. & Hendry, I. A. Enhanced serotonin response in the hippocampus of Galphaz protein knock-out mice. *Neuroreport* **16**, 921–925 (2005).
71. Deganutti, G. et al. Deciphering the agonist binding mechanism to the adenosine A_1. *Receptor. ACS Pharm. Transl. Sci.* **4**, 314–326 (2021).
72. Cheng, R. K. Y. et al. Structures of human A_1 and A_{2A} adenosine receptors with xanthines reveal determinants of selectivity. *Structure* **25**, 1275–1285.e1274 (2017).
73. Bussi, G. & Laio, A. Using metadynamics to explore complex free-energy landscapes. *Nat. Rev. Phys.* **2**, 200–212 (2020).
74. Flock, T. et al. Selectivity determinants of GPCR-G-protein binding. *Nature* **545**, 317–322 (2017).
75. Okashah, N. et al. Variable G protein determinants of GPCR coupling selectivity. *Proc. Natl Acad. Sci. USA* **116**, 12054–12059 (2019).
76. Dror, R. O. et al. Activation mechanism of the β2-adrenergic receptor. *Proc. Natl. Acad. Sci. USA* **108**, 18684–18689 (2011).
77. Draper-Joyce, C. J. et al. Structure of the adenosine-bound human adenosine A_1 receptor-Gi complex. *Nature* **558**, 559–563 (2018).
78. Glukhova, A. et al. Structure of the adenosine A_1 receptor reveals the basis for subtype selectivity. *Cell* **168**, 867–877 e813 (2017).
79. Rosenbaum, D. M., Rasmussen, S. G. & Kobilka, B. K. The structure and function of G-protein-coupled receptors. *Nature* **459**, 356–363 (2009).
80. Kato, H. E. et al. Conformational transitions of a neurotensin receptor 1-Gi1 complex. *Nature* **572**, 80–85 (2019).
81. Liu, X. et al. Structural insights into the process of GPCR-G protein complex formation. *Cell* **177**, 1243–1251 e1212 (2019).
82. Kooistra, A. J. et al. GPCRdb in 2021: integrating GPCR sequence, structure and function. *Nucleic Acids Res.* **49**, D335–D343 (2020).
83. GPCRdb. Human A_1R mutations. https://gpcrdb.org/mutations/protein/aa1r_human/ (2020).
84. Asano, T. et al. The G-protein Go in mammalian cardiac muscle: localization and coupling to A_1 adenosine receptors. *J. Biochem* **117**, 183–189 (1995).
85. Wolf, W. P., Spicher, K., Haase, H. & Schulze, W. Immunocytochemical localization of the G-protein sub-unit, Go alpha, in rat heart. Implications for a role of Go alpha in secretion of cardiac hormones. *J. Mol. Cell Cardiol.* **30**, 1149–1162 (1998).
86. McGrath, M. F. & de Bold, A. J. Transcriptional analysis of the mammalian heart with special reference to its endocrine function. *BMC Genomics* **10**, 254 (2009).
87. Jiang, M. & Bajpayee, N. S. Molecular mechanisms of Go signaling. *Neurosignals* **17**, 23–41 (2009).

88. Kawai, Y. & Arinze, I. J. Differential localization and development-dependent expression of G-protein subunits, Go alpha and G beta, in rabbit heart. *J. Mol. Cell Cardiol.* **28**, 1555–1564 (1996).
89. Belardinelli, L., Shryock, J. C., Song, Y., Wang, D. & Srinivas, M. Ionic basis of the electrophysiological actions of adenosine on cardiomyocytes. *FASEB J.* **9**, 359–365 (1995).
90. Kim, S. H. & Chung, J. M. An experimental model for peripheral neuropathy produced by segmental spinal nerve ligation in the rat. *Pain* **50**, 355–363 (1992).
91. Fayaz, A., Croft, P., Langford, R. M., Donaldson, L. J. & Jones, G. T. Prevalence of chronic pain in the UK: a systematic review and meta-analysis of population studies. *BMJ Open* **6**, e010364 (2016).
92. Yong R. J., Mullins P. M., Bhattacharyya N. Prevalence of chronic pain among adults in the United States. *Pain* **163**, e328–e332 (2021).
93. Vos, T. et al. Global, regional, and national incidence, prevalence, and years lived with disability for 328 diseases and injuries for 195 countries, 1990–2016: a systematic analysis for the Global Burden of Disease Study 2016. *Lancet* **390**, 1211–1259 (2017).
94. Chincholkar, M. Analgesic mechanisms of gabapentinoids and effects in experimental pain models: a narrative review. *Br. J. Anaesth.* **120**, 1315–1334 (2018).
95. Li, A. H., Moro, S., Melman, N., Ji, X. D. & Jacobson, K. A. Structure-activity relationships and molecular modeling of 3, 5-diacyl-2,4-dialkylpyridine derivatives as selective A_3 adenosine receptor antagonists. *J. Med. Chem.* **41**, 3186–3201 (1998).
96. Alnouri, M. W. et al. Selectivity is species-dependent: characterization of standard agonists and antagonists at human, rat, and mouse adenosine receptors. *Purinergic Signal* **11**, 389–407 (2015).
97. Chen, Z. et al. Controlling murine and rat chronic pain through A_3 adenosine receptor activation. *FASEB J.* **26**, 1855–1865 (2012).
98. Ford, A. et al. Engagement of the GABA to KCC2 signaling pathway contributes to the analgesic effects of A_3AR agonists in neuropathic pain. *J. Neurosci.* **35**, 6057–6067 (2015).
99. Lucarini, E. et al. Acute visceral pain relief mediated by A3AR agonists in rats: involvement of N-type voltage-gated calcium channels. *Pain* **161**, 2179–2190 (2020).
100. Imlach, W. L., Bhola, R. F., May, L. T., Christopoulos, A. & Christie, M. J. A positive allosteric modulator of the adenosine A_1 receptor selectively inhibits primary afferent synaptic transmission in a neuropathic pain model. *Mol. Pharm.* **88**, 460–468 (2015).
101. Little, J. W. et al. Endogenous adenosine A_3 receptor activation selectively alleviates persistent pain states. *Brain* **138**, 28–35 (2015).
102. Dunwiddie, T. V., Diao, L., Kim, H. O., Jiang, J. L. & Jacobson, K. A. Activation of hippocampal adenosine A_3 receptors produces a desensitization of A_1 receptor-mediated responses in rat hippocampus. *J. Neurosci.* **17**, 607–614 (1997).
103. Colca, J. R. Discontinued drugs 2011: endocrine and metabolic. *Expert Opin. Investig. Drugs* **21**, 1619–1624 (2012).
104. Fatholahi, M. et al. A novel partial agonist of the A_1 adenosine receptor and evidence of receptor homogeneity in adipocytes. *J. Pharmacol. Exp. Ther.* **317**, 676–684 (2006).
105. Drury, A. N. & Szent-Gyorgyi, A. The physiological activity of adenine compounds with especial reference to their action upon the mammalian heart. *J. Physiol.* **68**, 213–237 (1929).
106. Finnerup, N. B. et al. Neuropathic pain clinical trials: factors associated with decreases in estimated drug efficacy. *Pain* **159**, 2339–2346 (2018).
107. Imam, M. Z., Kuo, A., Ghassabian, S. & Smith, M. T. Progress in understanding mechanisms of opioid-induced gastrointestinal adverse effects and respiratory depression. *Neuropharmacology* **131**, 238–255 (2018).
108. Wall, M. J. & Dale, N. Neuronal transporter and astrocytic ATP exocytosis underlie activity-dependent adenosine release in the hippocampus. *J. Physiol.* **591**, 3853–3871 (2013).
109. Anderson, W. W. & Collingridge, G. L. Capabilities of the WinLTP data acquisition program extending beyond basic LTP experimental functions. *J. Neurosci. Methods* **162**, 346–356 (2007).
110. Frenguelli, B. G. & Wall, M. J. Combined electrophysiological and biosensor approaches to study purinergic regulation of epileptiform activity in cortical tissue. *J. Neurosci. Methods* **260**, 202–214 (2016).
111. Weston, C. et al. Receptor activity-modifying protein-directed G protein signaling specificity for the calcitonin gene-related peptide family of receptors. *J. Biol. Chem.* **291**, 25763 (2016).
112. Barkan, K. et al. Pharmacological characterisation of novel adenosine receptor A_3R antagonists. *Sci. Rep.* **27**, 20781 (2019).
113. Stoddart, L. A. et al. Fragment screening at adenosine-A_3 receptors in living cells using a fluorescence-based binding assay. *Chem. Biol.* **19**, 1105–1115 (2012).
114. Vernall, A. J., Stoddart, L. A., Briddon, S. J., Hill, S. J. & Kellam, B. Highly potent and selective fluorescent antagonists of the human adenosine A_3 receptor based on the 1,2,4-triazolo[4,3-a]quinoxalin-1-one scaffold. *J. Med. Chem.* **55**, 1771–1782 (2012).
115. Stoddart, L. A. et al. Application of BRET to monitor ligand binding to GPCRs. *Nat. Methods* **12**, 661–663 (2015).
116. Huang, J. & MacKerell, A. D. CHARMM36 all-atom additive protein force field: validation based on comparison to NMR data. *J. Comput. Chem.* **34**, 2135–2145 (2013).
117. Huang, J. et al. CHARMM36m: an improved force field for folded and intrinsically disordered proteins. *Nat. Methods* **14**, 71–73 (2017).
118. Vanommeslaeghe, K. & MacKerell, A. D. Jr. Automation of the CHARMM General Force Field (CGenFF) I: bond perception and atom typing. *J. Chem. Inf. Model.* **52**, 3144–3154 (2012).
119. Vanommeslaeghe, K., Raman, E. P. & MacKerell, A. D. Automation of the CHARMM General Force Field (CGenFF) II: assignment of bonded parameters and partial atomic charges. *J. Chem. Inf. Model.* **52**, 3155–3168 (2012).
120. Yu, W., He, X., Vanommeslaeghe, K. & MacKerell, A. D. Extension of the CHARMM general force field to sulfonyl-containing compounds and its utility in biomolecular simulations. *J. Comput. Chem.* **33**, 2451–2468 (2012).
121. Doerr, S., Harvey, M. J., Noé, F. & De Fabritiis, G. HTMD: high-throughput molecular dynamics for molecular discovery. *J. Chem. Theory Comput.* **12**, 1845–1852 (2016).
122. Humphrey, W., Dalke, A. & Schulten, K. VMD: visual molecular dynamics. *J. Mol. Graph* **14**, 33–38 (1996). 27-38.
123. Mayne, C. G., Saam, J., Schulten, K., Tajkhorshid, E. & Gumbart, J. C. Rapid parameterization of small molecules using the Force Field Toolkit. *J. Comput Chem.* **34**, 2757–2770 (2013).
124. Berman, H., Henrick, K. & Nakamura, H. Announcing the worldwide Protein Data bank. *Nat. Struct. Biol.* **10**, 980 (2003).
125. Berman, H. M. et al. The protein data bank. *Nucleic Acids Res* **28**, 235–242 (2000).
126. Fiser, A. & Sali, A. Modeller: generation and refinement of homology-based protein structure models. *Methods Enzymol.* **374**, 461–491 (2003).
127. Sali, A. & Blundell, T. L. Comparative protein modelling by satisfaction of spatial restraints. *J. Mol. Biol.* **234**, 779–815 (1993).
128. Dal Maso, E. et al. Extracellular loops 2 and 3 of the calcitonin receptor selectively modify agonist binding and efficacy. *Biochem. Pharmacol.* **150**, 214–244 (2018).
129. Liang, Y.-L. et al. Cryo-EM structure of the active, Gs-protein complexed, human CGRP receptor. *Nature* **561**, 492–497 (2018).
130. Dolinsky, T. J., Nielsen, J. E., McCammon, J. A. & Baker, N. A. PDB2PQR: an automated pipeline for the setup of Poisson-Boltzmann electrostatics calculations. *Nucleic Acids Res.* **32**, W665–667 (2004).
131. Olsson, M. H. M., Søndergaard, C. R., Rostkowski, M. & Jensen, J. H. PROPKA3: consistent treatment of internal and surface residues in empirical pK predictions. *J. Chem. Theory Comput* **7**, 525–537 (2011).
132. Sommer, B. Membrane packing problems: a short review on computational membrane modeling methods and tools. *Comput Struct. Biotechnol. J.* **5**, e201302014 (2013).
133. Lomize, M. A., Lomize, A. L., Pogozheva, I. D. & Mosberg, H. I. OPM: orientations of proteins in membranes database. *Bioinformatics* **22**, 623–625 (2006).
134. Jorgensen, W. L., Chandrasekhar, J., Madura, J. D., Impey, R. W. & Klein, M. L. Comparison of simple potential functions for simulating liquid water. *J. Chem. Phys.* **79**, 926 (1983).
135. Harvey, M. J., Giupponi, G. & Fabritiis, G. D. ACEMD: accelerating biomolecular dynamics in the microsecond time scale. *J. Chem. Theory Comput.* **5**, 1632–1639 (2009).
136. Berendsen, H. J. C., Postma, J. P. M., van Gunsteren, W. F., DiNola, A. & Haak, J. R. Molecular dynamics with coupling to an external bath. *J. Chem. Phys.* **81**, 3684 (1984).
137. Loncharich, R. J., Brooks, B. R. & Pastor, R. W. Langevin dynamics of peptides: the frictional dependence of isomerization rates of N-acetylalanyl-N'-methylamide. *Biopolymers* **32**, 523–535 (1992).
138. Deganutti, G. & Moro, S. Estimation of kinetic and thermodynamic ligand-binding parameters using computational strategies. *Future Med. Chem.* **9**, 507–523 (2017).
139. Sabbadin D., Salmaso V., Sturlese M., Moro S. Supervised molecular dynamics (sumd) approaches in drug design 1824:287–298 (2018).
140. Cuzzolin, A. et al. Deciphering the complexity of ligand-protein recognition pathways using supervised molecular dynamics (SuMD) simulations. *J. Chem. Inf. Model* **56**, 687–705 (2016).
141. Deganutti, G., Cuzzolin, A., Ciancetta, A. & Moro, S. Understanding allosteric interactions in G protein-coupled receptors using supervised molecular dynamics: a prototype study analysing the human A_3 adenosine receptor positive allosteric modulator LUF6000. *Bioorg. Med. Chem.* **23**, 4065–4071 (2015).

142. Deganutti, G. & Moro, S. Supporting the identification of novel fragment-based positive allosteric modulators using a supervised molecular dynamics approach: a retrospective analysis considering the human A_{2A} adenosine receptor as a key example. *Molecules* **22**, 818 (2017).
143. Deganutti G., Salmaso V., Moro S. Could adenosine recognize its receptors with a stoichiometry other than 1:1? *Mol Inform* **37**, e1800009 (2018).
144. Deganutti, G., Welihinda, A. & Moro, S. Comparison of the human A_{2A} adenosine receptor recognition by adenosine and inosine: new insight from supervised molecular dynamics simulations. *ChemMedChem* **12**, 1319–1326 (2017).
145. Sabbadin, D. & Moro, S. Supervised molecular dynamics (SuMD) as a helpful tool to depict GPCR-ligand recognition pathway in a nanosecond time scale. *J. Chem. Inf. Model* **54**, 372–376 (2014).
146. Salmaso, V., Sturlese, M., Cuzzolin, A. & Moro, S. Exploring protein-peptide recognition pathways using a supervised molecular dynamics approach. *Structure* **25**, 655–662.e652 (2017).
147. Branduardi, D., Gervasio, F. L. & Parrinello, M. From A to B in free energy space. *J. Chem. Phys.* **126**, 054103 (2007).
148. Laio, A. & Parrinello, M. Escaping free-energy minima. *Proc. Natl Acad. Sci. USA* **99**, 12562–12566 (2002).
149. Laio, A., Rodriguez-Fortea, A., Gervasio, F. L., Ceccarelli, M. & Parrinello, M. Assessing the accuracy of metadynamics. *J. Phys. Chem. B* **109**, 6714–6721 (2005).
150. Tribello, G. A., Bonomi, M., Branduardi, D., Camilloni, C. & Bussi, G. PLUMED 2: New feathers for an old bird. *Comput. Phys. Commun.* **185**, 604–613 (2014).
151. Deganutti, G. et al. Impact of protein–ligand solvation and desolvation on transition state thermodynamic properties of adenosine A_{2A} ligand binding kinetics. *Silico Pharm.* **5**, 16 (2016).
152. Barducci, A., Bussi, G. & Parrinello, M. Well-tempered metadynamics: a smoothly converging and tunable free-energy method. *Phys. Rev. Lett.* **100**, 020603 (2008).
153. Baker, J. G. & Hill, S. J. A comparison of the antagonist affinities for the Gi- and Gs-coupled states of the human adenosine A_1 receptor. *J. Pharm. Exp. Ther.* **320**, 218–228 (2007).
154. Hill, S. J. & Baker, J. G. The ups and downs of Gs- to Gi-protein switching. *Br. J. Pharm.* **138**, 1188–1189 (2003).
155. Klein Herenbrink, C. et al. The role of kinetic context in apparent biased agonism at GPCRs. *Nat. Commun.* **7**, 10842 (2016).

Acknowledgements

We gratefully acknowledge the support of the University of Warwick (URSS Awards to S.H. and J.O.; Warwick Ventures Proof of Concept Fund awards to M.J.W. & B.G.F.), the Leverhulme Trust (RPG-2017-255, CAR and G.L. to fund K.B. and G.D.), the BBSRC (BB/M00015X/2, G.L., and BB/M01116X/1, Ph.D. studentship to E.H.), the MRC (MR/J003964/1; I.W. and 2270402, iCASE PhD Studentship with NeuroSolutions to C.L.M.) and The Swiss National Science Foundation (PP00P2_123536 and PP00P2_146321, M.Lo). A.S. is supported by a European Scholarship from the Cambridge Trust, S.C. is funded by an AstraZeneca Ph.D. studentship and X.H. is funded by a China Scholarship Council Cambridge International Scholarship. RH is supported by an MRC Discovery Award (MC_PC_15070). C.A.R. is a Royal Society Industry Fellow. We would like to thank: Stephen Hill, Stephen Briddon, and Mark Soave (University of Nottingham) for gifting the Nluc-tagged adenosine receptor cell lines, the fluorescent antagonist AV039, and technical advice; Kathleen Caron and Duncan Mackie (University of North Carolina) for the β-arrestin1/2-YFP constructs, and Annette Gilchrist (Midwestern University) and Heidi Hamm (Vanderbilt University) for assistance with the Gαo interfering peptide plasmids. We are grateful to Kevin Moffat and the Biochemistry students of the School of Life Sciences at the University of Warwick for access to their frog heart preparations; Nick Dale, Mark Wigglesworth, Jens Kleinjung for discussions and comments on draft manuscripts, and Arthur Christopoulos for a pre-publication copy of the adenosine A_1R cryo-EM structure. In vivo studies on neuropathic pain were funded and undertaken by NeuroSolutions Ltd. Illustrative figures in Figs. 1bi, c; 2a–d, i, j; 3i, j; 5a; 6a; 7a, b were created with BioRender.com. Venn diagram in Fig. 2e was made at http://bioinformatics.psb.ugent.be/webtools/Venn/.

Author contributions

Experiments were designed by M.J.W., R.H., G.D., C.A.R., G.L., F.Y.Z., W.I., D.Sp., B.G.F., and were performed by M.J.W., E.H., R.H., K.B., I.W., S.C, A.S., H.F.W., D.Sa., X.H., W.I., C.L.M., E.D., C.H., S.H., J.O. Compounds were synthesised by M.Le., B.P., M.Lo. Molecular dynamics and docking simulations were designed and carried out by G.D. and C.A.R. Work was originally conceived by M.J.W. and B.G.F. The manuscript was written by M.J.W., G.D., C.A.R., G.L., B.G.F., with valuable input from E.H., R.H., K.B., M.Lo., I.W., W.I. and D.Sp.

Competing interests

The University of Warwick has filed a patent application for uses of BnOCPA in which M.W. and B.G.F. are named as the inventors and M.Lo., R.H., G.L., D.Sp., C.A.R. and G.D. are named as contributors. F.Y.Z., H.F.W, and D.Sp. are employees and/or hold shares in NeuroSolutions, which holds a licence to this patent. The remaining authors declare no competing interests.

Additional information

Supplementary information The online version contains supplementary material available at https://doi.org/10.1038/s41467-022-31652-2.

Correspondence and requests for materials should be addressed to Mark J. Wall, Graham Ladds or Bruno G. Frenguelli.

Peer review information *Nature Communications* thanks Kenneth Jacobson, Daniela Salvemini and the anonymous reviewer(s) for their contribution to the peer review of this work.

Appendix 3. Preti, et al. 2022

This appendix contains:

Preti B.*, **Suchankova A.***, Deganutti G.*, Leuenberger M., Barkan K., Manulak I., Huang X., Carvalho S., Ladds G, Lochner M., 2022. Discovery and Structure-Activity Relationship Studies of Novel Adenosine A_1 Receptor-Selective Agonists. Submitted to J. Med. Chem (* all three authors contributed equally).

Discovery and Structure-Activity Relationship Studies of Novel Adenosine A_1 Receptor-Selective Agonists

Barbara Preti,[†,#] Anna Suchankova,[‡,#] Giuseppe Deganutti,[§,#] Michele Leuenberger,[†] Kerry Barkan,[‡] Iga Manulak,[‡] Xianglin Huang,[‡] Sabrina Carvalho,[‡] Graham Ladds,[‡,*] and Martin Lochner[†,*]

[†]Institute of Biochemistry and Molecular Medicine, University of Bern, Bühlstrasse 28, 3012 Bern, Switzerland.

[‡]Department of Pharmacology, University of Cambridge, Tennis Court Road, Cambridge CB2 1PD, UK.

[§]Centre for Sport, Exercise and Life Sciences, Faculty of Health and Life Sciences, Coventry University, Coventry CV1 5FB, UK.

Running Title: SAR study of novel adenosine A_1 receptor agonists.

Keywords: G protein-coupled receptors; adenosine receptors; agonist; structure-activity relationship study; subtype selectivity; cAMP; functional assay; forskolin; BRET; binding affinity; ligand residence time.

Abstract

A series of benzyloxy and phenoxy derivatives of the adenosine receptor agonists N^6-cyclopentyl adenosine (CPA) and N^6-cyclopentyl 5'-*N*-ethylcarboxamidoadenosine (CP-NECA) were synthesized, and their potency and selectivity assessed using 3',5'-cyclic adenosine monophosphate (cAMP) accumulation assay. We observed that the most potent were the compounds with a halogen in *meta* position on the aromatic ring of the benzyloxy- or phenoxycyclopentyl substituent. In general, the NECA-based compounds displayed greater A_1R selectivity than the adenosine-based compounds, with N^6-2-(3-bromobenzyloxy)cyclopentyl-NECA and N^6-2-(3-methoxyphenoxy)cyclopentyl-NECA showing ~1500-fold improved A_1R selectivity compared to NECA. In addition, we quantified the compounds' affinity and kinetics of binding at both the human and rat A_1R using a NanoBRET binding assay and found that the halogen substituent in the benzyloxy- or phenoxycyclopentyl moiety seems to confer high affinity for the A_1R, with chloride being preferential over bromide for binding to the A_1R for both the human and rat receptors. Molecular modelling studies suggested a hydrophobic sub-pocket as contributing to the A_1R selectivity displayed. We believe that the identified very selective potent A_1R agonists are valuable tool compounds for adenosine receptor research and it is worthwhile to explore their therapeutical potential.

Introduction

The adenosine A_1 receptor (A_1R) is a G protein-coupled receptor (GPCR) that belongs to the adenosine receptor family consisting of four receptor subtypes (A_1R, $A_{2A}R$, $A_{2B}R$ and A_3R). All four receptor subtypes are non-selectively activated by the endogenous ligand adenosine, a naturally occurring purine nucleoside. The adenosine receptors are widely expressed in the body and therefore implicated in various pathological conditions including cancer, sleep regulation, cardiovascular, neurodegenerative and inflammatory diseases.[1-9] The wide expression pattern has led to the reality that despite more than four decades of intense medicinal research very few compounds have actually made it to the clinic, due to unacceptable side effects based on insufficient subtype selectivity and/or low efficacy, leaving a big untapped need for subtype-selective compounds.[10,11]

The selective activation of the A_1R, in particular, is a very promising strategy for the treatment of glaucoma, type 2 diabetes mellitus, pain, epilepsy, heart arrhythmias and cerebral ischemia, in which there are clear unmet clinical needs that could be addressed with novel more selective therapeutics.[11,12] Although all members of the adenosine receptor family are activated by endogenous adenosine, the A_1R and A_3R receptors are predominantly $G_{i/o}$-coupled, while the $A_{2A}R$ and $A_{2B}R$ are predominantly G_s coupled. The classical pathway following $G_{i/o}$ activation is the inhibition of adenylyl cyclase (AC) and subsequent inhibition of 3',5'-cyclic adenosine monophosphate (cAMP) accumulation in the cell, while activation of G_s activates AC resulting in the promotion of cAMP accumulation.

Several potent and A_1R-selective agonists are based on the endogenous adenosine scaffold. Substitution at the purine C-2 position, e.g. with chloride, and at the N^6 position with cycloalkyl- and bicycloalkyl groups, has led to potent and A_1R-selective agonists.[11-15] In addition, the ribose moiety has been the focus of synthetic modifications in AR agonist development. The ribose C-5' position tolerates certain substitutions, such as a 5'-carboxamido group in the prototypical, very potent, albeit not highly subtype-selective, AR agonist 5'-*N*-ethylcarboxyamidoadenosine (NECA). Small 5'-chlorine substituents have also been used and it was shown that together with N^6-bicycloalkyl groups lead to high-affinity and

highly selective human A_1R agonists, which have antinociceptive effects in mice without affecting motor or cardiovascular functions.[16,17] More bulky pyrazole groups have also been employed at this C-5' position and yielded potent and selective A_1R agonists that showed analgesic effects in mice.[15] Other successful selective and CNS active A_1R agonist examples feature conformationally constrained ribose ring systems.[14] Alternatively, non-nucleoside 3,5-dicyanopyridines have been synthetically optimized to yield potent and A_1R-selective full agonists, which have also been developed into PET tracers very recently.[18] Rather than modulating receptor activity by orthosteric exogenous agonists, Christopoulos and collaborators have recently presented MIPS521, a positive allosteric modulator of the A_1R, with which they were able to show *in vivo* analgesic efficacy in rats.[19] Their cryo-EM structural study of the human A_1R, bound to adenosine, MIPS521 and a G_{i2} protein heterotrimer (PDB code 7LD3), revealed the allosteric binding pocket at the lipid interface that could spark structure-based drug design campaigns.

We have previously reported the adenosine-based potent and highly A_1R-selective full agonist BnOCPA (Chart), which emerged from a structure-activity relationship (SAR) study with respect to cyclic and bicyclic purine N^6 substituents.[13] Our SAR study also showed that the synthetic NECA derivatives, such as BnOCP-NECA (Chart), were generally less subtype-selective than the adenosine ones. BnOCPA and BnOCP-NECA are extension derivatives of the prototypical, non-subtype selective AR agonist N^6-cyclopentyl adenosine (CPA). The N^6-hydroxycyclopentyl moiety is present in known A_1R-selective partial agonist CVT-3619 (later re-named GS 9667) and full agonist GR79236X. It should be noted that the stereochemical configuration of the N^6-hydroxycyclopentyl group in GR79236X is opposite to that in CVT-3619 and BnOCPA (Chart). Both GR79236X and CVT-3619 are able to increase insulin sensitivity and thus have been evaluated in clinical trials for treatment of type II diabetes, however their development was not successful and later discontinued.[20,21] Appending a benzyl group to the N^6-hydroxylcyclopentyl moiety we have found previously that BnOCPA retained high potency at A_1R and displayed very high A_1R-selectivity, compared to the non-benzylated congener.[13]

Chart. Known N^6-Cyclopentyl Adenosine A_1R Agonists, Previously Synthesized A_1R Agonists and Derivatives Presented in This Work

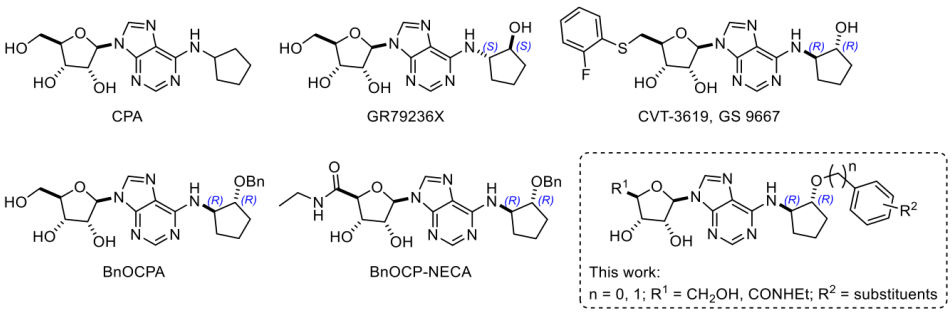

Subsequently, we demonstrated that BnOCPA was able to specifically activate $G\alpha_{ob}$ protein subtype-mediated signaling, which translated into potent *in vivo* analgesia without causing sedation, bradycardia, hypotension or respiratory depression.[22] Molecular dynamics (MD) simulations using the cryo-EM structure of the active adenosine-bound A_1R-heterotrimeric G_{i2} protein complex (PDB code 6D9H[23]) proposed four binding modes of BnOCPA[22] due to high flexibility of the N^6-appended benzyloxy group.[24]

Based on these molecular modelling studies we have designed a series of adenosine- and NECA-based compounds with extended N^6-benzyloxy- and N^6-phenoxycyclopentyl substituents (Chart) with the aim of improving the potency at A_1R while maintaining or improving the subtype-selectivity. To test the potency, selectivity and affinity of the designed compounds at the adenosine receptors, we have employed the cAMP accumulation and NanoBRET binding assays previously validated and employed at ARs.[25] We explored subtype selectivity at human A_1R, $A_{2A}R$, $A_{2B}R$ and A_3R in mammalian CHO-K1 cells and confirmed binding of the compounds at both human and rat A_1R in HEK293 cells. Kinetic studies were performed to dissect the binding properties of the compounds to hA_1R and rA_1R, and outline their structure-kinetic relationship (SKR). Finally, we have also used MD modelling to evaluate the binding pose of some of the agonists and validated the findings using mutagenesis. Together, this approach has identified novel adenosine- and NECA-based derivatives with improved potency, selectivity and affinity at the A_1R

receptor. Hence, these compounds constitute valuable tools for cellular studies of the A_1R receptor and show interesting therapeutic promise.

Results and Discussion

Chemistry

Our initial synthetic strategy was designed for keeping the route as concise as possible and entailed a projected *O*-alkylation of ribose-protected N^6-hydroxycyclopentyl adenosine and NECA precursors. After exploring different *O*-alkylation protocols and ribose hydroxyl protecting groups we abandoned this synthetic plan, as our attempts resulted in low conversions, trace amounts of desired products and many side products stemming from loss or migration of protecting groups, elimination reactions and *N*-alkylation of amine and amide groups (Scheme S1).

We therefore adapted our strategy and carried out the *O*-alkylation on *N*-protected (1*R*,2*R*)-2-aminocyclopentanol **1**[26] (Scheme 1). Under optimized conditions, treating a mixture of **1** and benzyl bromide (1 equivalent) in THF at 0°C with sodium hydride (2 equivalents) yielded 58% of desired **2a** after 4 hours. It was important to monitor this reaction carefully, as after a certain time (2-4 hours) side products started to emerge that diminished the isolated yields. These optimized conditions were applied for the preparation of benzyloxycyclopentyl intermediates **2b-i**, which were isolated in moderate to very good yields (30-91%).

Scheme 1. Synthesis of Benzyloxycyclopentyl and Phenoxycyclopentyl Amine Building Blocks[a]

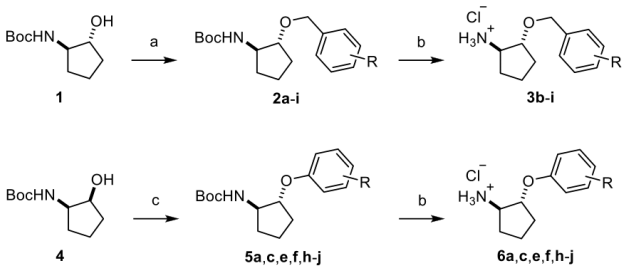

a: R = H; **b**: R = *p*-*i*-Pr; **c**: R = *p*-*t*-Bu; **d**: R = *p*-CN; **e**: R = *m*-OMe; **f**: R = *m*-Br; **g**: R = *p*-Br; **h**: R = *o*-Cl; **i**: R = *m*-Cl; **j**: R = *p*-Cl

[a]Reagents and conditions: (a) R-BnBr (1 equiv), NaH (2 equiv), THF, 0°C, 2-4 h, 30-91%; (b) HCl (4M in dioxane), 1,4-dioxane, rt, 4-18 h, 50%-quant. (c) R-PhOH, PPh_3, DIAD, THF, 0°C to rt, 18 h, 51-62%.

For the introduction of the phenoxy substituents on the cyclopentyl ring we first tosylated epimeric *N*-protected (1*S*,2*R*)-2-aminocyclopentanol **4** (*p*-TsCl, pyridine, rt, 24 h, 57% yield), which was followed by S_N2-type substitution with phenoxide (Figure S1). However, the latter reaction required forcing conditions (phenol, K_2CO_3, DMF, 70°C, 3 d) to obtain **5a** with the desired (1*R*,2*R*) stereochemistry in acceptable 61% yield. We therefore sought a milder, more efficient method and hypothesized that the Mitsunobu reaction[27] might allow us to directly access protected phenoxycyclopentyl amines **5** from **4** (Scheme 1). The Mitsunobu reaction is commonly used to convert primary and secondary alcohols to a variety of functional groups with inversion at the alcohol stereogenic center and requires an acidic nucleophile (e.g. carboxylic acids). In rare cases phenols (pK_a ~ 9-10) were employed as nucleophiles, but to the best of our knowledge cyclic secondary alcohols were not reported as Mitsunobu substrates to date. We were therefore pleased to find that adding diisopropyl azodicarboxylate (DIAD) to a solution of **4**, phenol and triphenylphosphine at 0°C, and subsequent stirring at room temperature overnight, delivered **5a** in 60% yield. ^{1}H NMR spectra of **5a** obtained via Mitsunobu reaction and of **5a** isolated after S_N2 phenoxide

substitution of tosylated **4** were identical, confirming full inversion at C-1 during the Mitsunobu reaction (Figure S1). For comparison, reaction with epimeric **1** under identical Mitsunobu conditions yielded the C-1 epimer of **5a** with a distinctively different ^{1}H NMR spectrum. Overall, our new synthetic strategy efficiently produced phenoxycyclopentyl building blocks **5** in moderate to good yields. Clean removal of the Boc-protecting group from **2** and **5** was achieved with HCl in dioxane to deliver ammonium salts **3** and **6** (Scheme 1).

Nucleophilic aromatic substitution (S_NAr) of 6-chloropurines **7** and **31** with amines **3** and **6** assembled the final agonist scaffolds (Scheme 2). Chloropurines **7** and **31** were synthesized starting from inosine using procedures adopted from Kotra *et al.*[28] and Middleton *et al.*,[29] with minor experimental modifications. Removal of the acetate groups was carried out with potassium carbonate in methanol at room temperature, while removal of the ribose acetonide group was accomplished with acetic acid in water at 80°C, yielding final adenosine derivatives **15**-**30** and NECA derivatives **44**-**55** in high purity and sufficient quantity.

In the adenosine series we observed partial cleavage of the acetate groups during the S_NAr reaction for some substrates, which led to complex but separable mixtures of desired nucleosides **8**-**14** and various deacetylated side products. We found that it was more convenient to take these crude mixtures into the subsequent deprotection step and isolate the fully deacetylated final products **15**-**30** (Scheme 2). Primary carboxamide derivative **18** was obtained from protected nitrile nucleoside **10** through hydrolysis with basic hydrogen peroxide in methanol at elevated temperature.[30]

Scheme 2. Synthesis of Benzyloxy- and Phenoxycyclopentyl Adenosine and NECA Derivatives[a]

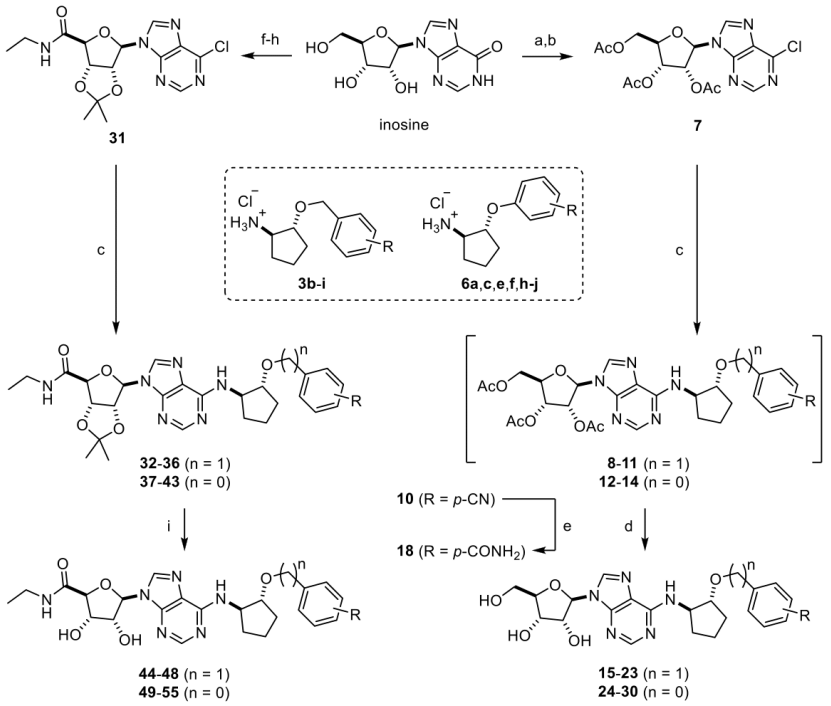

[a]Reagents and conditions: (a) Ac_2O, pyridine, rt 18 h, quant.; (b) $SOCl_2$, DMF, CH_2Cl_2, 50°C, 18 h, 86%; (c) **3b-i** or **6a**,**c**,**e**,**f**,**h-j**, $NaHCO_3$, *i*-PrOH, 105°C, 18 h, 36%-quant. (d) K_2CO_3, MeOH, rt, 30 min, 36-93%; (e) K_2CO_3, H_2O_2 (aq. 30%), MeOH, 40°C, 7 h, 83%. (f) 2,2-dimethoxypropane, *p*-TsOH, acetone, rt, 18 h, 32%; (g) TEMPO, DAIB, MeCN/H_2O, rt, 18 h, 80%; (h) $SOCl_2$, DMF, CH_2Cl_2, 50°C, 18 h; then $EtNH_2$ (2M in THF), 0°C to rt, 30 min, 41%; (i) AcOH, H_2O, 80°C, 18 h, 43-73%.

Biological Activity at Human A_1 Receptor

BnOCPA has previously been identified as a high potency A_1R-selective full agonist.[13,22] Using insights from BnOCPA MD simulations[22,24] and with the aim of further improving the A_1R selectivity and potency, we designed extended BnOCPA derivatives **15**-**18**. Their binding and activity at human A_1R (hA_1R) were then explored using both a NanoBRET binding assay and a cAMP accumulation assay, respectively (Table 1). In order to determine the A_1R mediated $G_{i/o}$ response, CHO-K1-A_1R cells were co-stimulated for 30 minutes with 10 μM forskolin (which promotes cAMP production by activating adenylyl cyclase) and the test compounds **15**-**18** were added in a range of concentrations (10^{-13} M to 10^{-4} M).

Table 1. Affinity (pK_i) and Potency (pEC_{50}) of Extended BnOCPA Derivatives at Human A_1R[a]

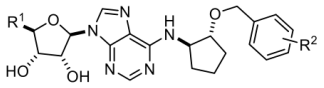

Compd	R^1	R^2	pEC_{50} (hA_1R)[b]	E_{max}[c]	pK_i (hA_1R)[d]
BnOCPA	$-CH_2OH$	H	8.43 ± 0.09	51.49 ± 1.9	6.18 ± 0.09
15	$-CH_2OH$	*p*-*i*-Pr	7.87 ± 0.16	51.95 ± 3.1	5.77 ± 0.08
16	$-CH_2OH$	*p*-*t*-Bu	8.20 ± 0.13	54.59 ± 2.8	5.58 ± 0.10
17	$-CH_2OH$	*p*-CN	7.40 ± 0.19	58.03 ± 4.2	5.85 ± 0.06
18	$-CH_2OH$	*p*-$CONH_2$	7.71 ± 0.13	59.51 ± 4.1	5.98 ± 0.05

[a]Data are the mean ± SEM of at least three independent repeats, conducted in duplicate. [b]The negative logarithm of the agonist concentration required to produce a half-maximal inhibition response of the 10 μM forskolin-induced cAMP accumulation in CHO-K1-A_1R cells. [c]The % maximal inhibition of cAMP accumulation for each agonist. Calculated as the % inhibition of the 10 μM forskolin response. [d]Binding affinity (pK_i) determined through NanoBRET binding assay in HEK293 cells stably expressing human Nluc-A_1R. The resulting concentration-dependent decrease in NanoBRET ratio at 10 min was used to

calculate pK_i. Statistical significance (* $p < 0.05$) determined using one-way ANOVA and Dunnett's post-test, and presented as described by Curtis *et al.*[31]

All four compounds were found to be agonists at the hA_1R using the inhibiting forskolin-stimulated cAMP accumulation assay with equivalent E_{max} values to that of full agonist BnOCPA. **16** showed the highest potency with pEC_{50} of 8.20 ± 0.13, which was similar to BnOCPA (pEC_{50} of 8.43 ± 0.09). **15**-**18** were further tested for their ability to displace the specific binding of CA200645, a fluorescent A_1R/A_3R antagonist, in HEK293 cells stably expressing an N-terminally tagged human Nanoluc-hA_1R (Nluc-hA_1R), as described previously.[25] All four explored BnOCPA derivative compounds **15**-**18** displayed similar affinity for Nluc-hA_1R with K_i in the range of 1-3 μM, which remained similar or lower than BnOCPA (K_i of 0.66 μM). Since none of the derivatives **15**-**18** improved upon BnOCPA potency or affinity at the A_1R, we have decided to not continue with these compounds further and instead designed a new series of compounds based on adenosine (**19**-**30**) and their structural analogs based on NECA (**44**-**55**). Full cAMP inhibition curves in the CHO-K1-hA_1R cells were obtained as described above (Figure 1, Table 2 and 3). Except for **27**, **48**, **49** and **53**, which showed partial activity, all the tested compounds behaved as full agonists at the hA_1R. **27** was the most potent (pEC_{50} of 10.0 ± 0.24), closely followed by **26**, **45**, **49** and **51**-**54**. Furthermore, all these compounds displayed higher potency than adenosine, NECA or BnOCPA, making them very promising candidate compounds. It is interesting to note that except for **49** and **53** the most potent compounds have a substituent in the *meta* position and except for **26**, **49** and **51** all have a halogen substituent. Therefore, it seems that a halogen in *meta* position on the aromatic ring confers high potency at the hA_1R. In addition, all most potent hA_1R agonists but **45** feature a N^6-phenoxycyclopentyl moiety.

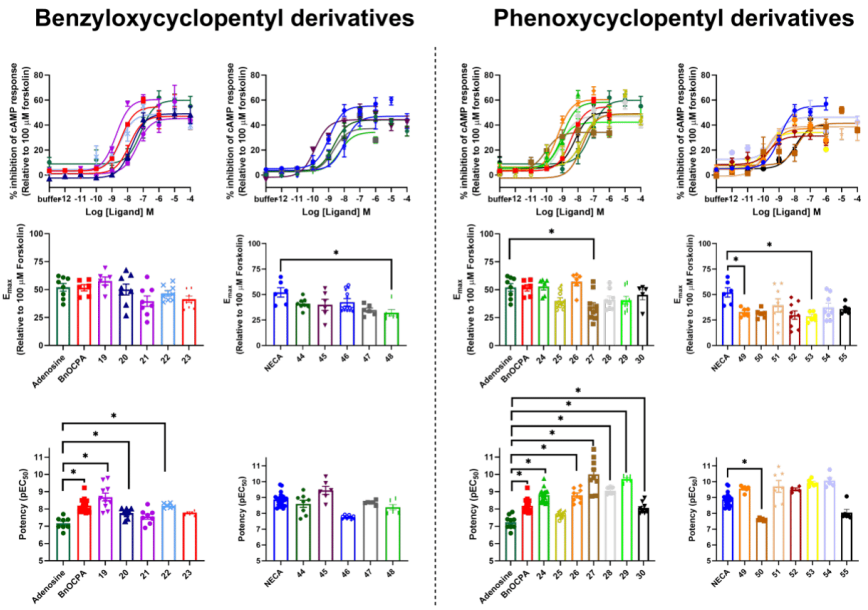

Figure 1. Efficacy and Potency of Synthetic Benzyloxy- and Phenoxycyclopentyl Adenosine and NECA Derivatives at A_1R. cAMP response in CHO-K1 cells stably expressing human A_1R in response to varying concentrations of AR ligands and 10 μM forskolin. E_{max} and pEC_{50} values for individual repeats are plotted at the bottom. Data are the mean ± SEM of at least three independent repeats, conducted in duplicate. Statistical significance (* $p < 0.05$) determined using one-way ANOVA and Dunnett's post-test, presented as described in ref 31.

Table 2. Affinity (pK_i) and Potency (pEC$_{50}$) of Synthetic Adenosine and NECA Benzyloxycyclopentyl Derivatives

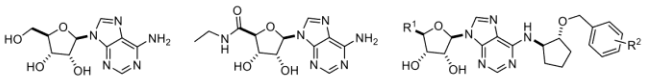

adenosine NECA BnOCPA, **19-23**, **44-48**

Compd	R[1]	R[2]	hA$_1$R		hA$_{2A}$R		hA$_{2B}$R		hA$_3$R		hA$_1$R	rA$_1$R
			pEC$_{50}$[a]	E$_{max}$[b]	pEC$_{50}$[a]	E$_{max}$[c]	pEC$_{50}$[a]	E$_{max}$[c]	pEC$_{50}$[a]	E$_{max}$[b]	pK_i[d]	pK_i[d]
Adenosine	-	-	7.16 ± 0.23	51.09 ± 4.9	7.60 ± 0.11	21.53 ± 0.9	7.28 ± 0.12	59.07 ± 2.9	7.87 ± 0.23	24.71 ± 2.5	6.09 ± 0.06	6.06 ± 0.05
BnOCPA	-CH$_2$OH	H	8.43 ± 0.09*	51.49 ± 1.9	4.95 ± 0.38*	17.13 ± 4.6	N.D.[e]		N.R.[f]		6.18 ± 0.09	6.41 ± 0.06*
19	-CH$_2$OH	*m*-OMe	8.74 ± 0.10*	57.41 ± 2.4	N.D.		N.D.		5.98 ± 0.47*	9.52 ± 2.1*	6.67 ± 0.10*	6.55 ± 0.06*
20	-CH$_2$OH	*m*-Br	7.74 ± 0.13*	51.44 ± 2.8	N.R.		N.D.		5.08 ± 0.26*	12.59 ± 1.8*	6.16 ± 0.10	6.13 ± 0.08
21	-CH$_2$OH	*p*-Br	7.39 ± 0.16	44.25 ± 3.2	N.D.		N.D.		N.R.		5.94 ± 0.07	6.06 ± 0.07
22	-CH$_2$OH	*o*-Cl	8.47 ± 0.24*	44.66 ± 4.3	5.17 ± 0.33*	18.55 ± 3.5	4.57 ± 0.12*	96.93 ± 8.1*	N.R.		6.56 ± 0.07*	6.56 ± 0.04*
23	-CH$_2$OH	*m*-Cl	7.88 ± 0.17	45.97 ± 3.3	N.D.		N.D.		N.R.		6.15 ± 0.07	6.43 ± 0.03*
NECA	-	-	8.96 ± 0.11	50.11 ± 2.4	7.95 ± 0.26	22.03 ± 2.4	7.20 ± 0.07	68.12 ± 2.0	7.83 ± 0.26	34.34 ± 3.7	6.61 ± 0.06	6.38 ± 0.04
44	-CONHEt	*m*-OMe	8.67 ± 0.19	41.15 ± 3.3	N.R.		4.42 ± 0.16*	73.07 ± 8.9	5.38 ± 0.09*	46.56 ± 2.1	6.39 ± 0.08	6.11 ± 0.07*
45	-CONHEt	*m*-Br	9.85 ± 0.19	46.12 ± 5.2	N.R.		N.D.		5.56 ± 0.10*	49.17 ± 2.4*	6.54 ± 0.15	6.46 ± 0.07
46	-CONHEt	*p*-Br	7.97 ± 0.24	43.32 ± 4.5	N.D.		N.D.		5.82 ± 0.20*	30.56 ± 2.8	6.15 ± 0.06*	6.38 ± 0.03
47	-CONHEt	*o*-Cl	8.67 ± 0.15	34.67 ± 2.2	5.68 ± 0.32	20.34 ± 3.1	5.36 ± 0.08*	87.58 ± 3.3	5.85 ± 0.13*	43.92 ± 2.8	6.63 ± 0.07	6.85 ± 0.05*
48	-CONHEt	*m*-Cl	8.29 ± 0.16	31.57 ± 2.1*	5.04 ± 0.29*	17.18 ± 2.9	4.72 ± 0.11*	96.14 ± 6.8*	5.83 ± 0.39*	31.06 ± 5.7	6.49 ± 0.08	6.90 ± 0.05*

[a]The negative logarithm of the agonist concentration required to produce a half-maximal response in the cAMP accumulation assay in CHO-K1 cells stably expressing a human AR subtype. 10 and 1 μM forskolin is included in the assay for A$_1$R and A$_3$R, respectively. [b]The % maximal inhibition of cAMP accumulation for each agonist. 10 and 1 μM forskolin is included in the assay for A$_1$R and A$_3$R, respectively. [c]The % maximal accumulation of for each agonist relative to 10 μM forskolin stimulation.

[d]Binding affinity (pK_i) determined through NanoBRET binding assay in HEK293 cells stably expressing human or rat Nluc-A_1R. The resulting concentration-dependent decrease in NanoBRET ratio at 10 min was used to calculate pK_i. [e]N.D., not determined. Full dose-response curve was not feasible. [f]N.R., no response detected in the assay. All data are the mean ± SEM of at least three independent repeats, conducted in duplicate. Statistical significance (* $p < 0.05$) determined using one-way ANOVA and Dunnett's post-test, presented according to ref [31]. Adenosine derivatives were compared to adenosine, while NECA derivatives were compared to NECA.

Table 3. Affinity (pK_i) and Potency (pEC$_{50}$) of Synthetic Adenosine and NECA Phenoxycyclopentyl Derivatives

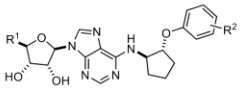

24-30, 49-55

Compd	R^1	R^2	hA_1R		$hA_{2A}R$		$hA_{2B}R$		hA_3R		hA_1R	rA_1R
			pEC$_{50}$[a]	E$_{max}$[b]	pEC$_{50}$[a]	E$_{max}$[c]	pEC$_{50}$[a]	E$_{max}$[c]	pEC$_{50}$[a]	E$_{max}$[b]	pK_i[d]	pK_i[d]
Adenosine	-	-	7.16 ± 0.23	51.09 ± 4.9	7.60 ± 0.11	21.53 ± 0.9	7.28 ± 0.12	59.07 ± 2.9	7.87 ± 0.23	24.71 ± 2.5	6.09 ± 0.06	6.06 ± 0.05
24	-CH$_2$OH	H	8.98 ± 0.14*	52.71 ± 3.1	N.D.[e]		4.90 ± 0.14*	64.19 ± 5.4	5.78 ± 0.42*	17.83 ± 3.7	6.84 ± 0.06*	6.60 ± 0.02*
25	-CH$_2$OH	*p*-*t*-Bu	7.74 ± 0.28	42.14 ± 5.1	N.D.[f]		N.D.		N.R.		6.35 ± 0.08	6.70 ± 0.05*
26	-CH$_2$OH	*m*-OMe	9.28 ± 0.10*	56.74 ± 2.4	5.24 ± 0.55*	17.25 ± 5.0	N.D.		N.R.		6.61 ± 0.07*	6.56 ± 0.06*
27	-CH$_2$OH	*m*-Br	10.0 ± 0.24*	30.55 ± 3.3*	N.D.		4.63 ± 0.12*	82.53 ± 6.2	N.R.		7.55 ± 0.11*	6.94 ± 0.08*
28	-CH$_2$OH	*o*-Cl	9.03 ± 0.19*	44.15 ± 3.6	5.96 ± 0.28*	17.01 ± 2.2	5.31 ± 0.09*	96.77 ± 4.4*	6.73 ± 0.42	13.42 ± 2.4*	7.17 ± 0.06*	7.28 ± 0.04*
29	-CH$_2$OH	*m*-Cl	9.21 ± 0.19*	38.25 ± 3.0	6.26 ± 0.34	13.63 ± 2.1	5.29 ± 0.07*	96.93 ± 8.1*	6.81 ± 0.47	11.77 ± 2.3*	7.19 ± 0.07*	7.36 ± 0.03*
30	-CH$_2$OH	*p*-Cl	8.19 ± 0.18*	45.06 ± 3.6	4.86 ± 0.58*	15.15 ± 5.5	N.D.		6.88 ± 0.60	12.5 ± 3.2*	6.23 ± 0.11	6.22 ± 0.06
NECA	-	-	8.96 ± 0.11	50.11 ± 2.4	7.95 ± 0.26	22.03 ± 2.4	7.20 ± 0.07	68.12 ± 2.0	7.83 ± 0.26	34.34 ± 3.7	6.61 ± 0.06	6.38 ± 0.04
49	-CONHEt	H	9.53 ± 0.20	32.68 ± 2.5*	5.48 ± 0.42*	15.41 ± 3.0	6.04 ± 0.09*	87.99 ± 3.7*	7.17 ± 0.16	51.24 ± 3.4*	7.30 ± 0.05*	7.41 ± 0.03*
50	-CONHEt	*p*-*t*-Bu	7.81 ± 0.41*	33.66 ± 6.1	4.84 ± 0.30*	20.11 ± 3.8	4.77 ± 0.08*	96.35 ± 5.0*	6.63 ± 0.19*	39.85 ± 3.2	6.35 ± 0.07	6.85 ± 0.05*
51	-CONHEt	*m*-OMe	9.88 ± 0.29	39.71 ± 5.9	5.20 ± 1.11*	5.16 ± 3.1*	5.10 ± 0.07*	84.76 ± 3.3	5.56 ± 0.14*	59.38 ± 4.0*	7.26 ± 0.14*	6.85 ± 0.06*
52	-CONHEt	*m*-Br	9.62 ± 0.35	39.71 ± 5.9	4.58 ± 0.87*	11.48 ± 6.7	5.37 ± 0.11*	61.12 ± 3.3	5.52 ± 0.12*	68.26 ± 3.8*	7.05 ± 0.16*	6.82 ± 0.10*
53	-CONHEt	*o*-Cl	9.91 ± 0.23	28.65 ± 2.7*	5.67 ± 0.46*	14.69 ± 3.2	6.22 ± 0.09*	80.91 ± 3.1	7.00 ± 0.19*	41.6 ± 3.3	7.39 ± 0.04*	7.60 ± 0.04*
54	-CONHEt	*m*-Cl	9.28 ± 0.28	34.67 ± 2.1	5.86 ± 0.41	13.32 ± 2.6	6.01 ± 0.09*	78.81 ± 3.4	6.79 ± 0.14*	44.20 ± 2.6	7.43 ± 0.05*	7.51 ± 0.06*
55	-CONHEt	*p*-Cl	7.99 ± 0.15	35.07 ± 2.5	4.86 ± 0.32*	25.01 ± 5.2	5.10 ± 0.09*	83.73 ± 4.5	6.92 ± 0.17*	47.16 ± 3.3	6.86 ± 0.10	7.08 ± 0.04*

[a]The negative logarithm of the agonist concentration required to produce a half-maximal response in the cAMP accumulation assay in CHO-K1 cells stably expressing a human AR subtype. 10 and 1 μM forskolin is included in the assay for A_1R and A_3R, respectively. [b]The % maximal inhibition of cAMP accumulation for each agonist. 10 and 1 μM forskolin is included in the assay for A_1R and A_3R, respectively. [c]The % maximal accumulation of for each agonist relative to 10 μM forskolin stimulation. [d]Binding affinity (pK_i) determined through NanoBRET binding assay in HEK293 cells stably expressing human or rat Nluc-A_1R. The resulting concentration-dependent decrease in NanoBRET ratio at 10 min was used to calculate pK_i. [e]N.D., not determined. Full dose-response curve was not feasible. [f]N.R., no response detected in the assay. All data are the mean ± SEM of at least three independent repeats, conducted in duplicate. Statistical significance (* $p < 0.05$) determined using one-way ANOVA and Dunnett's post-test, presented according to ref [31]. Adenosine derivatives were compared to adenosine, while NECA derivatives were compared to NECA.

Subtype Selectivity of Adenosine and NECA Derivatives

As the structural similarity between the orthosteric site of the four adenosine receptor subtypes often results in reduced selectivity of the compounds targeting them, we utilized CHO-K1 cells stably expressing human $A_{2A}R$, $A_{2B}R$ or A_3R ($hA_{2A}R$, $hA_{2B}R$ or hA_3R) and incubated them with increasing concentrations of the tested compounds (10^{-13} M to 10^{-4} M) to measure the cAMP accumulation in the cells in response to the agonists. For the $G_{i/o}$-coupled hA_3R 1 µM forskolin was also included. This addition was not required for $hA_{2A}R$ or $hA_{2B}R$ since both are G_s-coupled and thus stimulate cAMP production. All the tested compounds displayed only weak efficacy at either the $hA_{2A}R$ or $hA_{2B}R$, with many failing to generate full dose-dependent response curves at the concentrations tested, resulting in adenosine and NECA remaining the only potent compounds at these two receptors (Tables 2 and 3). At the hA_3R, the adenosine derivatives showed either a loss of efficacy or partial activity, while all the NECA-based compounds (**44-55**) behaved as full agonists, although with reduced potency compared to NECA alone. To further asses the compound selectivity, we have calculated the relative activity (RA) for all agonists at the different receptor subtypes (Figure 2).

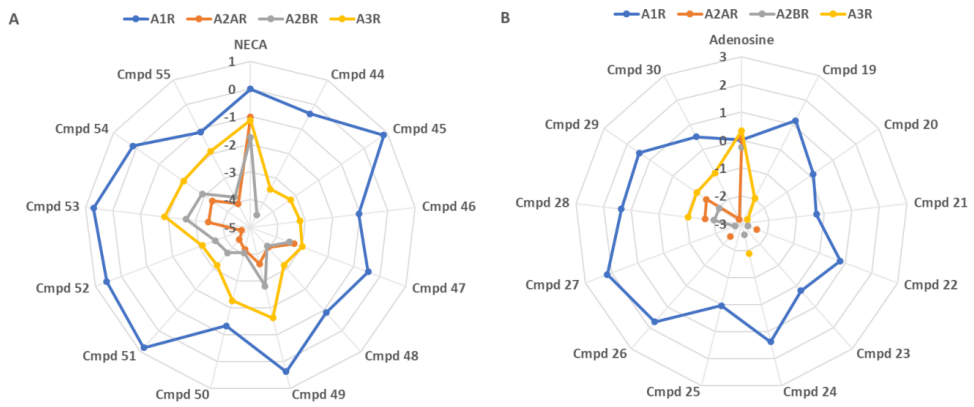

Figure 2. Adenosine and NECA Derivatives Show Selectivity towards A_1R Subtype. Log (RA) values of AR ligands at human A_1R, $A_{2A}R$, $A_{2B}R$ and A_3R normalized to (**A**) NECA or (**B**) adenosine response at A_1R.

Overall, all the compounds display at least partial selectivity for hA_1R except adenosine that is close to being an equipotent agonist at all the receptors. From the adenosine-based derivatives, compounds **22**, **23**,

26 and **27** display the most hA_1R selectivity, while compounds **28**-**30** also show activity at hA_3R. However, with NECA itself being hA_1R selective by ~10-fold, it is the NECA-based compounds that display the highest hA_1R selectivity, in particular compounds **44**, **45**, **51**-**53**. Compounds **45** and **51** are ~1500 fold more hA_1R selective than NECA itself, suggesting >10000-fold selectivity overall.

Differences between Adenosine and NECA Derivatives

When comparing the adenosine and NECA analogs, the compounds based on NECA seem to be generally more potent at inhibiting cAMP accumulation at the hA_1R receptor. Their potencies are either equivalent to or reduced, compared to NECA at the other three AR subtypes. As a result, the NECA-based derivatives are more hA_1R-selective than the adenosine derivatives. When we looked more closely at the adenosine and NECA-derived analog pairs, most of them displayed very similar selectivity across all AR subtypes (Tables 2 and 3). For example, adenosine-derived **29** and its NECA-derived analog **54** are both potent hA_1R full agonists (pEC_{50} = 9.21 ± 0.19 and 9.28 ± 0.28, respectively), whereas **30** and **55** are relatively less potent dual hA_1R and hA_3R agonists (pEC_{50} = 8.19 ± 0.18, 7.99 ± 0.15 (hA_1R) and 6.88 ± 0.60, 6.92 ± 0.17 (hA_3R), respectively). Therefore, for these compounds it seems to be the position of the substituent on the phenoxy group that has the most effect on compound selectivity. For some analog pairs, however, the patterns do not show such a close relationship. **27** and **52** are both potent agonists at hA_1R (pEC_{50} = 10.0 ± 0.24 and 9.62 ± 0.35, respectively), but **52** also weakly activated hA_3R (pEC_{50} = 5.52 ± 0.12), while **27** showed no response for this subtype. Consequently, in this case the ribose C-5' substituent group also affects the selectivity of the compounds with the adenosine-derived compound being more hA_1R selective.

Kinetics of Binding of Adenosine and NECA Derivatives at Human and Rat A_1R

Since A_1R agonists are promising compounds for the treatment of glaucoma, type 2 diabetes mellitus, pain, epilepsy and cerebral ischemia, it is important to assess their binding properties at both human and rat A_1R (rA_1R), as the latter is commonly used as a model in preclinical studies.[2,11,12] We have tested the compounds' ability to displace the specific binding (at equilibrium) of CA200645 in HEK293 cells stably expressing human and rat Nluc-A_1R (Figure 3, Tables 2 and 3).

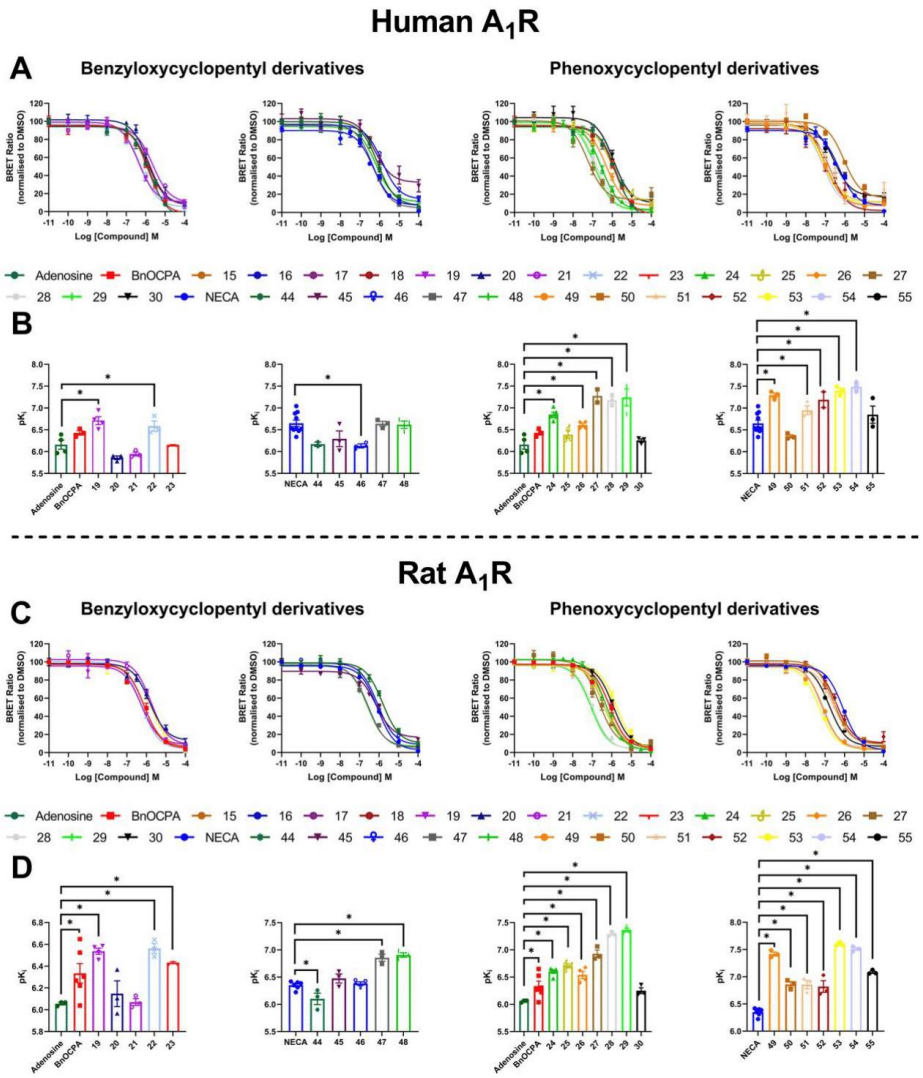

Figure 3. Binding Affinity of AR Ligands at Human and Rat A1R Measured by NanoBRET. HEK293 cells stably expressing human (**A**) or rat Nluc-A_1R (**C**) were treated with 20 nM CA200645 and increasing concentrations of unlabeled AR ligand. pK_i values for individual repeats from human A Nluc-A_1R (**B**) and rat Nluc-A_1R (**D**). Data are the mean ± SEM of at least three independent repeats, conducted in duplicate. Statistical significance (* $p < 0.05$) determined using one-way ANOVA and Dunnett's post-test, presented as described in ref 31.

The NanoBRET binding assay can also enable determination of real-time kinetics and affinities of the compound binding, as was previously described at the ARs.[25,32-34] Values were derived using the 'kinetics of competitive binding' model[35] build into GraphPad Prism v9.1 enabling determinations of the compounds' k_{on} and k_{off} values (Tables 4 and 5).

The reciprocal of the k_{off} enables a determination of the residence time (RT) of a compound.[25] RT is a quantification of the time a ligand spends bound to the receptor and it is increasingly considered in drug design because of its correlation with pharmacodynamics.[36] Beyond this, we also determined the pK_d of the compounds (k_{off}/k_{on}) from the kinetics assays and compared these values to those determined from the saturation binding assays. The kinetic parameters for CA200645 binding at the human Nluc-A_1R were determined as k_{on} (k_1) = 3.67 ± 0.34 × 10^6 M^{-1} min^{-1}, k_{off} (k_2) = 0.064 ±0.0023 min^{-1} with a K_d = 18.29 ± 2.4 nM. For the rA_1R, the kinetics of binding for CA200645 were determined as k_{on} (k_1) = 2.93 ± 0.24 × 10^6 M^{-1} min^{-1}, k_{off} (k_2) = 0.066 ± 0.0022 min^{-1} with a K_d = 32.96 ± 2.8 nM. With the help of these parameters, we were then able to provide estimates of the kinetics of binding for adenosine and NECA benzyloxycyclopentyl and phenoxycyclopentyl derivatives **19**-**30**, **44**-**55** at the human and rat A_1R (Tables 4 and 5).

The adenosine and NECA benzyloxycyclopentyl derivatives (Table 4) displayed RT comparable to adenosine and NECA on hA_1R (~ 21 min), while the phenoxycyclopentyl analogs generally had RT > 20 min (Table 5). As a general trend, the compounds are faster binders at rA_1R, regardless of linker length. The reason for this could be the divergent amino acid composition of the extracellular loops between hA_1R and rA_1R, which would favor different binding paths to the orthosteric site.[24]

Overall, the compounds displayed a very similar binding profile across the human and rat A_1R, suggesting that further studies in rats would be highly relevant for the potential use of the compounds in humans. The adenosine and NECA-derived analog pairs also display very similar affinities for both human and rat A_1R, suggesting it is the R^2 substituent on the phenoxy or benzyloxy ring that is key in determining the compound affinity for A_1R. At the hA_1R the compounds with the highest affinity are **27**-**29**, **49**, **51**, **53** and **54**. All of these have higher affinity at hA_1R than adenosine and NECA alone and are all phenoxycyclopentyl derivatives. It is interesting to note that except for **49** and **51**, all of these compounds have a halogen (chloride or bromide) substituent, mostly in the *meta*-position of the aromatic phenoxy ring. **27**, **49**, **51**, **53** and **54** all also have RT = 29-43 min at the human A_1R, while the RT for the rest of the compounds is lower. By

comparison, the benzyloxycyclopentyl derivatives generally display weaker binding and lower RT. At the rA_1R, compounds with the highest affinity are **28**, **29**, **49**, **53** and **54**. **27** and **52**, which have the bromide substituent on the aromatic ring, display reduced affinity at the rA_1R as well as the hA_1R when compared to **29** and **54**, respectively, which bear the chloride substituent at the same position. Considering the substitution position on the phenoxy ring, we observed the highest affinity with the chloride in the *meta*-position (**29**, **54**), followed by *ortho*- (**28**, **53**) and the *para*-position (**30**, **55**). Overall, halogen substituents as the R^2 group on the aromatic ring seem to confer high affinity for the A_1R, with chloride being preferential over bromide for binding at both the human and rat version of the receptor.

Table 4. Kinetics of Binding for Synthetic Adenosine and NECA Benzyloxycyclopentyl Derivatives to the Orthosteric Binding Site at Human and Rat A_1R

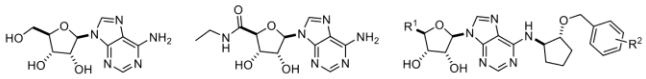

Compd	R^1	R^2	hA_1R				rA_1R			
			k_{on} (k_3) × 10^5 ($M^{-1}min^{-1}$)[a]	k_{off} (k_4) (min^{-1})[b]	pK_d[c]	RT (min)[d]	k_{on} (k_3) × 10^5 ($M^{-1}min^{-1}$)[a]	k_{off} (k_4) (min^{-1})[b]	pK_d[c]	RT (min)[d]
Adenosine	-	-	1.65 ± 0.24	0.048 ± 0.002	6.53 ± 0.07	21.15 ± 0.84	0.52 ± 0.22	0.079 ± 0.007	5.71 ± 0.17	12.86 ± 1.10
BnOCPA	$-CH_2OH$	H	1.47 ± 0.33	0.068 ± 0.002	6.30 ± 0.09	14.75 ± 0.56	1.57 ± 0.54	0.054 ± 0.007	6.40 ± 0.11	19.42 ± 2.21
NECA	-	-	2.04 ± 0.07	0.049 ± 0.005	6.63 ± 0.06	20.97 ± 1.98	2.29 ± 0.39	0.066 ± 0.008	6.53 ± 0.04	15.84 ± 2.05
19	$-CH_2OH$	*m*-OMe	2.51 ± 0.36	0.041 ± 0.004	6.77 ± 0.02	24.64 ± 1.98	2.52 ± 0.31	0.083 ± 0.016	6.49 ± 0.03	13.22 ± 2.10
20	$-CH_2OH$	*m*-Br	0.56 ± 0.12	0.080 ± 0.016	5.84 ± 0.02	14.84 ± 3.83	1.50 ± 0.29	0.097 ± 0.008	6.17 ± 0.09	10.56 ± 0.81
21	$-CH_2OH$	*p*-Br	0.66 ± 0.02	0.065 ± 0.010	6.02 ± 0.06	16.72 ± 3.01	1.13 ± 0.09	0.066 ± 0.010	6.24 ± 0.03	16.05 ± 2.09
22	$-CH_2OH$	*o*-Cl	2.75 ± 0.14	0.055 ± 0.012	6.74 ± 0.10	22.22 ± 6.21	5.07 ± 0.26	0.090 ± 0.015	6.77 ± 0.06	12.10 ± 2.06
23	$-CH_2OH$	*m*-Cl	1.40 ± 0.08	0.051 ± 0.015	6.48 ± 0.09	24.12 ± 5.29	2.85 ± 0.22	0.060 ± 0.006	6.68 ± 0.06	17.13 ± 1.54
44	-CONHEt	*m*-OMe	1.12 ± 0.09	0.110 ± 0.024	6.04 ± 0.10	10.59 ± 2.34	1.96 ± 0.13	0.141 ± 0.018	6.15 ± 0.06	7.41 ± 0.82
45	-CONHEt	*m*-Br	0.83 ± 0.06	0.095 ± 0.011	5.94 ± 0.02	10.78 ± 1.28	2.95 ± 0.41	0.121 ± 0.012	6.38 ± 0.06	8.51 ± 0.82
46	-CONHEt	*p*-Br	1.01 ± 0.06	0.076 ± 0.007	6.13 ± 0.03	13.55 ± 1.36	2.14 ± 0.14	0.058 ± 0.003	6.56 ± 0.01	17.30 ± 1.02
47	-CONHEt	*o*-Cl	3.64 ± 0.33	0.044 ± 0.009	6.94 ± 0.08	25.70 ± 4.63	7.31 ± 0.61	0.046 ± 0.002	7.20 ± 0.03	21.98 ± 1.13
48	-CONHEt	*m*-Cl	1.80 ± 0.17	0.040 ± 0.006	6.67 ± 0.05	27.96 ± 5.57	7.54 ± 0.30	0.073 ± 0.004	7.02 ± 0.03	13.90 ± 0.72

[a] k_{on} (k_3) for ligands as determined using NanoBRET binding assays, using either human or rat Nluc-A_1R expressing HEK 293 cells and determined through fitting with the 'kinetics of competitive binding' model.[35] [b] k_{off} (k_4) for ligands determined as in [a]. [c] Kinetic dissociation constant (pK_d) for each ligand as determined from k_{off}/k_{on}. [d] Residence time of each ligand as determined by the reciprocal of the k_{off}. All data are the mean ± SEM of at least three independent repeats, conducted in duplicate.

Table 5. Kinetics of Binding for Synthetic Adenosine and NECA Phenoxycyclopentyl Derivatives to the Orthosteric Binding Site at Human and Rat A_1R

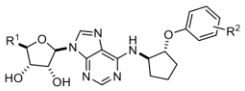

24-30, 49-55

Compd	R^1	R^2	hA$_1$R				rA$_1$R			
			k_{on} (k_3) ×10^5 (M^{-1}min^{-1})^a	k_{off} (k_4) (min^{-1})^b	pK_d^{c}	RT (min)^d	k_{on} (k_3) ×10^5 (M^{-1}min^{-1})^a	k_{off} (k_4) (min^{-1})^b	pK_d^{c}	RT (min)^d
24	-CH$_2$OH	H	4.78 ± 0.93	0.048 ± 0.004	6.97 ± 0.06	21.56 ± 2.13	2.70 ± 0.34	0.053 ± 0.001	6.70 ± 0.06	18.91 ± 0.30
25	-CH$_2$OH	*p*-*t*-Bu	1.48 ± 0.04	0.054 ± 0.005	6.44 ± 0.03	19.12 ± 2.01	4.84 ± 0.37	0.484 ± 0.173	6.17 ± 0.30	5.53 ± 3.31
26	-CH$_2$OH	*m*-OMe	2.97 ± 0.27	0.037 ± 0.003	6.90 ± 0.01	27.61 ± 2.09	3.32 ± 0.52	0.085 ± 0.007	6.58 ± 0.03	12.06 ± 1.03
27	-CH$_2$OH	*m*-Br	10.12 ± 1.29	0.038 ± 0.012	7.47 ± 0.09	33.13 ± 10.40	13.30 ± 1.21	0.050 ± 0.005	7.42 ± 0.03	20.40 ± 1.86
28	-CH$_2$OH	*o*-Cl	11.61 ± 1.31	0.052 ± 0.004	7.34 ± 0.04	19.55 ± 1.48	17.92 ± 1.30	0.048 ± 0.005	7.58 ± 0.01	21.46 ± 2.08
29	-CH$_2$OH	*m*-Cl	25.90 ± 2.14	0.040 ± 0.003	7.81 ± 0.02	25.37 ± 1.70	30.07 ± 4.02	0.071 ± 0.010	7.63 ± 0.12	15.20 ± 2.50
30	-CH$_2$OH	*p*-Cl	1.01 ± 0.31	0.056 ± 0.009	6.22 ± 0.13	19.46 ± 3.34	2.51 ± 0.90	0.056 ± 0.001	6.58 ± 0.15	17.90 ± 0.25
49	-CONHEt	H	16.43 ± 2.81	0.028 ± 0.002	7.63 ± 0.01	32.82 ± 1.02	25.12 ± 2.08	0.037 ± 0.002	7.83 ± 0.05	27.61 ± 1.66
50	-CONHEt	*p*-*t*-Bu	1.53 ± 0.11	0.091 ± 0.010	6.23 ± 0.06	11.47 ± 1.48	6.29 ± 0.62	0.070 ± 0.007	6.95 ± 0.01	14.76 ± 1.64
51	-CONHEt	*m*-OMe	4.27 ± 0.03	0.027 ± 0.007	7.23 ± 0.11	42.68 ± 10.88	11.91 ± 1.33	0.030 ± 0.006	7.62 ± 0.11	38.05 ± 8.74
52	-CONHEt	*m*-Br	5.57 ± 2.56	0.075 ± 0.038	6.91 ± 0.04	27.87 ± 14.23	4.46 ± 1.28	0.056 ± 0.008	6.85 ± 0.13	19.17 ± 2.68
53	-CONHEt	*o*-Cl	17.27 ± 1.12	0.041 ± 0.010	7.66 ± 0.11	29.44 ± 6.91	37.59 ± 1.91	0.048 ± 0.003	7.90 ± 0.00	21.23 ± 1.22
54	-CONHEt	*m*-Cl	20.28 ± 1.11	0.043 ± 0.013	7.75 ± 0.16	34.70 ± 13.43	35.85 ± 3.95	0.062 ± 0.007	7.76 ± 0.10	16.78 ± 2.22
55	-CONHEt	*p*-Cl	3.75 ± 1.04	0.076 ± 0.024	6.71 ± 0.03	17.48 ± 4.79	11.62 ± 0.26	0.064 ± 0.003	7.26 ± 0.01	15.65 ± 0.78

$^a k_{on}$ (k_3) for ligands as determined using NanoBRET binding assays, using either human or rat Nluc-A$_1$R expressing HEK 293 cells and determined through fitting with the 'kinetics of competitive binding' model.[35] $^b k_{off}$ (k_4) for ligands determined as in ^{a}. ^{c}Kinetic dissociation constant (pK_d) for each ligand as determined from k_{off}/k_{on}. ^{d}Residence time of each ligand as determined by the reciprocal of the k_{off}. All data are the mean ± SEM of at least three independent repeats, conducted in duplicate.

Finally, we performed a comparison of the affinity data obtained from the NanoBRET binding assay with the potency for inhibition of cAMP accumulation for the hA_1R, which showed a clear positive correlation (r = 0.82) with compounds **27**, **29**, **49**, **51**-**54** identified as both the most potent and strongest binders (Figure 4A). A similar correlation was also observed between potency and compounds' residence time (Figure 4B, r = 0.65). Overall, in this work, we have identified high affinity, very selective potent hA_1R agonists, namely **27**, **49** and **51**-**54**.

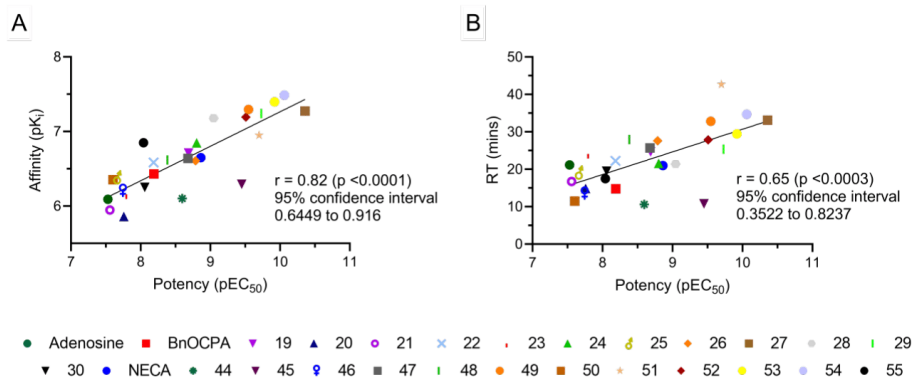

Figure 4. NECA and Adenosine Derivatives Show Correlation between Potency and Affinity or Residence Time at the hA_1R. (**A**) Potency pEC_{50} values of individual compounds from cAMP inhibition experiments plotted against pK_i values from NanoBRET experiments at hA_1R. (**B**) Potency pEC_{50} values of individual compounds from cAMP inhibition experiments plotted against RT values from NanoBRET experiments at hA_1R.

Molecular Dynamics Simulations

To retrieve insight into the possible binding mode of the studied agonists and rationalize the selectivity displayed, *in silico* experiments were performed on the phenoxycyclopentyl adenosine derivative **27**, the most A_1R-selective and potent agonist, and its benzyloxycyclopentyl congener **20**. A_1R and $A_{2A}R$

structures solved in complex with adenosine or NECA (or homology models obtained from them, see *Experimental Section*) present a closed conformation of the extracellular vestibule due to the lack of induced fit by N^6 substituents, not present on adenosine or NECA. This structural feature does not allow molecular docking of compounds bearing bulky N^6 groups to reproduce the binding mode of AR full agonists (Figure S2), which is characterized by the fundamental hydrogen bonds between the purine scaffold and the conserved Asn residue in position 6.55 and between the ribose ring and the Ser/Thr$^{7.42}$ or His$^{7.43}$. Therefore, molecular dynamics (MD) simulations of the four ARs subtypes were performed in the absence of any orthosteric agonists to sample receptors' conformations more open at the extracellular loop 2 (ECL2) and ECL3 levels. Molecular docking results for **20** and **27** on the MD-derived ARs structures were remarkably enhanced in the case of experimental structures A_1R and $A_{2A}R$, slightly improved for the structural A_3R model, and produced very little improvement for the $A_{2B}R$ model (Figure S3).

The best pose (in terms of similarity to adenosine) of **20** within A_1R and the best pose of **27** within A_1R or $A_{2A}R$ were further evaluated during 6 μs of MD simulations. For a complete comparison (Movie S1) of all four ARs subtypes, the best docking pose of **27** obtained on $A_{2A}R$ was superimposed on both $A_{2B}R$ and A_3R and subjected to MD simulations. During the MD trajectories, **27** remained stably bound to A_1R and $A_{2A}R$ but displayed less stable binding modes within A_3R and, in particular, the $A_{2B}R$ orthosteric site (Movie S1, Figure S4A). Compound **20** within A_1R was steady throughout the simulations (Movie S2), as indicated by RMSD values in line with **27** (Figure S4A)**.** In terms of flexibility, N^6 substituents explored divergent conformations in the different systems (Figure 5A, Movies S1 and S2): the 3-bromophenyl group of **27** was highly flexible in A_3R or $A_{2A}R$, more stable in A_1R, while the 3-bromobenzyl group of **20** displayed intermediate flexibility.

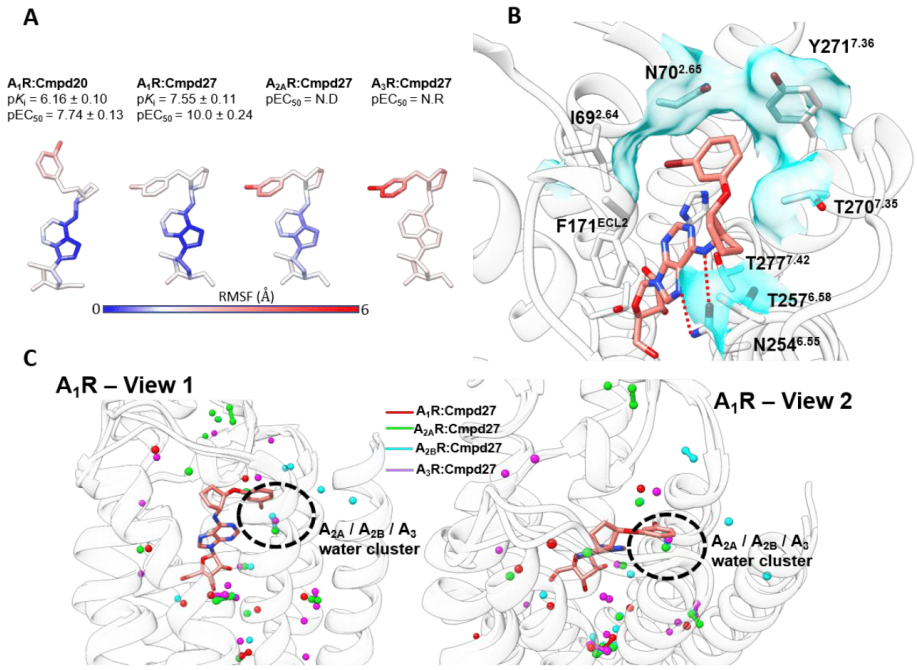

Figure 5. Molecular Dynamics Docking of 20 and 27. (**A**) Atomic root mean square fluctuation (RMSF) of **20** within A_1R and **27** within A_1R, $A_{2A}R$, and A_3R, plotted on the agonists' structure. (**B**) Compound **27** (salmon stick representation) binding mode within A_1R (white ribbon and sticks); the key hydrogen bonds with $N254^{6.55}$ are shown as red dotted lines, while the hydrophobic sub-pocket is shown as cyan transparent surface. (**C**) Two side view comparison of the structural water molecules detected in A_1R (red spheres), $A_{2A}R$ (green), $A_{2B}R$ (cyan), and A_3R (purple). The position of the stable water cluster only present in $A_{2A}R$, $A_{2B}R$ and A_3R is highlighted. Binding mode of **27** (salmon sticks) within A_1R is superimposed for reference.

Compound **27** bound to A_1R formed key hydrogen bonds with $N254^{6.55}$, hydrophobic contacts with $F171^{ECL2}$, and oriented the 3-bromophenyl moiety in a hydrophobic sub-pocket formed by $I69^{2.64}$, $N70^{2.65}$, $Y271^{7.36}$, and $T270^{7.35}$ (Figure 5B, Movies S1 and S2). The bulkier analog **20** was not able to completely

accommodate the 3-bromobenzyl group within this pocket and therefore displayed higher flexibility at the N^6 level (Figure 5A, Movie S2). It is plausible that this contributes to the reduced A_1R affinity and potency of **20** (pK_i = 6.16 ± 0.10, pEC_{50} = 7.74 ± 0.13) compared to **27** (pK_i = 7.55 ± 0.11, pEC_{50} = 10.0 ± 0.24). On the other hand, the interaction fingerprints of **20** (bound to A_1R) and **27** are unique for each simulated complex (Figure S4B) and do not allow a straightforward rationalization of the selectivity displayed by the agonists. We therefore focused on the water molecule network present in the apo forms of the four AR subtypes (Figure 5C, Figure S4C-F). Our data suggest the presence of structural water molecules (A_{2A} / A_{2B} / A_3 water cluster in Figure 5C) in the proximity of positions 2.64 and 2.65 of A_2AR, $A_{2B}R$, and A_3R but not A_1R, stabilized by the short polar side chain of $Ser^{2.65}$ ($Asn^{2.65}$ in A_1R, Figure S4B). It follows that the hydrophobic sub-pocket is putatively present only in A_1R, hence, **27** cannot be completely stabilized by the other AR subtypes.

Taken together, computational results suggest that a one-atom linker between the N^6-cyclopentane and the phenyl rings is optimal for stable binding to the hydrophobic pocket in A_1R. The absence of this pocket and the presence of stable water molecules competing with the ligands in $A_{2A}R$, $A_{2B}R$, and A_3R are probably responsible for the loss in affinity and potency of the tested agonists. The better complementarity with hA_1R could explain why adenosine and NECA benzyloxycyclopentyl derivatives (Table 4) displayed RT comparable to adenosine and NECA at hA_1R (~ 21 min), while the phenoxycyclopentyl analogs generally had RT > 20 min (Table 5). Indeed, the shorter linker, as present in **27**, would stabilize the compounds and increase the energy required to produce dissociation.

Validating the Predictions from the In Silico Experiments for A_1R Bound to 20 and 27

As described in Figure 5B, MD simulations suggested that the 3-bromophenyl moiety binds in a hydrophobic sub-pocket formed by $I69^{2.64}$, $N70^{2.65}$, $Y271^{7.36}$, and $T270^{7.35}$ while **20** was not able to completely accommodate the 3-bromobenzyl group within this pocket (Movie S2). To test these

observations, we made use of previously described mutants (I69$^{2.64}$A, N70$^{2.65}$A, Y271$^{7.36}$A) of the Nluc-A_1R[24] which enables comparison of ligand affinities with the wild type receptor. We also included the mutant T257$^{6.58}$A since we have previously shown that this residue is a good discriminator between different A_1R agonists.[24] We did not consider mutations of N254$^{6.55}$ or F171^{ELC2} since these are known to prevent ligand binding to the A_1R (including CA200645) and therefore cannot be studied.[24,37] Furthermore, we did not consider mutating T270$^{7.35}$ since, when we compared the sequences of the hA_1R and the rA_1R, we observed that in the rA_1R the equivalent residue at position T270$^{7.35}$ is an Ile. Comparison of the binding affinities (pK_i) for **20** and **27** between the hA_1R and the rA_1R show that **20** is equipotent between the two species while **27** has reduced affinity at the rA_1R (pK_i (hA_1R) = 7.55 ± 0.11; pK_i (rA_1R) = 6.94 ± 0.08). Initially, we determined the K_d for CA200645 at each of the four A_1R mutants (I69$^{2.64}$A, N70$^{2.65}$A, T257$^{6.58}$A, Y271$^{7.36}$A) and found the values to show close agreement with those previously reported.[24] We next performed a NanoBRET competition binding assay for the four mutants with BnOCPA (as a reference agonist), **20** and **27** (Table 6, Figure S5).

Consistent with MD simulation predictions, mutation of I69$^{2.64}$ and Y271$^{7.36}$ reduced affinity of BnOCPA, **20** and **27**. Interestingly, while the affinity at the A_1R of BnOCPA and **27** was not affected by mutation of N70$^{2.65}$, **20** was significantly reduced. A closer analysis of the MD simulations suggested that the side chain of N70$^{2.65}$ orients differently between **20** and **27**. For **20**, simulations predicted N70$^{2.65}$ amidic side chain group interactions with the purine ring (Figure S6, Movie S2) which are lost in N70$^{2.65}$A. Conversely, for **27**, the N70$^{2.65}$ amidic side chain group does not interact with the purine ring, but instead, it forms hydrophobic interactions through its methylene group with the bromobenzene ring (Figure 5B, Movie S2), implying the mutation to Ala plays not a significant role in binding. Finally, as we have previously reported,[24] mutation of T257$^{6.58}$A did provide a clear discriminator between the three different agonists. **27** together with BnOCPA both showed increases in binding affinity, while **20** displayed no significant change. In our previous studies we observed that both CPA and BnOCPA displayed increased affinities at the T257$^{6.58}$A mutant, while NECA showed reduced affinity and there was no change for

adenosine. We attributed these changes to an increase in lipophilicity of the protein environment underneath extracellular loop 3 (ECL3), which surrounds the cyclopentyl groups of the molecules. It is therefore apparent that the small molecule **27** favors a more hydrophobic environment within the binding pocket which is already suitable for **20**.

Table 6. NanoBRET Competition-Binding Assay at Human Wild Type and Mutant Nluc-A_1R[a]

A_1R	pK_i[a] (cmpd)					
	BnOCPA	***n***	**20**	***n***	**27**	***n***
WT	6.24 ± 0.04	3	6.38 ± 0.17	3	7.20 ± 0.16	3
$I69^{2.64}A$	5.03 ± 0.02*	3	5.06 ± 0.04*	3	6.37 ± 0.10*	3
$N70^{2.65}A$	6.01 ± 0.05	3	5.48 ± 0.15*	3	7.00 ± 0.24	3
$T257^{6.58}A$	6.93 ± 0.10*	3	6.23 ± 0.02	3	8.09 ± 0.18*	3
$Y271^{7.36}A$	5.40 ± 0.23*	3	5.19 ± 0.13*	3	6.33 ± 0.10*	3

[a]Compound affinity (pK_i) determined through NanoBRET competition-binding assays with CA200645 in wild type (WT) or mutant Nluc-A_1R stably expressing HEK293 cells. The resulting concentration-dependent decrease in BRET ratio at 10 minutes was used to calculate pK_i. Data are expressed as mean ± SEM obtained in *n* separate experiments. All individual experiments were conducted in duplicate. Statistical significance (* $p < 0.05$) compared to WT was determined by one-way ANOVA with Dunnett's post-test, and presented according to ref 31.

Conclusions

Herein, we report the synthesis of novel N^6-benzyloxycyclopentyl and N^6-phenoxycyclopentyl derivatives of adenosine and NECA. These compounds were evaluated using cAMP accumulation assay in

CHO-K1 cells and NanoBRET binding assay in HEK293 cells for potency, selectivity and binding at ARs. Our pharmacology data show that compounds including halogen substituents, chloride in particular, on the aromatic phenoxy and benzyloxy rings confer high affinity for the human and rat A_1R. These compounds have also high potency at the A_1R, particularly ones with a *meta* substituent on the aromatic rings. Furthermore, we also show that NECA-based derivatives have generally higher A_1R selectivity over the other AR subtypes. Molecular modeling studies suggest that the selectivity is driven by a short linker and the absence of stable water molecules within a sub-pocket of the hA_1R orthosteric site. It is worth noting that compounds **45** and **51** show approximately 1500 times improved A_1R selectivity over NECA itself. Overall, we have identified very selective and very potent A_1R agonists with high affinity for the receptor, namely phenoxycyclopentyl compounds **27**, **49**, **51-54**, which have great therapeutic promise for overcoming insufficient receptor selectivity and potency that many current compounds face.

Experimental Section

General Chemistry. All reactions were performed in dry glassware under an inert argon atmosphere. Anhydrous solvents were purchased as dry over molecular sieves from Sigma-Aldrich (Merck). Solvents were evaporated under reduced pressure at approximately 45ºC using a Büchi Rotavapor or under high vacuum on a Schlenk line. Reagents were purchased from Sigma-Aldrich (Merck), Fluorochem or Brunschwig and used without further purification. Reactions were monitored by thin layer chromatography (TLC) using aluminum sheets pre-coated with 0.2 mm silica (Macherey-Nagel ALUGRAM Xtra SII, G/UV_{254}) or aluminum oxide (Macherey-Nagel POLYGRAM Alox N/UV_{254}). Detection was under UV light source (λ_{max} 254 nm or 366 nm) or through staining with vanillin solution, with subsequent heating. Flash column chromatography was carried out on a Teledyne ISCO CombiFlash using pre-packed RediSep® Normal-phase Silica Flash Columns.

Proton nuclear magnetic resonance (^{1}H NMR) and carbon nuclear magnetic resonance (^{13}C NMR) spectra were recorded at room temperature using a Bruker Avance IIIHD-400, II-400 or IIIHD-300 spectrometer operating at 400 or 300 MHz, respectively, for ^{1}H and at 101 and 75 MHz, respectively, for ^{13}C. Chemical shifts (δ) are reported in parts per million (ppm) and are referenced to the residual solvent peak (DMSO-d_6: δ_H = 2.50 ppm, δ_C = 39.52 ppm; $CDCl_3$: δ_H = 7.26 ppm, δ_C = 77.16 ppm; Methanol-d_4: δ_H = 3.31 ppm, δ_C = 49.00 ppm) or Me_4Si (δ_H = 0.00 ppm). The order of citation in parentheses is (1) multiplicity: s (singlet), d (doublet), t (triplet), q (quartet), quint (quintet), m (multiplet) *etc* and br (broad), (2) coupling constants (*J*) in Hertz (Hz) and (3) number of equivalent nuclei (by integration). COSY, HSQC and DEPT were routinely used to assign peaks in ^{1}H and ^{13}C NMR spectra. Addition of D_2O was used to confirm the assignment of OH and NH peaks. High resolution mass spectra (HRMS) were recorded on a Thermo-Scientific LTQ Orbitrap XL spectrometer consisting of a linear ion trap (LTQ) featuring a HCD collision cell, coupled to the Orbitrap mass analyzer, equipped with a nanoelectrospray ion source (NSI). HRMS spectra were determined by the Mass Spectrometry Group at the Department of Chemistry, Biochemistry and Pharmaceutical Sciences, University of Bern, Switzerland (Prof. Dr. S. Schürch).

The purity of the compounds was determined with UPLC-MS on a Dionex UltiMate 3000 Rapid Separation LC system using a reversed-phase column (Acclaim™ RSLC, 120 C18, 3 × 50 mm, 2.2 µm, 120Å pore size, flow rate 1.2 mL/min), which was coupled to a ESI-MS Micromass Platform (quadrupole mass spectrometer). The gradient used was 100%A to 100%D over 7 min, with A (MilliQ H_2O + 0.1% TFA) and D (10% MilliQ H_2O/90% HPLC-grade MeCN + 0.1% TFA). Compounds **24** and **29** were measured on a Thermo-Scientific UltiMate 3000 HPLC equipped with a reverse-phase column (Acclaim™ 120 C18, 4.6 × 150 mm, 5 µm, 120Å pore size) and eluted with a gradient of MilliQ H_2O/HPLC-grade MeCN + 0.1% TFA. Purity was determined by total absorbance at 254 nm. All tested compounds were >95% pure, except **24** and **29** which were 95% and 94% pure, respectively (Tables S1 and S2).

Established Adenosine Receptor Agonists. Adenosine and 5'-*N*-ethylcarboxamidoadenosine (NECA) were purchased from R & D Systems (Bristol, UK). Where possible, compounds were prepared as 10mM stocks in DMSO.

Chemical Synthesis. Intermediates **1**, **7** and **31**, and BnOCPA were synthesized as described previously.[13,38]

General Procedure A (*O*-Alkylation) for the Synthesis of Intermediates 2a-i. Boc-protected (1*R*,2*R*)-2-aminocyclopentanol **1** and the appropriate benzyl bromide were dissolved in dry THF (50-100 mM). The reaction mixture was cooled to 0°C and NaH (60% dispersion in mineral oil) was added. After stirring at 0°C the reaction was quenched with MeOH (0.1 mL) and sat. aq. NH_4Cl. The reaction mixture was extracted with EtOAc, the organic phase was dried over Na_2SO_4 and concentrated under reduced pressure. The crude material was purified by flash column chromatography.

General Procedure B (Mitsunobu) for the Synthesis of Intermediates 5a,c,e,f,h-j. Boc-protected (1*S*,2*R*)-2-aminocyclopentanol **4**, the appropriate phenol and PPh_3 were dissolved in dry THF (50-100 mM) and cooled to 0°C. DIAD was added dropwise. Cooling was removed, the reaction mixture was left to warm to room temperature and stirred overnight. Water was added and the aqueous phase was extracted with EtOAc. The organic phase was dried over Na_2SO_4 and concentrated under reduced pressure. The crude material was purified by flash column chromatography.

General Procedure C (Boc Deprotection) for the Synthesis of Intermediates 3b-i and 6a,c,e,f,h-j. Boc-protected precursors **2b-i** and **5a,c,e,f,h-j** were dissolved in dioxane (85-830 mM) and HCl (4M in dioxane) was added. After stirring the reaction mixture at room temperature the solvent was removed under reduced pressure. The residual ammonium chloride salt was co-evaporated with CH_2Cl_2 and dried.

General Procedure D (S_NAr Reaction) for the Synthesis of Intermediates 8-14 and 32-43. The appropriate 6-chloropurine (**7** or **31**) and the appropriate benzyloxy- or phenoxycyclopentyl amine

intermediate (**3b-i** or **6a**,**c**,**e**,**f**,**h-j**) were dissolved in *i*-PrOH (11-36 mM). $NaHCO_3$ was added and the reaction mixture heated at reflux (*ca*. 105°C) overnight. After cooling, the solid was filtered off, washed with EtOH and the solvents were removed under reduced pressure. The crude material was purified by flash column chromatography. In some examples loss of acetate groups on the secondary alcohols was observed during the S_NAr reaction with **7**. In these cases the crude material was subjected directly to the deprotection protocol (see *General Procedure G*).

General Procedure E (Acetate Deprotection) for the Synthesis of Compounds 15-17, 19, 24, 26 and 30. Acetate-protected intermediates **8-14** were dissolved in MeOH (9-22 mM) and K_2CO_3 was added. The reaction mixture was stirred at room temperature, filtered and concentrated under reduced pressure. The crude material was purified by flash column chromatography.

General Procedure F (Acetonide Deprotection) for the Synthesis of Compounds 44-55. Acetonide-protected intermediates **32-43** were dissolved in water (38-75 mM) and acetic acid, and stirred at 80°C overnight. The water and acetic acid were removed in vacuo and the crude material purified by flash column chromatography.

General Procedure G (S_NAr Reaction and Subsequent Acetate Deprotection) for the Synthesis of Compounds 20-23, 25 and 27-29. 6-Chloropurine **7** and the appropriate benzyloxy- or phenoxycyclopentyl amine intermediate (**3f-i** or **6c**,**f**,**h**,**i**) were dissolved in *i*-PrOH (23-46 mM). $NaHCO_3$ was added and the reaction mixture heated at reflux (*ca*. 105°C) overnight. After cooling, the solid was filtered off, washed with EtOH and the solvents were removed under reduced pressure. The crude material was dissolved in MeOH (11-17 mM) and K_2CO_3 was added. The reaction mixture was stirred at room temperature, filtered and concentrated under reduced pressure. The crude material was purified by flash column chromatography.

Cell Culture. CHO-K1-hA_1R, CHO-K1-hA_{2A}R, CHO-K1-hA_{2B}R and CHO-K1-hA_3R cells were routinely cultured in Hams F-12, supplemented with 10% fetal bovine serum (FBS). HEK293 human Nluc-A_1R and HEK293 rat Nluc-A_1R, made by Kerry Barkan (University of Cambridge, UK), were cultured in

Dulbecco's modified Eagle's medium (DMEM)/Nutrient mixture F12 supplemented with 10% FBS. All cells were maintained at 37 °C with 5% CO2 in humified air.

cAMP Accumulation Assay. cAMP accumulation experiments were performed using a LANCE® Ultra cAMP detection kit as described previously.[25,39] Briefly, CHO-K1 cells stably expressing human WT A_1R, $A_{2A}R$, $A_{2B}R$ and A_3R were seeded at 2000 cells per well in a white 384-well optiplate. Cells were then incubated with adenosine receptor ligands (ranging between 100 μM to 1 pM) for 30 min at room temperature. For A_1R and A_3R expressing cells, 10 μM and 1 μM forskolin, respectively, was added at the same time as the addition of the adenosine receptor ligands, as we have described previously.[13,24,25]

NanoBRET Assay for Binding. To determine the affinity (pK_i) of adenosine receptor ligands, a NanoBRET competition binding assay was performed as described previously.[24,25] Briefly, CA200645 was used at 20 nM. Kinetic data was fitted with the 'kinetic of competitive binding' model[35] (built into Prism v9.1 (GraphPad Software, San Diego, CA)) to determine affinity (pK_i) values and the association rate constant (k_{on}) and dissociation rates (k_{off}) for AR ligands. In agreement with our previous studies, we determined the K_d of CA200645 at the human A_1R to be 18.29 ± 2.4 nM and at the rat A_1R 32.96 ± 2.8 nM.[25,39] The "one-site–K_i model" derived from the Cheng and Prusoff correction and available in Prism was fitted with the BRET ratio at 10 min post simulation and affinity (pK_i) constant values at equilibrium for adenosine receptor ligands were determined.

Data and Statistical Analysis. Data were analyzed using Prism v9.1 (GraphPad Software, San Diego, CA). Dose-response curves were fitted using a three-parameter logistic equation to calculate response range and pEC_{50}, and normalized to forskolin stimulation ($A_{2A}R$ and $A_{2B}R$) or forskolin inhibition (A_1R and A_3R), expressed as percentage of 100 μM forskolin. Adenosine and NECA stimulations were used as an intrinsic controls across all experiments.

Receptor binding kinetics was determined as described previously[25] using the Motulsky and Mahan method[35] (built into Prism v9.1) to determine the test compound association rate constant and dissociation

rate constant. The k_{on} and k_{off} values for binding of CA200645 at the human A_1R were determined to be k_{on} = 3.67 ± 0.34 × 10^6 $M^{-1}min^{-1}$ and k_{off} = 0.064 ± 0.0023 min^{-1} and at the rat A_1R k_{on} = 2.93 ± 0.24 × 10^6 $M^{-1}min^{-1}$ and k_{off} = 0.066 ± 0.0022 min^{-1}.

To calculate the relative activities (RA) of compounds (Figure 2) equation 1 was used,

$$RA = \frac{EC_{50} \times E_{max}\ (reference\ compound)}{EC_{50} \times E_{max}\ (compound)} \quad \text{(eq. 1)}$$

where E_{max} is the maximal response and EC_{50} is the agonist concentration required to produce a half-maximal response, and web plot was plotted using Microsoft Excel. Since the receptors are expressed in the same cell background and adenosine or NECA are full potent agonists across all the adenosine subtypes, we reasoned that changes in log (RA) for a given ligand, relative to NECA or adenosine at A_1R, would provide a quantitative means of comparing receptor selectivity of individual adenosine receptor ligands.

The statistical analysis was performed in Prism v9.1 using one-way ANOVA with a Dunnett's post-test for multiple comparisons following the guidelines as described by Curtis *et al.*[31] All experiments were performed in a minimum of three repeats, conducted in duplicates, and data were reported as mean ± SEM.

Adenosine Receptor Structures. The active state A_1R coordinates were retrieved from the Protein Data Bank (PDB) database[40] entry 7LD4.[19] The PDB ID 5G53[41] was used for $A_{2A}R$ in active conformation. $A_{2B}R$ in active conformation was modelled using 5G53 as a template through Modeller 9.19.[42] The $A_{2B}R$ ECL2 ($L142^{ECL2}$-$K170^{ECL2}$) was retrieved from the inactive state model by AlphaFold2[43] (entry P29275) and inserted in the homology model by superposition. A_3R in active conformation was modelled using 7LD4 as a template through Modeller 9.19.[42] The A_3R ECL2 ($K152^{ECL2}$-$S165^{ECL2}$) was retrieved from the inactive state model by AlphaFold2 (entry P0DMS8) and inserted in the homology model by superposition. All the ARs structures did not present neither the ICL3 nor the G protein bound to its intracellular binding site.

Force Field and Ligand Parameters for MD Simulations. The CHARMM36[44,45]/CGenFF 3.0.1[46-48] force field combination was employed in this work. Force field, topology and parameter files for **20** and **27** were obtained from the ParamChem webserver.[46]

System Preparations for MD Simulations. For all systems, hydrogen atoms were added by means of the pdb2pqr[49] and propka[50] software (considering a simulated pH of 7.0). The protonation of titratable side chains was checked by visual inspection. The resulting receptors were separately inserted in a square 90 Å x 90 Å 1-palmitoyl-2-oleyl-sn-glycerol-3-phosphocholine (POPC) bilayer (previously built by using the VMD Membrane Builder plugin 1.1, Membrane Plugin, Version 1.1. at http://www.ks.uiuc.edu/Research/vmd/plugins/membrane/), through an insertion method,[51] along with their co-crystallized ligand (and the crystallographic water molecules within 5 Å of the ligand). The receptor orientation was obtained by superposing the coordinates on the corresponding structure retrieved from the OPM database.[52] Lipids overlapping the receptor transmembrane helical bundle were removed and TIP3P water molecules[53] were added to the simulation box by means of the VMD Solvate plugin 1.5 (Solvate Plugin, Version 1.5. at http://www.ks.uiuc.edu/Research/vmd/plugins/solvate/). Finally, overall charge neutrality was reached by adding Na^+/Cl^- counter ions up to the final concentration of 0.150 M), using the VMD Autoionize plugin 1.3 (Autoionize Plugin, Version 1.3. at http://www.ks.uiuc.edu/Research/vmd/plugins/autoionize/).

System Equilibration and MD Settings. The MD engine ACEMD[54] was employed for both the equilibration and productive simulations. The equilibration was achieved in isothermal-isobaric conditions (NPT) using the Berendsen barostat[55] (target pressure 1 atm) and the Langevin thermostat[56] (target temperature 300 K) with low damping of 1 ps^{-1}. A multi-stage procedure was performed (integration time step of 2 fs): first, clashes between protein and lipid atoms were reduced through 1500 conjugate-gradient minimization steps, then 1 kcal mol^{-1} $Å^{-2}$ positional restraints on lipid phosphorus atoms, protein atoms other than Cα, and protein Cα atoms were gradually removed over 2 ns, 60 ns, and 80 ns respectively. The last 20 ns of equilibration was performed without any positional restraints. Productive trajectories were

computed with an integration time step of 4 fs in the canonical ensemble (NVT). The target temperature was set at 300 K, using a thermostat damping of 0.1 ps^{-1}. The M-SHAKE algorithm[57,58] was employed to constrain the bond lengths involving hydrogen atoms. The cut-off distance for electrostatic interactions was set at 9 Å, with a switching function applied beyond 7.5 Å. Long-range Coulomb interactions were handled using the particle mesh Ewald summation method (PME)[59] by setting the mesh spacing to 1.0 Å.

Molecular Docking. A first attempt to dock **20** and **27** into all the four ARs subtypes was performed on structures prepared as reported above using Vina[60] in a 30 Å x 30 Å x 30 Å cube centered on the atom CZ of the ECL2 conserved phenylalanine residue (F171 in A_1R, F168 in $A_{2A}R$, F173 in $A_{2B}R$, and F168 in A_3). Successive molecular docking simulations of **20** and **27**, with the same settings, were performed into AR structure extracted from MD simulations (see below). A_1R, $A_{2A}R$, and $A_{2B}R$ were extracted from adiabatic MD simulations, while the A_3R structure was the equilibrated apo structure.

Adiabatic MD of the apo Adenosine Receptors. The apo AR structures were prepared and equilibrated as reported above. A_1R, $A_{2A}R$, and $A_{2B}R$ were subjected to 50 ns of adiabatic MD.[61] A target distance of 13 Å and a force constant of 100 kJ mol^{-1} $Å^{-2}$ were set to favour the opening of the salt bridge between ECL2 and ECL3: $E172^{ECL2}$ (Cδ)-$K265^{ECL3}$ (Nζ) on A_1R, $E169^{ECL2}$(Cδ)-H264(Hε2) on $A_{2A}R$, E174(Cδ)-K265(Nζ) and K267(Nζ) on $A_{2B}R$.

MD Analysis. Root mean square deviations (RMSD) and fluctuation (RMSF) were computed using VMD.[62] Interatomic contacts and hydrogen bonds were detected using the GetContacts scripts tool (https://getcontacts.github.io). Contacts and hydrogen bond persistency are quantified as the percentage of frames (over all the frames obtained by merging the different replicas) in which protein residues formed contacts or hydrogen bonds with the ligand. Structural water molecules were detected in the apo ARs using AquaMMapS.[63] Short 10 ns simulations were performed with time step 2 fs, restraining the Cα atoms and saving a frame every 20 ps of simulation.

Residues Numbering System. Throughout the manuscript, the Ballesteros-Weinstein residues numbering system for GPCRs is adopted.[64]

Supporting Information

Summary of *O*-alkylation studies (Scheme S1), synthetic confirmation of 2-aminocyclopentanol stereochemistry (Figure S1), molecular docking of **20** and **27** (Figures S2-S3), molecular dynamics simulations (Movies S1-S2, Figures S4 and S6) and mutagenesis study (Figure S5). Purity assessment (Tables S1 and S2), molecular formula strings (Table S3) and reproduction of ^{1}H and ^{13}C NMR spectra for tested compounds. This material is available free of charge via the Internet at http://pubs.acs.org.

Author Information

Corresponding authors:

*M.Lo.: orcid.org/0000-0003-4930-1886; E-mail martin.lochner@ibmm.unibe.ch; phone +41 (0)31 684 3311

*G.L.: orcid.org/0000-0001-7320-9612; E-mail grl30@cam.ac.uk; phone +44 (0)1223 334 020

Notes:

The authors declare no competing financial interest.

#B.P., A.S. and G.D. contributed equally to this work. M.Lo. and G.H. also contributed equally.

Acknowledgments

This study was supported by the Swiss National Science Foundation (B.P., M.Le. and M.Lo.), the Cambridge Trust (A.S.), the Leverhulme Trust (K.B. and G.L.), an AstraZeneca studentship (S.C.), a British Pharmacological Society Vacation Studentship (I.M.), a China Scholarship Council Cambridge International Scholarship (X.H.) and the BBSRC (G.L.). We thank Matt Ladds for his help with proof checking the statistical analysis and the Analytical Services from the Department of Chemistry, Biochemistry and Pharmaceutical Sciences, University of Bern, Switzerland for measuring NMR and MS spectra of synthetic intermediates and final compounds.

Abbreviations Used

AC, adenylyl cyclase; AR, adenosine receptor; A_1R, adenosine A_1 receptor; $A_{2A}R$, adenosine A_{2A} receptor; $A_{2B}R$, adenosine A_{2B} receptor; A_3R, adenosine A_3 receptor; BRET, bioluminescence resonance energy transfer; DAIB, (diacetoxyiodo)benzene; DIAD, diisopropyl azodicarboxylate; NECA, 5'-*N*-ethylcarboxamidoadenosine; RA, relative activity; RT, residence time; TEMPO, (2,2,6,6-tetramethylpiperidin-1-yl)oxyl.

References

(1) Jacobson, K. A.; Müller, C. E. Medicinal chemistry of adenosine, P2Y and P2X receptors. *Neuropharmacology* **2016**, *104*, 31-49.

(2) Sawynok, J. Adenosine receptor targets for pain. *Neuroscience* **2016**, *338*, 1-18.

(3) Huang, Z. L.; Qu, W. M.; Eguchi, N.; Chen, J. F.; Schwarzschild, M. A.; Fredholm, B. B.; Urade, Y.; Hayaishi, O. Adenosine A_{2A}, but not A_1, receptors mediate the arousal effect of caffeine. *Nat. Neurosci.* **2005**, *8*, 858-859.

(4) Lazarus, M.; Shen, H. Y.; Cherasse, Y.; Qu, W. M.; Huang, Z. L.; Bass, C. E.; Winsky-Sommerer, R.; Semba, K.; Fredholm, B. B.; Boison, D.; Hayaishi, O.; Urade, Y.; Chen, J. F. Arousal effect of caffeine depends on adenosine A_{2A} receptors in the shell of the nucleus accumbens. *J. Neurosci.* **2011**, *31*, 10067-10075.

(5) Eltzschig, H. K.; Sitkovsky, M. V.; Robson, S. C. Purinergic signaling during inflammation. *N. Engl. J. Med.* **2012**, *367*, 2322-2333.

(6) Eltzschig, H. K. Adenosine: an old drug newly discovered. *Anesthesiology* **2009**, *111*, 904-915.

(7) Fredholm, B. B. Adenosine, an endogenous distress signal, modulates tissue damage and repair. *Cell Death Differ.* **2007**, *14*, 1315-1323.

(8) Haskó, G.; Linden, J.; Cronstein, B.; Pacher, P. Adenosine receptors: therapeutic aspects for inflammatory and immune diseases. *Nat. Rev. Drug Discov.* **2008**, *7*, 759-770.

(9) Eltzschig, H. K.; Carmeliet, P. Hypoxia and inflammation. *N. Engl. J. Med.* **2011**, *364*, 656-665.

(10) Jacobson, K. A.; Gao, Z. G. Adenosine receptors as therapeutic targets. *Nat. Rev. Drug Discov.* **2006**, *5*, 247-264.

(11) Chen, J. F.; Eltzschig, H. K.; Fredholm, B. B. Adenosine receptors as drug targets – what are the challenges? *Nat. Rev. Drug Discov.* **2013**, *12*, 265-286.

(12) Jacobson, K. A.; Tosh, D. K.; Jain, S.; Gao, Z. G. Historical and current adenosine receptor agonists in preclinical and clinical development. *Front. Cell. Neurosci.* **2019**, *13*, 124.

(13) Knight, A.; Hemmings, J. L.; Winfield, I.; Leuenberger, M.; Frattini, E.; Frenguelli, B. G.; Dowell, S. J.; Lochner, M.; Ladds, G. Discovery of novel adenosine receptor agonists that exhibit subtype selectivity. *J. Med. Chem.* **2016**, *59*, 947-964.

(14) Tosh, D. K.; Rao, H.; Bitant, A.; Salmaso, V.; Mannes, P.; Lieberman, D. I.; Vaughan, K. L.; Mattison, J. A.; Rothwell, A. C.; Auchampach, J. A.; Ciancetta, A.; Liu, N.; Cui, Z.; Gao, Z. G.; Reitman, M. L.; Gavrilova, O.; Jacobson, K. A. Design and in vivo characterization of A_1 adenosine receptor agonists in the native ribose and conformationally constrained (N)-methanocarba series. *J. Med. Chem.* **2019**, *62*, 1502-1522.

(15) Petrelli, R.; Scortichini, M.; Belardo, C.; Boccella, S.; Luongo, L.; Capone, F.; Kachler, S.; Vita, P.; Del Bello, F.; Maione, S.; Lavecchia, A.; Klotz, K. N.; Cappellacci, L. Structure-based design, synthesis, and in vivo antinociceptive effects of selective A_1 adenosine receptor agonists. *J. Med. Chem.* **2018**, *61*, 305-318.

(16) Franchetti, P.; Cappellacci, L.; Vita, P.; Petrelli, R.; Lavecchia, A.; Kachler, S.; Klotz, K.-N.; Marabese, I.; Luongo, L.; Maione, S.; Grifantini, M. N^6-Cycloalkyl- and N^6-bicycloalkyl-*C*5′(*C*2′)-modified adenosine derivatives as high-affinity and selective agonists at the human A_1 adenosine receptor with antinociceptive effects in mice. *J. Med. Chem.* **2009**, *52*, 2393-2406.

(17) Luongo, L.; Petrelli, R.; Gatta, L.; Giordano, C.; Guida, F.; Vita, P.; Franchetti, P.; Grifantini, M.; Novellis, V. D.; Cappellacci, L.; Maione, S. 5'-Chloro-5'-deoxy-(±)-ENBA, a potent and selective adenosine A_1 receptor agonist, alleviates neuropathic pain in mice through functional glial and microglial changes without affecting motor or cardiovascular functions. *Molecules* **2012**, *17*, 13712-13726.

(18) Guo, M.; Bakhoda, A.; Gao, Z. G.; Ramsey, J. M.; Li, Y.; O'Conor, K. A.; Kelleher, A. C.; Eisenberg, S. M.; Kang, Y.; Yan, X.; Javdan, C.; Fowler, J. S.; Rice, K. C.; Hooker, J. M.; Jacobson, K. A.; Kim, S. W.; Volkow, N. D. Discovery of highly potent adenosine A_1 receptor agonists: targeting positron emission tomography probes. *ACS Chem. Neurosci.* **2021**, *12*, 3410-3417.

(19) Draper-Joyce, C. J.; Bhola, R.; Wang, J.; Bhattarai, A.; Nguyen, A. T. N.; Cowie-Kent, I.; O'Sullivan, K.; Chia, L. Y.; Venugopal, H.; Valant, C.; Thal, D. M.; Wootten, D.; Panel, N.; Carlsson, J.; Christie, M. J.; White, P. J.; Scammells, P.; May, L. T.; Sexton, P. M.; Danev, R.; Miao, Y.; Glukhova, A.;

Imlach, W. L.; Christopoulos, A. Positive allosteric mechanisms of adenosine A_1 receptor-mediated analgesia. *Nature* **2021**, *597*, 571-576.

(20) Elzein, E.; Zablocki, J. A_1 adenosine receptor agonists and their potential therapeutic applications. *Expert Opin. Invest. Drugs* **2008**, *17*, 1901-1910.

(21) Staehr, P. M.; Dhalla, A. K.; Zack, J.; Wang, X.; Ho, Y. L.; Bingham, J.; Belardinelli, L. Reduction of free fatty acids, safety, and pharmacokinetics of oral GS-9667, an A_1 adenosine receptor partial agonist. *J. Clin. Pharmacol.* **2013**, *53*, 385-392.

(22) Wall, M. J.; Hill, E.; Huckstepp, R.; Barkan, K.; Deganutti, G.; Leuenberger, M.; Preti, B.; Winfield, I.; Carvalho, S.; Suchankowa, A.; Wei, H.; Safitri, D.; Huang, X.; Imlach, W.; La Mache, C.; Dean, E.; Hume, C.; Hayward, S.; Oliver, J.; Zhao, F.-Y.; Spanswick, D.; Reynolds, C. A.; Lochner, M.; Ladds, G.; Frenguelli, B. G. Selective activation of Gαob by an adenosine A_1 receptor agonist elicits analgesia without cardiorespiratory depression. *Nat. Commun.* **2022**, *13*, 4150.

(23) Draper-Joyce, C. J.; Khoshouei, M.; Thal, D. M.; Liang, Y.-L.; Nguyen, A. T. N.; Furness, S. G. B.; Venugopal, H.; Baltos, J.-A.; Plitzko, J. M.; Danev, R.; Baumeister, W.; May, L. T.; Wootten, D.; Sexton, P. M.; Glukhova, A.; Christopoulos, A. Structure of the adenosine-bound human adenosine A_1 receptor–G_i complex. *Nature* **2018**, *558*, 559-563.

(24) Deganutti, G.; Barkan, K.; Preti, B.; Leuenberger, M.; Wall, M.; Frenguelli, B. G.; Lochner, M.; Ladds, G.; Reynolds, C. A. Deciphering the agonist binding mechanism to the adenosine A_1 receptor. *ACS Pharmacol. Transl. Sci.* **2021**, *4*, 314-326.

(25) Barkan, K.; Lagarias, P.; Stampelou, M.; Stamatis, D.; Hoare, S.; Safitri, D.; Klotz, K. N.; Vrontaki, E.; Kolocouris, A.; Ladds, G. Pharmacological characterisation of novel adenosine A_3 receptor antagonists. *Sci. Rep.* **2020**, *10*, 20781.

(26) Jagtap, P. Adenosine compounds and their use thereof. WO2011/119919 A1, 2011.

(27) Mitsunobu, O.; Masaaki, Y. Prepration of esters of carboxylic and phosphoric acid via quaternary phosphonium salts. *Bull. Chem. Soc. Jpn.* **1967**, *40*, 2380-2382.

(28) Kotra, L. P.; Manouilov, K. K.; Cretton-Scott, E.; Sommadossi, J. P.; Boudinot, F. D.; Schinazi, R. F.; Chu, C. K. Synthesis, biotransformation, and pharmacokinetic studies of 9-(*β*-D-arabinofuranosyl)-6-azidopurine: a prodrug for Ara-A designed to utilize the azide reduction pathway. *J. Med. Chem.* **1996**, *39*, 5202-5207.

(29) Middleton, R. J.; Briddon, S. J.; Cordeaux, Y.; Yates, A. S.; Dale, C. L.; George, M. W.; Baker, J. G.; Hill, S. J.; Kellam, B. New fluorescent adenosine A_1-receptor agonists that allow quantification of ligand-receptor interactions in microdomains of single living cells. *J. Med. Chem.* **2007**, *50*, 782-793.

(30) Murthy, S.; Desantis, J.; Verheugd, P.; Maksimainen, M. M.; Venkannagari, H.; Massari, S.; Ashok, Y.; Obaji, E.; Nkizinkinko, Y.; Lüscher, B.; Tabarrini, O.; Lehtiö, L. 4-(Phenoxy) and 4-(benzyloxy)benzamides as potent and selective inhibitors of mono-ADP-ribosyltransferase PARP10/ARTD10. *Eur. J. Med. Chem.* **2018**, *156*, 93-102.

(31) Curtis, M. J.; Alexander, S.; Cirino, G.; Docherty, J. R.; George, C. H.; Giembycz, M. A.; Hoyer, D.; Insel, P. A.; Izzo, A. A.; Ji, Y.; MacEwan, D. J.; Sobey, C. G.; Stanford, S. C.; Teixeira, M. M.; Wonnacott, S.; Ahluwalia, A. Experimental design and analysis and their reporting II: updated and simplified guidance for authors and peer reviewers. *Br. J. Pharmacol.* **2018**, *175*, 987-993.

(32) Guo, D.; Heitman, L. H.; IJzerman, A. P. Kinetic aspects of the interaction between ligand and G protein-coupled receptor: the case of the adenosine receptors. *Chem. Rev.* **2017**, *117*, 38-66.

(33) Sykes, D. A.; Stoddart, L. A.; Kilpatrick, L. E.; Hill, S. J. Binding kinetics of ligands acting at GPCRs. *Mol. Cell. Endocrinol.* **2019**, *485*, 9-19.

(34) Vauquelin, G. Effects of target binding kinetics on *in vivo* drug efficacy: k_{off}, k_{on} and rebinding. *Br. J. Pharmacol.* **2016**, *173*, 2319-2334.

(35) Motulsky, H. J.; Mahan, L. C. The kinetics of competitive radioligand binding predicted by the law of mass action. *Mol. Pharmacol.* **1984**, *25*, 1-9.

(36) Lu, H.; Tonge, P. J. Drug–target residence time: critical information for lead optimization. *Curr. Opin. Chem. Biol.* **2010**, *14*, 467-474.

(37) Suchankova, A.; Stampelou, M.; Koutsouki, K.; Pousias, A.; Dhingra, L.; Barkan, K.; Pouli, N.; Marakos, P.; Tenta, R.; Kolocouris, A.; Lougiakis, N.; Ladds, G. Discovery of a high affinity adenosine A_1/A_3 receptor antagonist with a novel 7-amino-pyrazolo[3,4-*d*]pyridazine scaffold. *ACS Med. Chem. Lett.* **2022**, *13*, 923-934.

(38) Frenguelli, B. G.; Wall, M. J. Adenosine receptor agonists. WO2020/188288 A1, 2020.

(39) Deganutti, G.; Barkan, K.; Ladds, G.; Reynolds, C. A. Multisite model of allosterism for the adenosine A_1 receptor. *J. Chem. Inf. Model.* **2021**, *61*, 2001-2015.

(40) Berman, H. M.; Westbrook, J.; Feng, Z.; Gilliland, G.; Bhat, T. N.; Weissig, H.; Shindyalov, I. N.; Bourne, P. E. The protein data bank. *Nucleic Acids Res.* **2000**, *28*, 235-242.

(41) Carpenter, B.; Nehmé, R.; Warne, T.; Leslie, A. G.; Tate, C. G. Structure of the adenosine A_{2A} receptor bound to an engineered G protein. *Nature* **2016**, *536*, 104-107.

(42) Fiser, A.; Sali, A. Modeller: generation and refinement of homology-based protein structure models. *Methods Enzymol.* **2003**, *374*, 461-491.

(43) Jumper, J.; Evans, R.; Pritzel, A.; Green, T.; Figurnov, M.; Ronneberger, O.; Tunyasuvunakool, K.; Bates, R.; Žídek, A.; Potapenko, A.; Bridgland, A.; Meyer, C.; Kohl, S. A. A.; Ballard, A. J.; Cowie, A.; Romera-Paredes, B.; Nikolov, S.; Jain, R.; Adler, J.; Back, T.; Petersen, S.; Reiman, D.; Clancy, E.; Zielinski, M.; Steinegger, M.; Pacholska, M.; Berghammer, T.; Bodenstein, S.; Silver, D.; Vinyals, O.; Senior, A. W.; Kavukcuoglu, K.; Kohli, P.; Hassabis, D. Highly accurate protein structure prediction with AlphaFold. *Nature* **2021**, *596*, 583-589.

(44) Huang, J.; MacKerell, A. D., Jr. CHARMM36 all-atom additive protein force field: validation based on comparison to NMR data. *J. Comput. Chem.* **2013**, *34*, 2135-2145.

(45) Huang, J.; Rauscher, S.; Nawrocki, G.; Ran, T.; Feig, M.; de Groot, B. L.; Grubmüller, H.; MacKerell, A. D., Jr. CHARMM36m: an improved force field for folded and intrinsically disordered proteins. *Nat. Methods* **2017**, *14*, 71-73.

(46) Vanommeslaeghe, K.; MacKerell, A. D., Jr. Automation of the CHARMM General Force Field (CGenFF) I: bond perception and atom typing. *J. Chem. Inf. Model.* **2012**, *52*, 3144-3154.

(47) Vanommeslaeghe, K.; Raman, E. P.; MacKerell, A. D., Jr. Automation of the CHARMM General Force Field (CGenFF) II: assignment of bonded parameters and partial atomic charges. *J. Chem. Inf. Model.* **2012**, *52*, 3155-3168.

(48) Yu, W.; He, X.; Vanommeslaeghe, K.; MacKerell, A. D., Jr. Extension of the CHARMM General Force Field to sulfonyl-containing compounds and its utility in biomolecular simulations. *J. Comput. Chem.* **2012**, *33*, 2451-2468.

(49) Dolinsky, T. J.; Nielsen, J. E.; McCammon, J. A.; Baker, N. A. PDB2PQR: an automated pipeline for the setup of Poisson-Boltzmann electrostatics calculations. *Nucleic Acids Res.* **2004**, *32*, W665-W667.

(50) Olsson, M. H.; Søndergaard, C. R.; Rostkowski, M.; Jensen, J. H. PROPKA3: consistent treatment of internal and surface residues in empirical pK_a predictions. *J. Chem. Theory Comput.* **2011**, *7*, 525-537.

(51) Sommer, B. Membrane packing problems: a short review on computational membrane modeling methods and tools. *Comput. Struct. Biotechnol. J.* **2013**, *5*, e201302014.

(52) Lomize, M. A.; Lomize, A. L.; Pogozheva, I. D.; Mosberg, H. I. OPM: orientations of proteins in membranes database. *Bioinformatics* **2006**, *22*, 623-625.

(53) Jorgensen, W. L.; Chandrasekhar, J.; Madura, J. D.; Impey, R. W.; Klein, M. L. Comparison of simple potential functions for simulating liquid water. *J. Chem. Phys.* **1983**, *79*, 926-935.

(54) Harvey, M. J.; Giupponi, G.; Fabritiis, G. D. ACEMD: accelerating biomolecular dynamics in the microsecond time scale. *J. Chem. Theory Comput.* **2009**, *5*, 1632-1639.

(55) Berendsen, H. J. C.; Postma, J. P. M.; Gunsteren, W. F. v.; DiNola, A.; Haak, J. R. Molecular dynamics with coupling to an external bath. *J. Chem. Phys.* **1984**, *81*, 3684-3690.

(56) Loncharich, R. J.; Brooks, B. R.; Pastor, R. W. Langevin dynamics of peptides: the frictional dependence of isomerization rates of *N*-acetylalanyl-*N'*-methylamide. *Biopolymers* **1992**, *32*, 523-535.

(57) Forester, T. R.; Smith, W. SHAKE, rattle, and roll: efficient constraint algorithms for linked rigid bodies. *J. Comput. Chem.* **1998**, *19*, 102-111.

(58) Kräutler, V.; van Gunsteren, W. F.; Hünenberger, P. H. A fast SHAKE algorithm to solve distance constraint equations for small molecules in molecular dynamics simulations. *J. Comput. Chem.* **2001**, *22*, 501-508.

(59) Essmann, U.; Perera, L.; Berkowitz, M. L.; Darden, T.; Lee, H.; Pedersen, L. G. A smooth particle mesh Ewald method. *J. Chem. Phys.* **1995**, *103*, 8577-8593.

(60) Trott, O.; Olson, A. J. AutoDock Vina: improving the speed and accuracy of docking with a new scoring function, efficient optimization, and multithreading. *J. Comput. Chem.* **2010**, *31*, 455-461.

(61) Marchi, M.; Ballone, P. Adiabatic bias molecular dynamics: a method to navigate the conformational space of complex molecular systems. *J. Chem. Phys.* **1999**, *110*, 3697-3702.

(62) Humphrey, W.; Dalke, A.; Schulten, K. VMD: visual molecular dynamics. *J. Mol. Graph.* **1996**, *14*, 33-38.

(63) Cuzzolin, A.; Deganutti, G.; Salmaso, V.; Sturlese, M.; Moro, S. AquaMMapS: an alternative tool to monitor the role of water molecules during protein-ligand association. *ChemMedChem* **2018**, *13*, 522-531.

(64) Ballesteros, J. A.; Weinstein, H. Integrated methods for the construction of three-dimensional models and computational probing of structure-function relations in G protein-coupled receptors. In *Methods in Neurosciences*; Stuart, C. S., Ed.; Academic Press: San Diego, 1995; Vol. 25, pp 366-428.

Table of Contents Graphic

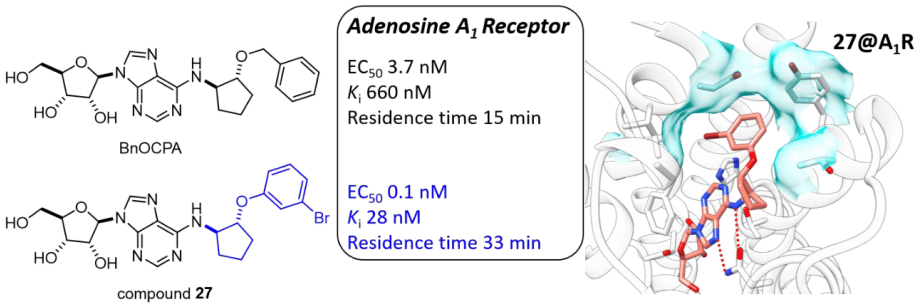

Appendix 4. Stampelou, et al. 2022

This appendix contains:

Stampelou M.*, **Suchankova A.***, Tzortzini E., Dhingra L., Barkan K., Lougiakis N., Marakos P., Pouli N., Ladds G., Kolocouris A., 2022. Novel 7-Anilino-Pyrazolo[3,4-c]pyridine as High Affinity Dual A_1, A_3 Adenosine Receptor Antagonists and SARs Study Using Alchemical Perturbation Binding Free-Energy Calculations. Accepted to J. Med. Chem (* both authors contributed equally).

* Unknown * | ACSJCA | JCA11.2.5208/W Library-x64 | manuscript.3f (R5.2.i3:5013 | 2.1) 2022/08/03 13:05:00 | PROD-WS-121 | rq_209648 | 9/13/2022 08:54:41 | 23 | JCA-DEFAULT

Journal of Medicinal Chemistry

pubs.acs.org/jmc Article

Dual A1/A3 Adenosine Receptor Antagonists: Binding Kinetics and SAR Studies Using Mutagenesis and Alchemical Binding Free Energy Calculations

Margarita Stampelou, Anna Suchankova, Efpraxia Tzortzini, Lakshiv Dhingra, Kerry Barkan, Nikolaos Lougiakis, Panagiotis Marakos, Nicole Pouli,* Graham Ladds,* and Antonios Kolocouris*

Cite This: https://doi.org/10.1021/acs.jmedchem.2c01123 Read Online

ACCESS | Metrics & More | Article Recommendations | Supporting Information

ABSTRACT: Drugs targeting adenosine receptors (AR) can provide treatment for diseases. We report the identification of 7-(phenylamino)-pyrazolo[3,4-*c*]pyridines **L2**−**L10**, **A15**, and **A17** as low-micromolar to low-nanomolar A_1R/A_3R dual antagonists, with 3-phenyl-5-cyano-7-(trimethoxyphenylamino)-pyrazolo[3,4-*c*]-pyridine **A17** displaying the highest affinity at both receptors with a long residence time of binding, as determined using a NanoBRET-based assay. Two binding orientations of **A17** produce stable complexes inside the orthosteric binding area of A_1R in molecular dynamics (MD) simulations, and we selected the most plausible orientation based on the agreement with alanine mutagenesis supported by affinity experiments. Interestingly, for drug design purposes, the mutation of $L250^{6.51}$ to alanine increased the binding affinity of **A17** at A_1R. We explored the structure−activity relationships against A_1R using alchemical binding free energy calculations with the thermodynamic integration coupled with the MD simulation (TI/MD) method, applied on the whole G-protein-coupled receptor−membrane system, which showed a good agreement (r = 0.73) between calculated and experimental relative binding free energies.

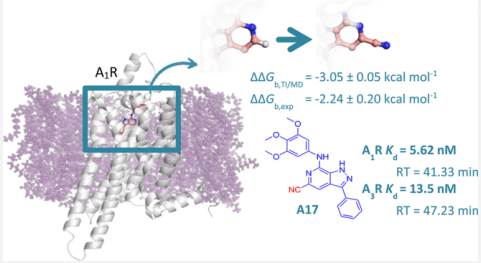

■ INTRODUCTION

Adenosine, a naturally occurring purine nucleoside, is an endogenous agonist of adenosine receptors (ARs).[1] ARs are G-protein-coupled receptors (GPCRs) comprising four subtypes: A_1, A_{2A}, A_{2B}, and A_3. The $A_{2A}R$ and $A_{2B}R$ subtypes act synergistically with the G_s protein resulting in the stimulation of adenylyl cyclase, increasing 3′,5′-cyclic adenosine monophosphate (cAMP) levels. In contrast, A_1R and A_3R subtypes inhibit adenylyl cyclase and decrease cAMP levels within cells by coupling to $G_{i/o}$. $A_{2A}R$ has been extensively studied over the last few decades because, until recently, it had been the only one of the four subtypes that had its structure resolved.[2−9] Indeed, the binding mode of several antagonists,[5−9] or agonists,[2−4] [e.g., **adenosine** and 5′-*N*-ethylcarboxamidoadenosine (**NECA**)], bound to the $A_{2A}R$ has been revealed by X-ray crystallography or more recently with cryo-electron microscopy (cryo-EM).[4] Since 2017, two X-ray structures of A_1R in complex with antagonists[10,11] and one cryo-EM of A_1R in complex with an agonist[12] were solved.

These experimental structures can help to understand the binding interactions of ARs with ligands and provide templates for structure-based drug design as others[13−19] and we[20] have shown previously. For example, in our previous work, from in silico screening of Maybridge HitFinder Library[20] using the experimental structure of $A_{2A}R$ with ZM241385 (PDB ID 3EML),[5] we identified new hits with low micromolar affinities against A_3R.[20] The affinities were, in most cases, consistent with antagonistic receptor activities determined using inhibition of cAMP accumulation.[21] With the agonist **NECA** and the specific N_6-(3-iodobenzyl)-adenosine-5′-*N*-methylcarboxamide (**IB-MECA**) for A_3R and our identified antagonists, we investigated the structural features of the experimentally unresolved A_3R orthosteric binding area using molecular dynamics (MD) simulations, mutagenesis, and functional assays.[21−23]

Different therapeutic applications have been identified in preclinical and clinical studies of A_1R antagonists as potassium-sparing diuretic agents with kidney-protecting properties.[24,25] These types of compounds can be useful in the treatment of chronic heart diseases.[26] A_1R antagonists may offer a

Received: July 13, 2022

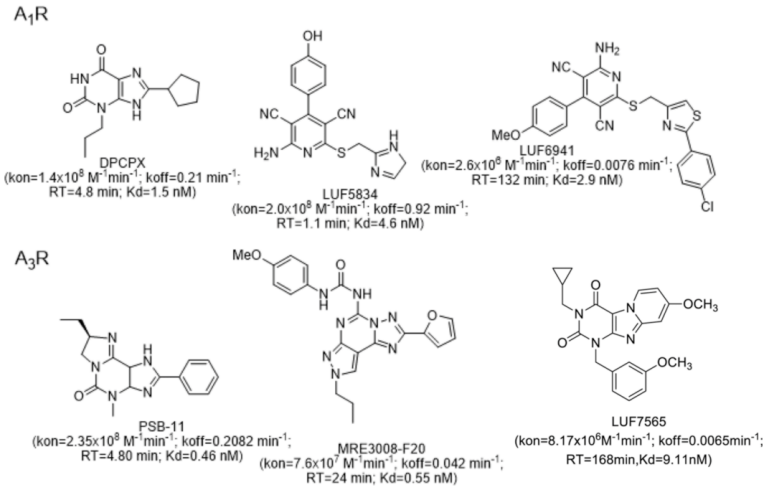

Figure 1. Association (K_{on}) and dissociation (K_{off}) rate constants of selected A_1R (DPCPX,[40] LUF5834,[41] and LUF6941[42]) and A_3R ligands (PSB-11,[43] MRE3008-F20,[44] and LUF7565[39]).

A15: A=H, B=CN, R=H
A17: A=OMe, B=CN, R=Ph
L2: A=OMe, B=Cl, R=iPr
L3: A=OMe, B=CN, R=iPr
L4: A=H, B=CN, R=Ph
L5: A=OMe, B=Cl, R=Ph
L6: A=OMe, B=H, R=Ph
L7: A=OMe, B=CH_2NH_2, R=Ph
L8: A=OMe, B=CH_2NHCH_2Ph, R=Ph
L9: A=OMe, B=CH_2NHCH_2(3-py), R=Ph
L10: A=OMe, B=CH_2NHCH_2(N-methyl-4-piperidinyl), R=Ph

A26: G=NHPh, Z=H, Y=CH_2NHPh, R_1=Me
L12: G=NHPh, Z=H, Y=CH_2NHPh, R_1=H
L15: G=NHPh, Z=H, Y=Ph, R_1=Me
L21: G=H, Z=NHPh, Y=NHPh, R_1=Me

Figure 2. General chemical structure and numbering of 7-aminophenyl-3-alkyl-5-substituted-pyrazolo[3,4-*c*]pyridine (left) and 1-alkyl-3-acylamino-pyrazolo[3,4-*c*]pyridine (right) scaffolds. The tested compounds have substituents shown below the chemical structures.

therapeutic opportunity for chronic lung diseases, such as asthma, chronic obstructive pulmonary disease (COPD), and pulmonary fibrosis.[24,27] The observation of the effects of **caffeine**, a classical non-selective **adenosine** antagonist, on the central nervous system (CNS),[24] such as improvement of awareness and learning, encouraged the search of selective antagonists endowed with CNS activity. Selective A_1R antagonists induce cognition enhancement,[24] leading to a general improvement in memory performance, and these actions are potentially useful in the treatment of dementia and anxiety disorders.[28] Moreover, it has been reported that treatment with the A_1R antagonist **CPT** (8-cyclopentyl-1,3-dimethylxanthine) in a model of Parkinson's disease produced a dose-dependent improvement in locomotion, suggesting that, although the role of A_1R in Parkinson's disease is still unclear, the A_1R antagonism may produce therapeutic effects, particularly at the beginning of treatment.[29]

Beyond inhibiting cAMP accumulations, the A_3R has been suggested to modulate mitogen-activated protein kinase (MAPK) activity, which may explain the role of this receptor in cell proliferation and differentiation[30,31] and in tumor development and progression. A_3R is overexpressed in several types of cancer cells and is thus considered as a possible biological marker for tumors.[30] It is well established that MAPK pathways are involved in tubulointerstitial fibrosis, which is a common feature of kidney diseases leading to chronic renal failure.[32] In a recent study, the potent and selective A_3R antagonist **LJ-1888** ((2*R*,3*R*,4*S*)-2-[2-chloro-6-(3-iodobenzylamino)-9*H*-purine-9-yl]tetrahydrothiophene-3,4-diol) blocked the development and attenuated the progression of renal interstitial fibrosis.[32] These findings

https://doi.org/10.1021/acs.jmedchem.2c01123
J. Med. Chem. XXXX, XXX, XXX−XXX

Journal of Medicinal Chemistry pubs.acs.org/jmc Article

Table 1. Binding Affinities Measured Using Schild Regression (K_d) or BRET Method (K_i) and Functional Activities for A15, A17, and L2–L10 and A26, L12, L15, and L21 against A_3R or A_1R

COMPOUND		A_3R			A_1R		
		pIC_{50} in presence of **NECA** [a]	pK_d [b]	pK_i [c]	pIC_{50} in presence of **NECA** [a]	pK_d [b]	pK_i [c]
A15	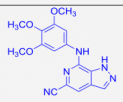	8.71 ± 0.14	5.91 ± 0.19	5.49 ± 0.10	7.99 ± 0.14	6.91 ± 0.18	6.64 ± 0.08
A17	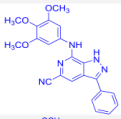	7.12 ± 0.13	7.87 ± 0.18	8.01 ± 0.06	6.70 ± 0.10	8.25 ± 0.15	8.36 ± 0.10
L2	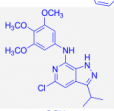	8.55 ± 0.13	6.26 ± 0.18	6.20 ± 0.06	8.30 ± 0.15	6.54 ± 0.19	6.54 ± 0.07
L3	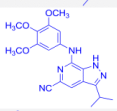	8.42 ± 0.19	6.45 ± 0.23	6.22 ± 0.10	8.49 ± 0.17	6.28 ± 0.20	7.91 ± 0.09
L4	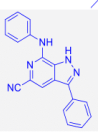	7.22 ± 0.09	7.77 ± 0.16	7.36 ± 0.05	7.87 ± 0.10	7.04 ± 0.14	6.67 ± 0.18
L5	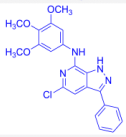	7.91 ± 0.10	7.05 ± 0.2	7.26 ± 0.03	8.54 ± 0.14	6.20 ± 0.18	6.66 ± 0.14
L6	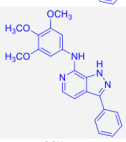	8.29 ± 0.10	6.60 ± 0.24	7.00 ± 0.10	8.72 ± 0.23	6.84 ± 0.23	6.78 ± 0.30
L7	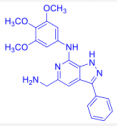	8.31 ± 0.21	6.59 ± 0.25	6.88 ± 0.08	7.64 ± 0.14	7.29 ± 0.18	7.64 ± 0.57
L8	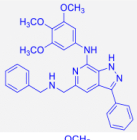	8.14 ± 0.20	6.80 ± 0.24	7.19 ± 0.10	8.41 ± 0.22	7.18 ± 0.25	6.69 ± 0.30
L9	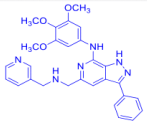	8.05 ± 0.10	6.89 ± 0.20	7.19 ± 0.07	7.92 ± 0.11	6.99 ± 0.16	7.20 ± 0.04

https://doi.org/10.1021/acs.jmedchem.2c01123
J. Med. Chem. XXXX, XXX, XXX−XXX

Table 1. continued

COMPOUND		A_3R			A_1R		
		pIC_{50} in presence of **NECA** [a]	pK_d [b]	pK_i [c]	pIC_{50} in presence of **NECA** [a]	pK_d [b]	pK_i [c]
L10	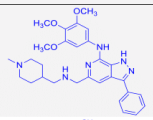	8.56 ± 0.20	6.24 ± 0.24	6.72 ± 0.09	8.33 ± 0.15	6.50 ± 0.19	6.13 ± 0.08
A26	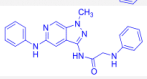	7.91 ± 0.19	7.05 ±0.22	7.07 ± 0.08	8.58 ± 0.10	6.13 ± 0.17	6.53 ± 0.27
L12	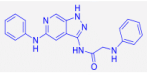	8.52 ± 0.21	6.31± 0.24	6.33 ± 0.09	8.16 ± 0.09	6.71 ± 0.14	6.44 ± 0.11
L15	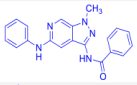	8.17 ± 0.20	6.77 ± 0.24	6.95 ± 0.08	8.30 ± 0.14	6.54 ± 0.17	6.02 ± 0.14
L21	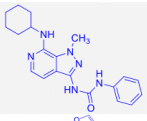	8.37 ± 0.19	6.52 ± 0.2	6.60 ± 0.13	8.85 ± 0.12	<6.0	<6.0
MRS 1220	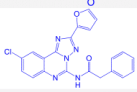	-	10.01 ±[#]	9.94 ±0.11	7.32 ± 0.09	7.62 ± 0.14	7.29 ± 0.27
NECA	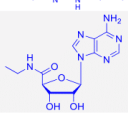	9.03 ± 0.13	-	6.63 ± 0.15	8.95 ± 0.10	-	7.08 ± 0.05

[a]Functional activity (pIC_{50} values in the presence of **NECA**) for a ligand as mean ± standard error of the mean (SEM) of at least three independent repeats, conducted in duplicate—values obtained from Figure 4. [b]Dissociation constant (pK_d) of a ligand as mean ± SEM of at least three independent repeats, conducted in duplicate as determined using the Schild analysis, see eq 1. [c]Equilibrium binding affinity constant (pK_i) of a ligand measured with NanoBRET against WT A_3R or A_1R; **NECA** was used as a positive control as described in ref 21. [#]Value obtained from ref 21 using **IB-MECA** as an agonist.

suggest that A_3R antagonists might become new therapeutic tools for the treatment of both chronic renal disease and acute renal ischemia and reperfusion injury.[33] Furthermore, A_3R antagonists have demonstrated efficacy in eye pathologies.[30] Indeed, it has been reported that the potent A_3R antagonist **MRS1220** (*N*-[9-chloro-2-(2-furanyl)-1,2,4-triazolo[1,5-*c*]-quinazolin-5-yl]benzeneacetamide) prevented oligodendrocyte damage and myelin loss triggered by ischemia or by activation of the A_3R in the rat optic nerve.[34] Hence, blockage of the A_3R has proven to be useful for the treatment of diverse diseases; however, its role is still to be elucidated in other pathophysiological conditions, such as inflammation, cancer, or pain.[30] The identification of new potent and selective ligands which clarify the therapeutic potential arising from blocking or stimulating the A_3R remains an attractive objective.[30,35]

Selecting ligands based on their affinity, an equilibrium parameter, does not necessarily predict in vitro activity. Kinetic profiling in the drug discovery process allows the resolution of ligand−receptor interactions into both molecular recognition (dependent on the association constant K_{on}) and complex stability (dependent on ligand's dissociation constant K_{off}). Significantly, this enables estimation of the residence time (RT = $1/K_{off}$) of that ligand upon its target.[36,37] In fact, a ligand's kinetic properties may provide a better indication of how a ligand will perform in vivo. Selected antagonists for A_1R[36] and A_3R[38,39] are shown in Figure 1.

In this study, we performed two rounds of screening for compounds that acted as antagonists of the A_3R [in total, we tested 52 molecules with chemical structures defining 7 classes of compounds against ARs (Table S1)]. The tested compounds belonged to our in-house compound library. We found that pyrazolo[3,4-*c*]pyridine (shown with blue color in Figure 2) as a novel pharmacophore, which after suitable substituents led to high-affinity antagonist activity against both the A_1R and A_3R. We identified potent antagonists in two classes of pyrazolo[3,4-*c*]pyridines, the 7-aminoaryl-3-aryl-(alkyl)-5-substituted-pyrazolo[3,4-*c*]pyridines and 3-(*N*-acyl)-amino-5-aminoaryl-pyrazolo[3,4-*c*]pyridines, as shown in Figure 2. These compounds were characterized for their pharmacological activity using both functional inhibition of cAMP accumulation assays and competition for binding of a fluorescent tracer.[21] These studies revealed that compound **A17** displayed a high K_{on} and a low K_{off} for both the A_1R and

https://doi.org/10.1021/acs.jmedchem.2c01123
J. Med. Chem. XXXX, XXX, XXX−XXX

Journal of Medicinal Chemistry pubs.acs.org/jmc Article

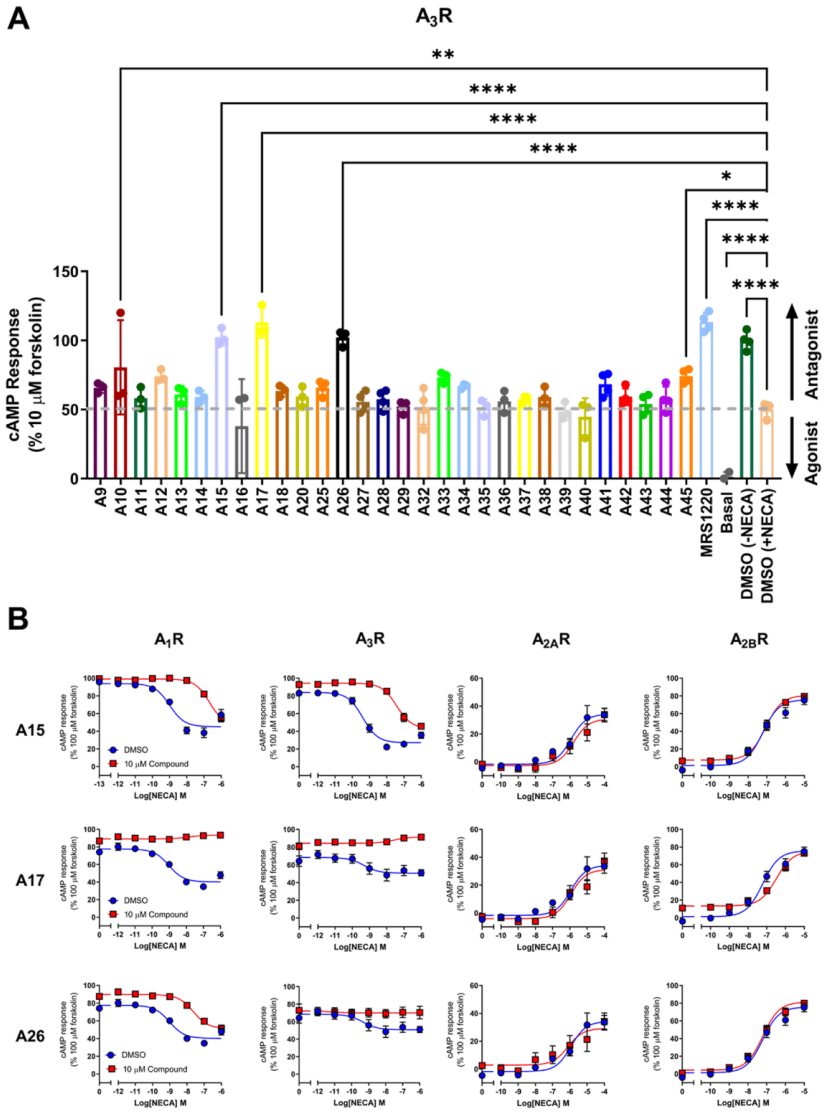

Figure 3. Screening and characterization of potential antagonists at the ARs. (A) cAMP accumulation was determined in Flp-In CHO cells stably expressing A_3R co-stimulated for 30 min with 10 μM forskolin, **NECA** at the pre-determined IC_{80} concentration (3.16 nM), and 1 μM of compound/DMSO control. An elevation in cAMP accumulation above that of 10 μM forskolin and **NECA**, as indicated by the gray dotted line, suggests that the compound is acting as an antagonist (black upwards arrow). Included is MRS 1220 (1 μM) as a positive control for a competitive antagonist of A_3R. A reduction of cAMP accumulation (black downwards arrow) could indicate a compound is acting as an agonist. All values are mean ± SEM expressed as % 10 μM forskolin response ("DMSO") where $n = 3$ independent experimental repeats, conducted in duplicate. Gray downward arrow indicates potential antagonists with a cAMP level >80%. The initial functional screen against A_3R included 30 compounds from our in-house library; from this functional screen, we identified compounds, **A15**, **A17**, and **A26** as potential A_3R antagonists. (B) Selectivity of **A15**, **A17**, and **A26** at individual AR subtypes (A_1R, $A_{2A}R$, $A_{2B}R$, and A_3R). cAMP accumulation or inhibition in response to varying **NECA** concentrations in the absence (blue) or presence of 10 μM tested compound (red) and forskolin for G_i-coupled receptors. Data were determined as statistically different (*, $p < 0.05$; **, $p < 0.01$; ****, $p < 0.0001$) compared to NECA with DMSO using a one-way ANOVA and Dunnett's posthoc test.

https://doi.org/10.1021/acs.jmedchem.2c01123
J. Med. Chem. XXXX, XXX, XXX−XXX

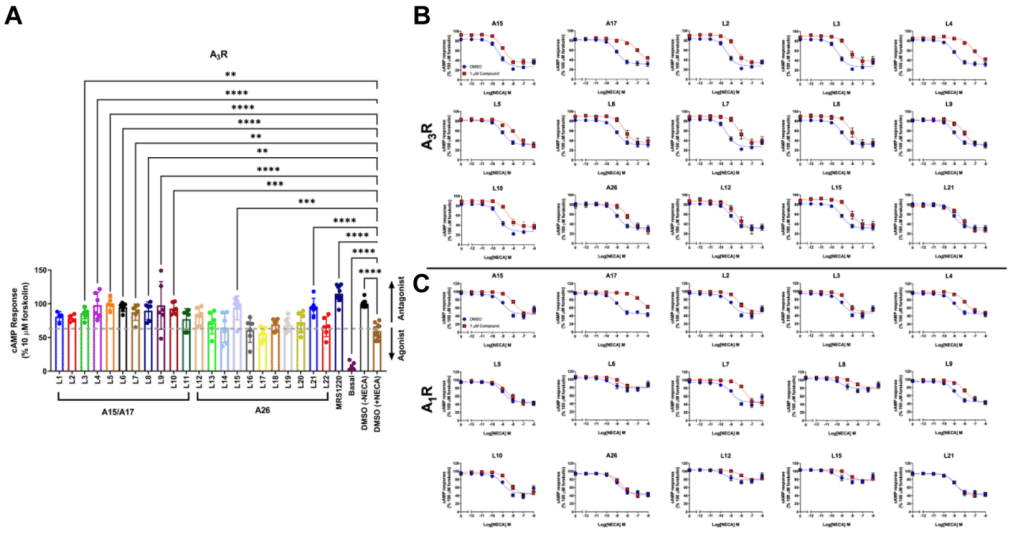

Figure 4. Screening and characterization of **A15**, **A17**, and **A26** analogues, at A_3R and A_1R. (A) 22 analogues of the **A15**/**A17** and **A26** scaffold (**L1**−**L22**) were screened for antagonist activity at the A_3R. Compounds **L2**−**L10**, **L12**, **L15**, and **L21** were determined to display significant antagonist activity and progressed to further characterization (B,C). A_3R Flp-In CHO cells (B) or CHO-K1 cells expressing A_1R (C) were stimulated with 10 μM forskolin varying concentrations of **NECA**, and either 1 μM potential antagonist (red curves) or **DMSO** (blue curves) for 30 min and cAMP accumulation detected. **NECA** inhibition data were fitted using a three-parameter logistic equation to determine the pIC_{50} of **NECA** in each condition; $n = 3$ independent repeats, each conducted in duplicate. All values are mean ± SEM, expressed as % 100 μM forskolin response. Data were determined as statistically different (*, $p < 0.05$; **, $p < 0.01$; ***, $p < 0.001$; ****, $p < 0.0001$) compared to NECA with DMSO using a one-way ANOVA and Dunnett's post hoc test.

A_3R, which resulted in a low nanomolar affinity; **A17**, at the A_1R, had a K_d of 5.62 nM and a residence time (RT of 41.33 min) and at the A_3R, the K_d was 13.5 nM with a RT of 47.23 min.

We next performed MD simulations and mutagenesis experiments to explore the binding pose of **A17** and some of its analogues at the A_1R and A_3R. For both these ARs, we also aimed to explore if binding free energy calculation methods could be used to accurately calculate the change in binding free energy affected by two similar substituents attached at the same position of a heterocyclic scaffold. We used the molecular mechanics-generalized Born surface area (MM-GBSA) method[45] with an implicit membrane[46] and also explicitly took into account the water molecules inside the binding area.[47] For the accurate description of structure−activity relationships (SARs), we additionally applied thermodynamic integration coupled with MD simulations (TI/MD) and a thermodynamic cycle method while including the whole ligand−GPCR membrane system in the calculations. We explored how the experimentally measured relative binding free energies correlated with the calculated values. The accuracy of relative binding free energy calculation for ligand−GPCR systems has been previously shown with free-energy perturbation coupled with MD simulations (FEP/MD) and a thermodynamic cycle method.[48]

■ RESULTS

Biological Results. *Compound Selection.* We performed a functional screen, initially of 30 compounds (**A9**−**18**, **A20**, **A25**−**29**, and **A32**−**A45**), from our in-house library for the identification of A_3R antagonists (Table S1). Compounds were selected for screening, following computation of their TanimotoCombo coefficient (Tc)[49] and subsequent comparison of chemical structure similarity, based on Tc values, with compounds in the CHEMBL[115] database, which were reported to be AR ligands.[50,51] The 7-anilino-3-phenyl pyrazolo-[3,4-*c*]pyridines (e.g., **A17**) had a calculated Tc = 0.4 when compared to 9-anilino imidazo[4,5-*c*]quinoline A3R antagonists,[52] while the 3-(*N*-acyl)amino 5-anilino pyrazolo-[3,4-*c*]pyridines (e.g., **A26**) had a Tc = 0.2−0.3 when compared to 2,4-diaminoquinazoline A3R antagonists, the *N*-piperazinyl acetamide of aminopyridino quinazolines (e.g., **A10**, see Table S1)[53] had a Tc = 0.22−0.35 when compared to *N*-piperazinyloacetamido aminopyrimidines with antagonistic activity against all ARs,[54] and so forth. Finally, nucleoside derivatives (see **A37**−**A44** in Table S1) had a Tc = 0.3−0.6 when compared to known agonists or antagonists of all ARs.[55−58]

Screening the In-House Library Using Functional Assays Revealed Three New Leads as AR Antagonists. For our screen,[59,60] the A_3Rs were expressed in Flp-In CHO cells. In order to allow the A_3R-mediated $G_{i/o}$ response to be determined, cells were co-stimulated for 30 min with 10 μM forskolin (which promoted cAMP production by activating adenylyl cyclase),[61] a predetermined IC_{80} of **NECA** (which reduces forskolin-induced cAMP production by agonizing the $G_{i/o}$-coupled A_3R), and either **DMSO** (negative control) or 1 μM of the test compound. A putative antagonist would diminish **NECA's** ability to inhibit forskolin-induced cAMP production, resulting in an elevated cAMP level when compared to **DMSO**; this was confirmed by the positive

https://doi.org/10.1021/acs.jmedchem.2c01123
J. Med. Chem. XXXX, XXX, XXX−XXX

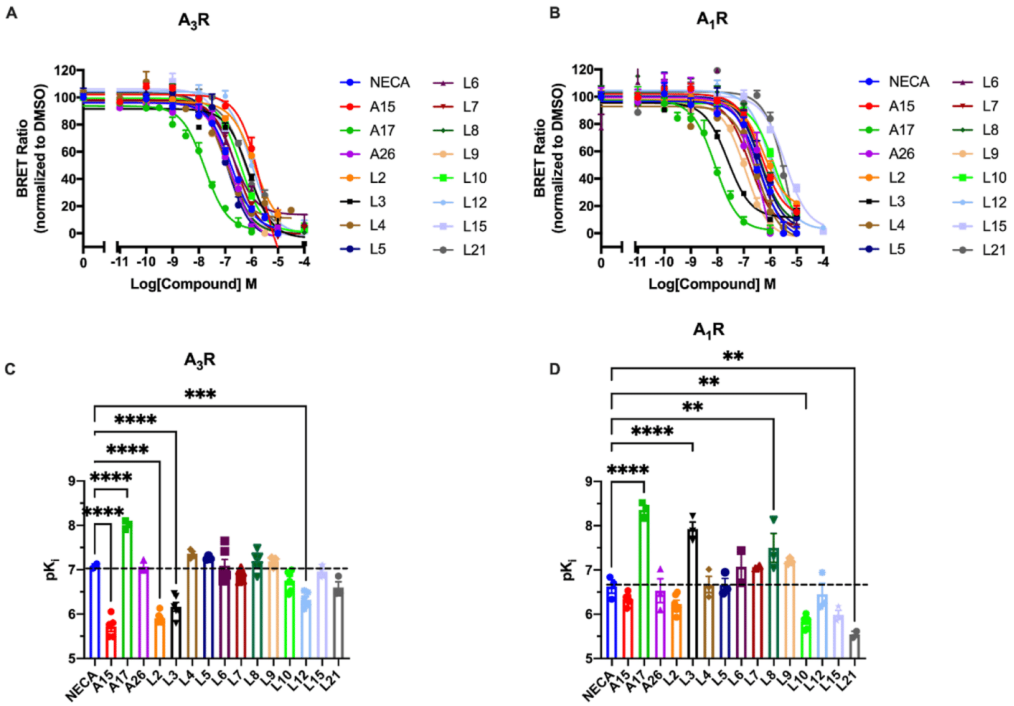

Figure 5. Inhibition of BRET between Nluc and CA200645 at the A_3R and A_1R by **A15**/**A17** and **A26** and their analogues. HEK293 cells expressing Nluc-A_3R (**A**) or Nluc-A_1R (**B**) were treated with 5 nM or 20 nM CA200645, respectively, enabling concentration-dependent decreases in the BRET ratio at 10 min to be determined with the response normalized to DMSO. Binding curves were fitted with the Cheng Prusoff equation built into Prism to enable estimates of the pK_i. Comparison of pK_i values for the A_3R (**C**) and A_1R (**D**) as determined via BRET binding. Dashed line represents the mean pK_i value of **NECA** for comparison. Each data point represent mean ± SEM of at least three experiments performed in duplicate.

control **MRS 1220**, a known A_3R antagonist (Table 1). From this functional screen, we identified five compounds, **A10**, **A15**, **A17**, **A26**, and **A45** as potential A_3R antagonists (Figure 3A). The nucleosides **A10** and **A45** were discontinued in the study because they showed the weakest activity ($p = 0.0041$ and $p = 0.0245$ vs **NECA**, respectively: Figure 3A). The three remaining compounds were all pyrazolo[3,4-*c*]pyridines. Compounds **A15** and **A17** shared the same substituents at positions 5 and 7 but had isopropyl and phenyl groups at the 3-position, respectively. Compound **A26** had a different substitution pattern with an acetamido and anilino groups at the 3- and 5-positions.

Three New Lead Compounds Have A_1R and A_3R Subtype Selectivity. The similarities between the four AR subtypes often results in reduced selectivity of potential antagonists. As we described previously,[21] we utilized A_3R expressing Flp-In CHO cells or A_1R, $A_{2A}R$, or $A_{2B}R$ expressing CHO-K1 cells incubated with a single high concentration of potential antagonist (10 μM) and increasing concentrations of **NECA**, to determine the subtype selectivity of **A15**/**A17** and **A26** in a functional cAMP assay. Both **A15** and **A26** showed a lack of efficacy at the **NECA**-stimulated $A_{2A}R$ and $A_{2B}R$ (Figure 3B, Table S2) but antagonized the A_1R, although **A15** showed weaker efficacy than **A26**. **A17** also antagonized the A_1R alongside the A_3R with high efficacy (Table 1) and also displayed weak efficacy at the $A_{2B}R$ ($pK_d = 5.49 \pm 0.17$). These data indicate that **A15**, **A17**, and **A26** displayed high subtype selectivity for both the A_1R and A_3R (Figure 3B).

*Additional Screening Based upon **A15**/**A17** and **A26** Revealed Pyrazolo[3,4-c]pyridine as a Novel Scaffold for the Development of AR Antagonists.* Having identified that **A15**/**A17** and **A26** contained a potential scaffold for the design of A_1R/A_3R antagonists, we performed a second round of compound screening using only **A15**/**A17** and **A26** analogues. The compounds **L1**−**L11** were analogues of **A15**/**A17**, while **L12**−**L22** were analogues of **A26** (Table S1). All were screened as potential antagonists of the A_3R, in the first instance, using the same method assay as described in previously (Figure 3A). From this screen, 12 additional compounds **L2**−**L10**, **L12**, **L15**, and **L21** (Figure 4A, Table 1) were identified as statistically significant potential antagonists of the A_3R. All 12 compounds were then subsequently screened for AR selectivity. All of them were able to antagonize the A_1R but most (11 out of 12) showed a lack of efficacy at **NECA**-stimulated $A_{2A}R$ and $A_{2B}R$ except for **L4**, which, analogous to **A17**, showed very weak efficacy at the $A_{2B}R$ ($pK_d = 5.77 \pm 0.12$; Figure S1, Tables S2 and S3).

https://doi.org/10.1021/acs.jmedchem.2c01123
J. Med. Chem. XXXX, XXX, XXX−XXX

Table 2. Kinetics of Binding for the A17- and A26-Panels of Compounds to the Orthosteric Binding Area at the A_3R and A_1R

	A_3R				A_1R			
compound	K_{on} (k_3) × 10^5 M^{-1} [a]	K_{off} (k_4) min^{-1} [b]	pK_D kinetics [c]	RT (min) [d]	K_{on} (k_3) × 10^5 M^{-1} [a]	K_{off} (k_4) min^{-1} [b]	pK_D kinetics [c]	RT (min) [d]
A15	**<50**	**<0.4**	**N.D.**	**>2**	3.18 ± 1.0	0.03 ± 0.006	6.99 ± 0.21	38.7 ± 8.8
A17	21.3 ± 1.2	0.021 ± 0.003	8.00 ± 0.32	47.23 ± 8.2	139.7 ± 1.5	0.024 ± 0.009	8.76 ± 0.07	41.31 ± 4.56
L2	**<50**	**<0.4**	**N.D.**	**>2**	1.72 ± 0.3	0.048 ± 0.01	6.55 ± 0.03	22.9 ± 4.3
L3	**<50**	**<0.4**	**N.D.**	**>2**	45.07 ± 3.4	0.061 ± 0.002	7.86 ± 0.45	16.3 ± 0.3
L4	8.2 ± 0.5	0.026 ± 0.006	7.58 ± 0.32	46.72 ± 4.5	11.5 ± 4.0	0.051 ± 0.004	7.21 ± 0.51	20.61 ± 3.4
L5	3.65 ± 0.6	0.031 ± 0.01	7.07 ± 0.22	32.05 ± 6.3	2.79 ± 0.29	0.055 ± 0.001	6.70 ± 0.54	18.2 ± 4.37
L6	24.7 ± 3.8	0.18 ± 0.02	7.13 ± 0.55	5.55 ± 2.6	5.23 ± 0.45	0.036 ± 0.005	6.88 ± 0.23	27.72 ± 3.7
L7	4.8 ± 2.4	0.105 ± 0.04	6.59 ± 0.73	9.55 ± 3.5	9.63 ± 2.5	0.039 ± 0.004	7.39 ± 0.40	25.34 ± 4.9
L8	9.33 ± 1.4	0.173 ± 0.067	**6.73 ± 0.45**	**5.78**	2.34 ± 0.6	0.054 ± 0.005	6.37 ± 0.11	18.50 ± 2.6
L9	5.62 ± 1.0	0.054 ± 0.02	7.0 ± 0.33	17.85 ± 4.3	8.17 ± 1.4	0.02 ± 0.015	7.54 ± 0.10	43.96 ± 2.1
L10	3.38 ± 1.1	0.01 ± 0.001	6.56 ± 0.43	10.85 ± 3.4	1.65 ± 0.4	0.04 ± 0.007	6.64 ± 0.03	31.43 ± 7.1
A26	12.45 ± 1.8	0.096 ± 0.03	7.11 ± 0.45	10.4 ± 3.4	3.36 ± 1.6	0.134 ± 0.003	6.40 ± 0.18	7.47 ± 2.2
L12	1.45 ± 0.3	0.051 ± 0.03	6.45 ± 0.22	19.04 ± 5.6	1.84 ± 0.4	0.052 ± 0.003	6.55 ± 0.40	19.23 ± 4.5
L15	**<50**	**<0.4**	**N.D.**	**>2**	0.834 ± 0.3	0.071 ± 0.004	6.07 ± 0.22	14.06 ± 2.4
L21	**<50**	**<0.4**	**N.D**	**>2**	**<50**	**<0.4**	**ND**	**>2**
MRS1220	3250 ± 2.8 [e]	0.0250.005 [e]	10.11 [e]	40.32 [e]	14.54 ± 0.4	0.023 ± 0.0008	7.80 ± 0.2	43.67 ± 5.6

[a] K_{on} (k_3) for ligands as determined using NanoBRET binding assays using either Nluc-A_3R or Nluc-A_1R expressing HEK 293 cells and determined through fitting with the "kinetics of competitive binding" model. [b] K_{off} (k_4) for ligands determined as in (a). [c] Kinetic dissociation constant (pK_d) for each ligand as determined from K_{on}/K_{off}. [d] Residence time of each ligand as determined by the reciprocal of the K_{off}. [e] Value obtained from ref 21. Note—values in bold could not be fitted using the "kinetics of competitive binding" model.

Structural Novelty of the Compounds as AR Antagonists. The compounds **A15**/**A17** and their analogues **L2**−**L10** were all pyrazolo[3,4-*c*]pyridines and contained an alkyl or phenyl group at the 3-position, an anilino group at the 7-position, and a cyano- or chloro- or aminomethyl or *N*-(arylmethyl)-2-aminomethyl group at the 5-position (Table 1). Compounds **A26** and its analogues **L12**, **L15**, or **L21** were four pyrazolo[3,4-*c*]pyridines, with substituted 3-(*N*-anilinoacetyl)-amino, 3-(*N*-benzoyl)amino, or 3-(*N*-phenylureido) groups, respectively. Compounds **A26**, **L12**, and **L15** were also substituted with a 5-anilino group and compound **21** with the 7-(*N*-cyclohexanylamino) group.

The identified pyrazolo[3,4-*c*]pyridine derivatives provide a novel scaffold for the development of AR antagonists. Representative nonxanthine pyrazolo derivatives that have been reported as AR ligands include pyrazolo-[4,3-*e*]-1,2,4-triazolo-[1,5-*c*]pyrimidines, pyrazolo-[3,4-*c*] or -[4,3-*c*]-quinolines, pyrazolo-[4,3-*d*]pyrimdinones, pyrazolo-[3,4-*d*]-pyrimidines, and pyrazolo-[1,5-*a*]pyridines.[62] When we screened in ChEMBL using similarity-based parameters for **A15**/**A17** or **A26**, that is, a Tc value >0.85, we were unable to find similar compounds or any other pyrazolo[3,4-*c*]pyridines as AR antagonists.

Functional Activity Measurements of the 15 Pyrazolo[3,4-c]pyridines Identified Nanomolar Antagonists for A_1R and A_3R. Full dose-dependent inhibition curves were obtained for compounds **A15**, **A17**, **L2**−**L10**, **A26**, **L12**, **L15**, and **L21** by stimulating cells with 10 μM forskolin and measuring forskolin-induced cAMP accumulation in CHO-K1-A_1R or A_3R Flp-In CHO cells in the presence of **NECA** in a range of concentrations (10^{-13} to 10^{-4} M), and either **DMSO** or 1 μM potential antagonist (Figure 4B,C). All compounds caused a reduction in **NECA** potency at the A_3R, characteristic of competitive antagonism albeit with varying extents (Table 1). Moreover, some of the compounds also displayed antagonism at A_1R, although compounds **L5** and **A26** displayed only weak effects on **NECA** potency while **L21** was inactive (Tables 1 and Table S4, Figure 4B,C).

The data in Figure 4B,C enable a crude estimation of the dissociation constant (pK_d) of each antagonist (Table 1) at the two AR subtypes when analyzed using Schild analysis and eq 1.[63] Due to their weak activities, we used 10 μM of **A26**, **L5**, and **L21** for our analysis. However, we were still unable to detect any activity for **L21** at A_1R.

Competition Binding Assays and Determination of Kinetic Parameters of Antagonist Binding at A_3R and A_1R Using NanoBRET. To provide a more quantitatively accurate estimate of the pK_d for all 15 pyrazolo[3,4-*c*]pyridines at the A_3R and A_1R, we performed a BRET-based competition binding assay (Figure 5, Tables 1 and S5). The compounds were assessed for their ability to displace the specific binding of CA200645,[64] a fluorescent xanthine-based antagonist of A_3R and A_1R, using Nluc-A_3R HEK293 and Nluc-A_1R expressed in HEK293 cells.[21] The NanoBRET binding assay also enables the determination of the kinetics of the compound binding, which Schild regression does not. Indeed, we[21] and others[64] have described the use of NanoBRET binding techniques to determine the real-time kinetics[36,37,65] and affinities of ligand binding at the ARs. Values were derived using the "kinetics of competitive binding" model build into GraphPad Prism 9.0, which enables determinations of the test compounds K_{on} (k_3) and K_{off} (k_4) (Table 2). The reciprocal of the K_{off} enables a determination of the residence time (RT) of the compound.[21] Beyond this, we also determined the pK_D of the compounds (k_4/k_3) from the kinetics assays and compared these values to those determined from the saturation binding assays and the Schild analysis.

The kinetic parameters for CA200645 binding at the Nluc-A_3R were determined as K_{on} (k_1) = 2.86 ± 0.45 × 10^6 M^{-1} min^{-1} and K_{off} (k_2) = 0.064 ± 0.0023 min^{-1} with a K_D = 25 ± 4.6 nM. Conversely, the kinetics of binding for CA200645 binding at the Nluc-A_1R were determined as K_{on} (k_1) = 3.67 ± 0.34 × 10^6 M^{-1} min^{-1} and K_{off} (k_2) = 0.067 ± 0.005 min^{-1}

https://doi.org/10.1021/acs.jmedchem.2c01123
J. Med. Chem. XXXX, XXX, XXX−XXX

Journal of Medicinal Chemistry pubs.acs.org/jmc Article

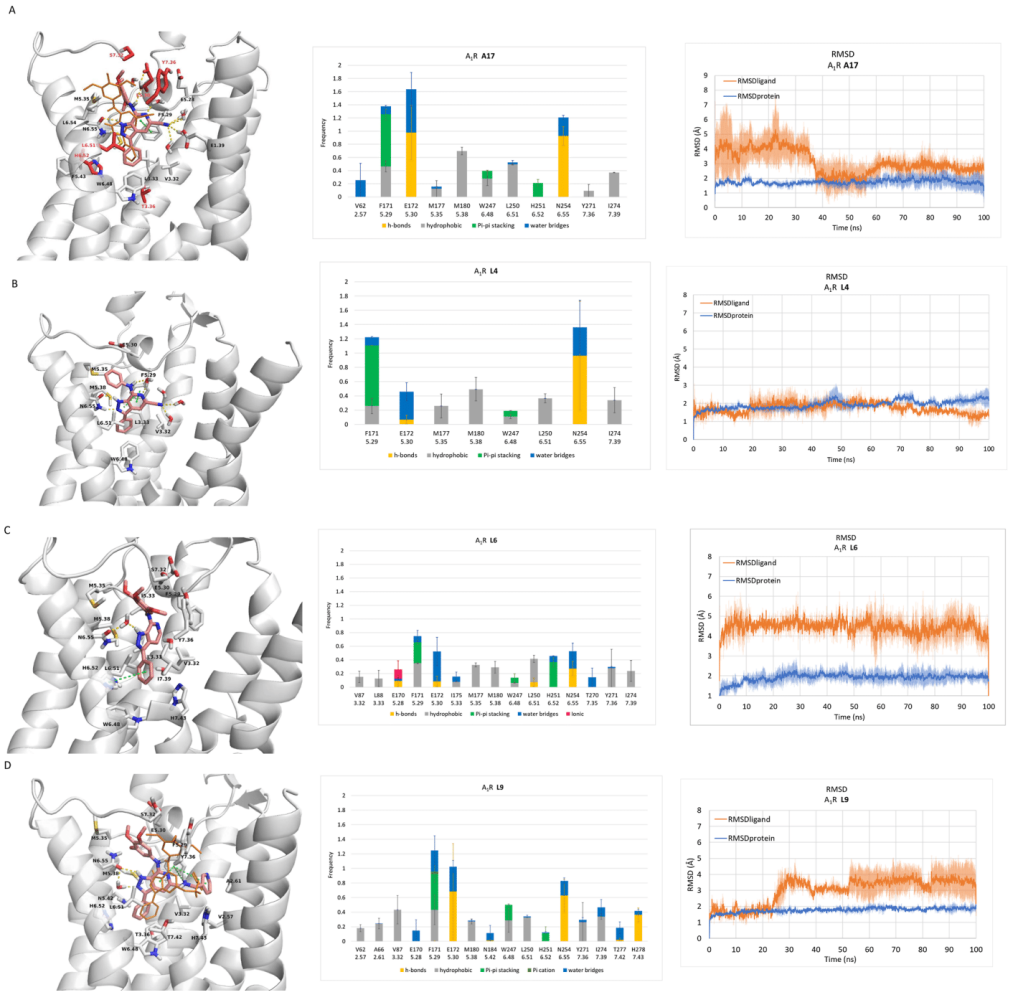

Figure 6. (A) Representative frames, receptor–ligand interaction frequency histograms, and rmsd plots of (A) **A17**, (B) **L4**, (C) **L6**, and (D) **L9** inside the orthosteric binding area of WT A_1R from 100 ns MD simulations using the amber99sb[68,69] force field using **docking pose 1** (see text) as the starting structure. Compared to **A17**, in **L4** or **L6** (B,C) either the trimethoxy group or the cyano group is missing while in **L9** a sizeable group has been installed at the 5-position of pyrazolo[3,4-*c*]pyridine ring. Bars are plotted only for residues with interaction frequencies ≥0.2. Color figure in frames or bar plots: ligand is shown with pink sticks and ligand's starting position with an orange wire, receptor is shown with a white cartoon and sticks, hydrogen bonding interactions are shown with yellow dashes or bars, π–π interactions are shown with green dashes or bars; hydrophobic interactions are shown with gray bars; and water bridges are shown with blue bars. Mutagenesis experiments were performed for A_1R with point mutations to alanine of residues shown in red sticks and/or noted in red color in the frame shown in (A). For MD simulations, we used the experimental structure of the inactive form of A_1R (PDB ID 5UEN[10]) in complex with an antagonist.

with a K_D = 18.29 ± 2.4 nM. Using these parameters, we were able to provide estimates of the kinetics of binding for most of the **A17**- and **A26**-based derivatives with the exception of **A15**, **L2**, and **L3** at the A_3R and **L21** at the A_1R, which failed to provide a reliable fit to the data, likely due to their low pK_d values (Table 2).

Many of the compounds showed a good agreement between the different methods used to determine their affinities, as compared in Tables 1 and 2. Thus, consistent with the Schild analysis compound, **A17** displayed the highest affinity at the A_3R followed by **L4** > **L6** = **L5** = **A26** = **L9**. At A_1R, **A17** also had the highest affinity with the rank order of affinities being **A17** > **L3** > **L9** > **L7** > **L4**. All the other compounds displayed weaker affinities. The comparison of the affinity constants calculated by the NanoBRET binding assays and the single dose Schild analysis once again showed a close agreement

https://doi.org/10.1021/acs.jmedchem.2c01123
J. Med. Chem. XXXX, XXX, XXX–XXX

Table 3. Binding Affinities for CA200645, NECA, and A17 Measured Using NanoBRET against WT and Mutant A_1Rs

residue's region in the binding area	mutation	K_d (nM)[a]	pK_d	
		CA200645	**A17**	NECA
	WT	76.37 ± 9.37	7.87 ± 0.06	6.67 ± 0.05
bottom	T91$^{3.36}$A	166.35 ± 17.36	8.37 ± 0.07 **	n.b.[b]
upper	E172$^{5.30}$A	116.04 ± 12.22	7.63 ± 0.08	5.38 ± 0.06 **
middle	L250$^{6.51}$A	158.28 ± 17.37	8.44 ± 0.05 **	n.b.[a]
middle	H251$^{6.52}$A	145.19 ± 19.13	8.03 ± 0.10*	8.04 ± 0.10 **
upper	S267$^{7.32}$A	70.99 ± 7.03	8.10 ± 0.16 **	6.31 ± 0.10
upper	Y271$^{7.36}$A	71.10 ± 7.68	7.82 ± 0.04	5.45 ± 0.06 **

[a]Affinity constant for CA200645 binding to mutant A_1R receptors. [b]n.b. **NECA** was unable to displace CA200645 at the mutant receptor. Statistical significance (*$p < 0.05$, **$p < 0.01$) determined using ANOVA and Dunnett' s post-test.

except for compound **L3** at the A_1R, where the affinities determined in the NanoBRET binding assays were ∼50-fold higher than in the Schild analysis. This may indicate that **L3** has unusual properties compared to the other compounds tested here.

From this data, we observed that the most interesting potencies at 1 μM concentration (indicated in bold in Table 1) include: (a) **L3** or **L4**, **L5**, **L7**,**L8**, **L9**, and **A17**, which are pyrazolo-[3,4-*c*]pyridines with a isopropyl or phenyl group at the 3-position, respectively, a cyano or chloro or aminomethyl or *N*-(arylmethyl)aminomethyl group at the 5-position, and an anilino group at the 7-position, and (b) **A26**, which is 3-(*N*-acyl)amino-5-anilino pyrazolo-[3,4-*c*]pyridine. The affinity range for the **A17** series, including compounds **L2**−**L10**, **A15** was between low micromolar to low nanomolar. The affinity range for the **A26** series, including compounds **L12**, **L15**, and **L21**, was between low micromolar to 100 nM.

Using these different methods revealed that, at the A_3R, both **A17** and **L4** displayed a low nanomolar affinity, while **A26**, **L5**, **L8**, and **L9** had mid-nanomolar affinities with the remaining compounds showing low affinities. At the A_1R, only **A17** displayed a low nanomolar affinity, while the five compounds **L4** and **L6**−**L9** displayed mid-nanomolar to low nanomolar affinities. We also observed that **A26** displayed a 5-fold selectivity for A_3R over the A_1R, while **L7** was 6-fold selective for A_1R over the A_3R.

Compared to **A15**, the phenyl group in **A17** increased the binding affinity by ∼17-fold at A_1R and considerably increased it at A_3R (Tables 1 and 2). The affinity was increased with the size of the 3-substituent according to the pK_d values for **L3** and **A17**, showing that the phenyl group was favored over the isopropyl group. Removal of the 5-cyano group in compound **L6** resulted in a reduction of affinity of ∼100-fold at the A_1R and 7-fold against A_3R. Similarly, when the cyano group in **A17** was changed to a chlorine group (**L5**), we again observed ∼100-fold reduction in affinity for A_1R and a 5-fold reduction for A_3R. Changing the cyano group in **A17** to an aminomethyl group in **L7** reduced its affinity at both receptors by ∼25-fold. Affinity was increased by ∼3-fold at both the A_1R and A_3R, when three methoxy groups (**A17**) were added to the phenyl group of **L4**. No change was observed in the affinity against A_3R between **L8** and **L9**. However, the presence of a pyridinyl group in **L9** (compared to a phenyl group in **L8**) led to a 15-fold increase in affinity for **L9** against A_1R compared to **L8**. The molecular basis of these changes for A_1R−ligand complexes, that is, the structure−activity relationships, will be discussed in the TI/MD calculations section.

The highest affinity compounds at the A_3R (i.e., **A17**, **L4**, and **L5**), displayed the longest residence times (RT) = 35−50 min. Some of the compounds, which displayed the highest affinity (**A17** and **L9**) at the A_1R, also displayed the longest RTs (40−50 min).

Structure−Activity Relationships. *MD Simulations and Mutagenesis Experiments.* To investigate the binding profile of the antagonists shown in Table 1 at the A_1R [for which an X-ray structure of A_1R in complex with an antagonist have been resolved (e.g. PDB ID 5UEN[10])], we next performed MD simulations. Using GOLD software[66] and the ChemScore as a scoring function,[2,67] we performed molecular docking calculations of these compounds into the orthosteric binding site of the A_1R. All docking poses showed that the anilino group oriented toward the extracellular side of the membrane. The anilino group was oriented toward extracellular loop 2 (EL2) (as in **docking pose 1** shown in Figure 6A) or toward the water environment (**docking pose 2** shown in Figure S5B). Similar binding poses for the antagonist **ZM241385** in complex with A_{2A}R have been observed in the X-ray structures PDB ID 4EIY[7] or 3EML,[5] respectively. However, only **docking pose 1** agreed with our mutagenesis data described below (readers are referred to mutagenesis experiment sub-section).

MD Simulations of the A_1R−A17 Complex. The selected docking pose were embedded in a 12 Å hydrated POPE lipid buffer and the system was subjected to 100 ns MD simulations with the amberff99sb force field.[74] Using **docking pose 1**, in which the anilino group was oriented toward the EL2, the MD simulations of the A_1R−**A17** complex showed that **A17** made interactions (>20% frequency) with F171$^{5.29}$, E172$^{5.30}$, M180$^{5.38}$, W247$^{6.48}$, L250$^{6.51}$, H251$^{6.52}$, N254$^{6.55}$, andI274$^{7.39}$ (Figure 6A). Further, we observed that the **A17**−A_1R complex was stabilized by: (a) direct hydrogen bonding interactions between both the pyrazolo 1-NH and anilino NH groups of the ligand and the amide side chain carbonyl of N254$^{6.55}$ and between anilino NH group and carboxylate side chain of E172$^{5.30}$, (b) hydrogen bonds between the cyano group of the ligand with waters that were inserted in the region between the ligand and TM1−TM2 (Figure 4A), (c) π−π stacking interactions between the core pyrazolo-[3,4-*c*]pyridine scaffold and the side-chain phenyl of F171$^{5.29}$ and between the ligand phenyl substituent and the imidazole of H251$^{6.52}$ or indole of W247$^{6.48}$, and (d) hydrophobic interactions between, (i) the trimethoxy-phenyl group of the ligand, which was directed either toward EL2 and I274$^{7.39}$; (ii) the pyrazole ring of the ligand and M180$^{5.38}$ and L246$^{6.51}$; and (iii) the phenyl ring of the ligand, which was oriented deeper into the receptor from the pyrazole scaffold and W247$^{6.48}$. In comparison, starting from **docking pose 2**, in which the anilino group was oriented toward the water environment, the MD simulations showed that **A17** did not form hydrogen bonding interactions with

https://doi.org/10.1021/acs.jmedchem.2c01123
J. Med. Chem. XXXX, XXX, XXX−XXX

Table 4. Relative Binding Free Energies Computed by TI/MD Calculations ($\Delta\Delta G_{b,TI/MD}$ in kcal mol^{-1}) Using Alchemical Transformations and a Thermodynamic Cycle, Experimental Values ($\Delta\Delta G_{b,exp}$ in kcal mol^{-1}) and Deviation of Calculated from Experimental Values ($|\Delta\Delta G_{b,TI/MD} - \Delta\Delta G_{b,exp}|$ in kcal mol^{-1}) for Pairs of Compounds Complexed to A_1R

alchemical perturbation	$\Delta\Delta G_{b,TI/MD}$	$\Delta\Delta G_{b,exp}$ [a]	$\lvert\Delta\Delta G_{b,TI/MD} - \Delta\Delta G_{b,exp}\rvert$
A15 → **L3**; 3H → 3iPr	−0.66 ± 0.07	−1.80 ± 0.09	1.14
A15 → **A17**; 3H → 3Ph	−1.06 ± 0.09	2.44 ± 0.09	1.38
L3 → **A17**; 3iPr → 3Ph	−0.87 ± 0.09	−0.63 ± 0.09	0.24
L4 → **A17**; 7Ph → 7Ph(OMe)$_3$	−3.34 ± 0.10	−2.39 ± 0.15	0.95
L6 → **A17**; 5H → 5CN	−3.05 ± 0.05	−2.24 ± 0.20	0.81
L6 → **L5**; 5H → 5Cl	−0.67 ± 0.04	0.16 ± 0.22	0.83
L5 → **A17**; 5Cl → 5CN	−1.09 ± 0.07	−2.40 ± 0.12	1.31
L2 → **L5**; 5Cl → 5CN	−0.37 ± 0.07	−0.18 ± 0.11	0.19
L9 → **L8**; py → Ph [b]	0.71 ± 0.08	0.72 ± 0.17	0.01
			mue = 0.87 kcal mol^{-1}

[a]Experimental relative binding free energies ($\Delta\Delta G_{b,exp}$) are estimated using the experimental binding affinities (pK_d) determined using binding kinetic data (Table 2) according to eq 3 in Experimental section. [b]In the substituent at the 5-position of the pyrazole ring.

E172$^{5.30}$ but did form hydrogen bonds with L250$^{6.51}$, H251$^{6.55}$, and T270$^{7.35}$. We next considered the hydrophobic interactions; **A17** had diminished interactions with M180$^{5.38}$, W247$^{6.48}$, and L250$^{6.51}$ but formed contacts with Y271$^{7.36}$ and π−π interactions with H251$^{6.52}$. We did not obtain a docking pose, where the 3-phenyl group was oriented extracellularly and the flexible 7-anilino group was oriented toward the bottom of the receptor. To achieve such a pose, we used manual docking; however, the MD simulations showed that the complex with A_1R was unstable due to the Pauli repulsion of the 7-anilino group with the bottom part of the receptor. MD simulations results of A26 series can be found in the Supporting Information.

*Mutational Analysis of **A17** and **A26** Binding at the A_1R.* We next used mutagenesis combined with NanoBRET-based[21] competition binding (using CA200645 as the fluorescent tracer) to experimentally investigate residues that were suggested to be important for the binding affinity of **A17** and **A26** (Table 3). For completeness, the affinity of the A_1R agonist **NECA** at each mutant was determined. The amino acid residues tested are shown in Figures 6A or S5B for **docking pose 1** and **docking pose 2**, respectively, of the most potent antagonist **A17** in red sticks and noted in red color.

The A_1R mutants T91$^{3.36}$A, E172$^{5.3}$A, L250$^{6.54}$A, and H251$^{6.52}$A all displayed reduced affinity for the fluorescent tracer CA200645 compared to the WT A_1R while mutants S267$^{7.32}$A and Y271$^{7.36}$A showed little difference in effect. For the agonist **NECA**, the A_1R mutants E172$^{5.3}$A and Y271$^{7.36}$A displayed reduced affinity with S267$^{7.32}$A maintaining affinity and H251$^{6.52}$A displaying increased affinity. Previous findings have also shown that mutation of S267$^{7.32}$A, significantly reduces **NECA's** affinity to the $A_{2A}R$.[70] We were unable to determine any binding for **NECA** at T91$^{3.36}$A or L250$^{6.51}$A mutants because in agreement to similar observations for $A_{2A}R$[72] and our findings for A_3R,[22] **NECA** binds to the orthosteric binding area through hydrogen bonding to T$^{3.36}$ at the bottom of the binding area.

The mutations H251$^{6.52}$A or S267$^{7.32}$A in the middle or upper regions of the orthosteric binding area increased the affinity of **A17** but only by ∼1.5-fold (Table 3). The H251$^{6.52}$A mutation equally affected antagonist binding at A_3R[21−23,73] and $A_{2A}R$.[70] Alanine mutation of T91$^{3.36}$ or L250$^{6.51}$ in the bottom or middle region caused a 3.2- or 3.8-fold increase in the affinity for **A17**, respectively (Table 3), while displaying no significant effect for **A26** (see Table S6). This was in agreement with other reports describing how mutating T91$^{3.36}$ to Ala increased the affinity of antagonist **LUF5834** to $A_{2A}R$[74] and of other non-nucleoside antagonists to A_1R.[70,71] Previously, we and other groups showed that mutation of residue T91$^{3.36}$ had a negligible effect on the affinity of antagonists to A_3R.[21−23,73] The result for L250$^{6.51}$A was a bit more unexpected because L250$^{6.51}$ is a highly conserved residue in all four AR subtypes and its mutation to Ala often causes a reduction or blockade of binding (see for examples our results for A_3R in refs 20 and 21). The mutant E172$^{5.30}$A in the upper region of the receptor displayed reduced affinity by ∼10% while mutation of Y271$^{7.36}$ did not change the affinity of the A_1R to **A17**.

From the simulations of WT A_1R−**A17** complex, starting from **docking pose** 1 (Figure 6A), we observe that **A17** had small π−π interactions with H251$^{6.52}$ and strong hydrophobic interactions with L250$^{6.51}$, strong hydrogen bonding interactions E172$^{5.30}$, and almost no interaction with Y271$^{7.36}$, while T91$^{3.36}$ and S267$^{7.32}$ were at a distance >4 Å from the ligand and their effect was allosteric.

From the MD simulations of WT A_1R−**A17** complex starting from **docking pose 2** (Figure S5B), we observed that **A17** had strong π−π interactions with H251$^{6.52}$ and strong hydrogen bonding interactions with L250$^{6.51}$. Hydrogen bonding interactions with E172$^{5.30}$ were not observed nor were interactions with Y271$^{7.36}$, while both T91$^{3.36}$ and S267$^{7.32}$ were again distant from **A17**.

To select which of the two docking poses agreed with the mutagenesis data (Table 3), we performed MD simulations of Y271$^{7.36}$A A_1R in complex with **A17** in each competing pose. The simulations (Figure S6) show that Y271$^{7.36}$A-A_1R reduced the binding interactions of **A17** in **docking pose 2** but maintained the interactions in **docking pose 1**, which agreed with our mutagenesis data. We further evaluated **docking pose 1** by exploring the effects of mutating S267$^{7.32}$, T91$^{3.36}$, H251$^{6.52}$, and L250$^{6.51}$, all to Ala, on the stability of **A17**−A_1R complex. We performed MD simulations for the individual mutant A_1Rs in complex with **A17** using **docking pose 1**. We observed that in all cases, although the ligand lost hydrogen bonding interactions with E172$^{5.29}$, the orthosteric binding area displayed plasticity with flexible residues recruited to the binding region to aid binding to **A17** (Figure S7). These findings agreed with the observations from our mutagenesis experiments that E172$^{5.30}$ was not very important for binding of **A17** to A_1R and that its mutation to Ala caused only a small

https://doi.org/10.1021/acs.jmedchem.2c01123
J. Med. Chem. XXXX, XXX, XXX−XXX

reduction in affinity (Table 3). Based on these findings, we selected **docking pose 1** to carry out the simulations of **A17** analogues.

SAR Analysis of Ligand Binding Using Free Energy Calculations. Alchemical Free Energy Calculations with TI/MD. FEP/MD[48,75−79] and TI/MD[134] simulations have been applied for ligand optimization in class A GPCRs[58,131−137] including ARs.[75−80] For example, FEP/MD calculations have been applied for lead fragment or lead compound optimization against the $A_{2A}R$[75,77] or for SAR interpretation, for example, 3-deazaadenosine agonists against $A_{2A}R$[81] and thiazolo[5,4-*d*]pirimidines ligands against $A_{2A}R$.[82] The FEP/MD[83] and TI/MD[84,85] methods can provide accurate results for relative binding free energies with a method error of 1 kcal mol^{-1}. We performed TI/MD calculations for nine alchemical transformations of the ligand complexes with A_1R, as listed in Table 4. The set of the studied compounds **A15**, **L2**−**L6**, **L8**, and **L9** cover ∼100 units of pK_ds range. The MD simulations of **A15**, **L2**−**L6**, **L8**, and **L9** in complex with A_1R converged during the 100 ns of production (performed in duplicate) with an $rmsd_{protein}$ value no higher than ∼2 Å (Table S5). These refinements produced suitable structures of the complexes between A_1R and **A15**, **L2**−**L6**, **L8**, and **L9** for performing TI/MD calculations (Figures 6 and S2). Generally, calculations were performed using a one-step protocol, which changed the charges and van der Waals interactions in a single simulation by activating both Lennard-Jones and Coulomb softcore potentials simultaneously so reducing the computational cost (see also description in the Experimental section). In our TI/MD simulations, the last frames of the complexes from the alchemical perturbation calculations match the last frames of the complexes from the 100 ns-MD simulations.

We observed that compared to **A15**, the presence of an alkyl substituent at the 3-position, for example, a 3-isopropyl (**L3**) or 3-phenyl (**A17**), anchored the ligand deeper into the receptor where it formed hydrophobic interactions mostly with $F182^{5.43}$ and $W243^{6.48}$ but also with $L91^{3.32}$. Thus, the presence of the isopropyl group in **L3**, or the phenyl group in **A17**, at the 3-position led to stronger binding as shown in the relative binding free energy values, which are for **A15** → **L3** $\Delta\Delta G_{b,exp}$ = −1.80 ± 0.09 kcal mol^{-1}, $\Delta\Delta G_{b,TI/MD}$ = −0.66 kcal mol^{-1}, and for **A15** → **A17** $\Delta\Delta G_{b,exp}$ = −2.44 ± 0.09 kcal mol^{-1}, $\Delta\Delta G_{b,TI/MD}$ = −1.06 kcal mol^{-1}. The binding affinity was increased with the size of the substituent at the 3-position as measured in the alchemical perturbation **L3** → **A17** with $\Delta\Delta G_{b,exp}$ = −0.63 kcal mol^{-1}, $\Delta\Delta G_{b,TI/MD}$ = −2.54 kcal mol^{-1} (Table 4) and in **L2** → **L5** with $\Delta\Delta G_{b,exp}$ = −0.18 ± 0.11 kcal mol^{-1}, $\Delta\Delta G_{b,TI/MD}$ = −0.37 ± 0.07 mol^{-1} confirming that the phenyl group was favored over the isopropyl group (Table 3).

An important effect in binding free energy from replacing the hydrogen at the 5-position with a chlorine or with a cyano group was examined with the alchemical perturbations **L6** → **L5** or **L6** → **A17** or **L5** → **A17** with $\Delta\Delta G_{b,exp}$ = 0.16 ± 0.22 kcal mol^{-1}, $\Delta\Delta G_{b,TI/MD}$ = −0.67 ± 0.04 kcal mol^{-1} or $\Delta\Delta G_{b,exp}$ = −2.24 ± 0.20 kcal mol^{-1}, $\Delta\Delta G_{b,TI/MD}$ = −3.05 ± 0.05 kcal mol^{-1} or $\Delta\Delta G_{b,exp}$ = −2.40 ± 0.12 kcal mol^{-1}, $\Delta\Delta G_{b,TI/MD}$ = −1.09 ± 0.09 kcal mol^{-1}, respectively. These results show that changing the hydrogen at the 5-position with a chlorine or a cyano group increased the binding free energy. Compared to **L5** and **L6** in **A17**, the combination of the 5-cyano group and nitrogen at the 6-position increased polarity, which attracted waters to enter the binding area between the ligand and TM2, TM3 according to the MD simulations. Thus, compared to **L5** and **L6**, in **A17** and **L4**, the 5-cyano group could form hydrogen bonding interactions with waters positioned between the ligand and transmembrane (TM)2 and TM3 (Figure 6A,B). It is worth noting that a B3LYP/6-31G(d,p) geometry optimization of **A17** with the 5-cyano group and nitrogen at the 6-position surrounded by three waters resulted in a stable complex (Figure S4). In **L6**, which lacked the 5-cyano group, the hydrogen bonding interactions with $N254^{6.55}$ and $E172^{5.30}$ as well as the hydrogen bonding interactions with waters that enter the area between the ligand and TM2, TM3, and the hydrophobic interactions with $M180^{5.38}$ and $W247^{6.48}$ were all reduced (Figure 6A,C).

By adding three methoxy groups in the phenyl group of the 7-anilino substituent, the lipophilicity of the ligand was enhanced and the desolvation penalty of **A17** compared to **L4** to reach the orthosteric binding area was reduced thus increasing binding affinity. Due to the deletion of the methoxy groups in **L4**, the hydrophobic interactions with $M180^{5.38}$ and $W247^{6.48}$ were also diminished. This effect in binding free energy was predicted by the TI/MD calculations using the alchemical perturbation **L4** → **A17** calculation, which produced $\Delta\Delta G_{b,TI/MD}$ = −2.39 ± 0.15 kcal mol^{-1} with $\Delta\Delta G_{b,exp}$ = −3.34 ± 0.10 kcal mol^{-1}.

The orthosteric binding pocket could accommodate sizeable substituents at the 5-position, for example, the phenylmethyl group in **L8** or the 3-(pyridinyl)methyl group in **L9** that were linked to a 5-aminomethyl group present in compound **L7**, leading to a pK_d = 6.37 for **L8** or pK_d = 7.54 for **L9** at A_1R (Table 2). The TI/MD predictions suggested that pyridinyl instead of phenyl, as is described by the alchemical transformation, **L8** → **L9** was favored with $\Delta\Delta G_{b,exp}$ ($\Delta\Delta G_{b,TI/MD}$) binding free energy values $\Delta\Delta G_{b,exp}$ = −0.72 kcal mol^{-1} and $\Delta\Delta G_{b,TI/MD}$ = −0.71 kcal mol^{-1} for A_1R. In **L9**, the increased length of the 5-substituent resulted in contacts with residues $A69^{2.61}$ and $V72^{2.63}$ of TM2 and the formation of direct water-bridged hydrogen bonding with $E19^{1.39}$, while the pyrazole ring was positioned close to TM5−TM7, thus increasing the π−π interactions with $F168^{5.29}$ and $L246^{6.51}$ and forming new interactions with $I249^{6.51}$ and $H272^{7.43}$ (Figure 6D). It seemed that compared to **L8**, in **L9**, the increased hydrophobic interactions between the pyridinylmethyl group and $V62^{2.57}$, $A66^{2.61}$, $V87^{3.32}$, and $I274^{7.39}$ but particularly the hydrogen bonding interaction of pyridinyl nitrogen with $H278^{7.43}$ caused the ∼15-fold increased affinity that **L9** displays compared to **L8**.

We obtained calculated relative binding free energy values that were quite close to the experimental values with mean unsigned error (mue) = 0.87 kcal mol^{-1} (Table 3). Furthermore, we showed a very good correlation coefficient r = 0.73 (p = 0.026) (Figure 7) between the calculated and the experimental relative binding free energies suggesting that the binding model used is reliable and the TI/MD calculations accurately describe the binding interactions of the ligands tested at A_1R.[58,132−134,137] Finally, the predictive index (PI) of Pearlman,[86] a measure for the correctness of the relative ranking of ligands according to binding free energy, was also high (PI = 0.73). Overall, the TI/MD simulations could accurately calculate the changes in binding affinity between different substituents that could be described only qualitatively in MD simulations using the height of protein−ligand interactions frequency bars (see Figures 6 and S2).

MM-GBSA Calculations with an Implicit Membrane Model. A postprocessing analysis of the MD simulations of

https://doi.org/10.1021/acs.jmedchem.2c01123
J. Med. Chem. XXXX, XXX, XXX−XXX

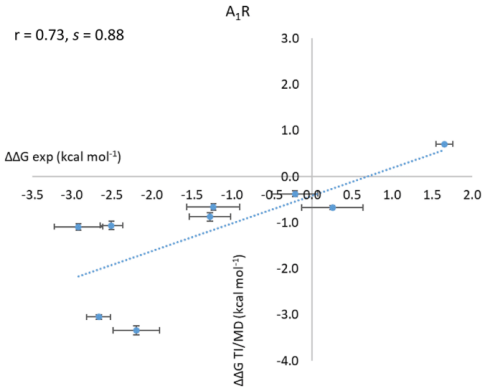

Figure 7. Computed $\Delta\Delta G_{b,TI/MD}$ values plotted against $\Delta\Delta G_{b,exp}$ values estimated by the experimental binding affinities pK_d (Table 2) for A_1R; *r*: correlation coefficient, *s*: slope.

the tested compounds **A15**, **L2**−**L10**, and **A17** in complex with A_1R was also applied using a MM-GBSA method, which applied a hydrophobic slab as an implicit membrane model and included water molecules in the orthosteric binding area, to a radius of 4 Å from the center of mass of the ligand,[46,87] and the OPLS2005[88,89] force field for the calculation of ligand−protein interactions.

Applying this approach showed that, compared to the highest affinity compound **A17** (ΔG_{eff} = −120.32 ± 7.25 kcal mol^{-1}), **L6** lacked the 5-electronegative substituent and had more positive binding free energy values, ΔG_{eff} = −105.14 ± 6.99 kcal mol^{-1} (Table S5). Moreover, **L4**, which compared to **A17**, lacked the trimethoxy substitution from the 7-anilino substituent also had a more positive binding free energy value, ΔG_{eff} = −91.10 ± 6.62 kcal mol^{-1}. Further, **L3** which contained a 3-isopropyl instead of 3-phenyl group had a ΔG_{eff} = −118.06 ± 7.18 kcal mol^{-1}, and **A15** (devoid of any substitution at 3-position) had a ΔG_{eff} = −99.37 ± 6.88 kcal mol^{-1}.

However, the MM-GBSA method performed poorly at predicting other changes, for example, in **L7** the presence of the 3-aminomethyl group or the 3-chloro group in **L7** or **L5** lead to ΔG_{eff} = −126.67 kcal mol^{-1} or ΔG_{eff} = −125.22 ± 7.60 kcal mol^{-1}, respectively, suggesting stronger binding affinity compared to **A17**. In **L8** and **L9**, the benzyl and *N*-(3-pyridinylmethyl)aminomethyl at the 3-position lead to ΔG_{eff} values of −143.08 ± 7.68 and −140.46 ± 7.41 kcal mol^{-1} showing erroneously stronger binding affinity compared to **L7** but also compared to **A17**. Similarly, **L10** had a ΔG_{eff} = −162.67 ± 8.79 kcal mol^{-1}, which suggested that **L10** was a stronger binder compared to **A17**.

Compared to the most potent compound **A17**, the MM-GBSA calculations reported correctly that the deletion of a group or substituent from **A17** (i.e., changing the substituent with hydrogen) resulted in more positive ΔG_{eff} values, that is, weaker binding without providing accurate relative free energy values (Figure 8). Such accuracy was possible using the perturbation methods based on statistical mechanics as also suggested by studies related to the comparative performance of FEP/MD and MM-PBSA methods for water soluble protein−ligand complexes[47,90] and membrane protein−ligand complexes, for example, complexes of A_1R and $A_{2A}R$.[78]

DISCUSSION

Other groups[13−19] and we[20] are motivated to identify new hits from virtual screening of ARs[20,23] and modify them to lead compounds. However, the possibility of re-purposing com-

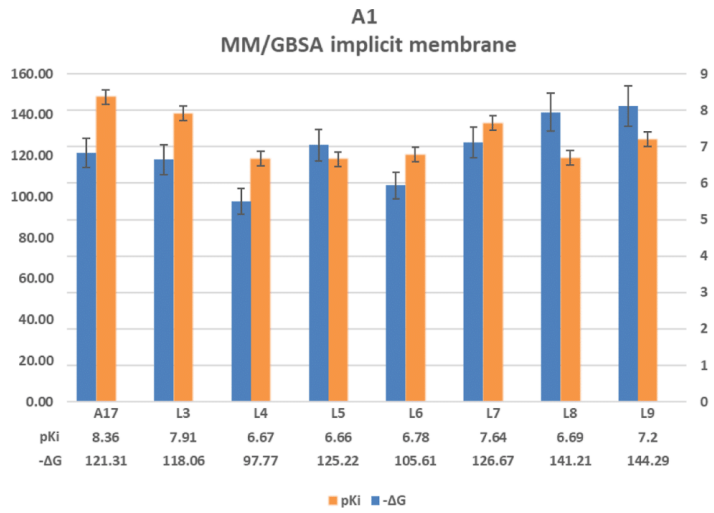

Figure 8. ΔG_{eff} values from MM-GBSA calculations using a model that is taking into account the membrane as a hydrophobic slab (brown bars) and experimental binding affinities calculated using the pK_d values measured using BRET (blue bars) for A_1R. For the protein model of A_1R the experimental structure of the inactive form of A_1R in complex with an antagonist (PDB ID 5UEN[10]) was used.

https://doi.org/10.1021/acs.jmedchem.2c01123
J. Med. Chem. XXXX, XXX, XXX−XXX

pounds from in-house libraries[16] is an exciting and a cost-effective process. We identified here the pyrazolo[3,4-*c*]-pyridines **L2**−**L10**, **A15**, and **A17** with a phenyl or isopropyl group at the 3-position, an anilino group at the 7-position, and a cyano- or chloro- or aminomethyl group or *N*-(arylmethyl)-2-aminomethyl group at the 5-position as nanomolar to mid-nanomolar antagonists at A_1R and A_3R. Another second series, including 3-(*N*-acyl)amino-5-anilino-pyrazolo-[3,4-*c*]pyridine **A26** and its analogues **L12**, **L15**, and **L21** displayed low micromolar to 100 nM binding affinity against A_1R and A_3R.

The binding areas of ARs are broad so it is very interesting to observe that small changes in ligand's structure resulted in significant changes in affinity/activity and receptor selectivity. For example, the replacement in **A17** of the 5-cyano group by the chloro group in **L5** reduced the affinity by ca. 30-fold and the deletion of the cyano group reduced the affinity by ca. 100-fold against A_1R. These changes reduced the affinity at A_3R by ca. 7-fold and 20-fold, respectively.

Some compounds showed high affinities and a diverse range of kinetic profiles. We found A_3R and A_1R antagonists with medium RTs and much longer RTs. For compounds acting at the A_3R, **A17**, **L4**, and **L5** had the longer residence time with RT values between ca. 32−50 min and **L6**, **L7**, **L10**, and **A26** the shortest residence with RT values between ca. 5.6−11 min. For compounds acting at the A_1R, **A15**, **A17**, **L9**, and **L10** had the longer residence time with RT values between ca. 30−44 min and **L3**, **L5**, **L8**, **A26**, and **L15** the shortest residence with RT values (between ca. 7.5−19 min). Compounds, which displayed high affinity at the A_3R, had RT between ca. 5−50 min, and at A_1R between ca. 18−40 min (**L4**, **L6**−**L8**). The kinetic data showed that compared to not potent congeners the active compounds, which displayed high affinity have a similar association rate, for example, at A_3R $K_{on} = 21.3 \times 10^5$ M^{-1} (**A17**) versus $K_{on} = 4.8 \times 10^5$ M^{-1} (**L7**) but a much lower dissociation rate of $K_{off} = 0.021$ min^{-1} (**A17**) versus 0.105 min^{-1} (**L7**), resulting in lower K_d's. Knowledge of target binding kinetics has been discussed to be very important for developing and selecting new AR antagonists in the early phase of drug discovery.[38,91]

The binding orientation of **A17** inside A_1R was selected between **docking pose 1** or **docking pose 2**, which produces stable **A17**−A_1R complexes in MD simulations, based on the agreement with alanine scanning mutagenesis experiments and affinities measured with the NanoBRET method. We observed that mutations $H251^{6.52}A$ and $S267^{7.32}A$ increased the affinity of **A17** by ∼1.5- and 1.7-fold, respectively, while $T91^{3.36}A$ and $L250^{6.51}A$ increased the affinity of **A17** by 3.2- and 3.8-fold (Table 4). Residues $Y271^{7.36}$ or $E172^{5.30}$ were not important for binding of **A17** to A_1R because their mutation to alanine had little effect upon **A17** affinity. The result for $L250^{6.51}A$ was a bit unexpected because $L250^{6.51}$ is highly conserved residue in all four AR subtypes where it is key to ligand recognition. Indeed, mutation of $L250^{6.51}$ to Ala has been reported to reduce or block affinity as we also showed previously[20,21] at the A_3R. We selected **docking pose 1** with the anilino group oriented toward EL2 because the MD simulations of **A17** with the mutant A_1R-$Y271^{7.36}A$ maintained binding interactions with **A17**, which was in agreement with our mutagenesis experiments. The MD simulations of **A17** in complex with the A_1R mutants $S267^{7.32}A$ or $T91^{3.36}A$ or $H251^{6.52}A$ or $L250^{6.51}A$ starting from **docking pose 1** produce complexes with binding interactions that also agreed with our mutagenesis data. A novel observation from mutagenesis data for drug design purposes that when the $L250^{6.51}$ was changed to alanine the binding affinity of **A17** was significantly increased at A_1R.

Our MD simulations starting from **docking pose 1** for the complexes of **A15**, **L2**−**L10**, and **A17** with A_1R showed that **A17**, the most potent antagonist against A_1R, was stabilized inside the binding area by an array of co-operative interactions. Compound **A17** binds to A_1R and interacts with TM5 $E170^{5.28}$, $F171^{5.29}$, $E172^{5.30}$, $M180^{5.38}$, $N184^{5.42}$, TM6 $W247^{6.48}$, $L250^{6.51}$, $H251^{6.52}$, $N254^{6.55}$, TM7 $T270^{7.35}$, and $Y271^{7.36}$ in A_1R;[92] its 5-cyano group in **A17** seems to be stabilized through hydrogen bonding interactions with waters that enter the binding area between the ligand and TM2 and TM3.

When we compared **A17** to **L4** or **L6** or **A15** (Figure 6B,C), we found that either the trimethoxy substitution or the cyano group or the 5-phenyl were replaced by hydrogens. In **L5** or **L7**, we observed that the cyano group in **A17** was changed to either chlorine groups or aminomethyl groups, respectively. In **L9** or **L8**, the sizeable *N*-(3-pyridinylmethyl)aminomethyl or *N*-benzylaminomethyl group, respectively, replaced the 5-cyano group of **A17** in the pyrazolo[3,4-*c*]pyridine ring. **L3** or **L2** had a 3-isopropyl group compared to the 3-phenyl in **A17** or **L5**, respectively. To explore a method that enabled the quantitative description of these SARs, we performed MM-GBSA calculations, using an implicit membrane model[46] and taking into account the waters inside the binding area,[47] and TI/MD simulations using the alchemical perturbations of these ligands, which are in very good agreement with the experimental relative binding free energies. The TI/MD method produced a very good correlation coefficient (r = 0.73) between the calculated and experimental relative binding free energies for A_1R showing that the method can be used for heat-to-lead optimization of **A17**.

■ EXPERIMENTAL SECTION

Biological Methods. *Cell Lines.* Stable Flp-In-CHO cell lines expressing the WT A_3R were generated and maintained as previously described.[59,60] CHO-K1 cells stably expressing WT A_1R, $A_{2A}R$, or $A_{2B}R$ were routinely cultured in Hams F-12, supplemented with 10% fetal bovine serum. All were annually checked for mycoplasma infection using an EZ-PCR mycoplasma test kit (Biological Industries, Kibbutz Beit-Haemek, Israel). Production and analysis of the mutant versions of the A_1R were as described in ref 93.

Compounds. **NECA** was purchased from Sigma-Aldrich and dissolved in dimethyl sulfoxide (DMSO). The 52 compounds tested were available from an in-house library of the Laboratory of Medicinal Chemistry, Section of Pharmaceutical Chemistry, Department of Pharmacy, National and Kapodistrian University of Athens. All compounds used for the in vitro testing were >95% pure by elemental analysis. Representatively, the purity data of compound **A17** (96.73%) as determined by HPLC is shown in the Supporting Information.

cAMP Accumulation Assay. cAMP inhibition experiments were performed using a LANCE cAMP kit as described previously.[59,60] Briefly, Flp-In-CHO cells expressing WT A_3R and CHO-K1 cells expressing WT A_1R, $A_{2A}R$, or $A_{2B}R$ were seeded in a white 384-well optiplate at a density of 2000 cells per well and stimulated for 30 min in a range of **NECA** concentrations, with or without potential antagonists, in the presence of 0.1% BSA and 25 μM rolipram, and 10 μM forskolin (to enable the detection of A_1R- or A_3R-mediated inhibition of cAMP). For the initial screening, IC_{80} (6.32 nM) of **NECA** was used. Because the $A_{2A}R$ and $A_{2B}R$ promote cAMP accumulation,[61] the addition of forskolin was not included when assaying these receptors.

Schild Analysis. **NECA** concentration-dependent response curves were constructed in the presence or either DMSO alone or 1 μM test compound or 1 μM **MRS1220**. **NECA** concentrations ranged from 1

https://doi.org/10.1021/acs.jmedchem.2c01123
J. Med. Chem. XXXX, XXX, XXX−XXX

pM to 1 μM. Estimates of the EC_{50} values in the presence and absence of the antagonist were determined using the three-parameter logistic equation built into Prism.

NanoBRET Assays for Binding. NanoBRET competition binding assays were conducted to determine the affinity constant (pK_i) of various potential antagonists at the A_1R and A_3R as described previously.[21] For both the A_1R and A_3R, the CellAura fluorescent A_3R antagonist (**CA200645**) with a xanthine amine congener (XAC) structure was used at 20 and 5 nM concentrations for A_1R and A_3R, respectively, because it has a slow off rate. Kinetic data was fitted with the "kinetic of competitive binding" model (see ref 94; built into Prism) to determine pK_i values and K_{on} and K_{off} rates for unlabeled A_3R antagonists. In agreement with our previous studies,[21,93] we determined the pK_d of **CA200645** at the A_1R to be 18.29 ± 2.4 nM and at the A_3R 26.95 ± 3.2 nM.[21] The BRET ratio at 10 min poststimulation was fitted with the "one-site—K_i model" derived from the Cheng and Prusoff correction and built into Prism to determine the affinity constant (pK_i) at equilibrium values for all unlabeled antagonists at the A_1R and A_3Rs.

Data and Statistical Analyses. All in vitro assay data were analyzed using Prism 9.0 (GraphPad software, San Diego, CA), with all dose−inhibition curves being fitted using a three-parameter logistic equation to calculate response range and pIC_{50}/pEC_{50}. Experimental design ensured random distribution of treatments across 96/384-well plates to avoid systematic bias. Agonist stimulation alone was used as an intrinsic control across all experiments. Dose-inhibition/dose−response curves were normalized to forskolin stimulation ($A_{2A}R$ and $A_{2B}R$) or forskolin inhibition (A_1R and A_3R) relative to **NECA** (agonist allowing comparison across AR subtypes), expressed as percentage forskolin inhibition for G_i-coupled A_1R and A_3R (1 or 10 μM, respectively) or stimulation for $A_{2A}R$ and $A_{2B}R$ (100 μM, representing the maximum cAMP accumulation of the system), relative to **NECA**. For cAMP experiments on A_1R mutants, data was normalized to 100 μM forskolin, representing the maximum cAMP accumulation possible for each cell line.

Schild analysis was performed to obtain the dissociation constant (pK_d) using eq 1[63]

$$\frac{D'}{D} = 1 + [A]K_2 \quad (1)$$

where D' and D are the IC_{50} values of **NECA** with and without the presence of an antagonist, respectively, [A] isthe concentration of antagonist present, and K_2 is the affinity constant (K_A) of the antagonist used.[63] Receptor binding kinetics was determined as described previously[21] using the Motulsky and Mahan method[94] (built into Prism 9.0) to determine the test compound association rate constant and dissociation rate constant. The K_{on} and K_{off} values for binding of CA200645 at the A_1R were determined to be (A_1R) K_{on} = 3.67 ± 0.34 × 10^6 M^{-1} min^{-1} and K_{off} = 0.06715 ± 0.0045 min^{-1} and (A_3R) K_{on} = 2.86 ± 0.45 × 10^6 M^{-1} min^{-1} and K_{off} = 0.064 ± 0.0023 min^{-1}. These values are in agreement with previous estimates at both receptors.[95] The data and statistical analysis comply with the recommendations on experimental design and analysis in pharmacology.[96] Statistical significance (*, $p < 0.05$;**, $p < 0.01$;***, $p < 0.001$;****, $p < 0.0001$) was calculated using a one-way ANOVA with Dunnett's post-test for multiple comparisons. Compounds taken forward for further experiments after initial screening were identified as having the highest statistical significance [p value of 0.001 (***) or <0.0001 (****)]. All statistical analysis was performed using Prism 9.0 on data, which were acquired from experiments performed a minimum of five times, conducted in duplicate.

Computational Medicinal Chemistry. *Ligand Preparation.* The 2D structures of the compounds **A15**, **L2**−**L10**, **A17**, **L12**, **L15**, **L21**, and **A26** were sketched with Marvin Program (Marvin version 21.17.0, ChemAxon) and a model built with the Schrödinger 2021-1 platform (Schrödinger Release 2021-1: Protein Preparation Wizard; Epik, Schrödinger, LLC, New York, NY, 2021; Impact, Schrödinger, LLC, New York, NY; Prime, Schrödinger, LLC, New York, NY, 2021) and minimized using the CG method, the MMFF94 force field,[97] and a distance-dependent dielectric constant of 4.0 until a convergence threshold of 2.4 × 10^{-5} kcal mol^{-1} $Å^{-1}$ was reached. Ionization states of the compounds at pH 7.5 were tested using the Epik program[98] implemented in Schrödinger suite (Prime, Schrödinger, LLC, New York, NY, 2021). Energy minimization of the compounds' 3D structures was performed using the OPLS2005[88,89] force field.

3D Similarity Calculations. All of the 3D similarity calculations were performed with Canvas program (Schrödinger Release 2021-1: Canvas, Schrödinger, LLC, New York, NY, 2021).[99] Similar compound structures were ranked according to the TanimotoCombo[49] coefficient as metric.

Protein Models. Model of the WT A_1R−Antagonist Complex. The X-ray WT A_1R—DU172 structure with PDB ID 5UEN[10] was processed using the Protein Preparation Wizard in Schrödinger suite (Schrödinger Release 2021-1: Protein Preparation Wizard; Epik, Schrödinger, LLC, New York, NY, 2021; Impact, Schrödinger, LLC, New York, NY; Prime, Schrödinger, LLC, New York, NY, 2021).[100] In this process, the bond orders and disulfide bonds were assigned, and missing hydrogen atoms were added. Additionally, N- and C-termini of the protein model were capped by acetyl and *N*-methylamino groups, respectively. His residues have the Nε-protonation state. All hydrogens of each protein complex were minimized with the OPLS2005[88,89] force field by means of Maestro/Macromodel 9.6[101] using a distance-dependent dielectric constant of 4.0. The molecular mechanics minimizations were performed with the conjugate-gradient (CG) method and a threshold value of 2.4 × 10^{-5} kcal mol^{-1} $Å^{-1}$ as the convergence criterion. Each protein was subjected to an all atom minimization using the OPLS2005[88,89] force field with heavy atom rmsd (root mean square deviation) value constrained to 0.30 Å until the rms (root mean square) of conjugate-gradient value reached <0.05 kcal·mol^{-1}·$Å^{-1}$. The model of WT A_1R−DU172[10] was utilized for the molecular docking calculations.

Models of Mutant A_1R−A17 Complexes. For the generation of $T91^{3.36}A$, $E172^{5.3}A$, $L250^{6.54}A$, $H251^{6.52}A$ $S267^{7.32}A$, and $Y271^{7.36}A$ A_1Rs in complex with **A17** point mutations were applied in the last frame from the MD simulation of A1R in complex with **A17**.

Molecular Docking Calculations. The molecular docking calculations of the 14 tested pyrazolo[3,4-*c*]pyridines **A15**, **L2**−**L10**, **A17**, **L12**, **L15**, **L21**, and **A26** with structures shown in Table 1, with A_1R, were performed using GOLD software[66] (GOLD Suite, Version 5.2; Cambridge Crystallographic Data Centre: Cambridge, U.K., 2015. GOLD Suite, version 5.2; Cambridge Crystallogr. Data Cent. Cambridge, U.K., 2015) and ChemScore[67] as the scoring function. The model of WT A_1R−DU172[10] generated as described above was used as a template for the molecular docking calculations of the antagonists to the binding area of each of the receptors. Each compound was docked in the binding site of DU172 in the A_1R−DU172[10] model in an area of 15 Å around the ligand using the experimental coordinates of DU172 and 20 genetic algorithm runs were applied for each docking calculation. The top-scoring docking poses were used for MD simulations to investigate the binding profile of the tested pyrazolo[3,4-*c*]pyridines at A_1R.

MD Simulations. Each protein−ligand complex was inserted in a pre-equilibrated hydrated 1-palmitoyl-2-oleoyl-*sn*-glycero-3-phosphoethanolamine (POPE) membrane bilayer according to orientations of proteins in membranes (OPM) database.[102] The orthorhombic periodic box boundaries were set 12 Å away from the protein using a System Builder utility of Desmond v4.9 (Schrödinger Release 2021-1: Desmond Molecular Dynamics System, D. E. Shaw Research, New York, NY, 2021. Maestro-Desmond Interoperability Tools, Schrödinger, New York, NY, 2021). The membrane bilayer consisted of ca. 170 lipids and 16,000 TIP3P[103] water molecules. Sodium and chloride ions were added randomly in the water phase to neutralize the system and reach an experimental salt concentration of 0.150 M NaCl. The total number of atoms of the complex was approximately 75,000 and the simulation box dimensions were (88 × 76 × 113 $Å^3$). We used the Desmond Viparr tool to assign the amber99sb[68,69] force field parameters for the calculation of the proteins, lipids, and intermolecular interactions, and the generalized Amber force field (GAFF)[104] parameters for the ligands. Ligand atomic charges were computed using the RESP[105] fitting for the

https://doi.org/10.1021/acs.jmedchem.2c01123
J. Med. Chem. XXXX, XXX, XXX−XXX

electrostatic potentials calculated with Gaussian03[106] at the HF/6-31G*[107] level of theory and the antechamber of AmberTools18.[108]

The MD simulation of each protein−ligand complex inside the lipid bilayer was performed using the default protocol provided with Desmond v4.9 program. The MD simulation protocol consists of a series of MD simulations designed to relax the system, while not deviating substantially from the initial coordinates. During the first stage, a simulation was run for 200 ps at 10 K in the *NVT* ensemble (constant volume, temperature, and number of atoms), with solute-heavy atoms restrained by a force constant of 50 kcal mol $Å^{-2}$. The temperature was raised to 310 K during a 200 ps MD simulation in the *NPT* ensemble (constant pressure, temperature and number of atoms), with the same force constant applied to the solute atoms. A temperature of 310 K was used in MD simulations in order to ensure that the membrane state is above the main phase transition temperature of 298 K for POPE bilayers.[109] The heating was then followed by equilibration simulations. First, two 1 ns stages of *NPT* equilibration were performed. In the first 1 ns stage, the heavy atoms of the system were restrained by applying a force constant of 10 kcal mol^{-1} $Å^{-2}$, and in the second 1 ns stage, the heavy atoms of the protein−ligand complex were restrained by applying a force constant of 2 kcal mol^{-1} $Å^{-2}$ to equilibrate water and lipid molecules. In the production phase, the relaxed systems were simulated without restraints in the *NPT* ensemble for 100 ns. Replicas of the system were saved every 10 ps.[110,111]

In the MD simulations, the particle mesh Ewald (PME)[82] method was employed to calculate long-range electrostatic interactions with a grid spacing of 0.8 Å. The SHAKE method was used to constrain heavy atom-hydrogen bonds at ideal lengths and angles.[112] Van der Waals and short-range electrostatic interactions were smoothly truncated at 12 Å.[113] A Nosé−Hoover thermostat[114] was utilized to maintain a constant temperature in all MD simulations, and the Martyna−Tobias−Klein method[115] was used to control the pressure. The equations of motion were integrated using the multistep reversible reference system propagator algorithm (RESPA)[116] integrator with an inner time step of 2 fs for bonded interactions and non-bonded interactions within a cutoff of 12 Å. An outer time step of 6.0 fs was used for non-bonded interactions beyond the cutoff.

The visualization of the MD simulation trajectories was performed using the graphical user interface (GUI) of Maestro and the protein−ligand interaction analysis was carried out with a simulation interaction diagram (SID) tool, available with a Desmond v4.9 program. For the calculation of hydrogen bond interactions, a distance of 2.5 Å between donor and acceptor heavy atoms, and angle ≥120° between donor-hydrogen-acceptor atoms and ≥90° between hydrogen-acceptor-bonded atom. Non-specific hydrophobic contacts were identified when the side chain of a hydrophobic residue fell within 3.6 Å from a ligand's aromatic or aliphatic carbon, while $\pi-\pi$ interactions were characterized by stacking of two aromatic groups face-to-face or face-to-edge. Water-mediated interactions were characterized when the distance between donor and acceptor atoms was 2.7 Å, as well as an angle ≥110° between donor-hydrogen-acceptor atoms and ≥80° between hydrogen-acceptor-bonded atoms.

100 ns MD simulations at constant pressure (*NPT*) were performed for the 14 most interesting ligands **A15**, **L2**−**L10**, **A17**, **L12**, **L15**, **L21**, and **A26** (Table 1) in complex with A_1R embedded in POPE bilayers using Desmond v4.9 software, the Desmond MD algorithm[117] with amber99sb[74] force field to investigate their binding interactions. Within the 100 ns MD simulation time, the total energy and rmsd of the protein backbone C_α atoms reached a plateau, and the systems were considered equilibrated and suitable for statistical analysis (Figure S3). The $rmsd_{prot}$ values were between 2 and 3 Å except in cases of the ligands **L8** and **L9**, which have increased girth produced $rmsd_{prot}$ values of 3−3.5 Å.

MD simulations were repeated twice for each complex using the same starting structure and applying randomized velocities. All the MD simulations with Desmond software were run on GTX 1060 GPUs in lab workstations or the ARIS Supercomputer.

MM-GBSA Calculations. For this, structural ensembles were extracted in intervals of 40 ps from the 20 ns MD simulation for each complex. Prior to the calculations, all water molecules, ions, and lipids were removed, except 20 water molecules in the vicinity of the ligand,[118] and the structures were positioned such that the geometric center of each complex was located at the coordinate origin. The MD trajectories were processed with the Python library MDAnalysis[119] in order to extract the 20 water molecules closest to any atom in the ligand for each of the 501 frames. During the MM-GBSA calculations, the explicit water molecules were considered as being part of the protein. Binding free energies of compounds in complex with A_1R and A_3R were estimated using the 1-trajectory MM-GBSA approach[45,90] and the OPLS2005[88,89] force field. For the calculation of binding free energy for each complex eqs 2−5 were used[120,121]

$$\Delta G_{bind} = \langle G_{complex} - G_{protein} - G_{ligand} \rangle_{complex} \quad (2)$$

$$G_i = V_{MM} - T\langle S_{MM} \rangle + \Delta G_{solv} \quad (3)$$

$$V_{MM} = V_{bonded} + V_{coul} + V_{LJ} \quad (4)$$

$$\Delta G_{solv} = \Delta G_P + \Delta G_{NP} \quad (5)$$

The binding free energy for each complex was thus calculated using eq 6

$$\Delta G_{bind} = \langle \Delta E_{coul} + \Delta E_{LJ} \rangle - T\langle \Delta S_{MM} \rangle + \Delta\Delta G_{solv} \quad (6)$$

In eqs 2−5, G_i is the free energy of system *i*, that being the ligand, the protein, or the complex; V_{MM} is the potential energy in vacuum as defined by the molecular mechanics (MM) model, which is composed of the bonded potential energy terms (V_{bonded}) and nonbonded Coulombic (V_{coul}) and Lennard-Jones (V_{LJ}) terms; S_{MM} is the entropy; ΔG_{solv} is the free energy of solvation for transferring the ligand from water in the binding area calculated using the PBSA model, composed by a polar (ΔG_P) and nonpolar (ΔG_{NP}) term; and *T* is the temperature and angle brackets represent an ensemble average. Molecular mechanics energies for Lennard-Jones (V_{LJ}) and Coulombic electrostatic (V_{coul}) were calculated with OPLS2005[88,89] force field; in these calculations $\Delta V_{bonded} = 0$, as the single trajectory method was adopted and $\Delta V_{MM} = \Delta V_{LJ}$ and ΔV_{coul}. The polar part of the solvation free energy was determined by calculations using the generalized-Born model.[122] The nonpolar term was considered proportional to the solvent accessible surface area (SASA), $\Delta G_{NP} = \gamma \cdots SASA$, where $\gamma = 0.0227$ kJ mol^{-1} $Å^{-2}$. The entropy term was neglected because we were interested in binding free energies between ligands in the same series and in this case, ΔG_{bind} is termed as effective binding energy, ΔG_{eff} (Table S5).[123] We applied a dielectric constant $\varepsilon_{solute} = 1$ to the binding area and to account for the lipophilic environment of the protein, an heterogeneous dielectric implicit membrane model was used along the bilayer *z*-axis.[96] The post-processing thermal_mmgbsa.py script of the Schrodinger Suite was used which takes snapshots from the MD simulations trajectory and calculates ΔG_{eff}.

Alchemical TI/MD Binding Free Energies Calculated with the MBAR Method. Method's Principles. The TI/MD method has been described in ref 124. Free energy is a state function, thus the free energy difference between states is independent of the path that connects them. To compare two ligands 0 and 1 binding to a receptor, the calculation of ΔA_1(b) and ΔA_0(b), respectively, is needed and then the difference $\Delta\Delta A_{\vec{0}\to 1}$ (b) or $\Delta\Delta A_{0,1}$ (b). The calculation of ΔA_1(b) and ΔA_0(b) is demanded because it includes large changes between the two states. Thus, the calculation of the relative binding free energies for two ligands bound to A_1R or A_3R (for pairs of ligands shown in Table 2) can be performed instead using the MBAR method[125] and applying a thermodynamic cycle[84,85,126] (Scheme 1), that is, using the ΔG values obtained for the transformations of the ligands in the bound (b), [($\Delta G_{0,1}$(b)], and the solvent (s) (water) state, respectively, $\Delta G_{0,1}$(b) and $\Delta G_{0,1}$(s), according to eq 7

https://doi.org/10.1021/acs.jmedchem.2c01123
J. Med. Chem. XXXX, XXX, XXX−XXX

Scheme 1. Thermodynamic Cycle Used for the Calculation of Relative Binding Free Energies

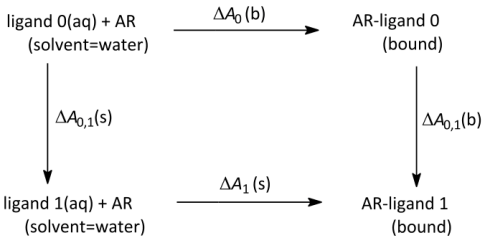

$$\Delta\Delta A_{b,\vec{0}\to 1} \text{ or } \Delta\Delta A_{b,0,1} = \Delta A_1(b) - \Delta A_0(b) = \Delta A_{0,1}(b) - \Delta A_{0,1}(s) \quad (7)$$

Using this method, we can calculate the difference between $\Delta A_{0,1}(b)$ and $\Delta A_{0,1}(s)$, which corresponds to the unphysical alchemical transformation 0 → 1 in the bound state and in the water, known as alchemical transformation which may be chosen to include a small change or perturbation of ligand structure (e.g., from H at 5-position of pyrazolo[3,4-*c*]pyridine to Cl) to lower the error for the free energy perturbation calculation $\Delta A_{0,1}(b)$ or $\Delta A_{0,1}(s)$.

Because the phase space overlap between two states 0, 1 of interest can be near zero, doing free energy calculations for the two states alone will often have very large errors. Free energy is a state function, we can construct a thermodynamic path that takes us through a set of states that improves phase space overlap between states that can be unphysical. By this, we mean that our intermediate states do not have to be observable experimentally. To put this mathematically, we can improve our results by constructing high phase space overlap intermediates and calculating our free energy difference $\Delta\Delta A_{\vec{0}\to 1}$ by the sum of the binding free energy differences between the intermediate states.

Briefly, a thermodynamic parameter λ can be used that smoothly connects states 0 and 1 through a λ-dependent potential $U(r^N; \lambda)$, such that $U(r^N; 0) = U_0(r^N)$ and $U(r^N; 1) = U_1(r^N)$. The transformation is broken down into a series of M steps corresponding to a set of λ values $\lambda_1, \lambda_2, ..., \lambda_M$ ranging from 0 to 1, such that there is sufficient phase space overlap between neighboring intermediate λ states. The TI method computes the free energy change of transformation 0 → 1 by integrating the Boltzmann averaged $dU(\lambda)/d\lambda$ as is described in eq 8

$$\Delta A_{\vec{0}\to 1} = \int_0^1 d\lambda \left\langle \frac{dU(r^N; \lambda)}{d\lambda} \right\rangle_\lambda = \Delta A_{\vec{0}\to 1} \approx \sum_{k=1}^{M} w_k \left\langle \frac{dU(r^N; \lambda)}{d\lambda} \right\rangle_{\lambda_k} \quad (8)$$

where the second sum indicates numerical integration over M quadrature points (λ_k, for $k = 1, ..., M$) with associated weights, w_k. A linear extrapolation between states can be applied for the construction of $U_1(r^N; \lambda)$, while with Amber18 softcore[85,127] the LJ and Coulomb term potentials are described according to eq 9

$$U(r^N; \lambda) = U_0^{SC}(r^N; \lambda) + \lambda\Delta U^{SC}(r^N; \lambda) = U_0^{SC}(r^N; \lambda) + \lambda(U_1^{SC}(r^N; 1 - \lambda) - U_0^{SC}(r^N; \lambda)) \quad (9)$$

The ΔA values for the alchemical transformations of the ligands in the bound (b) and the solvent (s) (water) state, $\Delta A_{0,1}(b)$ and $\Delta A_{0,1}(s)$, respectively, were computed using the MBAR method.[125] MBAR[125] calculates the free energy difference between neighboring intermediate states using eq 10

$$\Delta A_{\lambda\to\lambda+1} = -\ln \frac{\langle w \exp(-\beta U_{\lambda+1})\rangle_\lambda}{\langle w \exp(-\beta U_{\lambda+1})\rangle_{\lambda+1}} \quad (10)$$

where w is a function of $A(\lambda)$ and $A(\lambda + 1)$ and $\beta = 1/k_BT$. The equation is solved iteratively to give the free energy change of neighboring states $\Delta A_{\lambda\to\lambda+1}$, which via combination yield the overall free energy change. MBAR method has been shown to minimize the variance in the calculated free energies, by making more efficient use of the simulation data.[125,128]

TI/MD Calculation Protocol. For the TI/MD calculations, the relaxed complexes of compounds **A15**, **L3**−**L6**, **L8**, **L9**, **A17**, **L12**, and **A26** at A_1R from the 100 ns MD simulations in a POPE lipid bilayer with the amber99sb[74] force field were used as starting structures for the calculations of the alchemical transformations described in Table 3. TI/MD calculations were also performed for the ligands in solution.

Setups were performed with CHARMM-GUI[129] using structures of the complexes that were already equilibrated from the 100 ns MD simulations with Desmond and amber ff99sb[74] force field. The relaxed complexes were embedded in a POPE lipid bilayer extending 12 Å beyond the solutes using the CHARM-GUI web-based graphical user tool.[129] Sodium and chloride ions were randomly added in the aqueous phase to neutralize the system based on a Monte-Carlo approach, as implemented in CHARMM-GUI.[129] Each ligand−A_1R complex in the bilayer was processed by the LEaP module in AmberTools18 under the Amber18 software package.[130] Proteins, ligands, and water were described with ff14sb[131] GAFF1.8,[104] and TIP3P force fields,[103] respectively, and intermolecular interactions with ff14sb[131] force field. Atom types, bonded, and van der Waals parameters for ligands were added using Antechamber[132] and Parmchk2 in the Amber18 tool set.[130] Partial charges for ligands were obtained using RESP[105] fitting for the electrostatic potentials calculated with Gaussian03[106] at the Hartree−Fock (HF)/6-31G*[107] level of theory and the antechamber of AmberTools18.[130]

For each λ, a 500 ps constant volume equilibration (NVT) was followed by 2 ns NVT production simulation without restraints. Production simulations re-calculated the potential energy at each λ value every 1 ps for later analysis with MBAR.[125,128]

Thus, initial geometries were minimized using 20,000 steps of steepest descent minimization at $\lambda = 0.5$. These minimized geometries were then used for simulations at all λ values. Eleven λ values were applied equally spaced between 0.0 to 1.0. Each MD simulation was heated to 310 K for 500 ps using a Langevin thermostat (dynamics)[108] for temperature control, as implemented in Amber18,[130] employing a Langevin collision frequency of 2.0 ps^{-1} in the presence of harmonic restraint with a force constant of 10 kcal mol^{-1} $Å^{-2}$ on all membranes, proteins, and ligand atoms. A temperature of 310 K was used in MD simulations in order to ensure that the membrane state is above the main phase transition temperature of 298 K for POPE bilayers.[109] A Berendsen barostat[136] was used to adjust the density over 500 ps at constant pressure ($NPT\gamma$) (with $\gamma = 10$ dyn cm^{-1}), with a target pressure of 1 bar and a 2 ps coupling time. Then, the 500 ps of constant volume equilibration (NVT) was followed by 2 ns NVT production simulation without restraints. Energies were recorded every 1 ps, and coordinates were saved every 10 ps. Production simulations recalculated the potential energy at each λ value every 1 ps for later analysis with MBAR.[125,128]

The bond constraint SHAKE[112] algorithm was disabled for TI mutations in AMBER GPU-TI module pmemdGTI[137] and therefore, a time step of 1 fs was used for all MD simulations. Long-range electrostatics were calculated using PME,[82] with a 1 Å grid, and short-range non-bonding interactions were truncated at 12 Å with a continuum model long-range correction applied for energy and pressure.

For each alchemical calculation, the one-step protocol was performed, that is, disappearing one ligand and appearing the other ligand simultaneously, and the electrostatic and van der Waals interactions are scaled simultaneously using softcore potentials from

https://doi.org/10.1021/acs.jmedchem.2c01123
J. Med. Chem. XXXX, XXX, XXX−XXX

real atoms that are transformed into dummy atoms.[85] Alternatively, in the three-step "decharge-vdW-recharge" protocol, the atoms of the first ligand are first decharged, then undergo a van der Waals interaction transformation using softcore potentials, and then recharged to the final state (second ligand).[85] The one-step protocol is a less computationally expensive and more accurate approach to free energy estimates according to recent studies.[127] However, for the **L9** → **L8** transformation, the three-step protocol was applied because it has been observed that TI calculation converges poorly with one-step protocol if the substituent that is involved in the transformation includes a large numbers of atoms.[138]

The final states 0 and 1 of the alchemical calculations 0 → 1 or 1 → 0, that is, the structures of ligand 0−AR and 1−AR complexes as resulted from the alchemical transformations were compared with these complexes structure resulted from converged 100 ns MD simulations. This was performed to certify that the 2 ns MD simulation for each λ-state during the alchemical calculations was enough for the complexes 0−AR and 1−AR to converge to the same structure with 100 ns MD simulations.

Two repeats were performed for the TI/MD calculations for each alchemical transformation shown in Table 3.

Experimental relative binding free energies were estimated using the experimental binding affinities pK_d in Table 2 according to eq 11

$$\Delta\Delta G_{\bar{0}\to 1}(\mathrm{b})\mathrm{exp} = -1.9872\ T\ (pK_d,\ 1 - pK_d,\ 2) \quad (11)$$

■ ASSOCIATED CONTENT

Supporting Information

The Supporting Information is available free of charge at https://pubs.acs.org/doi/10.1021/acs.jmedchem.2c01123.

Pharmacological experiments, simulation methods, MD simulation results; chemical structures of compounds from our in-house library; functional activities for **A15**, **A17**, and **A27** against $A_{2A}R$ and $A_{2B}R$ and for **L2**−**L10**, **L12**, **L15**, and **L21** against $A_{2A}R$ and $A_{2B}R$; pIC_{50} of **NECA** in the presence of DMSO and in the presence of a potential antagonist in A_3R and A_1R Flp-In CHO cells; pK_ds measured through BRET and the rmsd values of the ligand and protein Ca carbons at A_1R; binding affinities for **A26** measured using NanoBRET against WT and mutant A_1Rs; characterization of **A15**/**A17** and **A26** analogues' selectivity, at the $A_{2A}R$ and $A_{2B}R$; frames, rmsd plots, and frequency interaction plots for A_1R in complex with antagonists not shown in the article; sequence alignment of the residues surrounding the binding site of A_1R, A_3R; complex of a cyanopyridine ring in complex with three waters stabilized through hydrogen bonding interactions; two docking poses 1 or 2 of **A17**; and representative frames and plots of $Y271^{7.36}A$ A_1Rs with the docking poses 1 and 2 of **A17** or $T91^{3.36}A$, $H251^{6.52}A$, $S267^{7.32}A$, and A_1Rs with docking pose 1 of **A17** from 100 ns MD simulations (PDF)

SMILES biological activity (CSV)

MD of **A17** (PDB)

MD of **A26** (PDB)

MD of **L2** (PDB)

MD of **L3** (PDB)

MD of **L4** (PDB)

MD of **L5** (PDB)

MD of **L6** (PDB)

MD of **L7** (PDB)

MD of **L8** (PDB)

MD of **L9** (PDB)

MD of **L10** (PDB)

MD of **L12** (PDB)

■ AUTHOR INFORMATION

Corresponding Authors

Nicole Pouli − *Laboratory of Medicinal Chemistry, Section of Pharmaceutical Chemistry, Department of Pharmacy, School of Health Sciences, National and Kapodistrian University of Athens, 15771 Athens, Greece*; Email: pouli@pharm.uoa.gr

Graham Ladds − *Department of Pharmacology, University of Cambridge, Cambridge CB2 1PD, U.K.*; orcid.org/0000-0001-7320-9612; Phone: +44 (0) 12023 334020; Email: grl30@cam.ac.uk

Antonios Kolocouris − *Laboratory of Medicinal Chemistry, Section of Pharmaceutical Chemistry, Department of Pharmacy, School of Health Sciences, National and Kapodistrian University of Athens, 15771 Athens, Greece*; orcid.org/0000-0001-6110-1903; Phone: 210-727-4834; Email: ankol@pharm.uoa.gr

Authors

Margarita Stampelou − *Laboratory of Medicinal Chemistry, Section of Pharmaceutical Chemistry, Department of Pharmacy, School of Health Sciences, National and Kapodistrian University of Athens, 15771 Athens, Greece*

Anna Suchankova − *Department of Pharmacology, University of Cambridge, Cambridge CB2 1PD, U.K.*

Efpraxia Tzortzini − *Laboratory of Medicinal Chemistry, Section of Pharmaceutical Chemistry, Department of Pharmacy, School of Health Sciences, National and Kapodistrian University of Athens, 15771 Athens, Greece*

Lakshiv Dhingra − *Department of Pharmacology, University of Cambridge, Cambridge CB2 1PD, U.K.*

Kerry Barkan − *Department of Pharmacology, University of Cambridge, Cambridge CB2 1PD, U.K.*; Present Address: Socei Heptares, Steinmetz Building, Granta Park, Cambridge CB21 6DG, UK

Nikolaos Lougiakis − *Laboratory of Medicinal Chemistry, Section of Pharmaceutical Chemistry, Department of Pharmacy, School of Health Sciences, National and Kapodistrian University of Athens, 15771 Athens, Greece*

Panagiotis Marakos − *Laboratory of Medicinal Chemistry, Section of Pharmaceutical Chemistry, Department of Pharmacy, School of Health Sciences, National and Kapodistrian University of Athens, 15771 Athens, Greece*

Complete contact information is available at: https://pubs.acs.org/10.1021/acs.jmedchem.2c01123

Author Contributions

M.S., A.S., G.L., and A.K. contributed equally. This research represents part of M.S. and A.S. Ph.D. theses. A.K. and G.L. conceived and designed the research; M.S. performed the computational work; A.S., L.D., and K.B. performed the mammalian assays; E.T. performed some initial docking calculations; M.S., A.S., G.L., and A.K. analyzed the data; N.L., P.M., and N.P. provided the compound library; and A.K., M.S., and G.L. wrote the manuscript.

Notes

The authors declare no competing financial interest.

Representative structures of the ligands from MD simulations and a movie for **A17**−A_1R complex are available at https://github.com/margstab/A1R-Pyrazolo-3-4-c-pyridine-Antagonists.git.

■ ACKNOWLEDGMENTS

This research represents part of the Ph.D. thesis of M.S. We gratefully acknowledge the support of Chiesi Hellas (A.K.), the Cambridge Trust (A.S.), the Leverhulme Trust (K.B. and G.L.), and the BBSRC (G.L.). This work was supported by the computational time granted from the Greek Research & Technology Network (GRNET) in the National HPC facility ARIS (pr001007). We thank Dr Lin Song in Prof. Kenneth Merz group for his assistance with the TI/MD code in AMBER software. We thank Ioannis Stylianakis for carrying out the DFT calculations shown in Figure S4.

■ ABBREVIATIONS

ARs, adenosine receptors; CG, conjugate gradient; CNS, central nervous system; cAMP, 3′,5′-cyclic adenosine monophosphate; COPD, chronic obstructive pulmonary disease; CPT, 8-cyclopentyl-1,3-dimethylxanthine; DMSO, dimethyl sulfoxide; GAFF, generalized Amber Force Field; EL2, extracellular loop; FEP, free energy perturbation; GB, generalized Born; GUI, graphical user interface; GPCRs, G-protein coupled receptors; HF, Hartree−Fock; **IB-MECA**, N_6-(3-iodobenzyl)-adenosine-5′-*N*-methylcarboxamide; IL, intracellular loop; **LJ-1888**, ((2*R*,3*R*,4*S*)-2-[2-chloro-6-(3-iodobenzylamino)-9*H*-purine-9-yl]tetrahydrothiophene-3,4-diol); m.a.e., mean assigned error; MM-GBSA, molecular mechanics-generalized Born surface area; MARK, mitogen-activated protein kinase; MD, molecular dynamics; **MRS1220**, *N*-[9-chloro-2-(2-furanyl)-1,2,4-triazolo[1,5-*c*]quinazolin-5-yl]-benzeneacetamide; NanoBRET, nano-bioluminescence resonance energy transfer; **NECA**, 5′-*N*-ethylcarboxamidoadenosine; *NPT*, constant pressure, temperature, and number of atoms; *NVT*, constant volume, temperature, and number of atoms; OPM, orientations of proteins in membranes; PDB, protein data bank; PME, particle mesh Ewald method; POPE, 1-palmitoyl-2-oleoyl-*sn*-glycero-3-phosphoethanolamine; RT, residence time; SEM, standard error of the mean; RESPA, reversible multiple time scale molecular dynamics; rms, root mean square; rmsd, root-mean-square deviation; SAR, structure−activity relationship; SASA, solvent accessible surface area; SID, simulation interaction diagram; TM, transmembrane; TI/MD, thermodynamic integration coupled with MD simulations; Tc, TanimotoCombo coefficient; XAC, xanthine amine congener

■ REFERENCES

(1) Fredholm, B. B.; IJzerman, A. P.; Jacobson, K. A.; Linden, J.; Müller, C. E.; Müller, C. E. International Union of Basic and Clinical Pharmacology. LXXXI. Nomenclature and Classification of Adenosine Receptors-An Update. *Pharmacol. Rev* **2011**, *63*, 1−34.

(2) Lebon, G.; Warne, T.; Edwards, P. C.; Bennett, K.; Langmead, C. J.; Leslie, A. G. W.; Tate, C. G. Agonist-Bound Adenosine A2A Receptor Structures Reveal Common Features of GPCR Activation. *Nature* **2011**, *474*, 521−525.

(3) Carpenter, B.; Nehmé, R.; Warne, T.; Leslie, A. G. W.; Tate, C. G. Structure of the Adenosine A2A Receptor Bound to an Engineered G Protein. *Nature* **2016**, *536*, 104−107.

(4) García-Nafría, J.; Lee, Y.; Bai, X.; Carpenter, B.; Tate, C. G. Cryo-EM structure of the adenosine A2A receptor coupled to an engineered heterotrimeric G protein. *Elife* **2018**, *7*, No. e35946.

(5) Jaakola, V.-P.; Griffith, M. T.; Hanson, M. A.; Cherezov, V.; Chien, E. Y. T.; Lane, J. R.; IJzerman, A. P.; Stevens, R. C. The 2.6 Angstrom Crystal Structure of a Human A 2A Adenosine Receptor Bound to an Antagonist. *Science* **2008**, *322*, 1211−1217.

(6) Doré, A. S.; Robertson, N.; Errey, J. C.; Ng, I.; Hollenstein, K.; Tehan, B.; Hurrell, E.; Bennett, K.; Congreve, M.; Magnani, F.; Tate, C. G.; Weir, M.; Marshall, F. H. Structure of the Adenosine A2A Receptor in Complex with ZM241385 and the Xanthines XAC and Caffeine. *Structure* **2011**, *19*, 1283−1293.

(7) Liu, W.; Chun, E.; Thompson, A. A.; Chubukov, P.; Xu, F.; Katritch, V.; Han, G. W.; Roth, C. B.; Heitman, L. H.; IJzerman, A. P.; Cherezov, V.; Stevens, R. C. Structural Basis for Allosteric Regulation of GPCRs by Sodium Ions. *Science* **2012**, *337*, 232−236.

(8) Sun, B.; Bachhawat, P.; Chu, M. L.-H.; Wood, M.; Ceska, T.; Sands, Z. A.; Mercier, J.; Lebon, F.; Kobilka, T. S.; Kobilka, B. K. Crystal Structure of the Adenosine A 2A Receptor Bound to an Antagonist Reveals a Potential Allosteric Pocket. *Proc. Natl. Acad. Sci. U.S.A.* **2017**, *114*, 2066−2071.

(9) Amelia, T.; van Veldhoven, J. P. D.; Falsini, M.; Liu, R.; Heitman, L. H.; van Westen, G. J. P.; Segala, E.; Verdon, G.; Cheng, R. K. Y.; Cooke, R. M.; van der Es, D.; IJzerman, A. P. Crystal Structure and Subsequent Ligand Design of a Nonriboside Partial Agonist Bound to the Adenosine A2A Receptor. *J. Med. Chem.* **2021**, *64*, 3827−3842.

(10) Glukhova, A.; Thal, D. M.; Nguyen, A. T.; Vecchio, E. A.; Jörg, M.; Scammells, P. J.; May, L. T.; Sexton, P. M.; Christopoulos, A. Structure of the Adenosine A1 Receptor Reveals the Basis for Subtype Selectivity. *Cell* **2017**, *168*, 867−877.

(11) Cheng, R. K. Y.; Segala, E.; Robertson, N.; Deflorian, F.; Doré, A. S.; Errey, J. C.; Fiez-Vandal, C.; Marshall, F. H.; Cooke, R. M. Structures of Human A 1 and A 2A Adenosine Receptors with Xanthines Reveal Determinants of Selectivity. *Structure* **2017**, *25*, 1275−1285.

(12) Draper-Joyce, C. J.; Khoshouei, M.; Thal, D. M.; Liang, Y. L.; Nguyen, A. T. N.; Furness, S. G. B.; Venugopal, H.; Baltos, J. A.; Plitzko, J. M.; Danev, R.; Baumeister, W.; May, L. T.; Wootten, D.; Sexton, P. M.; Glukhova, A.; Christopoulos, A. Structure of the Adenosine-Bound Human Adenosine A1 Receptor-Gi Complex. *Nature* **2018**, *558*, 559−563.

(13) Katritch, V.; Jaakola, V. P.; Lane, J. R.; Lin, J.; IJzerman, A. P.; Yeager, M.; Kufareva, I.; Stevens, R. C.; Abagyan, R. Structure-Based Discovery of Novel Chemotypes for Adenosine A2A Receptor Antagonists. *J. Med. Chem.* **2010**, *53*, 1799−1809.

(14) Carlsson, J.; Yoo, L.; Gao, Z. G.; Irwin, J. J.; Shoichet, B. K.; Jacobson, K. A. Structure-Based Discovery of A2A Adenosine Receptor Ligands. *J. Med. Chem.* **2010**, *53*, 3748−3755.

(15) Lenselink, E. B.; Beuming, T.; van Veen, C.; Massink, A.; Sherman, W.; van Vlijmen, H. W. T.; IJzerman, A. P. In Search of Novel Ligands Using a Structure-Based Approach: A Case Study on the Adenosine A2A Receptor. *J. Comput.-Aided Mol. Des.* **2016**, *30*, 863−874.

(16) Cescon, E.; Bolcato, G.; Federico, S.; Bissaro, M.; Valentini, A.; Ferlin, M. G.; Spalluto, G.; Sturlese, M.; Moro, S. Scaffold Repurposing of in-House Chemical Library toward the Identification of New Casein Kinase 1 δ Inhibitors. *ACS Med. Chem. Lett.* **2020**, *11*, 1168−1174.

(17) Langmead, C. J.; Andrews, S. P.; Congreve, M.; Errey, J. C.; Hurrell, E.; Marshall, F. H.; Mason, J. S.; Richardson, C. M.; Robertson, N.; Zhukov, A.; Weir, M. Identification of Novel Adenosine A2A Receptor Antagonists by Virtual Screening. *J. Med. Chem.* **2012**, *55*, 1904−1909.

(18) Jazayeri, A.; Andrews, S. P.; Marshall, F. H. Structurally Enabled Discovery of Adenosine A2a Receptor Antagonists. *Chem. Rev.* **2017**, *117*, 21−37.

(19) Tian, S.; Wang, X.; Li, L.; Zhang, X.; Li, Y.; Zhu, F.; Hou, T.; Zhen, X. Discovery of Novel and Selective Adenosine A2A Receptor Antagonists for Treating Parkinson's Disease through Comparative Structure-Based Virtual Screening. *J. Chem. Inf. Model.* **2017**, *57*, 1474−1487.

(20) Lagarias, P.; Vrontaki, E.; Lambrinidis, G.; Stamatis, D.; Convertino, M.; Ortore, G.; Mavromoustakos, T.; Klotz, K.-N. K. N.; Kolocouris, A. Discovery of Novel Adenosine Receptor Antagonists through a Combined Structure- and Ligand-Based Approach

https://doi.org/10.1021/acs.jmedchem.2c01123
J. Med. Chem. XXXX, XXX, XXX−XXX

Followed by Molecular Dynamics Investigation of Ligand Binding Mode. *J. Chem. Inf. Model.* **2018**, *58*, 794−815.

(21) Barkan, K.; Lagarias, P.; Stampelou, M.; Stamatis, D.; Hoare, S.; Safitri, D.; Klotz, K.-N. N.; Vrontaki, E.; Kolocouris, A.; Ladds, G. Pharmacological Characterisation of Novel Adenosine A3 Receptor Antagonists. *Sci. Rep.* **2020**, *10*, 20781.

(22) Stamatis, D.; Lagarias, P.; Barkan, K.; Vrontaki, E.; Ladds, G.; Kolocouris, A. Structural Characterization of Agonist Binding to an A3 Adenosine Receptor through Biomolecular Simulations and Mutagenesis Experiments. *J. Med. Chem.* **2019**, *62*, 8831−8846.

(23) Lagarias, P.; Barkan, K.; Tzortzini, E.; Stampelou, M.; Vrontaki, E.; Ladds, G.; Kolocouris, A.; Stampelou, M.; Vrontaki, E.; Ladds, G.; Kolocouris, A. Insights to the Binding of a Selective Adenosine A3 Receptor Antagonist Using Molecular Dynamic Simulations, MM-PBSA and MM-GBSA Free Energy Calculations, and Mutagenesis. *J. Chem. Inf. Model.* **2019**, *59*, 5183−5197.

(24) Schenone, S.; Brullo, C.; Musumeci, F.; Bruno, O.; Botta, M. A1 Receptors Ligands: Past, Present and Future Trends. *Curr. Top. Med. Chem.* **2010**, *10*, 878−901.

(25) Modlinger, P. S.; Welch, W. J. Adenosine A1 Receptor Antagonists and the Kidney. *Curr. Opin. Nephrol. Hypertens.* **2003**, *12*, 497−502.

(26) Shah, R. H.; Frishman, W. H. Adenosine1 Receptor Antagonism. *Cardiol. Rev.* **2009**, *17*, 125−131.

(27) Wilson, C. N.; Nadeem, A.; Spina, D.; Brown, R.; Page, C. P.; Mustafa, S. J. Adenosine Receptors and Asthma. In *Handbook of Experimental Pharmacology*; Springer, 2009; Vol. *193*, pp 329−362.

(28) Maemoto, T.; Tada, M.; Mihara, T.; Ueyama, N.; Matsuoka, H.; Harada, K.; Yamaji, T.; Shirakawa, K.; Kuroda, S.; Akahane, A.; Iwashita, A.; Matsuoka, N.; Mutoh, S. Pharmacological Characterization of FR194921, a New Potent, Selective, and Orally Active Antagonist for Central Adenosine A1 Receptors. *J. Pharmacol. Sci.* **2004**, *96*, 42−52.

(29) Trevitt, J.; Vallance, C.; Harris, A.; Goode, T. Adenosine antagonists reverse the cataleptic effects of haloperidol: Implications for the treatment of Parkinson's disease. *Pharmacol., Biochem. Behav.* **2009**, *92*, 521−527.

(30) Borea, P. A.; Varani, K.; Vincenzi, F.; Baraldi, P. G.; Tabrizi, M. A.; Merighi, S.; Gessi, S. The A3Adenosine Receptor: History and Perspectives. *Pharmacol. Rev.* **2015**, *67*, 74−102.

(31) Schulte, G.; Fredholm, B. B. Signaling Pathway from the Human Adenosine A3Receptor Expressed in Chinese Hamster Ovary Cells to the Extracellular Signal-Regulated Kinase 1/2. *Mol. Pharmacol.* **2002**, *62*, 1137−1146.

(32) Lee, J.; Hwang, I.; Lee, J. H.; Lee, H. W.; Jeong, L.-S.; Ha, H. The Selective A3AR Antagonist LJ-1888 Ameliorates UUO-Induced Tubulointerstitial Fibrosis. *Am. J. Pathol.* **2013**, *183*, 1488−1497.

(33) Rabadi, M. M.; Lee, H. T. Adenosine Receptors and Renal Ischaemia Reperfusion Injury. *Acta Physiol.* **2015**, *213*, 222−231.

(34) González-Fernández, E.; Sánchez-Gómez, M. V.; Pérez-Samartín, A.; Arellano, R. O.; Matute, C. A3Adenosine receptors mediate oligodendrocyte death and ischemic damage to optic nerve. *Glia* **2014**, *62*, 199−216.

(35) Baraldi, P. G.; Preti, D.; Borea, P. A.; Varani, K. Medicinal Chemistry of A3 Adenosine Receptor Modulators: Pharmacological Activities and Therapeutic Implications. *J. Med. Chem.* **2012**, *55*, 5676−5703.

(36) Guo, D.; Heitman, L. H.; IJzerman, A. P. Kinetic Aspects of the Interaction between Ligand and G Protein-Coupled Receptor: The Case of the Adenosine Receptors. *Chem. Rev.* **2017**, *117*, 38−66.

(37) Sykes, D. A.; Stoddart, L. A.; Kilpatrick, L. E.; Hill, S. J. Binding Kinetics of Ligands Acting at GPCRs. *Mol. Cell. Endocrinol.* **2019**, *48S*, 9−19.

(38) Xia, L.; Burger, W. A. C.; van Veldhoven, J. P. D.; Kuiper, B. J.; van Duijl, T. T.; Paasman, E. B.; Heitman, E.; IJzerman, L. H.; Ijzerman, A. P. Structure-Affinity Relationships and Structure-Kinetics Relationships of Pyrido[2,1-f]Purine-2,4-Dione Derivatives as Human Adenosine A3 Receptor Antagonists. *J. Med. Chem.* **2017**, *60*, 7555−7568.

(39) Bouzo-Lorenzo, M.; Stoddart, L. A.; Xia, L.; IJzerman, A. P.; Heitman, L. H.; Briddon, S. J.; Hill, S. J. A Live Cell NanoBRET Binding Assay Allows the Study of Ligand-Binding Kinetics to the Adenosine A3 Receptor. *Purinergic Signalling* **2019**, *15*, 139−153.

(40) Guo, D.; van Dorp, E. J. H.; Mulder-Krieger, T.; van Veldhoven, J. P. D.; Brussee, J.; IJzerman, A. P.; Heitman, L. H. Dual-Point Competition Association Assay: A Fast and High-Throughput Kinetic Screening Method for Assessing Ligand-Receptor Binding Kinetics. *J. Biomol. Screening* **2013**, *18*, 309−320.

(41) Guo, D.; Venhorst, S. N.; Massink, A.; van Veldhoven, J. P. D.; Vauquelin, G.; IJzerman, A. P.; Heitman, L. H. Molecular mechanism of allosteric modulation at GPCRs: insight from a binding kinetics study at the human A1adenosine receptor. *Br. J. Pharmacol.* **2014**, *171*, 5295−5312.

(42) Louvel, J.; Guo, D.; Soethoudt, M.; Mocking, T. A. M.; Lenselink, E. B.; Mulder-Krieger, T.; Heitman, L. H.; IJzerman, A. P. Structure-Kinetics Relationships of Capadenoson Derivatives as Adenosine A 1 Receptor Agonists. *Eur. J. Med. Chem.* **2015**, *101*, 681−691.

(43) Müller, C. E.; Diekmann, M.; Thorand, M.; Ozola, V. [3H]8-Ethyl-4-Methyl-2-Phenyl-(8R)-4,5,7,8-Tetrahydro-1H-Imidazo[2,1-i]-Purin-5-One ([3H]PSB-11), a Novel High-Affinity Antagonist Radioligand for Human A3 Adenosine Receptors. *Bioorg. Med. Chem. Lett.* **2002**, *12*, 501−503.

(44) Varani, K.; Merighi, S.; Gessi, S.; Klotz, K. N.; Leung, E.; Baraldi, P. G.; Cacciari, B.; Romagnoli, R.; Spalluto, G.; Borea, P. A. [3H]MRE 3008F20: A Novel Antagonist Radioligand for the Pharmacological and Biochemical Characterization of Human A3 Adenosine Receptors. *Mol. Pharmacol.* **2000**, *57*, 968−975.

(45) Massova, I.; Kollman, P. A. Combined Molecular Mechanical and Continuum Solvent Approach (MM- PBSA/GBSA) to Predict Ligand Binding. *Perspect. Drug Discov. Des.* **2000**, *18*, 113−135.

(46) Greene, D.; Qi, R.; Nguyen, R.; Qiu, T.; Luo, R. Heterogeneous Dielectric Implicit Membrane Model for the Calculation of MMPBSA Binding Free Energies. *J. Chem. Inf. Model.* **2019**, *59*, 3041−3056.

(47) Aldeghi, M.; Bodkin, M. J.; Knapp, S.; Biggin, P. C. Statistical Analysis on the Performance of Molecular Mechanics Poisson-Boltzmann Surface Area versus Absolute Binding Free Energy Calculations: Bromodomains as a Case Study. *J. Chem. Inf. Model.* **2017**, *57*, 2203−2221.

(48) Lenselink, E. B.; Louvel, J.; Forti, A. F.; van Veldhoven, J. P. D.; de Vries, H.; Mulder-Krieger, T.; McRobb, F. M.; Negri, A.; Goose, J.; Abel, R.; van Vlijmen, H. W. T.; Wang, L.; Harder, E.; Sherman, W.; IJzerman, A. P.; Beuming, T. Predicting Binding Affinities for GPCR Ligands Using Free-Energy Perturbation. *ACS Omega* **2016**, *1*, 293−304.

(49) Hawkins, P. C. D.; Skillman, A. G.; Nicholls, A. Comparison of Shape-Matching and Docking as Virtual Screening Tools. *J. Med. Chem.* **2007**, *50*, 74−82.

(50) Gaulton, A.; Bellis, L. J.; Bento, A. P.; Chambers, J.; Davies, M.; Hersey, A.; Light, Y.; McGlinchey, S.; Michalovich, D.; Al-Lazikani, B.; Overington, J. P. ChEMBL: A Large-Scale Bioactivity Database for Drug Discovery. *Nucleic Acids Res.* **2012**, *40*, D1100−D1107.

(51) Bento, A. P.; Gaulton, A.; Hersey, A.; Bellis, L. J.; Chambers, J.; Davies, M.; Krüger, F. A.; Light, Y.; Mak, L.; McGlinchey, S.; Nowotka, M.; Papadatos, G.; Santos, R.; Overington, J. P. The ChEMBL Bioactivity Database: An Update. *Nucleic Acids Res.* **2014**, *42*, D1083−D1090.

(52) Kim, Y.; de Castro, S.; Gao, Z.-G.; IJzerman, A. P.; Jacobson, K. A. Novel 2- and 4-Substituted 1H-Imidazo[4,5-c]quinolin-4-amine Derivatives as Allosteric Modulators of the A3 Adenosine Receptor. *J. Med. Chem.* **2009**, *52*, 2098−2108.

(53) Heitman, L. H.; Göblyös, A.; Zweemer, A. M.; Bakker, R.; Mulder-Krieger, T.; van Veldhoven, J. P. D.; de Vries, H.; Brussee, J.; IJzerman, A. P. A Series of 2,4-Disubstituted Quinolines as a New Class of Allosteric Enhancers of the Adenosine A3 Receptor. *J. Med. Chem.* **2009**, *52*, 926−931.

(54) Slee, D. H.; Chen, Y.; Zhang, X.; Moorjani, M.; Lanier, M. C.; Lin, E.; Rueter, J. K.; Williams, J. P.; Lechner, S. M.; Markison, S.;

Malany, S.; Santos, M.; Gross, R. S.; Jalali, K.; Sai, Y.; Zuo, Z.; Yang, C.; Castro-Palomino, J. C.; Crespo, M. I.; Prat, M.; Gual, S.; Díaz, J.-L.; Saunders, J. 2-Amino-N-pyrimidin-4-ylacetamides as A2A Receptor Antagonists: 1. Structure−Activity Relationships and Optimization of Heterocyclic Substituents. *J. Med. Chem.* **2008**, *51*, 1719−1729.

(55) Francis, J. E.; Webb, R. L.; Ghai, G. R.; Hutchison, A. J.; Moskal, M. A.; DeJesus, R.; Yokoyama, R.; Rovinski, S. L.; Contardo, N. Highly Selective Adenosine A2 Receptor Agonists in a Series of N-Alkylated 2-Aminoadenosines. *J. Med. Chem.* **1991**, *34*, 2570−2579.

(56) Siddiqi, S. M.; Jacobson, K. A.; Esker, J. L.; Olah, M. E.; Ji, X.; Melman, N.; Tiwari, K. N.; Secrist, J. A.; Schneller, S. W. Search for New Purine- and Ribose-Modified Adenosine Analogs as Selective Agonists and Antagonists at Adenosine Receptors. *J. Med. Chem.* **1995**, *38*, 1174−1188.

(57) Roelen, H.; Veldman, N.; Spek, A. L.; von Frijtag Drabbe Künzel, J.; Mathôt, R. A. A.; IJzerman, A. P. N6,C8-Disubstituted Adenosine Derivatives as Partial Agonists for Adenosine A1 Receptors. *J. Med. Chem.* **1996**, *39*, 1463−1471.

(58) Tchilibon, S.; Joshi, B. V.; Kim, S.-K.; Duong, H. T.; Gao, Z.-G.; Jacobson, K. A. (N)-Methanocarba 2,N6-Disubstituted Adenine Nucleosides as Highly Potent and Selective A3 Adenosine Receptor Agonists. *J. Med. Chem.* **2005**, *48*, 1745−1758.

(59) Weston, C.; Poyner, D.; Patel, V.; Dowell, S.; Ladds, G. Investigating G Protein Signalling Bias at the Glucagon-like Peptide-1 Receptor in Yeast. *Br. J. Pharmacol.* **2014**, *171*, 3651−3665.

(60) Knight, A.; Hemmings, J. L.; Winfield, I.; Leuenberger, M.; Frattini, E.; Frenguelli, B. G.; Dowell, S. J.; Lochner, M.; Ladds, G. Discovery of Novel Adenosine Receptor Agonists That Exhibit Subtype Selectivity. *J. Med. Chem.* **2016**, *59*, 947−964.

(61) Zhang, G.; Liu, Y.; Ruoho, A. E.; Hurley, J. H. Structure of the Adenylyl Cyclase Catalytic Core. *Nature* **1997**, *386*, 247−253.

(62) Cheong, S. L.; Venkatesan, G.; Paira, P.; Jothibasu, R.; Mandel, A. L.; Federico, S.; Spalluto, G.; Pastorin, G. Pyrazolo Derivatives as Potent Adenosine Receptor Antagonists: An Overview on the Structure-Activity Relationships. *Int. J. Med. Chem.* **2011**, *2011*, 1−15.

(63) Tallarida, R. J.; Murray, R. B. *Manual of Pharmacologic Calculations*; Springer New York: New York, NY, 1986.

(64) Stoddart, L. A.; Vernall, A. J.; Denman, J. L.; Briddon, S. J.; Kellam, B.; Hill, S. J. Fragment Screening at Adenosine-A3 Receptors in Living Cells Using a Fluorescence-Based Binding Assay. *Chem. Biol.* **2012**, *19*, 1105−1115.

(65) Vauquelin, G. Effects of target binding kinetics onin vivodrug efficacy: koff, konand rebinding. *Br. J. Pharmacol.* **2016**, *173*, 2319−2334.

(66) Jones, G.; Willett, P.; Glen, R. C.; Leach, A. R.; Taylor, R. Development and Validation of a Genetic Algorithm for Flexible Docking. *J. Mol. Biol.* **1997**, *267*, 727−748.

(67) Eldridge, M. D.; Murray, C. W.; Auton, T. R.; Paolini, G. V.; Mee, R. P. Empirical Scoring Functions: I. The Development of a Fast Empirical Scoring Function to Estimate the Binding Affinity of Ligands in Receptor Complexes. *J. Comput.-Aided Mol. Des.* **1997**, *11*, 425−445.

(68) Wang, J.; Cieplak, P.; Kollman, P. A. How Well Does a Restrained Electrostatic Potential (RESP) Model Perform in Calculating Conformational Energies of Organic and Biological Molecules? *J. Comput. Chem.* **2000**, *21*, 1049−1074.

(69) Hornak, V.; Abel, R.; Okur, A.; Strockbine, B.; Roitberg, A.; Simmerling, C. Comparison of Multiple Amber Force Fields and Development of Improved Protein Backbone Parameters. *Proteins: Struct., Funct., Genet.* **2006**, *65*, 712−725.

(70) Jespers, W.; Schiedel, A. C.; Heitman, L. H.; Cooke, R. M.; Kleene, L.; van Westen, G. J. P.; Gloriam, D. E.; Müller, C. E.; Sotelo, E.; Gutiérrez-de-Terán, H. Structural Mapping of Adenosine Receptor Mutations: Ligand Binding and Signaling Mechanisms. *Trends Pharmacol. Sci.* **2018**, *39*, 75−89.

(71) Kim, J.; Wess, J.; van Rhee, A. M. M.; Schöneberg, T.; Jacobson, K. A. Site-directed Mutagenesis Identifies Residues Involved in Ligand Recognition in the Human A2a Adenosine Receptor. *J. Biol. Chem.* **1995**, *270*, 13987−13997.

(72) Jiang, Q.; Van Rhee, A. M.; Kim, J.; Yehle, S.; Wess, J.; Jacobson, K. A. Hydrophilic side chains in the third and seventh transmembrane helical domains of human A2A adenosine receptors are required for ligand recognition. *Mol. Pharmacol.* **1996**, *50*, 512−521.

(73) Gao, Z.-G. G.; Chen, A.; Barak, D.; Kim, S. K.; Müller, C. E.; Jacobson, K. A. Identification by Site-directed Mutagenesis of Residues Involved in Ligand Recognition and Activation of the Human A3 Adenosine Receptor. *J. Biol. Chem.* **2002**, *277*, 19056−19063.

(74) Lane, J. R.; Klein Herenbrink, C. K.; van Westen, G. J. P.; Spoorendonk, J. A.; Hoffmann, C.; IJzerman, A. P. A Novel Nonribose Agonist, LUF5834, Engages Residues That Are Distinct from Those of Adenosine-Like Ligands to Activate the Adenosine A2a Receptor. *Mol. Pharmacol.* **2012**, *81*, 475−487.

(75) Matricon, P.; Vo, D. D.; Gao, Z.-G.; Kihlberg, J.; Jacobson, K. A.; Carlsson, J. Fragment-Based Design of Selective GPCR Ligands Guided by Free Energy Simulations. *Chem. Commun.* **2021**, *57*, 12305−12308.

(76) Deflorian, F.; Perez-Benito, L.; Lenselink, E. B.; Congreve, M.; van Vlijmen, H. W. T.; Mason, J. S.; Graaf, C.; Tresadern, G. Accurate Prediction of GPCR Ligand Binding Affinity with Free Energy Perturbation. *J. Chem. Inf. Model.* **2020**, *60*, 5563−5579.

(77) Matricon, P.; Ranganathan, A.; Warnick, E.; Gao, Z.-G.; Rudling, A.; Lambertucci, C.; Marucci, G.; Ezzati, A.; Jaiteh, M.; Dal Ben, D.; Jacobson, K. A.; Carlsson, J. Fragment Optimization for GPCRs by Molecular Dynamics Free Energy Calculations: Probing Druggable Subpockets of the A 2A Adenosine Receptor Binding Site. *Sci. Rep.* **2017**, *7*, 6398.

(78) Wan, S.; Potterton, A.; Husseini, F. S.; Wright, D. W.; Heifetz, A.; Malawski, M.; Townsend-Nicholson, A.; Coveney, P. V. Hit-to-lead and lead optimization binding free energy calculations for G protein-coupled receptors. *Interface Focus* **2020**, *10*, 20190128.

(79) Cappel, D.; Hall, M. L.; Lenselink, E. B.; Beuming, T.; Qi, J.; Bradner, J.; Sherman, W. Relative Binding Free Energy Calculations Applied to Protein Homology Models. *J. Chem. Inf. Model.* **2016**, *56*, 2388−2400.

(80) Keränen, H.; Åqvist, J.; Gutiérrez-de-Terán, H. Free Energy Calculations of A2A Adenosine Receptor Mutation Effects on Agonist Binding. *Chem. Commun.* **2015**, *51*, 3522−3525.

(81) Matricon, P.; Suresh, R. R.; Gao, Z.-G.; Panel, N.; Jacobson, K. A.; Carlsson, J. Ligand Design by Targeting a Binding Site Water. *Chem. Sci.* **2021**, *12*, 960−968.

(82) Jespers, W.; Oliveira, A.; Prieto-Díaz, R.; Majellaro, M.; Åqvist, J.; Sotelo, E.; Gutiérrez-de-Terán, H. Structure-Based Design of Potent and Selective Ligands at the Four Adenosine Receptors. *Molecules* **2017**, *22*, 1945.

(83) Pohorille, A.; Jarzynski, C.; Chipot, C. Good Practices in Free-Energy Calculations. *J. Phys. Chem. B* **2010**, *114*, 10235−10253.

(84) He, X.; Liu, S.; Lee, T.-S.; Ji, B.; Man, V. H.; York, D. M.; Wang, J. Fast, Accurate, and Reliable Protocols for Routine Calculations of Protein-Ligand Binding Affinities in Drug Design Projects Using AMBER GPU-TI with ff14SB/GAFF. *ACS Omega* **2020**, *5*, 4611−4619.

(85) Song, L. F.; Lee, T.-S.; Zhu, C.; York, D. M.; Merz, K. M. Using AMBER18 for Relative Free Energy Calculations. *J. Chem. Inf. Model.* **2019**, *59*, 3128−3135.

(86) Pearlman, D. A.; Charifson, P. S. Are Free Energy Calculations Useful in Practice? A Comparison with Rapid Scoring Functions for the P38 MAP Kinase Protein System. *J. Med. Chem.* **2001**, *44*, 3417−3423.

(87) Tanizaki, S.; Feig, M. A Generalized Born Formalism for Heterogeneous Dielectric Environments: Application to the Implicit Modeling of Biological Membranes. *J. Chem. Phys.* **2005**, *122*, 124706.

(88) Kaminski, G. A.; Friesner, R. A.; Tirado-Rives, J.; Jorgensen, W. L. Evaluation and Reparametrization of the OPLS-AA Force Field for

https://doi.org/10.1021/acs.jmedchem.2c01123
J. Med. Chem. XXXX, XXX, XXX−XXX

Proteins via Comparison with Accurate Quantum Chemical Calculations on Peptides. *J. Phys. Chem. B* **2001**, *105*, 6474−6487.

(89) Shivakumar, D.; Williams, J.; Wu, Y. J.; Damm, W.; Shelley, J.; Sherman, W. Prediction of Absolute Solvation Free Energies Using Molecular Dynamics Free Energy Perturbation and the OPLS Force Field. *J. Chem. Theory Comput.* **2010**, *6*, 1509−1519.

(90) Wan, S.; Bhati, A. P.; Zasada, S. J.; Wall, I.; Green, D.; Bamborough, P.; Coveney, P. V. Rapid and Reliable Binding Affinity Prediction of Bromodomain Inhibitors: A Computational Study. *J. Chem. Theory Comput.* **2017**, *13*, 784−795.

(91) Hoare, S. R. J.; Fleck, B. A.; Williams, J. P.; Grigoriadis, D. E. The importance of target binding kinetics for measuring target binding affinity in drug discovery: a case study from a CRF1 receptor antagonist program. *Today* **2020**, *25*, 7−14.

(92) Dawson, E. S.; Wells, J. N. Determination of Amino Acid Residues that are Accessible from the Ligand Binding Crevice in the Seventh Transmembrane-Spanning Region of the Human A1Adenosine Receptor. *Mol. Pharmacol.* **2001**, *59*, 1187−1195.

(93) Deganutti, G.; Barkan, K.; Ladds, G.; Reynolds, C. A. Multisite Model of Allosterism for the Adenosine A1 Receptor. *J. Chem. Inf. Model.* **2021**, *61*, 2001−2015.

(94) Motulsky, H. J.; Mahan, L. C. The Kinetics of Competitive Radioligand Binding Predicted by the Law of Mass Action. *Mol. Pharmacol.* **1984**, *25*, 1−9.

(95) Stoddart, L. A.; Johnstone, E. K. M.; Wheal, A. J.; Goulding, J.; Robers, M. B.; Machleidt, T.; Wood, K. V.; Hill, S. J.; Pfleger, K. D. G. Application of BRET to monitor ligand binding to GPCRs. *Methods* **2015**, *12*, 661−663.

(96) Curtis, M. J.; Alexander, S.; Cirino, G.; Docherty, J. R.; George, C. H.; Giembycz, M. A.; Hoyer, D.; Insel, P. A.; Izzo, A. A.; Ji, Y.; MacEwan, D. J.; Sobey, C. G.; Stanford, S. C.; Teixeira, M. M.; Wonnacott, S.; Ahluwalia, A. Experimental Design and Analysis and Their Reporting II: Updated and Simplified Guidance for Authors and Peer Reviewers. *Br. J. Pharmacol.* **2018**, *175*, 987−993.

(97) Halgren, T. T. A. Merck Molecular Force Field. I. Basis, Form, Scope, Parameterization, and Performance of MMFF94. *J. Comput. Chem.* **1996**, *17*, 490−519.

(98) Shelley, J. C.; Cholleti, A.; Frye, L. L.; Greenwood, J. R.; Timlin, M. R.; Uchimaya, M. Epik: A Software Program for PK a Prediction and Protonation State Generation for Drug-like Molecules. *J. Comput.-Aided Mol. Des.* **2007**, *21*, 681−691.

(99) Duan, J.; Dixon, S. L.; Lowrie, J. F.; Sherman, W. Analysis and Comparison of 2D Fingerprints: Insights into Database Screening Performance Using Eight Fingerprint Methods. *J. Mol. Graphics Modell.* **2010**, *29*, 157−170.

(100) Sastry, G. M.; Adzhigirey, M.; Day, T.; Annabhimoju, R.; Sherman, W. Protein and Ligand Preparation: Parameters, Protocols, and Influence on Virtual Screening Enrichments. *J. Comput.-Aided Mol. Des.* **2013**, *27*, 221−234.

(101) Mohamadi, F.; Richards, N. G. J.; Guida, W. C.; Liskamp, R.; Lipton, M.; Caufield, C.; Chang, G.; Hendrickson, T.; Still, W. C. Macromodel?An Integrated Software System for Modeling Organic and Bioorganic Molecules Using Molecular Mechanics. *J. Comput. Chem.* **1990**, *11*, 440−467.

(102) Lomize, M. A.; Pogozheva, I. D.; Joo, H.; Mosberg, H. I.; Lomize, A. L. OPM database and PPM web server: resources for positioning of proteins in membranes. *Nucleic Acids Res.* **2012**, *40*, D370−D376.

(103) Jorgensen, W. L.; Chandrasekhar, J.; Madura, J. D.; Impey, R. W.; Klein, M. L. Comparison of Simple Potential Functions for Simulating Liquid Water. *J. Chem. Phys.* **1983**, *79*, 926−935.

(104) Wang, J.; Wolf, R. M.; Caldwell, J. W.; Kollman, P. A.; Case, D. A. Development and Testing of a General Amber Force Field. *J. Comput. Chem.* **2004**, *25*, 1157−1174.

(105) Bayly, C. I.; Cieplak, P.; Cornell, W. D.; Kollman, P. A. A Well-Behaved Electrostatic Potential Based Method Using Charge Restraints for Deriving Atomic Charges: The RESP Model. *J. Phys. Chem.* **1993**, *97*, 10269−10280.

(106) Risch, M. J.; Trucks, G. W.; Schlegel, H. B.; Scuseria, G. E.; Robb, M. A.; Cheeseman, J. R.; Montgomery, J. A., Jr.; Vreven, T.; Kudin, K. N.; Burant, J. C.; Millam, J. M.; Iyengar, S. S.; Tomasi, J.; Barone, V.; Mennucci, B.; Cossi, M.; Scalmani, G.; Re, J. A. *Gaussian 03*, 2007.

(107) Davidson, E. R.; Feller, D. Basis Set Selection for Molecular Calculations. *Chem. Rev.* **1986**, *86*, 681−696.

(108) Case, D. A.; Ben-Shalom, I. Y.; Brozell, S. R.; Cerutti, D. S.; Cheatham, T. E., III; Darden, T. A.; Duke, R. E.; Ghoreishi, D.; Gilson, M. K.; Gohlke, H.; Goetz, A. W.; Greene, D.; Harris, R.; Homeyer, N.; Izadi, S.; Kovalenko, A.; Kurtzman, T.; Lee, T. S.; LeGrand, S.; Li, P.; Lin, C.; Liu, J.; Luchko, T.; Luo, R.; Mermelstein, D. J.; Merz, K. M.; Miao, Y.; Monard, G.; Nguyen, C.; Nguyen, H.; Omelyan, I.; Onufriev, A.; Pan, F.; Qi, R.; Roe, D. R.; Roitberg, A.; Sagui, C.; Schott-Verdugo, S.; Shen, J.; Simmerling, C. L.; Smith, J.; Salomon-Ferrer, R.; Swails, J.; Walker, R. C.; Wang, J.; Wei, H.; Wolf, R. M.; Wu, X.; Xiao, L.; York, D. M.; Kollman, P. A. *AMBER 2018*; University of California, 2018.

(109) Koynova, R.; Caffrey, M. Phases and phase transitions of the phosphatidylcholines. *Biochim. Biophys. Acta, Rev. Biomembr.* **1998**, *1376*, 91−145.

(110) Darden, T.; York, D.; Pedersen, L. Particle mesh Ewald: AnN log(N) method for Ewald sums in large systems. *J. Chem. Phys.* **1993**, *98*, 10089−10092.

(111) Essmann, U.; Perera, L.; Berkowitz, M. L.; Darden, T.; Lee, H.; Pedersen, L. G. A Smooth Particle Mesh Ewald Method. *J. Chem. Phys.* **1995**, *103*, 8577−8593.

(112) Ryckaert, J.-P.; Ciccotti, G.; Berendsen, H. J. Numerical Integration of the Cartesian Equations of Motion of a System with Constraints: Molecular Dynamics of n-Alkanes. *J. Comput. Phys.* **1977**, *23*, 327−341.

(113) Balusek, C.; Hwang, H.; Lau, C. H.; Lundquist, K.; Hazel, A.; Pavlova, A.; Lynch, D. L.; Reggio, P. H.; Wang, Y.; Gumbart, J. C. Accelerating Membrane Simulations with Hydrogen Mass Repartitioning. *J. Chem. Theory Comput.* **2019**, *15*, 4673−4686.

(114) Martyna, G. J.; Klein, M. L.; Tuckerman, M. Nosé-Hoover chains: The canonical ensemble via continuous dynamics. *J. Chem. Phys.* **1992**, *97*, 2635−2643.

(115) Martyna, G. J.; Tobias, D. J.; Klein, M. L. Constant Pressure Molecular Dynamics Algorithms. *J. Chem. Phys.* **1994**, *101*, 4177−4189.

(116) Humphreys, D. D.; Friesner, R. A.; Berne, B. J. A Multiple-Time-Step Molecular Dynamics Algorithm for Macromolecules. *J. Phys. Chem.* **1994**, *98*, 6885−6892.

(117) Bowers, K. J.; Chow, E.; Xu, H.; Dror, R. O.; Eastwood, M. P.; Gregersen, B. A.; Klepeis, J. L.; Kolossvary, I.; Moraes, M. A.; Sacerdoti, F. D.; Salmon, J. K.; Shan, Y.; Shaw, D. E. Scalable Algorithms for Molecular Dynamics Simulations on Commodity Clusters. *Proceedings of the 2006 ACM/IEEE Conference on Supercomputing, SC'06*; ACM Press: New York, USA, 2006; p 84.

(118) Maffucci, I.; Contini, A. Explicit Ligand Hydration Shells Improve the Correlation between MM-PB/GBSA Binding Energies and Experimental Activities. *J. Chem. Theory Comput.* **2013**, *9*, 2706−2717.

(119) Michaud-Agrawal, N.; Denning, E. J.; Woolf, T. B.; Beckstein, O. MDAnalysis: A Toolkit for the Analysis of Molecular Dynamics Simulations. *J. Comput. Chem.* **2011**, *32*, 2319−2327.

(120) Genheden, S.; Ryde, U. The MM/PBSA and MM/GBSA Methods to Estimate Ligand-Binding Affinities. *Expert Opin. Drug Discovery* **2015**, *10*, 449−461.

(121) Homeyer, N.; Gohlke, H. Free Energy Calculations by the Molecular Mechanics Poisson−Boltzmann Surface Area Method. *Mol. Inf.* **2012**, *31*, 114−122.

(122) Qiu, D.; Shenkin, P. S.; Hollinger, F. P.; Still, W. C. The GB/SA Continuum Model for Solvation. A Fast Analytical Method for the Calculation of Approximate Born Radii. *J. Phys. Chem. A* **1997**, *101*, 3005−3014.

https://doi.org/10.1021/acs.jmedchem.2c01123
J. Med. Chem. XXXX, XXX, XXX−XXX

(123) Gohlke, H.; Case, D. A. Converging Free Energy Estimates: MM-PB(GB)SA Studies on the Protein-Protein Complex Ras-Raf. *J. Comput. Chem.* **2004**, *25*, 238−250.
(124) Kirkwood, J. G. Statistical Mechanics of Fluid Mixtures. *J. Chem. Phys.* **1935**, *3*, 300.
(125) Procacci, P. Multiple Bennett Acceptance Ratio Made Easy for Replica Exchange Simulations. *J. Chem. Phys.* **2013**, *139*, 124105.
(126) Genheden, S.; Nilsson, I.; Ryde, U. Binding Affinities of Factor Xa Inhibitors Estimated by Thermodynamic Integration and MM/GBSA. *J. Chem. Inf. Model.* **2011**, *51*, 947−958.
(127) Steinbrecher, T.; Joung, I.; Case, D. A. Soft-Core Potentials in Thermodynamic Integration: Comparing One- and Two-Step Transformations. *J. Comput. Chem.* **2011**, *32*, 3253−3263.
(128) Shirts, M. R.; Pande, V. S. Comparison of Efficiency and Bias of Free Energies Computed by Exponential Averaging, the Bennett Acceptance Ratio, and Thermodynamic Integration. *J. Chem. Phys.* **2005**, *122*, 144107.
(129) Jo, S.; Kim, T.; Iyer, V. G.; Im, W. CHARMM-GUI: A Web-Based Graphical User Interface for CHARMM. *J. Comput. Chem.* **2008**, *29*, 1859−1865.
(130) Case, D. A., Ben-Shalom, I. Y., Brozell, S. R., Cerutti, D. S., Cheatham, T. E., III, Cruzeiro, V. W. D.; Duke, R. E., Ghoreishi, D., Gilson, M. K., Gohlke, H., Goetz, A. W., Greene, D., Harris, R., Homeyer, N., Izadi, Y. H. S., Kovalenko, A., Kurtzman, T., Lee, T. S., LeGrand, S., Li, P., Lin, C., Liu, J., Luchko, T., Luo, R., Mermelstein, D. J., Merz, K. M., Miao, Y., Monard, G., Nguyen, C., Nguyen, H., Omelyan, I., Onufriev, A., Pan, F., Qi, R., Roe, D. R., Roitberg, A., Sagui, C., Schott-Verdugo, S., Shen, J., Simmerling, C. L., Smith, J., SalomonFerrer, R., Swails, J., Walker, R. C., Wang, J., Wei, H., Wolf, R. M., Wu, X., Xiao, L. *AMBER18*, 2018.
(131) Maier, J. A.; Martinez, C.; Kasavajhala, K.; Wickstrom, L.; Hauser, K. E.; Simmerling, C. Ff14SB: Improving the Accuracy of Protein Side Chain and Backbone Parameters from Ff99SB. *J. Chem. Theory Comput.* **2015**, *11*, 3696−3713.
(132) Wang, J.; Wang, W.; Kollman, P. A.; Case, D. A. Automatic atom type and bond type perception in molecular mechanical calculations. *J. Mol. Graphics Modell.* **2006**, *25*, 247−260.
(133) Feller, S. E.; Zhang, Y.; Pastor, R. W.; Brooks, B. R. Constant Pressure Molecular Dynamics Simulation: The Langevin Piston Method. *J. Chem. Phys.* **1995**, *103*, 4613−4621.
(134) Izaguirre, J. A.; Catarello, D. P.; Wozniak, J. M.; Skeel, R. D. Langevin Stabilization of Molecular Dynamics. *J. Chem. Phys.* **2001**, *114*, 2090−2098.
(135) Salomon-Ferrer, R.; Case, D. A.; Walker, R. C. An Overview of the Amber Biomolecular Simulation Package. *Wiley Interdiscip. Rev.: Comput. Mol. Sci.* **2013**, *3*, 198−210.
(136) Berendsen, H. J. C.; Postma, J. P. M.; van Gunsteren, W. F.; Haak, A.; Haak, J. R. Molecular Dynamics with Coupling to an External Bath. *J. Chem. Phys.* **1984**, *81*, 3684−3690.
(137) Lee, T. S.; Hu, Y.; Sherborne, B.; Guo, Z.; York, D. M. Toward Fast and Accurate Binding Affinity Prediction with pmemdGTI: An Efficient Implementation of GPU-Accelerated Thermodynamic Integration. *J. Chem. Theory Comput.* **2017**, *13*, 3077−3084.
(138) Su, P.-C.; Johnson, M. E. Evaluating Thermodynamic Integration Performance of the New Amber Molecular Dynamics Package and Assess Potential Halogen Bonds of Enoyl-ACP Reductase (FabI) Benzimidazole Inhibitors. *J. Comput. Chem.* **2016**, *37*, 836−847.

Appendix 5. Suchankova, et al. 2022

This appendix contains:

Suchankova, A.*, Stampelou, M.*, Koutsouki, K., Pousias, A., Dhingra, L., Barkan, K., Pouli, N., Marakos, P., Tenta, R., Kolocouris, A., Lougiakis, N., Ladds, G., 2022. Discovery of a High Affinity Adenosine A1/A3 Receptor Antagonist with a Novel 7-Amino-pyrazolo[3,4-d]pyridazine Scaffold. ACS Med. Chem. Lett. 13, 923–934. https://doi.org/10.1021/acsmedchemlett.2c00052 (* both authors contributed equally).

ACS Medicinal Chemistry Letters

pubs.acs.org/acsmedchemlett Letter

Discovery of a High Affinity Adenosine A_1/A_3 Receptor Antagonist with a Novel 7-Amino-pyrazolo[3,4-*d*]pyridazine Scaffold

Anna Suchankova,[†] Margarita Stampelou,[†] Klontiana Koutsouki,[†] Athanasios Pousias, Lakshiv Dhingra, Kerry Barkan, Nicole Pouli, Panagiotis Marakos, Roxane Tenta, Antonios Kolocouris,* Nikolaos Lougiakis,* and Graham Ladds*

Cite This: https://doi.org/10.1021/acsmedchemlett.2c00052 Read Online

ACCESS | Metrics & More | Article Recommendations | Supporting Information

ABSTRACT: Here we describe the design and synthesis of pyrazolo[3,4-*d*]pyridazines as adenosine receptor (AR) ligands. We demonstrate that the introduction of a 3-phenyl group, together with a 7-benzylamino and 1-methyl group at the pyrazolopyridazine scaffold, generated the antagonist compound **10b**, which displayed 21 nM affinity and a residence time of ∼60 min, for the human A_1R, 55 nM affinity and a residence time of ∼73 min, for the human A_3R and 1.7 μM affinity for the human A_{2B}R while not being toxic. Strikingly, the 2-methyl analog of **10b**, **15b**, had no significant affinity. Docking calculations and molecular dynamics simulations of the ligands inside the orthosteric binding area suggested that the 2-methyl group in **15b** hinders the formation of hydrogen bonding interactions with $N^{6.55}$ which are considered critical for the stabilization inside the orthosteric binding cavity. We, therefore, demonstrate that **10a** is a novel scaffold for the development of high affinity AR ligands. From the mutagenesis experiments the biggest effect was observed for the $Y271^{7.46}A$ mutation which caused an ∼10-fold reduction in the binding affinity of **10b**.

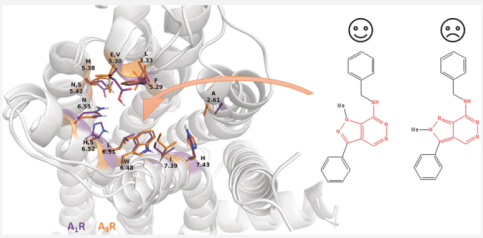

KEYWORDS: *Adenosine A_1 receptor, adenosine A_3 receptor, adenosine A_{2B} receptor, antagonist, binding kinetics, BRET, cAMP, cytotoxicity, molecular dynamics, mutagenesis, residence time*

Adenosine, a naturally occurring purine nucleoside, is the endogenous agonist of adenosine receptors (ARs).[1] ARs are G protein-coupled receptors (GPCRs) comprising four subtypes; A_1, A_{2A}, A_{2B}, and A_3. The A_{2A} and A_{2B} subtypes act synergistically with $G\alpha_s$ stimulating adenylyl cyclase and, therefore, increasing 3′,5′-cyclic adenosine monophosphate (cAMP) levels. In contrast, A_1 and A_3 receptor subtypes inhibit adenylyl cyclase and decrease cAMP levels by coupling to the $G_{i/o}$ family of G proteins.

In the last two decades numerous heterocyclic compounds have been synthesized as AR ligands including xanthines and bi- or tricyclic fused heterocyclic analogues, e.g., purines, deazapurines, pyrazolopyridines, imidazotriazines, thienopyridazines, naphthyridines, pyridopyrimidines, and pyrazoloquinolines.[2−4]

Different therapeutic applications have been identified in preclinical and clinical studies for A_1R antagonists as potassium-sparing diuretic agents with kidney-protecting properties,[2] treatments for chronic lung diseases such as asthma,[5,6] and possible use in Parkinson's disease.[7]

A_3R has been reported to be overexpressed in several types of cancer cells and is, thus, considered as a biological marker for tumors.[8] In a recent study, the potent and selective A_3R antagonist LJ-1888 ((2*R*,3*R*,4*S*)-2-[2-chloro-6-(3-iodobenzylamino)-9H-purine-9-yl]tetrahydrothiophene-3,4-diol) blocked the development and attenuated the progression of renal interstitial fibrosis,[9] while A_3R antagonists have demonstrated efficacy in eye pathologies by lowering intraocular pressure.[10]

While the binding mode of several agonists and antagonists at A_1R has been revealed with X-ray crystallography or cryogenic electron microscopy,[11−13] the experimental structures for A_3R and A_{2B}R have, to date, not been resolved, and only homology models can be used for these AR subtypes.

By the repurposing of antiproliferative aromatic condensed nitrogen heterocycles, we previously identified nanomolar affinity pyrazolo[3,4-*c*]pyridine A_1R/A_3R antagonists.[14] It has been reported that non-xanthine pyrazolo derivatives that potently bind ARs are pyrazolo[4,3-*d*]pyrimidines,[3] pyrazolo-

Received: February 11, 2022
Accepted: May 24, 2022

Scheme 1. Synthesis of 4a,b and 5a,b[a]

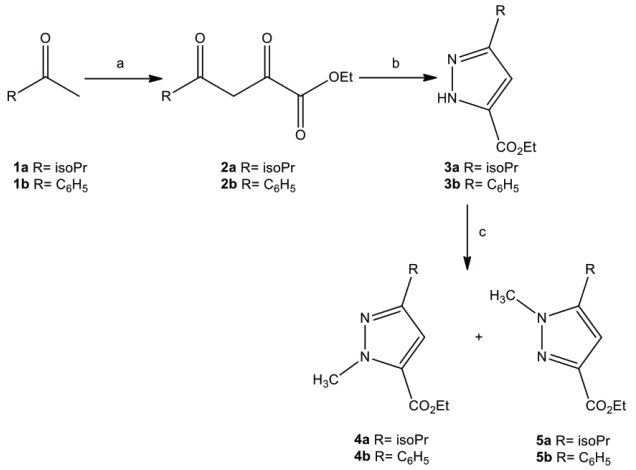

[a]Reagents and conditions: (a) diethyl oxalate, NaH 60%, toluene dry, 50°C, 2 h; (b) NH_2NH_2 80%, EtOH, reflux, 90 min; (c) (i) NaH 60%, DMF dry, 0 °C, 15 min, (ii) CH_3I, rt, 1 h.

Scheme 2. Synthesis of 10a−c[a]

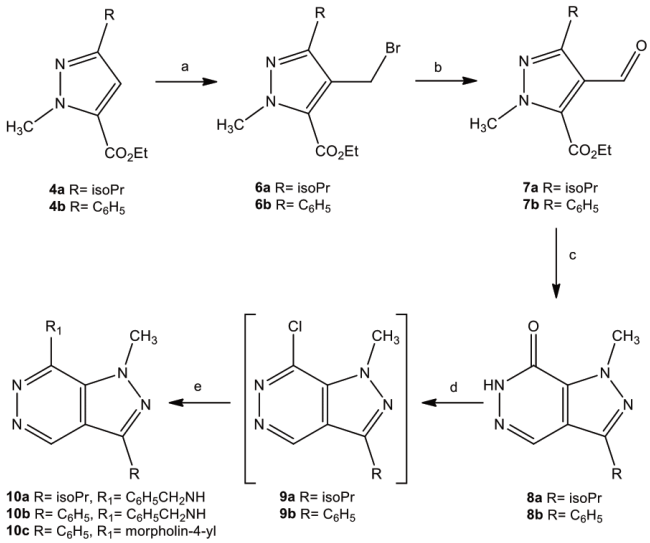

[a]Reagents and conditions: (a) paraformaldehyde, 33% HBr in AcOH, 90 °C, 3.5 h; (b) N-methylmorpholine-N-oxide, MeCN dry, rt, 24 h; (c) NH_2NH_2 (80%), HCl 36%, EtOH, 90°C, 1 h; (d) $POCl_3$, 110 °C, 2.5−8 h; (e) HNR_1R_2, EtOH, reflux, 2 h.

[1,5-*c*]quinazolines,[15] pyrazolo[3,4-*b*]pyridines,[16,17] pyrazolo-[3,4-*b*]pyridines, pyrazolo[4,3-*e*]-1,2,4-triazolo[1,5-*c*]-pyrimidines, pyrazolo[3,4-*c*]- or -[4,3-*c*]quinolines, pyrazolo-[4,3-*d*]pyrimidinones, pyrazolo[3,4-*d*]pyrimidines, and pyrazolo[1,5-*a*]pyridines.[18] After we previously identified the potent pyrazolo[3,4-*c*]pyridine A_1R/A_3R antagonists[14] and observed that certain substituted pyrazolo[3,4-*b*]pyridines had antagonistic potency against A_3R or A_1R,[16,17] we quantified the novel pyrazolo[3,4-*d*]pyridazine scaffold for activity at ARs. Here, we synthesized a series of new 3-alkyl- or 3-aryl-7-amino-pyrazolo-[3,4-d]pyridazine derivatives and determined their affinities against the different ARs using functional cAMP accumulation assays, fluorescent ligand displacement binding studies, and molecular dynamics (MD) simulations.[19,20] We

https://doi.org/10.1021/acsmedchemlett.2c00052
ACS Med. Chem. Lett. XXXX, XXX, XXX−XXX

Scheme 3. Synthesis of 15a−c[a]

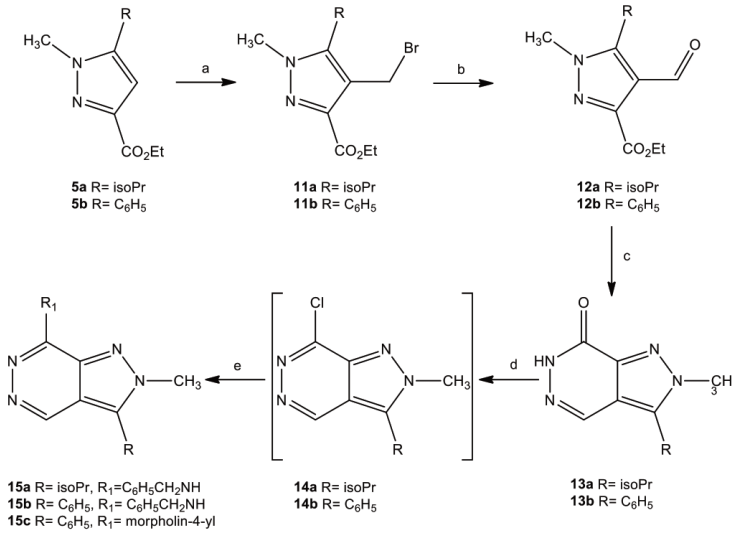

[a]Reagents and conditions: (a) paraformaldehyde, 33% HBr in AcOH, 90 °C, 3.5 h; (b) N-methylmorpholine-N-oxide, MeCN dry, rt, 24 h; (c) NH_2NH_2 (80%), HCl 36%, EtOH, 90 °C, 1 h; (d) $POCl_3$, 110 °C, 2.5−8 h; (e) HNR_1R_2, EtOH, reflux, 2 h.

identified the 21 nM A_1R/55 nM A_3R/<2 μM $A_{2B}R$ antagonist 1-methyl-3-phenyl-7-benzylaminopyrazolo[3,4-*d*]pyridazine (**10b**) as a lead compound. Strikingly, compound **15b**, the 2-methyl congener of **10b**, had lower affinity by >100-fold against 3AR subtypes since, we assumed, it cannot form hydrogen bonding interactions with $N^{6.55}$ which are considered critical for stabilization inside the orthosteric binding cavity. Finally, as these new compounds present structural similarity to antiproliferative purine analogues,[21] we evaluated their cytotoxic potential against the human fibroblasts cell line (WI-38) and prostatic (PC-3) and colonic (HCT116) cancer cell lines.

Similarity Calculations. Searching the CHEMBL[22] database to determine if pyrazolo[3,4-*d*]pyridazine has been used as a scaffold for ligands binding to ARs, using a TanimotoCombo (Tc)[23] coefficient > 0.85, we did not find any pyrazolo[3,4-*d*]pyridazine derivatives with potency against ARs, suggesting that it is a novel ring system for the development of AR ligands. When we considered the amide 7-benzylamino-3-phenylpyrazolo[3,4-*d*]pyridazine, we found the 4-(2-phenethyl)amino 1-phenylethylpyrazolo[3,4-*b*]pyridine (T_c = 0.15) had been reported to bind A_1R.[16,17] Thus, we proceeded with a structural activity relationship study around 7-benzylamino-3-phenyl pyrazolo[3,4-*d*]pyridazine and synthesized a series of 7-amino-pyrazolo[3,4-*d*]pyridazines for biological evaluation against ARs.

Chemistry. The synthesis of the target compounds was accomplished through the previously reported pyrazolecarboxylates **4a,b** and **5a,b** (Scheme 1). Briefly, commercial isopropylmethylketone (**1a**) or acetophenone (**1b**), was first converted to the ethyl 2,4-diketocarboxylates **2a** and **2b**, respectively,[24,25] which upon reaction with hydrazine monohydrate gave the pyrazolecarboxylates **3a,b**.[26] These were methylated using methyl iodide in the presence of sodium hydride and provided the regioisomers **4a,b**[27,28] and **5a,b**,[28] respectively. Interestingly, when we used tetrahydrofuran as solvent in the place of dimethylformamide (DMF), we exclusively obtained the N^1-methyl-5-carboxylate **4a** isomer.

Each of the isomeric pyrazoles **4a,b** or **5a,b** was subsequently treated with paraformaldehyde in the presence of a 33% HBr solution in acetic acid and was converted to the bromides **6a,b** (Scheme 2) or **11a,b** (Scheme 3), respectively. The bromomethyl group was then oxidized using *N*-methylmorpholine *N*-oxide to generate the carbaldehydes **7a,b** (Scheme 2) and **12a,b** (Scheme 3).

The aldehydes **7a,b** and **12a,b** were then treated with hydrazine, and upon ring closure the pyrazolopyridazinones **8a,b** and **13a,b** were obtained. The pyridazinones reacted with phosphorus oxychloride to give the corresponding chloro derivatives **9a,b** and **14a,b** with suitable purity that they could be introduced to the next reaction. These crude products were then treated with benzylamine or morpholine to result in the target compounds **10a−c** and **15a−c** (Figures S1−S3).

Assessing Biological Activity of Pyrazolo[3,4-*d*]-pyridazine Derivatives. *cAMP Assays Assessing Activity at Adenosine Receptors.* Having synthesized compounds **10a−c** and **15a−c**, we next tested their activity, as antagonists, against the different human AR subtypes using a single high concentration of the compound (1 μM) coadministered with NECA (5′-*N*-ethylcarboxamidoadenosine) in a cAMP accumulation assay (Figure 1A and B). Note that for A_1R and A_3R 10 μM forskolin was added since these are $G_{i/o}$-coupled receptors and reduce cAMP accumulation.[19,29] All compounds lacked efficacy at NECA-stimulated $A_{2A}R$ (even when tested at 10 μM) (Table S1). Compounds **10c**, **15b**, and **15c** also lacked efficacy at the other 3AR subtypes, with **15a** displaying weak efficacy only at A_3R, while compounds **10a** and **10b** displayed activity at all 3ARs although this was only detectable for $A_{2B}R$ when a 10 μM concentration of the compound was used (Table S1). Based

https://doi.org/10.1021/acsmedchemlett.2c00052
ACS Med. Chem. Lett. XXXX, XXX, XXX−XXX

ACS Medicinal Chemistry Letters pubs.acs.org/acsmedchemlett Letter

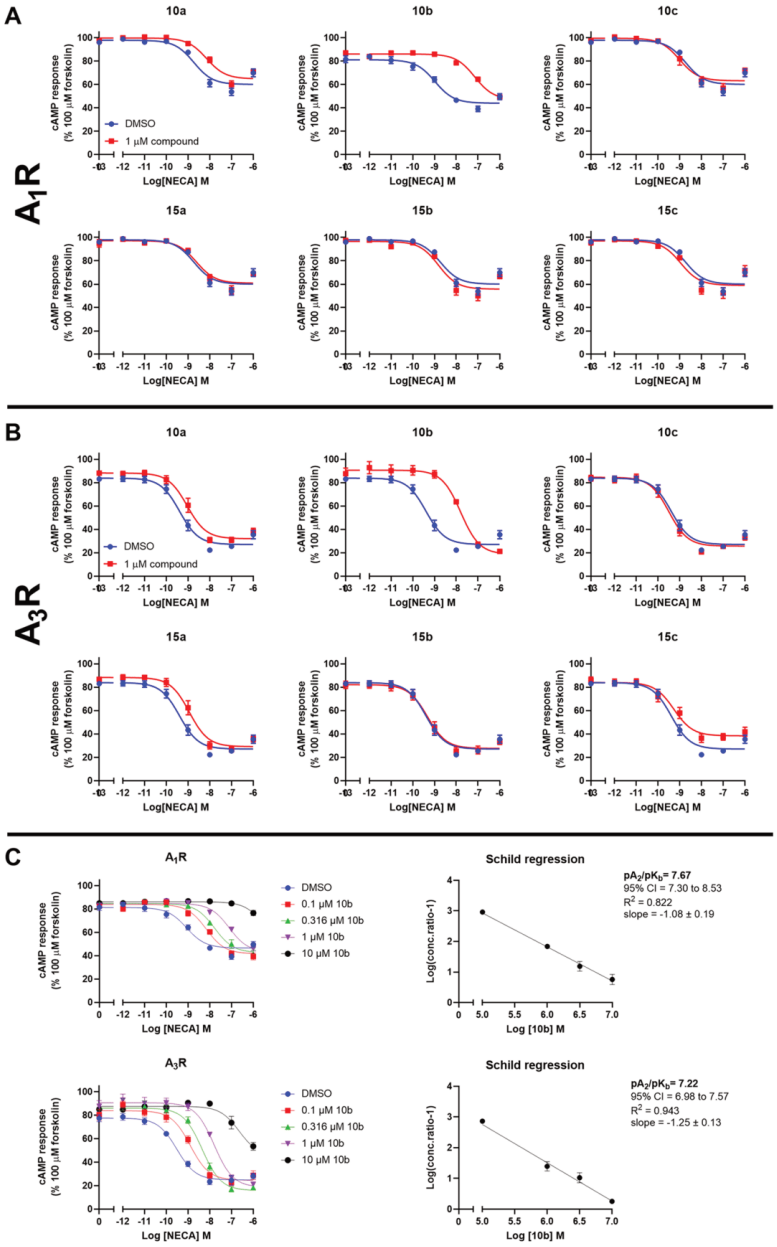

Figure 1. Characterization of 7-amino-pyrazolo[3,4-*d*]pyridazines at human A_1R and A_3R. (A and B) Cells expressing either human A_1R (A) or A_3R (B) were exposed to 10 μM forskolin and stimulated with increasing concentrations of NECA for 30 min in the presence of a 1 μM concentration of the test compound, and the cAMP accumulation was quantified. (C) cAMP accumulation was measured as detailed in part A using multiple concentrations of **10b**. Using pEC_{50} values, Schild regression analysis was conducted to calculate pA_2/pK_b values. All values are mean ± SEM expressed as percentage forskolin inhibition, relative to NECA. $n \geq 3$ independent experimental repeats were performed in duplicate.

https://doi.org/10.1021/acsmedchemlett.2c00052
ACS Med. Chem. Lett. XXXX, XXX, XXX−XXX

ACS Medicinal Chemistry Letters pubs.acs.org/acsmedchemlett Letter

Table 1. Chemical Structures, Antagonistic Potencies (pEC_{50} in the Presence of NECA[a]), and Affinities (pK_i[b]) of 7-Amino-pyrazolo[3,4-*d*]pyridazines 10a–c and 15a–c against A_1R and A_3R

	A_1R		A_3R	
Compound	pEC_{50} of NECA in presence of compound[a]	pK_i [b]	pEC_{50} of NECA in presence of compound[a]	pK_i [b]
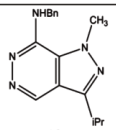 **10a**	8.15 ± 0.12**	5.17 ± 1.13#	9.04 ± 0.11	6.42 ± 0.28
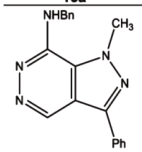 **10b**	7.15 ± 0.07***	7.95 ± 0.09***	7.80 ± 0.10***	7.89 ± 0.11*
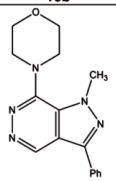 **10c**	9.01 ± 0.16	< 5.0	9.50 ± 0.12	< 5.0
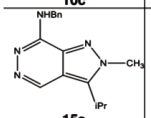 **15a**	8.62 ± 0.15	<5.0	8.94 ± 0.11*	5.77 ± 0.27#
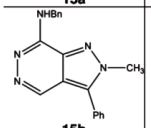 **15b**	8.82 ± 0.15	< 5.0	9.33 ± 0.13	< 5.0
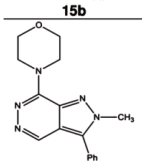 **15c**	8.96 ± 0.18	< 5.0	9.27 ± 0.16	6.44 ± 0.23#
DPCPX	6.03 ± 0.16	9.23 ± 0.08	-	-
MRS1220	7.32 ± 0.09	7.29 ± 0.27	7.44 ± 0.02#	9.94 ±0.11
NECA	8.74 ± 0.15	6.69 ± 0.10	9.39 ± 0.11	7.05 ± 0.07

[a]Mean ± SEM; functional activities (pEC_{50} values of NECA in the presence of either 1 μM ligands or vehicle) as mean ± standard error of the mean (SEM) of at least three independent repeats, conducted in duplicate—values obtained from Figure 1. [b]Mean ± SEM; equilibrium binding affinities of the ligands measured with NanoBRET against Nluc-A_3R or Nluc-A_1R; NECA was used as positive control.[3] #Due to the high affinity of MRS1220, 10 nM was used to enable measurement of the full dose–response curve of NECA to determine pEC_{50}. Statistical significance compared to NECA was determined, at $p < 0.05$, through one-way ANOVA with Dunnett's post-test (*, $p < 0.05$; **, $p < 0.01$; ***, $p < 0.001$; ****, $p < 0.0001$).

upon a single concentration of antagonist, we calculated the equilibrium dissociation constant (pK_d) of each compound (Table 1). Of the compounds tested, **10b** displayed the highest affinity at the different AR subtypes with greater selectivity toward A_1R and A_3R than $A_{2B}R$. We next performed a more extensive Schild analysis using multiple doses of the most potent antagonist, **10b**, only at A_1R and A_3R (Figure 1C). In both cases **10b** acted as a competitive antagonist, generating a Schild slope that did not significantly differ from unity. Using the Schild plot,

https://doi.org/10.1021/acsmedchemlett.2c00052
ACS Med. Chem. Lett. XXXX, XXX, XXX–XXX

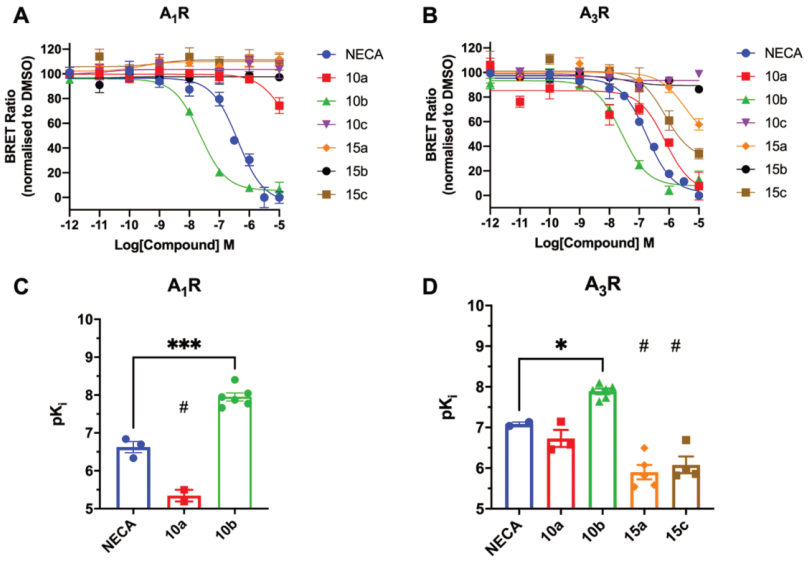

Figure 2. Inhibition of BRET between CA200645 at NLuc-A_1R and Nluc-A_3R by **10b** and **10a**. HEK293 cells expressing Nluc-A_1R (A) or Nluc-A_3R (B) were treated with 5 nM or 20 nM CA200645, respectively, enabling concentration-dependent decreases in the BRET ratio at 10 min to be determined with the response normalized to DMSO. Binding curves were fitted with the Cheng Prusoff equation built into GraphPad Prism 9.3 to enable estimates of the pK_i.[19] Comparison of pK_i values for A_1R (C) and A_3R (D) as determined via BRET binding. Each data point represents the mean ± SEM of at least three experiments performed in duplicate. The statistical significance compared to NECA was determined, at $p < 0.05$, through one-way ANOVA with Dunnett's post-test (*, $p < 0.05$; ***, $p < 0.001$). #Compounds did not fully displace CA200645, so pK_i values are estimates preventing statistical analysis.

we calculated **10b**'s affinity (pA_2/pK_b) to be 21 nM at A_1R and 55 nM at A_3R while only 1.7 μM at $A_{2B}R$ (Table S1).

Quantifying Binding Parameters Using a NanoBRET-Based Saturation Binding Assay. We next sought to independently verify the affinities determined using the Shield analysis by directly quantifying the potential antagonists' binding to A_1R and A_3R using a previously described saturation nano-bioluminescence resonance energy transfer (NanoBRET) binding assay.[19] We determined the ability of all the compounds to displace the specific binding of CA200645,[30] a fluorescent antagonist of A_3R and A_1R, using Nluc-A_3R expressing human embryonic kidney 293 (HEK293) and Nluc-A_1R HEK293 cells (Figure 2 and Table 1). $A_{2B}R$ was not included in this analysis since the pK_d values of **10a** and **10b** at $A_{2B}R$ were estimated to be below 1 μM (Figure 1 and Table 1). Consistent with the Schild analysis, compound **10b** displayed the highest affinity at A_1R and A_3R (A_1R, $pK_i = 7.95 \pm 0.09$; A_3R, $pK_i = 7.89 \pm 0.11$). Of the remaining compounds, **10a** displayed weak affinity at A_3R (pK_i, 6.42 ± 0.28), which agreed with the Schild regression estimate, but failed to fully displace CA200645 at A_1R, making an estimate for its affinity unreliable. All the other compounds failed to displace CA200645 at A_1R or A_3R except for **15a** and **15c**, which did display some binding at A_3R but, like **10a**, also failed to fully displace CA200645 at the concentrations tested. Significantly, **15b**, which contains an *N*-methyl substitution to 1-NH and 2-NMe compared to 1-NMe and 2-NH in **10b**, failed to bind either AR subtype.

*Determining Kinetic Parameters of **10b** Binding at A_3R and A_1R Using NanoBRET.* We next investigated the real-time binding kinetics[19,30] of **10b** at A_3R and A_1R using the NanoBRET binding method. Specifically, we quantified **10b**'s ability to inhibit specific binding of CA200645 to Nluc-A_3R and Nluc-A_1R expressed in HEK293 cells. The kinetic parameters for CA200645 binding at Nluc-A_3R were previously determined as $K_{on} = 32.5 \pm 0.28 \times 10^5$ M^{-1} min^{-1} and $K_{off} = 0.025 \pm 0.005$ min^{-1} with a pK_D of 10.11. Conversely the kinetics of CA200645 binding at Nluc-A_1R were determined as $K_{on} = 14.5 \pm 0.4 \times 10^5$ M^{-1} min^{-1}, $K_{off} = 0.023 \pm 0.001$ min^{-1}, and $pK_D = 7.80 \pm 0.2$ nM.[14] Applying these parameters into the "kinetics of competitive binding" model built into GraphPad Prism9.0, we were able to provide estimates of the kinetics of binding for **10b** against A_1R ($K_{on} = 51.4 \pm 0.26 \times 10^5$ M^{-1} min^{-1}, $K_{off} = 0.019 \pm 0.003$ min^{-1} with a $pK_D = 7.46 \pm 0.1$ and RT = 59.8 ± 12.7 min) and against the A_3R, ($K_{on} = 25.6 \pm 0.1 \times 10^5$ $M^{-1}min^{-1}$, $K_{off} = 0.0014 \pm 0.002$ min^{-1} with a $pK_D = 7.26 \pm 0.05$ and RT = 72.58 ± 8.8 min). None of the other compounds were analyzed using this method due to their extremely fast K_{off} rates (>min^{-1}). For compound **10b** there was an excellent agreement between pK_D (K_{on}/K_{off}) of the compounds from the kinetics assays and the Schild analysis (pA_2/pK_b) and fair agreement (~3.16-fold) with the saturation binding assays (pK_i).

Simulations. *Investigation of the Binding of the 7-Amino-pyrazolo[3,4-d]pyridazines to A_1R and A_3R.* Having pharmacologically evaluated the different compounds, we then used molecular docking to provide insights into how they bind to the ARs. We docked **10a**−**10c** into the orthosteric binding site of A_1R and **10b** and **15b** into $A_{2B}R$ and A_3R (the amino acid sequences of A_1R, A_3R, and $A_{2B}R$ in the orthosteric binding area

https://doi.org/10.1021/acsmedchemlett.2c00052
ACS Med. Chem. Lett. XXXX, XXX, XXX−XXX

ACS Medicinal Chemistry Letters pubs.acs.org/acsmedchemlett Letter

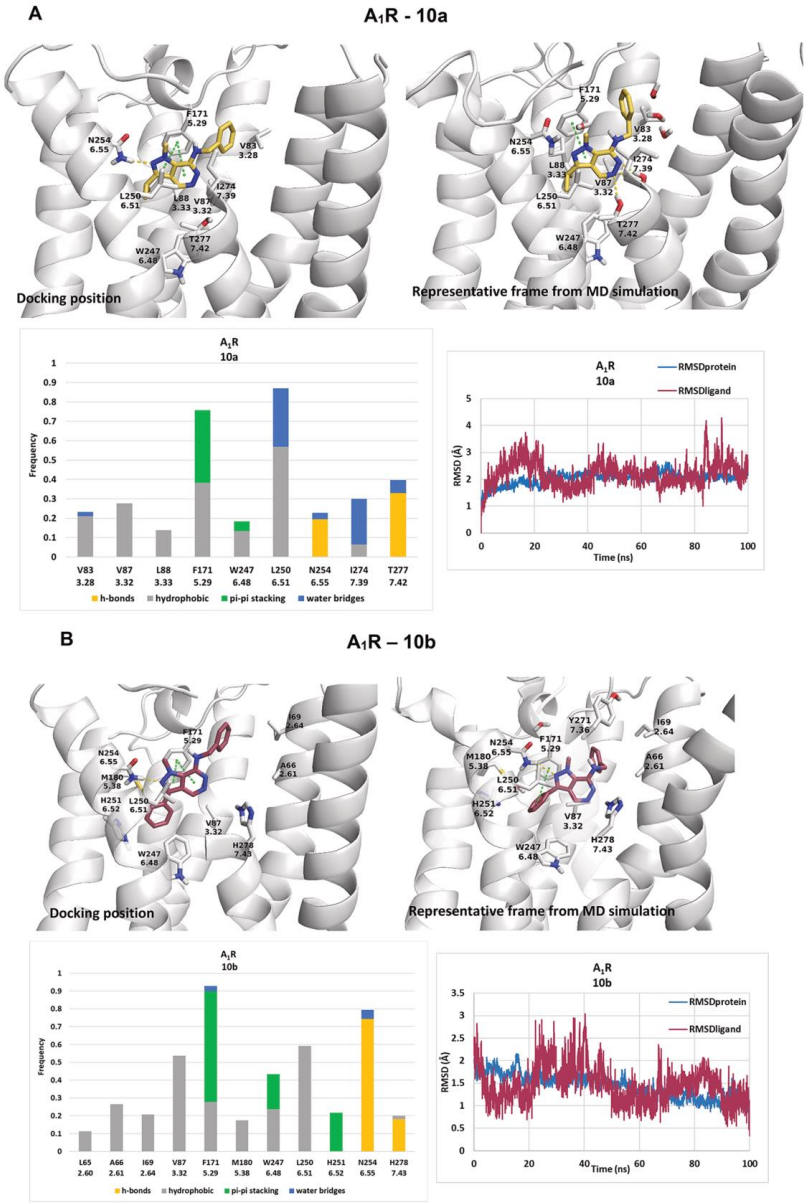

Figure 3. continued

https://doi.org/10.1021/acsmedchemlett.2c00052
ACS Med. Chem. Lett. XXXX, XXX, XXX−XXX

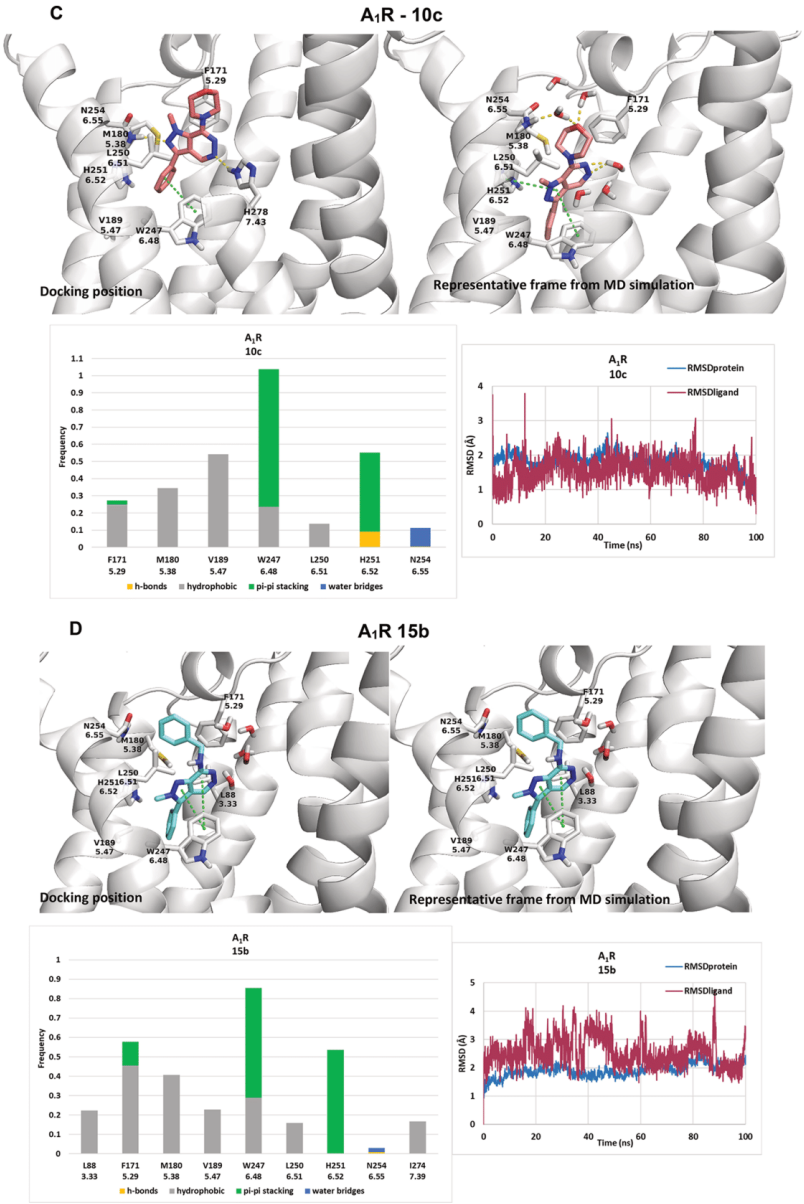

Figure 3. (A−C) 100 ns MD simulations of **10a−c** inside the orthosteric binding area of A_1R. (D) 100 ns MD simulations of **15b** inside the orthosteric binding area of A_1R. Starting structures are shown (docking pose), and representative frames from MD simulations, receptor−ligand interaction frequency histograms, and RMSD plots of proteins ($RMSD_{protein}$; blue plots) and ligand heavy atoms ($RMSD_{ligand}$; red plots) inside the orthosteric binding area of WT A_1R or A_3R. Bars are plotted only for residues with interaction frequencies ≥0.2. Color scheme: ligand = brown sticks, receptor = white cartoon and sticks, hydrogen bonding interactions = yellow (dashes or bars), $\pi-\pi$ interactions = green (dashes or bars), hydrophobic interactions = gray, water bridges = blue. For the protein models of A_1R in complex with **10a−c** or **15b**, the experimental structure of the inactive form of A_1R in complex with an antagonist (PDB ID 5UEN[4]) was used.

https://doi.org/10.1021/acsmedchemlett.2c00052
ACS Med. Chem. Lett. XXXX, XXX, XXX−XXX

are shown in Scheme S1) using ChemScore as the scoring function[31] with the highest score docking pose being inserted into a hydrated phosphatidylethanolamine bilayer. The complexes were subjected to 100 ns MD simulations with amber99sb,[32] and then, the MD simulations' trajectory was analyzed (Table S2). The MD simulations showed that the 7-benzylamino-pyrazolo[3,4-*d*]pyridazine **10b** substituted with N^1Me and a 3-phenyl group formed a stable complex with all 3ARs with $RMSD_{protein}$ values <2.1 Å. Starting from the same docking pose of **10b** in A_1R or A_3R (Figure 3), the mean frame from MD simulations was close to the starting docking pose in A_1R ($RMSD_{lig}$ = 1.21 Å) while in A_3R (Figure S2) the ligand moved considerably into the cleft between the transmembrane (TM)3, TM5, and TM6 helices ($RMSD_{lig}$ = 4.88 Å). Thus, starting from the same binding pose for **10b**, the MD simulations produced two different binding orientations at A_1R and A_3R. This is due to the fact that A_1R has a broader binding area, expanded toward TM1 and TM2, compared to the other ARs, according to the X-ray structures of A_1R in complex with antagonists.[11,12] A similar AR ligand reported in the literature is 4-(2-phenethyl)amino 1-phenylethyl pyrazolo[3,4-*b*]pyridine (Tc = 0.15), which binds with a similar docking pose to **10b** to A_1R.[16] We also docked a representative adenine derivative (*N*9-methyl,*N*6-benzyl adenine) to A_1R and found a similar docking pose (Figure S3).

Inside the A_1R orthosteric site, compound **10b** formed hydrogen bonds through its pyrazole or pyridazine nitrogen donor groups to the amide side chain of $N254^{6.5}$ or the imidazole side chain of $H278^{7.43}$. Furthermore, **10b** was stabilized in the orthosteric binding site through $\pi-\pi$ interactions between its pyrazolo[3,4-*d*]pyridazine or phenyl rings with $F171^{5.29}$, $H251^{6.2}$, and $W247^{6.48}$, respectively. The benzylamino group of **10b** oriented toward the widened TM2 area in A_1R, forming hydrophobic interactions with $A66^{2.61}$ and $I69^{2.64}$. Furthermore, **10b** was found to bind deep in the pocket interacting with $V87^{3.32}$ and $W247^{6.48}$ while 3-phenyl-pyrazole aligned close to the side chains of $M180^{5.38}$ and $L250^{6.1}$ (Figure 3A). In A_3R, compound **10b** was stabilized through formation of hydrogen bonding interactions with $N254^{6.5}$ and $H278^{7.43}$ and hydrophobic interactions with $L90^{3.32}$, $L91^{3.33}$, $F168^{5.29}$, $M177^{5.38}$, $L246^{6.1}$, and $I268^{7.39}$ (Figure S2B). Finally, the MD simulations for **10b** (Figure S2A) in complex with $A_{2B}R$ (Figure S2) show weak hydrogen bond interactions with $N254^{6.5}$.

Pharmacologically, compounds **10b** and **15b** differed considerably in their affinity to the ARs (Figures 1 and 2 and Table 1). Comparing MD simulations for **15b** with **10b** in the orthosteric binding area of A_1R, A_3R (and $A_{2B}R$) shows that starting from a similar docking pose, the substitution from N^1 Me and 2-NH (found in **10b**) to N^1H and N^2 Me (in **15b**) results in **15b** failing to generate hydrogen bonds with $N^{6.55}$ because of the steric repulsion between 2-methyl and the amide side chain of $N^{6.55}$; for this reason also **15a** and **15c** were inactive (Figure S2). Although many ligands can have similar docking poses, subtle changes in the ligand substitution pattern can result in significant changes in binding, and this can be followed only with MD simulations. Considering the two active compounds, **10b** and **10a**, replacement of the 3-phenyl group (found in **10b**) with a 3-isopropyl group (generating **10a**) results in a remarkable reduction of affinity. This is due to **10a** losing significant $\pi-\pi$ interactions with $H251^{6.2}$ and hydrophobic interactions with residues deeper in the binding site, e.g., $W247^{6.48}$, $L250^{6.1}$, and $V87^{3.32}$ (Figure 3). Finally, substitution of **10b**'s 7-benzylamino by the more rigid morpholinyl group (found in **10c**) resulted in reduced affinity to the ARs. The more rigid morpholino group in **10c** repels $F171^{5.29}$, so the ligand rotates and moves to the bottom of the binding area, losing hydrogen bonding interactions with $N254^{6.5}$ and weakening its hydrophobic interaction with critical residues, e.g., $F171^{5.29}$ and $L250^{6.1}$ (Figure 3). With an accuracy of ∼±4 kcal mol^{-1}, the MM-GBSA method[33,34] (Supporting Information) only provides an approximation when applied to structure−activity relationships for analogs in the same series. Nevertheless, the MM-GBSA binding free energy calculations for ligands **10a−c** against A_1R (Table S2), using the OPLS2005 force field[35,36] with a hydrophobic slab as an implicit membrane model and including the waters in the orthosteric binding area, predicted fairly well the stability of **10a−c** in complex with A_1R with binding free energy values (after neglecting entropy) ΔG_{eff} = −94.50, −96.42, and −85.35 kcal mol^{-1}.

*Mutagenesis Experiments to Study **10b** Binding to A_1R.* We have previously observed that mutation of residues that do not directly interact with the ligands (e.g., $V^{5.30}$ for A_3R, which is more than 4 Å apart from the ligand inside the orthosteric binding area) can, through allosteric interactions due to the plasticity of the binding area, significantly affect ligand affinity.[20,21,37] As such it is not always straightforward to determine the effects of a mutation on affinity properties. Despite this caveat, we next used mutational analysis combined with NanoBRET to determine the important residues required for **10b** binding to A_1R. The mutation of $L250^{6.1}$A resulted in only a slight reduction of binding affinity for **10b** (Table 2) despite the MD simulations suggesting that the ligand should be close enough to $L250^{6.1}$ to enable hydrophobic interactions. It is possible that residues $H251^{6.52}$ and $W247^{6.48}$ could contribute to the stabilization of **10b** with hydrophobic interactions even if $L250^{6.1}$ is mutated to alanine. It is noteworthy that mutation of $E172^{5.30}$ (which is also more than 4 Å apart from the ligand inside the orthosteric binding area) to alanine also did not significantly change the binding affinity (Table 2). This contrasts with our studies using 3-phenyl-7-anilinopyrazolo-[3,4-*c*]pyridines which showed a 1.5-fold decrease in affinity due to the $E172^{5.30}$A mutation.[14]

Table 2. Binding Affinities (pK_i) for 10b Measured Using Saturation NanoBRET Binding with CA200645 as the Fluorescent Tracer against WT A_1R and Mutant A_1Rs

A_1R	pK_i	Effect on affinity
WT	7.68 ± 0.11	baseline
$T91^{3.36}$A	7.68 ± 0.07	no change
$E172^{5.30}$ A	7.34 ± 0.06	no significant change
$L250^{6.51}$ A	7.57 ± 0.04	no significant change
$H251^{6.52}$A	7.62 ± 0.06	no significant change
$S267^{7.42}$A	7.86 ± 0.03	no significant change
$Y271^{7.46}$A	6.99 ± 0.05	∼10-fold reduction

In addition, mutation of $H251^{6.2}$A has been reported to reduce antagonist affinity against A_3R[20,21] although here it did not have any effect on **10b** affinity at A_1R. Other residues of interest to mutate were $T91^{3.36}$A and $S267^{7.42}$A, which are deep in the orthosteric pocket. Interestingly, we found that mutation to alanine of these residues also did not have a significant effect on the binding affinity of **10b** (Table 2). This is in contrast to our results for pyrazolo[3,4-*c*]pyridines which can interact directly with these residues.[9] The results for **10b** suggested that it is

https://doi.org/10.1021/acsmedchemlett.2c00052
ACS Med. Chem. Lett. XXXX, XXX, XXX−XXX

positioned above pyrazolo[3,4-*c*]pyridines,[9] in the A_1R pocket, and so unaffected by these mutations.

The biggest effect in this study was observed for the $Y271^{7.46}A$ A_1R mutation, which caused a ~10-fold reduction in the binding affinity of **10b** (Table 2). This effect is in contrast to that observed previously for pyrazolo[3,4-*c*]pyridines[14] for which we showed that the $Y271^{7.46}A$ mutation caused a slight increase in binding affinity. Since the MD simulations showed contacts with $H278^{7.43}$ and not $Y271^{7.46}$, the $Y271^{7.46}A$ mutation in A_1R might affect the binding of **10b** through contact with $H278^{7.43}$. We performed the MD simulations of **10b** in complex with A_1R-$Y271^{7.46}A$ and observed that the ligand loses its hydrogen bonding interactions with $N254^{6.5}$, which might weaken its binding interactions with the orthosteric binding area (Figure S4).

Preliminary Toxicological Analysis of Pyrazolo[3,4-d]-pyridazine Derivatives. Given the high affinity **10b** displays for A_1R and A_3R, and thus the potential for it to be a scaffold for future compound development, we wanted to evaluate its antiproliferative nature as an early indicator of its toxicological profile. We therefore evaluated **10b**, alongside the other compounds in this study, for cytotoxic activity against human fibroblasts (WI-38) and two cancer cell lines, namely the prostate cancer (PC-3) and colon cancer (HCT116) cell lines. Importantly, **10b** alongside all the compounds proved to be not cytotoxic against the cell lines, with IC_{50} values >10 μM. The only compound that did display any cytotoxicity was **15b**, which displayed moderate cytotoxicity against the PC-3 and HCT116 cell lines, showing IC_{50} values of 5.3 ± 0.1 μM against PC-3 cells and 4.15 ± 0.05 μM against HCT116 cells. As a result of these data, we are confident that **10b** is noncytotoxic and can be progressed for further development as a dual A_1R/A_3R antagonist.

■ ASSOCIATED CONTENT

Supporting Information

The Supporting Information is available free of charge at https://pubs.acs.org/doi/10.1021/acsmedchemlett.2c00052.

Scheme S1. Comparison of amino acid residue sequences of the binding area. Table S1. Chemical structures and antagonistic potencies of 7-amino-pyrazolo[3,4-*d*]-pyridazines **10a−c** and **15a−c** against A2AR and A2BR. Table S2. Mean RMSD values for all compounds against A_1R, $A_{2A}R$, and $A_{2B}R$ and ΔG_{eff} only for **10−10c** against A_1R. Figure S1. ^1H and ^{13}C NMR spectra of the target compounds. Figure S2. Results from the MD simulations of **10b** and **15b** against A_3R and $A_{2B}R$. Figure S3. Docking poses of 4-(2-phenethyl)amino-1-phenylethyl pyrazolo-[3,4-*b*]pyridine and N9-methyl,N6-benzyl adenine to A_1R. Figure S4. Representative frames from 100 ns MD simulations of **10b** inside the orthosteric binding area of WT A1R and **10b** inside mutant Y271A A_1R and the receptor−ligand interaction frequency histogram and RMSD graphs of protein Ca and ligand heavy atoms. Information for the methods and synthetic protocols. (PDF)

■ AUTHOR INFORMATION

Corresponding Authors

Antonios Kolocouris − *Laboratory of Medicinal Chemistry, Section of Pharmaceutical Chemistry, Department of Pharmacy, School of Health Sciences, National and Kapodistrian University of Athens, 15771 Athens, Greece;* orcid.org/0000-0001-6110-1903; Email: ankol@pharm.uoa.gr

Nikolaos Lougiakis − *Laboratory of Medicinal Chemistry, Section of Pharmaceutical Chemistry, Department of Pharmacy, School of Health Sciences, National and Kapodistrian University of Athens, 15771 Athens, Greece;* Email: nlougiak@pharm.uoa.gr

Graham Ladds − *Department of Pharmacology, University of Cambridge, Cambridge CB2 1PD, U.K.;* orcid.org/0000-0001-7320-9612; Email: grl30@cam.ac.ukz

Authors

Anna Suchankova − *Department of Pharmacology, University of Cambridge, Cambridge CB2 1PD, U.K.*

Margarita Stampelou − *Laboratory of Medicinal Chemistry, Section of Pharmaceutical Chemistry, Department of Pharmacy, School of Health Sciences, National and Kapodistrian University of Athens, 15771 Athens, Greece*

Klontiana Koutsouki − *Laboratory of Medicinal Chemistry, Section of Pharmaceutical Chemistry, Department of Pharmacy, School of Health Sciences, National and Kapodistrian University of Athens, 15771 Athens, Greece; Department of Nutrition & Dietetics, School of Health Sciences and Education, Harokopio University, 17671 Athens, Greece;* Present Address: Cyprus Pharmaceutical Organization Limited, 11 King Paul A' Street, 1096 Nicosia, Cyprus

Athanasios Pousias − *Laboratory of Medicinal Chemistry, Section of Pharmaceutical Chemistry, Department of Pharmacy, School of Health Sciences, National and Kapodistrian University of Athens, 15771 Athens, Greece*

Lakshiv Dhingra − *Department of Pharmacology, University of Cambridge, Cambridge CB2 1PD, U.K.*

Kerry Barkan − *Department of Pharmacology, University of Cambridge, Cambridge CB2 1PD, U.K.*

Nicole Pouli − *Laboratory of Medicinal Chemistry, Section of Pharmaceutical Chemistry, Department of Pharmacy, School of Health Sciences, National and Kapodistrian University of Athens, 15771 Athens, Greece*

Panagiotis Marakos − *Laboratory of Medicinal Chemistry, Section of Pharmaceutical Chemistry, Department of Pharmacy, School of Health Sciences, National and Kapodistrian University of Athens, 15771 Athens, Greece*

Roxane Tenta − *Department of Nutrition & Dietetics, School of Health Sciences and Education, Harokopio University, 17671 Athens, Greece*

Complete contact information is available at: https://pubs.acs.org/10.1021/acsmedchemlett.2c00052

Author Contributions

[†]A.S., M.S., and K.K. contributed equally. A.K., N.L. and G.L. contributed equally. A.K., N.L., G.L., and M.S. conceived and designed the research; K.K. and A.P. synthesized and characterized the compounds in the P.M., N.P., and N.L. lab; A.S. and L.D. performed the mammalian assays in the G.L. lab; M.S. performed the simulations in the A.K. lab; K.K., A.P., M.S., A.S., N.L., P.M., A.K., and G.L. analyzed the data; A.K., P.M., N.P., N.L., and G.L. wrote the manuscript; A.K., G.L., N.L., and M.S. edited the manuscript.

Notes

The authors declare no competing financial interest.

https://doi.org/10.1021/acsmedchemlett.2c00052
ACS Med. Chem. Lett. XXXX, XXX, XXX−XXX

ACKNOWLEDGMENTS

This research represents part of the master's thesis of K.K. and part of the Ph.D. theses of A.S. and M.S. We gratefully acknowledge the support of Chiesi Hellas (A.K.), the Cambridge Trust (A.S.), the Leverhulme Trust (G.L.), and the BBSRC (G.L.). This work was supported by computational time granted from the Greek Research & Technology Network (GRNET) in the National HPC facility - ARIS - under project ID pr001007.

ABBREVIATIONS

ARs, adenosine receptors; BRET, bioluminescence resonance energy transfer; GPCRs, G protein-coupled receptors; HEK, human embryonic kidney; MD, molecular dynamics; NECA, 5′-*N*-ethylcarboxamidoadenosine; PDB, Protein Data Bank; RMSD, root-mean-square deviation; T_c, TanimotoCombo; t_m, mixing time; TM, transmembrane

REFERENCES

(1) Fredholm, B. B.; IJzerman, A. P.; Jacobson, K. A.; Linden, J.; Muller, C. E.; Müller, C. E. International Union of Basic and Clinical Pharmacology. LXXXI. Nomenclature and Classification of Adenosine Receptors — An Update. *Pharmacol. Rev.* **2011**, *63*, 1−34.

(2) Schenone, S.; Brullo, C.; Musumeci, F.; Bruno, O.; Botta, M. A1 Receptors Ligands: Past, Present and Future Trends. *Curr. Top. Med. Chem.* **2010**, *10*, 878−901.

(3) Squarcialupi, L.; Catarzi, D.; Varano, F.; Betti, M.; Falsini, M.; Vincenzi, F.; Ravani, A.; Ciancetta, A.; Varani, K.; Moro, S.; Colotta, V. Structural Refinement of Pyrazolo[4,3-d]Pyrimidine Derivatives to Obtain Highly Potent and Selective Antagonists for the Human A3 Adenosine Receptor. *Eur. J. Med. Chem.* **2016**, *108*, 117−133.

(4) Sun, B.; Bachhawat, P.; Chu, M. L.-H.; Wood, M.; Ceska, T.; Sands, Z. A.; Mercier, J.; Lebon, F.; Kobilka, T. S.; Kobilka, B. K. Crystal Structure of the Adenosine A2A Receptor Bound to an Antagonist Reveals a Potential Allosteric Pocket. *Proc. Natl. Acad. Sci. U. S. A.* **2017**, *114*, 2066−2071.

(5) el-Hashim, A.; D'Agostino, B.; Matera, M. G.; Page, C. Characterization of adenosine receptors involved in adenosine-induced bronchoconstriction in allergic rabbits. *Br. J. Pharmacol.* **1996**, *119*, 1262−1268.

(6) Brown, R. A.; Spina, D.; Page, C. P. Adenosine receptors and asthma. *Br. J. Pharmacol.* **2008**, *153*, S446−S456.

(7) Johnson, J. A.; Montgomery, A. P.; Starr, E. R.; Ludwig, J.; Trevitt, J. Dose-dependent effects of adenosine antagonists on tacrine-induced tremulous jaw movements. *Eur. J. Pharmacol.* **2018**, *833*, 364−369.

(8) Cohen, S.; Fishman, P. Targeting the A3 Adenosine Receptor to Treat Cytokine Release Syndrome in Cancer Immunotherapy. *Drug Des. Devel. Ther.* **2019**, *13*, 491−497.

(9) Lee, J.; Hwang, I.; Lee, J. H.; Lee, H. W.; Jeong, L.-S.; Ha, H. The Selective A3AR Antagonist LJ-1888 Ameliorates UUO-Induced Tubulointerstitial Fibrosis. *Am. J. Pathol.* **2013**, *183*, 1488−1497.

(10) Wang, Z.; Do, C. W.; Avila, M. Y.; Peterson-Yantorno, K.; Stone, R. A.; Gao, Z.-G.; Joshi, B.; Besada, P.; Jeong, L. S.; Jacobson, K. A.; Civan, M. M. Nucleoside-Derived Antagonists to A3 Adenosine Receptors Lower Mouse Intraocular Pressure and Act across Species. *Exp. Eye Res.* **2010**, *90*, 146−154.

(11) Glukhova, A.; Thal, D. M.; Nguyen, A. T.; Vecchio, E. A.; Jörg, M.; Scammells, P. J.; May, L. T.; Sexton, P. M.; Christopoulos, A. Structure of the Adenosine A1 Receptor Reveals the Basis for Subtype Selectivity. *Cell* **2017**, *168*, 867−877.

(12) Cheng, R. K. Y.; Segala, E.; Robertson, N.; Deflorian, F.; Doré, A. S.; Errey, J. C.; Fiez-Vandal, C.; Marshall, F. H.; Cooke, R. M. Structures of Human A1 and A2A Adenosine Receptors with Xanthines Reveal Determinants of Selectivity. *Structure* **2017**, *25*, 1275−1285.

(13) Draper-Joyce, C. J.; Khoshouei, M.; Thal, D. M.; Liang, Y.-L.; Nguyen, A. T. N.; Furness, S. G. B.; Venugopal, H.; Baltos, J.-A.; Plitzko, J. M.; Danev, R.; Baumeister, W.; May, L. T.; Wootten, D.; Sexton, P. M.; Glukhova, A.; Christopoulos, A. Structure of the Adenosine-Bound Human Adenosine A1 Receptor-Gi Complex. *Nature* **2018**, *558*, 559−563.

(14) Stampelou, M.; Suchankova, A.; Tzortzini, E.; Dhingra, L.; Barkan, K.; Lougiakis, N.; Marakos, P.; Pouli, N.; Ladds, G.; Kolocouris, A. Novel Pyrazolo[3,4-c]Pyridine Antagonists with Nanomolar Affinity for A1/A3 Adenosine Receptors: Binding Kinetics and Exploration of Their Binding Profile Using Mutagenesis Experiments, MD Simulations and TI/MD Calculations. *ChemRxiv* **2021**, DOI: 10.26434/chemrxiv-2021-j18mg-v3.

(15) Catarzi, D.; Colotta, V.; Varano, F.; Poli, D.; Squarcialupi, L.; Filacchioni, G.; Varani, K.; Vincenzi, F.; Borea, P. A.; Dal Ben, D.; Lambertucci, C.; Cristalli, G. Pyrazolo[1,5-c]Quinazoline Derivatives and Their Simplified Analogues as Adenosine Receptor Antagonists: Synthesis, Structure-Affinity Relationships and Molecular Modeling Studies. *Bioorg. Med. Chem.* **2013**, *21*, 283−294.

(16) Manetti, F.; Schenone, S.; Bondavalli, F.; Brullo, C.; Bruno, O.; Ranise, A.; Mosti, L.; Menozzi, G.; Fossa, P.; Trincavelli, M. L.; Martini, C.; Martinelli, A.; Tintori, C.; Botta, M. Synthesis and 3D QSAR of new pyrazolo[3,4-b]pyridines: potent and selective inhibitors of A1 adenosine receptors. *J. Med. Chem.* **2005**, *48*, 7172−7185.

(17) Tuccinardi, T.; Zizzari, A. T.; Brullo, C.; Daniele, S.; Musumeci, F.; Schenone, S.; Trincavelli, M. L.; Martini, C.; Martinelli, A.; Giorgi, G.; Botta, M. Substituted pyrazolo[3,4-b]pyridines as human A1 adenosine antagonists: Developments in understanding the receptor stereoselectivity. *Org. Biomol. Chem.* **2011**, *9*, 4448−4455.

(18) Cheong, S. L.; Venkatesan, G.; Paira, P.; Jothibasu, R.; Mandel, A. L.; Federico, S.; Spalluto, G.; Pastorin, G. Pyrazolo Derivatives as Potent Adenosine Receptor Antagonists: An Overview on the Structure-Activity Relationships. *Int. J. Med. Chem.* **2011**, 480652.

(19) Barkan, K.; Lagarias, P.; Stampelou, M.; Stamatis, D.; Hoare, S.; Safitri, D.; Klotz, K.-N.; Vrontaki, E.; Kolocouris, A.; Ladds, G. Pharmacological Characterisation of Novel Adenosine A3 Receptor Antagonists. *Sci. Rep.* **2020**, *10*, 20781.

(20) Lagarias, P.; Barkan, K.; Tzortzini, E.; Stampelou, M.; Vrontaki, E.; Ladds, G.; Kolocouris, A. Insights to the Binding of a Selective Adenosine A3 Receptor Antagonist Using Molecular Dynamic Simulations, MM-PBSA and MM-GBSA Free Energy Calculations, and Mutagenesis. *J. Chem. Inf. Model.* **2019**, *59*, 5183−5197.

(21) Papastathopoulos, A.; Lougiakis, N.; Kostakis, I. K.; Marakos, P.; Pouli, N.; Pratsinis, H.; Kletsas, D. New Bioactive 5-Arylcarboximidamidopyrazolo[3,4-c]Pyridines: Synthesis, Cytotoxic Activity, Mechanistic Investigation and Structure-Activity Relationships. *Eur. J. Med. Chem.* **2021**, *218*, 113387.

(22) Bento, A. P.; Gaulton, A.; Hersey, A.; Bellis, L. J.; Chambers, J.; Davies, M.; Krüger, F. A.; Light, Y.; Mak, L.; McGlinchey, S.; Nowotka, M.; Papadatos, G.; Santos, R.; Overington, J. P. The ChEMBL Bioactivity Database: An Update. *Nucleic Acids Res.* **2014**, *42*, D1083−D1090.

(23) Hawkins, P. C. D.; Skillman, A. G.; Nicholls, A. Comparison of Shape-Matching and Docking as Virtual Screening Tools. *J. Med. Chem.* **2007**, *50*, 74−82.

(24) Pei, Y.; Wickham, B. O. S. Regioselective Syntheses of 3-Aminomethyl-5-Substituted Isoxazoles: A Facile and Chemoselective Reduction of Azide to Amine by Sodium Borohydride Using 1,3-Propanedithiol as a Catalyst. *Tetrahedron Lett.* **1993**, *34*, 7509−7512.

(25) Fadnavis, N. W.; Radhika, K. R. Enantio- and Regiospecific Reduction of Ethyl 4-Phenyl-2,4-Dioxobutyrate with Baker's Yeast: Preparation of (R)-HPB Ester. *Tetrahedron Asymmetry* **2004**, *15*, 3443−3447.

(26) Dang, T. T.; Dang, T. T.; Fischer, C.; Görls, H.; Langer, P. Synthesis of Pyrazole-3-Carboxylates and Pyrazole-1,5-Dicarboxylates by One-Pot Cyclization of Hydrazone Dianions with Diethyl Oxalate. *Tetrahedron* **2008**, *64*, 2207−2215.

(27) Yan, Z.; Liu, A.; Huang, M.; Liu, M.; Pei, H.; Huang, L.; Yi, H.; Liu, W.; Hu, A. Design, Synthesis, DFT Study and Antifungal Activity of the Derivatives of Pyrazolecarboxamide Containing Thiazole or Oxazole Ring. *Eur. J. Med. Chem.* **2018**, *149*, 170−181.

(28) Schmidt, A.; Habeck, T.; Kindermann, M. K.; Nieger, M. New Pyrazolium-Carboxylates as Structural Analogues of the Pseudo-Cross-Conjugated Betainic Alkaloid Nigellicine. *J. Org. Chem.* **2003**, *68*, 5977−5982.
(29) Knight, A.; Hemmings, J. L.; Winfield, I.; Leuenberger, M.; Frattini, E.; Frenguelli, B. G.; Dowell, S. J.; Lochner, M.; Ladds, G. Discovery of Novel Adenosine Receptor Agonists That Exhibit Subtype Selectivity. *J. Med. Chem.* **2016**, *59*, 947−964.
(30) Stoddart, L. A.; Vernall, A. J.; Denman, J. L.; Briddon, S. J.; Kellam, B.; Hill, S. J. Fragment Screening at Adenosine-A3 Receptors in Living Cells Using a Fluorescence-Based Binding Assay. *Chem. Biol.* **2012**, *19*, 1105−1115.
(31) Eldridge, M. D.; Murray, C. W.; Auton, T. R.; Paolini, G. V.; Mee, R. P. Empirical Scoring Functions: I. The Development of a Fast Empirical Scoring Function to Estimate the Binding Affinity of Ligands in Receptor Complexes. *J. Comput. Aided. Mol. Des.* **1997**, *11*, 425−445.
(32) Hornak, V.; Abel, R.; Okur, A.; Strockbine, B.; Roitberg, A.; Simmerling, C. Comparison of Multiple Amber Force Fields and Development of Improved Protein Backbone Parameters. *Proteins Struct. Funct. Genet.* **2006**, *65*, 712−725.
(33) Massova, I.; Kollman, P. A. Combined molecular mechanical and continuum solvent approach (MM-PBSA/GBSA) to predict ligand binding. *Per. Drug Discovery Design* **2000**, *18*, 113−135.
(34) Wang, E.; Sun, H.; Wang, J.; Wang, Z.; Liu, H.; Zhang, J. Z. H.; Hou, T. End-Point Binding Free Energy Calculation with MM/PBSA and MM/GBSA: Strategies and Applications in Drug Design. *Chem. Rev.* **2019**, *119*, 9478−9508.
(35) Kaminski, G.; Friesner, R. A.; Tirado-Rives, J.; Jorgensen, W. L. Evaluation and Reparametrization of the OPLS-AA Force Field for Proteins via Comparison with Accurate Quantum Chemical Calculations on Peptides. *Phys. Chem. B* **2001**, *105* (28), 6474−6487.
(36) Shivakumar, D.; Williams, J.; Wu, Y.; Damm, W.; Shelley, J.; Sherman, W. Prediction of Absolute Solvation Free Energies using Molecular Dynamics Free Energy Perturbation and the OPLS Force Field. *J. Chem. Theory Comput.* **2010**, *6*, 1509−19.
(37) Stamatis, D.; Lagarias, P.; Barkan, K.; Vrontaki, E.; Ladds, G.; Kolocouris, A. Structural Characterization of Agonist Binding to an A3 Adenosine Receptor through Biomolecular Simulations and Mutagenesis Experiments. *J. Med. Chem.* **2019**, *62*, 8831−8846.

https://doi.org/10.1021/acsmedchemlett.2c00052
ACS Med. Chem. Lett. XXXX, XXX, XXX−XXX